A NETWORK PROBE FOR THE MODE ANALYSIS OF PLANAR ANTENNAS

A thesis submitted to the Faculty of Science
of the University of London for the degree
of Doctor of Philosophy

by

Jonathan WHITEHURST
BSc. (London)

Department of Physics
Royal Holloway and Bedford New College

April 1988

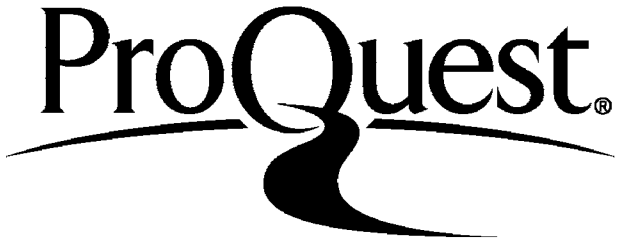

ABSTRACT

The current trend towards total circuit integration where the antenna, R.F., and baseband circuitry are incorporated on a single substrate precludes the use of measurement systems such as the network analyser since there are no suitable R.F. input or output ports.

This investigation has addressed the problem of performing "in-situ" circuit measurements on millimetre wave printed circuits using a small, capacitively coupled probe. The technique is applicable to any "open" printed circuit geometry, and does not require any physical connection to the circuit under test.

A computer controlled measurement system is described which allows either the mode of excitation of a circuit element to be determined from the $|E_z|^2$ distribution on its top surface, or else perform circuit measurements on individual elements using a technique analogous to the waveguide slotted line.

The suitability of various probe geometries for this purpose is assessed, and sources of measurement error inherent in the probe designs employed are described.

Emphasis has been placed on the characterization of integrated antenna elements and their associated feed network. Examples pertaining to microstrip patch antennas, the coplanar strip vee, and the tapered slotline antenna are presented.

CONTENTS

ABSTRACT 2

CONTENTS 3

CHAPTER (1) Introduction

1.1 Survey of Millimetre Wave Systems 23

1.2 Transmission Lines for Millimetre Wavelengths 26

1.3 Integrated Circuit Measurement Techniques 33

CHAPTER (2) The Mechanical Design and Computer Control of the Scanning Network Probe

2.1 Introduction 36

2.2 Mechanical Aspects of the Scanning Network Probe 36

2.3 The Computer Management System Part 1: Electronic Support Hardware 38

2.4 The Computer Management System Part 2: The Control Computer and Peripheral Support 41

2.5 The Computer Management System Part 3: The Management Software 42

2.5.1 Antenna Polar Pattern measurement 45

2.5.2 Linear Line Scan VSWR Measurements 47

2.5.3 Area Scan Measurements 52

2.6 Graphics Support Software 53

2.7 System Errors 54

CHAPTER (3) R.F. Probes and Detection Techniques

3.1 R.F. Probe Design 60

3.1.1 Introduction 60

3.1.2 Coplanar Strip Line Probes 63

3.1.3 The Coaxial Monopole Probe 73

3.1.4 Magnetic Field Probes 103

3.1.5 Electric Dipole Probes 105

3.2 R.F. Signal Detection Techniques 107

3.2.1 Introduction 107

3.2.2 Amplitude Only Detectors 108

3.2.3 Homodyne Detector Systems 115

CHAPTER (4) Investigation of Printed Microstrip Antennas Using the Scanning Network Probe

4.1 The End–Fed Microstrip Patch Antenna 121

4.1.1 Theoretical Aspects of the Rectangular Patch Antenna 121

4.1.2 Rectangular Patch Design and Manufacture 128

4.1.3 Initial Measurements 129

4.1.4 Scanning Network Probe Measurements 133

4.1.5 Comments on the Scanning Network Probe Results 139

4.2 The Triangular Patch Antenna 146

4.2.1 Theoretical Aspects of the Triangular Patch Antenna 146

4.2.2 Triangular Patch Design and Fabrication 149

4.2.3 Scanning Network Probe Measurements 156

4.2.4 Comments on the Triangular Resonator Investigation 167

4.3 The Edge–Fed Microstrip Disk Antenna 168

4.3.1 Theoretical Aspects of the Microstrip Disk 168

4.3.2 Microstrip Disk Design and Fabrication 171

4.3.3 Scanning Network Probe Measurements 177

4.4 The Microstrip Annular Disk Antenna 186

4.4.1 Design and Manufacture 186

4.4.2 Scanning Network Probe Measurements 188

4.5 Concluding Remarks 193

CHAPTER (5) The Printed Vee and Tapered Slot Antenna

5.1 Introduction 194

5.2 Vee Antenna Design Equations 196

5.3 Integrated Vee Detector and Mixer Module Design for Quasi–Optic Systems 202

5.4 Scanning Network Probe Investigation of a Two Wavelength Vee Antenna 224

5.5 A Brief Investigation of Tapered Slot Excitation Modes Using the Scanning Network Probe 230

CHAPTER (6) Printed Transmission Line Measurements Using the Scanning Network Probe

6.1 Theory of Reflections on Transmission Lines 235

6.2 The Principles of VSWR Measurements on Printed Transmission Lines using the Scanning Network Probe 240

6.3 VSWR Measurements on Printed Microstrip Using the Scanning Network Probe 250

6.3.1 Initial Investigation of Printed Microstrip 250

6.3.2 The Investigation of Microstrip Open Circuits 263

6.4 VSWR Measurements on Coplanar Strip Transmission Lines 271

CHAPTER (7) Microstrip Antenna Array Diagnostics

7.1 Introduction 286

7.2 A Linear 4–Element Rectangular Patch Array 286

7.2.1 Theoretical Design Considerations 286

7.2.2 4–Element Linear Array Performance 292

7.3 A 2×2 Element Rectangular Patch Array 304

7.3.1 Design Philosophy 304

7.3.2 Measurements on the 2×2 Patch Array 306

7.4 A Four Element Patch Array for Circularly Polarized Applications 313

7.4.1 Design Considerations 313

7.4.2 Array Measurements 314

7.5 Parasitic Coupling Between Close Spaced Rectangular Patch Antennas 323

7.6 Summary 324

CHAPTER (8) Conclusions and Future Areas of Research

8.1 Conclusions 331

8.2 Future Exploitation of the Scanning Network Probe System 335

REFERENCES 354

ACKNOWLEDGEMENTS 361

APPENDIX (1)

A.1 Scanning Network Probe Software 363

A.2 Antenna Design Software 396

LIST OF FIGURES

CHAPTER (1)

1.1 Average atmospheric absorbtion of millimetre waves 25

1.2 Transmission lines for millimetre wavelengths 29

1.3 The De Rhonde 4–port coupler 31

1.4 Some common dielectric waveguides 33

CHAPTER (2)

2.1 Schematic diagram of the scanning network probe hardware 39

2.2 The scanning network probe computer management hardware 40

2.3 Antenna radiation pattern measurement 46

2.4 Antenna radiation pattern measurement algorithm 48

2.5 The linear line scan algorithm 50

2.6 Typical experimental set up for the measurement of VSWR on microstrip circuits 51

2.7 Positional error against cross slide speed 55

2.8 Positional error as a function of scan increment 55

2.9 Theoretical TM_{11} $|E_z|^2$ distribution in a triangular patch 57

2.10 Theoretical TM_{11} $|E_z|^2$ distribution in a circular patch 58

CHAPTER (3)

3.1 The asymmetric loop probe 62

3.2 The coplanar strip probe 62

3.3 The eccosorb screening for the CPS probe 64

3.4 The coplanar strip probe measurement principle 64

3.5 Experimental arrangement for the CPS probe tests 68

3.6 Measured voltage standing wave on a CPS transmission line using a probe to substrate separation of 50 μm 70

3.7 Measured voltage standing wave on a CPS transmission line using a probe to substrate separation of 100 μm 71

3.8 Measured voltage standing wave on a CPS transmission line using a probe to substrate separation of 150 μm 72

3.9 The coaxial monopole probe 75

3.10 The evaluation of the probe output voltage 75

3.11 The effect of a bent probe monopole 77

3.12 Circuital *emf*s due to a transverse magnetic field 77

3.13a Amplitude error against frequency, $\epsilon_e = 1.7$ 81

3.13b Phase Error against frequency, $\epsilon_e = 1.7$ 81

3.13c Amplitude error against frequency, $\epsilon_e = 5.7$ 82

3.13d Phase error against frequency, $\epsilon_e = 5.7$ 82

3.14a Amplitude variation along an open circuit TEM transmission line 85

3.14b Phase variation along an open circuit TEM transmission line 85

3.15 Phasor diagrams illustrating the abrupt voltage phase change at a voltage minimum 86

3.16 Probe circuital *emf*s at a current standing wave minimum 86

3.17 Probe circuital *emf*s at an arbitary position in a current standing wave 88

3.18 Phasor representation of ξ_M and ξ_E 88

3.19a Amplitude error against frequency, $\epsilon_e = 1.7$ 93

3.19b Phase error against frequency, $\epsilon_e = 1.7$ 93

3.19c Amplitude error against frequency, $\epsilon_e = 5.7$ 94

3.19d Phase error against frequency, $\epsilon_e = 5.7$ 94

3.20 Q-band coaxial probe construction 96

3.21 The open circuit edge effect 100

3.22 Measured open circuit edge effect with the coaxial probes 100

3.23 The 0.3 *mm* diameter coaxial probe construction 101

3.24 The balanced loop probe 104

3.25 The measurement of an elliptically polarized B field 104

3.26 Q-band magnetic field schematic diagram 106

3.27 Balanced detector configuration 106

3.28 Typical high sensitivity detector design 109

3.29 Wide bandwidth detector configuration 109

3.30 Silicon point contact diode detector response 113

3.31 Calibration of diode response 113

3.32 Extended range lock-in voltmeter 114

3.33 The essential components of a superheterodyne detector 114

3.34 The basic homodyne detector 116

3.35 Phasor diagram illustrating the detection process 116

3.36 Proposed R.F. phase discriminator design 118

CHAPTER (4)

4.1 The rectangular patch equivalent circuit 122

4.2 Equivalent cavity representation of the rectangular microstrip patch 127

4.3 Low order rectangular patch modes 127

4.4 Patch and feed line outline 130

4.5 Measured rectangular patch return loss 132

4.6 Theoretical rectangular patch return loss 132

4.7 Rectangular patch excited below resonance, F=27.5 *GHz* 134

4.8 Rectangular patch excited just below resonance, F=30.1 *GHz* 136

4.9 Rectangular patch excited at resonance, F=30.6 *GHz* 137

4.10 Rectangular patch excited just above resonance, F=31.2 *GHz* 138

4.11 Rectangular patch excited above resonance, F=35.0 *GHz* 140

4.12 First minimum shift against frequency 142

4.13 Fringe field amplitude against frequency 142

4.14 Rectangular patch excitation, open substrate 143

4.15 Rectangular patch excitation, swam edged 144

4.16 Rectangular patch excitation, copper edged 145

4.17 The equilateral triangle patch radiator 147

4.18 $F_r.a$ product against radius r 147

4.19 Theoretical $|E_z|^2$ for the TM_{01} mode 151

4.20 Theoretical $|E_z|^2$ for the TM_{11} mode 152

4.21 Theoretical $|E_z|^2$ for the TM_{02} mode 153

4.22 Theoretical $|E_z|^2$ for the TM_{12} mode 154

4.23 Theoretical $|E_z|^2$ for the TM_{22} mode 155

4.24 Experimental $|E_z|^2$ for the TM_{01} mode, F=35.0 GHz 157

4.25 Cross–section of Figure (4.24) along feed axis 158

4.26 Triangle test point locations 158

4.27 Experimental $|E_z|^2$ for the TM_{11} mode, F=34.0 GHz 160

4.28 Experimental $|E_z|^2$ for the TM_{02} mode, F=35.1 GHz 161

4.29 Experimental $|E_z|^2$ for the TM_{12} mode, F=35.0 GHz 162

4.30 Experimental $|E_z|^2$ for the TM_{22} mode, F=34.4 GHz 163

4.31 Cross–section of Figure (4.27) along feed axis 164

4.32 Microstrip disk antenna geometry 169

4.33 Theoretical $|E_z|^2$ for the TM_{11} mode 172

4.34 Theoretical $|E_z|^2$ for the TM_{21} mode 173

4.35 Theoretical $|E_z|^2$ for the TM_{02} mode 174

4.36 Theoretical $|E_z|^2$ for the TM_{31} mode 175

4.37 Experimental $|E_z|^2$ for the TM_{11} mode, F=35.8 GHz 178

4.38 Experimental $|E_z|^2$ for the TM_{21} mode, F=35.5 GHz 179

4.39 Experimental $|E_z|^2$ for the TM_{02} mode, F=34.8 GHz 180

4.40 Experimental $|E_z|^2$ for the TM_{31} mode, F=35.5 GHz 181

4.41 Cross–section of experimental TM_{02} data along feed axis 183

4.42 Cross–section of experimental TM_{11} data along feed axis 183

4.43 Cross–section of experimental TM_{21} data along feed axis 184

4.44 The microstrip ring geometry 184

4.45 Experimental $|E_z|^2$ for the TM_{11} mode, F=35.0 *GHz* 190

4.46 Experimental $|E_z|^2$ for the TM_{21} mode, F=34.5 *GHz* 191

4.47 Experimental $|E_z|^2$ for the TM_{31} mode, F=33.5 *GHz* 192

CHAPTER (5)

5.1

(a) The printed vee geometry 195

(b) The tapered slot geometry 195

5.2 The equivalent wire vee geometry 198

5.3 The parallel coplanar strip geometry 198

5.4 The general form of the integrated vee–detector modeule 201

5.5 The vee antenna mounting arrangement 201

5.6

(a) $14.4\,\lambda_{220}$ vee antenna co–polar E–plane radiation pattern, F=221 *GHz* 205

(b) $14.4\,\lambda_{220}$ vee antenna co–polar H–plane radiation pattern, F=221 *GHz* 205

(c) $14.4\,\lambda_{220}$ vee antenna cross–polar E and H–plane radiation pattern, F=221 *GHz* 206

5.7 Cross–polar radiation sources at the vee aperture 206

5.8

(a) $14.4\,\lambda_{220}$ vee antenna co–polar E–plane radiation pattern, F=95 *GHz* 208

(b) 14.4 λ_{220} vee antenna co–polar H–plane radiation pattern, F=95 *GHz* 208

(c) 14.4 λ_{220} vee antenna cross–polar E and H–plane radiation pattern, F=95 *GHz* 209

5.9

(a) 14.4 λ_{220} vee antenna co–polar E–plane radiation pattern, F=33 *GHz* 209

(b) 14.4 λ_{220} vee antenna co–polar H–plane radiation pattern, F=33 *GHz* 210

(c) 14.4 λ_{220} vee antenna cross–polar E and H–plane radiation pattern, F=33 *GHz* 210

5.10 Radiation pattern distortion caused by R.F. coupling to the bias lines 212

5.11

(a) 2.0 λ_{220} vee antenna co–polar E–plane radiation pattern, F=221 *GHz* 212

(b) 2.0 λ_{220} vee antenna co–polar E–plane radiation pattern, F=237 *GHz* 213

(c) 2.0 λ_{220} vee antenna co–polar E–plane radiation pattern, F=240 *GHz* 213

(d) 2.0 λ_{220} vee antenna co–polar E–plane radiation pattern, F=245 *GHz* 214

(e) 2.0 λ_{220} vee antenna co–polar E–plane radiation pattern, F=250 *GHz* 214

(f) 2.0 λ_{220} vee antenna co–polar E–plane radiation pattern, F=255 *GHz* 215

5.12 2.0 λ_{220} vee antenna cross–polar E–plane radiation pattern, F=221 *GHz* 215

5.13

(a) $3.0\,\lambda_{220}$ vee antenna co-polar E-plane radiation pattern, F=221 *GHz* 216

(b) $3.0\,\lambda_{220}$ vee antenna co-polar H-plane radiation pattern, F=221 *GHz* 216

5.14 Beam lead diode equivalent circuit 221

5.15 Vee detector equivalent circuit 221

5.16 Proposed vee design employing a shunt mounted detector 223

5.17 Experimental arrangement for exciting the vee antenna 225

5.18 $|E_z|^2$ distribution measured on a $2\,\lambda_0$ vee antenna, F=34.6 *GHz* 226

5.19 Peak signal level against vee-to-lens separation 226

5.20

(a) $|E_z|^2$ distribution on a single vee element, short circuit load, F=34.1 *GHz* 227

(b) $|E_z|^2$ distribution on a single vee element, matched load, F=34.1 *GHz* 228

5.21 Revised radiation pattern calculation 229

5.22

(a) $|E_z|^2$ distribution on one half of a tapered slot antenna, short circuit load, F=34.1 *GHz* 232

(b) $|E_z|^2$ distribution on one half of a tapered slot antenna, matched load, F=34.1 *GHz* 233

CHAPTER (6)

6.1 Reflection on a transmission line due to an arbitrary load Z_L 236

6.2 Voltage standing waves on a lossless transmission line 241

6.3 Voltage standing waves on a lossy transmission line 241

6.4 Practical realization of a waveguide slotted line 241

6.5 Systematic errors introduced by the misalignment of the transmission line and scan axes

(a) example of lateral run–out 243

(b) example of vertical run–out 243

6.6 Flow graph representation of the probe coupling to the transmission line

(a) Flow graph of complete circuit 246

(b) Flow graph reduced to find incident voltage 246

(c) Flow graph reduced to find reflected voltage 246

6.7 The distortion of a voltage maximum produced by capacative loading 246

6.8 Voltage standing wave pattern near a minimum 248

6.9 Voltage standing wave pattern near a voltage minimum when V_{min} is below the detector noise floor 248

6.10 Experimental set up to compare VSWR measurements made using a slotted line and the scanning network probe 251

6.11

(a) Wave diagram showing the forward and reflected waves at the transition plane 251

(b) Phasor diagram showing the forward and reflected waves at the transition plane 251

6.12 Experimental set up for the initial microstrip line investigation 254

6.13

(a) Probe response transverse to the axis of the microstrip 255

(b) Probe response as a function of probe to substrate separation 255

6.14 Two port test piece measured return loss

(a) Into port (1) 257

(b) Into port (2) 257

6.15 Power standing wave plot measured on the two port test piece

(a) Waveguide short circuit set to zero 259

(b) Waveguide short circuit shifted by $\lambda_g/4$ 259

6.16

(a) Power standing wave plot, port (2) unmatched, input unmatched 261

(b) Power standing wave plot, port (2) matched, input unmatched 261

(c) Power standing wave plot, port (2) matched, input unmatched, SWAM covers on transitions 262

6.17 Power standing wave plot, port (2) matched, input matched, SWAM covers on transitions 262

6.18

(a) General microstrip open circuit test piece 265

(b) Waveguide to microstrip transition detail 266

6.19 Typical open circuit microstrip line scan measurements

(a) 105 Ω, F=36.5 *GHz* 268

(b) 78 Ω, F=36.5 *GHz* 268

(c) 50 Ω, F=36.5 *GHz* 269

(d) 40 Ω, F=36.5 *GHz* 269

(e) 30 Ω, F=36.5 *GHz* 270

(f) 22 Ω, F=36.5 *GHz* 270

6.20 Measured variation of λ_g with frequency 272

6.21 Measured variation of Δ_l/h with frequency 272

6.22 Theoretical variation of Δ_l/h with frequency[6.8] 273

6.23 Method employed to energize C.P.S. transmission lines for the scanning network probe measurements 274

6.24 Variation of the detected signal with probe to substrate separation 276

6.25 Variation of the probe signal transverse to the axis of the C.P.S. transmisssion line 276

6.26 Power standing wave plots illustrating stub matching in a 200 Ω transmission line 277

6.27 Details of the shunt stub construction 278

6.28 Power standing plot of a matched C.P.S. transmission line 280

6.29 Matched load construction 281

6.30 Vee rectenna design 281

6.31 Power standing wave measured on the passive vee rectenna 282

6.32 Power standing wave measured on a short circuit C.P.S. transmission line, $\epsilon_r = 9.4$

CHAPTER (7)

7.1 A linear point source array 287

7.2 4–element patch array outline 287

7.3 4–element linear array return loss 293

7.4 4–element linear array radiation pattern, F=33.8 *GHz*

(a) E–plane 294

(b) H–plane 294

7.5 4–element linear array radiation pattern, F=37.8 *GHz*

(a) E–plane 295

(b) H–plane 295

7.6 Radiation pattern distortion caused by direct coupling to the waveguide aperture 297

7.7 Measured $|E_z|^2$ distribution on the linear array, F=33.8 *GHz* 299

7.8 Array element excitation detail

(a) Left hand pair of elements 300

(b) Right hand pair of elements 300

7.9 Cross–sections of the inner pair of elements taken along the axis of the microstrip feed

(a) inner left hand element 301

(b) inner right hand element 301

7.10 Measured $|E_z|^2$ distribution on the linear array, F=37.8 *GHz* 303

7.11 2×2 patch array outline 305

7.12 2×2 patch array return loss 305

7.13 2×2 patch array radiation pattern at 35.8 *GHz*

(a) E–plane 307

(b) H–plane 307

7.14 Measured $|E_z|^2$ distribution on the 2×2 patch array, F=32.4 *GHz* 308

7.15 Measured $|E_z|^2$ distribution on the 2×2 patch array, F=35.6 *GHz* 309

7.16 Measured $|E_z|^2$ distribution on the 2×2 patch array, F=38.3 *GHz* 310

7.17 Measured $|E_z|^2$ distribution on the 2×2 patch array, F=36.8 *GHz* 311

7.18 C.P. array outline 315

7.19 C.P. array return loss 315

7.20 Measured $|E_z|^2$ distribution on the C.P. array, F=28.9 *GHz* 316

7.21 Measured $|E_z|^2$ distribution on the C.P. array, F=31.8 *GHz* 317

7.22 Measured $|E_z|^2$ distribution on the C.P. array, F=34.9 *GHz* 318

7.23 Measured $|E_z|^2$ distribution on the C.P. array, F=39.8 *GHz* 319

7.24 Measured $|E_z|^2$ distribution on the C.P. array, F=35.9 *GHz* 321

7.25 Measured C.P. array radiation pattern, F=35.9 *GHz*

(a) In the plane parallel to the principal microstrip feed 322

(b) In the plane perpendicular to the principal microstrip feed 322

7.26 Parasitic patch layout 325

7.27 Variation of parasite excitation with patch–parasite separation 325

7.28 The 90° hybrid coupler 326

7.29 Measured $|E_z|^2$ distribution on the monopulse array, F=34.9 *GHz* 327

CHAPTER (8)

8.1 Idealized result of a sliding load calibration 333

8.2 Equivalent circuit of a microstrip transmission line and probe 333

8.3 Microstrip sliding load construction 335

8.4 Sliding load calibration example

(a) Measured voltage standing wave, load position # 1 335

(b) Measured voltage standing wave, load position # 2 336

(c) Residual voltage standing wave 336

8.5 Measured $|E_z|^2$ distributions on microstrip transmission lines

(a) 78 Ω, F=34.5 *GHz* 339

(b) 50 Ω, F=34.5 *GHz* 340

(c) 40 Ω, F=34.5 *GHz* 341

(d) 30 Ω, F=34.5 *GHz* 342

(e) 22 Ω, F=34.5 *GHz* 343

8.6 Pentagonal patch return loss 345

8.7 Measured $|E_z|^2$ distribution on the pentagonal patch, F=29.5 *GHz* 347

8.8 E–field sources for the pentagonal patch linearly polarized mode 345

8.9 Pentagonal patch radiation pattern, F=29.5 *GHz*

(a) E–plane 349

(b) H–plane 349

8.10 Measured $|E_z|^2$ distribution on the pentagonal patch, F=30.35 *GHz* 351

8.11 Pentagonal patch radiation pattern, F=30.35 *GHz*

(a) In the plane parallel to the microstrip feed 352

(b) In the plane perpendicular to the microstrip feed 352

LIST OF PHOTOGRAPHIC PLATES

CHAPTER (2)

2.1 The scanning network probe system 37

2.2 The scanning network probe translator 43

CHAPTER (3)

3.1 Test circuit for evaluating the coplanar strip probe performance 65

3.2 The Q–band 0.5 *mm* coaxial probe 97

CHAPTER (4)

4.1 The completed rectangular patch antenna 131

4.2 The completed triangular patch antennas 150

4.3 The completed circular patch antennas 176

4.4 The completed annular disk antennas 189

CHAPTER (5)

5.1 The $3\,\lambda_{220}$ vee detector 217

CHAPTER (7)

7.1 The corporately fed rectangular patch arrays 330

CHAPTER (8)

8.1 The pentagonal patch antenna 344

LIST OF TABLES

CHAPTER (2)

2.1 Scanning Network Probe Driver Procedures 44

CHAPTER (3)

3.1 The Electrical Properties of Some Common Metals 98

3.2 The Comparison of Probe Performance at 35 *GHz* 102

CHAPTER (4)

4.1 Principal Resonant Mode Characteristics 149

4.2 TM_{01} Triangular Resonator Test Point Data 159

4.3 TM_{11} Triangular Resonator Test Point Data 165

4.4 TM_{02} Triangular Resonator Test Point Data 165

4.5 TM_{12} Triangular Resonator Test Point Data 166

4.6 TM_{22} Triangular Resonator Test Point Data 166

4.7 Roots of $J_n'(ka) = 0$ 170

4.8 Microstrip Disk Dimensions and Performance 177

4.9 The Relative Excitation and Angular Position of the Disk Resonator Nodes 182

4.10 Comparison of Scalar Network Analyser and Scanning Network Probe Return Loss Measurements on the Microstrip Disk Resonators 185

4.11 Microstrip Ring Design and Performance Data 188

4.12 The Relative Excitation and Angular Position of the Annular Resonator Nodes 193

CHAPTER (6)

6.1 Microstrip Open Circuit Design Data 264

CHAPTER (7)

7.1 Linear Array Performance Summary 292

7.2 C.P. Array Radiation Pattern Results 323

CHAPTER (8)

8.1 Residual VSWR as a Function of Probe–to–Substrate Separation 337

CHAPTER 1

Introduction

1.1 Survey of Millimetre Wave Systems

The term "millimetre waves" is generally used to describe the region of the electromagnetic spectrum between approximately 30 *GHz* and 300 *GHz*. The millimetre wave bands lie between the microwave and infrared regions, and consequently possess characteristics that are intermediate between the two regions. Millimetre waves are characterized by short wavelength, typically $10mm$–$1mm$, thus reducing component size. The reduced component size allows the construction of very compact and lightweight systems compared to an equivalent microwave system. In the case of antennas, an important factor is the degree of miniaturization that can be achieved; very narrow beamwidths can be obtained with physically small antennas by resorting to high operating frequencies. The obvious application for small narrow beamwidth antennas is in miniature radar systems for precision guided weapons. A 95 *GHz* seeker has been succesfully demonstrated[1.1] which used a 5.8 inch diameter reflector antenna with a beamwidth of 1.5 degrees. The same reference cites the future development of still smaller guidance systems for precision guided submunitions. A further advantage of narrow beamwidth antennas is that high resolution radar systems with the ability to track targets at very low elevation angles can be constucted.[1.2] Narrow beamwidth combined with sidelobe levels is also important for communications purposes where covertness and immunity to hostile electronic counter measures (ECM) are required.[1.3] Figure (1.1) shows the calculated atmospheric absorption over the centimetric and millimetric wavelengths. The principal transmission windows are at 35 *GHz*, 94 *GHz*, 140 *GHz*, and 220 *GHz*. These windows are very wide, possessing bandwidths of 16 *GHz*, 23 *GHz*, 26 *GHz*, and 70 *GHz* respectively. Such large bandwidths allow the use of very high speed data transmission, frequency diversity and spread spectrum communication systems. The high attenuation absorption windows at 60 *GHz*, 119 *GHz*, and 183 *GHz*, are of comparable width to the transmission windows and permit very secure short range communication with a low probability of intercept and high immunity to jamming. A good example of the exploitation of atmospheric attenuation is the american joint services satallite communication program "MILSTAR". MILSTAR uses uplink and downlink frequencies in the 35 *GHz* low attenuation window whilst the inter–satallite message

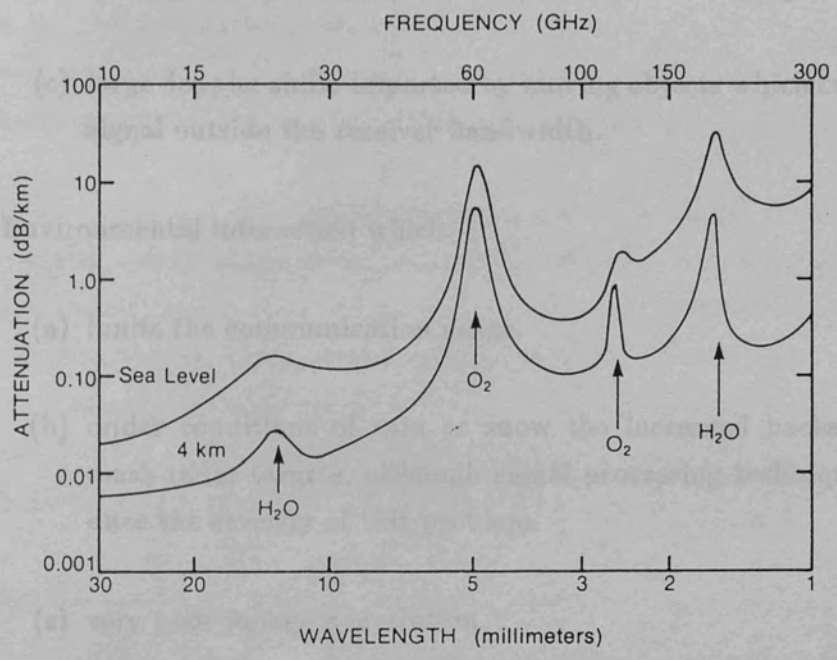

Figure (1.1) Average atmospheric absorption of millimetre waves[1.3]

routing is carried out at approximately 60 *GHz*. The use of 60 *GHz* for the inter–satallite communication ensures jamming of the inter–satallite link by an earth station is made virtually impossible.[1.4] The exploitation of the millimetre bands is not totally straightforward. The problems can be summarized as follows:

(1) The short wavelength results in:

   (a) small component sizes which require close tolerance manufacture.

   (b) small reception cross–section of a single antenna element, thus requiring the use of arrays or lens/reflector antenna systems.

   (c) large doppler shifts imparted by moving objects which can take the signal outside the receiver bandwidth.

(2) Environmental interaction which:

   (a) limits the communication range.

   (b) under conditions of rain or snow the increased backscatter can mask radar targets, although signal processing techniques can reduce the severity of this problem.

   (c) very poor foliage penetration.

(3) Technological difficulties:

   (a) the lack of high power solid state sources has hindered the development of highly miniaturized millimetre wave systems.

   (b) the shortage of accurate theoretical models for millimetre wave transmission lines and transmission line discontinuities makes circuit design difficult.

(4) Competition with mature technologies:

   (a) infrared and optical systems.

   (b) microwave systems.

Despite the above problems, millimetre waves are finding new applications in telecommunications and radar systems in addition to the well established areas such as plasma diagnostics and millimetre wave astronomy.

Numerical techniques and the advent of fast computers has enabled the solution of transmission line geometries and discontinuities which have proved insoluble by analytic methods. The recent introduction of commercial indium phosphide oscillators and amplifiers operating at millimetric wavelengths now provides the system designer with high power reliable solid state sources and power amplifiers. These two factors combined with the current military for total capability weapons systems has lead to a recent upsurge in millimetre wave component and systems design.[1.4]

1.2 Transmission Lines for Millimetre Wavelengths

The millimetre wave region occupies a unique position in the electromagnetic spectrum where beam mode and integrated optics guidance systems can be applied in addition to the low frequency microwave transmission techniques. Transmission line geometries used for millimetre wave circuits can be broadly categorized as follows:

(1) hollow metal waveguide

(2) printed circuit technology

(3) dielectric waveguides

(4) beam mode or quasi–optic techniques

Metal waveguide techniques find applications in high reliability systems up to 220 *GHz*. The manufacture of millimetric waveguide components is difficult and expensive due to the small size and the narrow tolerances that are placed on the dimensions and the surface finish. Metal waveguide components are invariably made by an electroforming technique which involves the electrolytic deposition of copper onto a precision former. In some instances such as waveguide tapers and pyramidal horns the mandrel can be removed and re–used, however for more complex structures such as couplers and corrugated waveguide components, the mandrel has to be dissolved away after electroforming. This makes the mass production of components by this technique highly uneconomic. The use of split block waveguide combined with a photolithographically produced

metal septum has been succesfully employed to manufacture cheap directional couplers.[1.5] The major disadvantage of waveguide as a millimetre wave transmission media is in the mechanical integration of semiconductor devices. The use of packaged devices, which is widespread at the lower microwave frequencies, is not straightforward in the millimetre wave region due to package parasitic problems. Devices such as mixer and detector diodes are often incorporated into waveguide sections known as "wafers",[1.7] but power devices are more generally obtained in a "micro–pill" package at the longer millimetric wavelengths. At short millimetric wavelengths the use of packaged devices becomes difficult due to the physical size of the package in relation to the waveguide dimensions. This necessitates the device being incorporated into the waveguide at chip level. The device integration problem combined with the demand for very small systems has led to an extensive study of photolithographically reproduced "printed circuit" geometries. Figure (1.2) shows some of the wide variety of printed circuit transmission lines that have been developed. Open microstrip has found widespread use at the lower microwave frequencies where the mode of propagation can be characterized with acceptable accuracy by static calculations; circuit design is therefore a relatively simple process. References(1.8) and (1.9) provide a useful bibliography and summary of equations for microstrip circuit design at low frequencies. Above 10 GHz the fundamental mode of propagation in microstrip becomes dispersive, and a full wave analysis is required in order to determine the microstrip propagation characteristics. In addition to the problem introduced by dispersion, the transmission line losses associated with microstrip are very high. The transmission line losses in microstrip can be attributed to:

(a) dielectric losses

(b) conductor losses due to the finite surface resistivity of the metal conductor

(c) radiation into free space and surface wave modes

Millimetre wave applications require the use of very low–loss substrate materials such as crystal quartz, although ptfe–glassfibre composites provide a cheaper alternative material for less demanding applications. The conductor losses depend not only on the intrinsic surface resistivity of the metal used, but also on the crystal structure and surface finish quality of the metallization. For example, it has been found[1.10] that rolled copper is a superior metallization to electrodeposited copper at a frequency of 90GHz. The circuit parasitic effects due to radiation and surface wave coupling become of increasing significance at

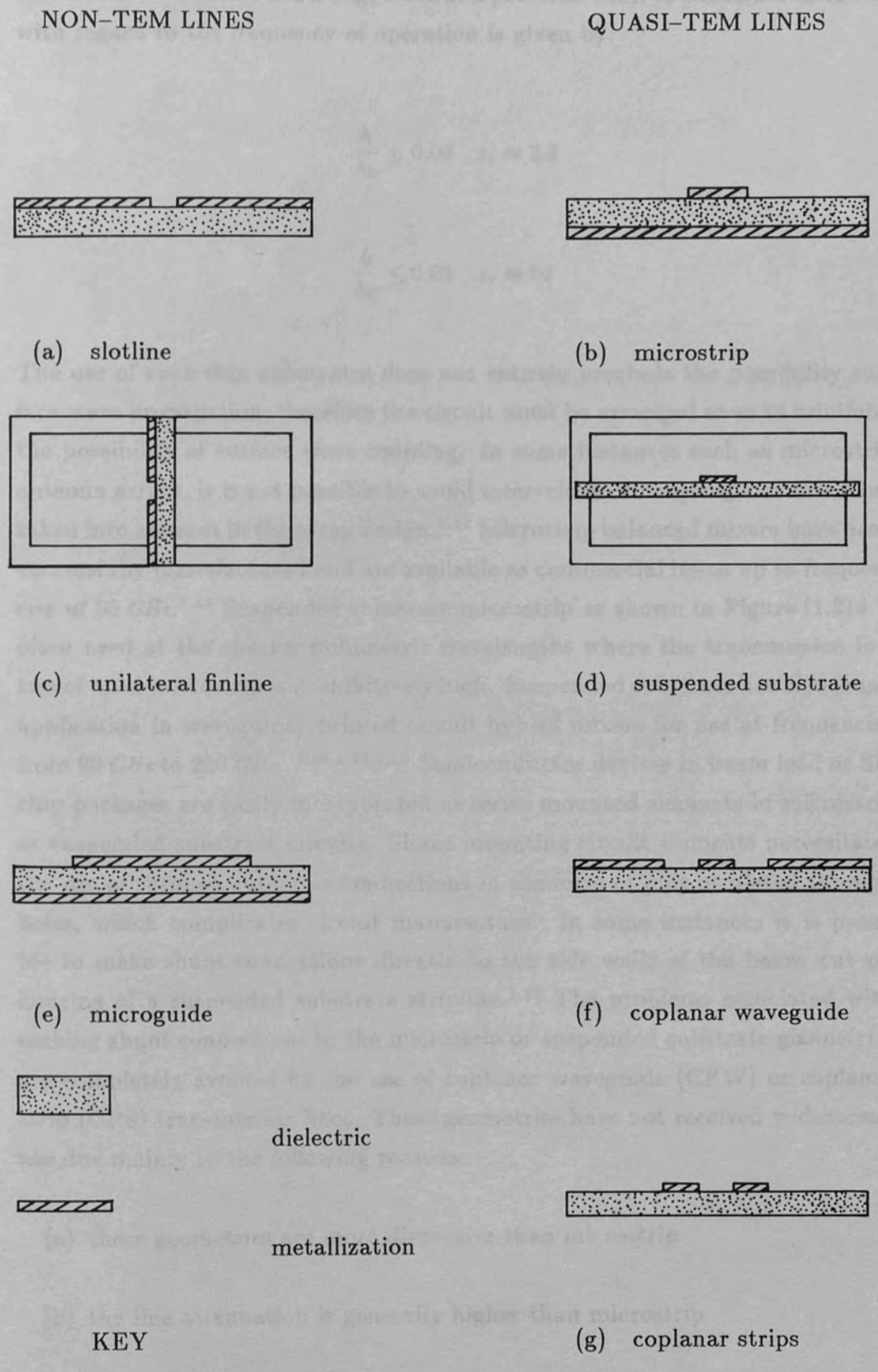

Figure (1.2) Transmission lines for millimetre wavelengths

millimetre wavelengths. A full wave treatment of the open circuit microstrip termination which includes surface wave effects has been given by James and Henderson.[1.11] Their results suggest that a practical limit to substrate thickness with regard to the frequency of operation is given by:

$$\frac{h}{\lambda_0} \leq 0.09 \quad \epsilon_r \approx 2.3$$

$$\frac{h}{\lambda_0} \leq 0.03 \quad \epsilon_r \approx 10$$

The use of such thin substrates does not entirely preclude the possibility surface wave propagation, therefore the circuit must be arranged so as to minimize the possibility of surface wave coupling. In some instances such as microstrip antenna arrays, it is not possible to avoid inter–element coupling and this must taken into account in the array design.[1.12] Microstrip balanced mixers have been successfully manufactured and are available as commercial items up to frequencies of 95 *GHz*.[1.13] Suspended substrate microstrip as shown in Figure (1.2)d is often used at the shorter millimetric wavelengths where the transmission line loss of open microstrip is prohibitively high. Suspended substrate has also found application in waveguide/ printed circuit hybrid mixers for use at frequencies from 90 *GHz* to 220 *GHz*. [1.14,1.15,1.16] Semiconductor devices in beam lead or flip chip packages are easily incorporated as series mounted elements in microstrip or suspended substrate circuits. Shunt mounting circuit elements necessitates the use of through substrate connections in the form of pins or plated through holes, which complicates circuit manufacture. In some instances it is possible to make shunt connections directly to the side walls of the below cut–off housing of a suspended substrate stripline.[1.17] The problems associated with making shunt connections in the microstrip or suspended substrate geometries are completely avoided by the use of coplanar waveguide (CPW) or coplanar strip (CPS) transmission lines. These geometries have not received widespread use due mainly to the following reasons:

(a) these geometries are more dispersive than microstrip

(b) the line attenuation is generally higher than microstrip

(c) the fringing fields are not localized to the substrate, (except when the substrate permittivity is high) thus requiring a large circuit enclosure.

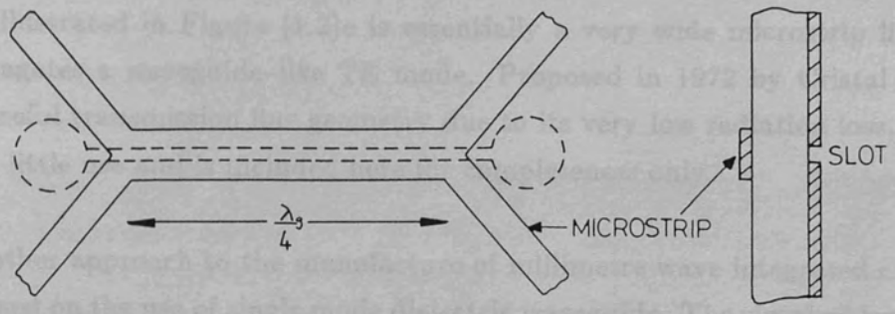

Figure (1.3) The De Rhonde 4–port coupler[1.8]

The slot transmission line shown in Figure (1.2)a was first proposed by Cohn in 1969[1.18] and is useful in situations where regions of elliptically polarized magnetic field are required, such as in the construction of non–reciprocal ferrite devices. Slotline has found extensive use in hybrid configurations such as the De Rhonde coupler shown in Figure (1.3). Chapter(7) of reference(1.8) highlights a number of novel circuit configurations using microstrip/slotline hybrid elements. A useful feature of slotline is the ease with which a slotline circuit can be combined with a high gain tapered slot antenna.[1.19,1.20] The finline geometry shown in Figure (1.2)c can be modelled as a printed equivalent of a ridged waveguide. Finline circuits can be designed with octave bandwidths, and with lower loss than equivalent open microstrip circuits.[1.21] In a similar manner to slotline, the finline geometry can be used with other printed circuit transmission lines to form hybrid circuits. High performance hybrid balanced mixer designs with very low local oscillator break–through have been demonstrated at Q–band[1.22] and W–band[1.23]. Finline has many attractive properties, but its use at frequencies above 220 *GHz* in fundamental mode waveguide is precluded by the physical size of the standard beamlead package. Finally, the microguide geomtry illustrated in Figure (1.2)e is essentially a very wide microstrip line that propagates a waveguide–like TE mode. Proposed in 1972 by Cristal et al[1.24] as useful transmission line geometry due to its very low radiation loss, it has found little use and is included here for completeness only.

Another approach to the manufacture of millimetre wave integrated circuits is based on the use of single mode dielectric waveguide. The simplest form of dielectric waveguide shown in Figure (1.4)a is unsuitable for general use due to the difficulty in providing mechanical support for the waveguide without causing unwanted radiation losses. The configurations that have received most attention[1.25,1.26,1.27,1.28] are shown in Figure (1.4)b and (1.4)c; These geomtries are known as image guide and insular guide respectively. The mechanical support for the waveguide is provided by the groundplane, however the finite conductivity of the groundplane metallization does result in an increased line attenuation compared with the simple dielectric waveguide geometry. Dielectric waveguides have three problems in common:

(a) the integration of semiconductor devices without causing spurious radiation

(b) the bias and low frequency signal lines have to be incorporated as additional circuit elements

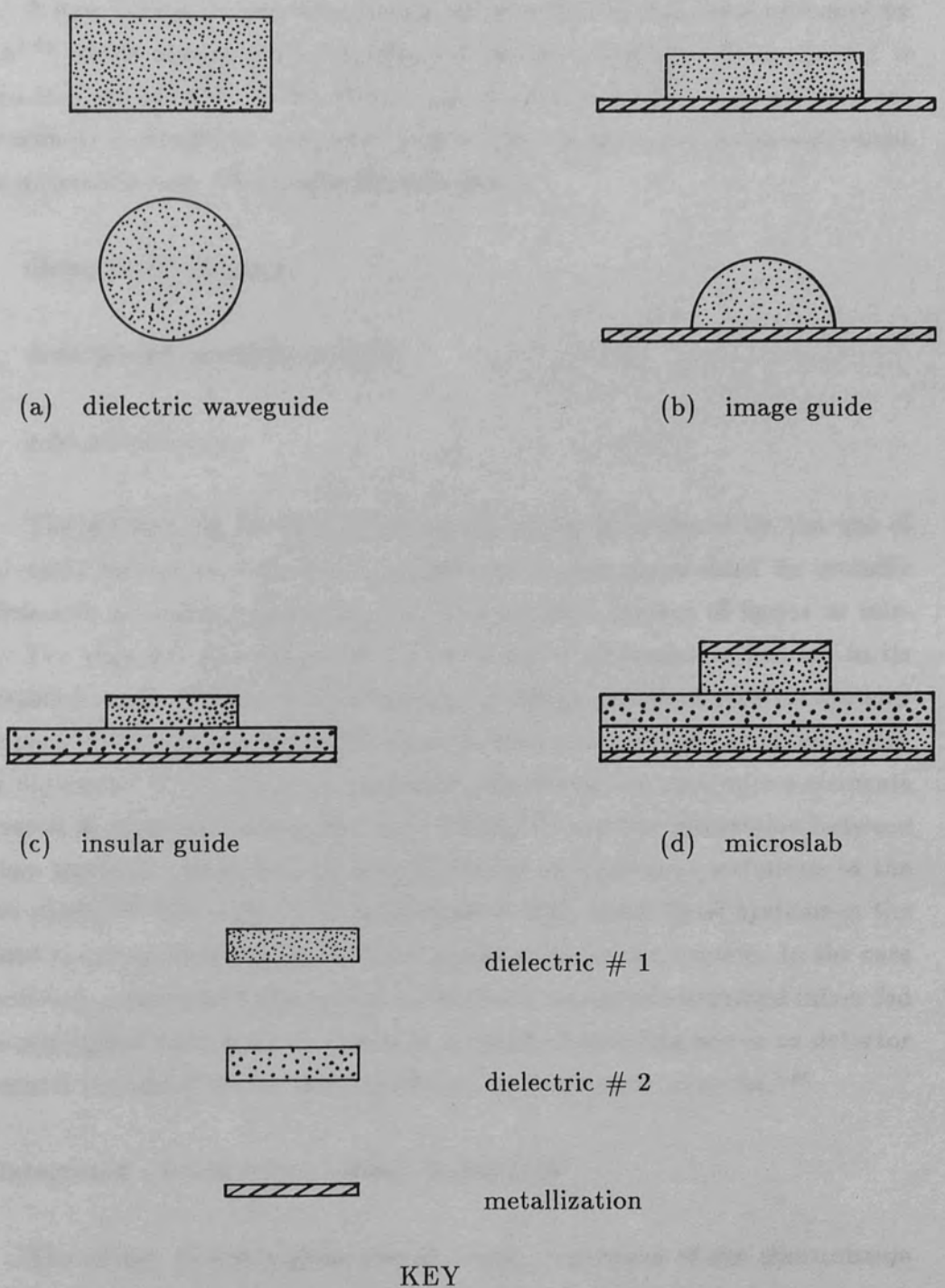

Figure (1.4) Some common dielectric waveguides

(c) circuit miniaturization is limited by the large radius bends in the dielectric waveguide that are required in order to reduce radiation loss at the bend.

A new hybrid transmission media called microslab has been proposed by Brian[1.28] which overcomes the problem of device coupling. The geometry is shown in Figure (1.4)d. Brian claims that the losses measured at 140 GHz are approximately .16 dB/cm compared with 1.2 dB/cm measured in an equivalent open microstrip line. The materials used were:

dielectric #1 =alumina

dielectric #2 =gallium arsenide

gold metallization

The ultimate in low loss transmission media is achieved by the use of quasi–optic techniques where the guided wave is not constrained by metallic or dielectric boundary conditions, but by a periodic system of lenses or mirrors. The very low loss nature of the quasi–optic transmission has led to its widespread use in millimetre wave astronomy. Many ingenious receiver systems have been developed which use frequency selective surfaces as signal/local osillator diplexers.[1.30,1.31] The wave propagation between the lens/mirror elements is treated as a series of gaussian beam modes,[1.32] and the interaction between the two gaussian beams can be determined by an analogous technique to the Smith chart.[1.33] The only problem associated with quasi–optic systems is the efficient coupling of power into and out of the transmission system. In the case of receivers, a common technique is to employ a waveguide mounted mixer fed by a corrugated conical horn. Another method of coupling power to detector systems is the use of multi–element printed antenna array systems.[1.34]

1.3 Integrated Circuit measurement Techniques

The ability to test a given circuit design, regardless of the transmission line technology employed, is clearly of importance. Vector and scalar network analysers using high frequency coaxial connectors are available up to 50 GHz, and waveguide systems are are available up to 140 GHz. A technique commonly used for waveguide systems is to develop and test each circuit element individually. However the integrated circuit engineer can only use such techniques as a first order design criterion because the integrated circuit elements often

perform in a different manner when combined on a single substrate due to parasitic coupling. As millimetre wave integrated circuit systems progress to greater levels of integration where, for example, the antenna is also fabricated on the same substrate as the R.F. circuitary, the need arises for a measurement system capable of:

(a) characterizing the performance of integrated circuit elements "in situ"

(b) performing antenna diagnostics

There appears to be only two previous accounts in the literature of attempts to perform measurements on "modern" printed transmission lines, these being due to Mao et al.[1.35], and Ladbroooke.[1.36] The work of Mao et al. includes no experimental technique or results for the probes mentioned, and does not appear to be a serious attempt to perform accurate circuit measurements.

In contrast the work of Ladbrooke is very complete, and describes a measurement technique based on a fixed probe beneath a microstrip line. The technique requires the fabrication of a purpose built circuit incorporating the probe and the circuit element element to be tested, therefore it is unsuited to the the task of general purpose circuit measurements on production MICs. The reference includes some data showing the variation of effective permittivity with frequency of an alumina based microstrip line over the frequency range 4 *GHz*–12 *GHz*, and a good treatment of measurement errors.

Towards the end of this research Schwarz and Turner[1.37] presented a balanced magnetic field probe using microbolometer detectors for the purpose of performing circuit measurements on coplanar waveguide. The paper is mostly concerned with the design and construction of the microbolometer detectors, and only very limited experimental work is presented. No discussion of potential measurement errors is given.

The chief aim of this research was to investigate the feasibility of performing such "in situ" measurements on millimetre wave integrated circuits by means of a non–contacting, scanning probe technique. Using very small electric or magnetic field probes, the quasi–stationary fields close $\leq \lambda_0/150$ to the surface of the transmission line are sampled on a regular mesh. The resulting amplitude data enables the either the voltage or current distributions in the transmission line or antenna to be observed. The technique utilizes a computer controlled probe translation mechanism which is capable of

positioning the probe with a small random error of $2\,\mu m$. The design requirements of the probe translator and the wide range of applications software developed are given in chapter(2). Chapter(3) describes the evolution of the probe designs and their relative merits; the detection techniques employed for the frequency ranges of interest are also described. Chapter(4) presents the results of an investigation of excitation modes in isolated microstrip antennas. Chapter(5) reviews the design of wide band printed vee antennas for use as quasi–optic detectors at $220\,GHz$. The results from a scanning network probe study of the vee and linearly tapered slot reception modes are given. The application of the scanning network probe to precision impedance measurements in planar printed transmission lines is described in chapter(6). This chapter considers the effect of the probe perturbation on the measured results, and presents experimental results from an investigation of microstrip open circuit transmission lines. Chapter(7) describes the application of the scanning network probe to printed microstrip array antenna diagnostics. Several examples of corporately fed arrays are presented. Finally, chapter(8) summarizes the results achieved and describes possible future avenues of research based on the scanning network probe measurement technique.

CHAPTER 2

The Mechanical Design and Computer Control of the Scanning Network Probe

2.1 Introduction

The scanning network probe system can be categorized into two components i.e.:

(a) a multi–axis stepper motor driven probe translator

(b) a comprehensive computer control and data management system

The mechanical design of the probe translator is determined by the desired scan area which sets the maximum limits of the probe travel, and the operational frequency of the circuit, which determines the minimum step size requirement and the acceptable positional error. The design criteria for a probe translator capable of measuring circuits up to $200mm$ by $200mm$ in area at frequencies up to 200 GHz are derived in section(2.2). The construction of the probe translator and its associated hardware are also described in section(2.2). The elements of the computer control system including all aspects of the hardware and software required are described in sections (2.3) to (2.6). Finally section(2.7) assesses the overall system errors due to the mechanical system and the data handling software.

2.2 Mechanical Aspects of the Scanning Network Probe

In order to map the fine structure in the electric or magnetic field variations close to the surface of the circuit, the probe translation mechanism must be capable of positioning the R.F. probe to an accuracy at least $\lambda_0/100$. At the frequency of interest, namely 220 GHz, the probe postion has to be maintained within approximately $\pm 2\mu m$. Accuracy of this order can be achieved by the use of crossed roller bearings located in very stable meehanite housings and precision ground leadscrews for the principal x–y movements. The crossed roller slides that form the principal x–y movement can be seen in plate(2.1). The robust construction of the cross slides enables large detector systems to be carried with minimal loading of the drive system, and negligable distortion

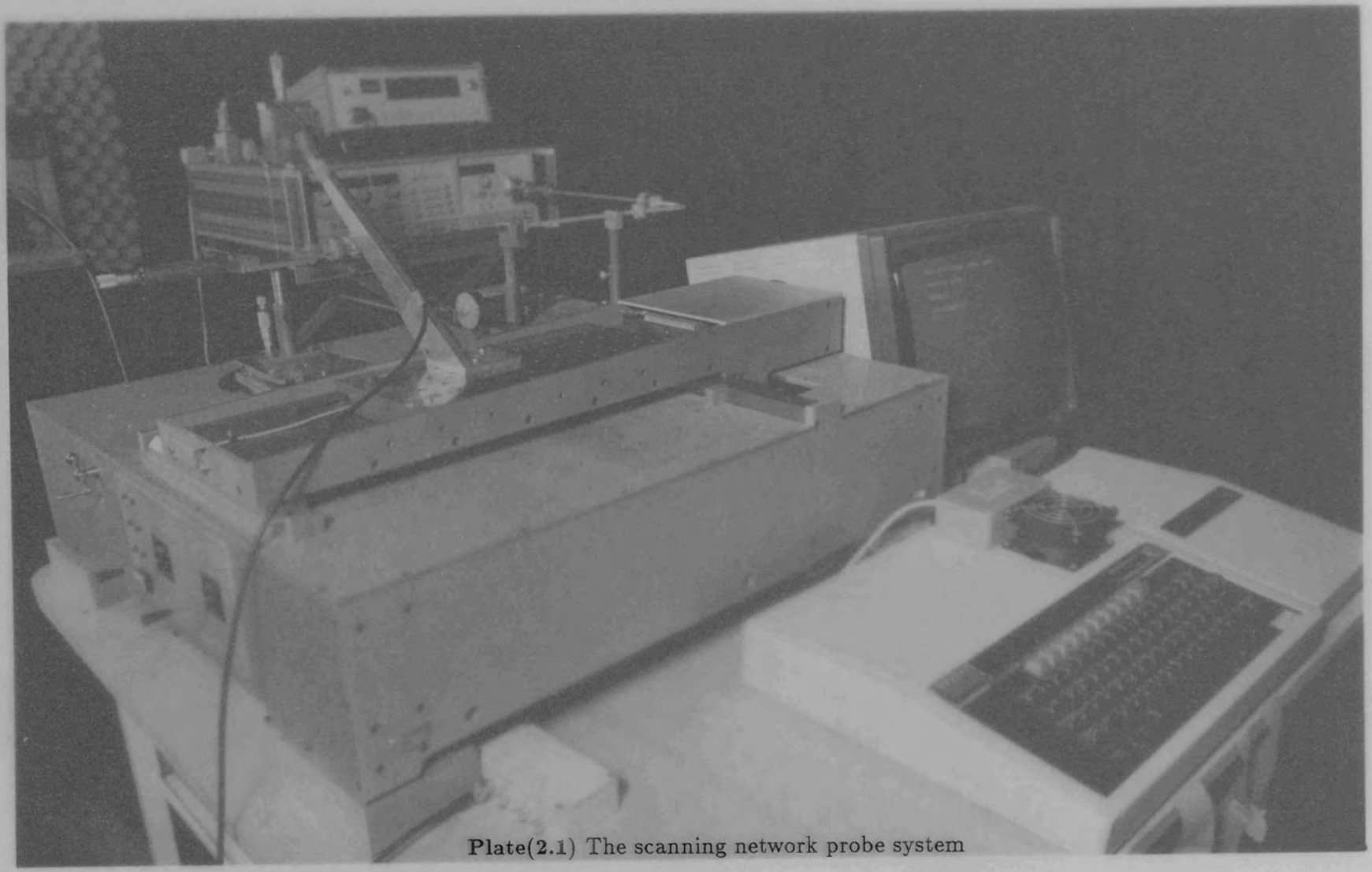

Plate(2.1) The scanning network probe system

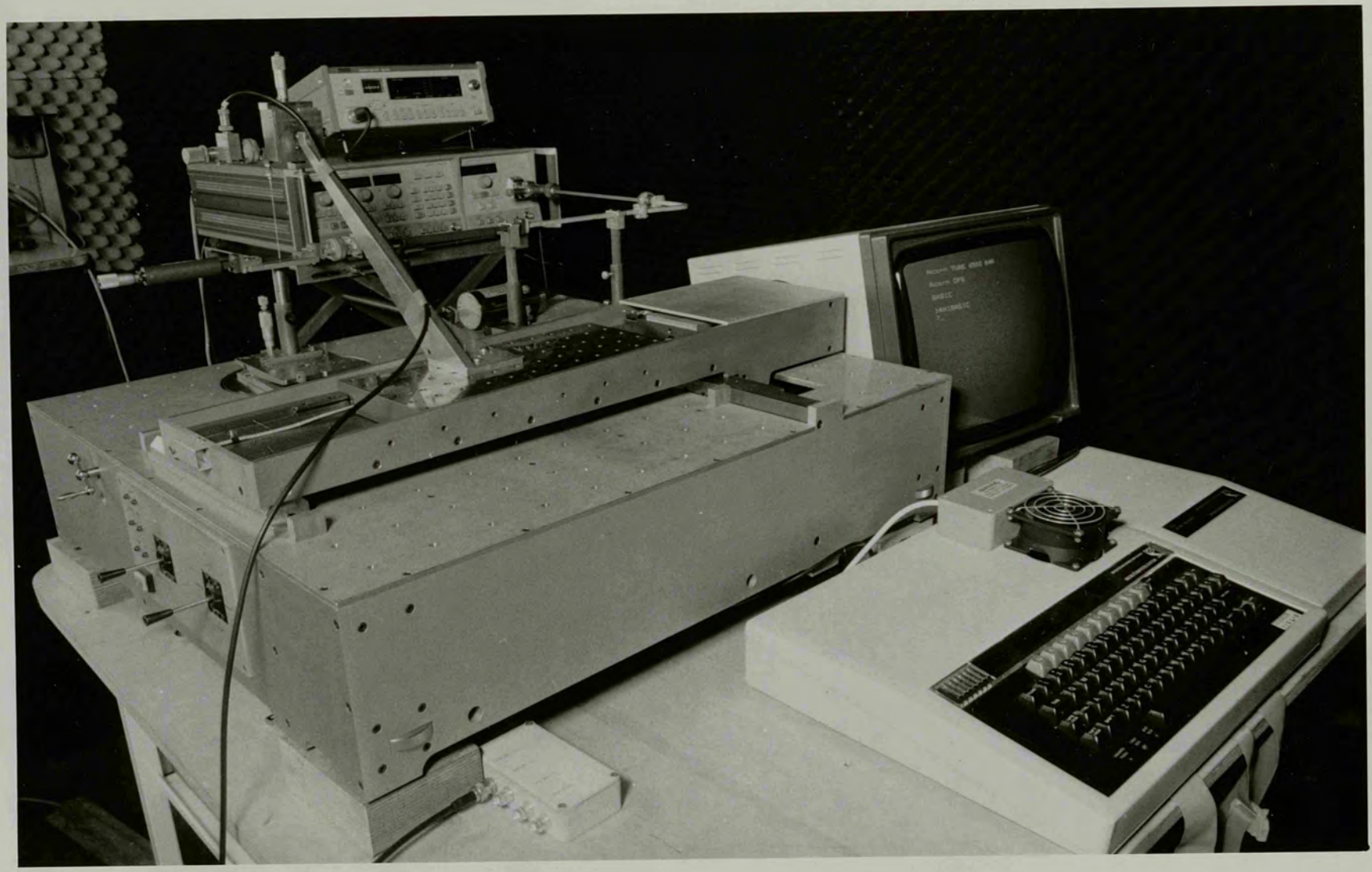

of the cross slide. Both cross–slides are actuated via $1mm$ pitch leadscrews which are driven directly from sine/cosine pole interpolating stepper motors. (These are often referred to as "microstep" motors) The electronic driver circuits for the stepper motors were arranged to provide 2000 steps per revolution, which results in a minimum step interval of $0.5\,\mu m$. An advantage of the microstep drive is that it is relatively smooth and vibration free compared with conventional pulse driven stepper motor systems. The smooth drive reduces lost steps due to motor bounce, and also reduces the settling time of the carriage, thus enabling rapid data collection. The x–y position of the probe is given by two 9 bit absolute optical shaft encoders mounted on the extended spindles of the stepper motors and a ROM based counter to record the number of leadscrew revolutions. The count direction is set by an analogue control line which changes the motor direction. The 9 bit angular resolution of the shaft encoder gives a spatial resolution of approximately $2\,\mu m$ on the x and y axes. The data from the shaft encoder is used to drive an LED display and the computer interface when required. In addition to the primary x–y movements, provision is made for z and θ movements in the form of a rotary/rising platform. This feature allows the probe–to–substrate separation and the angular postion of the circuit to be varied. The additional degrees of movement make the initial circuit alignment relatively simple. The rotary motion of the circuit mounting platform can also be employed to measure the radiation patterns of small antennas. Both these auxillary movements are driven by conventional four phase stepper motors, since the microstep facility was not required. The angular position of the platform is monitored by an 8 bit rotary shaft encoder, whilst the platform height can be monitored by an optional linear postion transducer if required. The 8 bit shaft encoder on the rotary platform has an angular resolution of 1.8 degrees. The x,y,z,θ movements are mounted on a substantial dural chassis, the top plate of which is drilled with a matrix of tapped holes to provide a secure, stable mounting for any ancilliary R.F. components, as illustrated in plate(2.1)

2.3 The Computer Management System Part(1): Electronic Support Hardware

The purpose of the computer management system is to carry out the laborious step and repeat measurements required by the scanning network probe technique. The scope of this section is to provide an outline of the electronic hardware necessary for the automatic control of the scanning network probe mechanics. A block diagram of the stepper motor drive and the shaft encoder position feedback loop is shown in Figure (2.1). The stepper motors can be controlled manually via a pair of dual axis joysticks and the analogue

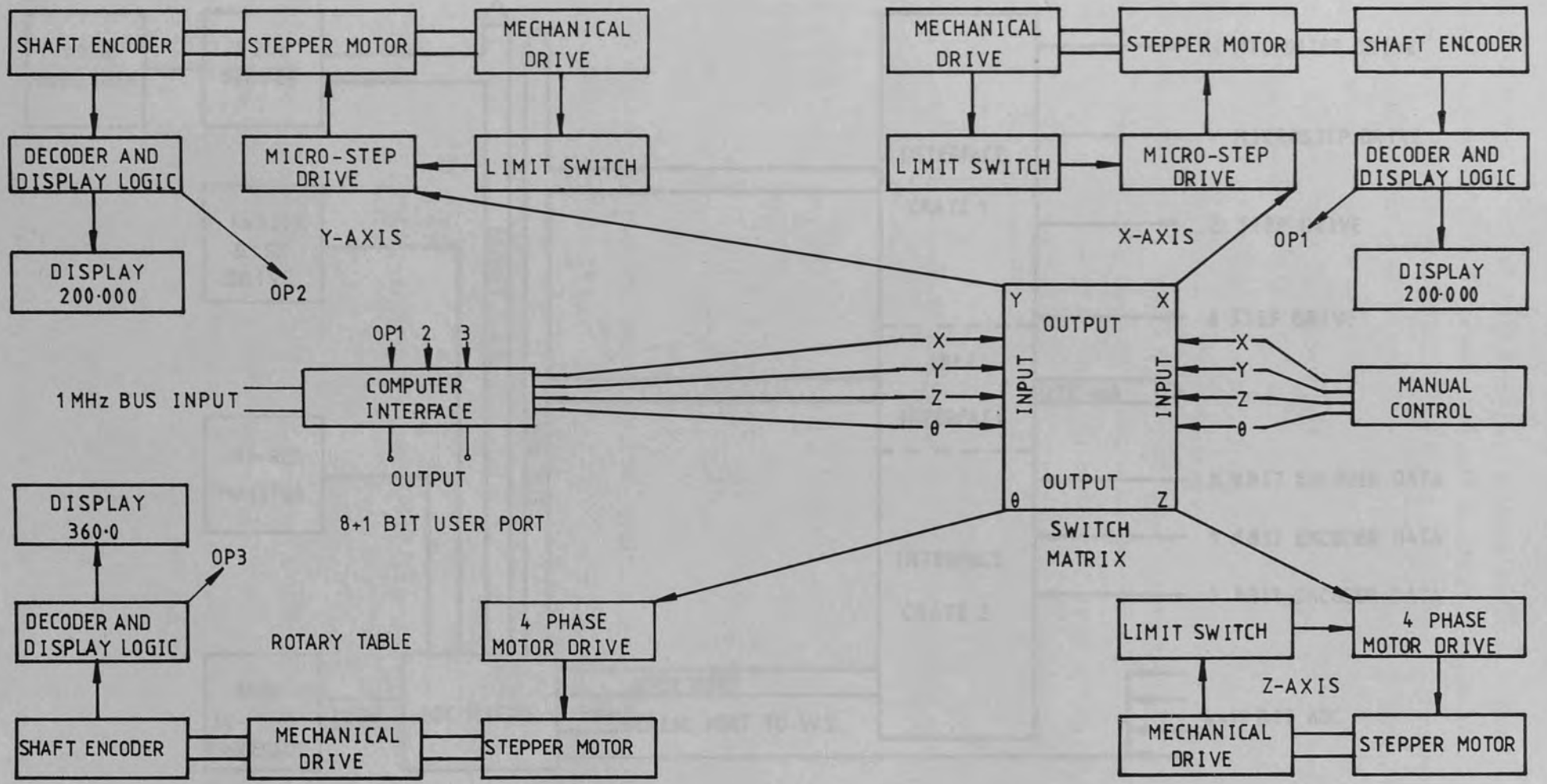

Figure(2.1) Schematic diagram of the scanning network probe hardware

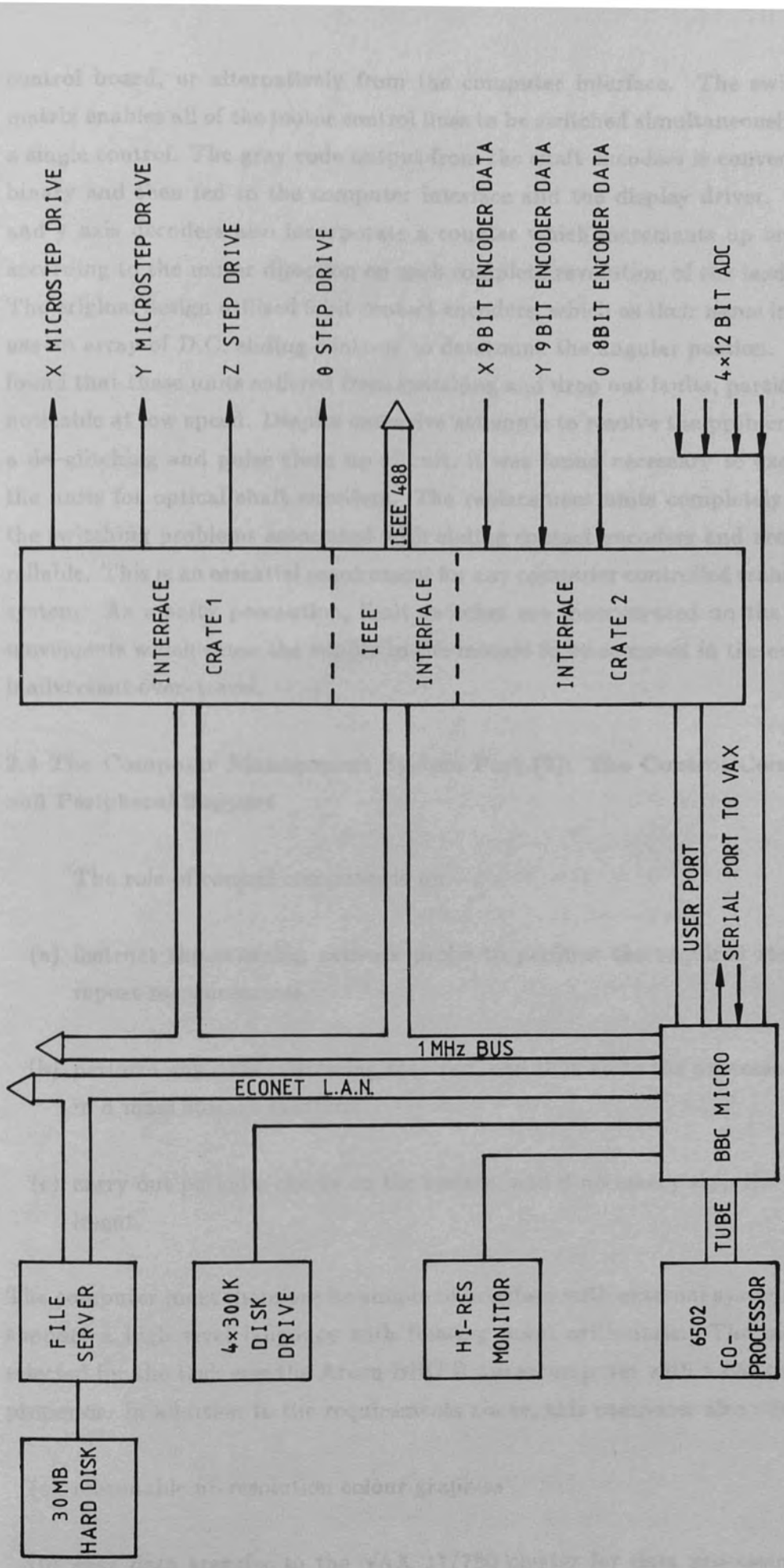

Figure(2.2) The scanning network probe computer management hardware

control board, or alternatively from the computer interface. The switching matrix enables all of the motor control lines to be switched simultaneously from a single control. The gray code output from the shaft encoders is converted to binary and then fed to the computer interface and the display driver. The x and y axis decoders also incorporate a counter which increments up or down according to the motor direction on each complete revolution of the leadscrew. The original design utilized 9 bit contact encoders, which as their name implies, use an array of D.C. sliding contacts to determine the angular postion. It was found that these units suffered from switching and drop out faults, particularly noticable at low speed. Despite extensive attempts to resolve the problem with a de–glitching and pulse clean up circuit, it was found necessary to exchange the units for optical shaft encoders. The replacement units completely cured the switching problems associated with sliding contact encoders and are 100% reliable. This is an essential requirement for any computer controlled transducer system. As a safty precaution, limit switches are incorporated on the linear movements which cause the supply to the motors to be removed in the event of inadvertant over–travel.

2.4 The Computer Management System Part (2): The Control Computer and Peripheral Support

The role of control computer is to:

(a) instruct the scanning network probe to perform the required step and repeat measurements.

(b) perform any data processing required, and then store the processed data in a mass storage medium.

(c) carry out periodic checks on the system, and if necessary stop the experiment.

The computer must therefore be simple to interface with external systems, and support a high level language with floating point arithmatic. The machine selected for the task was the Acorn BBC B microcomputer with a 6502 second processor. In addition to the requirements above, this computer also offered:

(a) reasonable hi–resolution colour graphics

(b) easy data transfer to the VAX 11/780 cluster for data processing and

presentation

(c) a cheap local area networking capability allowing multi user access to a centralized hard disk drive

For very basic fixed frequency measurements on small circuits the computer support hardware required is minimal and would comprise:

(a) BBC B computer and 6502 second processor

(b) dual floppy disk drive

(c) the scanning network probe interfaces

The system currently in use is shown in Figure (2.2). The addition of the GPIB interface allows the control computer to access external GPIB equipped devices such as a power meter or sweep oscillator. The scope of the control by the management software is greatly increased by this feature, and automated multiple frequency measurements and automatic calibration become possible. The econet local area network facility enables access to a 30 M byte hard disk for data storage. The hard disk unit has a much faster access time than floppy disk drive systems and considerably reduces the time to complete tasks such as loading and saving data. The multi user network also allows the data to be spooled and transferred to VAX mainframe immediately on completion of the experiment by a second network station. This leaves the control computer free to start another experiment. A bonus of the econet system is that the status of an experiment can be interrogated from any station on the network, and if necessary keyboard control can be transferred to the remote station.[2.2]

2.5 The Computer Management System Part(3): The Management Software

The management software replaces the human operator in the measurement process, and must be programmed with suitable "intelligence" to cater for factors such as R.F. power failiure, or encoder error. The software must also enable the operator to easily correct keyboard entry errors without the need to re–run the program. In order to simplify and standardize the scanning network probe software, a self contained software driver was written. The device driver routines are called from the BASIC control program as "procedures". The procedures available and their function are listed in table (2.1).

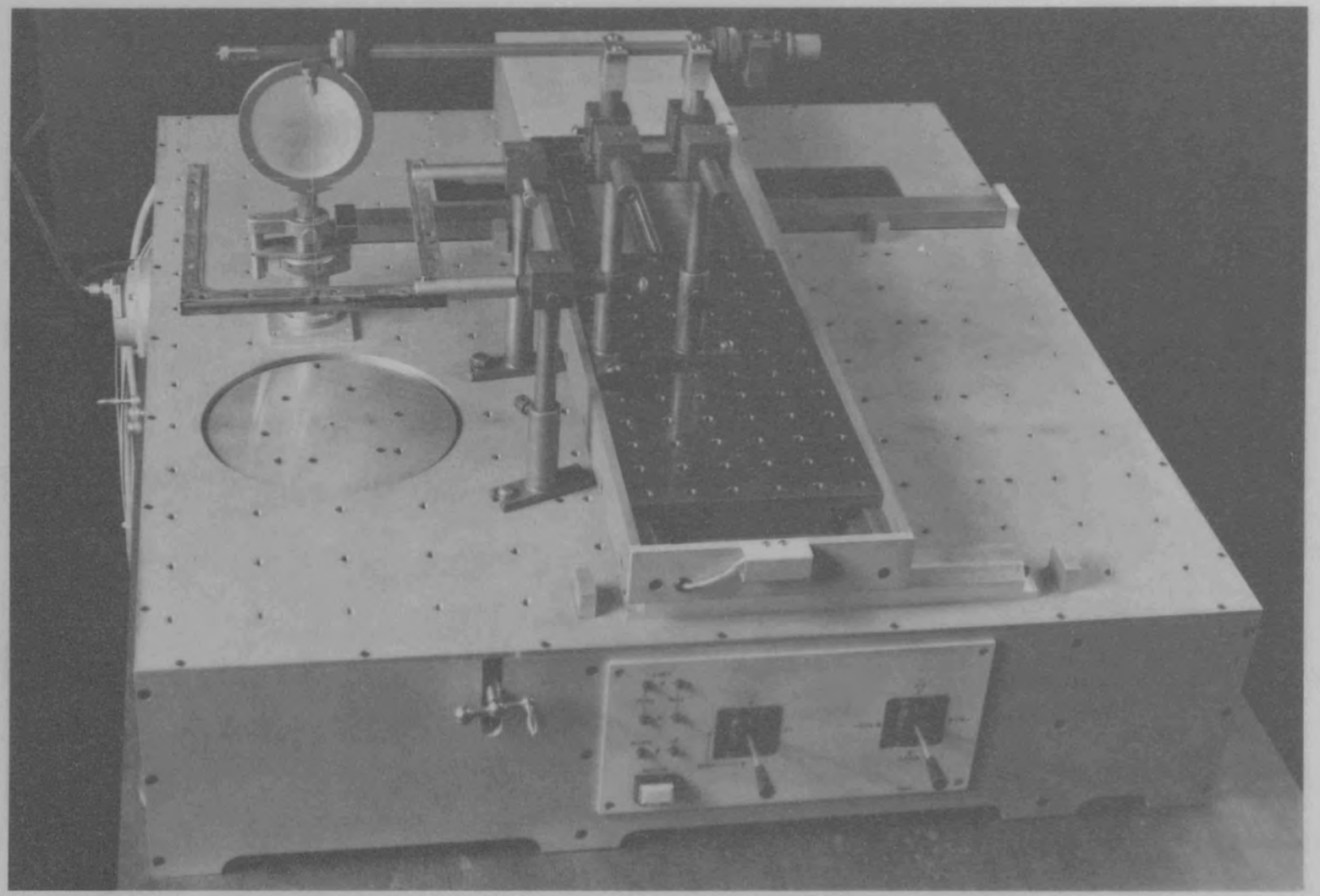

Plate(2.2) The scanning network probe translator

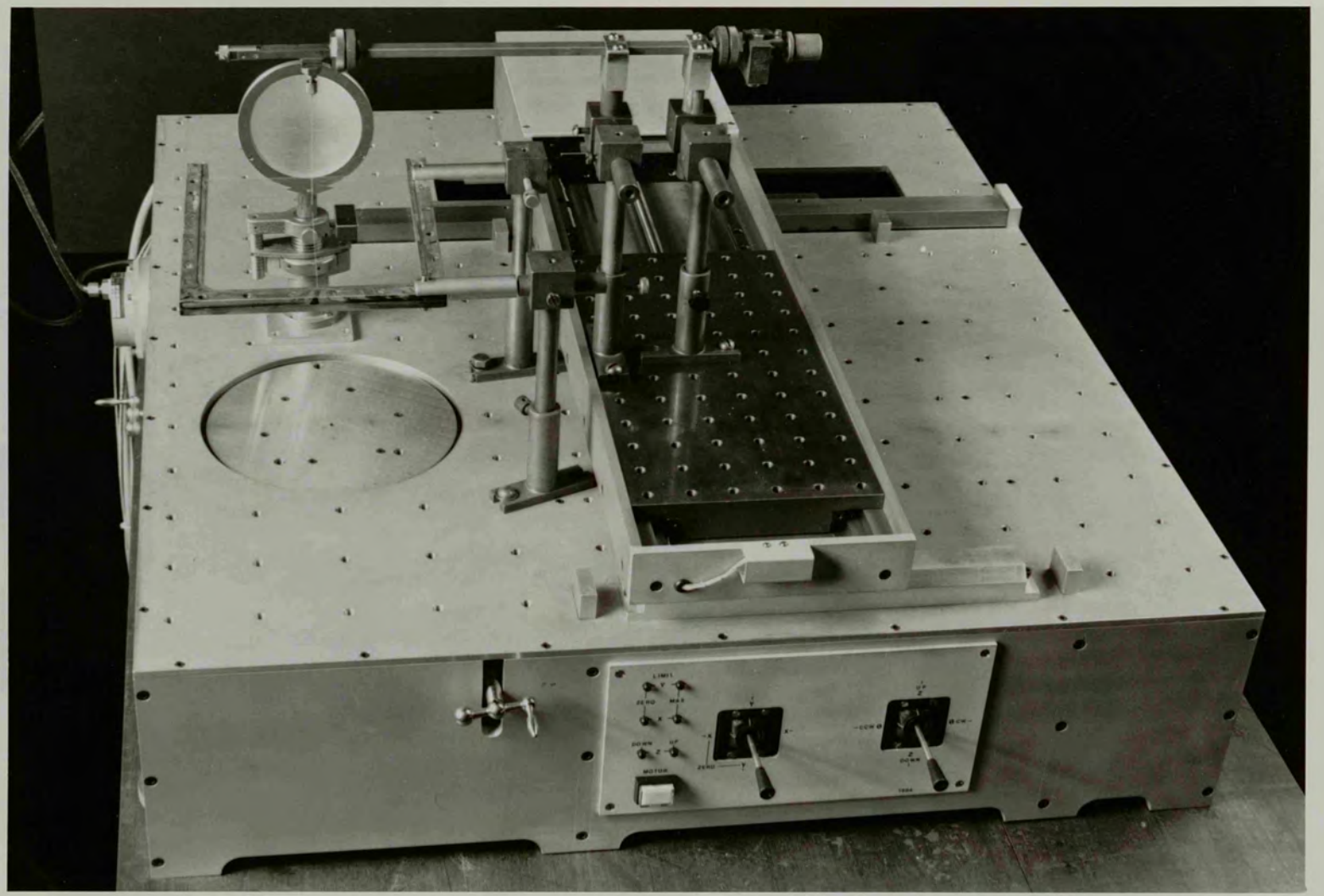

TABLE (2.1)

Scanning Network Probe Device Driver Procedures

PROCm1(ST%,DI%,SP%)	sets up x–axis motor
PROCm2(ST%,DI%,SP%)	sets up y–axis motor
PROCm3(ST%,DI%,SP%)	sets up z–axis motor
PROCm4(ST%,DI%,SP%)	sets up θ–axis motor
PROCms1	starts x–axis motor
PROCms2	starts y–axis motor
PROCms3	starts z–axis motor
PROCms4	starts θ–axis motor
PROCinhibit	stops all motors
PROCmstat	reads motor status
PROCyread	reads y–axis position in mm
PROCxread	reads x–axis position in mm
PROCtheta	reads θ position in degrees

where:

ST%= the number of steps (maximum of &FFF)

DI%= 0 for forward and &20 for reverse travel

SP%= speed select (integer between 0 and &10)

The variables ST%, DI%, and SP% passed in the parameter block of the motor set up procedures set the number of steps, the direction of travel, and the speed of translation. Any number of steps up to 4368 can be programmed into the counters, and the direction is set to forward or reverse by the value of DI%. The translation speed is set by the value of SP%, which is calculated from the following expression:

$$translation\ speed = \frac{motor\ clock\ rate}{steps\ per\ rev}\ \frac{1}{2^{SP\%}} \qquad 2.1$$

In the current system all of the motors are clocked at 10kHz, and the principal axes require 2000 steps per revolution, therefore the maximum and the minimum translation speeds of the x and y axes i.e. $1.25 mm S^{-1}$ (SP%=2) and

$0.15 \times 10^{-4} mmS^{-1}$ (SP%=15). Setting SP% to 0 or 1 inhibits the motor. This range of motor speeds is sufficient for most applications, the fast speeds being used for the set up procedure and the slow speeds for the actual measurement process. Once the desired motor parameters are entered, motor stepping is started by the relevant start procedure. For example, to execute 20 steps in a forward direction at the fastest speed on the x–axis the program would read as follows:

```
PROCm1(20,0,2)
PROCms1
```

The remaining two procedures, PROCinhibit and PROCmstat are used to inhibit all the motors and interrogate the motor status respectively. A more complete description of programming with the scanning network probe interface is given in appendix(1).

The measurements made with the scanning network probe can be divided into three categories:

(a) polar radiation plot measurements

(b) linear line scan VSWR measurements

(c) area scan measurements

A menu driven suite of programs has been developed that enables the the above measurements to be made with a variety of R.F. source and detector combinations, thus relieving the operator of entering labourious set commands. The menu is run by auto–booting the systems software on the local floppy disk drive or on the econet master disk. The required routine can then be selected by single key entries. The different measurement routines are now considered in more detail.

2.5.1 Antenna Polar Pattern Measurement

The diagram in Figure (2.3) illustrates the typical arrangement employed to measure antenna radiation patterns in reception. The antenna to be tested is mounted to the rotary table by a suitable jig, and the metallic surfaces of the scanning network probe are covered with microwave absorber.

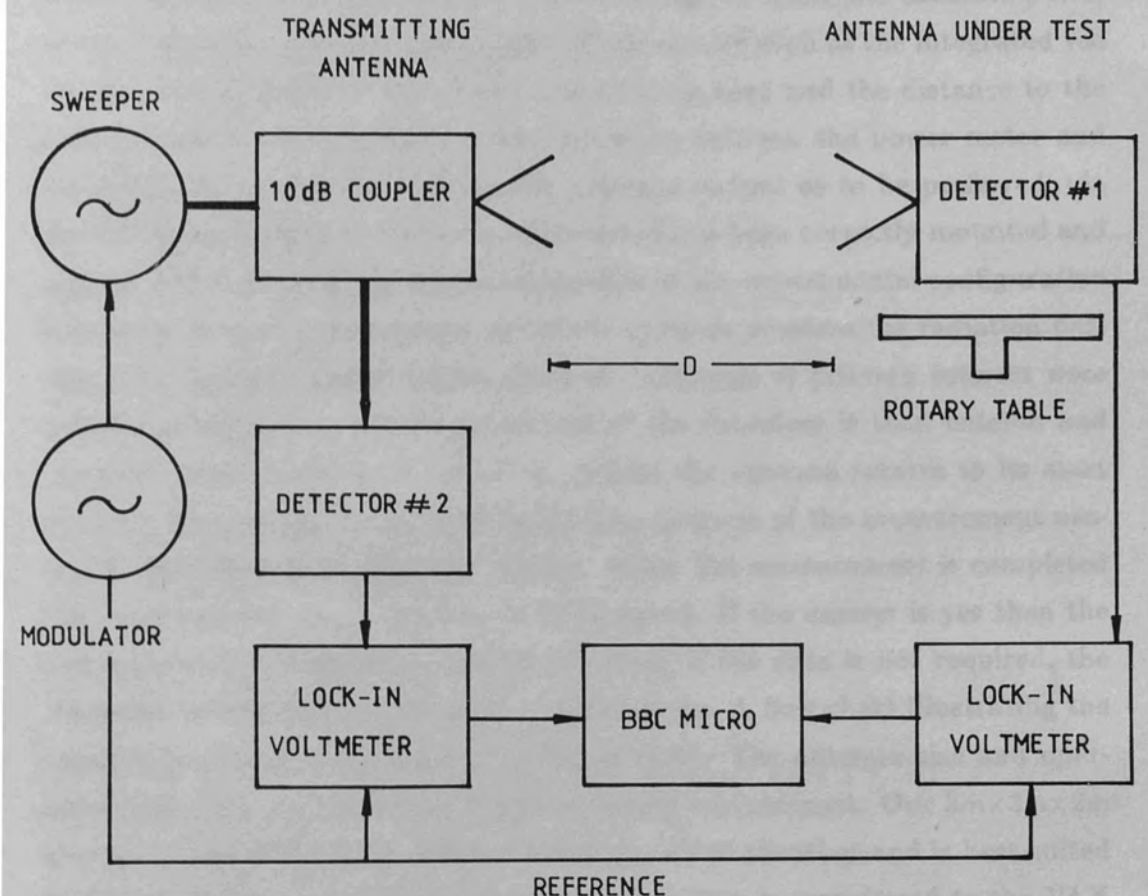

Figure (2.3) Antenna radiation pattern measurement

The transmitting and receiving antennas are aligned with a HeNe laser and boresight direction recorded. The second detector monitors the input power to the illuminating horn and is used to normalize the data from the antenna under test. The second detector can be replaced by an absolute reading power meter, such as the Anritsu ML83. The advantage of using the absolute power sensor is that the sensitivity of "rectenna" structures such as the integrated vee can be calculated if the gain of the transmitting horn and the distance to the antenna under test is known. Communication between the power meter and the computer is accomplished via the analogue output or to be preferred, via the GPIB bus. When the antenna to be tested has been correctly mounted and aligned, the measurement routine appropiate to the experimental configuration is selected from the main menu. All of the routines measure the radiation pattern ± 90 degrees from boresight, since the antennas of primary interest were half–plane radiators. The time constant of the detectors is then entered and the measurement routine is initiated. Whilst the antenna rotates to its start position, the anechoic room is vacated. The progress of the measurement process is monitored from a remote display. When the measurement is completed the computer will ask if the data is to be saved. If the answer is yes then the computer will prompt for an output filename. If the data is not required, the computer reverts back to the measurement mode. A flow chart illustrating the measurement procedure is given in Figure (2.4). The antenna size and operating frequency are limited by the surrounding environment. Our $3m \times 3m \times 2m$ anechoic room is clad with Plessey Materials AF40 absorber and is best suited for frequencies in excess of 10 GHz. The stored data is transferred to the VAX mainframe computer where the user can either:

(a) display the data on a suitable graphics terminal using the plotting routines described in section(2.6).

(b) plot the data on a Calcomp81 plotter.

(c) archive the data onto magnetic tape for long term storage.

The software routines for antenna polar pattern measurements are given in appendix(1).

2.5.2 Linear Line Scan VSWR Measurements

One of the two primary functions of the scanning network probe system is to measure the VSWR on printed transmission lines in a manner analagous

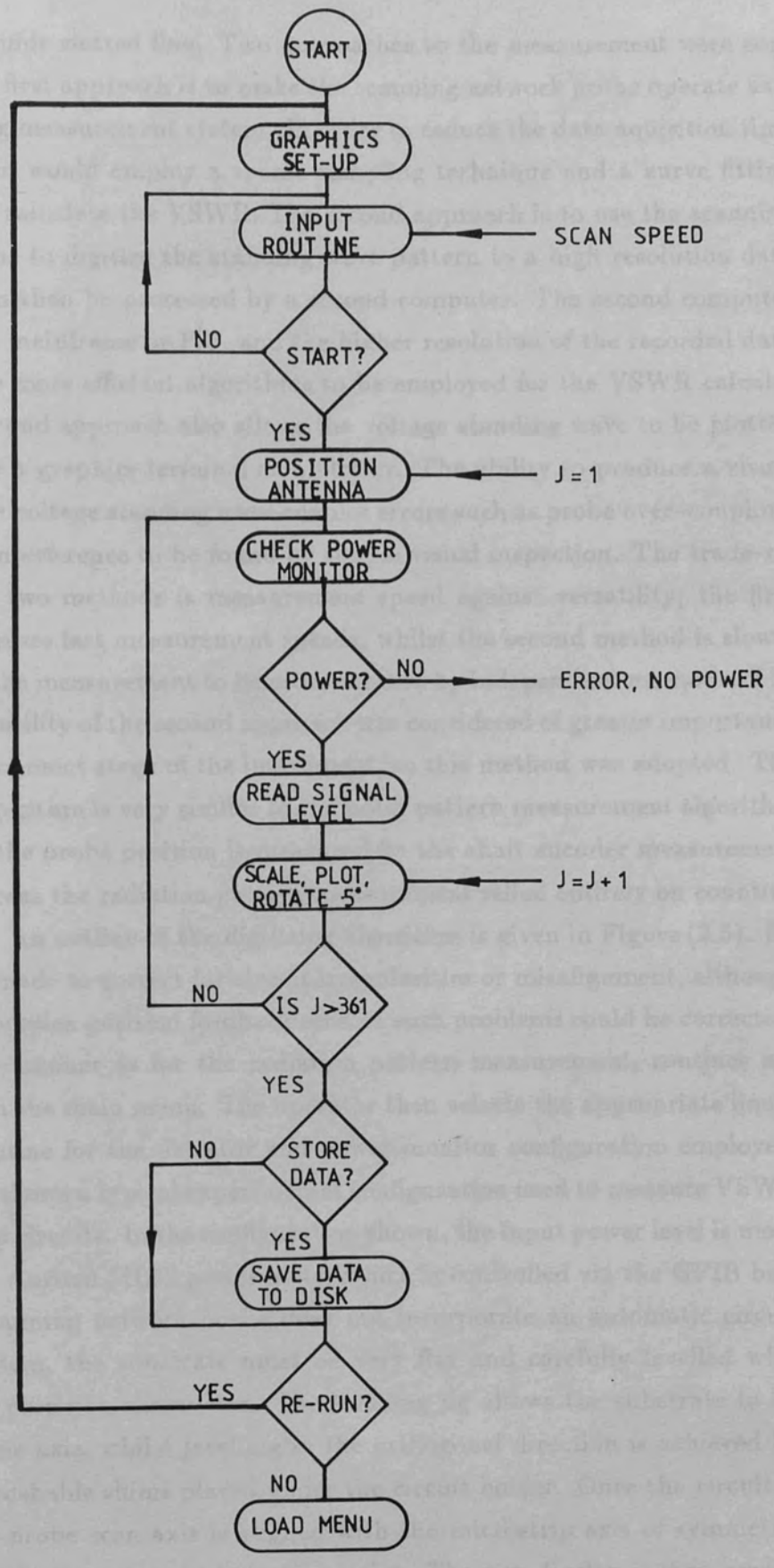

Figure (2.4) Antenna radiation pattern measurement algorithm

to the waveguide slotted line. Two approaches to the measurement were considered. The first approach is to make the scanning network probe operate as a direct reading measurement system. In order to reduce the data aquisition time such a system would employ a sparse sampling technique and a curve fitting algorithm to calculate the VSWR. The second approach is to use the scanning network probe to digitize the standing wave pattern to a high resolution data file which can then be processed by a second computer. The second computer can be a fast mainframe or P.C. and the higher resolution of the recorded data would enable more efficient algorithms to be employed for the VSWR calculation. The second approach also allows the voltage standing wave to be plotted out on either a graphics terminal or a plotter. The ability to produce a visual display of the voltage standing wave enables errors such as probe over–coupling, or multiple interference to be found by simple visual inspection. The trade–off between the two methods is measurement speed against versatility; the first method promises fast measurement speeds, whilst the second method is slower but enables the measurement to be cross checked by independant methods. The superior versatility of the second approach was considered of greater importance at this development stage of the instrument, so this method was adopted. The digitizing algorithm is very similar to the polar pattern measurement algorithm except that the probe position is measured by the shaft encoder measurement system, whereas the radiation pattern measurement relied entirely on counting motor steps. An outline of the digitizing algorithm is given in Figure (2.5). No provision is made to correct for circuit irregularities or misalignment, although with more complex position feedback sensors such problems could be corrected. In the same manner as for the radiation pattern measurement, routines are selected from the main menu. The operator then selects the appropriate linear line scan routine for the detector and power monitor configuration employed. Figure (2.6) shows a typical experimental configuration used to measure VSWR on microstrip circuits. In the configuration shown, the input power level is monitored by an Anritsu ML83 power meter which is controlled via the GPIB bus. Since the scanning network probe does not incorporate an automatic circuit levelling system, the substrate must be very flat and carefully levelled with the aid of a precision clinometer. The levelling jig allows the substrate to be levelled in one axis, whilst levelling in the orthogonal direction is achieved by the use of crushable shims placed under the circuit holder. Once the circuit is levelled, the probe scan axis is aligned with the microstrip axis of symmetry, and positioned at a convenient starting point. The x–y display is then zeroed and the line scan selected from the main menu. The software first prompts the user to enter the lock–in voltmeter time constant and *fsd*. After these have

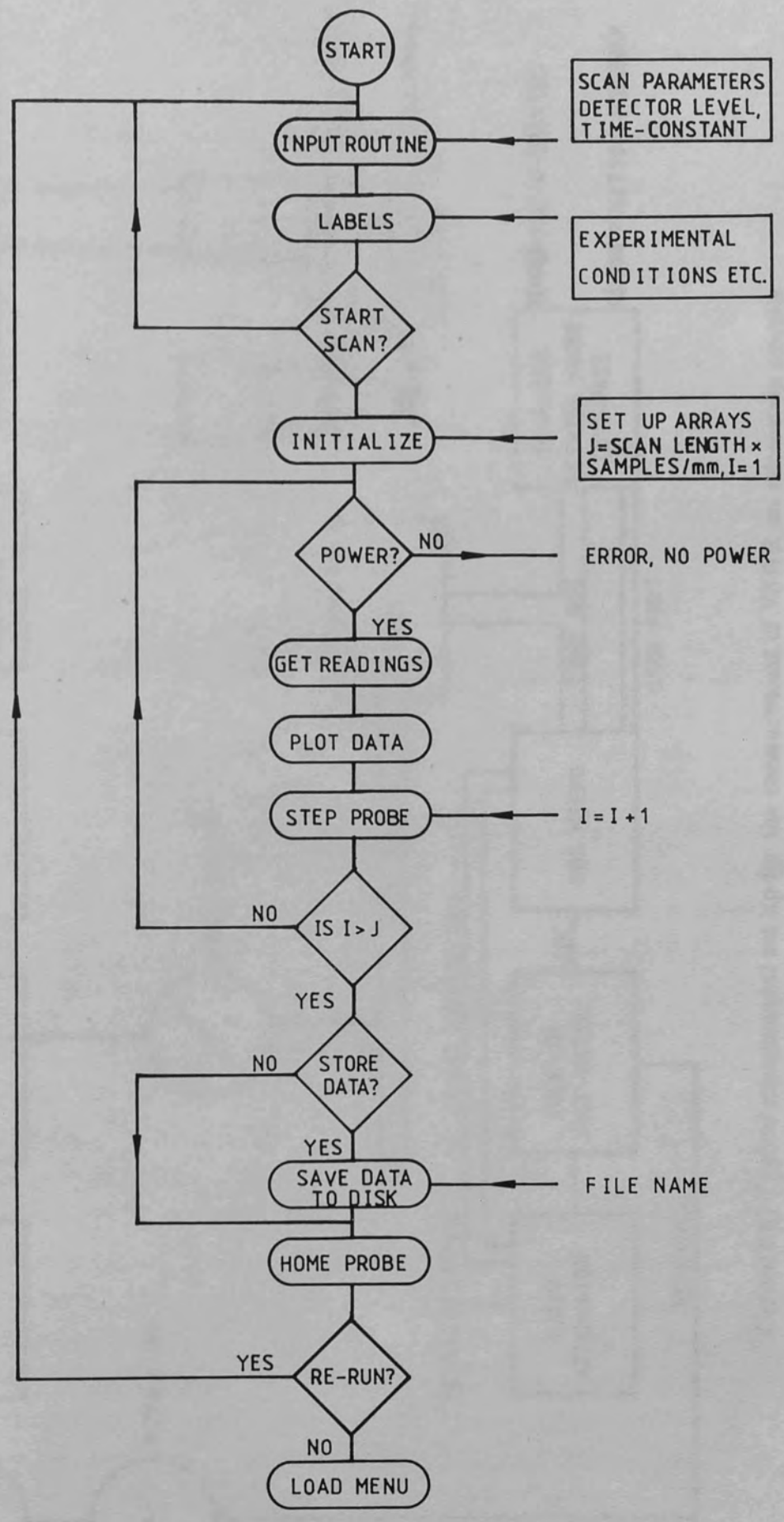

Figure (2.5) The linear line scan algorithm

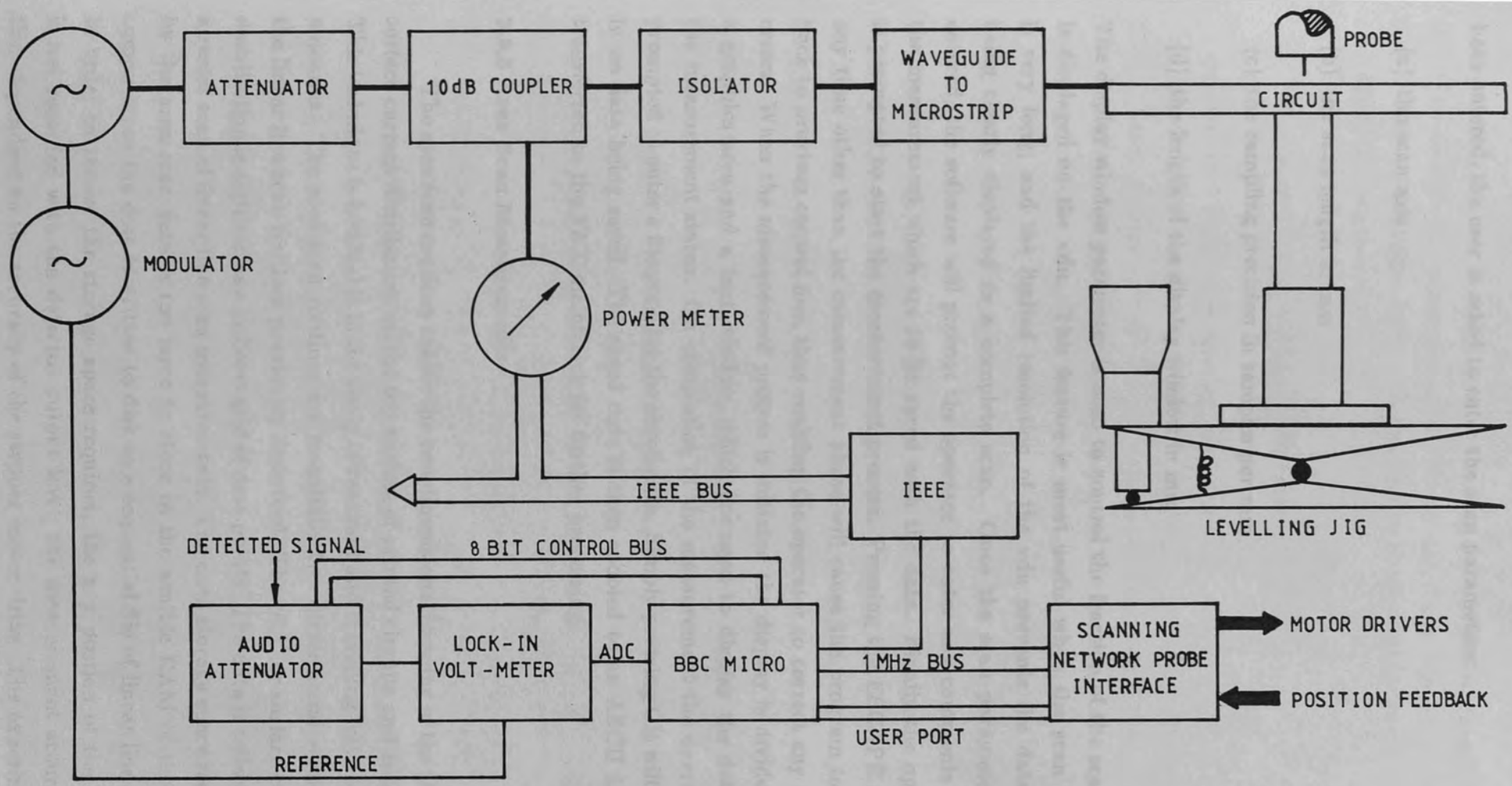

Figure(2.6) Typical experimental set up for the measurement of VSWR on microstrip circuits

been entered, the user is asked to enter the scan parameters:

(a) the scan axis

(b) the scan length in mm

(c) the sampling precision in samples per mm

(d) the length of the display window in mm

The display window parameter is used to control the fraction of the scan that is displayed on the vdu. This feature is most useful when the scan length is very long, and the limited resolution of the vdu prevents the data from being clearly displayed as a complete scan. Once the scan parameters are entered, the software will prompt the operator to enter any comments about the measurement which are to be saved with the data. Finally the operator is prompted to start the measurement process. Pressing the ESCAPE key at any time other than the measurement phase will cause the program to jump back to previous control line, thus enabling the operator to correct any typing errors. When the measurement process is initiated the display is divided into a graphics area and a text window, which are used to display the data and the measurement status. On completion of the measurement the operator is prompted to enter a filename for the saved data. Simply pressing CR will result in no data being saved. The saved data is then spooled to an ASCII file and transferred to the VAX mainframe for further processing.

2.5.3 Area Scan Measurements

The area scan routines enable the two dimensional imaging of the $|E_z|^2$ or surface current distribution on the top surface of printed circuits and antennas. This technique is invaluable in the study of resonant and travelling wave printed antennas. The area scan routines are essentially two dimensional versions of the linear line scan routines previously described. The $|E_z|^2$ or surface current distribution is digitized as a uniform grid of data points. The data is collected by a raster scan of linear line scan measurements. The data storage space required by the area scan data is too large to store in the avaible RAM of the BBC computer, so the data is written to disk as a sequential file of linear line scans. In order to reduce the storage space required, the x–y postion of the probe is not recorded with the detector output level; the measurement accuracy is thus dependant on the accuracy of the stepper motor drive. The experimental

set–up for area scan measurements on microstrip–like geometries is the same as for the linear line scan measurements previously described. The input routines to the area scan software are almost identical to those used for the linear line scan measurements except that:

(a) the scan length in x and y must be entered

(b) the output filename is entered before the measurement is initiated

The area scan routine and the various enhancements to suit different source and detector configurations is given in appendix(1). The completed data file is spooled and transferred to the VAX mainframe for data processing.

2.6 Graphics Support Software

Once the data is transferred to the VAX mainframe, graphical output is obtained via a suite of FORTRAN77 programs run from a DCL menu routine. The FORTRAN77 programs all employ DIMFILM[2.3] subroutines to generate the graphical output. The following plotting routines have been developed:

(a) GENERAL: a general purpose graphing utility

(b) RADIATION: cartesian radiation plot output

(c) VSWR: plots VSWR data

(d) CONTOUR: monochrome contouring routine, including zoom and sectioning options

(e) COLOUR CONTOUR: as above but with colour coded contour levels

(f) TEK: same as (d) but modified to enable use of the TEK4111 hardware

(g) SURFACE: 3D surface representation of the measured data

All the routines can be used with any of the DIMFILM compatible devices listed in reference(2.3), except the TEK routine which has been configured to drive the TEK4111 graphics terminal.

2.7 System Errors

The system errors can be divided into two groups:

(a) mechanical and electrical errors in the data collection

(b) software induced errors in the graphic output

The first group includes all of the typical errors associated with leadscrew driven systems i.e.:

(a) lost steps

(b) backlash in the leadscrew drive

(c) accuracy of the leadscrew pitch

The origin of lost or spurious steps in the stepper motor drive can be due to a number of factors, such as inadequite filtering of the noise generated by the computer system itself, or heavy loading of the cross slide. In order to check the scanning network probe system for lost steps, a short program was written which either the x or y cross slide can be driven over its entire travel in $10mm$ blocks. The difference between the intended distance of $10mm$ and the actual distance moved as measured by the shaft encoder measurement system was then recorded. The graph in Figure (2.7) illustrates the measured error in the programmed $10mm$ block as a function of cross slide speed for a step increment of $125\,\mu m$. The presence of lost steps is clearly indicated, and the problem is more severe at the higher cross slide speeds. This suggests that steps are being lost in the acceleration phase of the motor. As a further check, the positional error in a $10\,mm$ block is shown plotted as a function of the scan increment at constant cross slide speed in Figure (2.8). This graph shows that the positional error increases with decreasing step interval, which confirms that the acceleration phase is the most likely point at which steps are being lost since the motor undergoes more accelerations per $10\,mm$ block for a smaller scan increment. This source of error is extremely difficult to correct, however the cumulative error over $10\,mm$ is at worst less than 0.2%. For measurements on small circuits this would be a negligable source of error. In order to maintain accuracy, measurements should be made via the shaft encoder measurement system and not from the programmed number of steps. The backlash of the y–axis cross slide was measured using a test dial indicator. It was found that

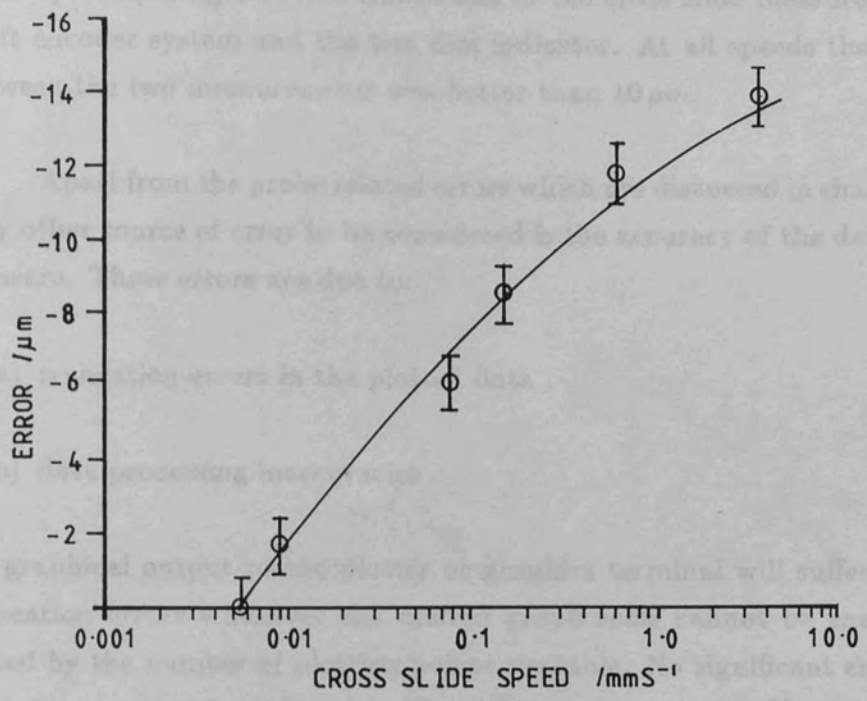

Figure (2.7) Positional error against cross slide speed

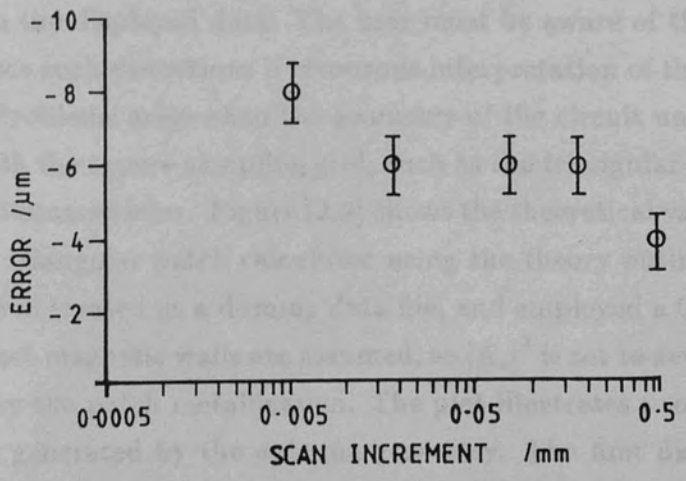

Figure (2.8) Positional error as a function of scan increment

when the cross slide was loaded with its normal payload, the backlash was barely detectable on the test dial indicator. At the fastest cross slide speed, this error was estimated to be approximately $20\,\mu m$, and considerably less at the slower speeds. The test dial indicator was also employed to check the leadscrew pitch by comparing a $10\,mm$ translation of the cross slide measured using the shaft encoder system and the test dial indicator. At all speeds the agreement between the two measurements was better than $10\,\mu m$.

Apart from the probe related errors which are discussed in chapter(3), the only other source of error to be considered is the accuracy of the data handling software. These errors are due to:

(a) truncation errors in the plotted data

(b) data processing inaccuracies

All graphical output to the plotter or graphics terminal will suffer from data truncation errors whenever the desired graph scale cannot be exactly represented by the number of plotting points available. No significant errors of this kind were expected, or found in the Calcomp 81 output. The low resolution real time display on the BBC computer is susceptable to this kind of error, and the accuracy of the real time display cannot be guaranteed. The same is also true for data that has been screen dumped from the real time display. The relatively simple 2 dimensional graphing routines use very little data processing, and hence will produce negligable error in the displayed output. The contour and surface plot routines have to perform considerable data processing in order to produce the required output, and under some circumstances can produce distortions in the displayed data. The user must be aware of the data types that will produce such distortions if erroneous interpretation of the results are to be avoided. Problems arise when the geometry of the circuit under test is imcompatible with the square sampling grid, such as the triangular and circular patch antennas discussed later. Figure (2.9) shows the theoretical variation of $|E_z|^2$ for the TM_{11} triangular patch calculated using the theory outlined in chapter(4). The plot was created as a dummy data file, and employed a $0.125\,mm$ sampling grid. Perfect magnetic walls are assumed, so $|E_z|^2$ is set to zero outside the area bounded by the patch metallization. The plot illustrates two distortions which have been generated by the antenna geometry. The first distortion is evident on the sides of the triangle that are not parallel to the scan axes; it is observed that the contours of constant $|E_z|^2$ have an undulating, zig–zag form, whereas the contours along the edge parallel to the y–axis vary in a smooth manner.

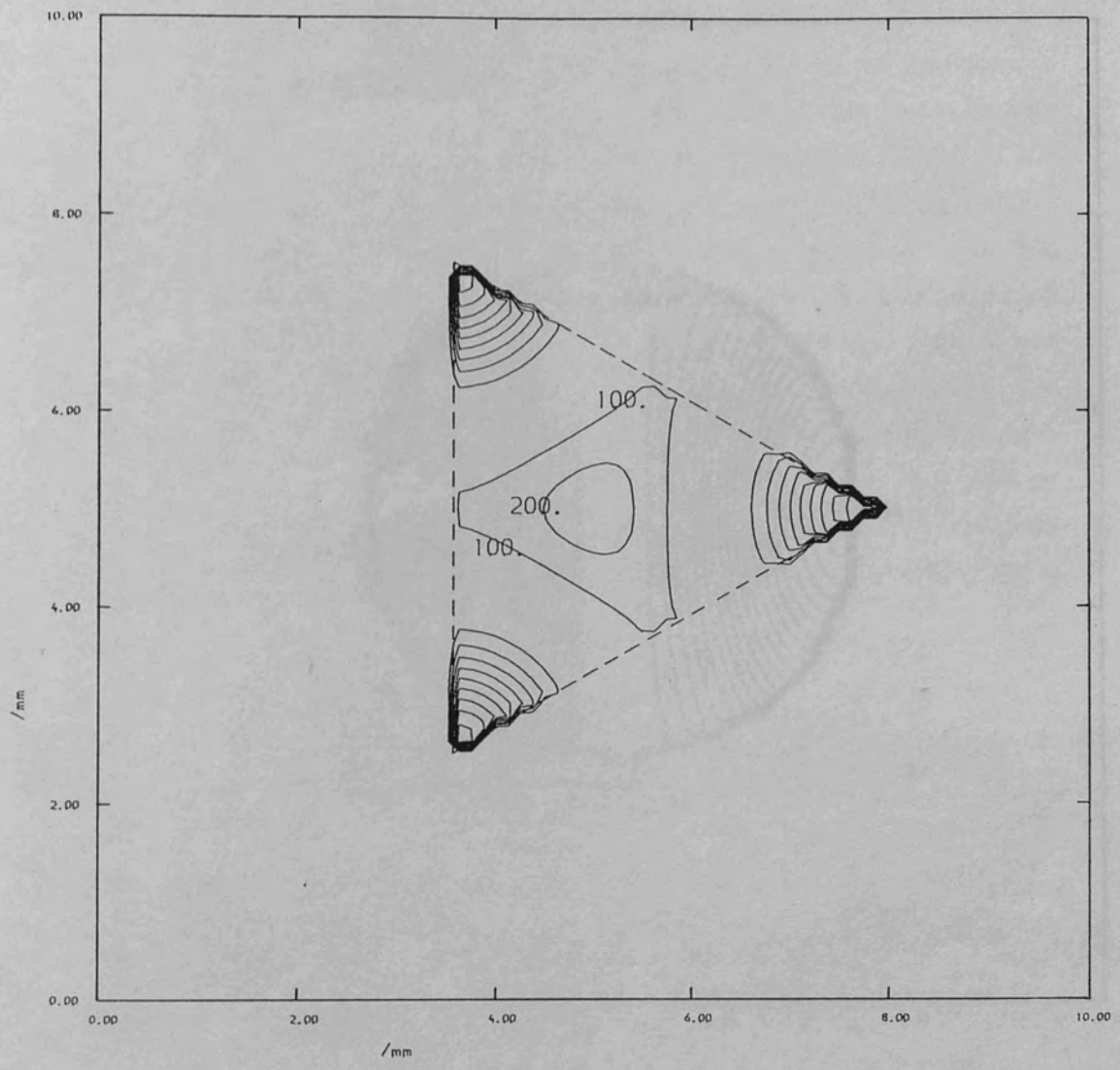

Figure (2.9) Theoretical TM_{11} $|E_z|^2$ distribution in a triangular patch

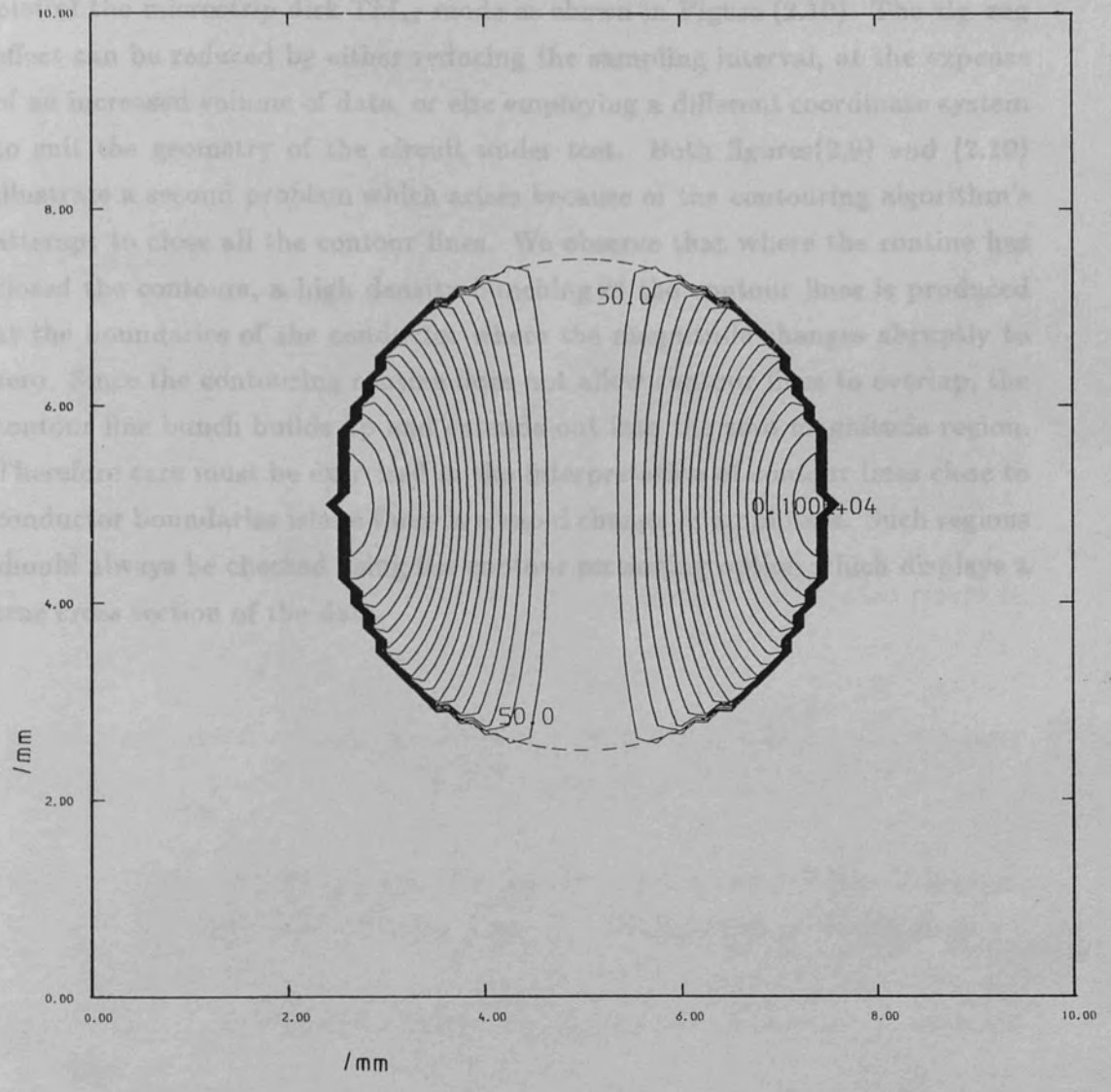

Figure (2.10) Theoretical TM_{11} $|E_z|^2$ distribution in a circular patch

The zig–zag effect is caused by the staircase of sample points that approximate the two sloping edges. The contouring software is restricted to linear interpolation between sample points, thus resulting in the zig–zag effect at the sloping boundaries. Similar distortion is also evident in the theoretical $|E_z|^2$ contour plot of the microstrip disk TM_{11} mode as shown in Figure (2.10). The zig–zag effect can be reduced by either reducing the sampling interval, at the expense of an increased volume of data, or else employing a different coordinate system to suit the geometry of the circuit under test. Both figures(2.9) and (2.10) illustrate a second problem which arises because of the contouring algorithm's attempt to close all the contour lines. We observe that where the routine has closed the contours, a high density bunching of the contour lines is produced at the boundaries of the conductor where the magnitude changes abruptly to zero. Since the contouring routine does not allow contour lines to overlap, the contour line bunch builds up and extends out into the zero magnitude region. Therefore care must be exercised in the interpretation of contour lines close to conductor boundaries where there is a rapid change in amplitude. Such regions should always be checked using the contour sectioning option which displays a true cross section of the data.

CHAPTER 3

R.F. Probes and Detection Techniques

3.1 R.F. Probe Design

3.1.1 Introduction.

The purpose of the R.F. probe is to sample the the electric or magnetic field over a small region of space, thus enabling the field variations in the region under investigation to be measured. In order that the measurements accurately reflect the field under study, the following probe requirements must be satisfied:

(a) it must have sufficient spatial resolution to observe any fine structure in the field distribution.

(b) it must provide enough signal to drive the detector over a useful dynamic range.

(c) the presence of the probe and its associated telemetry link (low frequency or R.F.) should not appreciably perturb the field under investigation.

(d) the probe should respond independantly to either the electric or magnetic field.

High spatial resolution may be achieved by the use of small diameter probes, but the ultimate resolution achieved will also be dependant on the sensitivity of the detection system employed. The requirement for low perturbation is met by the use of probes with diameters of less than $\lambda/20$. The spurious signal picked up by the transmission line link between the probe sensor and the detector (or the low frequency connections between the detector diode and amplifier when the probe incorporates a detector diode) may be reduced by:

(a) screening with an R.F. absorber

(b) using resistive transmission lines

Reference (3.1) contains a useful theoretical treatment of the measurement error introduced by scattered radiation from two wire balanced transmission line feeds. The same reference also includes experimental results that compare a short dipole response when the low frequency connections to an integrated diode detector are made using a low loss or a highly resistive transmission line. The conclusion reached from the theoretical and experimental investigations in reference (3.1) is that the telemetry link must have a low scattering cross section; a condition which is satisfied by the use of resistive transmission lines orientated such that the transmission line is perpendicular to the E–vector. A probe with an output proportional to a combination of the electric and magnetic field in the region under investigation is clearly undesirable. An example of such a probe is the asymmetric loop shown in Figure (3.1). The induced *emf* at the terminals a,b due to an electric field $\vec{E}$ is given by:

$$emf = \int_a^b \vec{E}.\vec{dl} \qquad 3.1$$

Assuming that the loop is a square of side A, the line integral in equation (3.1) can performed for each component of $\vec{E}$ as follows:

$$V_x = E_x\Delta \qquad 3.2a$$

$$V_y = 0 \qquad 3.2b$$

$$V_z = 0 \qquad 3.2c$$

The results in 3.2a–c indicate that for the loop orientation shown in Figure (3.1), only the component of the electric field parallel to the sides containing the line break will contribute to the *emf* appearing across the feed point terminals. The total *emf* across the terminals a,b will therefore be the sum of the *emfs* due to the local $\frac{\partial \vec{B}}{\partial t}$ and E_x. If the electric field were linearly polarized, then the loop could be orientated such that the asymmetric arms of the loop were always perpendicular to the electric field, thus allowing the components of $\vec{B}$ to be found without error. Section (3.1.4) will describe the construction and operation of loop probes in more detail.

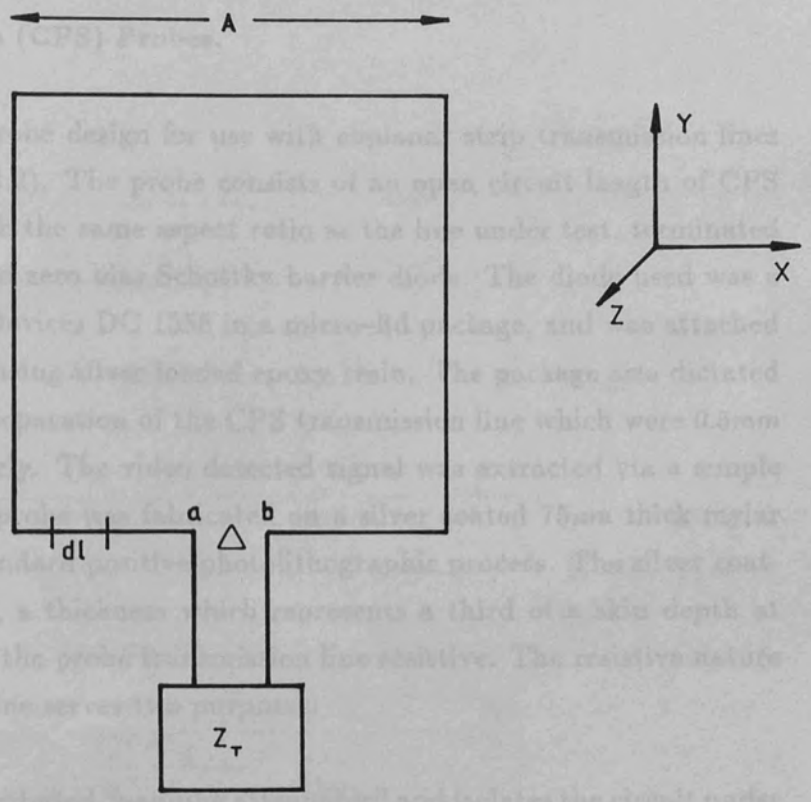

Figure (3.1) The asymmetric loop probe

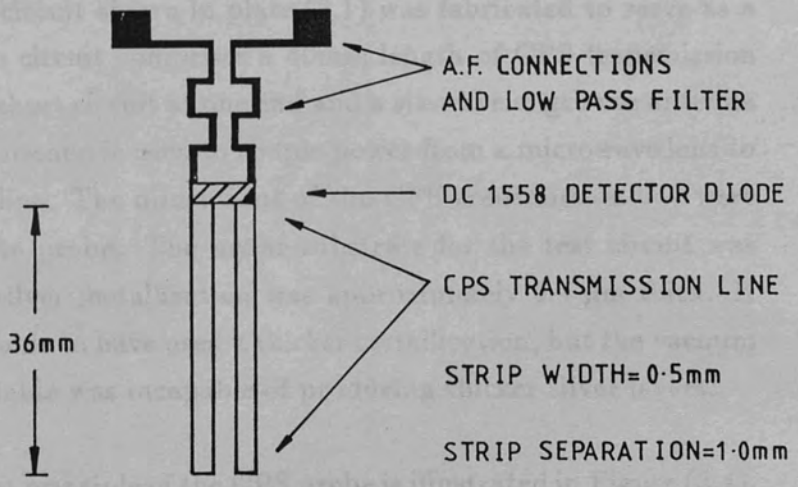

Figure (3.2) The coplanar strip probe

3.1.2 Coplanar Strip (CPS) Probes.

The original probe design for use with coplanar strip transmission lines is shown in Figure (3.2). The probe consists of an open circuit length of CPS transmission line with the same aspect ratio as the line under test, terminated with a shunt mounted zero bias Schottky barrier diode. The diode used was a Marconi Electronic Devices DC 1558 in a micro–lid package, and was attached to the probe circuit using silver loaded epoxy resin. The package size dictated the strip width and separation of the CPS transmission line which were $0.5mm$ and $1.0mm$ respectively. The video detected signal was extracted via a simple low pass filter. The probe was fabricated on a silver coated $75\mu m$ thick mylar substrate using a standard positive photolithographic process. The silver coating was $0.2\mu m$ thick, a thickness which represents a third of a skin depth at 35 GHz, thus making the probe transmission line resistive. The resistive nature of the transmission line serves two purposes:

(a) it acts as a distributed "padding attenuator" and isolates the circuit under test from reflections caused by the detector mismatch.

(b) it reduces the currents induced in the probe transmission line by direct radiation coupling.

The probe substrate was attached to a dural support frame using a cyanoacrylate adhesive. To prevent direct radiation coupling to the diode and low frequency lines, the probe assembly was encased in Eccosorb AN72 absorber. A small area approximately 10mm square was left uncovered at the probe tip. (see Figure (3.3)) The circuit shown in plate (3.1) was fabricated to serve as a probe test circuit. The circuit comprises a 40mm length of CPS transmission line terminated with a short circuit at one end and a six wavelength vee antenna at the other. The vee antenna is used to couple power from a microwave lens to the CPS transmission line. The dimensions of the CPS transmission line were identical to those of the probe. The mylar substrate for the test circuit was 75 μm thick, and the silver metallization was approximately 0.4 μm thick. It would have been preferable to have used a thicker metallization, but the vacuum coating technique available was incapable of producing thicker silver layers.

The measurement principle of the CPS probe is illustrated in Figure (3.4). The coupling from the transmission line under test to the probe is via the fringing electric field. The coupling magnitude is varied by adjusting the

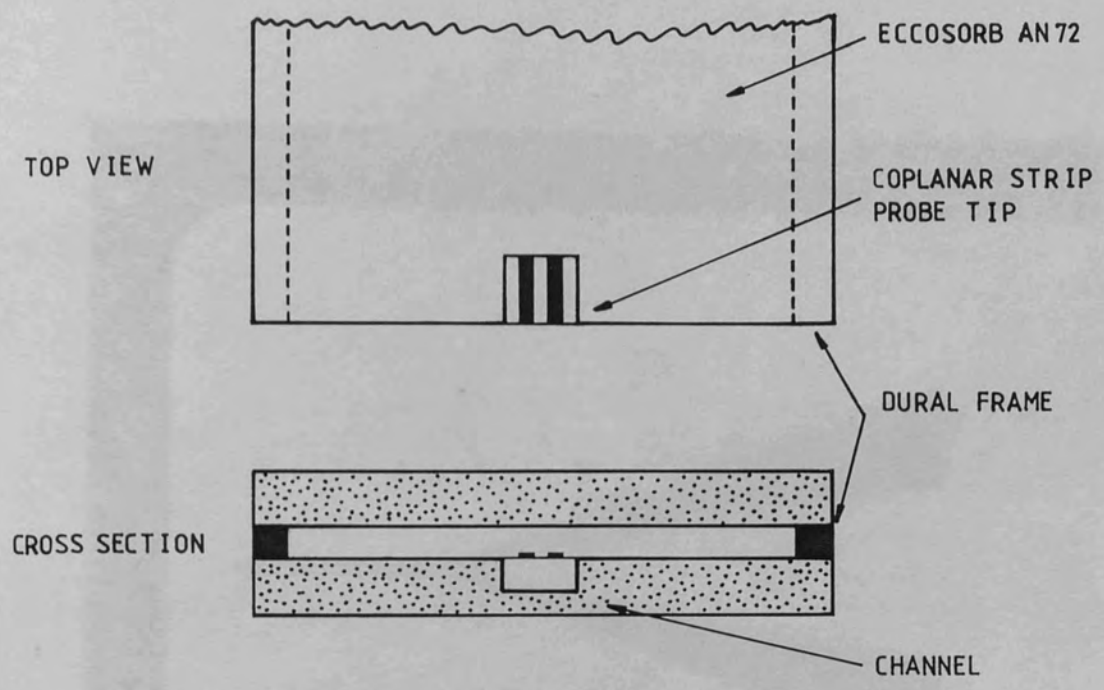

Figure (3.3) The eccosorb screening for the CPS probe

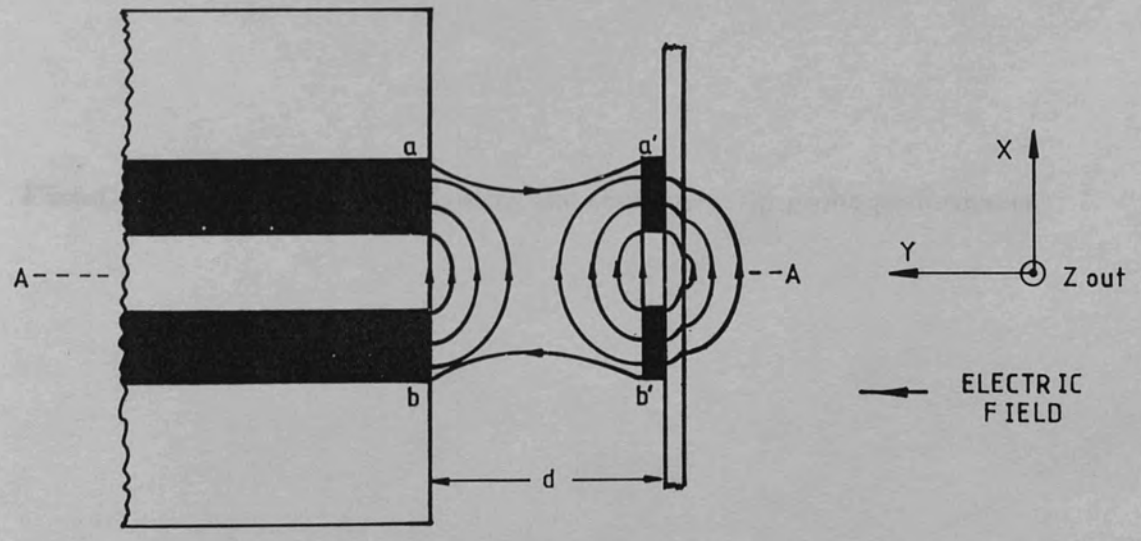

Figure (3.4) The coplanar strip probe measurement principle

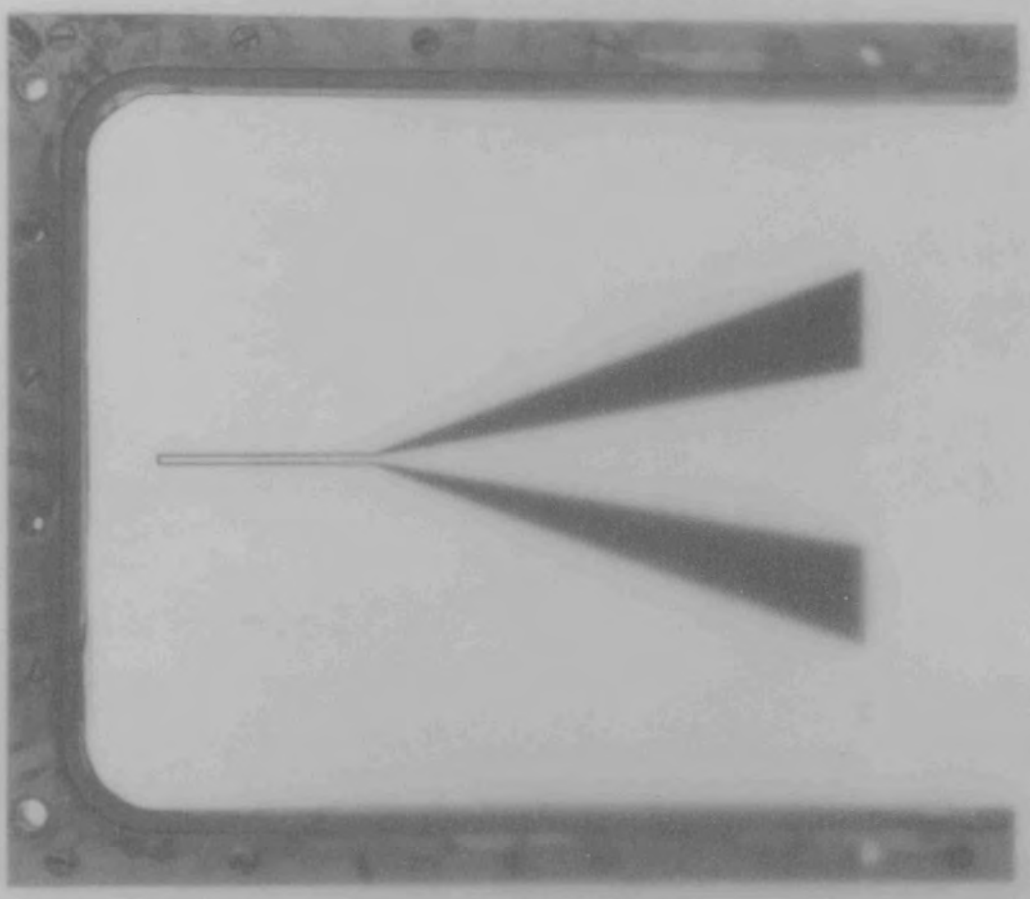

Plate(3.1) Test circuit for evaluating the coplanar strip probe performance

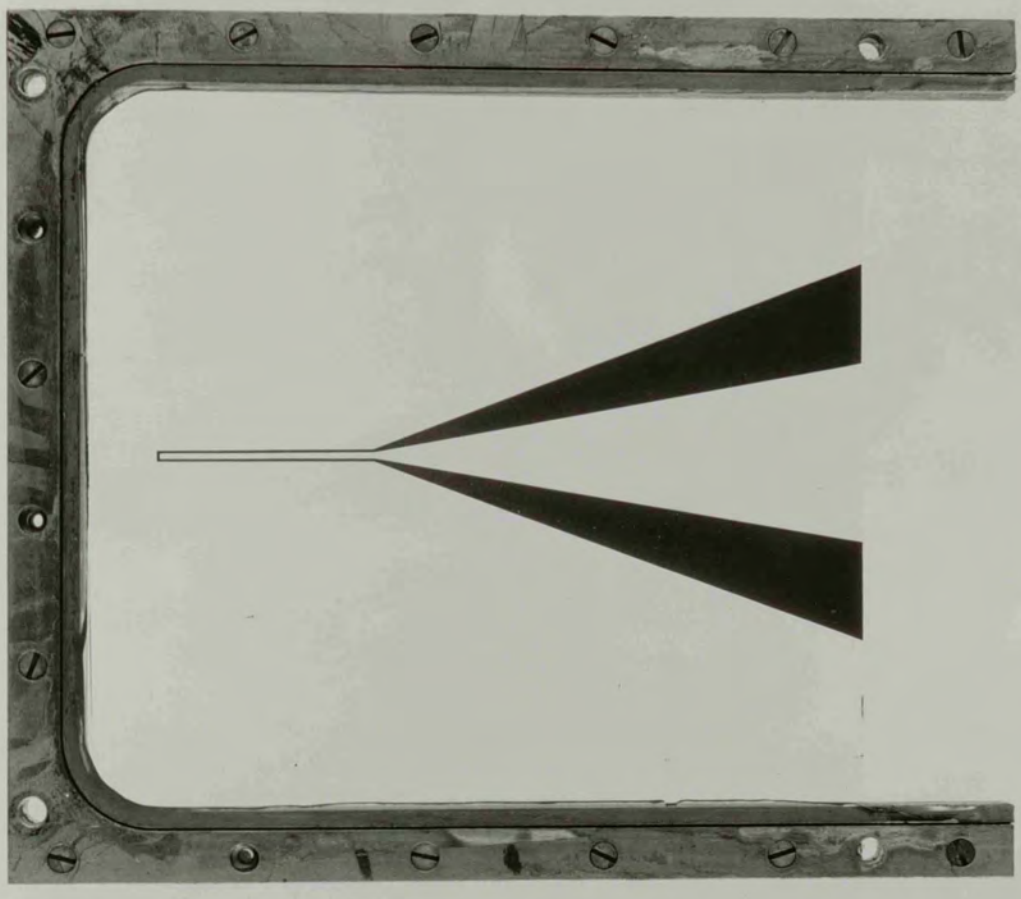

probe to substrate separation. The *emf* generated at the probe input due to the electric field surrounding the transmission line under test is found by evaluating the line integral of $\vec{E}.\vec{dl}$ around the path $a \rightarrow a' \rightarrow b' \rightarrow b$. This assumes that the conductor thickness is negligable with respect to a guide wavelength, and that the electric field fringing is localized to the region of the probe tip. Therefore:

$$emf = -\int_a^b \vec{E}.\vec{dl}$$

$$= -\int_a^{a'} \vec{E}.\vec{dl} + \int_{a'}^{b} \vec{E}.\vec{dl} - \int_{b'}^{b} \vec{E}.\vec{dl} \qquad 3.3$$

Since the problem is symmetric about the axis A-A then:

$$\int_a^{a'} \vec{E}.\vec{dl} = \int_{b'}^{b} \vec{E}.\vec{dl} \qquad 3.4$$

Therefore equation (3.3) becomes:

$$emf = \int_{a'}^{b} \vec{E}.\vec{dl} - 2\int_a^{a'} \vec{E}.\vec{dl} \qquad 3.5$$

The path $a' \rightarrow b'$ is tangential to the surface of the strip conductors, therefore the electric field can not have a component parallel to the integration path. The only contribution to the line integral along $a' \rightarrow b'$ is due to the x–component of the electric field between the conductors. In the limit of small d then the electric field lines in Figure (3.4) become parallel to the integration paths $a \rightarrow a'$ and $b \rightarrow b'$, thus the total line integral becomes:

$$emf = E_x s - 2E_y d \qquad 3.6$$

Where:

s= the strip separation

d= the probe to substrate separation

Therefore from the simple expression in equation (3.6) we can see that the *emf* generated at the probe tip decreases linearly with increasing probe to substrate separation. In the limit of d tending to zero, the *emf* generated at the probe input becomes equal to $E_x s$, which is simply the instantaneous voltage across the CPS transmission line. The relative magnitudes of the electric field components E_x and E_y only depends on the aspect ratio of the transmission line and the substrate parameters. (i.e. substrate thickness and permittivity) We also note that the CPS transmision line will support a near TEM mode if the substrate is very thin. If a standing wave exists on the transmission line then clearly both E_x and E_y will be weighted by the voltage standing wave envelope function, i.e.:

$$\xi(z) = A(z)[E_{x_0} - 2E_{y_0}] \qquad 3.7$$

where, E_{x_0}, E_{y_0} are the X and Y components of the electric field at voltage standing wave maximum
and $A(z)$ is given by:

$$A(z) = [1 + (1-\rho)^2 - \rho \sin(2\beta z - \phi_L)]^{\frac{1}{2}}$$

If d is maintained constant then the term in brackets in equation (3.7) becomes a constant, and the R.F. voltage generated across the probe input terminals becomes proportional to the voltage standing wave. Since there is no z–component of magnetic field, there can be no magnetic flux linking the path $a \rightarrow a' \rightarrow b' \rightarrow b$. Therefore the probe only couples to the x and y–components of the electric field.

The experimental arrangement used to energize the test circuit is shown in Figure (3.5). Any variations in the power output of the klystron source over the duration of the experiment are sensed by the power monitor circuit. The experimental procedure to make a vswr measurement using the CPS probe and the original Rockwell AIM–65 microcomputer controlled linear scanner is as follows:

(a) The transmission line under test is aligned to the scan axis of the probe.

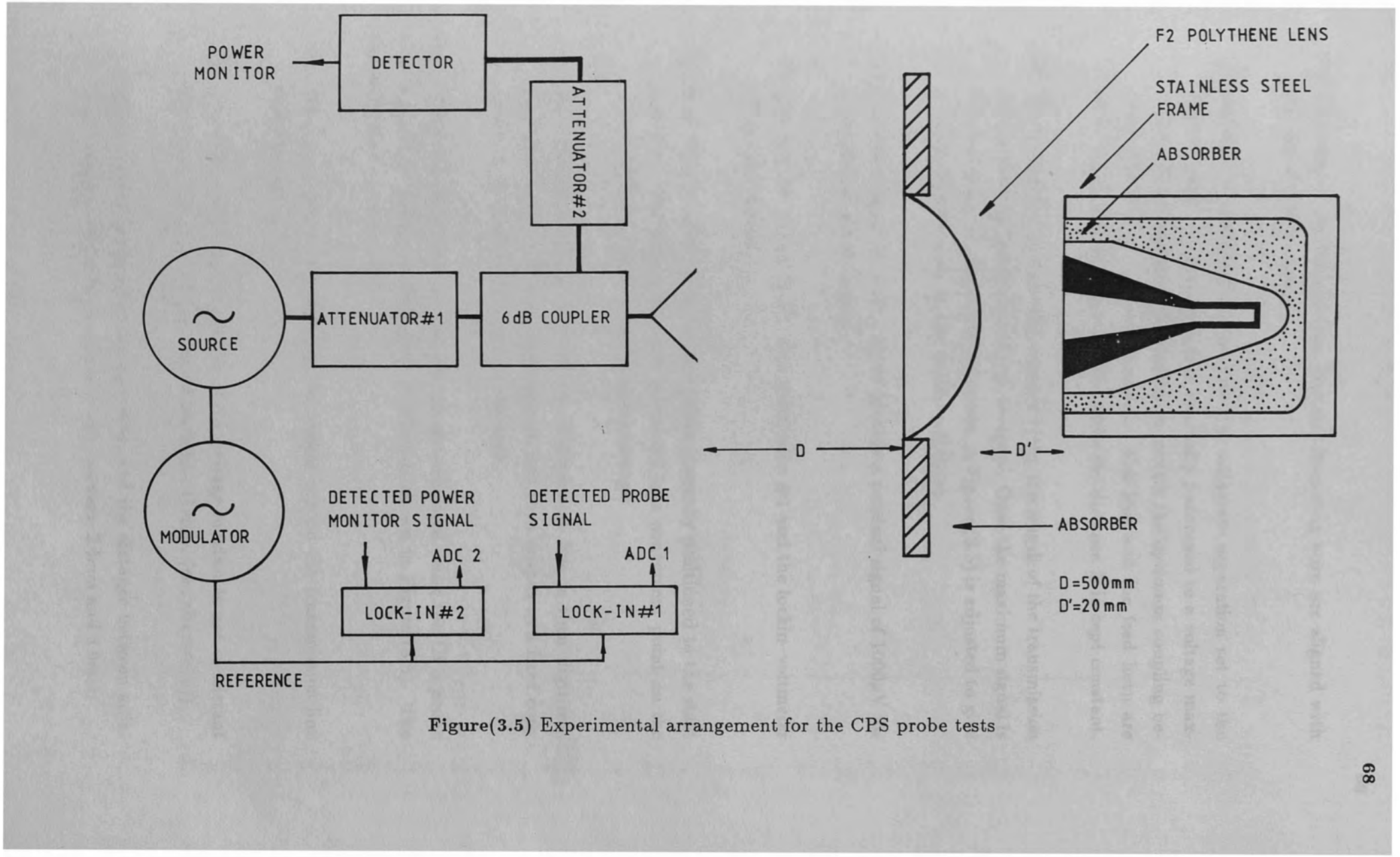

Figure(3.5) Experimental arrangement for the CPS probe tests

(b) The axes of the vee antenna, lens and launching horn are aligned with the aid of a HeNe laser.

(c) the R.F. is switched on, the probe to substrate separation set to the desired value. The probe is then manually positioned to a voltage maximum. The distance D' is adjusted to obtain the optimum coupling between the lens and the vee antenna. The lens and the feed horn are mounted on a sliding carriage, therefore the distance D is kept constant.

(d) The probe is then manually scanned along the length of the transmission line in order to locate the maximum signal. Once the maximum signal is located, then the attenuator #1 shown in Figure (3.5) is adjusted to give a full scale deflection on the lockin–voltmeter.

(e) The attenuator #2 is then set to provide a nominal signal of 1000μV for the power monitor system.

(f) The R.F. is "switched off" with attenuator #1 and the lockin–voltmeter offsets measured.

(g) The R.F. is switched on and the probe manually positioned to the start position. The start position is referenced to a convenient point on the circuit with the aid of a travelling microscope.

(h) The voltage standing wave on the transmission line is then digitized, corrected for source power fluctuations, and then output as a hard copy graph of detector output against distance.

The voltage standing wave on the test circuit measured using the CPS probe with a probe to substrate separation of $50\mu m$ is shown in Figure (3.6). The following features are noted:

(a) The probe picks up a signal in the region beyond the transmission line short circuit.

(b) The variation in the magnitude of the voltage maxima is not consistant that expected from simple transmission line theory. (see chapter(6))

(c) The shape of the maxima are distorted, and the distance between adjacent maxima and adjacent minima vary between $3.6mm$ and $3.9mm$.

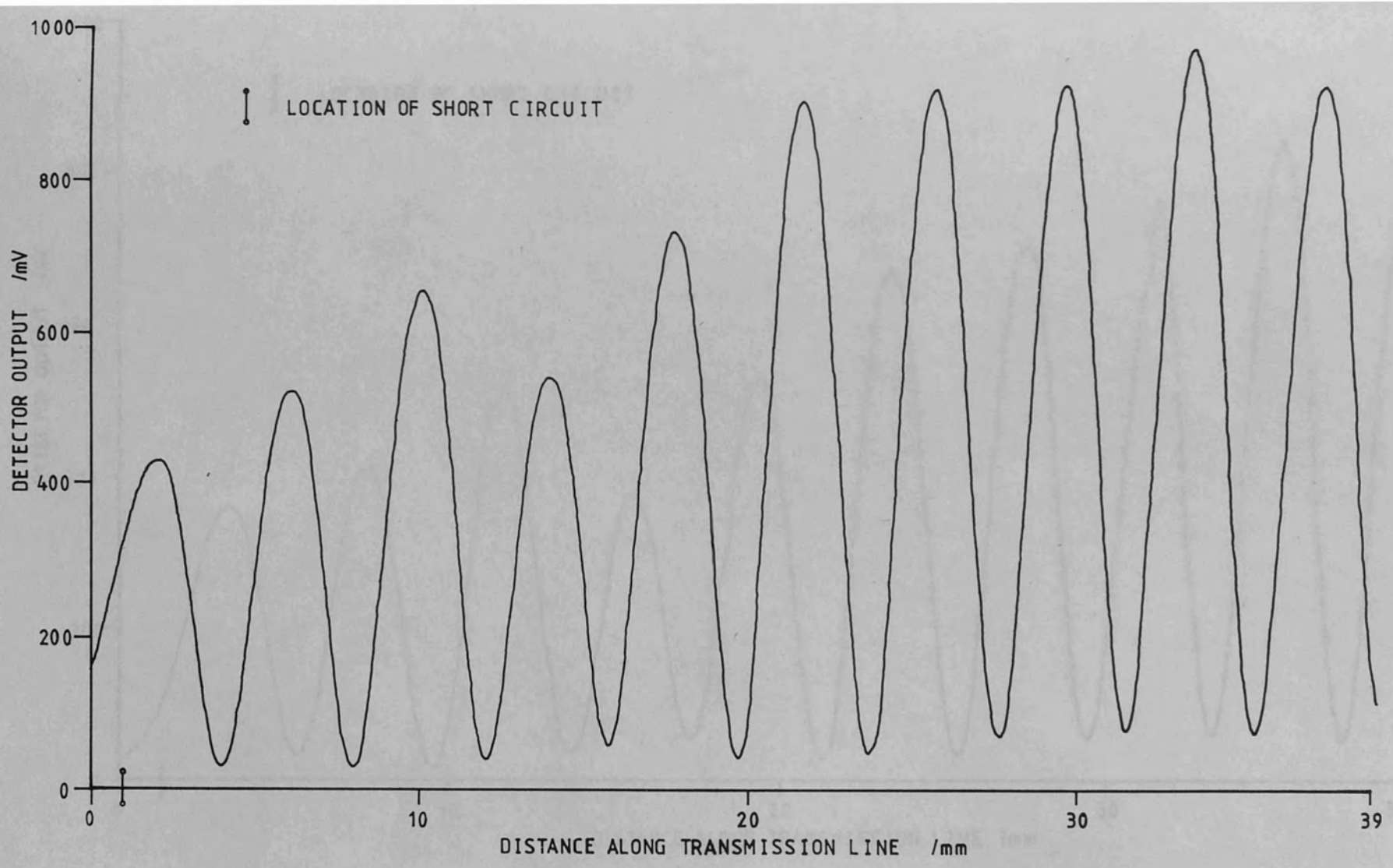

Figure(3.6) Measured voltage standing wave on a CPS transmission line using a probe to substrate separation of 50 μm

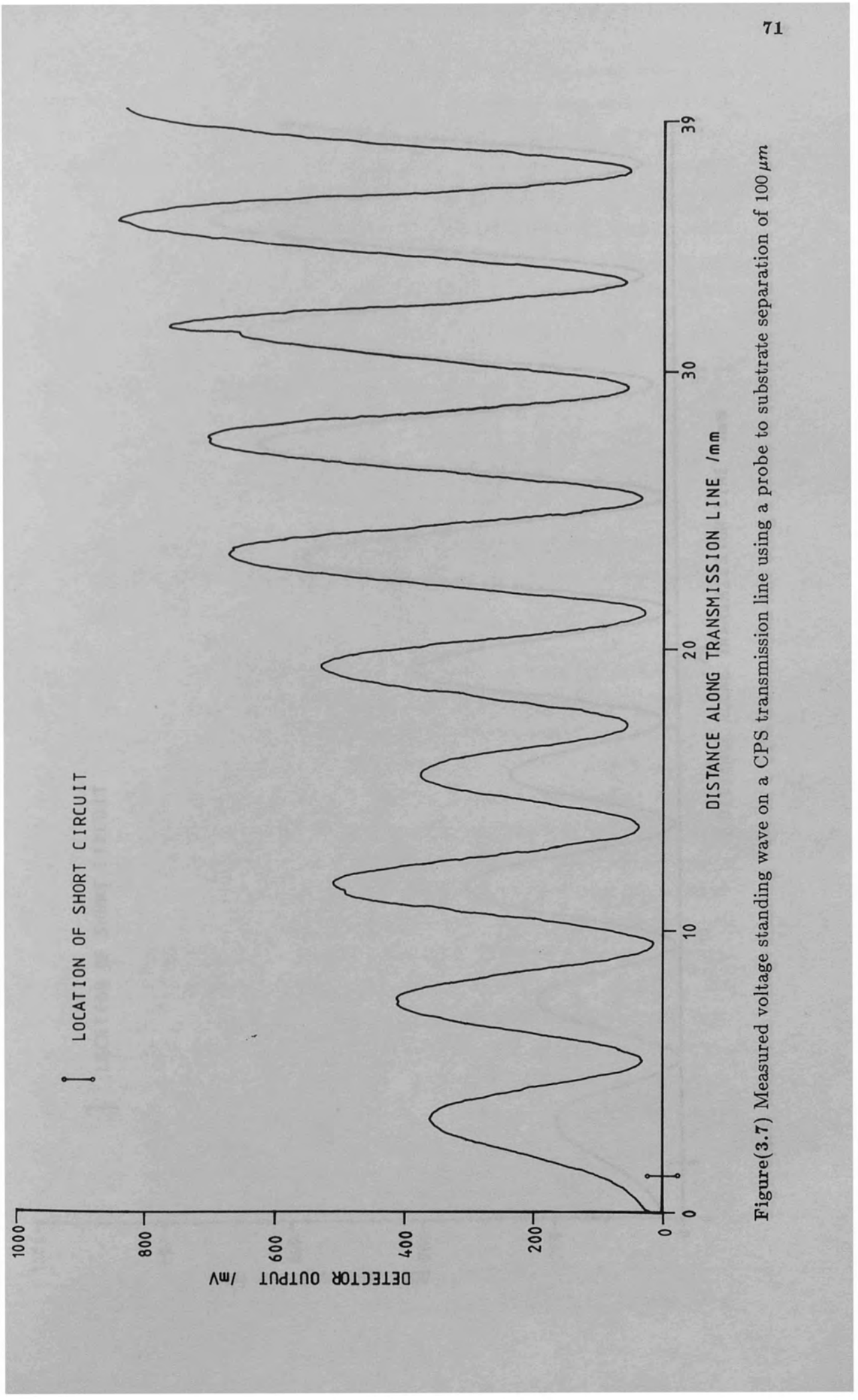

Figure(3.7) Measured voltage standing wave on a CPS transmission line using a probe to substrate separation of 100 μm

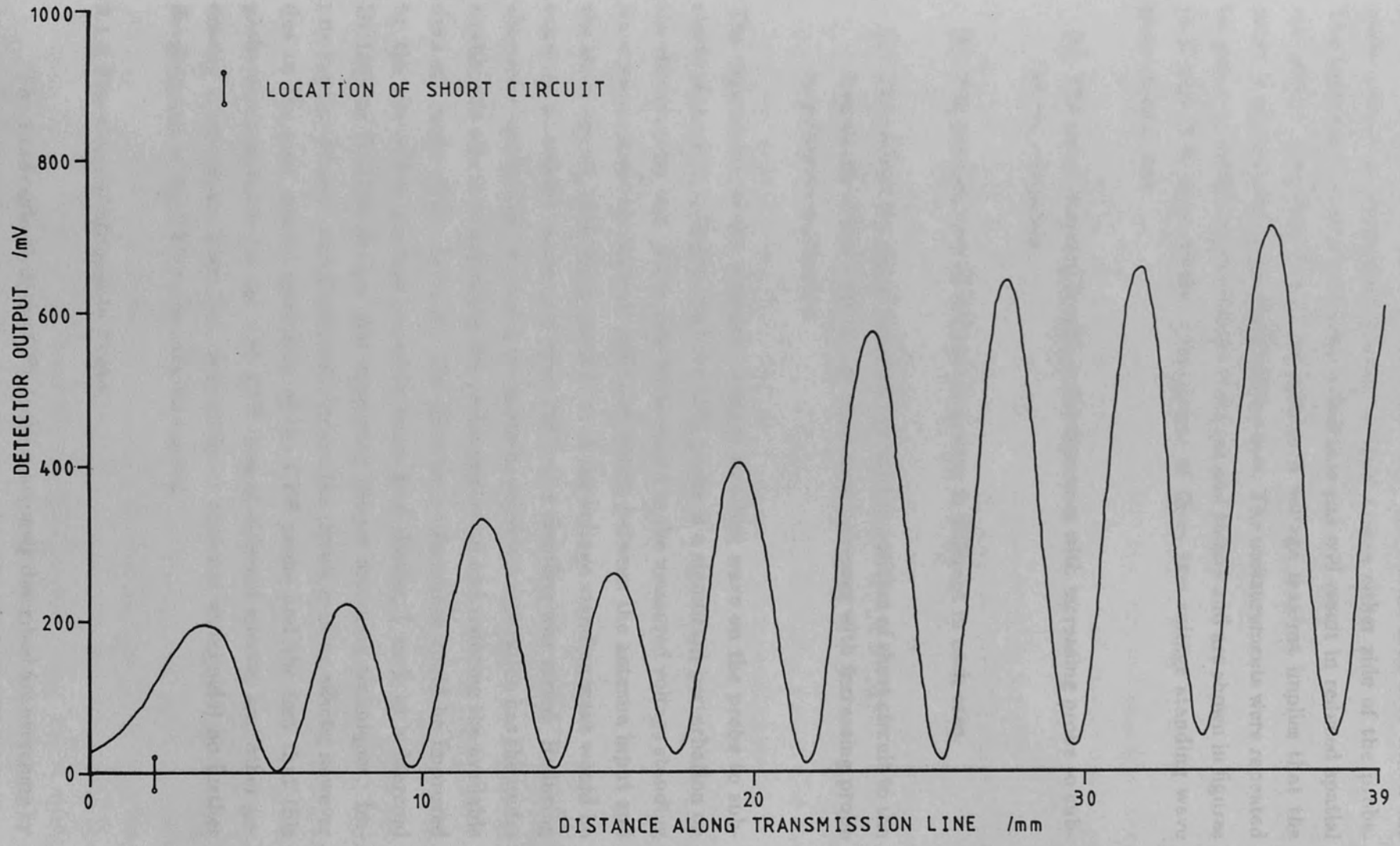

Figure(3.8) Measured voltage standing wave on a CPS transmission line using a probe to substrate separation of 150 μm

The finite probe response beyond the location of the transmission line short circuit indicates that the "capture area" (i.e. the circuit area over which the probe output is integrated) extends at least $1.0mm$ either side of the probe. The large capture area is clearly undesirable and will result in reduced spatial resolution. The distortion of the measured voltage maxima implies that the probe is overcoupled to the transmission line. The measurements were repeated for probe to substrate separations of $100\mu m$ and $150\mu m$ and are shown in figures (3.7) and (3.8) respectively. Comparison of these two voltage standing wave plots reveals that:

(a) The signal detected by the probe decreases with increasing probe to substrate separation.

(b) The general form of the standing wave is different in each case.

(c) The ratio of the signal detected beyond the position of short circuit to the magnitude of the first voltage maximum increases with increasing probe to substrate separation.

The dependance of the measured voltage standing wave on the probe to substrate separation indicates that the CPS probe is a significant perturbation on the circuit under test. If the non–uniformities in the measured voltage standing wave were caused by multiple reflection effects between the antenna input and the short circuit, then the general form of the voltage standing wave would be expected to remain unchanged when the probe coupling was varied. Reducing the probe coupling by increasing the probe to substrate separation has the undesirable side effects of degrading the probe resolution and reducing the available dynamic range of the detector. The detector performance could be improved by the use of low package parasitic beam lead diodes, (such as a Marconi DC1338 or DC1346 device) and employing proper matching techniques. Improving the detector matching would reduce the circuit loading effects; however due to the poor spatial resolution of the CPS probe and the fact that this probe was unsuitable for use with CPS lines of different spacing and other geometry transmission lines, (i.e. microstrip or coplanar waveguide) no further development of the CPS probe was attempted.

3.1.3 The Coaxial Monopole Probe.

The disadvantages of the CPS probe previously described are overcome by the use of the coaxial monopole probe illustrated in Figure (3.9). The coupling

from the circuit under test to the probe is by fringing electric field lines to the monopole and the coaxial outer conductor. Since the monopole is closer to the circuit under test more field lines will terminate on the monopole than on the sheath. This generates a potential difference across the coaxial inner and outer conductors and one can intuitively assert that this voltage will increase with increasing monopole height h since the number of electric field lines terminating on the monopole will increase, whilst the number of electric field lines terminating on the outer sheath will decrease. Clearly, the induced voltage will decrease with increasing probe to substrate separation d, the decay law being determined by the transmission line geometry. It is assumed that the probe interaction with the circuit is limited to the probe tip. This assumption is justifiable provided that the probe to substrate separation and monopole length are kept small with respect to the wavelength, and that the transmission line under test exhibits a rapid electric field decay with distance. The perturbing effect of the probe coaxial feed can be reduced by forming the outer sheath from a lossy metallization. The probe will produce a localized field distortion surrounding the transmission line under test which would be expected to give rise to an impedance discontinuity in the region of the probe, such perturbation is unavoidable and can only be minimized by employing probes that are physically small in comparison with the wavelength of the exciting source.

The voltage V generated across the inner and outer conductors is given by the line integral of the electric field around the contours $a \rightarrow b$ and $a' \rightarrow b'$ in Figure (3.10) or:

$$V = \int_a^b \vec{E}.\vec{dl} + \int_{a'}^{b'} \vec{E}.\vec{dl} \qquad 3.8$$

In order to calculate the voltage V by this method we must know the integration paths and the variation of the electric field on the integration paths. Even in the simple case considered, the calculation of V is an extremely difficult problem. The lack of an exact theory describing the nature of the probe coupling with factors such as probe to substrate separation, monopole length, and outer sheath diameter, required the effect of these factors to be investigated by experiment. Figure (3.10) also illustrates the manner in which the monopole probe will couple to a magnetic field; any magnetic flux linking the integration paths will give rise to a circuital *emf* in the detector circuit. When the magnetic field is uniform over the probe capture area, the circuital currents cancel in the probe monopole, leaving a net circuital *emf* around the path $b \rightarrow b'$. This path does not include the detector circuit, therefore the contribution to the detected probe output due to magnetic flux linkage will be zero. The coupling can also be visualized in terms of the electric displacement generated across the probe aperture by the circuital *emf*. In the case illustrated in Figure (3.10)

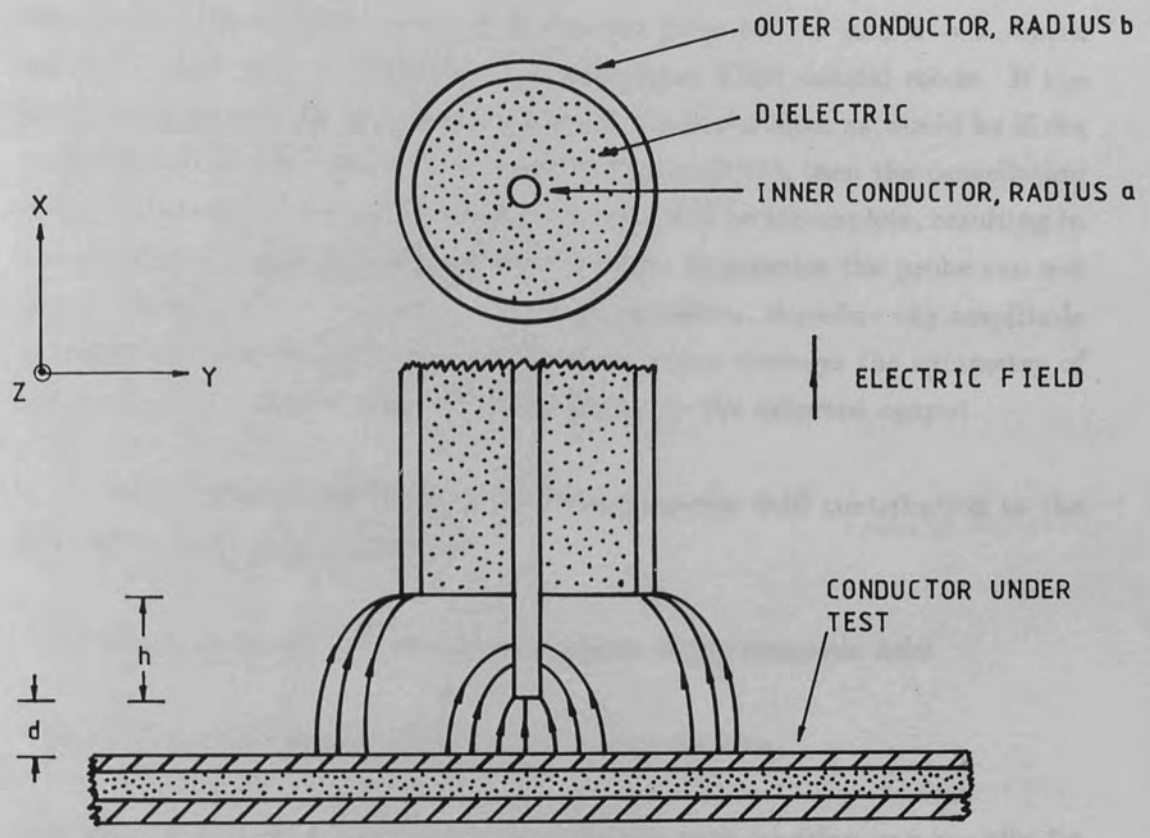

Figure (3.9) The coaxial monopole probe

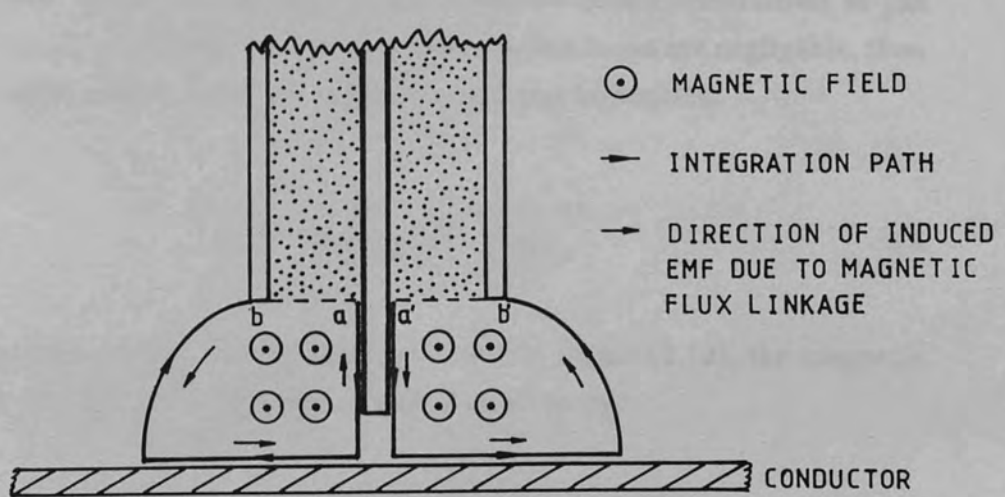

Figure (3.10) The evaluation of the probe output voltage

the electric displacement vector $\vec{D}$ is directed from $b' \rightarrow a'$ and $a \rightarrow b$, which will not couple very strongly to the fundamental TEM coaxial mode. If the integration paths were not symmetric about the probe axis, as would be if the probe monopole were bent as illustrated in Figure (3.11), then the cancellation of the currents i_1 and i_2 in the probe monopole will be incomplete, resulting in a magnetic contribution to the detector output. In practice the probe can not be considered small with respect to the field variations, therefore any amplitude or phase variation across the probe diameter which destroys the symmetry of the problem results in a magnetic contribution to the detected output.

To summarize, the magnitude of the magnetic field contribution to the detector output is dependant on:

(a) The local amplitude and phase gradient of the magnetic field.

(b) The size and symmetry of the probe capture area.

The rate of change of magnetic field intensity with position can usually be found without much difficulty, however the exact integration path that defines the probe capture area is not so easily calculated. We can use the approximate model developed for the probe response assuming that the transmission line is carrying a pure TEM wave (i.e. no component of electric or magnetic field in the direction of propagation) and that the probe response is limited to the vertical component of electric field over the conductor and the lateral magnetic field intensity. This approximate model enables an order of magnitude estimate of the relative weights of the electric and magnetic field contributions to the detector output. Assuming that the transmission line losses are negligable, then the longtitudinal variation of the magnetic field can be written:

$$B = B_0 \exp\big(j(\omega t - \beta z)\big) \qquad 3.9$$

Where: $B_0 = |\vec{B}|$ $\omega = 2\pi f$ $\beta = \frac{2\pi}{\lambda_g}$ With reference to Figure (3.12), the magnetic flux linking the two circuital paths A and A' is given by:

$$\xi = \oint \vec{E}.\vec{dl} = \frac{-\partial}{\partial t} \int_S \vec{B}.\vec{ds} \qquad 3.10$$

Assuming that the probe capture area is of the same order as the probe outer

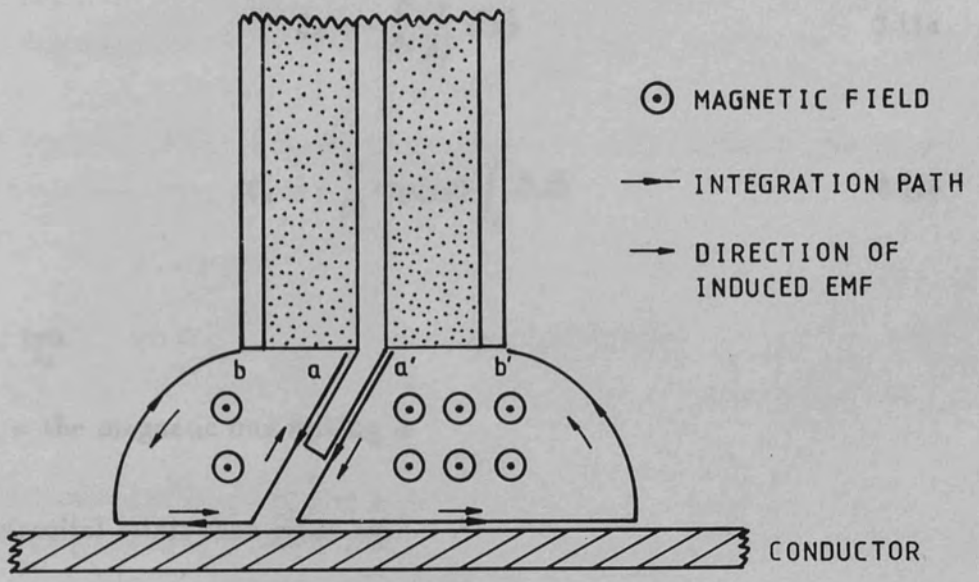

Figure (3.11) The effect of a bent probe monopole

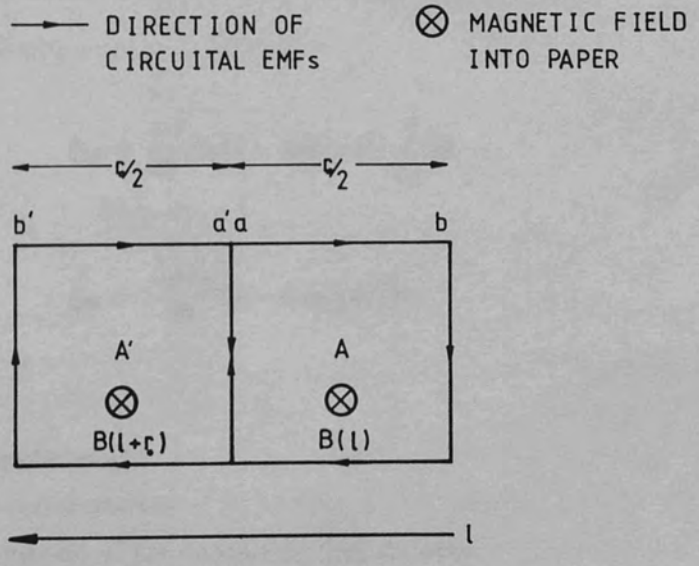

Figure (3.12) Circuital *emf*s due to a transverse magnetic field

sheath diameter then the difference in the magnetic flux density $\vec{B}$ linking the circuits A and A' is simply a phase difference of $2\pi r_0/\lambda_g$ radians where r_0 is the radius of the probe outer sheath. Therefore the circuital *emf*s in A and A' are:

$$\xi_A = -\frac{\partial}{\partial t}\int_S \vec{B}.\vec{ds} \qquad 3.11a$$

$$\xi'_A = -\frac{\partial}{\partial t}\exp(j\phi)\int_S \vec{B}.\vec{ds} \qquad 3.11b$$

Where:

$\phi = \frac{2\pi r_0}{\lambda_g}$

$\vec{B_A}$ = the magnetic flux linking A

The net circuital *emf* is then given by:

$$\xi_M = \xi'_A - \xi_A$$

$$\xi_M = -\frac{\partial}{\partial t}\int_S \vec{B_A}.\vec{ds}(1-\exp(j\phi)) \qquad 3.12$$

The induced *emf* due to the magnetic field can be expressed as:

$$\xi_M = \frac{-\partial}{\partial t}B_0(1-\exp(j\phi))\int_S ds$$

$$\xi_M = \frac{-\partial B_0}{\partial t}(1-\exp(j\phi))hr \qquad 3.13$$

Where:

h = the monopole length

r = the probe outer radius

B_0 = the magnitude of the magnetic flux density

Differentiating equation (3.13) with respect to time and separating into real and imaginary parts:

$$\xi_M = -\omega B_0[\sin(\phi) + j(1 - \cos(\phi))] \qquad 3.14$$

Where:

$\omega = 2\pi f$

f = frequency

Rewriting equation (3.14) in terms of the electric field intensity by the wave impedance relation then:

$$\xi_M = -\frac{\omega E_0 \sqrt{\epsilon_e}\mu_0}{377}[\sin(\phi) + j(1 - \cos(\phi))]hr \qquad 3.15$$

Where:

c =the velocity of light in free space

μ_0 =the permeability of free space

ϵ_e =the effective permittivity

Assuming that the probe to substrate separation is small, then the electric field contribution to the probe output will be approximately given by:

$$\xi_E = E_0 h \qquad 3.16$$

Therefore the total probe output is given by:

$$\xi_T = E_0 h - \frac{2\pi E_0 \sqrt{\epsilon_e} c\mu_0}{377\lambda_0}[\sin(\phi) + j(1 - cos(\phi))]hr$$

$$= E_0 h\left[1 - \frac{2\pi\sqrt{\epsilon_e} c\mu_0}{377\lambda_0}[\sin(\phi) + j(1 - cos(\phi))]r\right] \qquad 3.17$$

Separating equation (3.17) into real and imaginary parts and taking the modulus:

$$|\xi_T| = E_0 h\left\{1 - [2Ar\sin(\phi) + 2A^2r^2\cos(\phi) - 2A^2r^2]\right\}^{\frac{1}{2}} \qquad 3.18$$

Where:

$$A = \frac{2\pi\sqrt{\epsilon_e}\mu_0 c}{377\lambda_0}$$

Since the term in square brackets is small then using the binomial theorem we find:

$$|\xi_T| = E_0 h\{1 - [Ar\sin(\phi) + A^2 r^2 \cos(\phi) - A^2 r^2]\} \qquad 3.19$$

The phase error angle, defined as the deviation of $\arg(\xi_T)$ from $\arg(\xi_e)$ is given by:

$$\Delta\phi = \arctan\left\{\frac{Ar(1-\cos(\phi))}{(1 - Ar\sin(\phi)}\right\} \qquad 3.20$$

For the case when ϕ is small, equation (3.19) becomes:

$$|\xi_T| \approx E_0 h\left[1 - \frac{2\pi A' r^2}{{\lambda_0}^2}\right] \qquad 3.21$$

Where:

$$A' = \frac{2\pi\epsilon_e\mu_0 c}{377}$$

Therefore when the coaxial probe is being used to investigate a travelling wave excited on a TEM transmission line, then the amplitude measurement error, defined as ξ_M/ξ_E will decrease as the square of the wavelength, and increase linearly with increasing effective permittivity. Figures (3.13)a and(3.13)b show the variation of the amplitude and phase error ratio for coaxial probes with diameters of $0.5mm$, $0.25mm$, and $0.125mm$, and a monopole length equal to the radius. The line under test is assumed to have a relative effective permittivity of 1.7, which corresponds to a 50Ω line on RT–DUROID 5880 at a frequency of 35 GHz. At frequencies of 10 GHz and below the amplitude and phase errors predicted

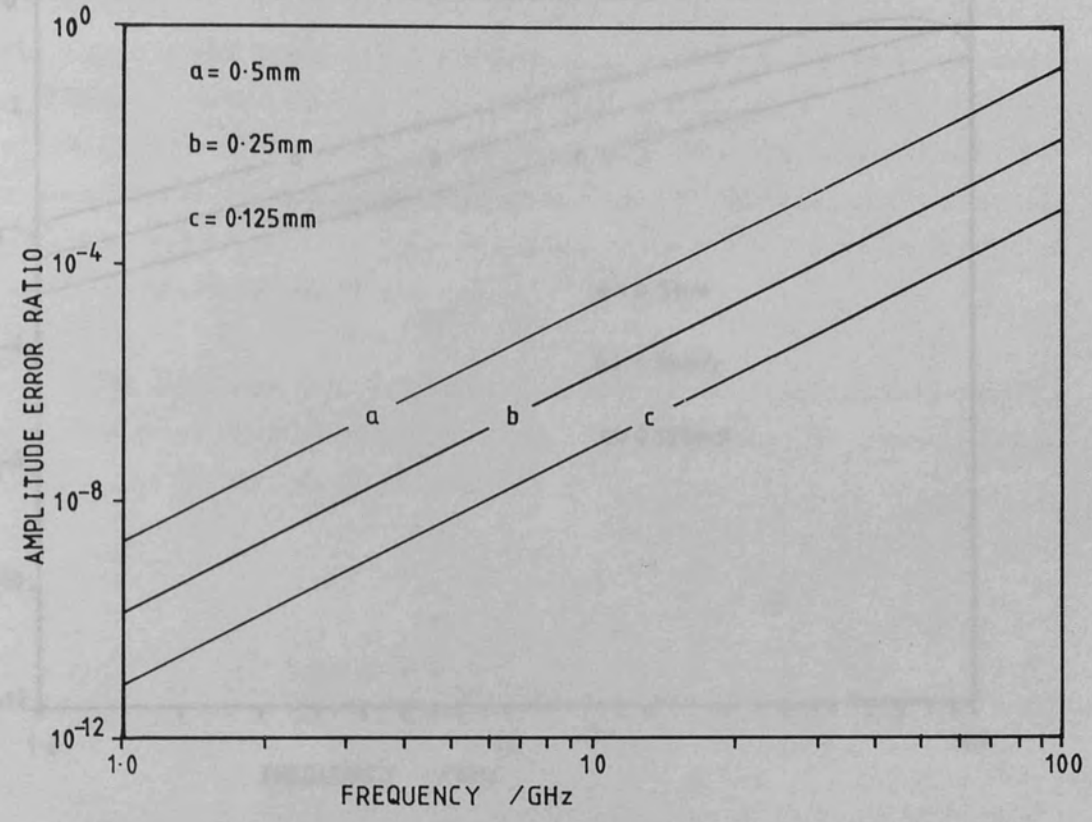

Figure (3.13)a Amplitude error against frequency, $\epsilon_e = 1.7$

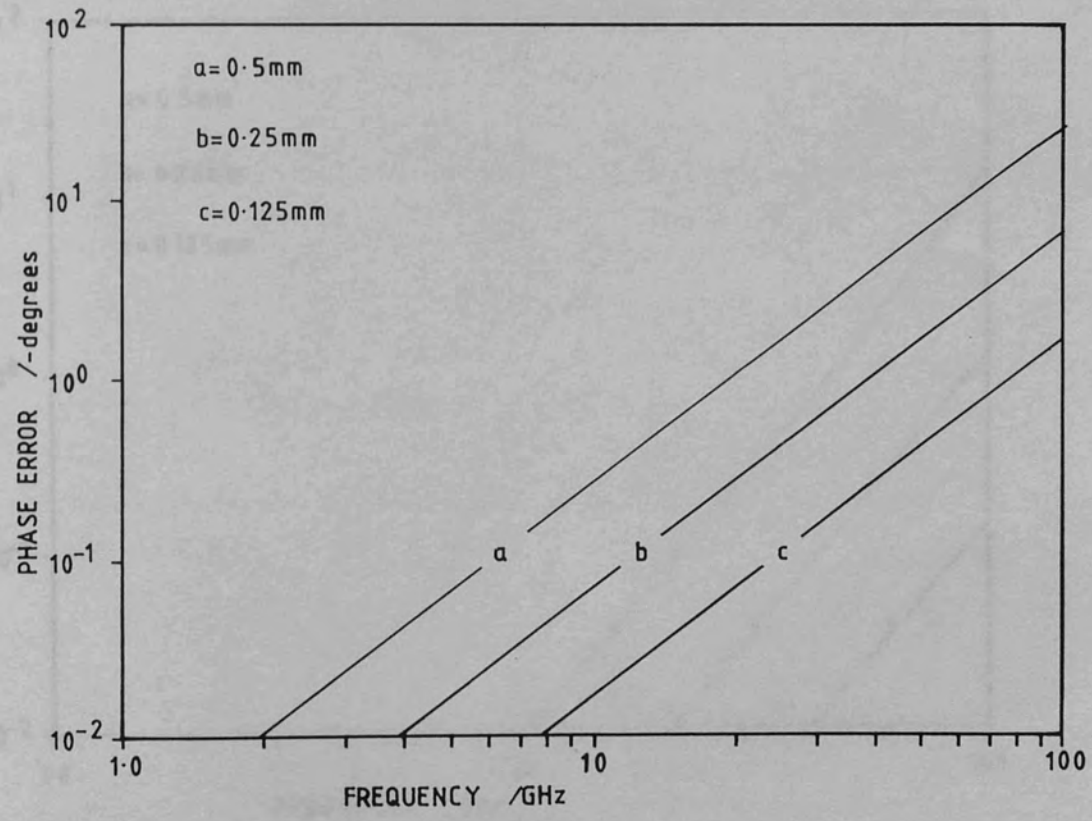

Figure (3.13)b Phase error against frequency, $\epsilon_e = 1.7$

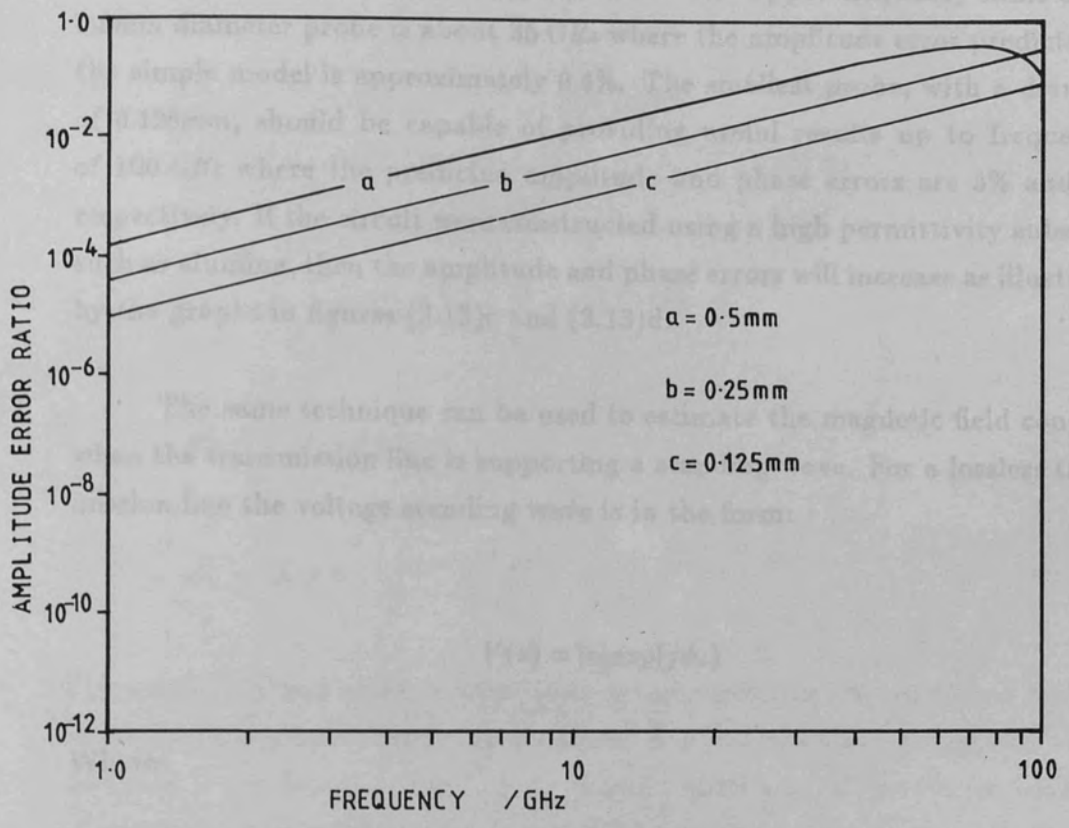

Figure (3.13)c Amplitude error against frequency, $\epsilon_e = 5.7$

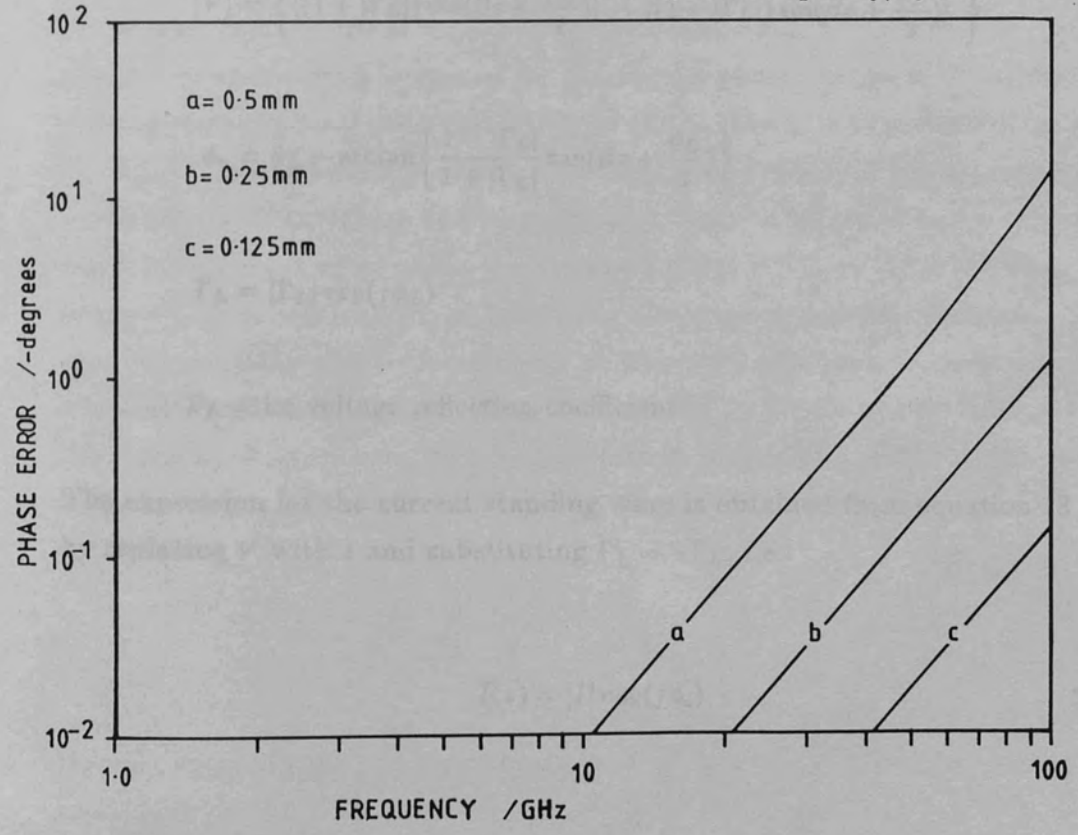

Figure (3.13)d Phase error against frequency, $\epsilon_e = 5.7$

are negligibly small for all the probe sizes. The upper frequency limit of the $0.5mm$ diameter probe is about 35 GHz where the amplitude error predicted by the simple model is approximately 0.6%. The smallest probe, with a diameter of $0.125mm$, should be capable of providing useful results up to frequencies of 100 GHz where the predicted amplitude and phase errors are 3% and 0.1° respectively. If the circuit were constructed using a high permittivity substrate such as alumina, then the amplitude and phase errors will increase as illustrated by the graphs in figures (3.13)c and (3.13)d.

The same technique can be used to estimate the magnetic field coupling when the transmission line is supporting a standing wave. For a lossless transmission line the voltage standing wave is in the form:

$$V(z) = |v| \exp(j\phi_v) \qquad 3.22$$

Where:

$$|V| = \left\{ [(1 + |\Gamma_L|) \cos(\beta z + \frac{\phi_L}{2})]^2 + [(1 - |\Gamma_L|) \sin(\beta z + \frac{\phi_L}{2})]^2 \right\}^{\frac{1}{2}}$$

$$\phi_v = \phi_L - \arctan\left\{ \frac{1 - |\Gamma_L|}{1 + |\Gamma_L|} \tan(\beta z + \frac{\phi_L}{2}) \right\}$$

$$\Gamma_L = |\Gamma_L| \exp(j\phi_L)$$

Γ_L =the voltage reflection coefficient

The expression for the current standing wave is obtained from equation (3.22) by replacing V with I and substituting $\Gamma'_L = -\Gamma_L$, i.e.:

$$I(z) = |I| \exp(j\phi_i) \qquad 3.23$$

Where:

$$|I| = \left\{ [(1 + |\Gamma'_L|)\cos(\beta z + \frac{\phi'_L}{2})]^2 + [(1 - |\Gamma'_L|)\sin(\beta z + \frac{\phi'_L}{2})]^2 \right\}^{\frac{1}{2}}$$

$$\phi_i = \phi'_L - \arctan\left\{ \frac{1 - |\Gamma'_L|}{1 + |\Gamma'_L|} \tan(\beta z + \frac{\phi'_L}{2}) \right\}$$

$$\Gamma'_L = |\Gamma_L| \exp(j\phi'_L)$$

$$\phi'_L = \phi_L + \pi$$

The amplitude and phase components are sketched in Figure (3.14) for the case of a perfect open circuit termination. The current and voltage amplitude variation is the familiar standing wave form, with a $\lambda_g/2$ periodicity between adjacent pairs of maxima or minima. The first maximum in the voltage and current standing waves occur at positions of $\lambda_g/2$ and $\lambda_g/4$ from the open circuit. The phase of the voltage and current standing waves are seen to vary in a "staircase" fashion, changing abruptly by π radians at the voltage or current minima respectively. The reason for the abrupt phase change is illustrated by the sequence of phasor diagrams in Figure (3.15). We note that the voltage and current phase is indeterminate when the forward and reflected voltage or current waves cancel. The voltage and current phase takes on values of $\phi_0 \pm \pi$ where ϕ_0 is the initial phase offset and n is an integer. If $|V_r| \neq |V_i|$, or $|I_r| \neq |I_i|$, then the phase will vary continuously in traversing a voltage or current minimum . The significance of the phase discontinuity at a current minimum to measurements made with coaxial monopole probes is illustrated by Figure (3.16). By applying the right hand screw rule, the circuital *emf*s in the circuits A and A' are found to be equal and add in phase. Therefore the net *emf* is given by:

$$\xi_T = \xi_A - \xi'_A \qquad 3.24$$

From equation (3.10) and the symmetry of the current standing wave about a minimum:

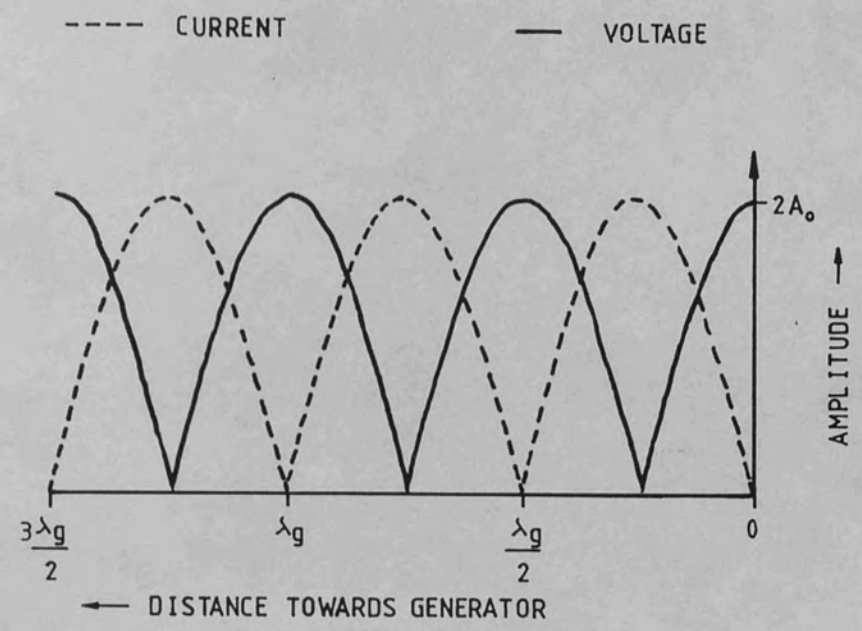

Figure (3.14)a Amplitude variation along an open circuit TEM transmission line

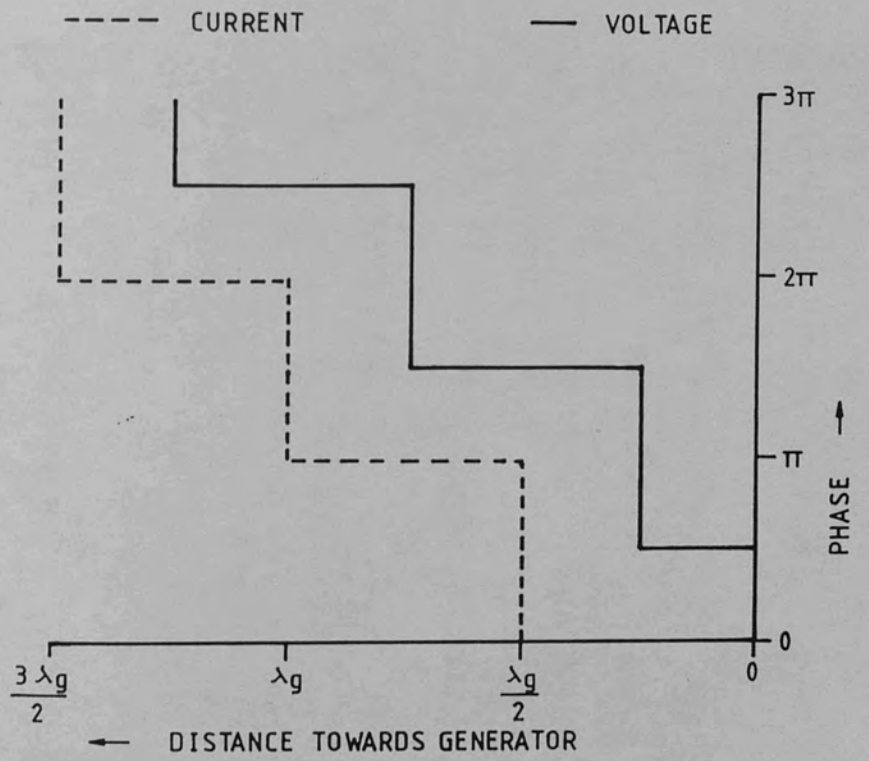

Figure (3.14)b Phase variation along an open circuit TEM transmission line

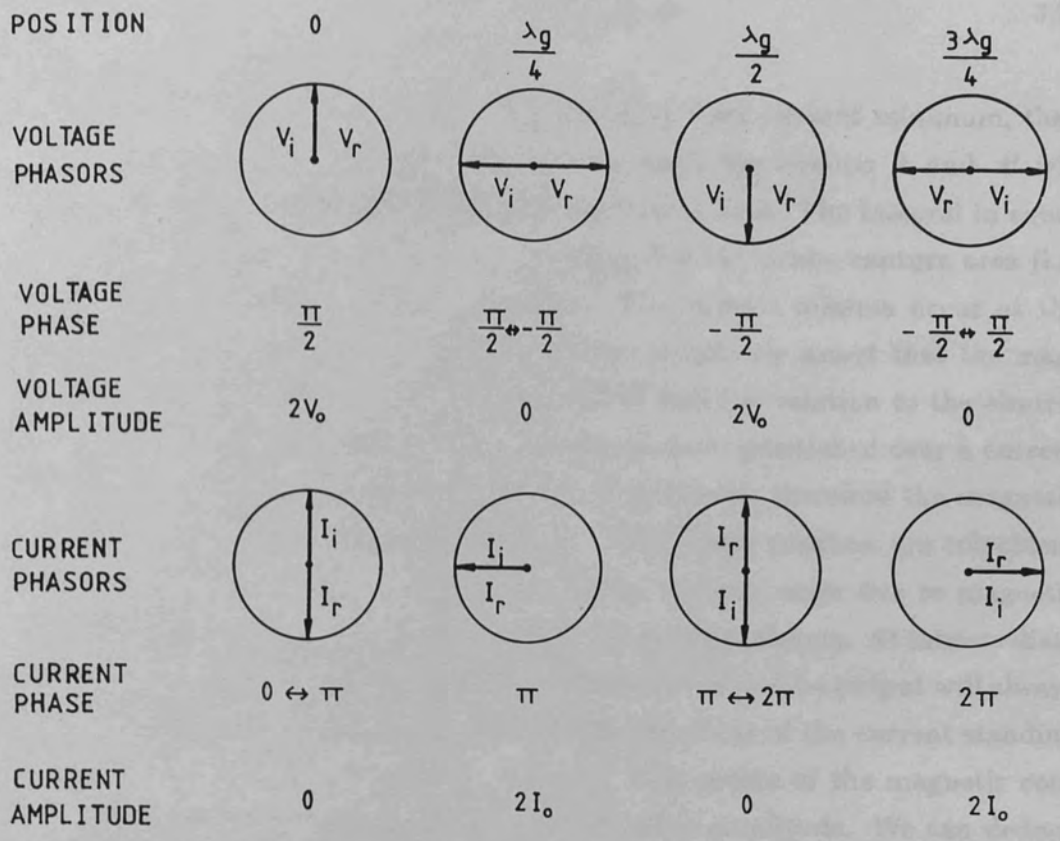

Figure (3.15) Phasor diagrams illustrating the abrupt phase change at a voltage minimum

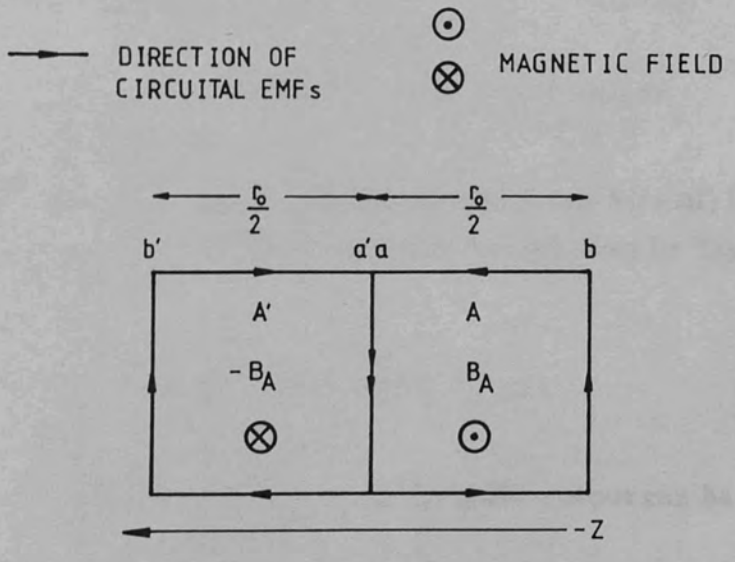

Figure (3.16) Probe circuital *emfs* at a current standing wave minimum

$$\xi_T = -2\frac{\partial}{\partial t}\int_s \vec{B_A}.\vec{ds} \qquad 3.25$$

Since we are considering the case of a standing wave current minimum, then the magnitude of the magnetic flux linking with the circuits A and A' will approach zero for the high VSWR case considered here. The integral in equation (3.25) will also approach zero providing that the probe capture area (i.e. the area enclosed by A and A') is small. The current minima occur at the same position as voltage maxima, so one can intuitively assert that the magnetic contribution to the probe output will be small in relation to the electric field contribution. When the probe is symmetrically positioned over a current maximum then the circuital *emf*s are found to cancel, therefore the magnetic contribution to the probe output is zero. The current maxima are coincident with the voltage minima, so ideally we expect minimal error due to magnetic field coupling when measuring the level of the voltage minima. At intermediate positions between the current maxima and minima the probe output will always contain a magnetic contribution even though the phase of the current standing wave is constant between adjacent minima. The source of the magnetic coupling is the gradient of the current standing wave amplitude. We can deduce from Figure (3.17) that the circuital *emf*s will oppose each other, however the cancellation is incomplete since the magnetic flux linkage though the circuits A and A' is not equal. To a good approximation the magnetic flux density linking with A and A' can be assumed to be uniform and given by the magnitude of $\vec{B}$ located at the mid points of the circuital paths. Therefore from equations (3.17) and (3.21) the net *emf* is given by:

$$\xi_M = -\frac{\partial}{\partial t}\int_S B(l+\Delta l).ds + \frac{\partial}{\partial t}\int_S B(l).ds \qquad 3.26$$

Where $B(l)$ is the magnetic flux density through A and $B(l+\Delta l)$ is the magnetic flux density through A'. If the probe radius is small, then by Taylor's theorem:

$$B(l+\Delta l) = B(l) + \frac{dB}{dl}\Delta l + ... \qquad 3.27$$

Therefore the magnetic contribution to the probe output can be written:

$$\xi_M = \frac{\partial}{\partial t}\int_S \frac{dB}{dl}\Delta l.ds \qquad 3.28$$

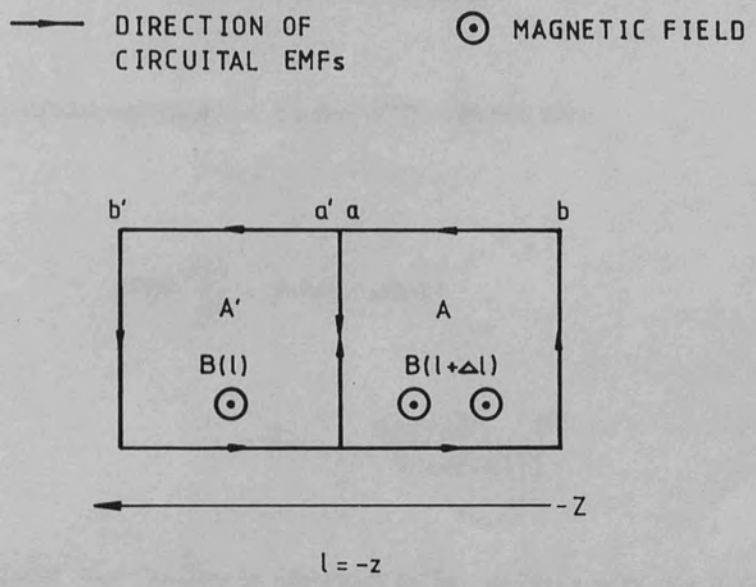

Figure (3.17) Probe circuital *emf*s at an arbitrary position in a current standing wave

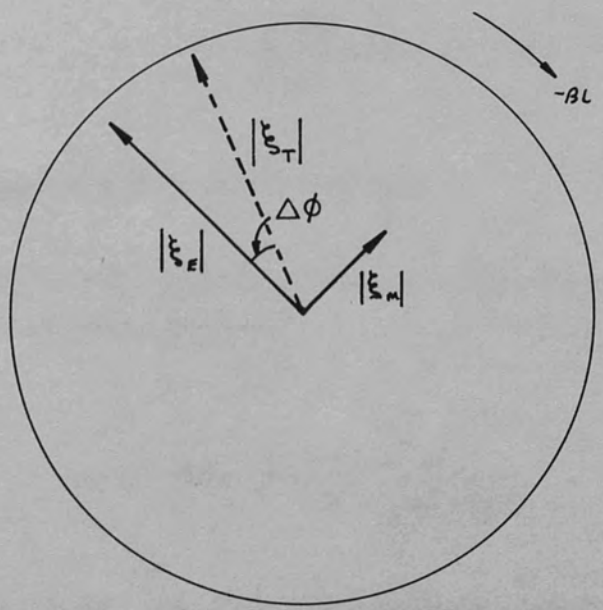

Figure (3.18) Phasor representation of ξ_M and ξ_E

The longtitudinal variation of the magnetic flux density B is of the same form as the longtitudinal variation of current in the transmission line, i.e.:

$$B(l) = B_0(2 - 2\cos(2\beta l))^{\frac{1}{2}} \qquad 3.29$$

Therefore differentiating equation (3.29) with respect to l:

$$2B(l)\frac{dB}{dl} = {B_0}^2 4\beta \sin(2\beta l)$$

$$\frac{dB}{dl} = 2B_0\left\{\frac{\beta\sin(2\beta l)}{(2 - 2\cos(2\beta l))}\right\}^{\frac{1}{2}} \qquad 3.30$$

Since the magnetic flux density is assumed to be uniform over the areas A and A', then equation (3.28) can be rearranged to give:

$$\xi_M = -\frac{\partial}{\partial t}\frac{dB}{dl}\Delta l \int_S ds$$

$$= -\frac{\partial}{\partial t}\frac{dB}{dl}\Delta l A_e \qquad 3.31$$

Where A_e is the area bound by the circuital loop.

Substituting for $\frac{dB}{dl}$ and differentiating equation (3.29) with respect to the implicitly assumed time factor $\exp(j\omega t)$:

$$\xi_M = -j2B_0\omega\Delta l A_e \frac{\sin(2\beta l)}{(2 - 2\cos(2\beta l))^{\frac{1}{2}}} \qquad 3.32$$

In order to find the relative magnitude of the magnetic contribution to the total voltage at the probe output terminals, equation (3.32) needs to be expressed in terms of the the peak electric field intensity E_0. The electric and magnetic field intensities are related by:

$$\frac{E}{H} = 377\left(\frac{\mu_e}{\epsilon_e}\right)^{\frac{1}{2}} \qquad 3.33$$

Where μ_e and ϵ_e are the effective permeability and permittivity of the transmission line. In terms of the magnetic flux density B, equation (3.33) becomes:

$$\frac{E}{B} = 377\left(\frac{\mu_e}{\epsilon_e}\right)^{\frac{1}{2}} \frac{1}{\mu_e \mu_0} \qquad 3.34$$

Combining equations (3.32) and (3.34) and assuming that the substrate material is non magnetic then:

$$\xi_M = -j2E_0\omega \frac{\sqrt{\epsilon_e}\mu_0}{377} \Delta l A_e \frac{\beta \sin(2\beta l)}{(2 - 2\cos(2\beta l))^{\frac{1}{2}}} \qquad 3.35$$

After some minor rearrangement, finally:

$$\xi_M = -j \frac{8E_0\epsilon_e\mu_0 c\pi^2}{377\lambda_0^2} A_e \Delta l \frac{\sin(2\beta l)}{(2 - 2\cos(2\beta l))^{\frac{1}{2}}} \qquad 3.36$$

Equation (3.36) clearly identifies the functional dependances of the induced *emf* due to magnetic coupling. It is noted that:

(a) The magnitude of ξ_M is proportional to the inverse square of the free space wavelength λ_0.

(b) ξ_M increases linearly with increasing effective permittivity. Therefore when investigating transmission line geometries such as microstrip, we would expect a higher measurement error due to magnetic coupling when the circuit is fabricated on a high dielectric constant material. Since the effective permittivity is a function of linewidth, the measurement error due to magnetic coupling will also be a function of linewidth.

(c) ξ_M is proportional to the product of the area enclosed by one circuital loop and the separation of the loop centres Δl. Both these factors are functions of the probe outer sheath diameter and the monopole length.

(d) ξ_M is always in phase quadrature with the electric field on the transmission line.

Assuming that the electric field in the region of the probe is parallel to probe monopole (i.e. perpendicular to the conductor surface) then the electric field contribution to the probe output is given by:

$$\xi_E = E(l)h \tag{3.37}$$

Where:

$$E(l) = E_0(2 + 2\cos(2\beta l))^{\frac{1}{2}}$$

The measured probe signal is given by $|\xi_T|$ or:

$$\begin{aligned}\xi_T &= \xi_E + \xi_M \\ &= E_0 h(2 + 2\cos(2\beta l))^{\frac{1}{2}} - j\frac{8E_0\epsilon_e\mu_0 c\pi^2}{377\lambda_0^2} A_e \Delta l \frac{\sin(2\beta l)}{(2 - 2\cos(2\beta l))^{\frac{1}{2}}}\end{aligned} \tag{3.38}$$

$$|\xi_T| = E_0 h(2 + 2\cos(2\beta l))^{\frac{1}{2}} \left\{1 + \left[\frac{8E_0\epsilon_e\mu_0 c\pi^2}{377\lambda_0^2}\right]^2 \frac{\sin^2(2\beta l)}{(2 - 2\cos(2\beta l))} \frac{r^4}{(2 + 2\cos(2\beta l))}\right\}^{\frac{1}{2}}$$

$$= E_0 h(2 + 2\cos(2\beta l))^{\frac{1}{2}} \left\{1 + \left[\frac{4\epsilon_e\mu_0 c\pi^2}{377\lambda_0^2}\right]^2 r^4\right\}^{\frac{1}{2}} \tag{3.39}$$

Since the fractional term in the square brackets is usually small compared to unity, then using the binomial expansion equation (3.39) becomes:

$$|\xi_T| = E_0 h(2 + 2\cos(2\beta l))^{\frac{1}{2}} \left\{1 + 8\left[\frac{\epsilon_e\mu_0 c\pi^2}{377\lambda_0^2}\right]^2 r^4\right\} \tag{3.40}$$

The phasor diagram in Figure (3.18) illustrates the quadrature relation between ξ_E and ξ_M. The phase error $\Delta\phi$ due to magnetic coupling is given simply by $\arg(\xi_T)$ or:

$$\Delta\phi = \arctan\left\{\frac{-4\epsilon_e\mu_0 c\pi^2}{377\lambda_0^2}r^2\right\} \qquad 3.41$$

The resulting expressions for the amplitude and phase of the probe output voltage show that the errors introduced by magnetic coupling are independant of the probe's position when measuring high VSWRs on TEM transmission lines. Both expressions decrease rapidly with increasing wavelength for a given probe outer sheath diameter. The graphs in Figure (3.19) illustrate the variation of the amplitude and phase errors as a function of frequency for probe diameters of $0.5mm$, $0.25mm$, and $0.125mm$. The probes are assumed to be operating with a small probe to substrate separation, and the transmission line under test assumed to have a relative permittivity of 1.7. The graphs show that amplitude and phase errors are completely negligable for the $0.5mm$ diameter probe at frequencies below 10 GHz. At frequencies of the order of 35 GHz, the amplitude and phase errors are 0.2% and 3° for the $0.5mm$ diameter probe. At frequencies approaching 100 GHz the errors become unacceptably high with the $0.5mm$ diameter probe, indicating that the smaller diameter probes must be employed. It is interesting to note that the $0.125mm$ diameter probe should be capable of providing useful results at frequencies around 100 GHz. Figures (3.19)c and (3.19)d indicate the magnitude of the amplitude and phase errors when the same probes are used to investigate a transmission line with a relative permittivity of 5.7.

These order of magnitude errors have been calculated assuming that:

(a) The transmission line propagates a pure TEM mode.

(b) The transmission line supports a pure standing wave, i.e. no account is taken of multiple standing wave effects such as generated by mismatched connectors or transitions.

(c) The probe 'capture area' is limited in extent to approximately the diameter of the probe outer sheath which is only a good approximation for small monopole lengths and small probe to substrate separations.

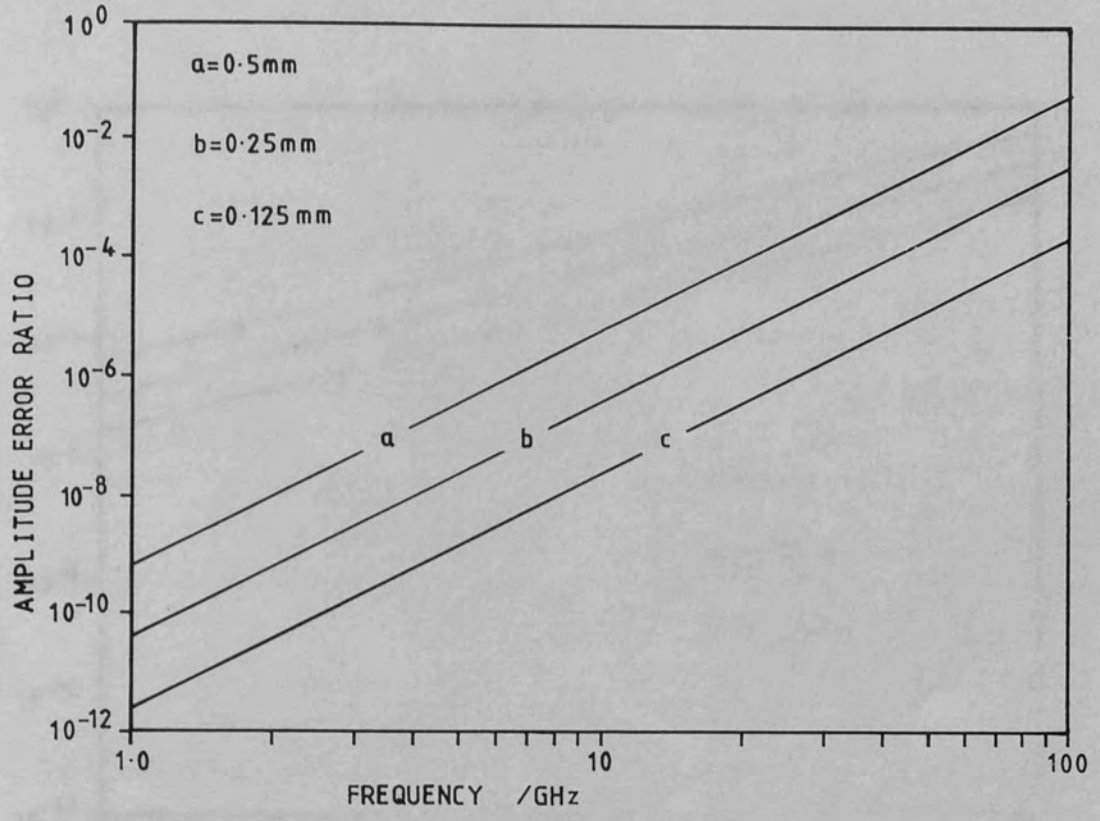

Figure (3.19)a Amplitude error against frequency, $\epsilon_e = 1.7$

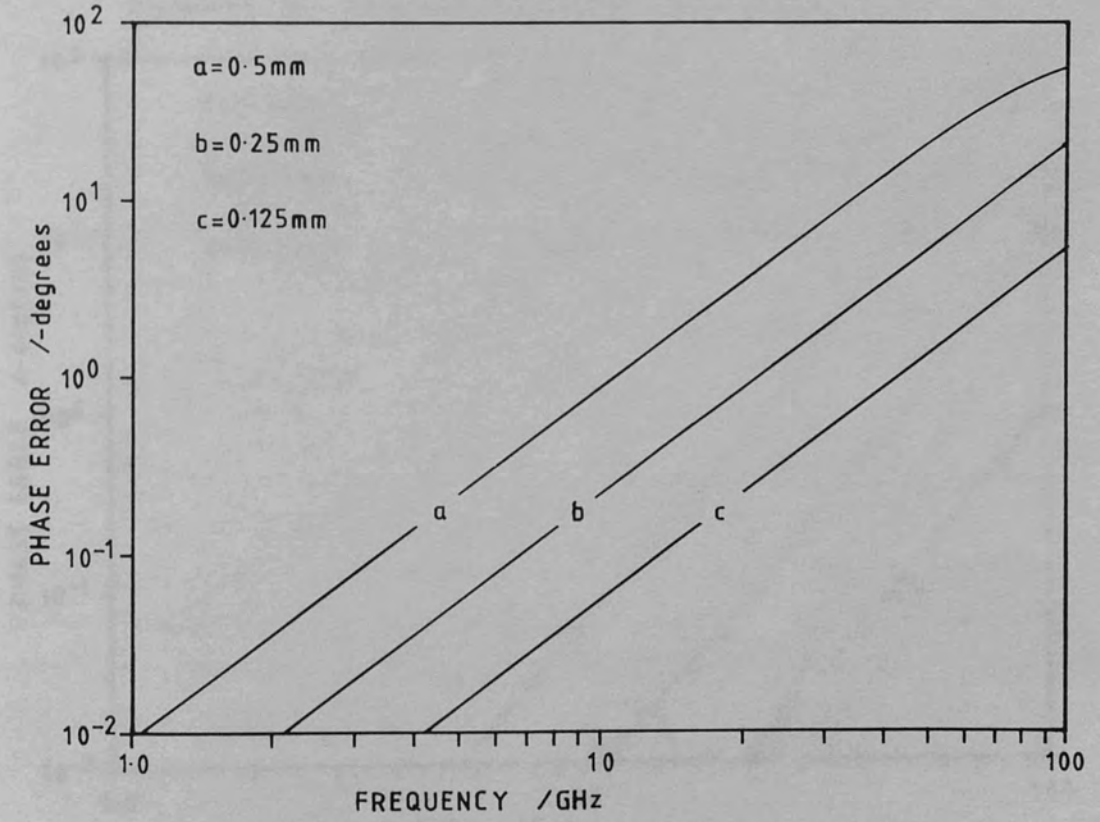

Figure (3.19)b Phase error against frequency, $\epsilon_e = 1.7$

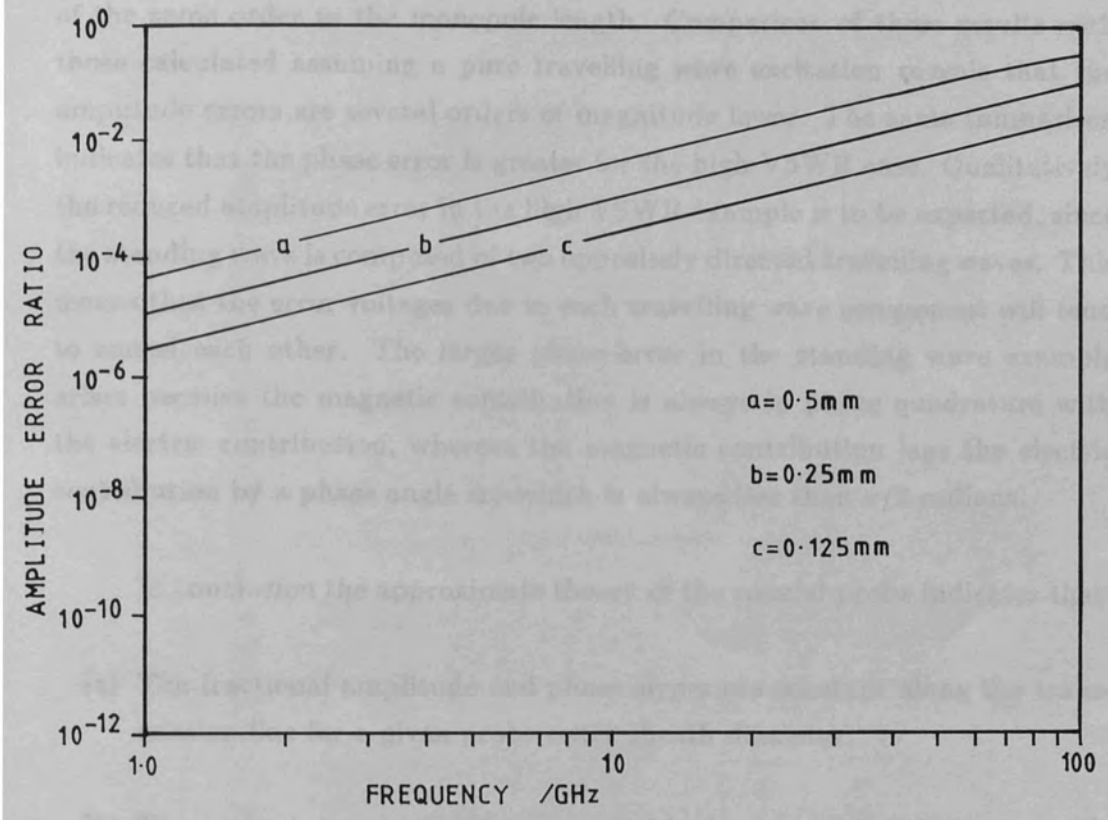

Figure (3.19)c Amplitude error against frequency, $\epsilon_e = 5.7$

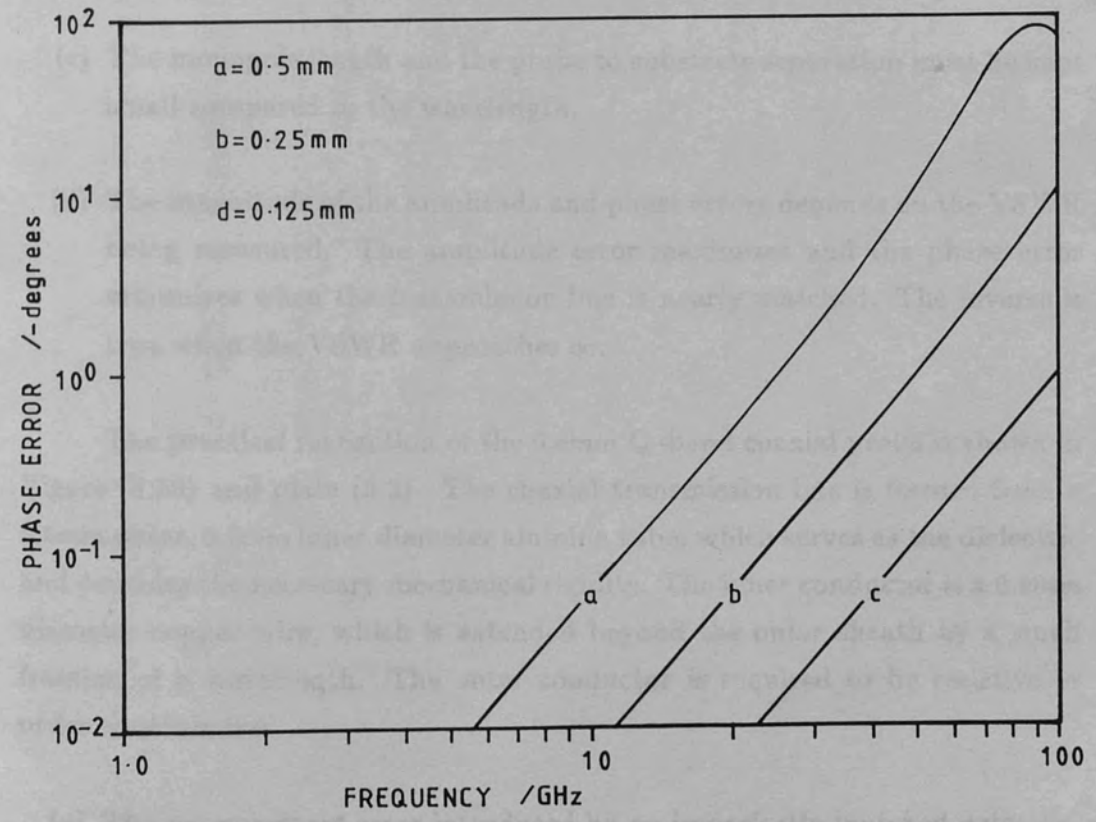

Figure (3.19)d Phase error against frequency, $\epsilon_e = 5.7$

These calculations are thus invalid when the probe is used to investigate non–TEM geometries such as slotline, or when the probe to substrate separation is of the same order as the monopole length. Comparison of these results with those calculated assuming a pure travelling wave excitation reveals that the amplitude errors are several orders of magnitude lower. The same comparison indicates that the phase error is greater for the high VSWR case. Qualitatively the reduced amplitude error in the high VSWR example is to be expected, since the standing wave is composed of two oppositely directed travelling waves. This means that the error voltages due to each travelling wave component will tend to cancel each other. The larger phase error in the standing wave example arises because the magnetic contribution is always in phase quadrature with the electric contribution, whereas the magnetic contribution lags the electric contribution by a phase angle $\Delta\phi$ which is always less than $\pi/2$ radians.

In conclusion the approximate theory of the coaxial probe indicates that:

(a) The fractional amplitude and phase errors are constant along the transmission line for a given probe outer sheath diameter.

(b) The probe outer sheath diameter must be kept small in relation to guide wavelength.

(c) The monopole length and the probe to substrate separation must be kept small compared to the wavelength.

(d) The magnitude of the amplitude and phase errors depends on the VSWR being measured. The amplitude error maximizes and the phase error minimizes when the transmission line is nearly matched. The inverse is true when the VSWR approaches ∞.

The practical realization of the $0.5mm$ Q–band coaxial probe is shown in Figure (3.20) and plate (3.2). The coaxial transmission line is formed from a $0.5mm$ outer, $0.2mm$ inner diameter alumina tube, which serves as the dielectric and provides the necessary mechanical rigidity. The inner conductor is a $0.1mm$ diameter copper wire, which is extended beyond the outer sheath by a small fraction of a wavelength. The outer conductor is required to be resistive in order to minimize:

(a) The measurement error introduced by an imperfectly matched detector.

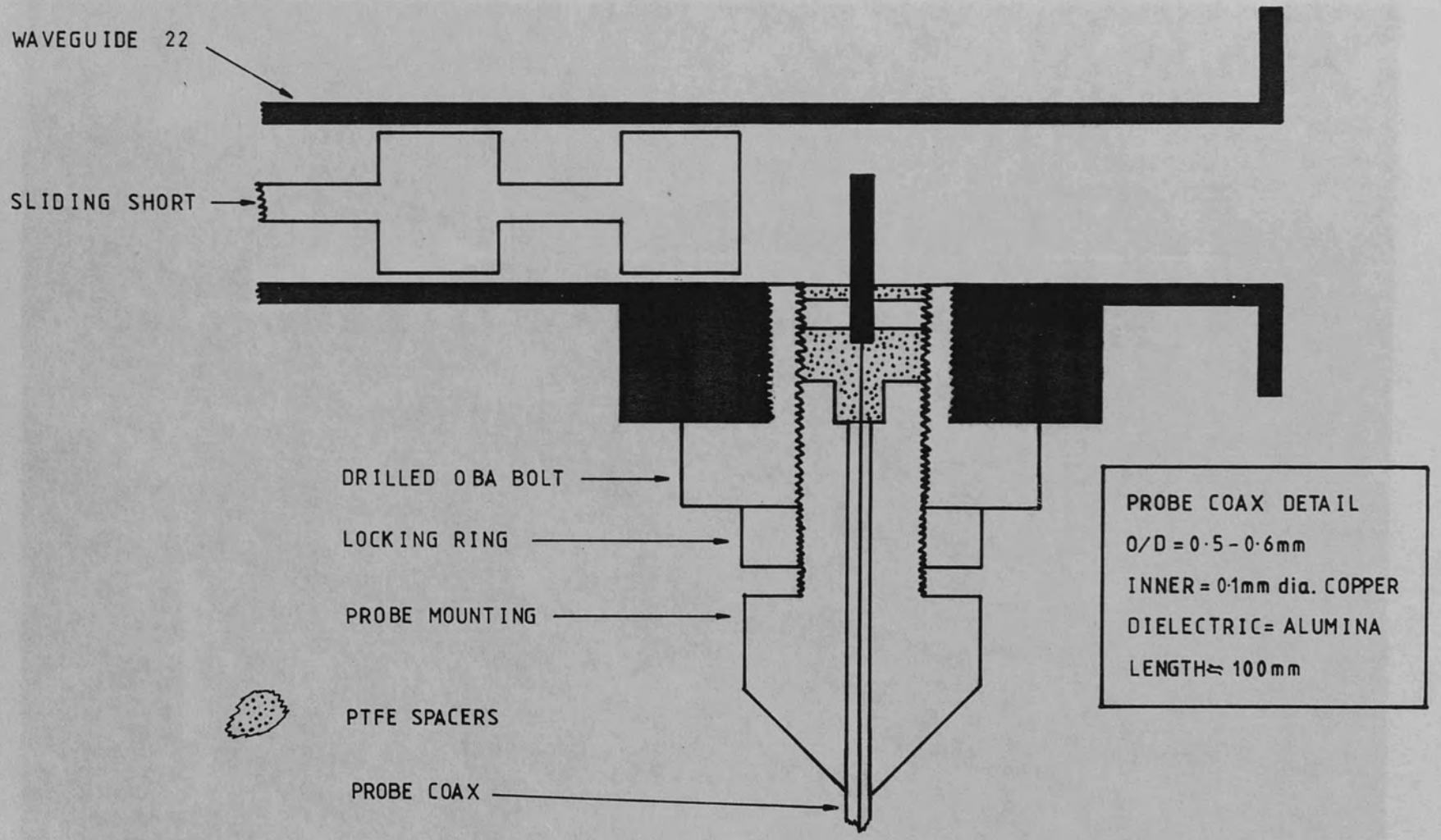

Figure(3.20) Q–band coaxial probe construction

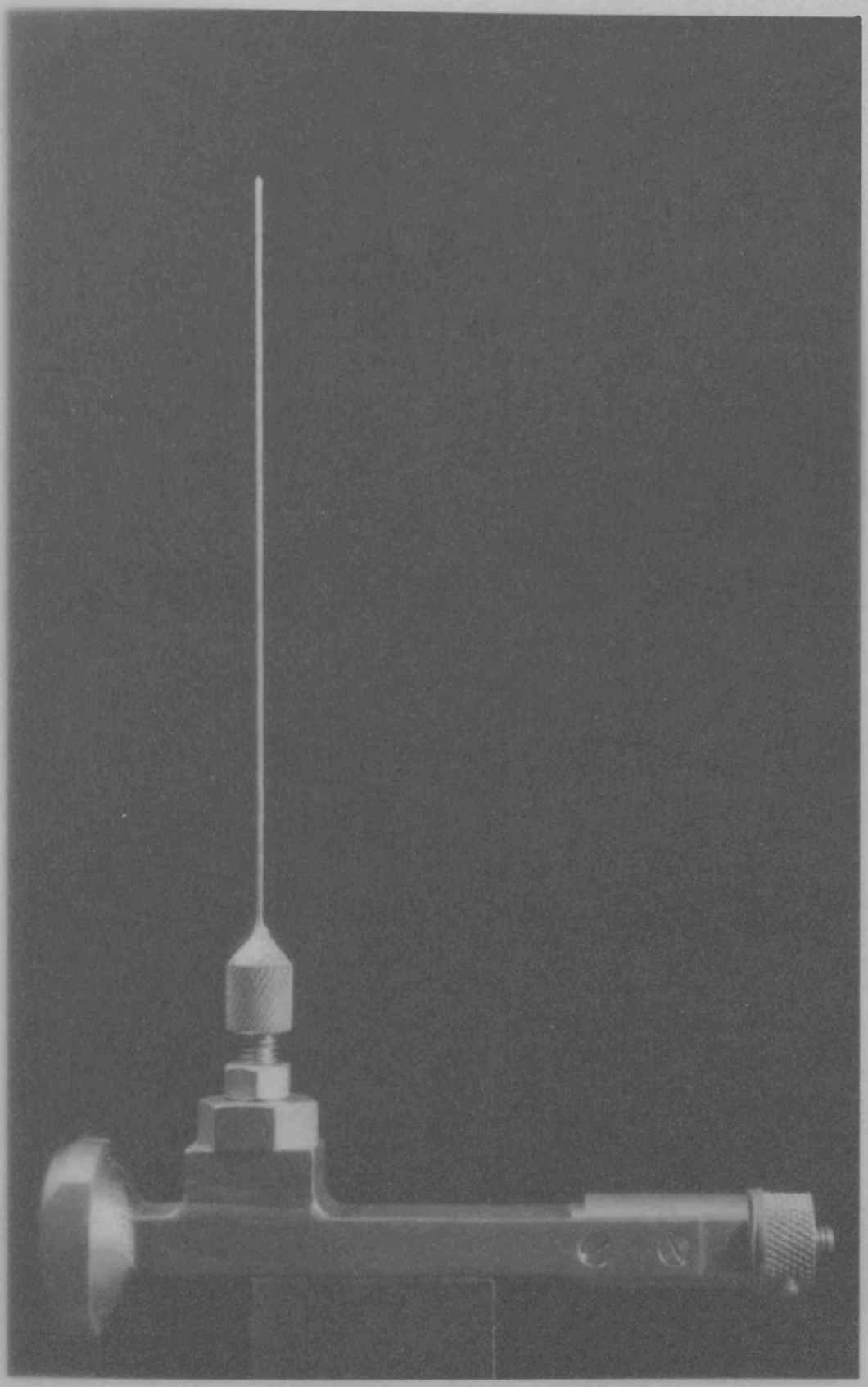

Plate(3.2) The Q–band 0.5 *mm* coaxial probe

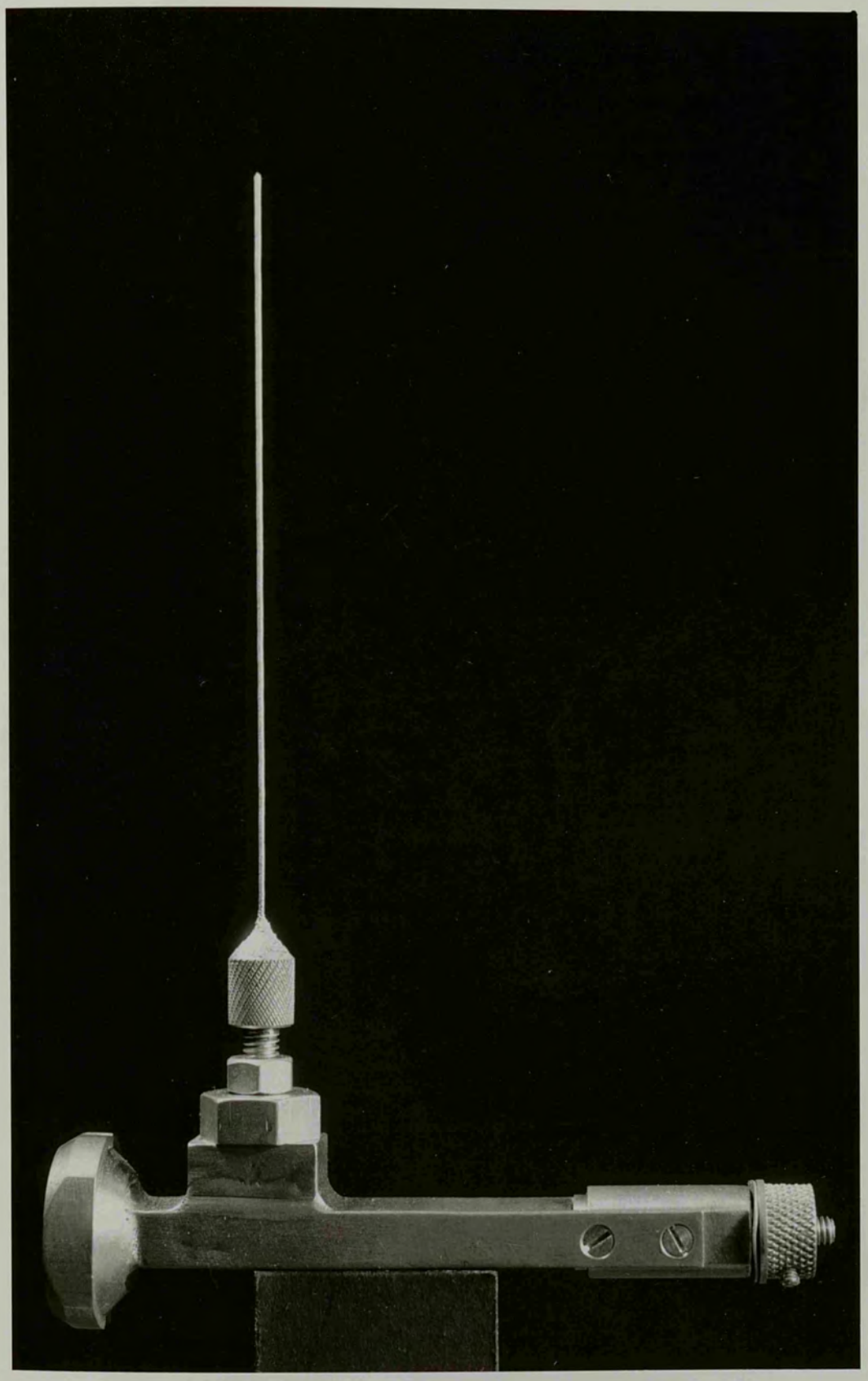

(b) The secondary scattering error.

The materials considered for the probe outer sheath were vacuum deposited silver approximately $0.2\mu m$ thick and drawn nickel tubing with a wall thickness of $50\mu m$ (valve cathode tubing) The relative merits of the two materials can be compared in Table (3.1) which lists the electrical properties of some common metals.

Table (3.1)

The Electrical Properties of Some Common Metals

metal	conductivity Mhos/m	μ_r	skin depth / μm	R_s Ω/square
copper	5.8×10^7	1.0	0.25	0.069
silver	6.15×10^7	1.0	0.24	0.068
nickel	1.3×10^7	100	0.053	1.45

It is apparent from Table (3.1) that nickel is more suitable for use as the probe outer conductor since the high surface resistance will suppress surface currents, and the small skin depth which enables the inner conductor to be effectively shielded from the external environment. The high surface resistance of nickel necessarily results in a high transmission loss. Using the equations in reference (3.2), the loss factor for the silver and nickel sheathed coaxial lines are found to be $\approx 85dB/m$ and $\approx 206dB/m$ respectively. The overall length of the coaxial section is of the order of $100mm$, thus the single pass loss incurred is $8.5dB$ and $20.6dB$ for the silver and nickel sheathed versions of the probes. The high transmission loss improves the detector isolation from the circuit under test, but will clearly reduce the probe's small signal performance if the detection system employed is of limited sensitivity.

The probe signal is coupled into WG–22 via an electric field probe through the centre of broad wall. Any mismatch at the probe/waveguide interface is matched out by adjusting the waveguide short circuit and the penetration depth of the waveguide probe. The advantages of launching into waveguide are twofold:

(a) The detector is screened from surface currents propagating on the outside of the probe.

(b) Detector systems can be made up and interchanged with relative ease in waveguide.

The screening effect of the waveguide detector is of great significance; it allows the use of unbalanced detectors without incurring error due to surface currents flowing on the outer conductor.

The influence of the monopole length and the probe to substrate separation was investigated using the open circuit edge of a rectangular patch antenna as a test circuit. From the simple transmission model of the rectangular patch, there should be a voltage maximum located at each open circuit edge. The coaxial probe has a finite integration area over which the electric field is sampled. Thus when the probe is located exactly over the edge of the patch, the average electric field intensity measured will be lower than slightly inside the metallization edge. As a result, the position of the measured voltage maximum will be shifted inside the edge of the patch metallization by a small amount Δl. This effect is illustrated by Figure (3.21). By measuring the shift Δl, the probe integration area can be estimated. Figure (3.22) shows the variation of the measured Δl with the probe to substrate separation for silver sheathed $0.5mm$ probes with monopole lengths of $0.044\lambda_0$, $0.032\lambda_0$, and $0.022\lambda_0$, where $\lambda_0 = 8.5mm$. The edge effect is seen to reduce with decreasing probe to substrate separation for all monopole lengths. It is apparent that the edge effect is minimized when monopole length is approximately one probe outer sheath radius in length. The edge effect becomes negligable for the optimimal probe configuration for probe to substrate separations of the order of $0.005\lambda_0$ or less. Figure (3.22) also shows the variation of Δl with the probe to substrate separation for the slightly larger diameter ($0.6mm$) nickel sheathed probe. The monopole length was trimmed to approximately one probe outer diameter in length. When compared to the results for the $0.5mm$ silver sheathed probe, it is clear that the edge effect is more pronounced when using the larger diameter nickel probe. The edge effect suffered by the nickel sheathed probe can be reduced to $0.0025\lambda_0$, which is negligable for most applications.

The smallest probe that has been constructed is shown in Figure (3.23). The probe tip is fabricated from a $0.3mm$ diameter nickel tube and employs a 50 S.W.G double cotton covered copper wire as an inner conductor and dielectric. In order to reduce the line loss and improve the rigidity of the probe assembley, the majority of the coaxial section, approximately $80mm$, is constructed using $0.5mm$ alumina tube with a nickel outer sheath. The design also incorporates a $\lambda_0/4$ wave trap which will prevent surface currents from flowing up the probe

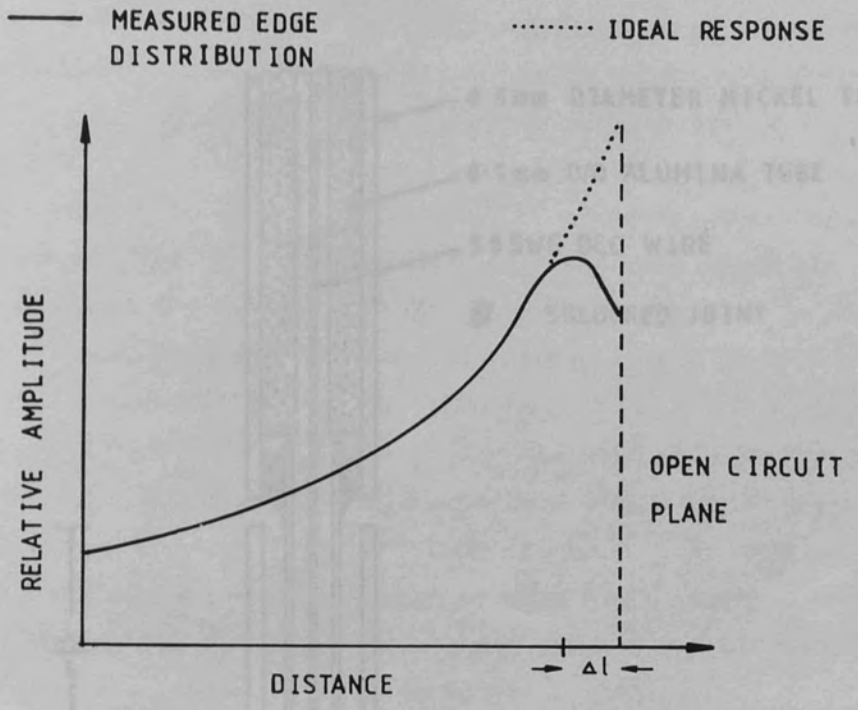

Figure (3.21) The open circuit edge effect

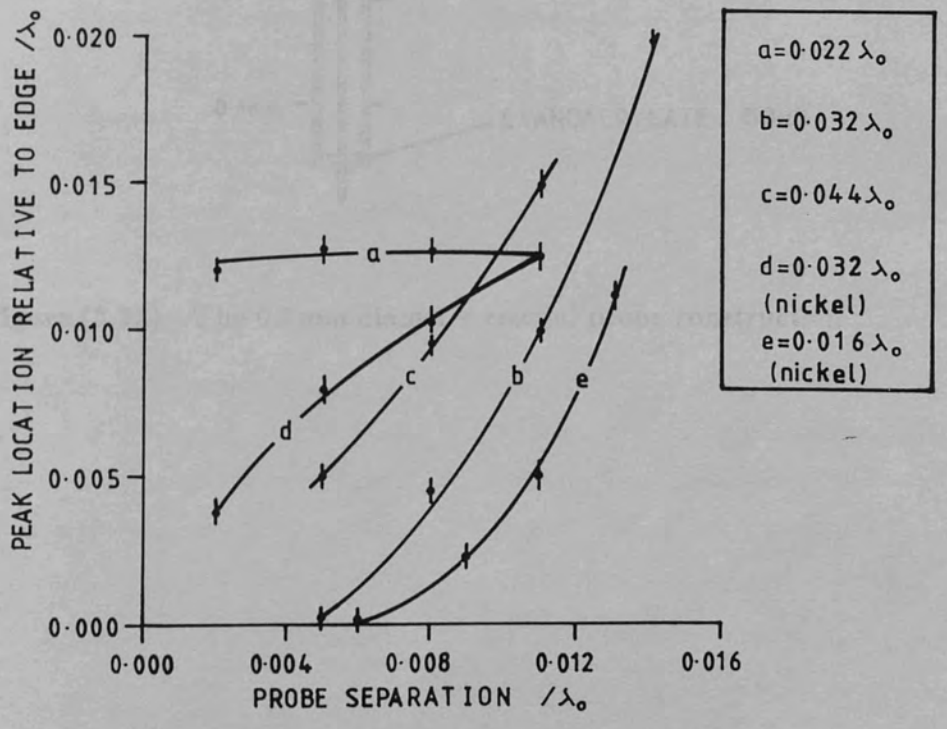

Figure (3.22) Measured open circuit edge effect with the coaxial probes

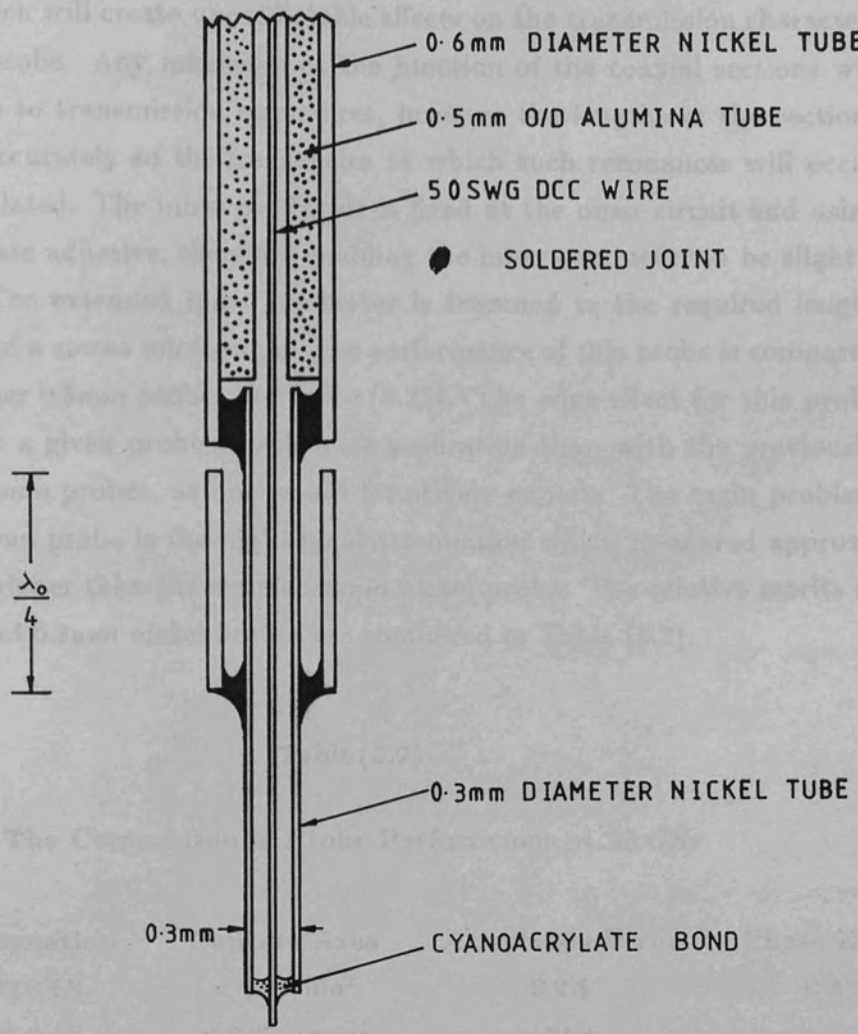

Figure (3.23) The 0.3 *mm* diameter coaxial probe construction

outer conductor. No attempt was made to match the impedances at the junction between the two sections, however care was exercised to ensure that the soldered junction between the outer conductors was made correctly. Failure to completely solder the joint will result in a series stub being formed at the junction, which will create unpredictable effects on the transmission characteristic of the probe. Any mismatch at the junction of the coaxial sections will also give rise to transmission resonances, however the lengths of the sections are known accurately so the frequencies at which such resonances will occur are easily isolated. The inner conductor is fixed at the open circuit end using a cyanoacrylate adhesive, therefore enabling the inner conductor to be slightly tensioned. The extended inner conductor is trimmed to the required length with the aid of a stereo microscope. The performance of this probe is compared with the larger $0.5mm$ probes in Figure (3.22). The edge effect for this probe is smaller for a given probe to substrate separation than with the previously described $0.5mm$ probes, as one would intuitively expect. The main problem with the $0.3mm$ probe is the high signal attenuation which measured approximately $7dB$ higher than the simple $0.5mm$ nickel probe. The relative merits of the $0.5mm$ and $0.3mm$ nickel probes are compared in Table (3.2).

Table (3.2)

The Comparison of Probe Performance at 35 *GHz*

Probe	Attenuation	Capture Area	Amplitude Error	Phase Error
$0.5mm$	$20.6\,dB$	$< 0.01\,mm^2$	0.2%	$< 3°$
$0.3mm$	$27.0\,dB$	$< 0.0002\,mm^2$	0.01%	$< 1°$

The phase and amplitude errors refer to the magnetic coupling error and are calculated using the approximate theory developed earlier in this chapter. The capture area is used as a figure of merit to compare the resolution of different probes and is defined using the measured edge effect Δl as:

$$A_c = \pi(\Delta l)^2 \qquad 3.42$$

The $0.3mm$ probe is clearly more superior in performance, possessing better

spatial resolution and lower magnetic coupling errors than the $0.5mm$ probe. The high attenuation of $0.3mm$ probe is a major disadvantage when the available signal is low and/or the detector sensitivity is poor, since this results in a loss of measurement dynamic range. The question of probe perturbation is difficult to quantify, however the results of the microstrip experiments given in chapters (5) and (6) indicate that the measured results using the coaxial probes are in good agreement with the available theory.

3.1.4 Magnetic Field probes.

The measurement of the tangential magnetic field very close to the top surface of a printed conductor enables the surface current distribution on the conductor to be observed. By taking two orthogonal measurements, the direction and magnitude of the surface current can be found. A magnetic field probe would prove useful for the study of microstrip patch radiators of arbitary geometry. Magnetic field probes suffer from two major drawbacks:

(a) As previously stated two orthogonal measurements are generally required, thus increasing the data aquisition time.

(b) The loop probe couples to both electric and magnetic fields.

At millimetre wavelengths an additional problem is that the probe dimensions required make the fabrication of loop probes very difficult without recourse to precision photolithographic techniques. The multiple measurement problem can be overcome by the use of multi–element probes, a technique which has been extensively exploited at UHF frequencies. (reference (3.3)) When the wavelength is of the order of $8.5mm$ or less the multi–element probe becomes impractical due the small dimensions of the structure. The electric field response of the loop probe can be reduced by employing a balanced loop construction as shown in Figure (3.24). The degree of reduction in the electric field component of the probe output voltage will depend on the similarities of the detector diode characteristics, or in the case of a modulated scattering loop, the symmetry of the load impedances in each arm. When the electromagnetic field under study is arbitrarily polarized, such as would be encountered if probing a non–TEM transmission line such as slotline, then four measurements are required in order to measure the three components of $\vec{B}$. The loop orientations required are shown in Figure (3.25) and the probe output corresponding to each orientation is given by:

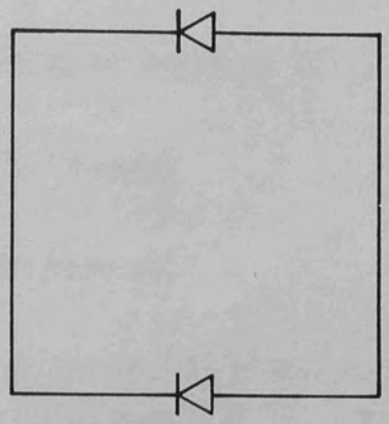

Figure (3.24) The balanced loop probe

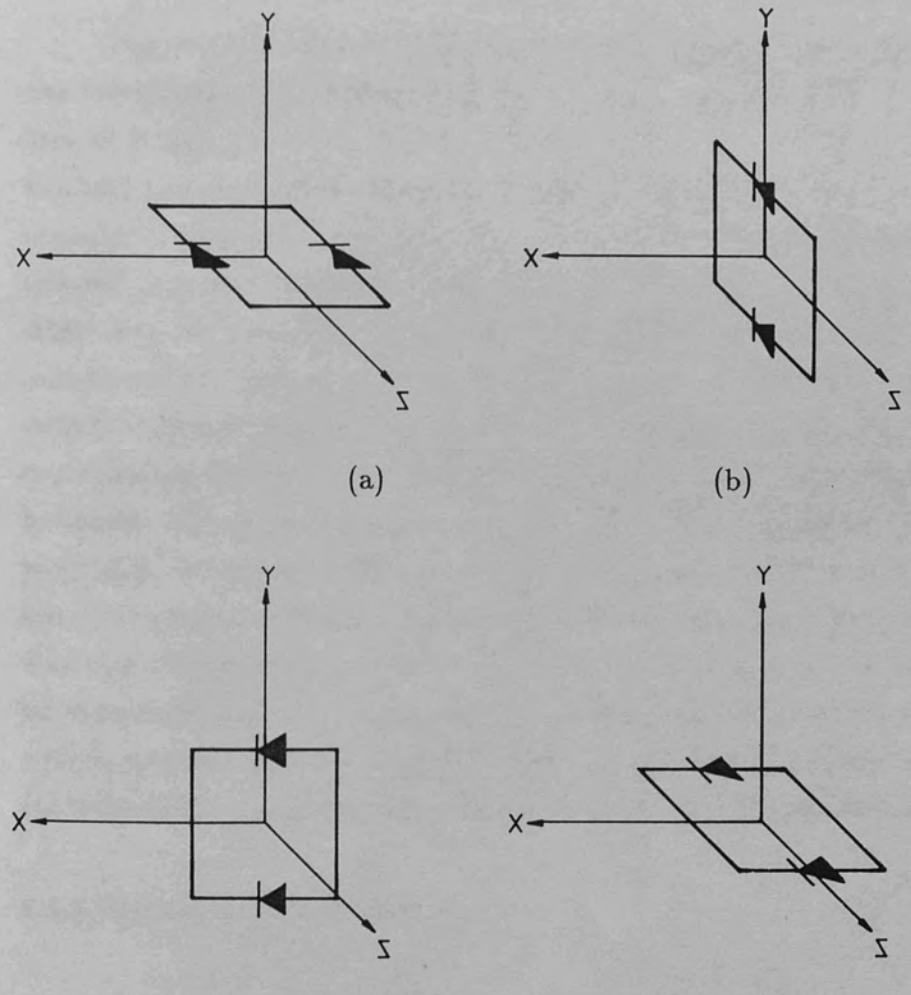

Figure (3.25) The measurement of an elliptically polarized **B** field

(a) B_x : E_x and E_y not measured

(b) B_y : E_x and E_y not measured

(c) B_y : E_x also measured

(d) B_z : E_x also measured

Clearly, B_x and B_y are unambiguously measured for the loop orientations (a) and (b) since the loaded arms of the loop are orthogonal to both the components of the electric field. By subtracting B_y as measured in orientation (b) from the combined effect of B_y and E_x in (c), we can determine E_x and hence deduce B_z from the measurement in orientation (d).

Figure (3.26) shows the construction of the magnetic loop probe which was fabricated to investigate the surface current distribution on printed conductors at Q–band frequencies. The loop is formed at the end of a self supporting shielded balanced transmission line fabricated from $1.0mm$ diameter twin bore alumina tube and 0.1mm diameter copper conductors. The probe signal is coupled into the tangential magnetic field close to the waveguide narrow wall, which has the advantage of partially suppressing the component of the probe output due the electric monopole mode of reception. The initial measurements with this probe on CPS transmission lines indicated that the electric monopole contribution was too large for accurate measurements of the magnetic field to be made. The electric monopole contribution can be totally removed by employing an integrated balanced detector such as shown in Figure (3.27). The circuit is only suitable for amplitude only measurements. If phase measurement was also required then a homodyne system such as described in section (3.2.3) must be employed. Due to the inherent problems associated with magnetic loop probes, and the fact that the surface currents can be deduced from electric field measurements, the use of magnetic probes was not pursued further.

3.1.5 Electric Dipole Probes

The electric dipole probe has found extensive use in the measurement of "open" electric fields, such as Fresnal near field measurements. The use of scattering dipoles for the measurement of low frequency electric fields is thoroughly described by King in reference (3.3). The problems associated with

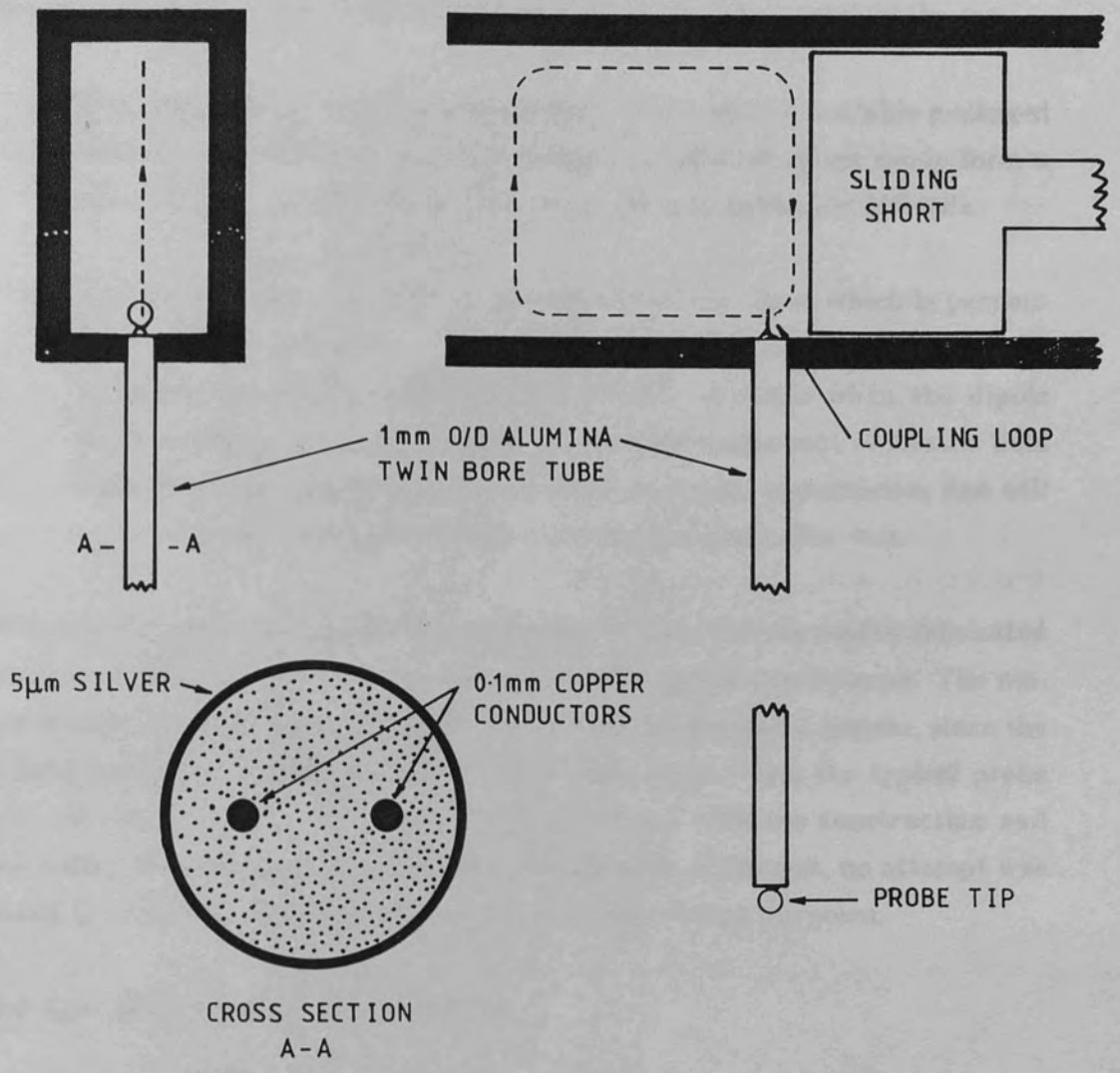

Figure (3.26) Q–band magnetic field probe schematic diagram

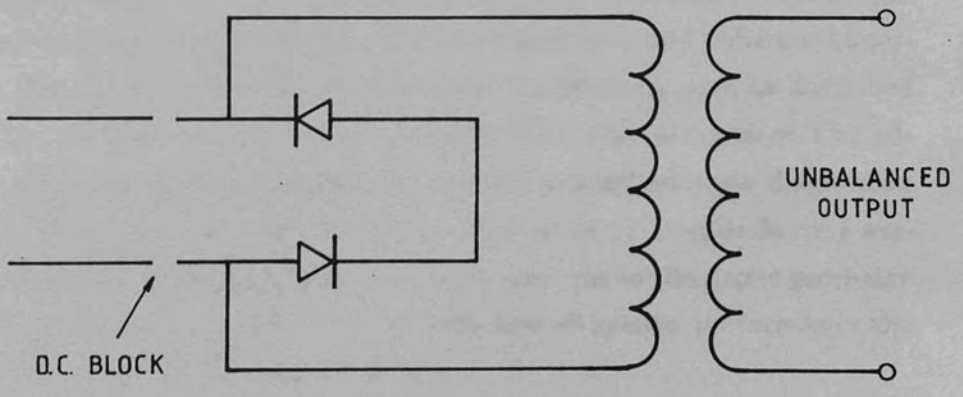

Figure (3.27) Balanced detector configuration

the use of dipole probes at millimetre and near millimetre wavelengths are:

(a) The small size of the dipole in relation to the size of available packaged devices. For example, the beam leads of a DC1346 mixer diode form a very effective $\lambda_g/2$ dipole at frequencies of approximately 220 GHz.

(b) The dipole requires a balanced transmission line input which is perpendicular to the dipole axis. Whilst this is not a serious drawback for the measurement of free space fields, it poses a problem when the dipole probe is being used to investigate the vertical component of electric field close to the surface of a conductor since the probe transmission line will be in very close proximity to the transmission line under test.

Very small dipoles with lengths of approximately $20\mu m$ can be readily fabricated on thin metallized dielectric films using photolithographic techniques. The major problem is the integration of the probe with the detection system, since the typical beam lead packaged diode is forty times larger than the typical probe size required. In view of the difficulties associated with the construction and operation of dipole probes at the short wavelengths of interest, no attempt was made to fabricate dipole probes for circuit measurement purposes.

3.2 R.F. Signal Detection Techniques

3.2.1 Introduction

R.F. signal detection techniques can be broadly classed as either amplitude only or simultaneous amplitude and phase detectors. The first class of detector encompasses all forms of direct video detection and incoherent superheterodyne systems. The second class of detectors are more complex, and hence more expensive systems and include the homodyne and coherent superheterodyne detectors. For circuit measurement applications such as described in chapter (6), a simple amplitude only system is all that is required.The addition of a phase measurement capability enables printed antenna diagnostics to be carried out more effectively than is possible with an amplitude only system. In the previous section the measurement errors due to the probe geometry were described, therefore in order to assess the overall system performance the detector errors must now be considered.

3.2.2 Amplitude Only Detectors

The most straightforward amplitude detector is the unbalanced video detector shown schematically in Figure (3.28). For waveguide detectors the impedance boosting network is realized by a sliding backshort positioned approximately $\lambda_g/4$ behind the diode. This type of detector offers the best sensitivity in terms of voltage output per unit of incident power. The disadvantage of this system is that it is bandwidth limited, typically a few hundred MHz. A configuration giving a wider bandwidth is shown in Figure (3.29); commercial detectors of this type have bandwidths extending from 10 MHz to 18 *GHz.* Whilst this configuration provides a very flat response as a function of frequency, the voltage available at the diode terminals is halved, thus resulting in poor sensitivity compared to the previous configuration. Both configurations operate with either a C.W., or a modulated carrier, the detected output being either a D.C. or A.C. voltage respectively. Detection of the incident R.F. occurs because of the non linear *I–V* characteristic of the diode, i.e.:

$$I = I_s\left\{\exp\left(\frac{V_j}{.028}\right) - 1\right\} \qquad 3.43$$

Where:

$V_j = V - IR_s$

$=$ the junction voltage

$R_s =$ the diode series resistance

Assuming that the D.C. current is held constant by a current regulator or a large bias resistor then the total junction current is given by:

$$I = I_0 + i\cos(\omega t) \qquad 3.44$$

Combining equations (3.43) and (3.44):

$$V_j = 0.028\ln\left(\frac{I_s + I_0 + i\cos(\omega t)}{I_s}\right) \qquad 3.45$$

At low power levels the R.F. current will be small, so equation (3.45) can be

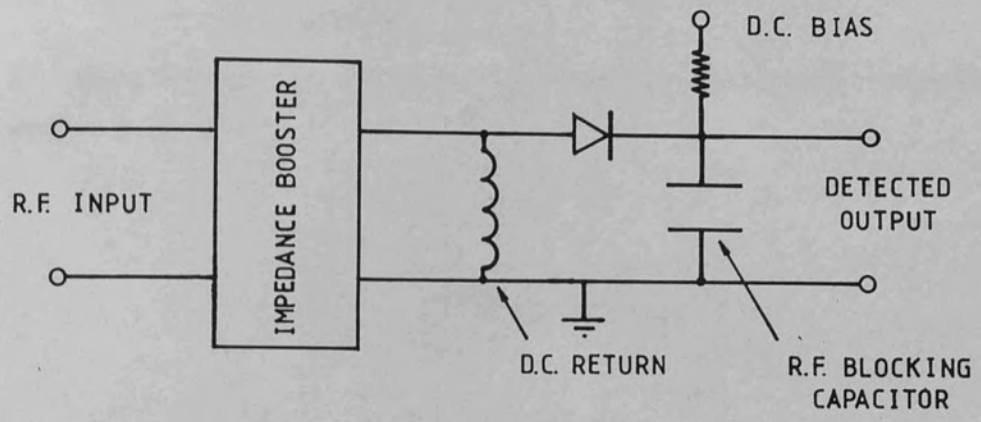

Figure (3.28) Typical high sensitivity detector design

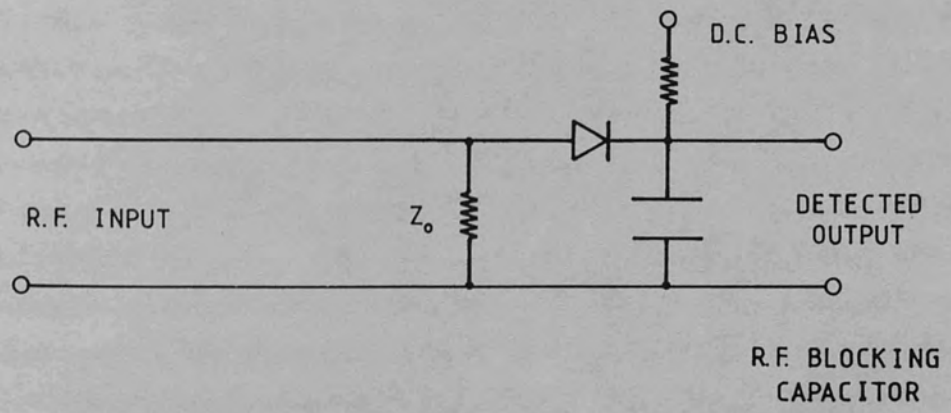

Figure (3.29) Wide bandwidth detector configuration

expanded as a Taylor series, i.e.:

$$V_j = 0.028\left(\frac{I_0 + I_s}{I_s}\right) + 0.028\left[\frac{i\cos(\omega t)}{I_0 + I_s} - \frac{i^2\cos^2(\omega t)}{2(I_0 + I_s)^2} + \frac{i^3\cos^3(\omega t)}{6(I_0 + I_s)^3} - .....\right] \quad 3.46$$

By taking the time average of equation (3.46) and ignoring all terms above the second order then:

$$V_{DC} = 0.028\ln\left(\frac{I_0 + I_s}{I_s}\right) - \frac{0.028i^2}{4(I_0 + I_s)^2}$$

$$= V_0 - \frac{V_j^2}{0.112} \quad 3.47$$

Where the constant $0.112 = 4nkT/e$

and:

$k =$	the Boltzmann constant
$T =$	the absolute temperature
$e =$	the electronic charge
$n =$	the diode ideality factor

Therefore to a first order the D.C. output voltage from the detector diode is proportional to the square of the R.F. voltage across the junction. In reality the contribution of higher order even terms of the Taylor expansion will generate a small D.C. voltage across the diode junction, but can be neglected in most practical situations. The higher order terms become more troublesome when the diode is operated in the linear region of its I–V characteristic. The second harmonic errors can be suppressed by employing a balanced detector arrangement such as the Wavetek Pacific Measurements WPM15176 unit described in reference (3.4). A further problem is the requirement for an extremely low drift D.C. amplifier when making low level measurements. The D.C. detection system is also prone to spurious low frequency pick up on the interconnecting leads between the diode and amplifier. Employing a modulated carrier and A.C. amplification after detection enables some of the problems associated with D.C. detection to be overcome. When the R.F. voltage across the diode junction is modulated with a sinusoidal waveform, it can be shown[3.5] that the most

significant terms in the detected output are:

$$V_{AC} \approx \frac{V_0^2}{2}\frac{d^2 I}{dV^2}\left\{\frac{1}{2} + \frac{m^2}{4} + m\sin(\omega_m t) - \frac{m^2}{4}\cos(2\omega_m t) + \textit{other R.F. terms}\right\} \quad 3.48$$

Where:

I is given by equation (3.43)
m = the modulation index
ω_m = the modulation frequency
V_0 = the peak R.F. voltage

The R.F. terms are usually filtered out by the detector mount, and the D.C. terms removed by a D.C. blocking capacitor. The remaining A.F. terms are then narrow band detected. The use of a lock–in voltmeter to perform the narrow band amplification and detection is particularly attractive since:

(a) The effective detection bandwidth can be made extremely narrow by increasing the integration time constant.

(b) The output is a D.C. voltage which is proportional to the *rms* A.C. input when the input waveform is sinusoidal.

The narrow detection bandwidth means that spurious electrical noise picked up on the interconnecting leads between the diode and lock–in voltmeter is no longer a source of serious error, since it is unlikely to be coherent with the modulation frequency. The D.C. output voltage from the lock–in voltmeter can be easily digitized by an analogue to digital converter and read into the controlling computer for analysis. Following through the calculation in reference (3.6) reveals that A.C. detection also suffers from second harmonic error when using an unbalanced detector. The second harmonic error is negligable when the diode is operated in its square law region, and can be totally eliminated by employing a balanced detector. The major advantage of A.C. detection is that the errors due to D.C. drift in the amplifier and thermal *emf*s at dissimilar metal junctions are completely eliminated.

A.C. detection combined with a lock–in amplifier was employed for all the amplitude measurements due to its superiority over D.C. detection. The initial

measurement of the combined lock–in voltmeter and silicon detector response as a function of frequency is shown in Figure (3.30). The response is seen to be square law down to detected output voltages of the order of 1μV. From the calibration of the diode response against absolute power measured using an Anritsu ML83a power meter shown in Figure (3.31), the square law response of the diode is confirmed and the sensitivity calculated to be $2400\mu V/\mu W$. The lock–in voltmeter employed was a Brookdeal 9503, which has a measurement range of $100nV$ to $10mV$ in ten ranges. The dynamic range of each range setting was approximately $20dB$, thus in order to make full use of the diode dynamic range a 6–bit programmable audio attenuator was incorporated into the detector circuit as shown in Figure (3.32). The attenuator can be programmed in $1.5dB$ steps up to a maximum of $-88.5dB$ via a 6–bit data bus. An additional two lines are incorporated to act as address lines, thus allowing up to four different attenuators to be addressed from the 8–bit parallel printer port of the BBC micro–computer. The attenuator was calibrated in $6dB$ steps from $0dB$ to $-42dB$. Therefore when the lock–in voltmeter is set to a $3\mu V$ *fsd* then measurements between $1\mu V$ and $50\,000\mu V$ can be made. This range effectively covers the square law region of the silicon detectors employed. The attenuation level is selected by the BBC micro–computer to obtain the highest output signal from the lock–in voltmeter without taking the instrument into an overload condition.

The disadvantages of the video detector are poor sensitivity and limited dynamic range. The measurement range of diode detectors can be extended into the linear region to give an effective dynamic range approaching $80dB$. This technique is useful for scalar network analysers where the power coupled to the detectors is significantly higher than for a detector coupled to small microwave probe. Sensitivity and dynamic range can be improved by the use of a superheterodyne detector. With careful design a Q–band superheterodyne detector can be made with a minimum detectable signal of the order of $-100dBm$ and a dynamic range in excess of $100dB$[3.5]. The only problem with such a system is the added complexity; in addition to the source power and frequency stabilization, the local oscillator must be power stabilized and servo controlled to track the signal. If full extent of the superheterodyne's dynamic range is to be exploited, then a programmable I.F. attenuator will be required as illustrated in Figure (3.32). The cost of a superheterodyne detection system is considerably more than a simple video detector, especially if wide bandwidth operation is required. As demonstrated in the later chapters, the A.C. video detection system has sufficient dynamic range and sensitivity for most applications. Where greater sensitivity and dynamic range are required, the homodyne

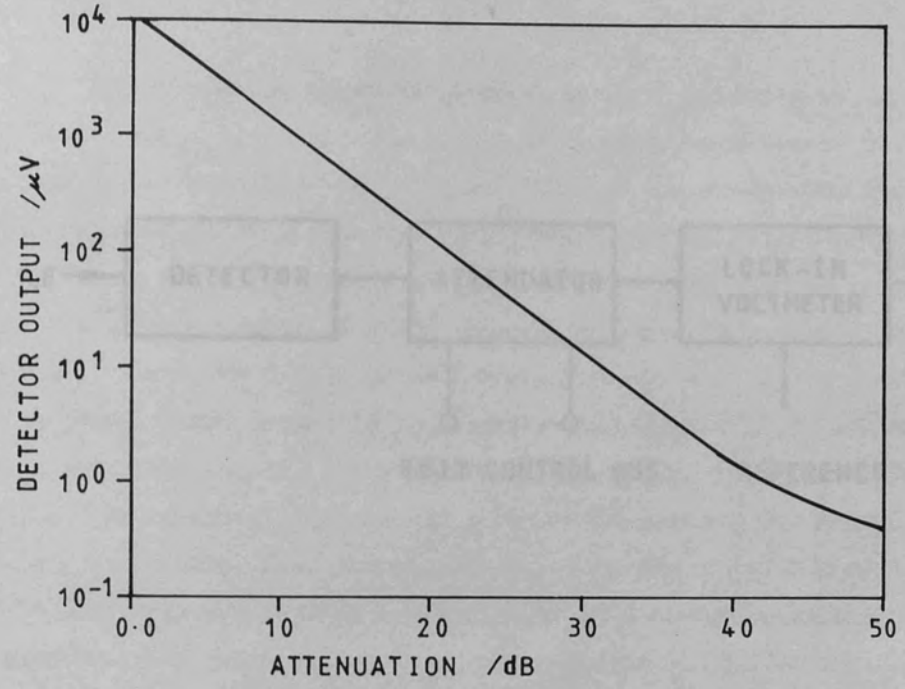

Figure (3.30) Silicon point contact diode detector response

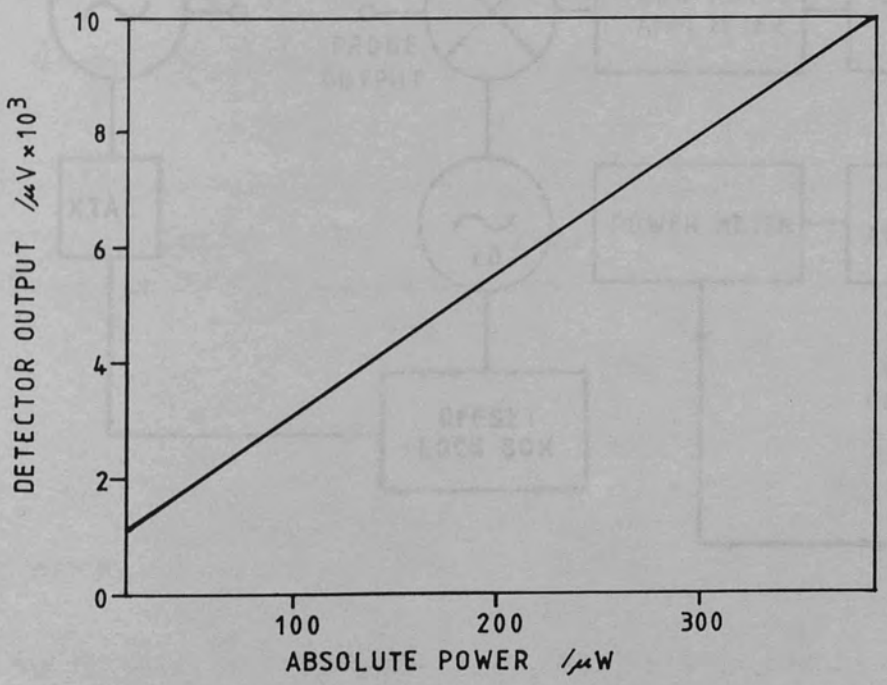

Figure (3.31) Calibration of diode response against the Anritsu power meter

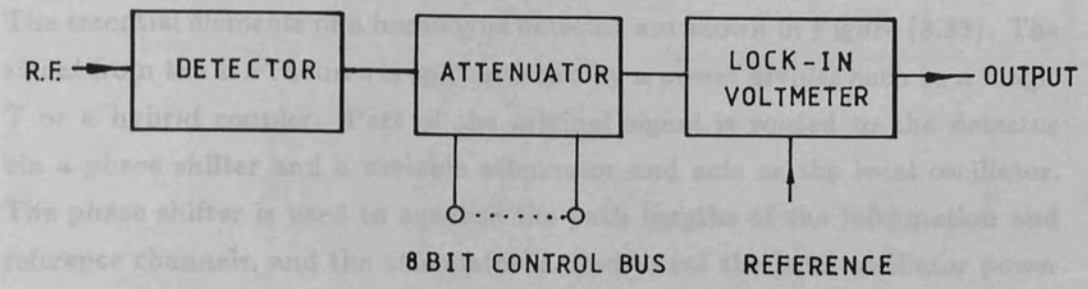

Figure (3.32) Extended range lock–in voltmeter

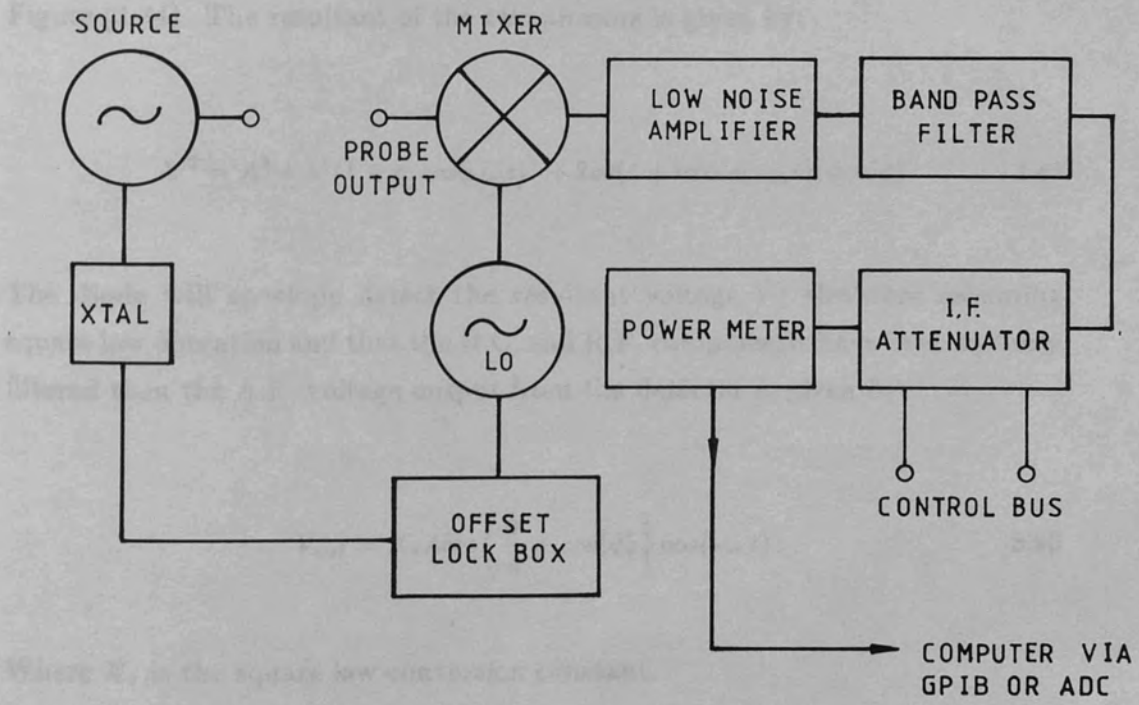

Figure (3.33) The essential components of a superheterodyne detector

system described in the following section is a cost effective alternative to the superheterodyne detector.

3.2.3 Homodyne Detector Systems

The homodyne detection principle involves summing an un-modulated reference signal of frequency ω with a modulated signal also of frequency ω in a non linear device, the output being taken at the modulation frequency ω_m. The essential elements of a homodyne detector are shown in Figure (3.33). The signal from the R.F. source is split into two by a power divider such as a magic T or a hybrid coupler. Part of the original signal is routed to the detector via a phase shifter and a variable attenuator and acts as the local oscillator. The phase shifter is used to equalize the path lengths of the information and reference channels, and the attenuator is used to set the local oscillator power level. The remaining signal is taken to the detector via the system under test and a modulator. The form of modulation employed depends on the application, but in general double sideband A.M. with carrier is the simplest form of modulation to produce, requiring only a simple pin diode reflection modulator. The modulated signal is then summed with the local oscillator signal by a power adding network, such as a magic T, and passed to the diode detector. The voltage across the detector is found with the aid of the phasor diagram in Figure (3.34). The resultant of the two phasors is given by:

$$V^2 = A^2 + b^2(1 + m\cos(\omega_m t)^2 + 2ab(1 + m\cos(\omega_m t))\cos(\phi) \qquad 3.49$$

The diode will envelope detect the resultant voltage V; therefore assuming square law operation and that the D.C. and R.F. components have been suitably filtered then the A.F. voltage output from the detector is given by:

$$V_{out} = K_s Abm\left\{\frac{b}{A} + \cos(\phi)\right\}\cos(\omega_m t) \qquad 3.50$$

Where K_s is the square law conversion constant.

Thus the phase of the R.F. signal can be found by adjusting the phase shifter in the reference channel to locate the zeros in the voltage output which occur

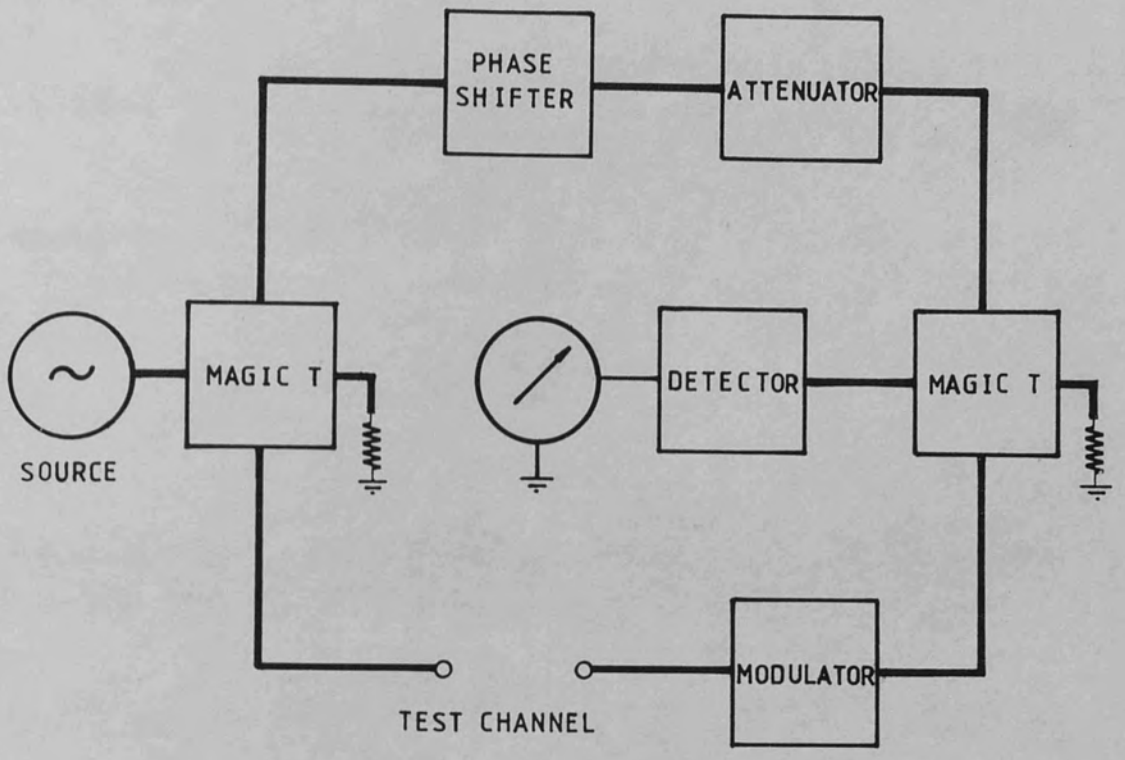

Figure (3.34) The basic homodyne detector

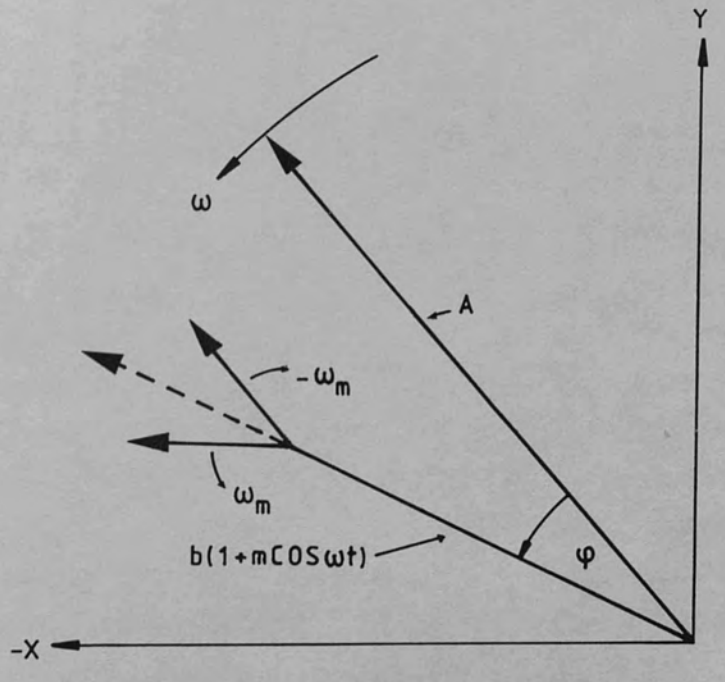

Figure (3.35) Phasor diagram illustrating the detection process

whenever $\cos(\phi) = -b/A$, or:

$$\phi = \pm\left[(2n+1)\frac{\pi}{2} + (-1)^n E_p\right] \quad n = 0, 1, 2, .. \qquad 3.51$$

Where:

$$E_p = \arcsin\left(\frac{b}{A}\right)$$

The amplitude of the signal can then be found zeroing the $\cos(\phi)$ term in equation (3.50) with the aid of the reference channel phase shifter, thus giving:

$$V_{out} = K_s b^2 m \cos(\omega_m t) \qquad 3.52$$

If the b/A term in equation (3.50) can be removed, or reduced to an insignificant level, then the measurement procedure is simplified because the detector output becomes:

$$V_{out} = K_s A b m \cos(\phi)\cos(\omega_m t) \qquad 3.53$$

This can be achieved by keeping the amplitude of the signal in the information channel small with respect to reference channel amplitude. A better solution is to employ double sideband suppressed carrier modulation, or else to use balanced detectors which have the effect of removing the carrier term from a double sideband with carrier signal. Despite the simplicity of equation (3.53), obtaining automated phase and amplitude measurements is not straightforward since a servo control loop is required to set the reference channel phase shifter. This undesirable feature increases the complexity of the computer control system and increases the data aquisition time. At the expense of a more sophisticated R.F. detector illustrated in Figure (3.35) it is possible to obtain a simultaneous measurement of amplitude and phase.[3.6] The reference signal A is split using a magic T to obtain two equal components that are out of phase by π radians. The information channel signal is split using a $3db$ coupler which imparts a $\pi/2$ phase shift to the two components. Assuming that the path lengths are all

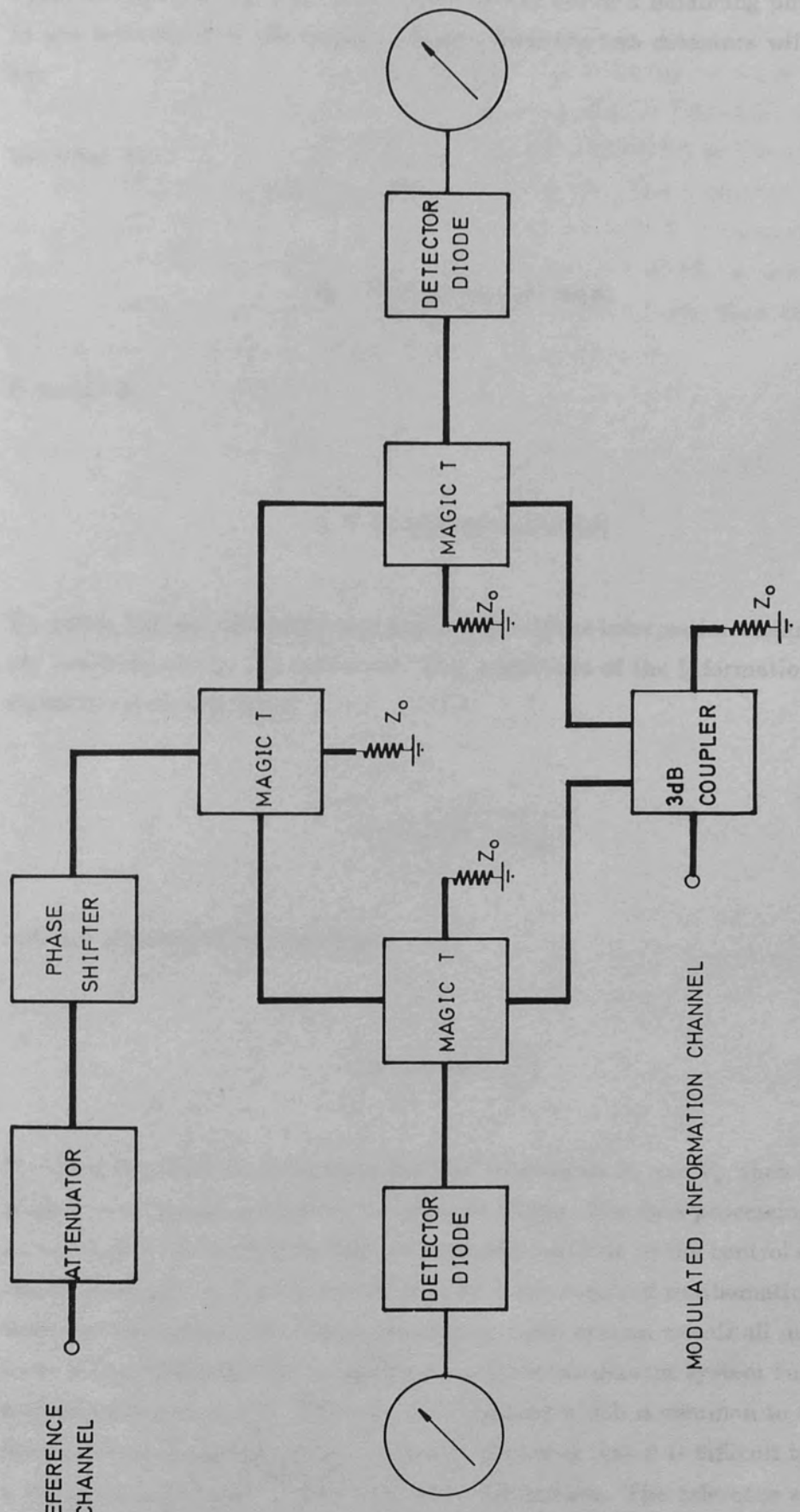

Figure (3.36) Proposed R.F. phase bridge design

equal multiples of $\lambda_g/2$ (or made equal by the use of a balancing phase shifter in one branch) then the output voltages from the two detectors will be given by:

Detector A:

$$V_x = K_s Amb \cos(\omega_m t) \cos(\phi) \qquad 3.54a$$

Detector B:

$$V_y = K_s Amb \cos(\omega_m t) \sin(\phi) \qquad 3.54b$$

Therefore the real and imaginary components of the information channel phasor are available at the two detectors. The amplitude of the information channel signal is calculated from:

$$|V_s| = \sqrt{V_x^2 + V_y^2} \qquad 3.55$$

and the phase is calculated from:

$$\phi = \arctan\{\frac{V_y}{V_x}\} \qquad 3.56$$

Provided that lock–in voltmeters are used to measure V_x and V_y, then the phase angle ϕ is unambiguously given by equation (3.56). The data processing is easily accomplished by feeding the lock–in voltmeter outputs to the control computer via an analogue to digital converter, where the required mathematical operations can be carried out. Since this measurement system avoids all mechanical servo loops, it is ideal for a rapid automatic measurement system such as the scanning network probe. The only disadvantage which is common to all homodyne systems being used with translatory probes is that it is difficult to provide a reference signal that is free from phase distortion. The reference signal has to be routed to the detector via some form of flexible linkage, such as a system of rotary waveguide joints or by coaxial cable. For measurements on circuits

requiring small area scans of the order of $40mm \times 40mm$, then a large diameter multi–turn coil of 0.010" semi–rigid cable should prove an effective means of coupling the reference signal to a homodyne detector operating at Q–band frequencies. The phase and amplitude detector shown in Figure (3.33) is still under development for use at Q–band. The only alternative to the homodyne system is the phase locked superheterodyne detector. These systems are complex to design and require considerable expenditure on R.F. components, as is evidenced by the high cost of vector network analysers which employ this detection principle. If a vector network analyser were available, then this would make an excellent detector for the scanning network probe.

CHAPTER 4

Investigation of Printed Microstrip Antennas Using a Scanning Network Probe

4.1 The End–Fed Microstrip Patch Antenna

4.1.1 Theoretical Aspects of the Rectangular Patch Antenna

The rectangular microstrip patch has been extensively investigated from a theoretical standpoint, and consequently several different models for the radiation and input impedance characteristics are available. Reference to Bahl and Bhartia[4.1] and James, Hall, and Wood[4.2] provides a vast bibliography on the development of the printed antenna up to 1981. For the purposes of this study the only models employed are the transmission line model of Munson[4.4] and Derneryd,[4.3] and the cavity model due to Lo et al.[4.5] The transmission line model treats the rectangular patch element as two radiating slots separated by a length of ideal transmission line. The radiating slots are replaced by a lumped conductance G which represnts the radiation resistance of the slot, and a lumped susceptance B is introduced to account for the fringing field capacitance at the open circuit edges. The lumped equivalent circuit is shown in Figure (4.1). The input admittance Y_{in} at the feed point is given by the admittance of one equivalent slot in parallel with the transformed admittance of the other slot. Therefore:

$$Y_{in} = G + jB + Y_L \left\{ \frac{G + j(B + Y_L \tan(\beta l)}{Y_L + jG \tan(\beta L) - B \tan(\beta L} \right\} \qquad 4.1$$

Where:

$$G = \frac{1 - \frac{(k_0 h)^2}{24}}{120\lambda_0} \qquad 4.2$$

$$B = Y_L k_0 \Delta l \sqrt{\epsilon_{ef}} \qquad 4.3$$

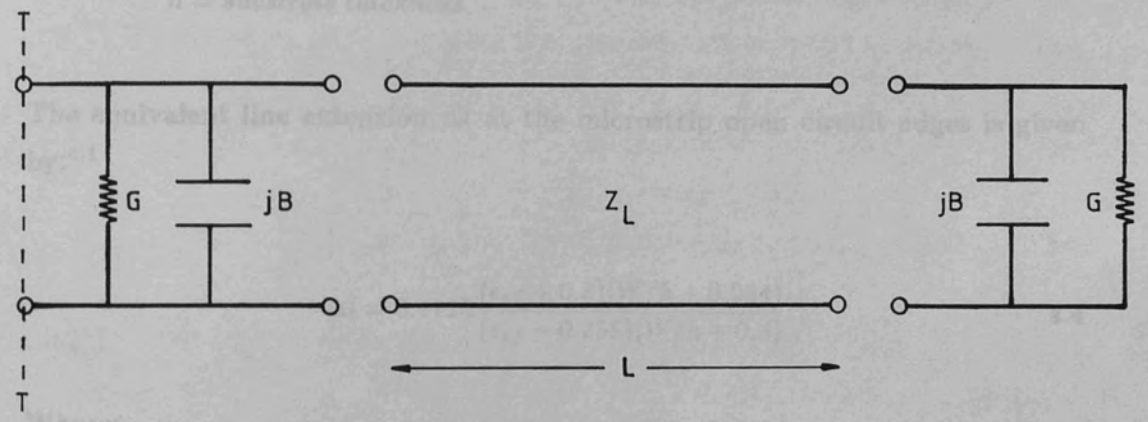

Figure (4.1) The rectangular patch equivalent circuit

and the symbols defined as follows:

$$Z_L = \textit{characteristic impedance of the transmission line}$$

$$Y_L = \frac{1}{Z_L}$$

$$\beta = \frac{2\pi}{\lambda_0}\sqrt{\epsilon_{ef}}$$

$$\epsilon_{ef} = \textit{effective dielectric constant of the patch transmission line}$$

$$k_0 = \frac{2\pi}{\lambda_0}$$

$$h = \textit{substrate thickness}$$

The equivalent line extension Δl at the microstrip open circuit edges is given by:[4.1]

$$\Delta l = 0.412h\frac{(\epsilon_{ef}+0.3)(W/h+0.264)}{(\epsilon_{ef}-0.258)(W/h+0.8)} \qquad 4.4$$

Where:

$$W = \textit{the patch width}$$

Separating Y_{in} into real and imaginary parts it is found that:

$$Y_{in} = G' + jB' \qquad 4.5$$

Where:

$$G' = G + Y_L\frac{(G(Y_L - \beta\tan(\beta L) + G\tan(\beta L)(B + Y_L\tan(\beta L))}{(Y_L - \beta\tan(\beta L)^2 + G^2\tan^2(\beta L)}$$

and:

$$B' = B + Y_L \frac{((B + Y_L \tan(\beta L))(Y_L - B\tan(\beta L)) - G^2 \tan(\beta L)}{(Y_L - \beta \tan(\beta L)^2 + G^2 \tan^2(\beta L)}$$

At resonance the imaginary part of Y_{in} is zero. Equating B' to zero gives the expression:

$$\tan(\beta L) = \frac{2Y_L B}{B^2 + G^2 - {Y_L}^2} \qquad 4.6$$

The resonant length of the patch can be from the above expression. In general $Y_L \gg B$ and $Y_L \gg G$ therefore the approximate solution of equation(4.6) becomes:

$$L = \frac{n\lambda_g}{\sqrt{\epsilon_{ef}}} - 2\Delta l \qquad 4.7$$

Where:

$$\lambda_g = \frac{\lambda_0}{\sqrt{\epsilon_{ef}}}$$

Thus the resonant length of the patch is given by any odd multiple of a half guide wavelength minus twice the line extension term Δl. The input impedance of the patch at the plane T—T in Figure (4.1) is given by:

$$Z_{in} = \frac{1}{Y_{in}}$$

$$Z_{in} = \frac{G'}{G'^2 + B'^2} - j\frac{B'}{G'^2 + B'^2} \qquad 4.8$$

The effect of attaching the patch to a microstrip line with an impedance Z_m can be quantified in terms of a complex reflection coefficient Γ given by:

$$\Gamma = \frac{Z_L - Z_m}{Z_L + Z_m} \tag{4.9}$$

Writing:

$$Z_{in} = R_L + jX \tag{4.10}$$

and assuming that Z_m is purely resistive and equal to R_m then:

$$\Gamma = \frac{R_L - R_m + jX}{R_L + R_m + jX} \tag{4.11}$$

Rationalizing and separating into real and imaginary components gives:

$$\Gamma = \frac{R_L^2 - R_m^2 + X^2}{(R_L + R_m)^2 + X^2} + j\frac{2XR_m}{(R_L + R_m)^2 + X^2} \tag{4.12}$$

The VSWR s is then given by:

$$s = \frac{1 + |\Gamma|}{1 - |\Gamma|} \tag{4.13}$$

The phase angle ϕ of the reflection coefficient is given by:

$$\phi = \arg(\Gamma)$$

$$\phi = \arctan\left(\frac{2XR_m}{R_L^2 - R_m^2 + X^2}\right) \tag{4.14}$$

The general form of the voltage standing wave produced in the high impedance microstrip feed is given by:

$$V = V_0\left[(1 + |\Gamma|)^2 - 4|\Gamma|\sin^2(\beta_m l - \phi/2)\right]^{\frac{1}{2}} \tag{4.15}$$

Where:

$$l = -z$$

$$\beta_m = \frac{2\pi}{\lambda_0}\sqrt{\epsilon_{em}}$$

$$\epsilon_{em} = effective\ permittivity\ of\ the\ microstrip\ feed$$

From equation(4.15) it is observed that the first maximum in the standing wave pattern occurs when:

$$\beta_m l - \frac{\phi}{2} = 0$$

or:

$$l = \frac{\phi}{2\beta_m} \qquad 4.16$$

It has been shown that the transmission line model enables a first order patch design to be made using equation(4.7), and predicts the patch input impedance characteristics in terms of the VSWR and phase angle of the complex reflection coefficient. However the model is not sufficiently general to enable the characterization of higher order transverse modes. In order to find the field variations beneath the patch metallization, the cavity model advanced by Lo et al is used. This model treats the rectangular patch as a dielectric loaded cavity of height $2h$ bounded by two electric walls and a magnetic boundary around the perimeter of the patch as shown in Figure (4.2). Since the height of the equivalent cavity is much less than a wavelength and the other cavity dimensions, then it can be assumed that there is only one component of electric field E_z, and two components of magnetic field H_x and H_y which are all independant of z. The electric and magnetic fields are then obtained from

$$\vec{E}_{mn} = \Psi_{mn}\hat{z} \qquad 4.17a$$

$$\vec{H}_{mn} = \frac{1}{j\omega\mu}\hat{z} \times \nabla_t \Psi_{mn} \qquad 4.17b$$

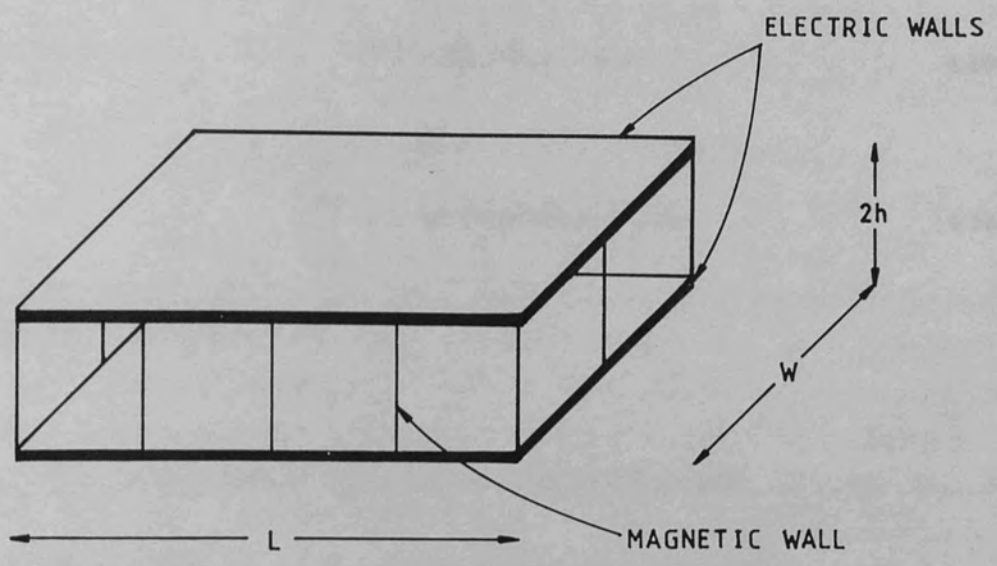

Figure (4.2) The cavity representation of the rectangular microstrip patch

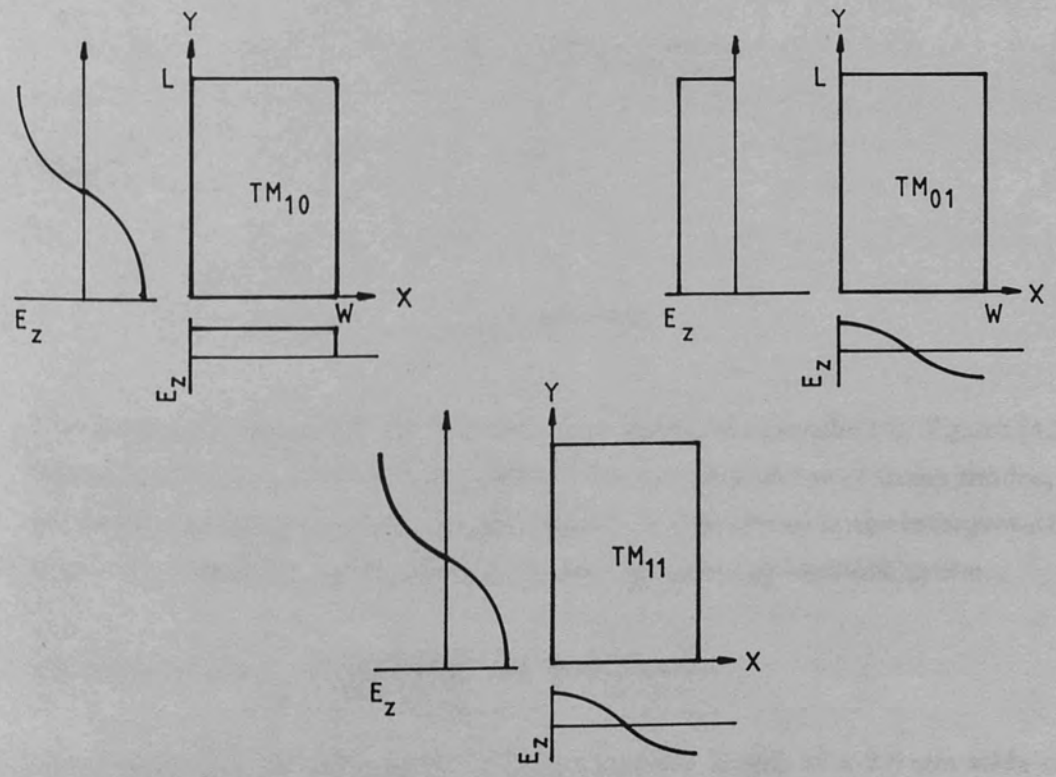

Figure (4.3) Low order rectangular patch modes

Subject to the boundary conditions:

$$(\nabla_t^2 + k_{mn}^2)\Psi_{mn} = 0 \qquad 4.18a$$

$$\frac{\partial \Psi_{mn}}{\partial n} = 0 \ \textit{on the patch perimeter} \qquad 4.18b$$

The symbols are defined as:

∇_t = *tranverse del operator with respect to the z axis*

Ψ_{mn} = *the field solution for the rectangular patch with a resonant wavenumber* k_{mn}

$k_{mn} = \omega_{mn}\sqrt{\mu\epsilon}$

For the most elementary case of perfect open circuit walls, the solution of equation(4.17)a becomes:[4.7]

$$E_z = A\cos(\frac{m\pi y}{L})\cos(\frac{n\pi x}{W}) \qquad 4.19$$

Where:

A = *constant*

The amplitude variations for the first three modes are sketched in Figure (4.3). The actual mode excited in the patch will be a superposition of many modes, as pointed out in reference(4.6), and this should be considered in the interpretation of the experimental results obtained using the scanning network probe.

4.1.2 Rectangular patch design and manufacture

With the aid of equation(4.7) the resonant length of a 2.5 *mm* wide microstrip line at 30.5 GHz when manufactured on RT–DUROID 5880 ($\epsilon_r = 2.2$)

was found to be $3.19\,mm$. The patch was edge fed by a $100\,\Omega$ microstrip line which was linearly tapered to $50\,\Omega$ over a distance of approximately one guide wavelength. The $50\,\Omega$ line was continued to the substrate edge to allow attachment to a ridged waveguide to microstrip transformer.

The outline of the antenna and feed is shown in Figure (4.4). The mask for antenna was produced using a CALMA CAD artwork system at Marconi Defence Systems Stanmore (MDS). The antenna was manufactured at MDS using a copper etch–back technique. In order to compensate for the unavoidable undercutting in this process, the patch and feed dimensions were expanded by one metallization thickness. After etching, the substrate was cut to size and soldered to a flat 1/4" thick brass plate which as a support for the flexible substrate and provides a rigid fixing for the waveguide to microstrip transformer. The completed antenna and the microstrip to waveguide transformer are shown in plate(4.1).

4.1.3 Initial Measurements

The initial assessment of the patch input characteristic was performed using a scalar network analyser. This instrument was employed owing to the relative ease with which resonances in the antenna system could be detected. A discussion of the errors associated with scalar network analyser measurements is given in reference(4.8). Using the expressions given in this reference, the accuracy of the scalar network analyser was estimated to be $\pm 1.5\,dB$. The frequency scale of the network analyser was calibrated against a precision absorbtion wavemeter and the accuracy of the frequency scale in the range 26.5–40 GHz was estimated to be $\pm$10MHz. The return loss of the end fed microstrip patch over the frequency range 26.5–40 GHz is given in Figure (4.5). The principle resonance occurs at 30.6 GHz and is associated with a return loss of approximately $18dB$. The bandwidth for a $10\,dB$ return loss is $\pm$415MHz

Figure (4.6) shows the theoretical return loss calculated by the FORTRAN77 program "PATCH" listed in appendix(1). The program makes use of the expressions developed in section(4.1.1) and the dispersion corrected formulae for the microstrip parameters given in reference(4.9). The program predicts the centre frequency of the patch resonance to be 30.5 GHz, and an associated return loss of $27\,dB$ with a $10\,dB$ bandwidth of ± 1.5 GHz. The agreement the centre frequency predicted by the transmission line model and the experimental value is very good, however the theoretical return loss and the $10\,dB$ bandwidth measurements exhibit a noticable deviation from the experimental

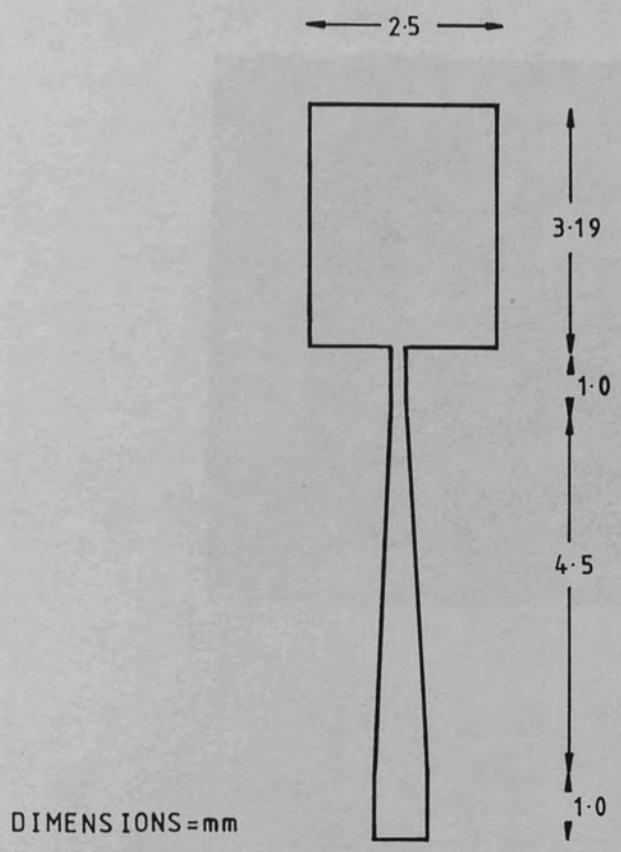

Figure (4.4) Patch and feed line outline

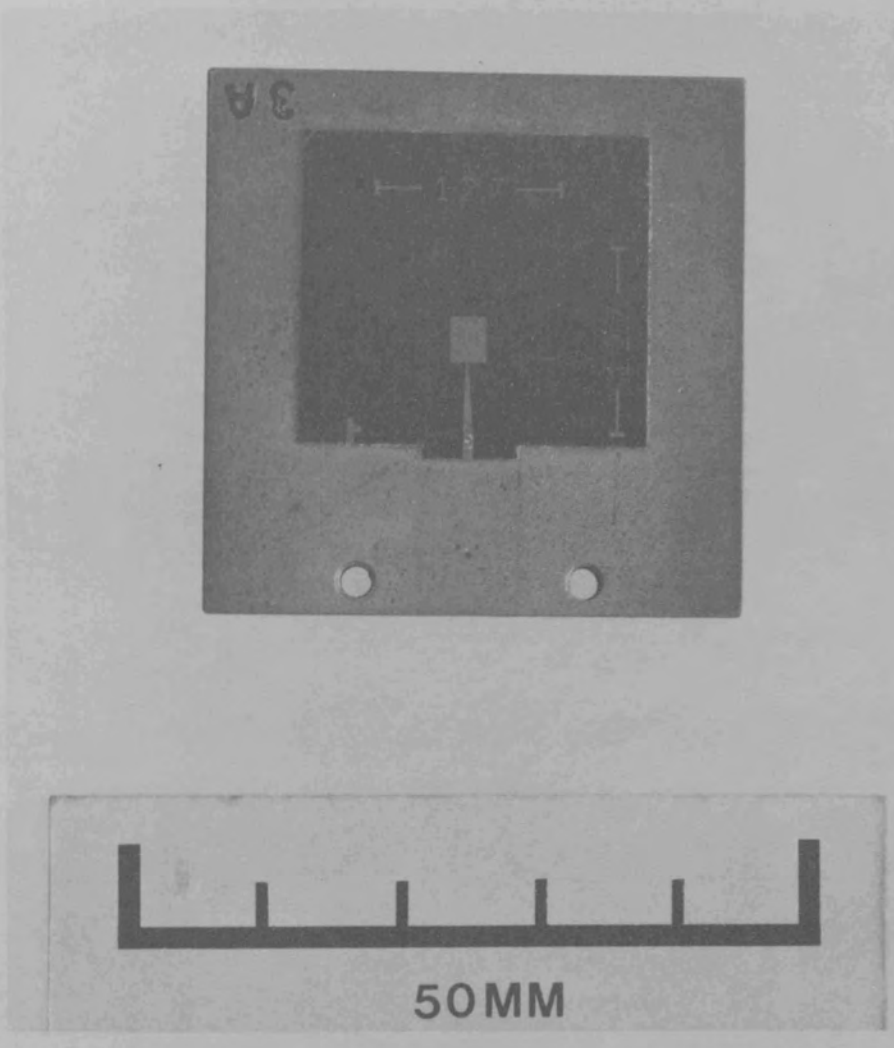

Plate(4.1) The completed rectangular patch antenna

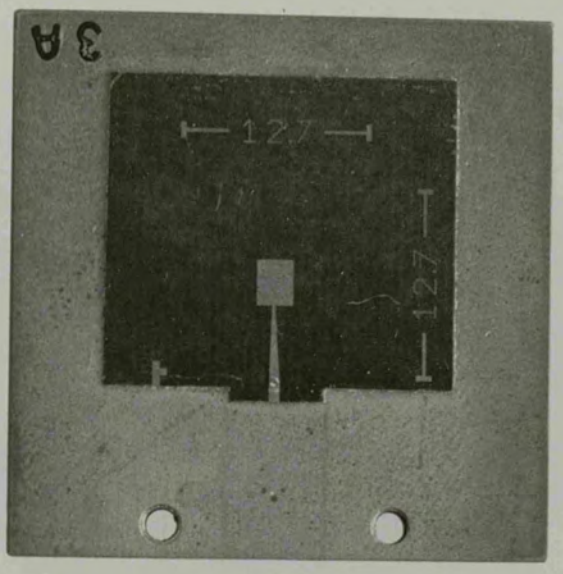
3A
127
127

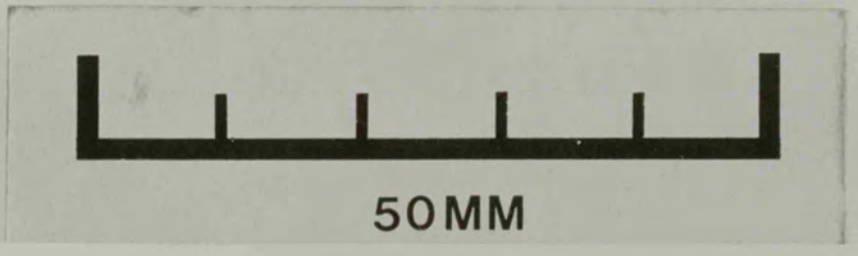
50MM

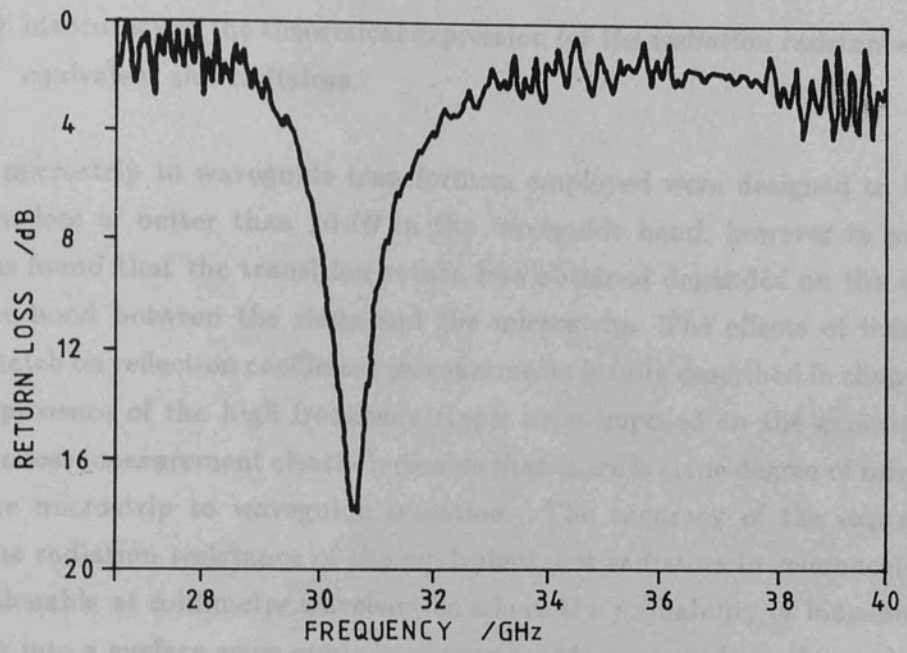

Figure (4.5) Measured rectangular patch return loss

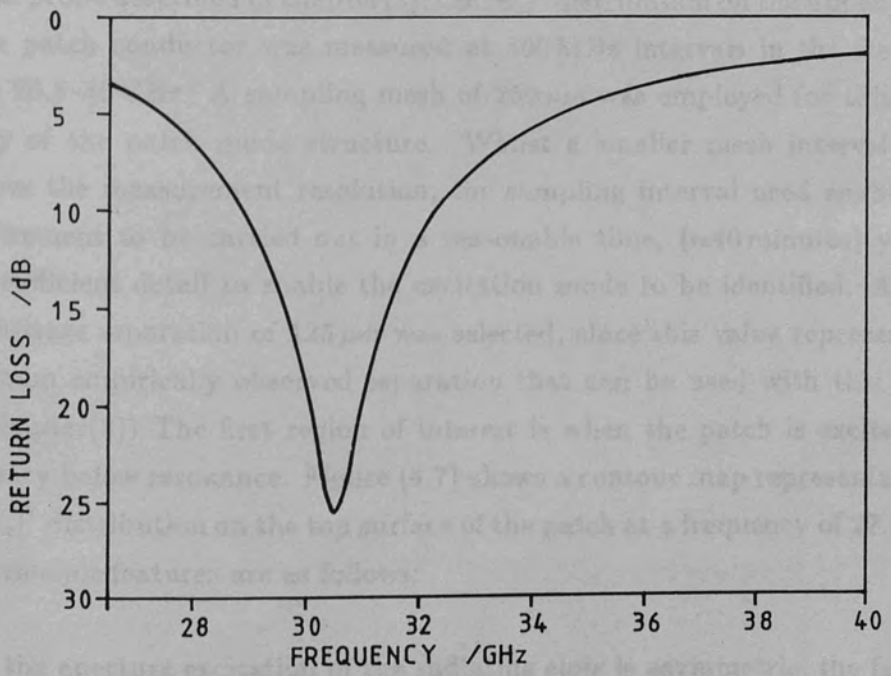

Figure (4.6) Theoretical rectangular patch return loss

values. Possible reasons for the discrepancy include:

(a) the finite mismatch of the waveguide to microstrip transition

(b) inaccuracy of the theoretical expression for the radiation resistance of the equivalent slot radiators.

The microstrip to waveguide transformers employed were designed to have a return loss of better than $20\,dB$ in the waveguide band, however in practice it was found that the transition return loss obtained depended on the quality of the bond between the ridge and the microstrip. The effects of transition mismatch on reflection coefficient measurements is fully described in chapter(6). The presence of the high frequency ripple superimposed on the experimental return loss measurement clearly indicates that there is some degree of mismatch at the microstrip to waveguide transtion. The accuracy of the expressions for the radiation resistance of the equivalent slot radiators in reference(4.1) is questionable at millimetre wavelengths where the probability of launching the power into a surface wave mode is of comparable magnitude to the probability of launching the incident power into a radiation mode.

4.1.4 Scanning Network Probe Measurements

Using the area scanning technique described in chapter(2) and the $0.5\,mm$ coaxial probe described in chapter(3), the $|E_z|^2$ distribution on the upper surface of the patch conductor was measured at 500 MHz intervals in the frequency range 26.5–40 GHz. A sampling mesh of $250\,\mu m$ was employed for this initial survey of the patch mode structure. Whilst a smaller mesh interval would improve the measurement resolution, the sampling interval used enabled the measurement to be carried out in a reasonable time, ($\approx$40 minutes) yet still yield sufficient detail to enable the excitation mode to be identified. A probe to substrate separation of $125\,\mu m$ was selected, since this value represents the maximum empirically observed separation that can be used with this probe. (see chapter(3)) The first region of interest is when the patch is excited at a frequency below resonance. Figure (4.7) shows a contour map representation of the $|E_z|^2$ distribution on the top surface of the patch at a frequency of 27.5 GHz. The principle features are as follows:

(a) the aperture excitation of the radiating slots is asymmetric; the far edge being more uniformly excited across the width whilst the input edge shows relatively little excitation.

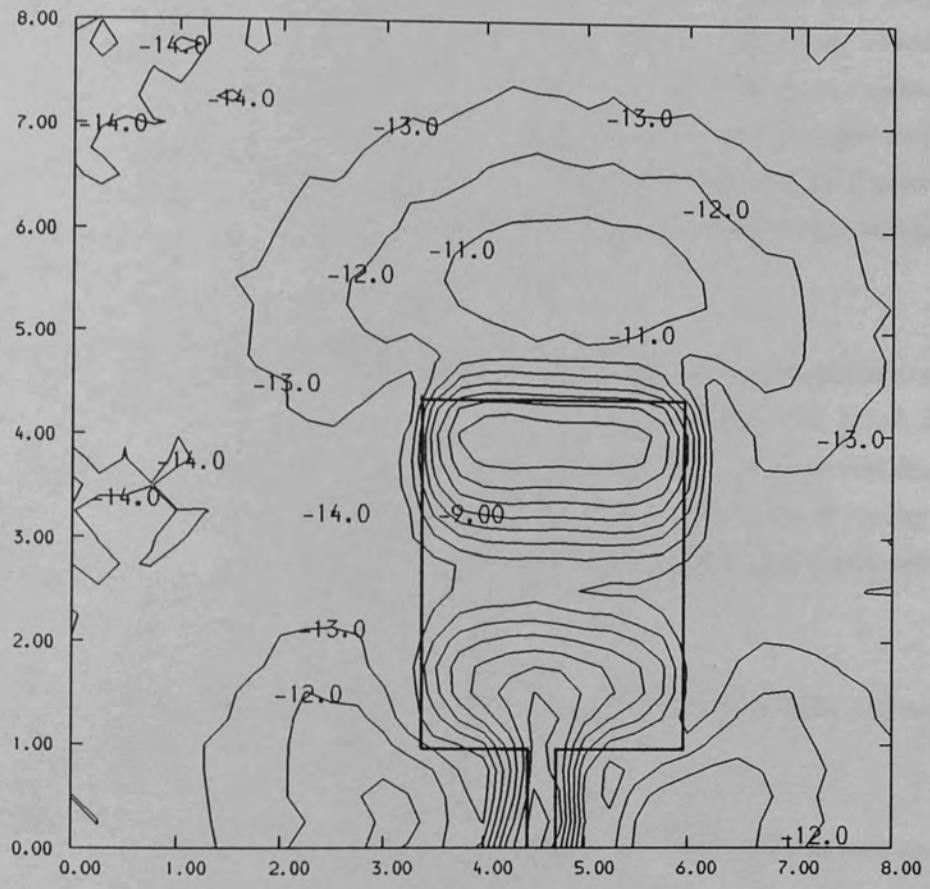

SCALE

$X, Y = 1.0\,mm/division \qquad Z = 1.0\,dB/level$

Figure (4.7) Rectangular patch excited below resonance, F=27.5 *GHz*

(b) the position of the standing wave minimum is not centrally located and is shifted towards the microstrip feed point

(c) regions of enhanced $|E_z|^2$ are present over the substrate area beyond the patch metallization

The features noted in (a) and (b) might be expected intuituively because below resonance the patch is physically shorter than half a guide wavelength and the feed point maximum is forced away from the patch edge and along the microstrip feed. The appearance of the low level region extending beyond the patch open circuit edges was not expected. The fringing effects associated with microstrip open circuits are usually considered to be limited to a few substrate thicknesses distant from the discontinuity. There is evidence in Figure (4.7) that there is a significant fringing effect extending over 10 substrate thicknesses beyond the physical position of the open circuit.

The second region of interest is the transition through resonance, and this process is illustrated with figures(4.8) to (4.10). When the patch is just below resonance, (30.1 GHz) as shown in Figure (4.8), it is observed that the aperture excitation is becoming more symmetric, and that the standing wave minimum is now located close to the centre line of the patch. Further interesting observations are:

(a) the magnitude of the detected signal is approximately 30% higher than that obtained at 27.5 GHz

(b) the amplitude of the standing wave on the microstrip feed is now reduced

Both these features indicate that a better feed point match was achieved at 30.1 GHz than at 27.5 GHz. The input power to the patch was externally levelled to $4dB_m$ in both cases. The field structure beyond the patch metallization is much less prominant just below resonance than at 27.5 GHz. On increasing the frequency to 30.6 GHz, the resonant frequency of the patch as determined by the return loss measurement the excitation mode of the patch changes. With reference to Figure (4.9) the following observations were made:

(a) the open circuit excitation is uniform across the patch width to within approximately 0.5 dB, and the balance of excitation between the two apertures is within a comparable figure.

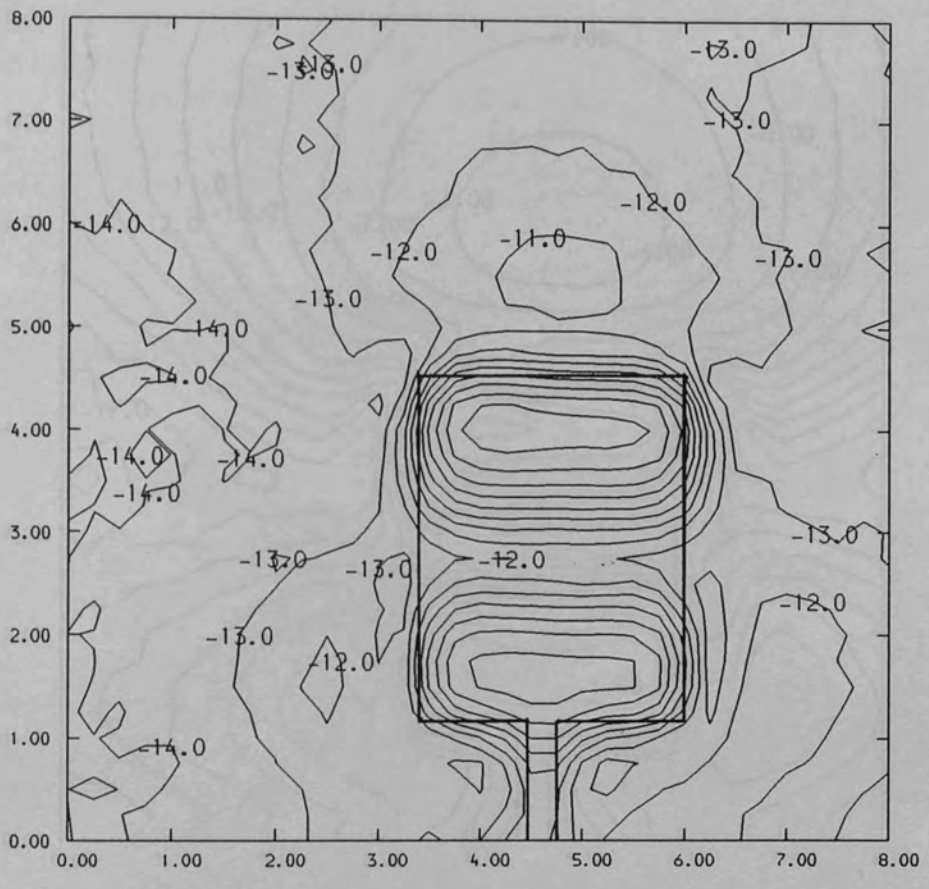

SCALE

$X, Y = 1.0\,mm/division \qquad Z = 1.0\,dB/level$

Figure (4.8) Rectangular patch excited just below resonance, F=30.1 *GHz*

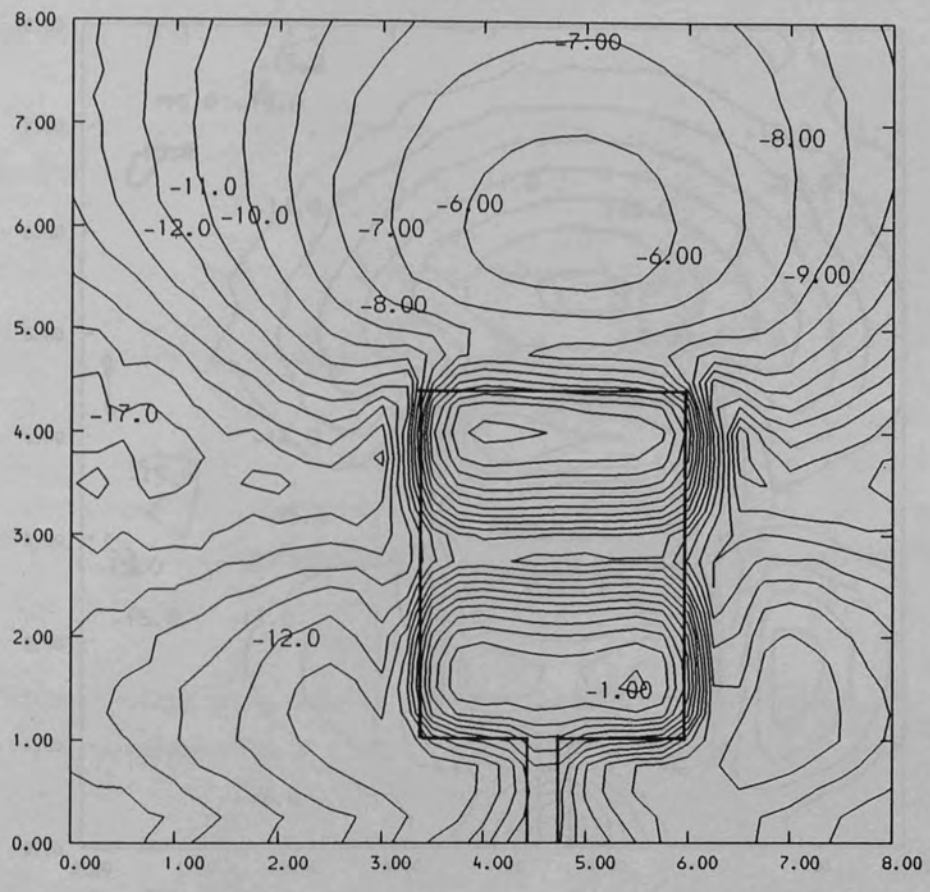

SCALE

$X, Y = 1.0\,mm/division \qquad Z = 1.0\,dB/level$

Figure (4.9) Rectangular patch excited at resonance, F=30.6 *GHz*

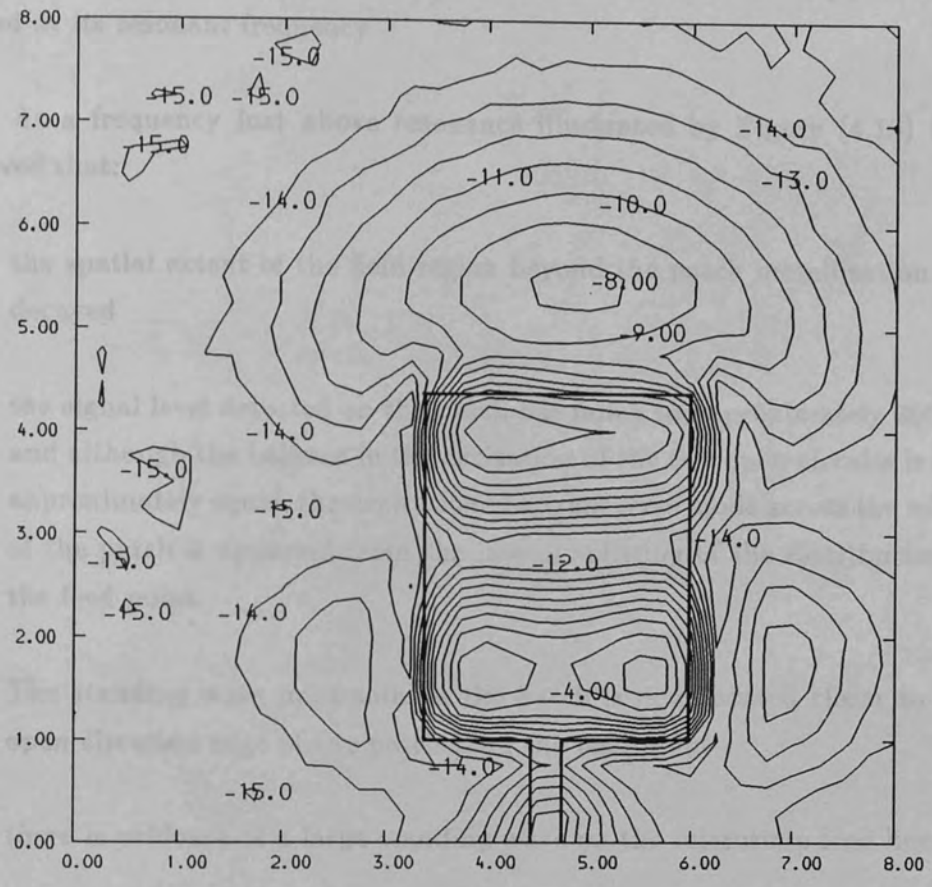

SCALE

$X, Y = 1.0\,mm/division \qquad Z = 1.0\,dB/level$

Figure (4.10) Rectangular patch excited just above resonance, F=31.2 *GHz*

(b) the magnitude of the signal maxima detected at the patch open circuits has now increased to $900\,\mu V$ for $4\,db_m$ of input power

(c) the minimum is located centrally between the open circuit edges

(d) The feature beyond the patch metallization has now become more prominent, and is only $5\,dB$ down in magnitude on the edge excitation

The features noted in (a),(b), and (c) are all consistant with the patch being excited at its resonant frequency.

At a frequency just above resonance illustrated by Figure (4.10) it is observed that:

(a) the spatial extent of the field region beyond the patch metallization has decayed

(b) the signal level detected on the patch has fallen to approximately $250\,\mu V$ and although the balance in the excitation of the two open circuits is still approximately equal, the excitation of a transverse mode across the width of the patch is apparent from the lateral splitting of the distribution at the feed point.

(c) The standing wave minimum on the patch is now located closer to the open circuited edge of the patch than the feed point

(d) there is evidence of a large standing wave on the microstrip feed line

The effect of increasing the frequency to a point where the cross polar TM_{11} mode is strongly excited (35 GHz in this case) is shown in Figure (4.11). It is observed that the patch excitation has become highly asymmetric, with two opposing corners being strongly excited. The asymmetry in this instance is attributed to the slight offset in the microstrip feed point from the mid point of the patch width. There is no indication of any significant field regions beyond the patch metallization in this example.

4.1.5 Further Comments on the Scanning Network Probe Results

In the previous section the pictorial nature of the two dimensional amplitude plots was exploited to enable the mode of excitation of a rectangular

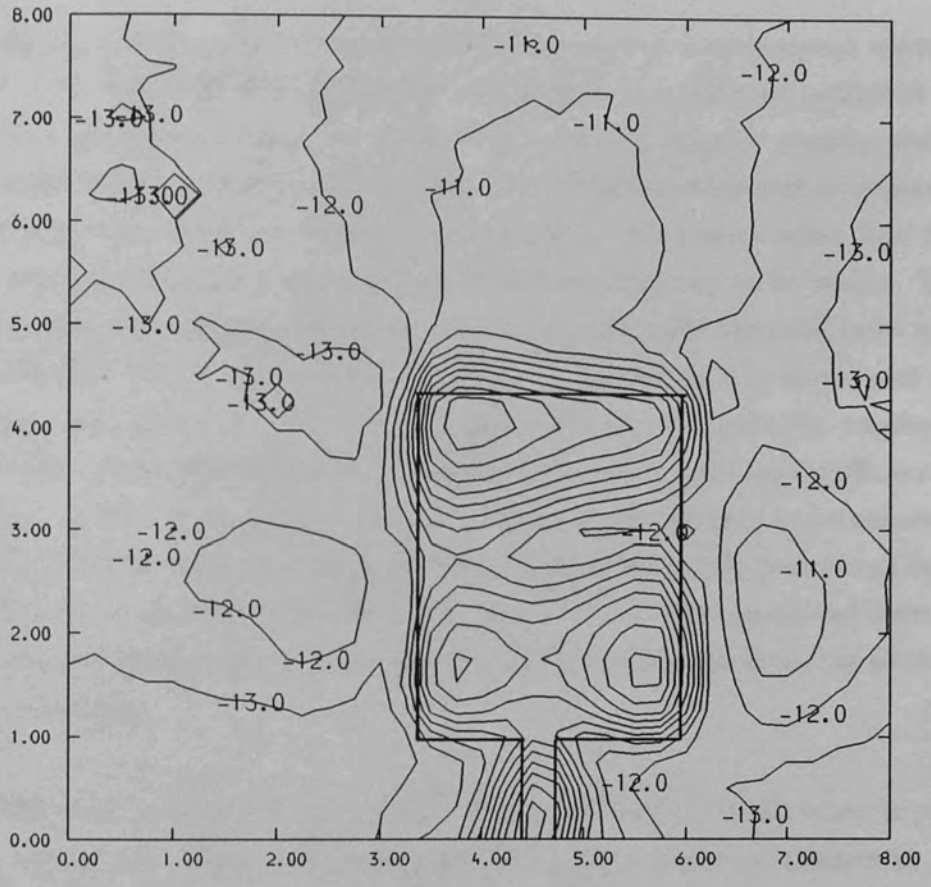

SCALE

$X, Y = 1.0\,mm/division \qquad Z = 1.0\,dB/level$

Figure (4.11) Rectangular patch excited above resonance, F=35 *GHz*

patch to be observed as a function of frequency. There are two more aspects worthy of further study:

(a) the input behaviour of the patch measured using the scanning network probe system

(b) the behaviour of the field regions beyond the patch metallization as a function of frequency

By using the scanning network probe transmission line measurement routines described in chapter(6) it is possible to characterize the input behaviour of the patch as a function of frequency by a series of spot frequency psuedo–slotted line measurements on the microstrip feed. One major problem was encountered in applying this technique, namely the length of the transmission line feed which was too short to enable good VSWR measurements to be made. This problem arose because the microstrip circuit was originally designed to be used in conjunction with a sub–miniature coaxial to microstrip transition, and not the larger waveguide to microstrip transformer that was actually employed. The length of the transmission line accessible to the probe was sufficient to enable the shift in the first maximum as a function of frequency to be observed. The experimental data is plotted in Figure (4.12) with the theoretical value calculated from equation(4.16), shown by the solid line. The agreement between the theory and experiment is good, which helps to validate the scanning network probe technique.

The amplitude of the field region beyond the patch metallization is plotted as a function of frequency in Figure (4.13). The graph maximizes at the resonant frequency of the patch, and also exhibits smaller maxima at frequency intervals of approximately 1.8 GHz. It was also observed that changes in the substrate boundary conditions, such as loading with R.F. absorber, or partially covering the substrate area with a copper sheet, have negligable effect on the these field regions. This is illustrated by figures(4.14) to (4.16) which shows the measured $|E_z|^2$ distribution with the surrounding substrate area:

(a) open

(b) covered with R.F. absorber

(c) covered with copper foil

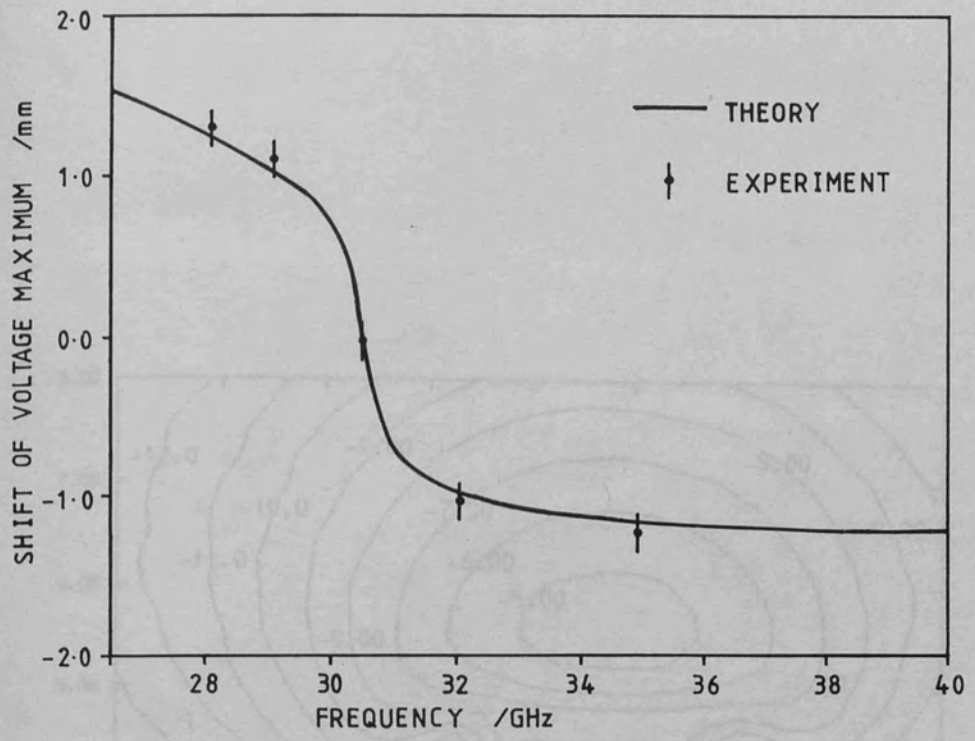

Figure (4.12) First minimum shift against frequency

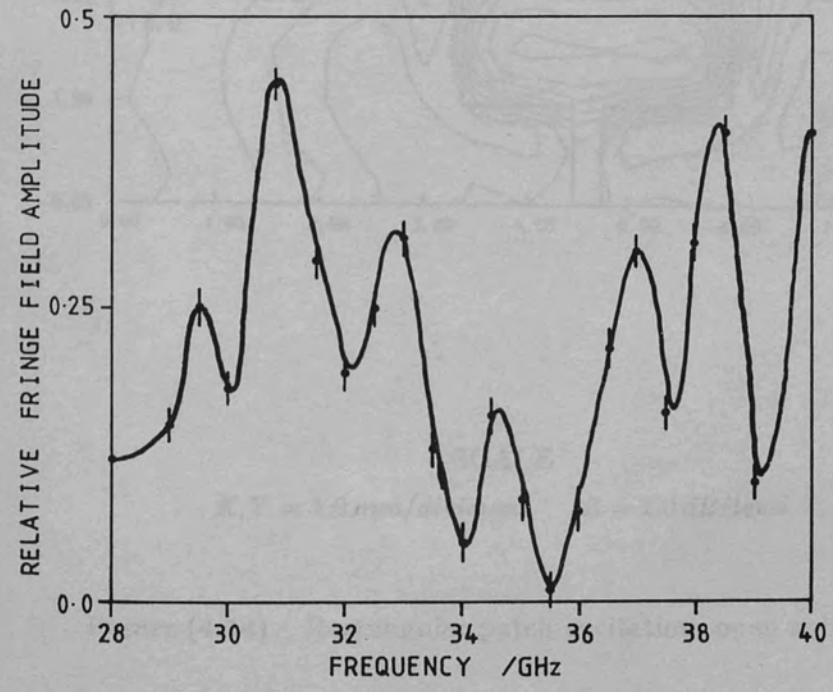

Figure (4.13) Fringe field amplitude against frequency

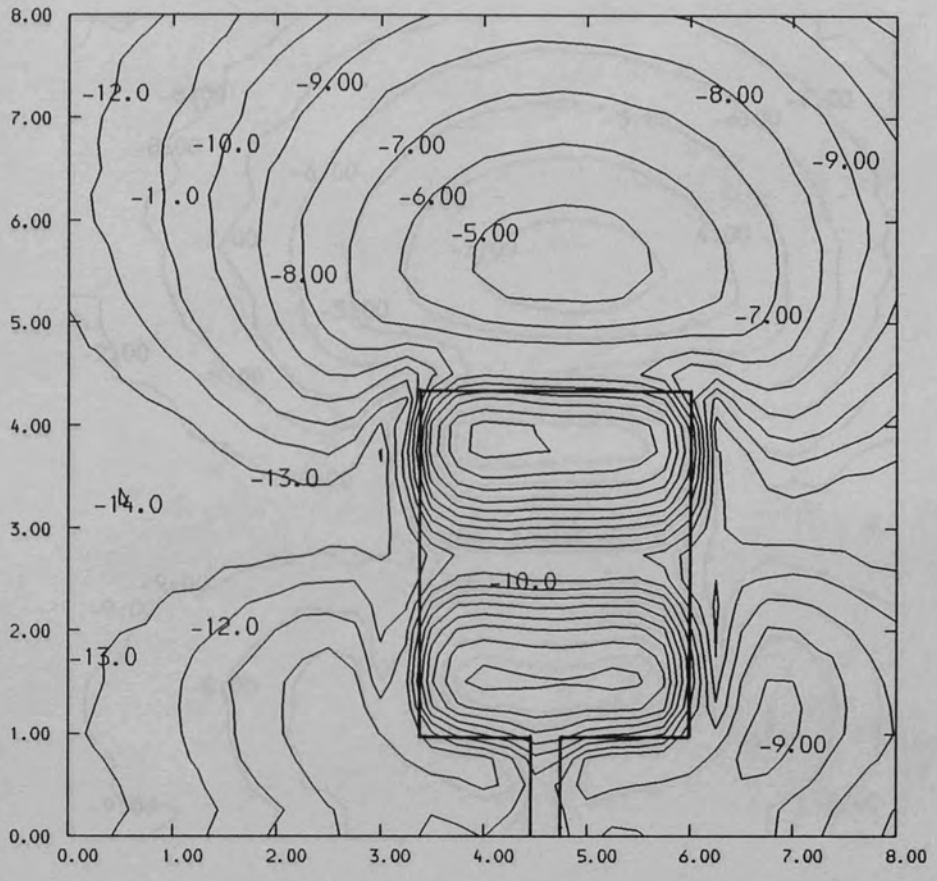

SCALE

$X, Y = 1.0\,mm/division \qquad Z = 1.0\,dB/level$

Figure (4.14) Rectangular patch excitation, open substrate

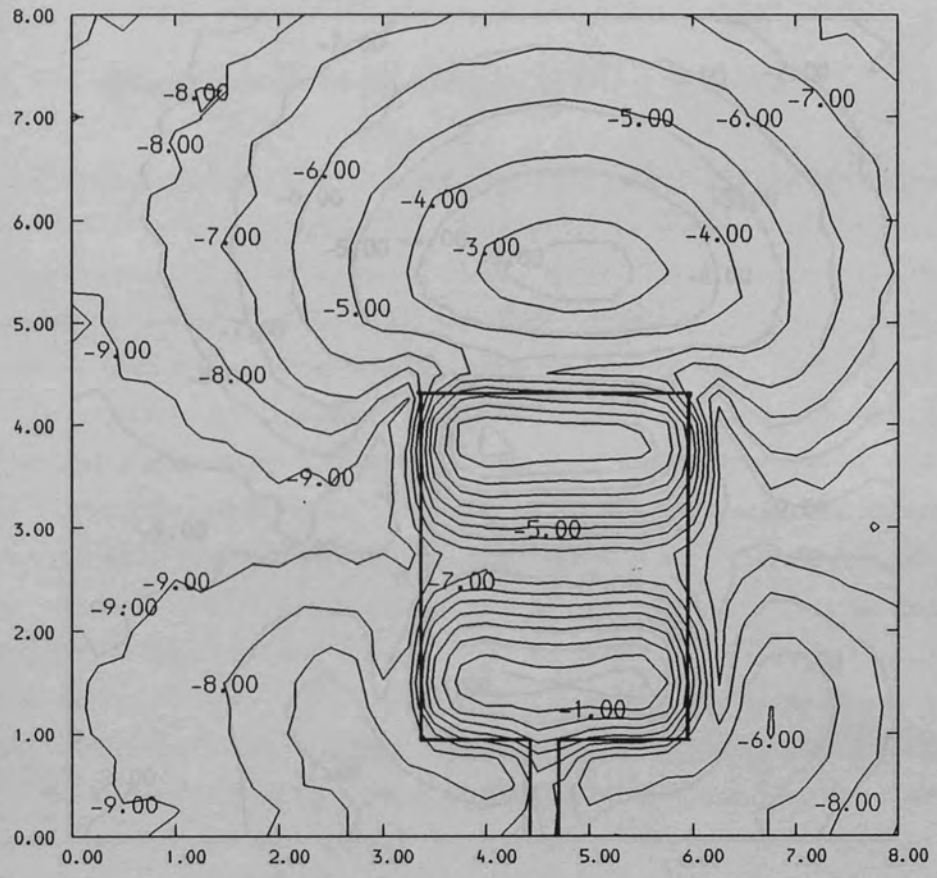

SCALE

$X, Y = 1.0\,mm/division \qquad Z = 1.0\,dB/level$

Figure (4.15) Rectangular patch excitation, swam edged substrate

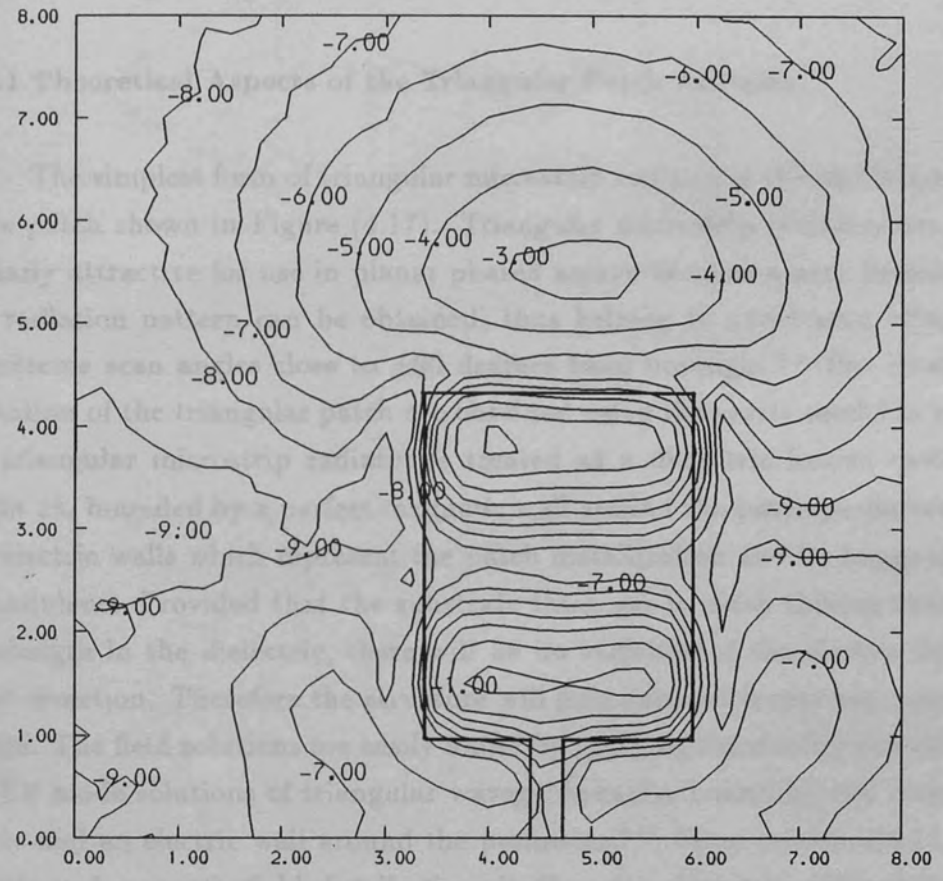

SCALE

$X, Y = 1.0\,mm/division \qquad Z = 1.0\,dB/level$

Figure (4.16) Rectangular patch excitation, copper edged substrate

If the external field regions were due to a propagating TM_0 surface wave, then modifying the substrate boundary conditions in the manner described would be expected to alter the observed field structure. This suggests that these field regions are evanescent and are not associated with a propagating wave in the near field region; the slight perturbation of the probe is assumed to be the cause of a power flow out from the evanescent region. The nature of these features will be discussed further in chapter(8).

4.2 The Triangular Patch Antenna

4.2.1 Theoretical Aspects of the Triangular Patch Antenna

The simplest form of triangular microstrip radiator is the equilateral triangle patch shown in Figure (4.17). Triangular microstrip radiators are particularly attractive for use in planar phased arrays because a near hemispherical radiation pattern can be obtained, thus helping to avoid scan blindness at extreme scan angles close to ± 90 degrees from boresight.[4.1] The modes of excitation of the triangular patch are obtained using the cavity model in which the triangular microstrip radiator is treated as a dielectric loaded cavity of height $2h$, bounded by a perfect magnetic wall around the patch perimeter and two electric walls which represent the patch metallization and its image in the groundplane. Provided that the substrate thickness is much thinner than the wavelength in the dielectric, there will be no variation of the electric field in the z–direction. Therefore the structure will only support transverse magnetic modes. The field solutions are easily found by applying the duality principle to the TE mode solutions of triangular waveguide cavity bound by two magnetic sheets and an electric wall around the perimeter.[4.11] From reference(4.12) the electric and magnetic field distributions in the equivalent triangular resonator are given by:

$$E_z = A_{m,n,l} T(x,y)_{m,n,l} \tag{4.20}$$

$$H_x = \frac{j}{\omega\mu} \frac{\partial E_z}{\partial y} \tag{4.21}$$

$$H_y = -\frac{j}{\omega\mu} \frac{\partial E_z}{\partial x} \tag{4.22}$$

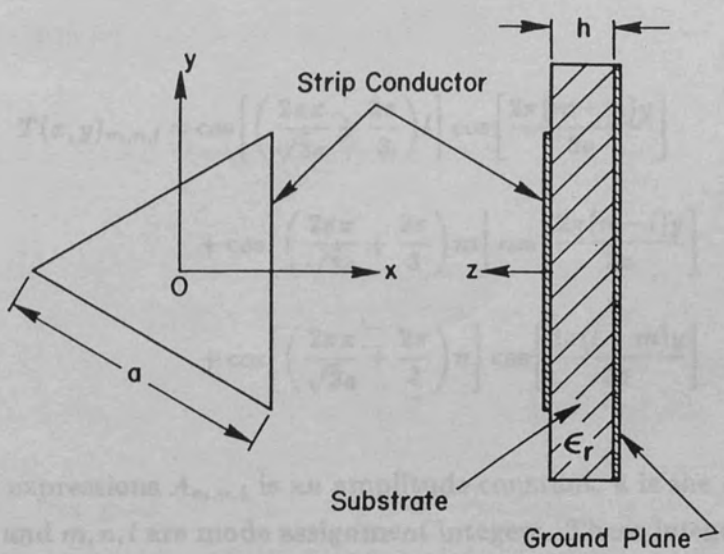

Figure (4.17) The equilateral triangle patch radiator

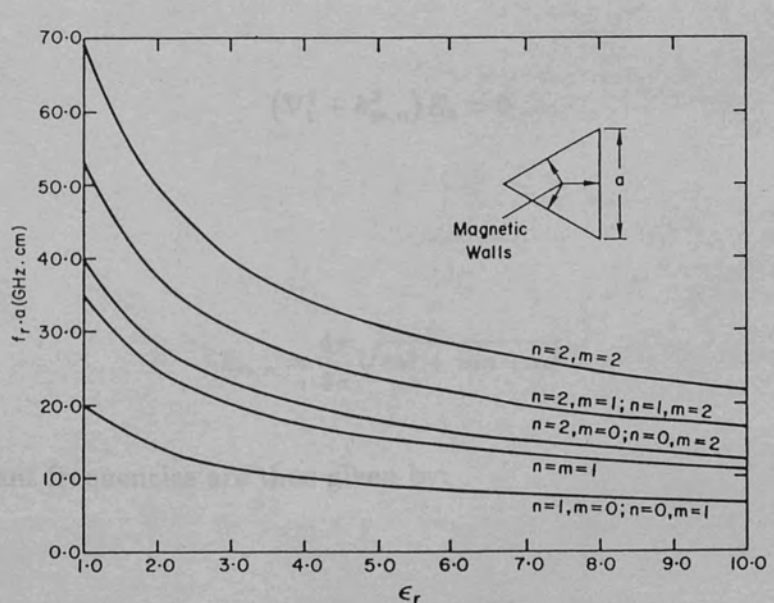

Figure (4.18) $F_r.a$ product against radius r

$$E_x = E_y = H_z = 0$$

Where:

$$T(x,y)_{m,n,l} = \cos\left[\left(\frac{2\pi x}{\sqrt{3}a} + \frac{2\pi}{3}\right)l\right]\cos\left[\frac{2\pi(m-n)y}{3a}\right]$$

$$+\cos\left[\left(\frac{2\pi x}{\sqrt{3}a} + \frac{2\pi}{3}\right)m\right]\cos\left[\frac{2\pi(n-l)y}{3a}\right]$$

$$+\cos\left[\left(\frac{2\pi x}{\sqrt{3}a} + \frac{2\pi}{3}\right)n\right]\cos\left[\frac{2\pi(l-m)y}{3a}\right] \qquad 4.23$$

In the above expressions $A_{m,n,l}$ is an amplitude constant, a is the length of the triangle side and m, n, l are mode assignment integers. These integers can never be simultaneously zero, and must also satisfy the condition:

$$m + n + l = 0 \qquad 4.24$$

The fields satisfy the wave equation:

$$\left(\nabla_t^2 + k_{m,n}^2\right) E_z = 0 \qquad 4.25$$

When:[4.12]

$$k_{m,n} = \frac{4\pi}{3a}\sqrt{m^2 + mn + n^2} \qquad 4.26$$

The resonant frequencies are thus given by:

$$f_{n,m} = \frac{ck_{m,n}}{2\pi\sqrt{\epsilon_r}}$$

$$= \frac{2c}{3a\sqrt{\epsilon_r}}\left(m^2 + mn + n^2\right)^{\frac{1}{2}} \qquad 4.27$$

Equation(4.27) is plotted in Figure (4.18) as a function of ϵ_r. (taken from reference(4.1) In order to visualize the theoretical $|E_z|^2$ distribution in the equivalent triangular resonator, equation(4.23) was incorporated into the FORTRAN77 program "TRIMODE" listed in appendix(1). The $|E_z|^2$ distributions for the first five modes are plotted in figures(4.19) to (4.23), and serve as a direct visual comparison for the measured results.

4.2.2 Triangular Patch Design and Fabrication

With the aid of equation(4.17) equilateral triangular patches were designed to be resonant in the TM_{01},TM_{11},TM_{02},TM_{12}, and TM_{22} modes at a frequency of 35 GHz when fabricated on RT–DUROID 5880. ($\epsilon_r = 2.2$) It was decided to feed the patches from one apex by a high impedance microstrip, which was tapered to $50\,\Omega$ for use with the waveguide to microstrip transformers that were available. The antennas were fabricated at the centre of a $50\,mm \times 50\,mm$ substrate a similar copper etch back method used at MDS Stanmore. The soldering of such large substrates to the brass support plate requires a special technique to obtain the high quality surface finish required. The technique involves soldering the substrate to a precision machined brass plate in a heated press, and the surface finish obtained is better than 0.0001" over the substrate area. The completed antennas are shown in plate(4.2). The initial tests to find the location of the patch resonant frequencies were performed using a scalar network analyser. The etched dimensions, resonant frequency and return loss at resonance are given in Table(4.1).

TABLE(4.1)

Principal Resonant Mode Characteristics

mode	a–theory/mm	a–measured/mm	frequency/GHz	return loss/dB
TM_{01}	3.9	3.77	35.0	4.8
TM_{11}	6.3	6.20	34.0	6.3
TM_{02}	7.5	7.25	35.1	12.0
TM_{12}	10.3	10.26	35.0	10.0
TM_{22}	13.4	13.31	34.4	15.0

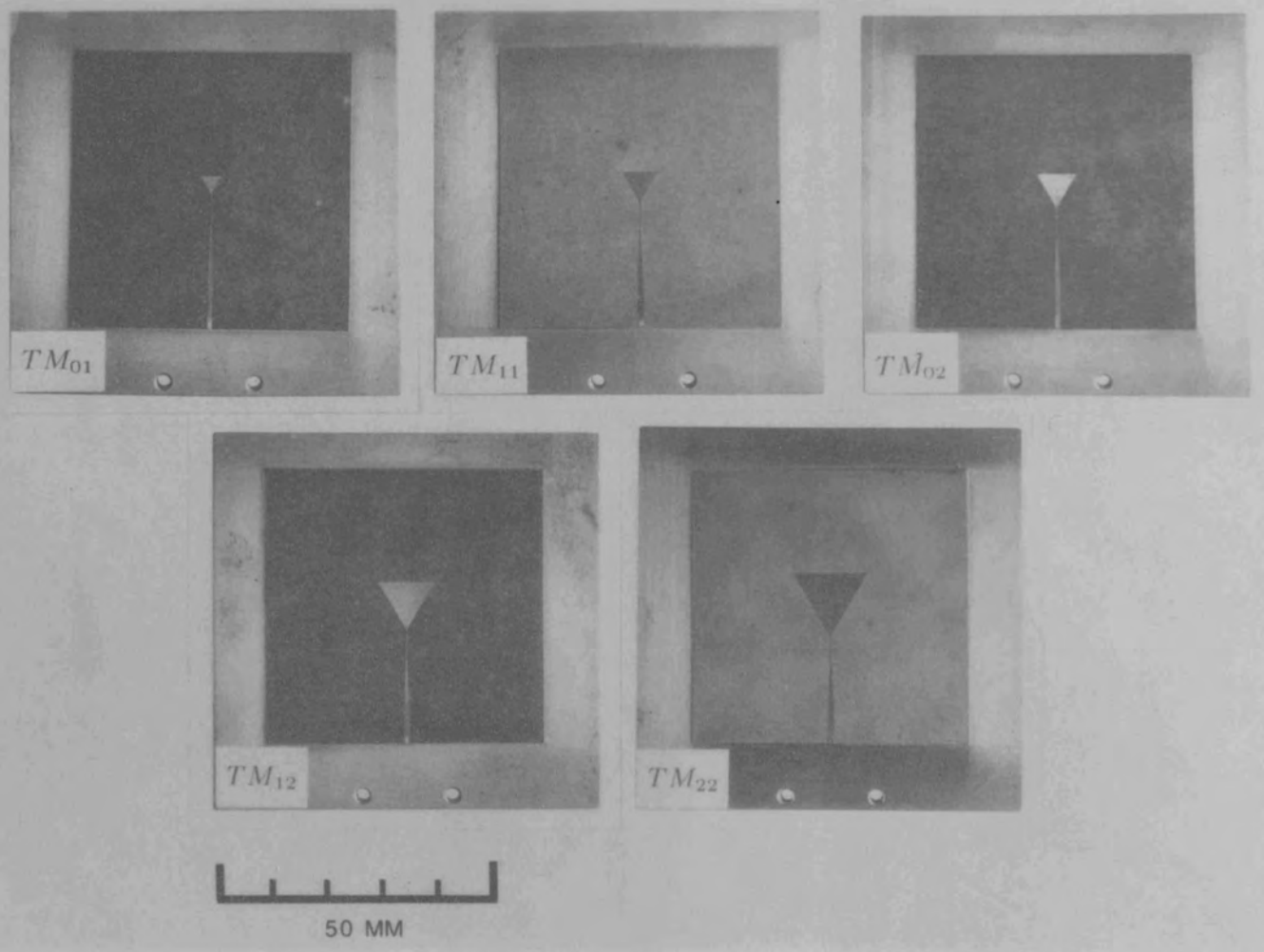

Plate(4.2) The completed triangular patch antennas

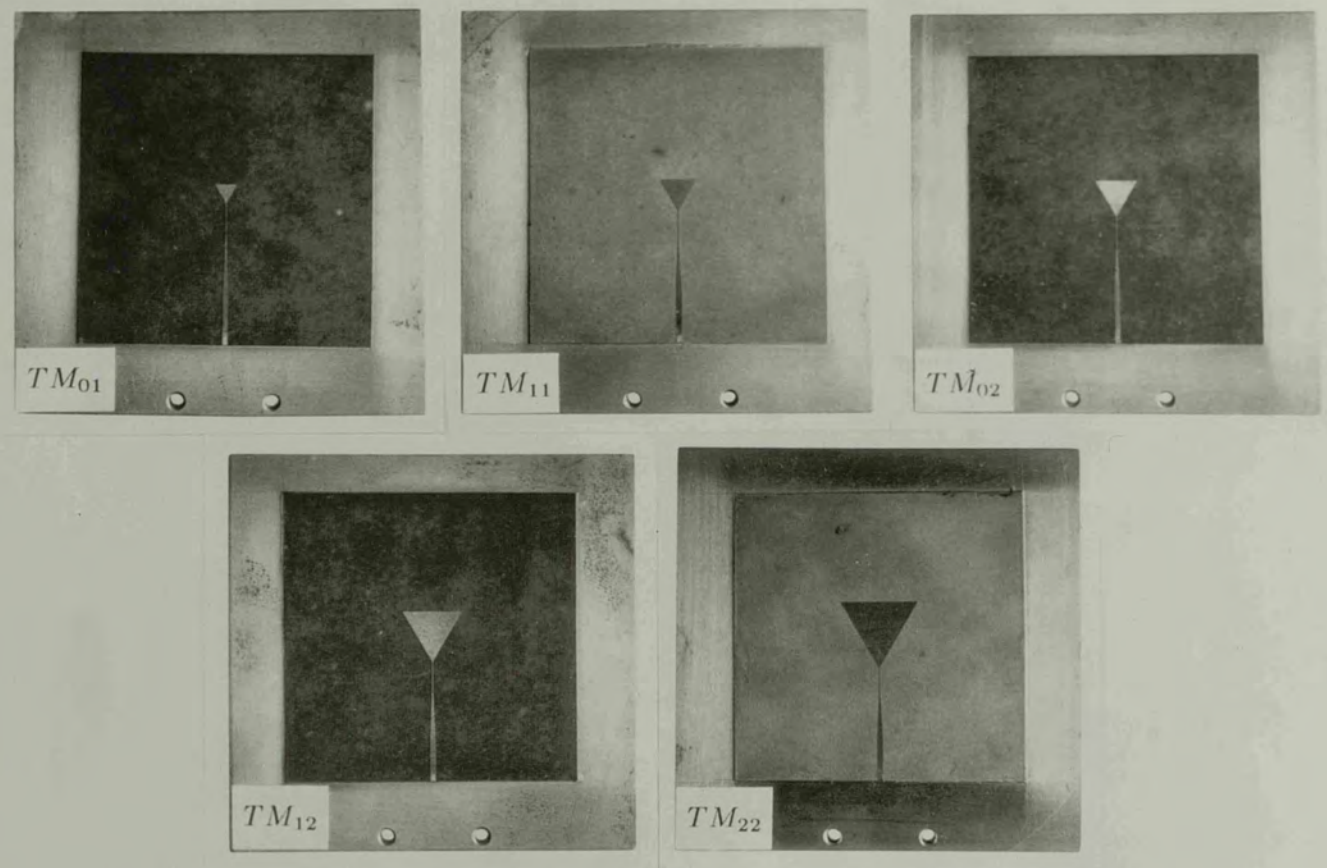
TM_{01}
TM_{11}
TM_{02}
TM_{12}
TM_{22}
50 MM

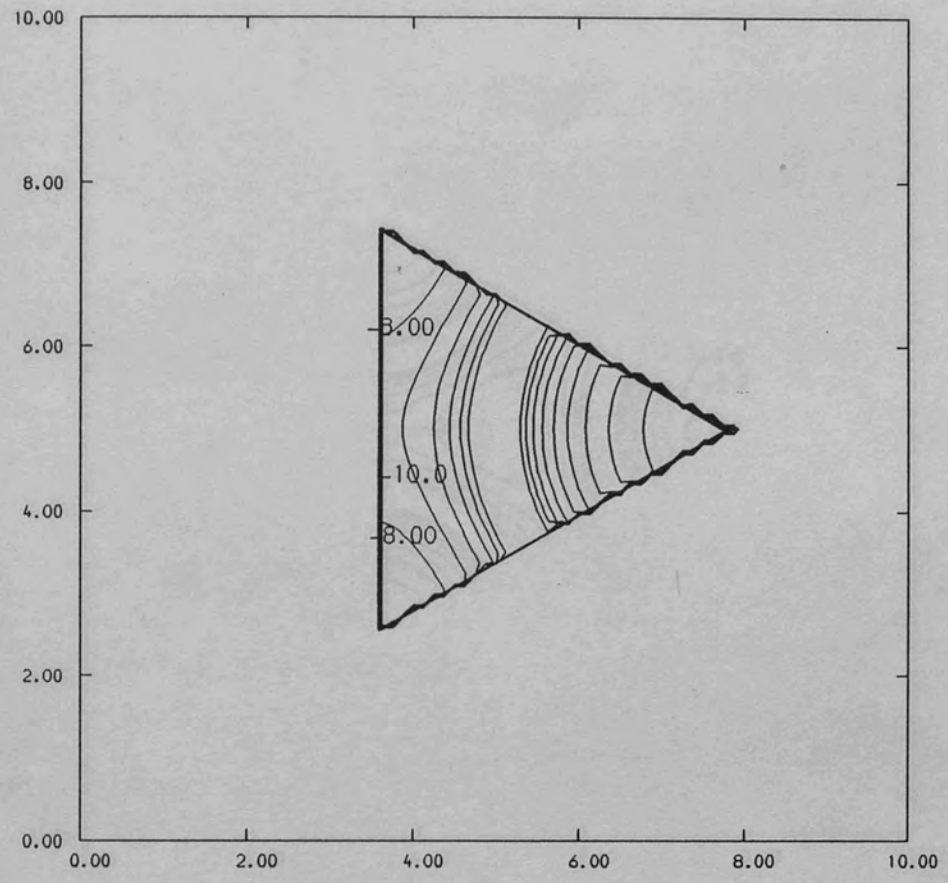

SCALE

$X, Y = 2.0\,mm/division \qquad Z = 2\,dB/level$

Figure (4.19) Theoretical $|E_z|^2$ for the TM_{01} mode

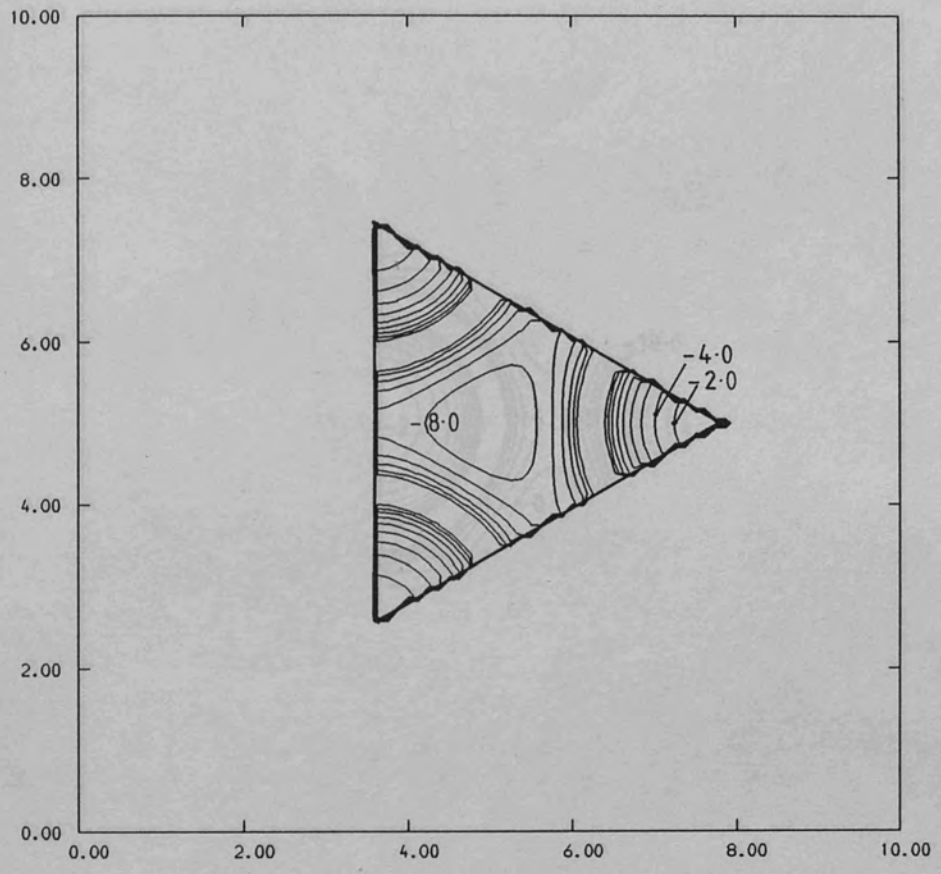

SCALE

$X, Y = 2.0\,mm/division \qquad Z = 2\,dB/level$

Figure (4.20) Theoretical $|E_z|^2$ for the TM_{11} mode

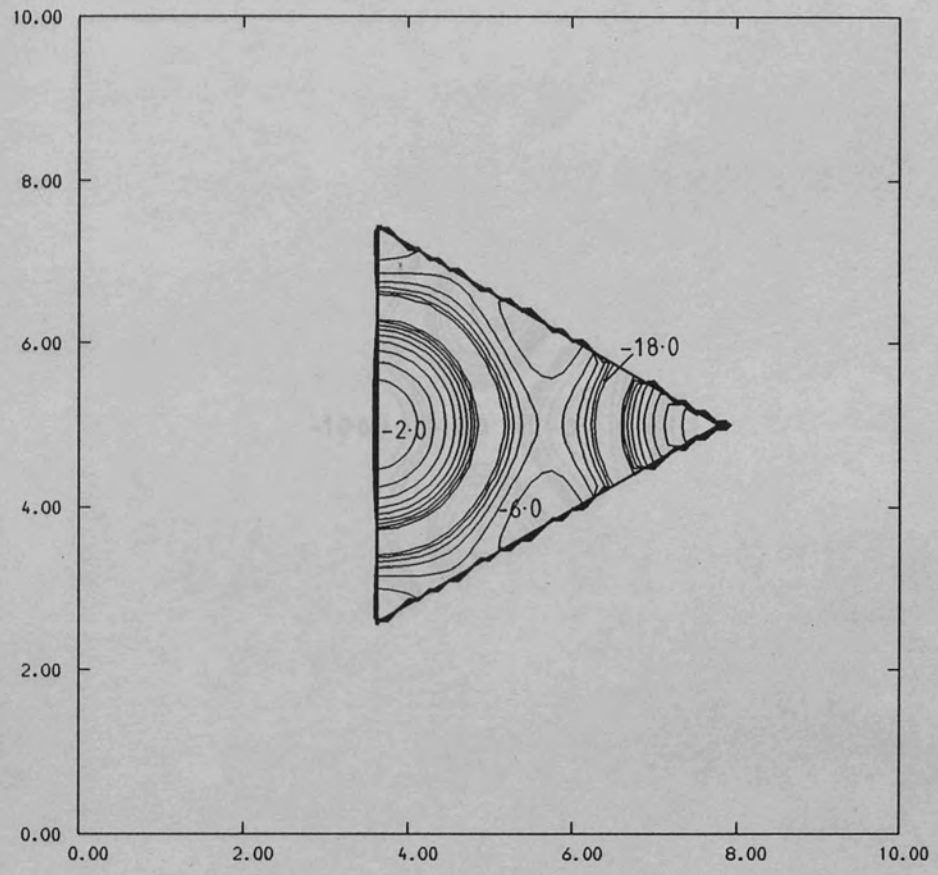

SCALE

$X, Y = 2.0\,mm/division \qquad Z = 2\,dB/level$

Figure (4.21) Theoretical $|E_z|^2$ for the TM_{02} mode

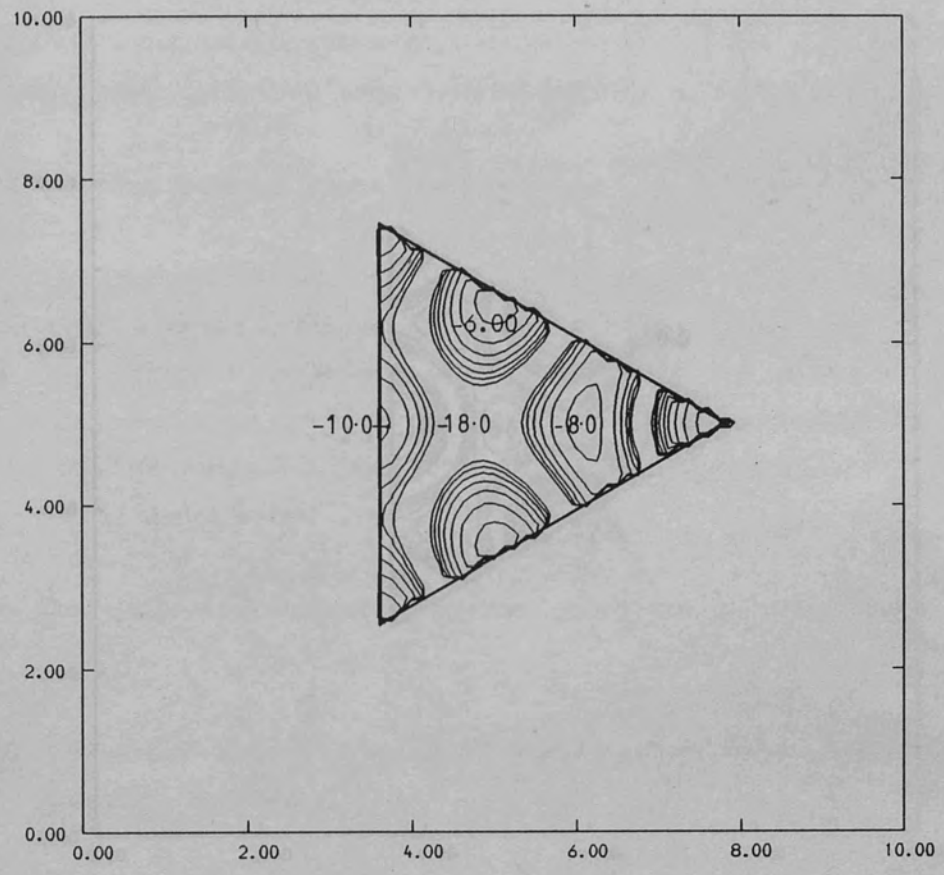

SCALE

$X, Y = 2.0\,mm/division \qquad Z = 2\,dB/level$

Figure (4.22) Theoretical $|E_z|^2$ for the TM_{12} mode

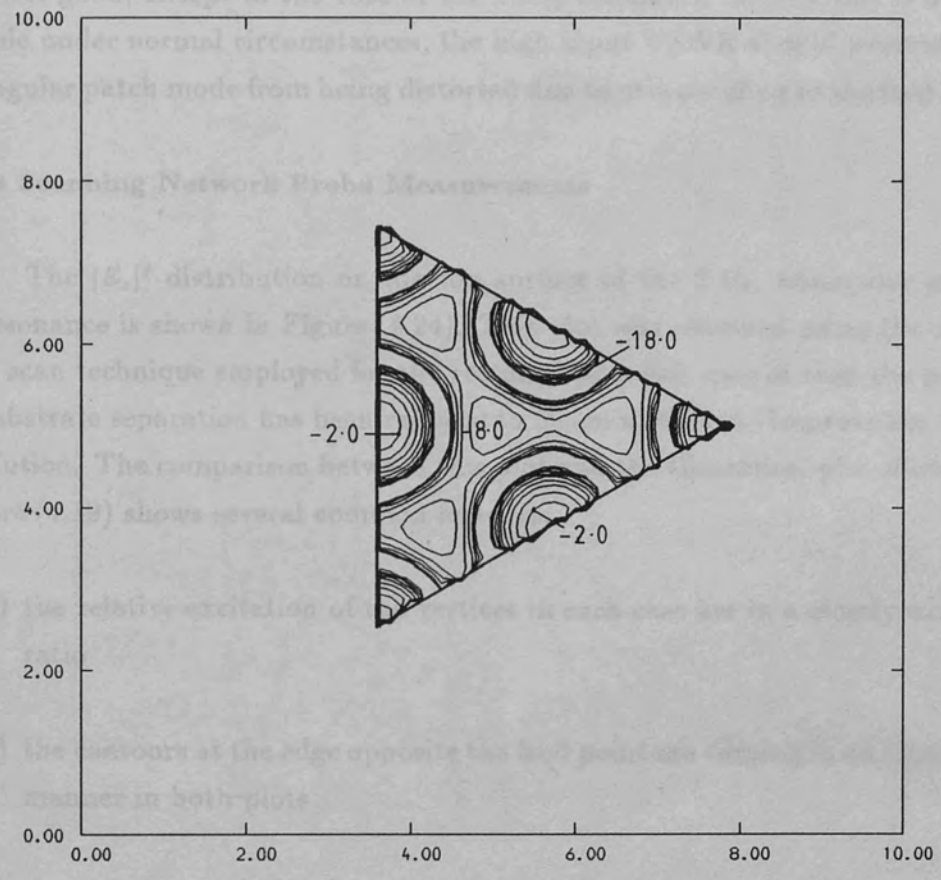

SCALE

$X, Y = 2.0\,mm/division \qquad Z = 2\,dB/level$

Figure (4.23) Theoretical $|E_z|^2$ for the TM_{22} mode

The resonant frequencies are quite close to the design frequency of 35 GHz, which is somewhat fortuitous agreement since the design equation took no account of fringing field effects. Neglecting the fringe field capacitance in this manner would normally be expected to lower the resonant frequency of the microstrip resonator. Reference to Table(4.1) shows that the etch undercut had reduced the patch dimensions, and partially compensated for the oversize dimensions calculated from equation(4.27). The return loss of the apex fed patches shows that the matching to the high impedance microstrip ($\approx 140\,\Omega$) was not good, except in the case of the TM_{22} resonator. Whilst this is undesirable under normal circumstances, the high input VSWR should prevent the triangular patch mode from being distorted due to overcoupling to the feed line.

4.2.3 Scanning Network Probe Measurements

The $|E_z|^2$ distribution on the top surface of the TM_{01} triangular patch at resonance is shown in Figure (4.24). This plot was obtained using the same area scan technique employed for the rectangular patch, except that the probe to substrate separation has been reduced to $50\,\mu m$ in order to improve the edge resolution. The comparison between this plot and the theoretical plot shown in Figure (4.19) shows several common features:

(a) the relative excitation of the vertices in each case are in a closely similar ratio

(b) the contours at the edge opposite the feed point are varying in an identical manner in both plots

(c) the experimental plot shows the contour bunching effect at the feed apex, which was also noted in the theoretical plot, and is due to the contouring software routine

Figure (4.25) shows the cross section of the TM_{01} plot along the axis of the microstrip feed. This plot shows the first standing wave maximum in the feeder occurs $3.25 \pm 0.125\,mm$ from the apex. This represents approximately a half guide wavelength in the high impedance microstrip feed, therefore implying that the input impedance of the TM_{01} triangle at resonance is very high. The input VSWR of the TM_{01} triangular patch works out to be 1.9, which corresponds to a return loss of $\approx 5\,dB$. This figure compares favourably with the the $4.8 \pm 1.8\,dB$ measured in the waveguide feed with the scalar network analyser. A more qualitative mode identification was made by a simple six point

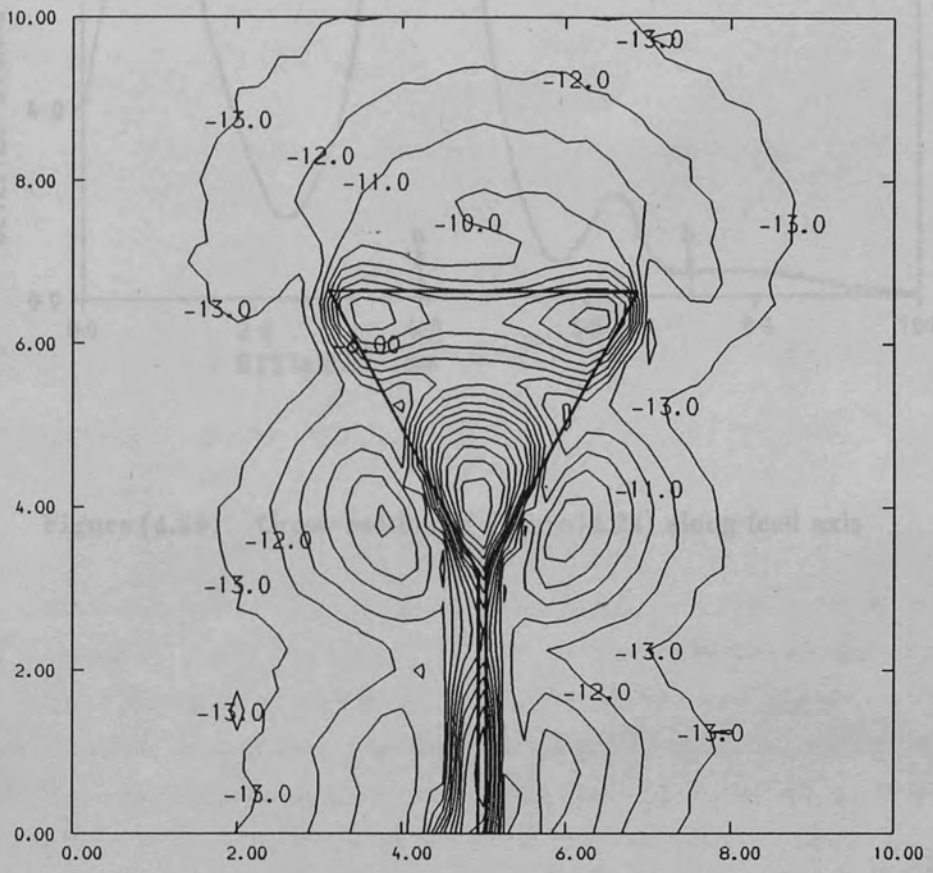

SCALE

$X, Y = 2.0\,mm/division \qquad Z = 1.0\,dB/level$

Figure (4.24) Experimental $|E_z|^2$ for the TM_{01} mode, F=35 GHz

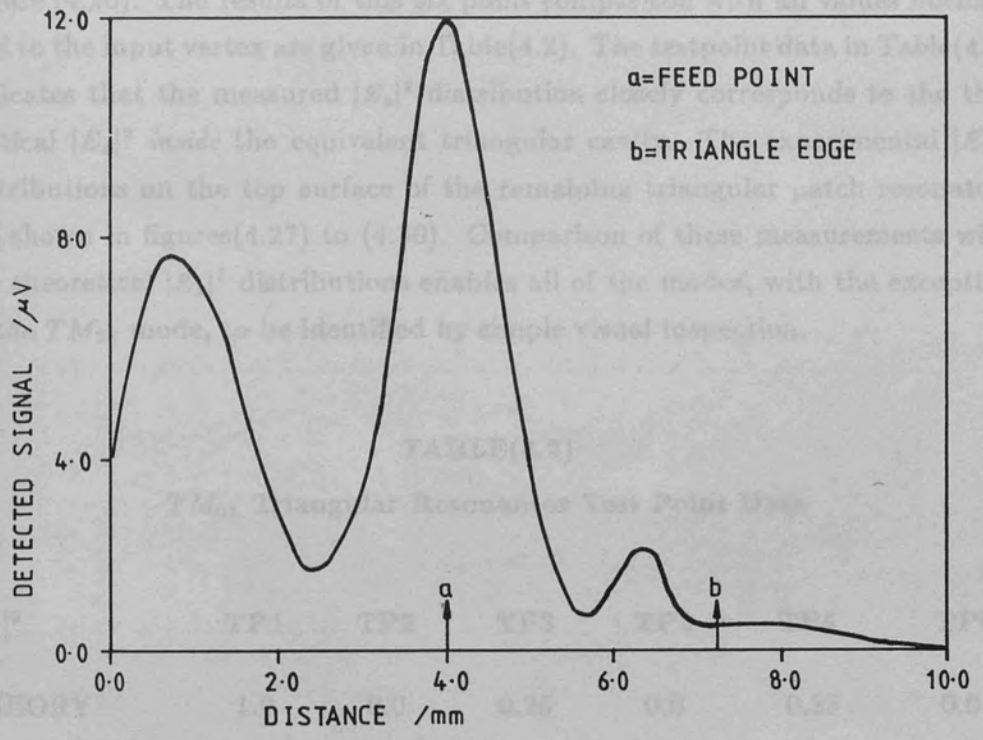

Figure (4.25) Cross–section of Figure (4.24) along feed axis

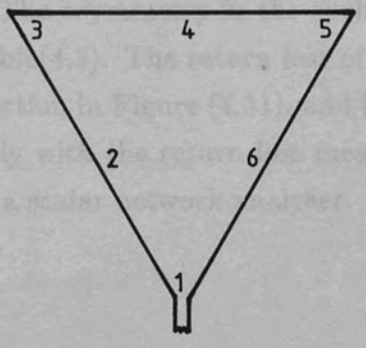

Figure (4.26) Triangle test point locations

amplitude comparison test. The test point pattern that was adopted is shown in Figure (4.26). The results of this six point comparison with all values normalized to the input vertex are given in Table(4.2). The testpoint data in Table(4.2) indicates that the measured $|E_z|^2$ distribution closely corresponds to the theoretical $|E_z|^2$ *inside* the equivalent triangular cavity. The experimental $|E_z|^2$ distributions on the top surface of the remaining triangular patch resonators are shown in figures(4.27) to (4.30). Comparison of these measurements with the theoretical $|E_z|^2$ distributions enables all of the modes, with the exception of the TM_{22} mode, to be identified by simple visual inspection.

TABLE(4.2)

TM_{01} Triangular Resonantor Test Point Data

$\lvert\frac{E_z}{E_0}\rvert^2$	**TP1**	**TP2**	**TP3**	**TP4**	**TP5**	**TP6**
THEORY	1.0	0.0	0.25	0.0	0.25	0.0
EXPERIMENT	1.0±.02	0.0±.02	0.27±.03	0.0±.02	0.34±.05	0.0±0.02

Considering the TM_{11} mode in more detail, it is apparent there is a slight asymmetry in the mode of excitation. With reference to Figure (4.27), the left hand vertex is more weakly excited than the other two which are of equal amplitude. It is interesting to note that the fringing field region is also slightly more pronounced at this vertex. The cause of this effect is uncertain, and cannot be related to defects in the patch resonator or the probe. Tracking errors in the probe height can also be ruled out since the amplitude of the fringing field region and the fields over the patch metallization both decay with increasing probe height. The asymmetry in the excitation is quantified by the six point test given in Table(4.3). The return loss of the antenna input can be deduced from the cross section in Figure (4.31), and is found to be $7.5\,dB$. This result compares favourably with the return loss measurement of $6\pm2\,dB$ made in the waveguide feed by a scalar network analyser.

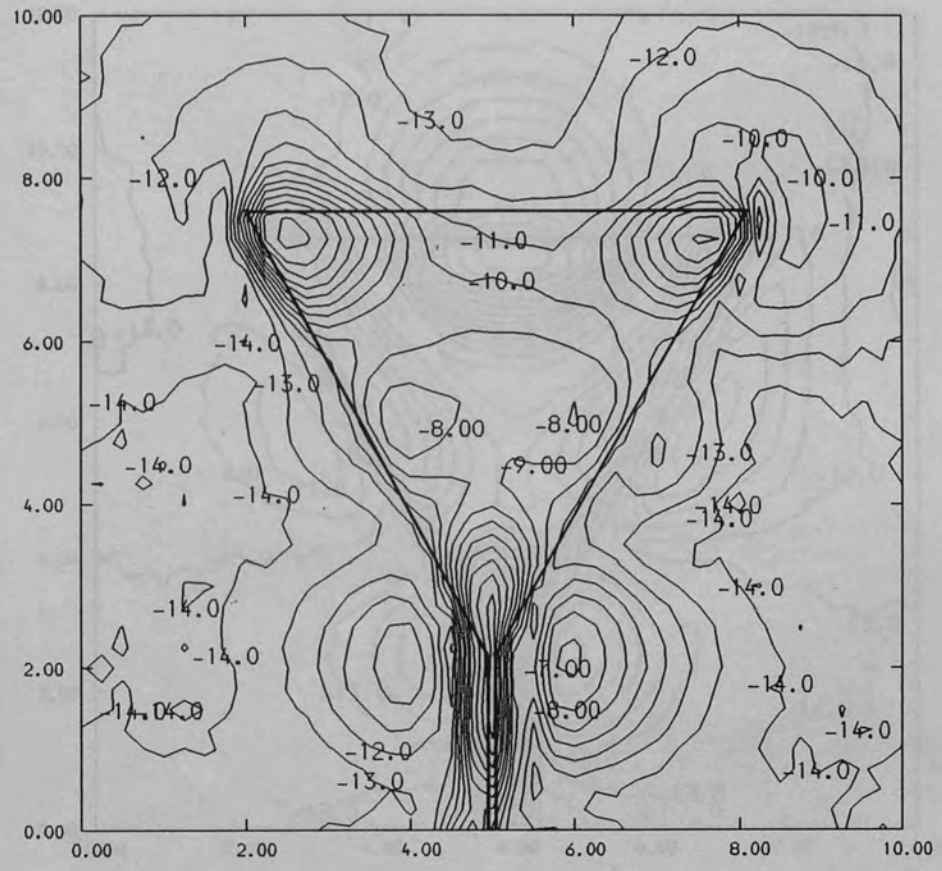

SCALE

$X, Y = 2.0\,mm/division \qquad Z = 1.0\,dB/level$

Figure (4.27) Experimental $|E_z|^2$ for the TM_{11} mode, F=34 *GHz*

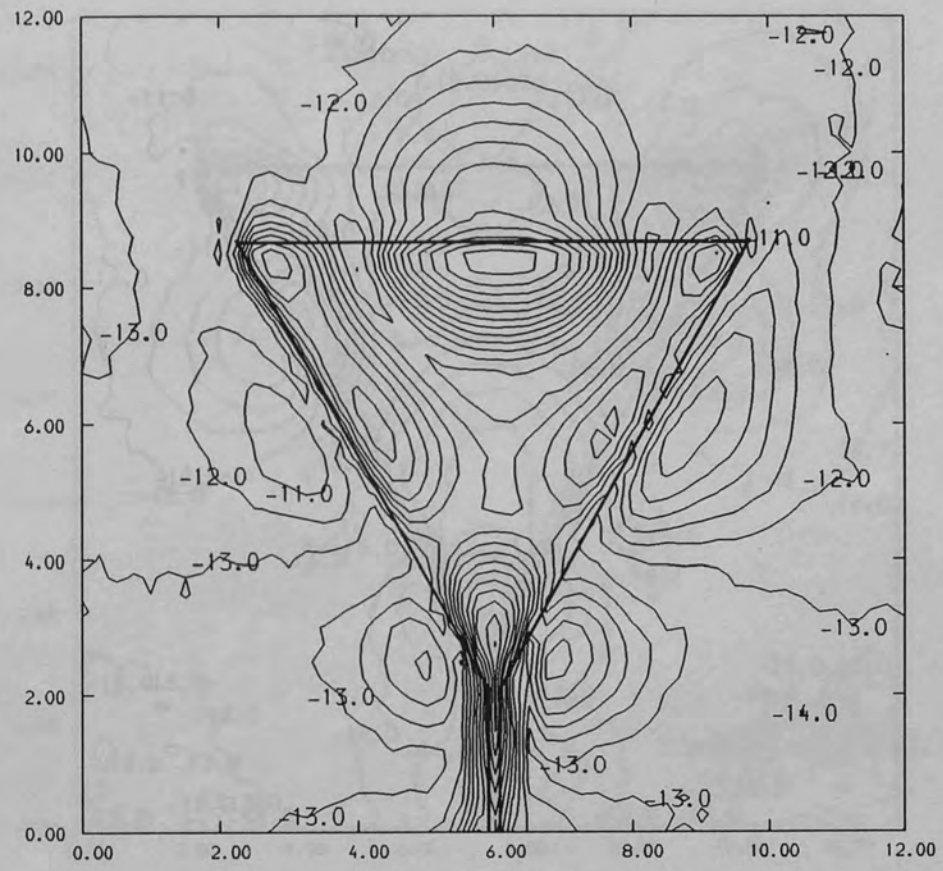

SCALE

$X, Y = 2.0\,mm/division \qquad Z = 1.0\,dB/level$

Figure (4.28) Experimental $|E_z|^2$ for the TM_{02} mode, F=35.1 *GHz*

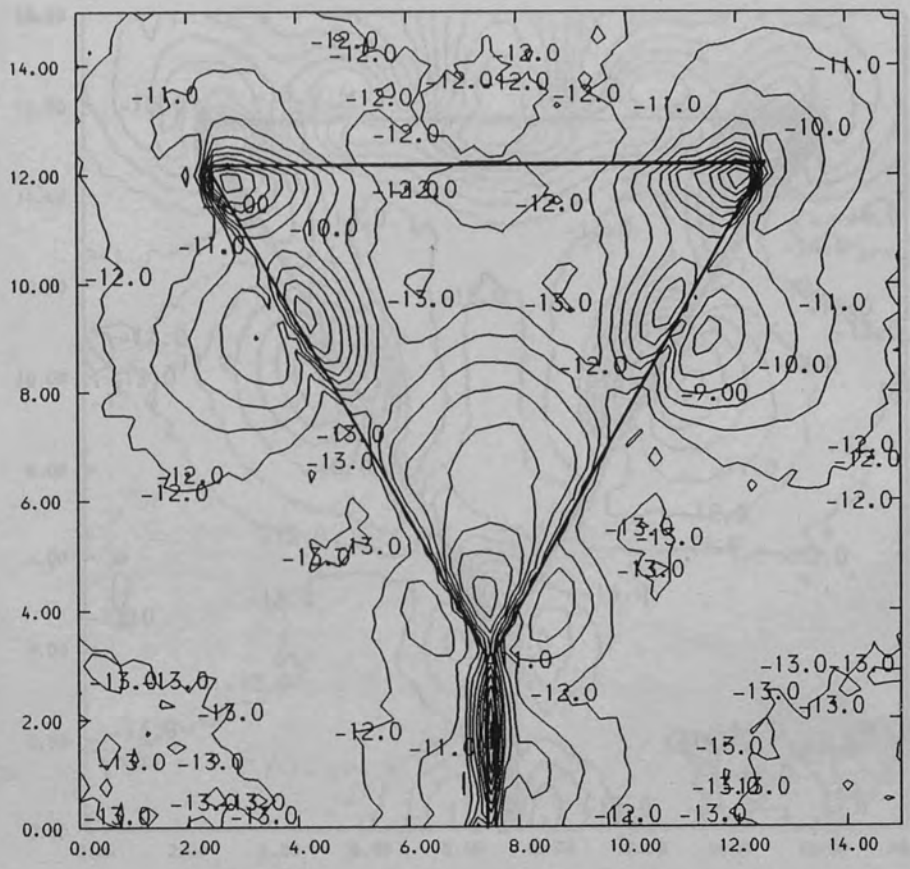

SCALE

$X, Y = 2.0\,mm/division \qquad Z = 1.0\,dB/level$

Figure (4.29) Experimental $|E_z|^2$ for the TM_{12} mode, F=35 GHz

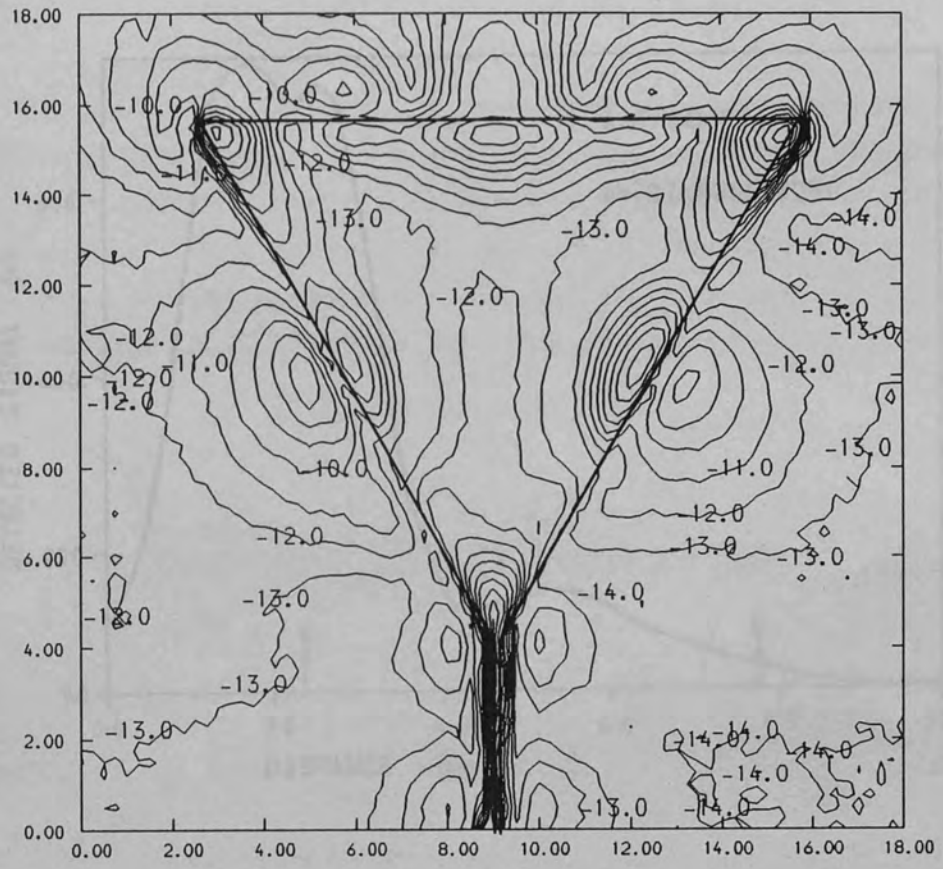

SCALE

$X, Y = 2.0\,mm/division \qquad Z = 1.0\,dB/level$

Figure (4.30) Experimental $|E_z|^2$ for the TM_{22} mode, F=34.4 GHz

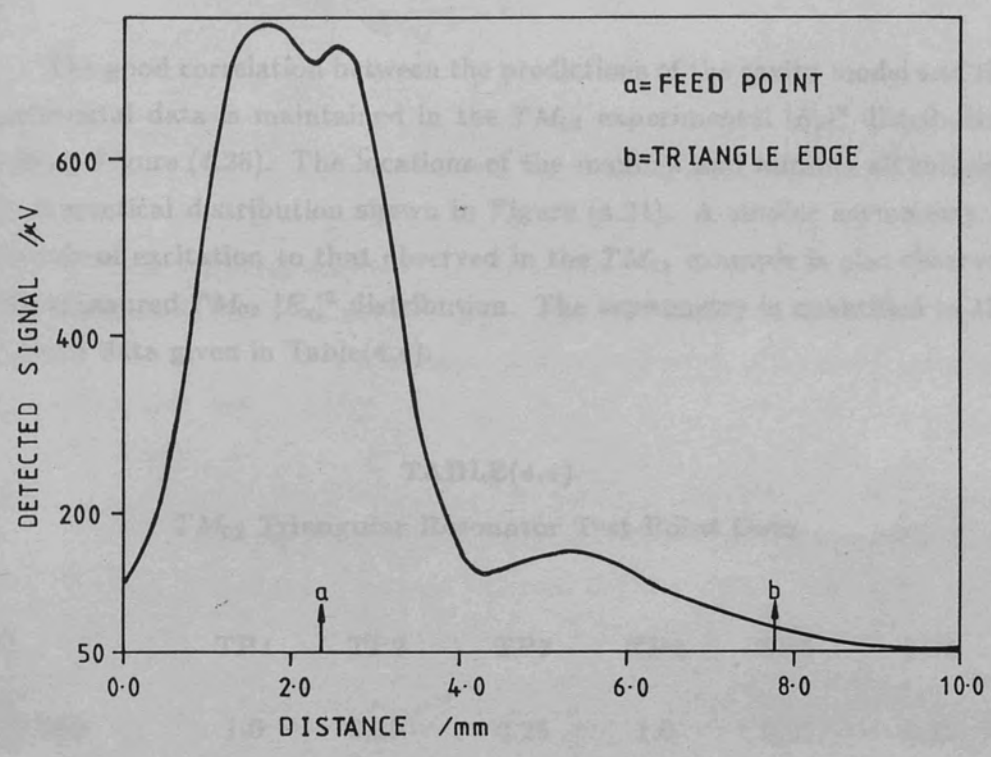

Figure (4.31) Cross–section of Figure (4.20) along feed axis

TABLE(4.3)

TM_{11} Triangular Resonator Test Point Data

$\lvert\frac{E_z}{E_0}\rvert^2$	TP1	TP2	TP3	TP4	TP5	TP6
THEORY	1.0	0.25	1.0	0.25	1.0	0.25
EXPERIMENTAL	1.0±.1	0.25±.03	0.7±.14	0.1±.05	1.0±.1	0.25±.03

The good correlation between the predictions of the cavity model and the experimental data is maintained in the TM_{02} experimental $|E_z|^2$ distribution shown in Figure (4.28). The locations of the maxima and minima all coincide with theoretical distribution shown in Figure (4.21). A similar asymmetry in the mode of excitation to that observed in the TM_{11} example is also observed in the measured TM_{02} $|E_z|^2$ distribution. The asymmetry is quantified in the test point data given in Table(4.4).

TABLE(4.4)

TM_{02} Triangular Resonator Test Point Data

$\lvert\frac{E_z}{E_0}\rvert^2$	TP1	TP2	TP3	TP4	TP5	TP6
THEORY	1.0	0.25	0.25	1.0	0.25	0.25
EXPERIMENT	1.0±.1	0.14±.02	0.14±.02	1.1±.1	0.4±.05	0.31±.04

The return loss at the antenna input is found to be $9.9\pm0.25\,dB$, and is in reasonable agreement with scalar network analyser measurement of $12.0\pm2\,dB$ in the waveguide feed.

A noticable deviation from the cavity model prediction and the experimental results is observed in the TM_{12} example shown in Figure (4.29). The positions of the maxima and minima are approximately as expected from the cavity model prediction shown in Figure (4.22), however the amplitude of the nodes and antinodes are not in the correct ratios as demonstrated by the test point data in Table(4.5).

TABLE(4.5)

TM_{12} Triangular Resonator Test Point Data

$\lvert\frac{E_z}{E_0}\rvert^2$	TP1	TP2	TP3	TP4	TP5	TP6
THEORY	1.0	0.0	0.25	0.0	0.25	0.0
EXPERIMENT	1.0±.1	0.0±0.02	0.69±.07	0.19±.03	1.1±.1	0.0±.02

The conclusion reached concerning this example is that the measured $|E_z|^2$ distribution is composed of two or more cavity modes. The same asymmetry in the fringing field regions found in the previous examples is observed. The return loss measured at the antenna input was found to be $9.8\pm.25\,dB$, which is in good ageement with the scalar network analyser result of $10\pm2\,dB$ measured in the waveguide feed.

The final example of triangular resonator that was investigated was the TM_{22} Triangle. A visual comparison between the theoretical and experimental $|E_z|^2$ distributions can be made from figures(4.23) and (4.30) respectively. The experimental distribution shows some similarity to the cavity mode, however there is a marked deviation in the relative amplitudes of the nodes, and the low level variations indicated in Figure (4.22) are not observed. The test point data in Table(4.6) provides a good indication of the deviation from the cavity model.

TABLE(4.6)

TM_{22} Triangular Resonator Test Point Data

$\lvert\frac{E_z}{E_0}\rvert^2$	TP1	TP2	TP3	TP4	TP5	TP6
THEORY	1.0	1.0	1.0	1.0	1.0	1.0
EXPERIMENT	1.0±.1	0.37±.04	1.1±.1	0.48±.05	0.79±.07	0.48±.05

The asymmetry in the fringing field regions is observed in this example, but on the opposite side of the patch to the previous examples. Since the same probe was employed for all the measurements, this implies that the effect is not related to asymmetries in the probe geometry. The actual mode excited in this example appears to be a combination of modes, rather than a pure TM_{22} mode. The return loss measured at the antenna input in this example is $14.4 \pm .25\, dB$, and compares favourably with the scalar network analyser result in the waveguide feed.

4.2.4 Final Comments on the Triangular Resonator Investigation

The most interesting discovery made during this investigation was the fact that the electric field distribution associated with the top surface of the patch is closely related to the electric field distribution underneath the patch metallization. The direct communication of charge between the upper and lower surfaces of the patch is not possible due to the skin effect. Consequently the fields on the top surface have to be set up via charge communication around the open circuit microstrip edges. The scanning network probe technique has also shown that the low order modes are excited with the classical field distributions predicted by the cavity model. The higher order modes suffer from field distortions which are thought to be due to feed point asymmetry. The potential use of the scanning network probe as a precision diagnostic technique for performing *in situ* circuit measurements on integrated circuits has been demonstrated by the consistant agreement between the scanning network probe and scalar network analyser results. The slight difference between the two sets of results is due to:

(a) the finite line loss in the microstrip feed

and more importantly:

(b) the finite mismatch of the waveguide to microstrip transition

Using the expressions given by Bahl and Bhartia[4.1] the transmission line loss of the microstrip feed was estimated to be $\approx 0.6\, dB$. (assuming a loss tangent of 0.005) The transmission line loss effectively improves the return loss measured by the waveguide scalar network analyser by twice the line loss, or $1.2\, dB$ in this case. The major cause of discrepancies between the two measurements is the mismatch of the waveguide to microstrip transition. The errors incurred in making measurements through waveguide to microstrip transitions with a finite

reflection coefficient are fully described in chapter(6).

4.3 The Edge Fed Microstrip Disk Antenna

4.3.1 Theoretical Aspects of the Microstrip Disk

The microstrip disk geometry and coordinate system is shown in Figure (4.32). Provided that the substrate thickness is much less than the wavelength in the dielectric then the system can be treated as a TM cavity in the same manner as the previous examples. In order to find the resonant modes and their associated field structure in the equivalent TM cavity, the wave equation must be solved subject to the cavity boundary conditions. When no current sources are present the wave equation is:

$$(\nabla^2 + k^2) = 0 \qquad 4.28$$

Where:

$k = \omega\sqrt{\mu\epsilon_r}$

$\nabla =$ *Laplacian operator in cylindrical coordinates*

Since the structure will only support TM modes, $\vec{E}$ is in the direction of $\hat{z}$. The magnetic wall boundary condition requires that:

$$\left(\frac{\partial E}{\partial \rho}\right)_{\rho=a} = 0 \qquad 4.29$$

Where ρ is the radial coordinate.

The solution of the wave equation in cylindrical coordinates is then given by:[4.1]

$$E_z = E_0 J_n(k\rho)\cos(n\phi) \qquad 4.30$$

Where $J_n(k\rho)$ is the Bessel function of order n.

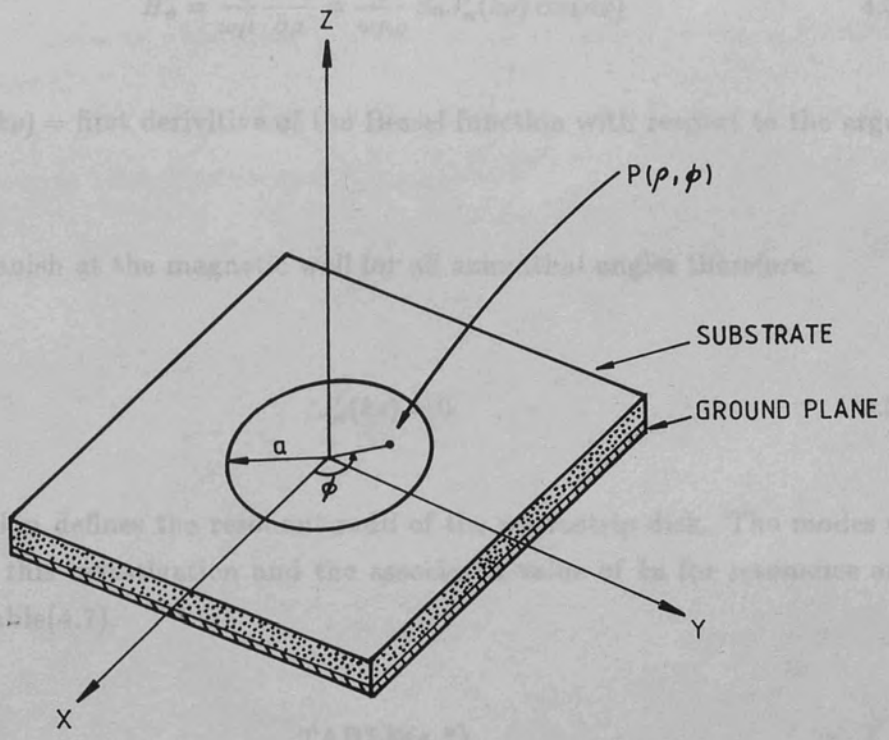

Figure (4.32) Microstrip disk antenna geometry

The components of H then follow:

$$H_\rho = \frac{j}{\omega\mu}\frac{1}{\rho}\frac{\partial E_z}{\partial \phi} = \frac{jn}{\omega\mu} E_0 J_n(k\rho)\sin(n\phi) \qquad 4.31$$

$$H_\phi = \frac{-j}{\omega\mu}\frac{\partial E_z}{\partial \rho} = \frac{-jk}{\omega\mu\rho} E_0 J_n'(k\rho)\cos(n\phi) \qquad 4.32$$

Where $J_n'(k\rho)$ = first derivitive of the Bessel function with respect to the argument.

H_ϕ must vanish at the magnetic wall for all azimuthal angles therefore:

$$J_n'(ka) = 0 \qquad 4.33$$

This equation defines the resonant radii of the microstrip disk. The modes of interest in this investigation and the associated value of ka for resonance are given in Table(4.7).

TABLE(4.7)

Roots of $J_n'(ka) = 0$

mode n,m	ka
1,1	1.84118
2,1	3.05424
0,2	3.83171
3,1	4.20119

In this notation the integer n represents the order of the Bessel function and corresponds to the number of of half wavelength changes around the edge of the disk, and the integer m represents the m^{th} zero of the Bessel function and

corresponds to the number of radial changes in in amplitude. Equation(4.30) was used in the FORTRAN77 program "DMODE" which generates the theoretical $|E_z|^2$ distribution in the equivalent cavity. The program is listed in appendix(1). The $|E_z|^2$ distribution for the TM_{11}, TM_{21}, TM_{02}, and TM_{31} are given in figures(4.33) to (4.36). The "corrugated" edges in these contour plots is due to the finite size of the sampling grid used in the computation process, which results in an un–even sample along the circular boundary. As explained in chapter(2), this computer simulation of the scanning network probe measurement process allows the idiosynchrocies in the software contouring routines to be identified.

4.3.2 Microstrip Disk Design and Fabrication

The resonant frequency of the nm^{th} mode is given by:[4.1]

$$f_r = \frac{k_{n,m}c}{2\pi a_e\sqrt{\epsilon_r}} \qquad 4.34$$

Where:

$c = velocity\ of\ light$

$k_{m,n} = m^{th}\ zero\ of\ the\ derivitive\ of\ the\ Bessel\ function\ of\ order\ n$

$$a_e = a\left[1+\frac{2h}{\pi a\epsilon_r}\left(\ln\left(\frac{\pi a}{2h}\right)+1.7726\right)\right]^{\frac{1}{2}} \qquad 4.35$$

The term a_e is called the effective radius and compensates for the fringing field capacitance at the open circuit boundary. Equation(4.34) was plotted as a function of radius ρ in order to find the required radius to resonate at 35 GHz for each of the modes listed in Table(4.7), when manufactured on RT–DUROID 5880. The patches were edge fed by an identical feed arrangement to that used for the triangular resonators. The antennas were etched and soldered to brass support plates by the same technique as previously employed except that the antenna dimensions were expanded by $17\,\mu m$ to allow for the etch undercut. The etched dimensions, resonant frequency, and the measured return loss in the waveguide feed are given in Table(4.8). A photograph of the completed antennas is shown in plate(4.3).

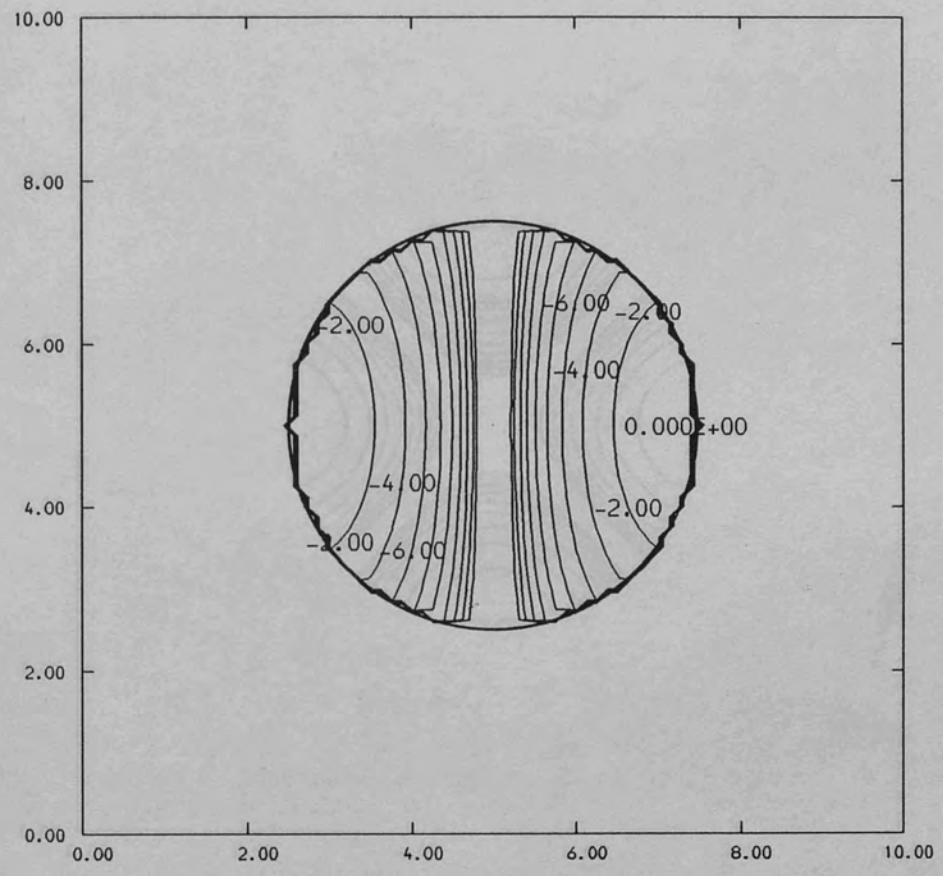

SCALE

$X, Y = 2.0\,mm/division \qquad Z = 2.0\,dB/level$

Figure (4.33) Theoretical $|E_z|^2$ for the TM_{11} mode

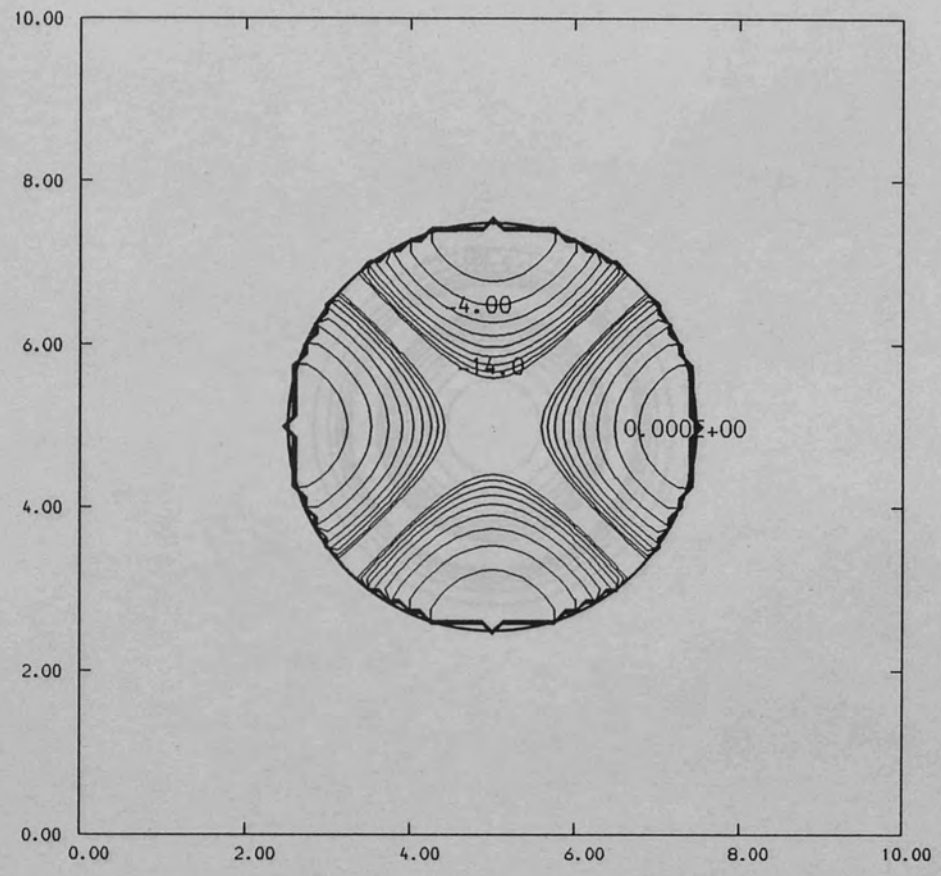

SCALE

$X, Y = 2.0\,mm/division \qquad Z = 2.0\,dB/level$

Figure (4.34) Theoretical $|E_z|^2$ for the TM_{21} mode

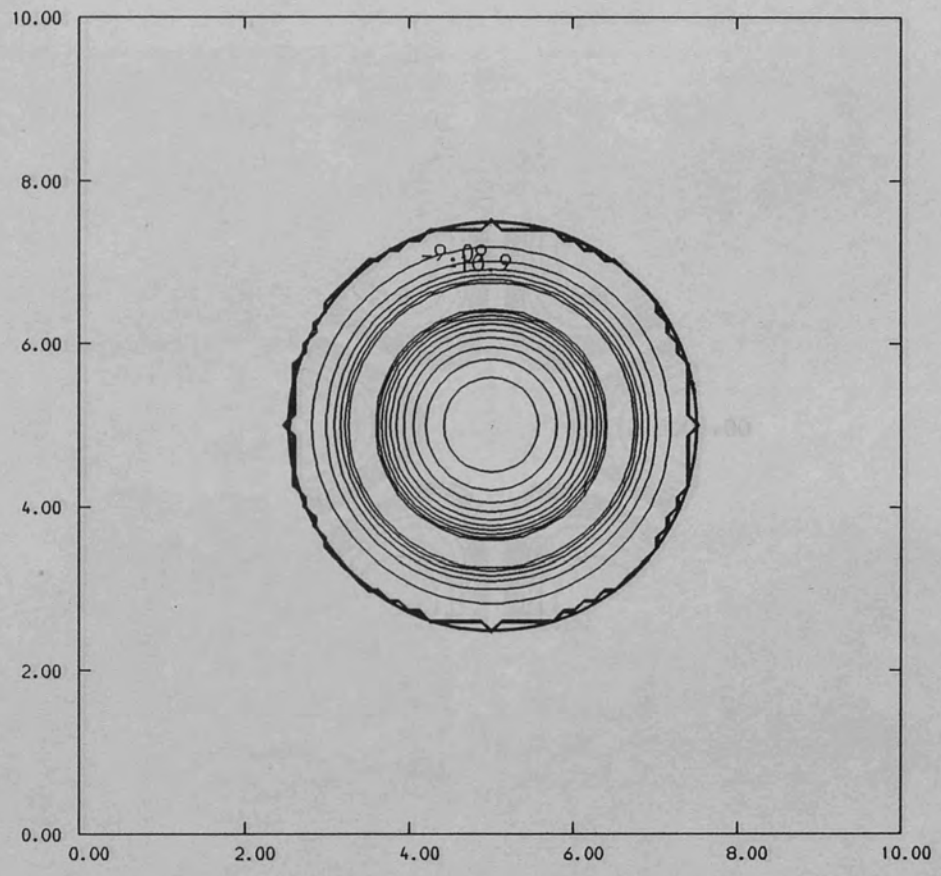

SCALE

$X, Y = 2.0\,mm/division \qquad Z = 2.0\,dB/level$

Figure (4.35) Theoretical $|E_z|^2$ for the TM_{02} mode

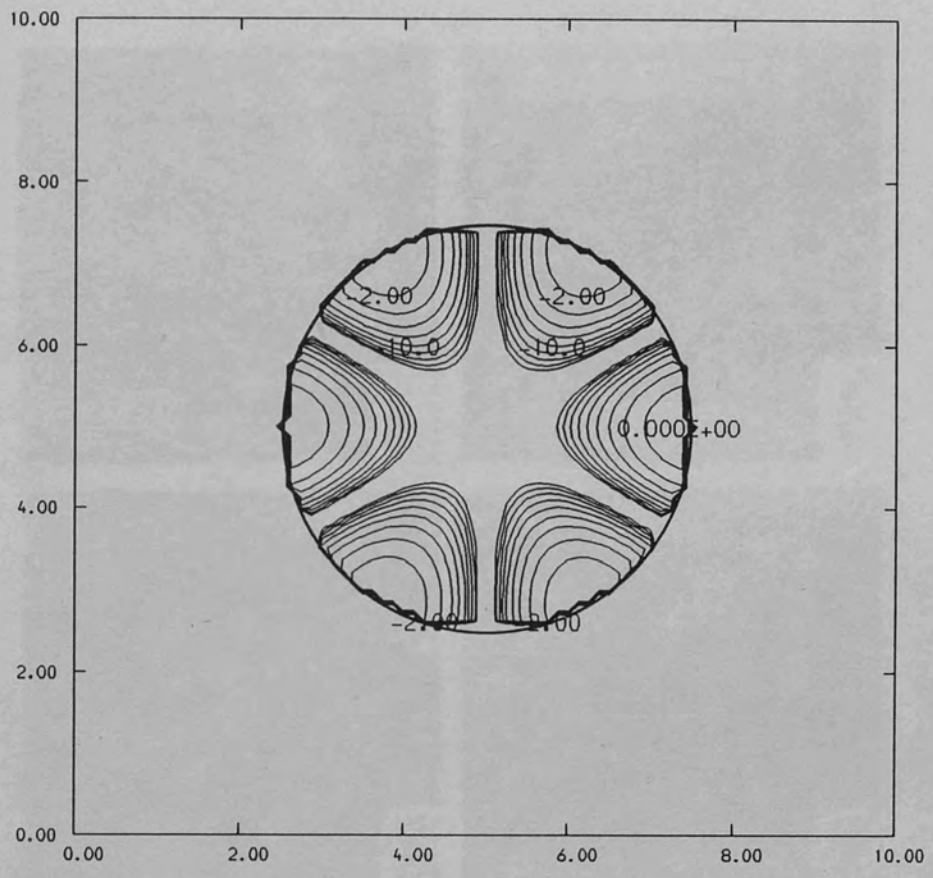

SCALE

$X, Y = 2.0\,mm/division \qquad Z = 2.0\,dB/level$

Figure (4.36) Theoretical $|E_z|^2$ for the TM_{31} mode

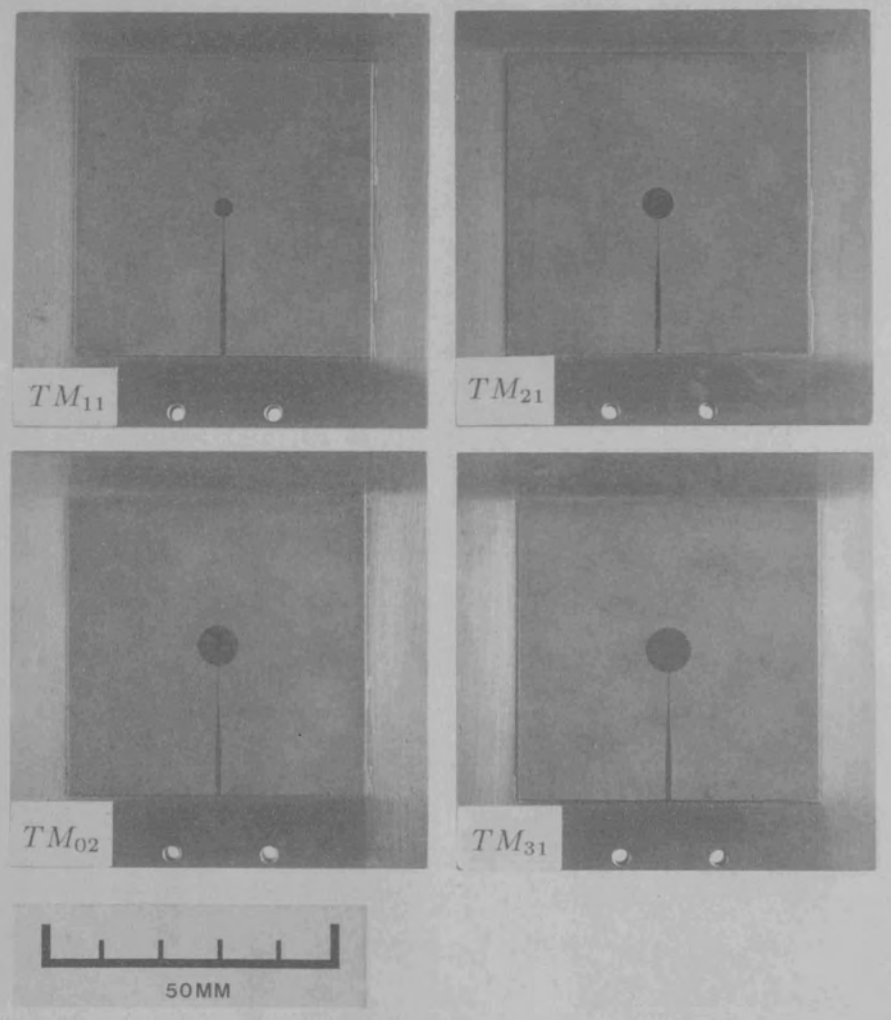

Plate(4.3) The completed circular patch antennas

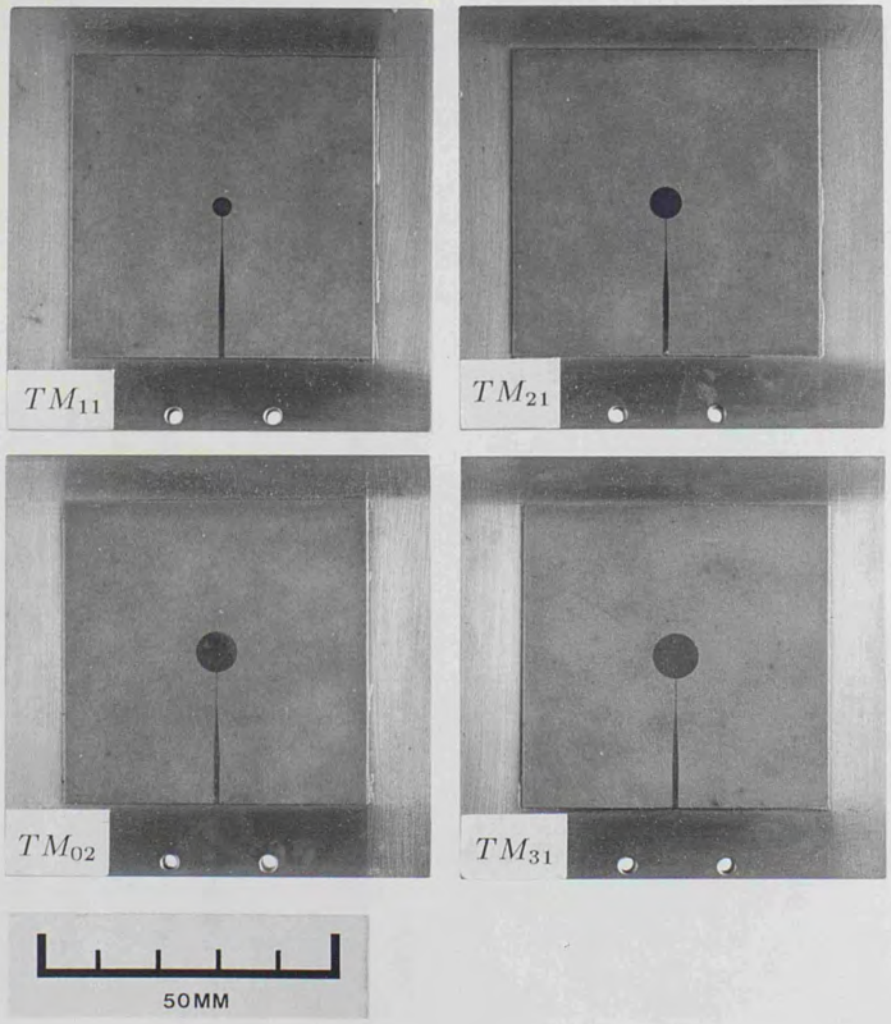

TABLE(4.8)

Microstrip Disk Dimensions and Performance

resonant mode	radius /mm	frequency /GHz	return loss /dB
TM_{11}	1.6	35.8	13.0
TM_{21}	2.31	35.5	11.0
TM_{02}	3.34	34.8	6.8
TM_{31}	3.71	35.5	22

4.3.3 Scanning Network Probe Measurements

Using the same area scan techniques previously employed for the triangular and rectangular patch resonator investigation, the $|E_z|^2$ distributions were obtained for the microstrip disks at the same resonant frequency indicated by the waveguide scalar network analyser measurements. The results for each of the modes are shown in figures(4.37) to (3.40). Simple visual comparison of these experimental plots with those derived for $|E_z|^2$ in the equivalent cavity enables all four modes to be unambiguously identified. From equation(4.30) it is observed that the amplitude of the nodes in the equivalent cavity are equal and equi–spaced by $360/2n$. Table(4.9) lists the relative excitation and angular positions of the nodes in each case. The excitation of the TM_{11} and TM_{21} modes is found to be azimuthally symmetric as expected, however the TM_{31} mode shows no such symmetry in the amplitude of the nodes. Close inspection of Figure (4.40) reveals that the low excitation level of a cavity node is again correlated with an enhanced fringing field region. Examination of the antenna revealed no obvious defects that might be responsible for this effect, such as poor quality etching. The probe was also examined and found to be free of any defects.

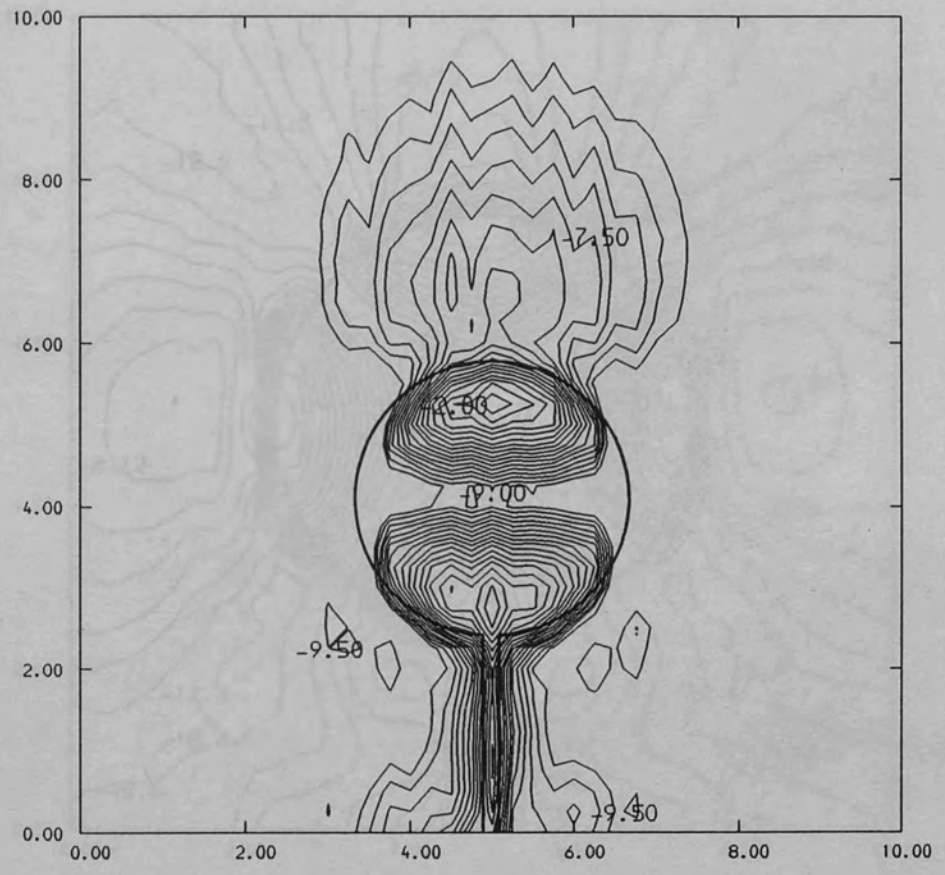

SCALE

$X, Y = 2.0\,mm/division \qquad Z = 0.5dB/level$

Figure (4.37) Experimental $|E_z|^2$ for the TM_{11} mode, F=35.8 *GHz*

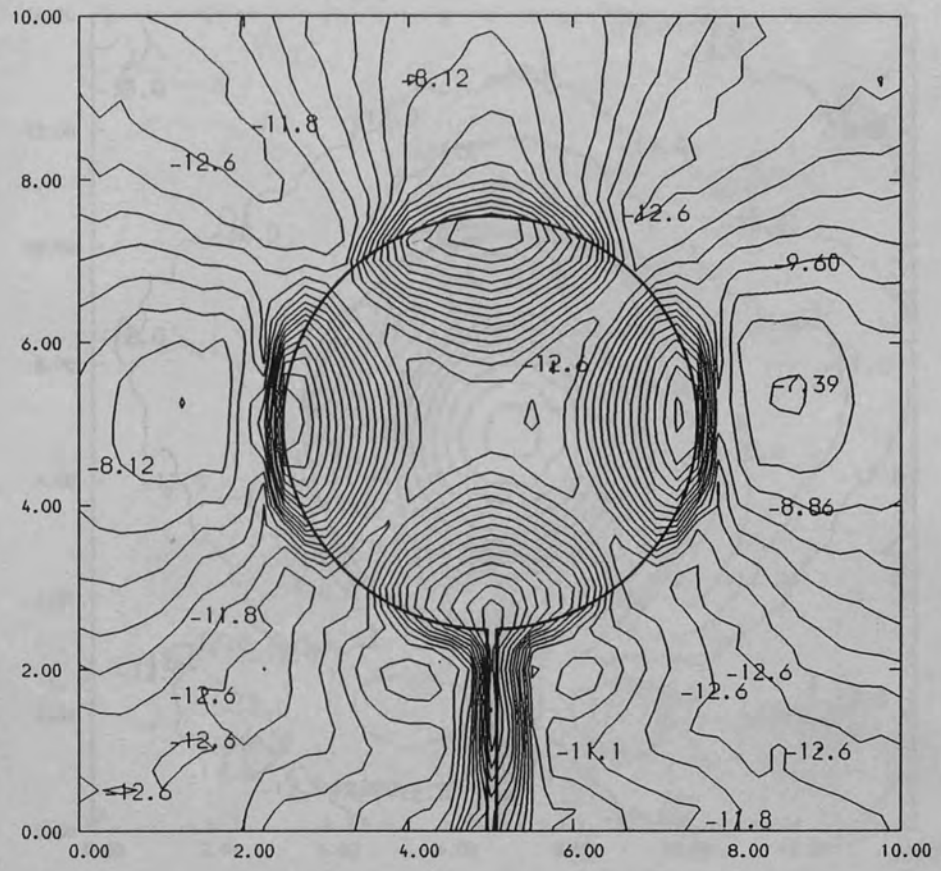

SCALE

$X, Y = 2.0\,mm/division \qquad Z = 0.8\,dB/level$

Figure (4.38) Experimental $|E_z|^2$ for the TM_{21} mode, F=35.5 *GHz*

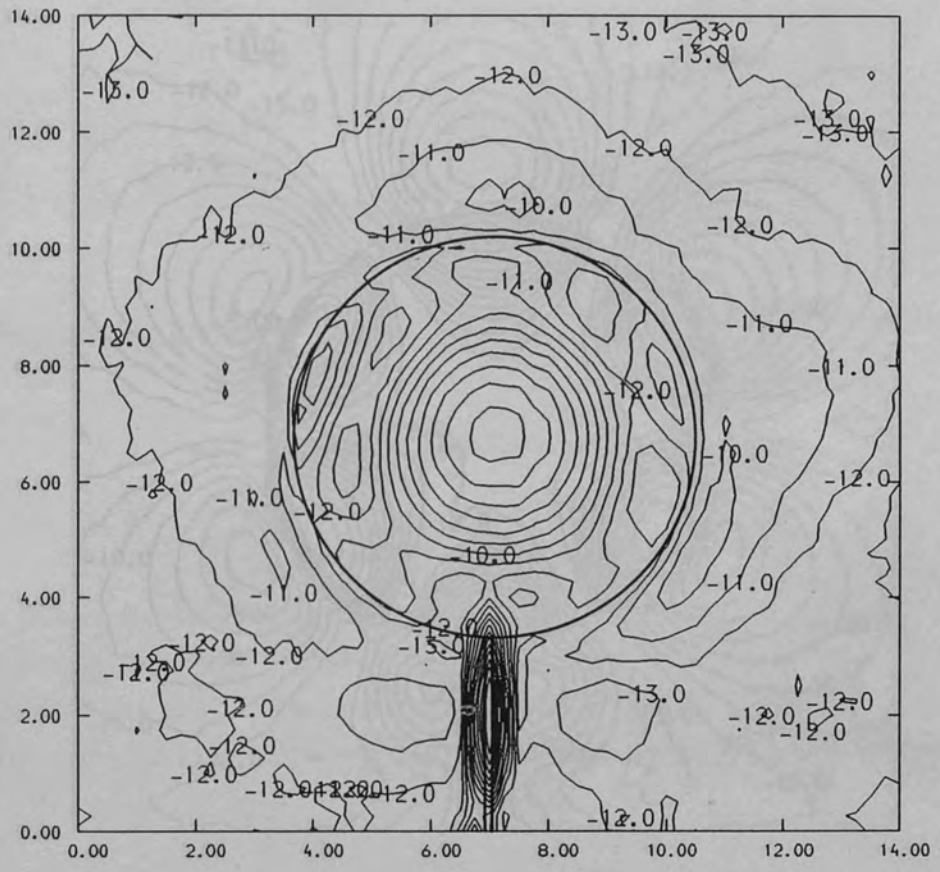

SCALE

$X, Y = 2.0\,mm/division \qquad Z = 1.0\,dB/level$

Figure (4.39) Experimental $|E_z|^2$ for the TM_{02} mode, F=34.8 GHz

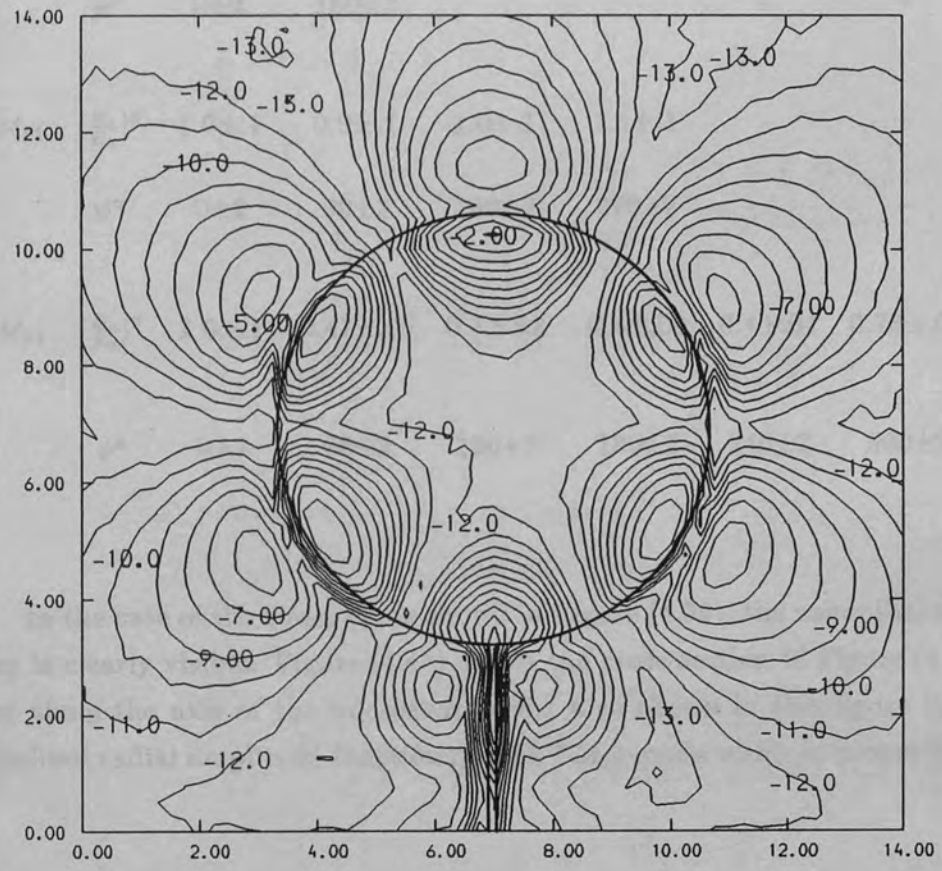

SCALE

$X, Y = 2.0\,mm/division \qquad Z = 1.0\,dB/level$

Figure (4.40) Experimental $|E_z|^2$ for the TM_{31} mode, F=35.5 *GHz*

TABLE(4.9)

The Relative Excitation $|\frac{E_x}{E_0}|^2$and angular postion of the Disk Resonator Nodes

mode		node 1	node 2	node 3	node 4	node 5	node 6
TM_{11}	$\|\frac{E_x}{E_0}\|^2$	1.0±.1	1.0±.1	–	–	–	–
	$\phi°$	0±2	180±2	–	–	–	–
TM_{21}	$\|\frac{E_x}{E_0}\|^2$	1.0±.1	0.9±.1	1.0±.1	1.1±.1	–	–
	$\phi°$	0±2	90±2	180±2	270±2	–	–
TM_{31}	$\|\frac{E_x}{E_0}\|^2$	1.0±.1	0.47±.05	0.3±.03	0.6±.06	0.4±.04	0.73±.07
	$\phi°$	0±2	60±2	120±2	180±2	240±2	300±2

In the case of the TM_{02} mode shown in Figure (4.39), the azimuthal symmetry is clearly visible. Figure (4.41) shows the cross section of Figure (4.39), taken along the axis of the microstrip feed. Also shown in this figure is the normalized radial amplitude function for the TM_{02} mode which is proportional to:

$$A_{(\rho)} = \frac{J_0^2(k\rho)}{J_0^2(0)} \qquad 4.36$$

The difference between the theoretical radial amplitude function and the experimental results is most apparent close to the edge of the disk, where the following differences are observed:

(a) the rate of decay of the experimental data is a slower function of radius

(b) the turning points in the theoretical amplitude function are absent from the experimental data

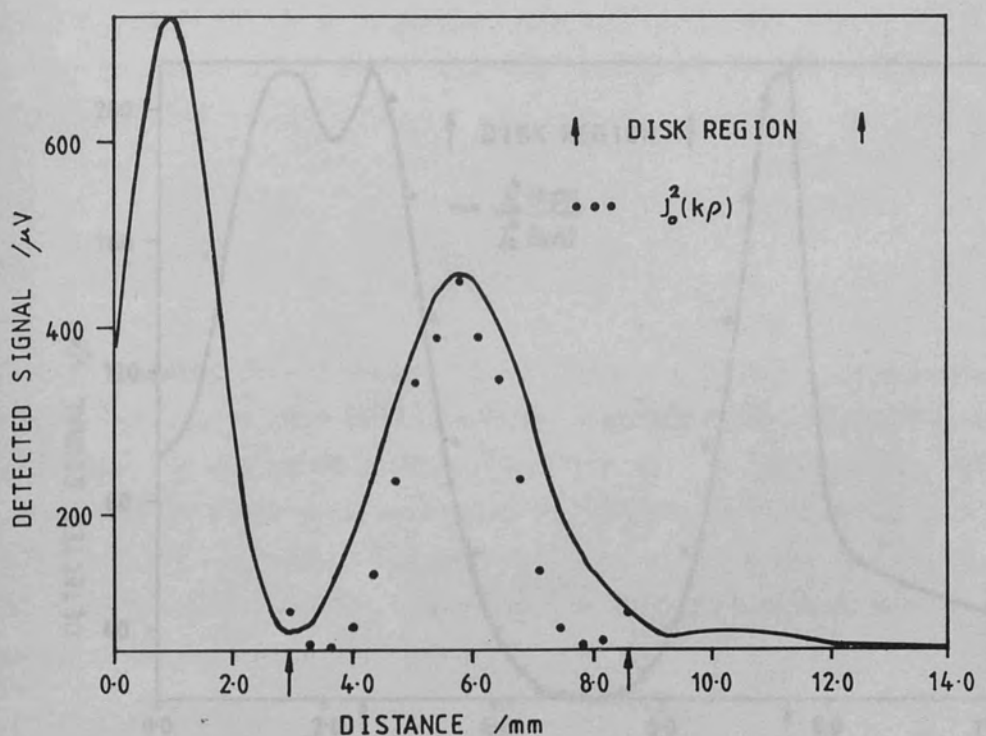

Figure (4.41) Cross–section of experimental TM_{02} data along feed axis

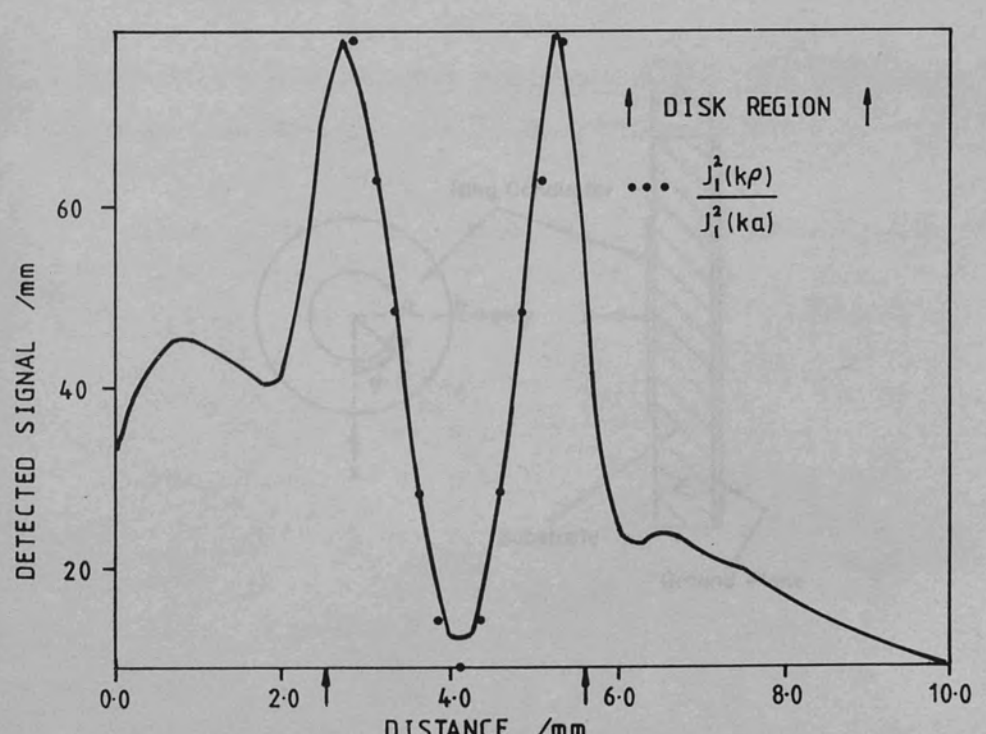

Figure (4.42) Cross–section of experimental TM_{11} data along feed axis

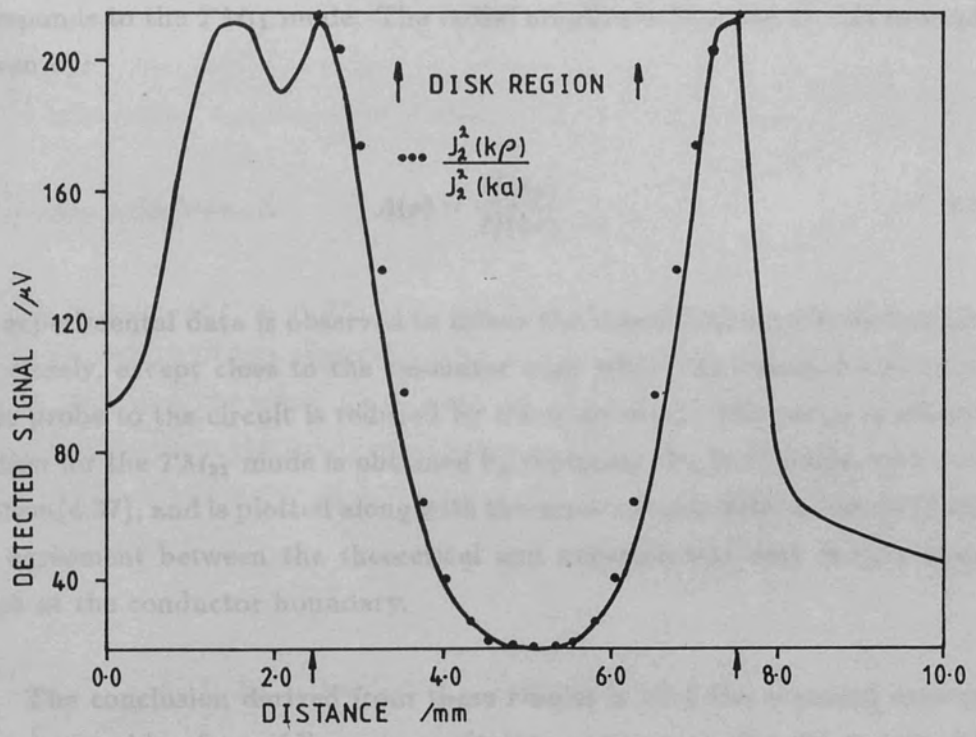

Figure (4.43) Cross–section of experimental TM_{21} data along feed axis

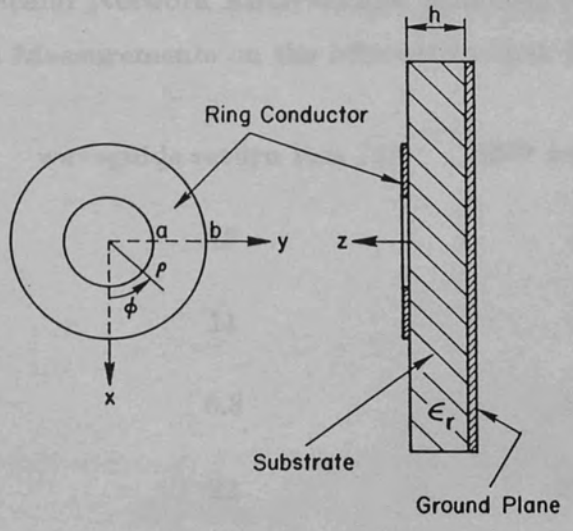

Figure (4.44) The microstrip ring geometry

Figure (4.42) shows a similar cross section through Figure (4.37) and corresponds to the TM_{11} mode. The radial amplitude function in this example is given by:

$$A(\rho) = \frac{J_1^2(k\rho)}{J_1^2(ka)} \qquad 4.37$$

The experimental data is observed to follow the theoretical amplitude function very closely, except close to the resonator edge where the capacitive coupling of the probe to the circuit is reduced by the edge effect. The radial amplitude function for the TM_{21} mode is obtained by replacing the J_1 function with J_2 in equation(4.37), and is plotted along with the experimental data in Figure (4.43). The agreement between the theoretical and experimental data is very good, except at the conductor boundary.

The conclusion derived from these results is that the scanning network probe is capable of providing a quantitative assessment of a microstrip disk resonator field distribution, the only errors of any significance occurring at the resonator boundaries. The comparison between the return loss measured in the waveguide feed by a scalar network analyser and that measured close to the antenna input by the scanning network probe is shown in Table(4.10).

TABLE(4.10)

Comparison of Scalar Network Analyser and Scanning Network Probe Return Loss Measurements on the Microstrip Disk Resonators

mode	waveguide return loss $/dB$	SNP return loss $/dB$
TM_{11}	13	12±.25
TM_{21}	11	9.5±.25
TM_{02}	6.8	5.9±.25
TM_{31}	22	21.2±.25

The results in Table(4.10) indicate that the scanning network probe measurements are consistant with the scalar network analyser results in the waveguide

feed, supporting the quantitative nature of the scanning network probe measurements.

4.4 The Microstrip Annular Disk Antenna

4.4.1 Design and Manufacture

The microstrip ring antenna geometry is shown in Figure (4.43). Assuming that the width of the ring conductor is much greater than the substrate thickness, and that the substrate thickness is much smaller than a wavelength in the dielectric, then the cavity model can be employed to calculate the field distribution underneath the microstrip ring. Quoting the results given in chapter(7) of reference(4.1):

$$E_z = E_0\Big[J_n(k\rho)Y_n'(k\rho) - J_n'(k\rho)Y_n'(k\rho)\Big]cos(n\phi) \qquad 4.38$$

Where:

J_n =*Bessel function of the first kind*

Y_n =*Bessel function of the second kind*

$'$*denotes differention with respect to the argument*

n =*azimuthal mode number*

The value of k for a given TM_{n1} mode is found from the solution of:[4.1]

$$J_n'(kb)Y_n'(ka) - J_n'(ka)Y_n'(k\underline{)} = 0 \qquad 4.39$$

The resonant wavenumber k must first be calculated from equation(4.38), or found from mode charts[4.13]. Alternatively the approximation given in reference(4.1) can be employed:

$$k = \frac{2n}{a+b} \qquad 4.40$$

Which is reported to be accurate provided that:

(a) a and b are in cm

(b) $(b-a)/(b+a) \leq 0.35$

(c) $n \leq 5$

Once k is determined then the resonant frequency is calculated from:

$$f_r = \frac{ck}{2\pi\sqrt{\epsilon_e}} \qquad 4.41$$

In this expression ϵ_e is the effective dielectric constant of a microstrip line of width $(b-a)$. With the aid of equations(4.40) and (4.41) and the microstrip design formulae found in reference(4.7), the values of a and b were calculated by an iterative computer program to produce a resonance at 35 GHz for the first three azimuthal modes when manufactured on RT–DUROID 5880. The annular patches were excited by a high impedance microstrip feed located at the resonator edge. The finished antennas are shown in plate(4.4), and the final etched dimensions are given in Table(4.11) together with the return loss measured with a scalar network analyser in the feed waveguide. Comparison of equation(4.30) for the electric field variation inside the equivalent disk cavity and equation(4.38) for the electric field inside the equivalent ring cavity reveals that they are both of a similar form i.e.:

$$E_z = F(\rho)cos(n\phi) \qquad 4.42$$

Where:

$$F(\rho)\ is\ a\ radial\ amplitude\ function$$

$$n = the\ azimuthal\ mode\ number$$

Consequently some similarity in the the azimuthal variations of the $|E_z|^2$ distribution in these two geometries would be expected.

TABLE(4.11)

Microstrip Ring Design and Performance Data

mode	outer radius /*mm*	inner radius /*mm*	frequency /GHz	return loss /*db*
TM_{11}	2.45	1.31	none found	1.5
TM_{21}	3.68	1.78	34.5	21.7
TM_{31}	6.04	2.14	33.5	31.6

4.4.2 Scanning Network Probe Measurements

From Table(4.11) it is apparent that the TM_{11} ring had no resonance in the frequency range 26.5 to 40 GHz. An area scan measurement at a frequency of 34.75 GHz shown in Figure (4.45) indicates that the system is nearer to a TM_{21} resonance than the desired TM_{11} resonance. Area scans of the remaining two annular patches at the resonant frequencies indicated by the scalar network analyser measurements in the waveguide feed are given in figures(4.46) and (4.47). In both examples the scanning network probe reveals that the actual mode of resonance is not consistant with that expected from the theoretical design formulae. By counting the number of azimuthal nodes it is found that:

(a) the TM_{21} design is operating in a TM_{31} mode

(b) the TM_{31} design is operating in a TM_{51} mode

The azimuthal symmetry of the electric field requires that the nodes should be of equal amplitude and spaced apart by $360/2n$ degrees. Table(4.12) indicates that the nodes are in the locations expected for the TM_{31} and TM_{51} modes, but the relative magnitude of the nodes is not equal. Examination of the TM_{31} and TM_{51} area scans reveals that the nodes that are more weakly excited over the patch metallization are linked with a region of enhanced excitation beyond the edge of the metallization. The cause of this effect is uncertain, there being no obvious mechanical defect in either the probe or the resonator under test.

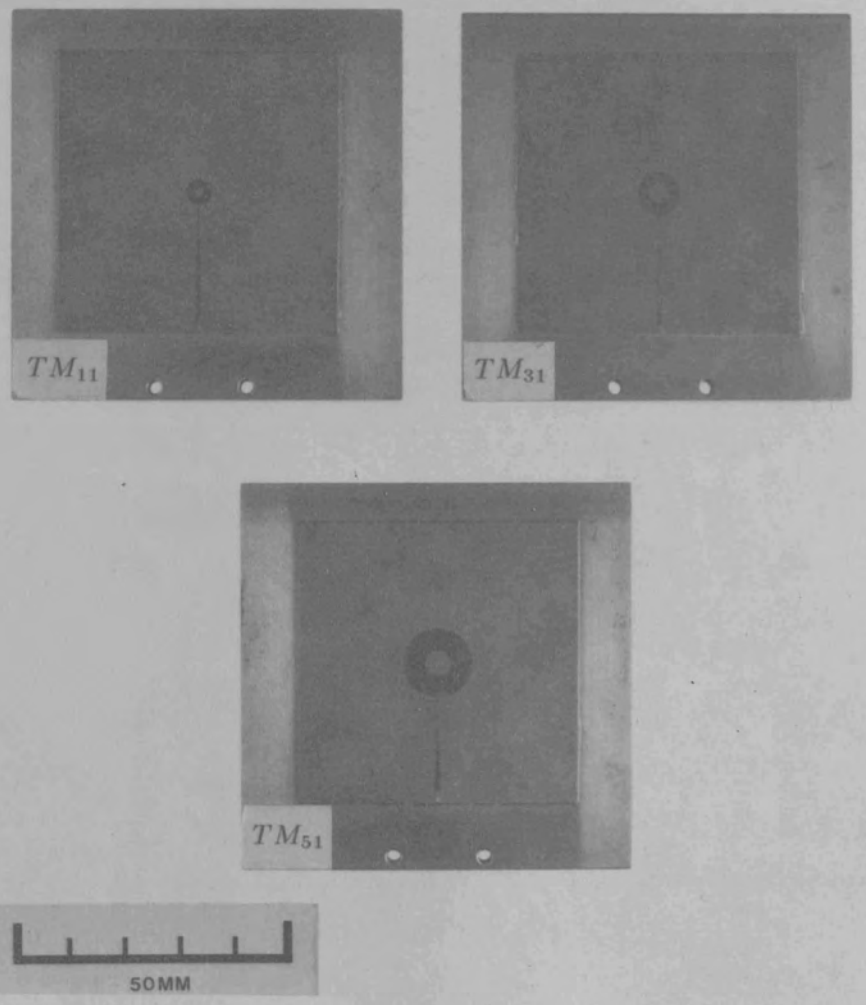

Plate(4.4) The completed annular patch antennas

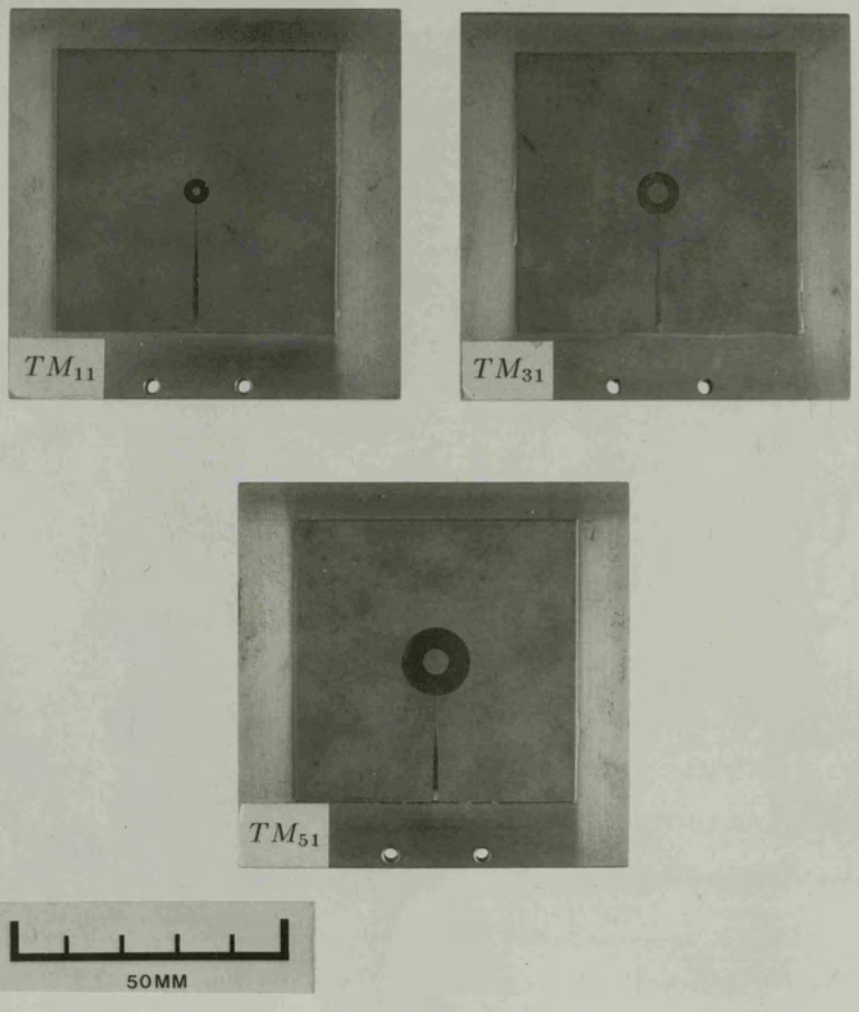
TM_{11}
TM_{31}
TM_{51}
50MM

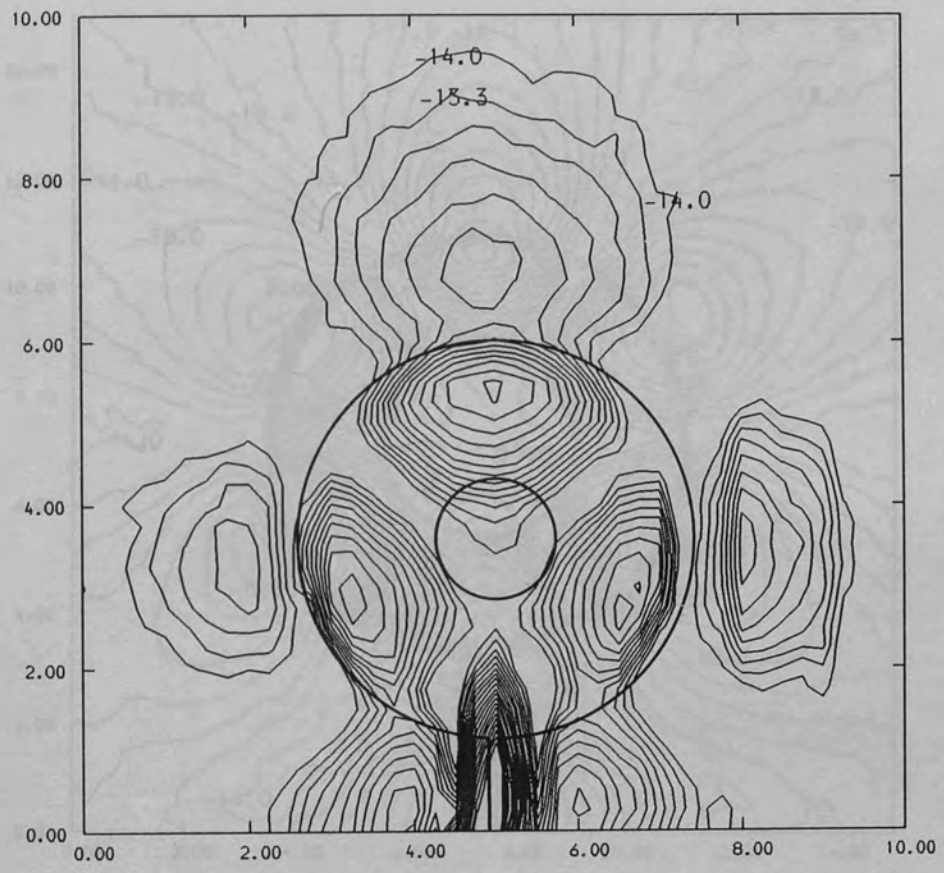

SCALE

$X, Y = 2.0\,mm/division \qquad Z = 0.7\,dB/level$

Figure (4.45) Experimental $|E_z|^2$ for the TM_{11} mode, F=35 *GHz*

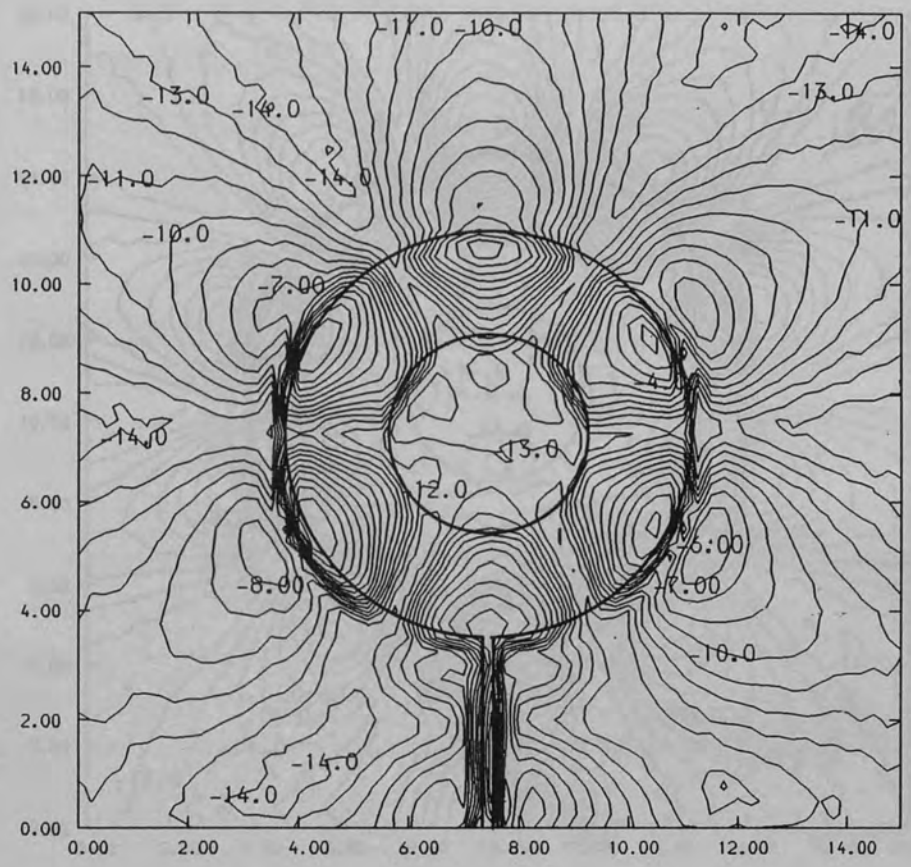

SCALE

$X, Y = 2.0\,mm/division \qquad Z = 1.0\,dB/level$

Figure (4.46) Experimental $|E_z|^2$ for the TM_{21} mode, F=34.5 *GHz*

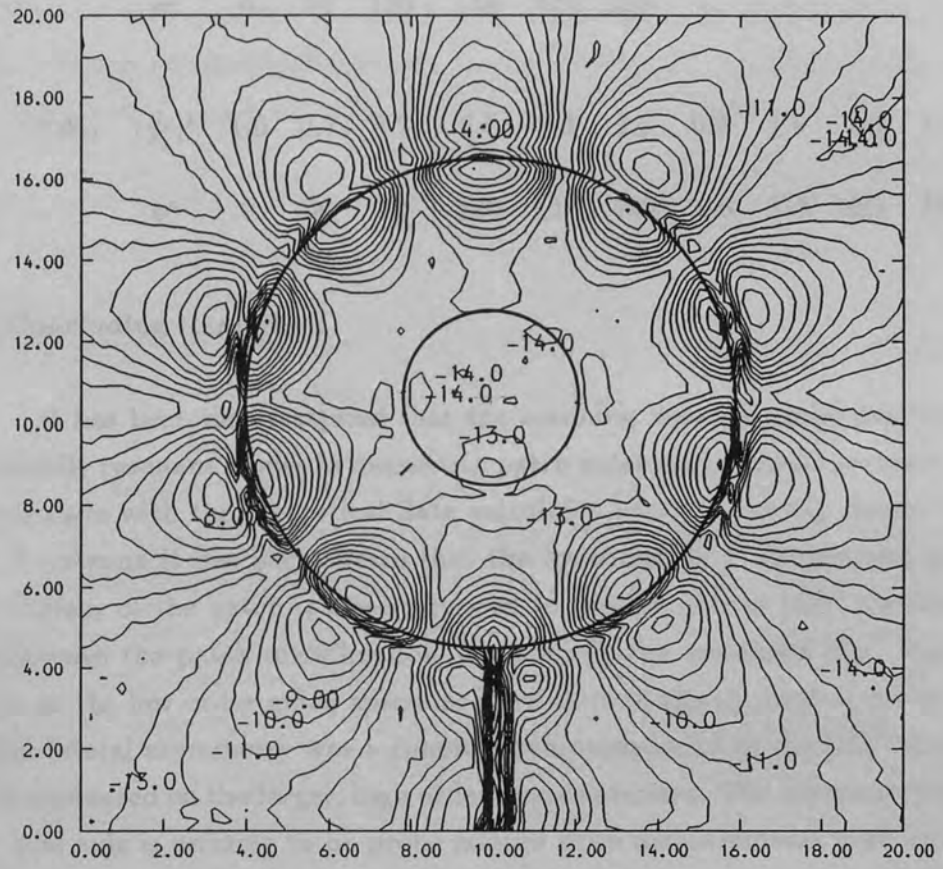

SCALE

$X, Y = 2.0\,mm/division \qquad Z = 1.0\,dB/level$

Figure (4.47) Experimental $|E_z|^2$ for the TM_{31} mode, F=33.5 *GHz*

TABLE(4.12)

The Relative Excitation $|\frac{E_z}{E_0}|^2$ and Angular Position of the Annular Resonator Nodes

mode		1	2	3	4	5	6	7	8	9	10
TM_{31}	$\|\frac{E_z}{E_0}\|^2$	1.0	1.1	1.0	1.1	1.5	1.5	–	–	–	–
	$\phi°$	0	60	120	180	240	300	–	–	–	–
TM_{51}	$\|\frac{E_z}{E_0}\|^2$	1.0	0.7	0.7	0.6	0.6	0.9	0.8	1.0	1.3	1.0
	$\phi°$	0	36	72	108	144	180	216	252	288	324

4.5 Concluding Remarks

It has been demonstrated that the scanning network probe can be used to identify resonant modes in microstrip patch antennas of simple geometry. By comparison with the theoretical data calculated using the cavity model of the patch antenna it has been shown that the measured $|E_z|^2$ distribution on the top surface of the patch is closely related to the theoretical $|E_z|^2$ distribution underneath the patch metallization. In general, the measured $|E_z|^2$ distributions on the low order mode antennas were close to the theoretical predictions whilst lateral asymmetry was a common symptom found in the $|E_z|^2$ distributions measured on the larger, high order mode antennas. The asymmetry about the feed axis is unlikely to be probe related since measurements with different probes yield the same asymmetries. Other possible causes include feed point asymmetry and imperfections in the dielectric substrate. These effects could be isolated by measurements on several examples of the same antenna, however since the effects were not related to the probe employed in the measurement no attempt was made to isolate the precise cause of the asymmetries. The theory for the probe magnetic interaction developed in Chapter (3) is only applicable to one dimensional TEM transmission lines, and is not easily extended to cater for two dimensional measurements on printed circuit elements of arbitrary shape. The difficulty arises due to the non-TEM nature of the microstrip resonators which were investigated, however since the error introduced by the magnetic interaction was expected to be small in comparison to the probe coupling errors in area scan measurements, its effect was assumed to be negligible.

CHAPTER 5

The Printed Vee and Tapered Slot Antenna

5.1 Introduction

The printed vee and tapered slot antennas illustrated in Figure (5.1) are relatively high gain endfire antennas. When the taper of the tapered slot antenna follows an exponential rather than a linear taper it is usually called a "Vivaldi antenna". Both antenna types exhibit two modes of operation:

(a) a broad band travelling wave mode obtained when the antenna is long compared to a wavelength and correctly matched at both ends

(b) a narrow band standing wave mode when the antenna is short compared to the wavelength, or incorrectly terminated

The travelling wave mode of operation is capable of providing a very broad band match. Gibson[5.1] claims to have constructed a Vivaldi antenna with an instantaneous bandwidth of 38 *GHz*, extending from 2 *GHz* to 40 *GHz*. The input impedance is not the only characteristic a designer must consider, radiation pattern control and antenna efficiency often limit the useful bandwidth of a travelling wave antenna before the input match to the feeder becomes unacceptable. The standing wave mode of operation is undesirable due to the bi–directional radiation pattern and the rapid variation of the input impedance with frequency.

The printed vee antennas considered in this investigation were designed to function as integrated detector or mixer elements in quasi–optic systems operating at 220 *GHz*. The first order design procedure and the results from practical integrated detectors are described. The effect matching of a two wavelength vee to a CPS transmission line was investigated by the use of the the scanning network probe and a large scale model operating at Q–band frequencies. The effect of the substrate thickness on the velocity factor of the vee antenna has been determined by the scanning network probe technique. A linearly tapered slot operating at Q–band frequencies has also been investigated using the scanning network probe.

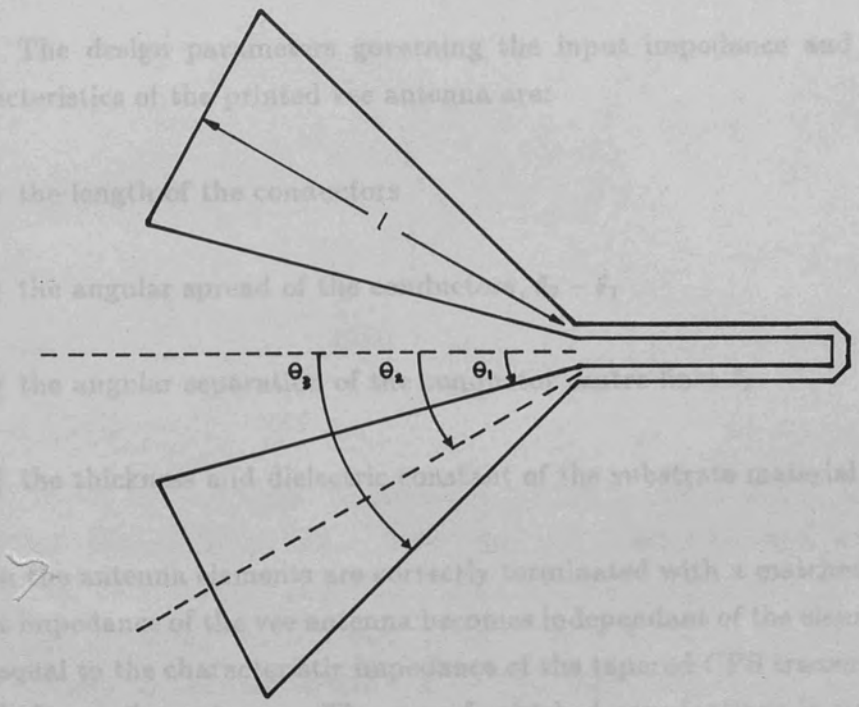

Figure (5.1)a The printed vee geometry

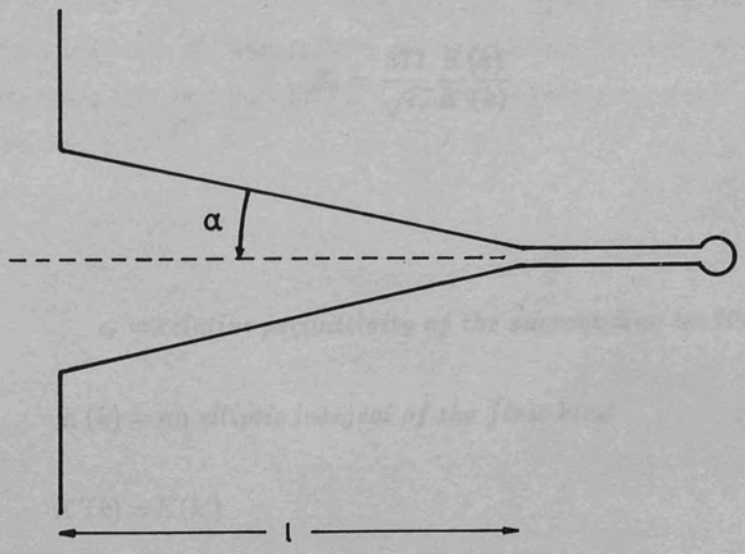

Figure (5.1)b The tapered slot geometry

5.2 Vee Antenna Design Equations

The design parameters governing the input impedance and radiation characteristics of the printed vee antenna are:

(a) the length of the conductors

(b) the angular spread of the conductors, $\theta_2 - \theta_1$

(c) the angular separation of the conductor centre lines θ_3

(d) the thickness and dielectric constant of the substrate material

When the antenna elements are correctly terminated with a matched load, the input impedance of the vee antenna becomes independant of the element length and equal to the characteristic impedance of the tapered CPS transmission line which forms the antenna. The use of matched terminations is unnecessary when the vee antenna is several wavelengths long, since the majority of the input power will have been radiated before the exciting wave reaches the open circuit discontinuity at the extremity of the vee. Rutledge et al[5.2] employ a conformal transformation to find the characteristic impedance of the tapered CPS transmission line. The two stage transformation maps the tapered CPS line geometry into the parallel CPS line geometry. The characteristic impedance is then given by:

$$Z_0 = \frac{377}{\sqrt{\epsilon_r}} \frac{K(k)}{K'(k)} \qquad 5.1$$

Where:

ϵ_r = *relative permittivity of the surrounding medium*

$K(k)$ = *an elliptic integral of the first kind*

$K'(k) = K(k')$

$k = \tan(\theta_1/2)/\tan(\theta_2/2)$

$k' = (1 - k^2)^{\frac{1}{2}}/cr$

The ratio of the elliptic integrals is easily found from the following closed form expressions:

$$\frac{K(k)}{K'(k)} = \frac{1}{\pi} \ln\left\{2\frac{1+\sqrt{k}}{1-\sqrt{k}}\right\} \qquad 0.707 \leq k \leq 1 \quad 5.2a$$

$$\frac{K(k)}{K'(k)} = \frac{\pi}{\ln\left\{2\frac{1+\sqrt{k}}{1-\sqrt{k}}\right\}} \qquad 0 \leq k \leq 0.707 \quad 5.2b$$

This method is exact when the vee antenna is embedded in an infinite dielectric medium. Equation(5.1) can still be used to calculate an approximate value of the vee characteristic impedance when the vee is fabricated on a dielectric substrate providing that the substrate can be assumed to be negligably thin with respect to the wavelength. A working criterion has been suggested by Cummins[5.4] that the substrate thickness must be thinner than $\lambda_0/100$. Under the assumption of negligable substrate thickness, equation(5.1) is used with ϵ_r equal to unity to evaluate the vee input impedance. Since this is a quasi–static technique, the results can only be taken as a first order approximation at millimetric wavelengths.

The radiation characteristics of the vee antenna can be modelled by replacing the fan vee geometry with an equivalent thin wire vee as illustrated by Figure (5.2). The angle between the equivalent wire vee elements is made equal to the angle between the centre lines of the fan vee conductors. For maximum directivity the angle 2α must be made equal to twice the angle of the principal lobe of one wire or:[5.5]

$$2\alpha \approx 4 \arcsin\left(\frac{0.431}{\sqrt{l/\lambda}}\right) \qquad 5.3$$

Where:

$l = the\ length\ of\ the\ antenna\ element$

$\lambda = wavelength$

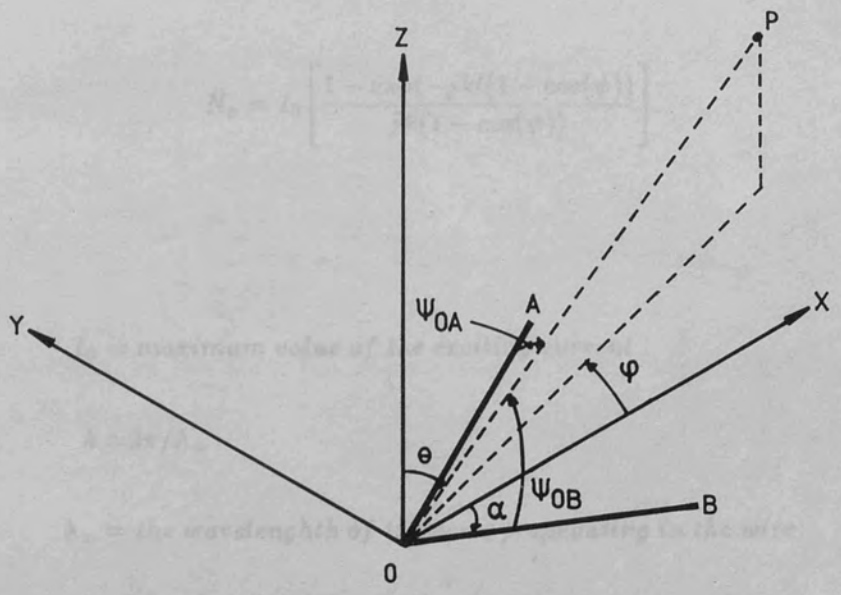

Figure (5.2) The equivalent wire vee geometry

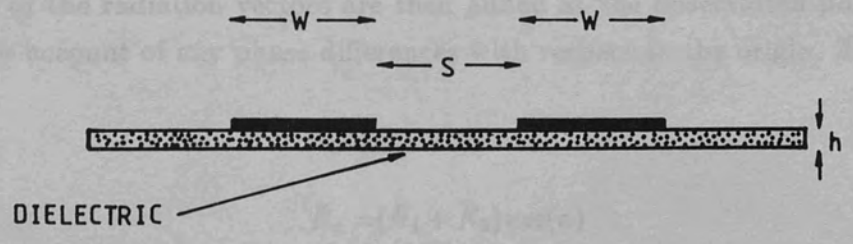

Figure (5.3) The parallel coplanar strip geometry

It can be shown[5.6] that the far field radiation vector $\bar{N}_x$ of a thin wire aligned with the x–axis and excited by a progressive wave of current $I = I_0 \exp(-jkx)$ is given by:

$$\bar{N}_x = I_0 \left[\frac{1 - \exp(-jkl(1 - \cos(\psi))}{jk(1 - \cos(\psi))} \right] \qquad 5.4$$

Where:

$I_0 =$ *maximum value of the exciting current*

$k = 2\pi/\lambda_w$

$\lambda_w =$ *the wavelenghth of the wave propagating in the wire*

$\psi =$ *the angular position of observation point*

For the wire vee geometry shown in Figure (5.2), ψ_{OA} and ψ_{OB} are the angles between the radius vector to a far field observation point P and the wires OA and OB respectively. Denoting the radiation of OA as $\bar{N}_1$ and OB as $\bar{N}_2$, then:

$$\bar{N}_1 = f(\psi) \qquad 5.5a$$

$$\bar{N}_2 = -f(\psi) \qquad 5.5b$$

The function $f(\psi)$ in equations(5.5)a, b is given by equation(5.4). The components of the radiation vectors are then added at the observation point taking proper account of any phase differences with respect to the origin. This gives:

$$\bar{N}_x = (\bar{N}_1 + \bar{N}_2)\cos(\alpha) \qquad 5.6a$$

$$\bar{N}_y = (-\bar{N}_1 + \bar{N}_2)\sin(\alpha) \qquad 5.6b$$

Since the exciting current has no component in the z–direction then $\bar{N}_z = 0$.

Defining the expressions $S_1(\psi_{OA}, \psi_{OB})$ and $S_2(\psi_{OA}, \psi_{OB})$ as:

$$S_1 = \frac{1 - \exp\left(-jkl(1 - \cos(\psi_{OA}))\right)}{1 - \cos(\psi_{OA})} - \frac{1 - \exp\left(-jkl(1 - \cos(\psi_{OB}))\right)}{1 - \cos(\psi_{OB})}$$

$$S_2 = \frac{1 - \exp\left(-jkl(1 - \cos(\psi_{OA}))\right)}{1 - \cos(\psi_{OA})} + \frac{1 - \exp\left(-jkl(1 - \cos(\psi_{OB}))\right)}{1 - \cos(\psi_{OB})}$$

The components of the total radiation vector in terms of spherical polar coordinates is then given by:

$$N_\theta = \frac{I_0}{jk}\left(S_1 \cos(\alpha)\cos(\phi) + S_2 \sin(\alpha)\sin(\phi)\right)\cos(\theta) \qquad 5.7a$$

$$N_\phi = \frac{I_0}{jk}\left(S_1 \cos(\alpha)\sin(\phi) + S_2 \sin(\alpha)\cos(\phi)\right) \qquad 5.7b$$

The directivity function $K(\theta, \phi)$ is then given by:

$$K = \frac{I_0^2 \eta}{32\pi^2}\left[N_\theta N_\theta^* + N_\phi N_\phi^*\right] \qquad 5.8$$

In the principal planes equation(5.8) becomes:

$$K_{H-plane} = \frac{I_0^2 \eta}{8\pi^2}\sin^2(\alpha)\left[\frac{(1 - \cos(kl(1 - \sin(\theta)\cos(\alpha)))^2}{(1 - \sin(\theta)\cos(\alpha))}\right] \qquad 5.9$$

and:

$$K_{E-plane} = \frac{I_0^2 \eta}{32\pi^2}\left[\left(f_1(\phi, \alpha) - f_2(\phi, \alpha)\right)^2 + \left(f_3(\phi, \alpha) - f_4(\phi, \alpha)\right)^2\right] \qquad 5.10$$

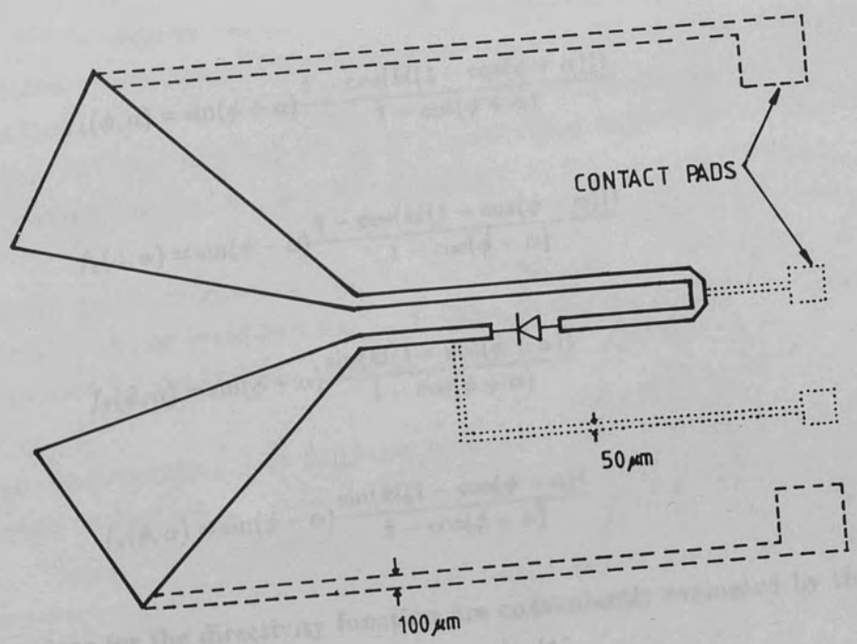

Figure (5.4) The general form of the integrated vee–detector module

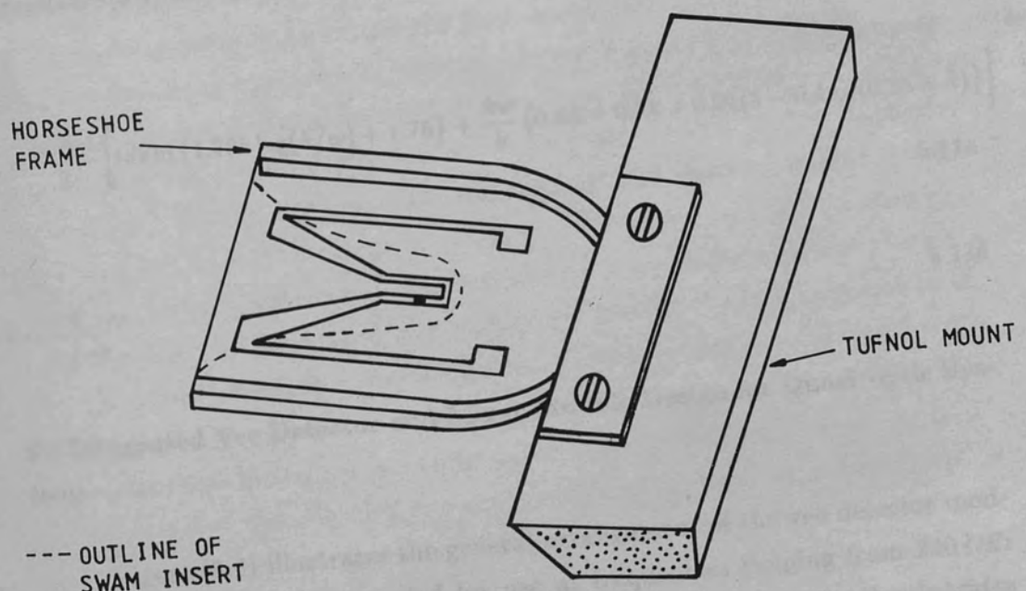

Figure (5.5) The vee antenna mounting arrangement

Where:

$$f_1(\phi,\alpha) = \sin(\phi+\alpha)\frac{1-\cos(kl(1-\cos(\phi+\alpha)))}{1-\cos(\phi+\alpha)}$$

$$f_2(\phi,\alpha) = \sin(\phi-\alpha)\frac{1-\cos(kl(1-\cos(\phi-\alpha)))}{1-\cos(\phi-\alpha)}$$

$$f_3(\phi,\alpha) = \sin(\phi+\alpha)\frac{\sin(kl(1-\cos(\phi+\alpha))}{1-\cos(\phi+\alpha)}$$

$$f_4(\phi,\alpha) = \sin(\phi-\alpha)\frac{\sin(kl(1-\cos(\phi-\alpha))}{1-\cos(\phi-\alpha)}$$

The expressions for the directivity function are conveniantly evaluated by the FORTRAN77 program "WIRE" listed in appendix(1).

Some form of transmission line is necessary for the construction of feed and matching networks. The ideal transmission line geometry for this purpose is the coplanar parallel strip, or CPS, geometry illustrated in Figure (5.3). The characteristic impedance of the CPS transmission line is calculated using Equations(5.1) and (5.2) with ϵ_r and k replaced by:

$$\epsilon_{re} = \frac{\epsilon_r+1}{2}\left[\tanh(\{1.785\log(h/w)+1.75\}+\frac{kw}{h}\{0.04-0.7k+0.01(1-0.1\epsilon_r)(0.25+k)\}\right] \qquad 5.11a$$

$$k = \frac{s}{s+w} \qquad 5.11b$$

5.3 Integrated Vee Detector and Mixer Module Design for Quasi–optic Systems

Figure (5.4) illustrates the general arrangement of the vee detector modules that have been constructed for use at frequencies ranging from 220 GHz to 260 GHz. Two designs were fabricated on 15 μm thick MYLAR substrates metallized with a 0.2 μm gold coating. The first design incorporated a $14.4\lambda_{220}$ vee with the bias arrangement shown dashed in Figure (5.4). The first order vee

design parameters were calculated using the BASIC program "V–IMP" listed in appendix(1). The program calculates the optimum angle 2α between the centrelines of the vee conductors for a given conductor length l using equation(5.3). The program then iterates equation(5.1) until the angular spread of the vee conductors is such that the input impedance of the travelling wave mode reaches the required value. The dimensions of a compatible CPS transmission line with a strip width of $100\,\mu m$ are then calculated using equations(5.1 and (5.11). The $100\,\mu m$ strip width is necessary so that a step discontinuity at the junctions between the diode beam leads and the CPS transmission line is avoided. The design parameters for the $14.4\lambda_{220}$ vee so obtained are:

(a) a vee conductor length of $19.75\,mm$ with an angular separation of $26°$ between centrelines

(b) a conductor spread of $\pm 5°$ about the centre line to obtain an input impedance of $200\,\Omega$

(c) a matching CPS transmission line with a strip width and separation of $100\,\mu m$ and $190\,\mu m$ respectively.

Due to the large package size of the DC 1346 beam lead diode at the near millimetric wavelengths of interest, the diode has to be series mounted in one of the strip conductors. The short circuit stub illustrated in Figure (5.4) functions as a matching network to cancel the package parasitics and as a D.C. return path for the diode bias circuit. The circuit was manufactured using standard photolithographic techniques, however the small dimensions of the circuit necessited the use of the electron beam lithography facility at the Rutherford Laboratory. During the substrate preparation and photolithographic stages the $15\,\mu m$ MYLAR substrate is supported on a 2" diameter stainless steel ring. After etching, the antenna is transferred to a small stainless steel horseshoe shaped support as illustrated in Figure (5.5). The MYLAR is attached to the horseshoe support using either a cyanoacrylate or epoxy resin adhesive. The substrate is maintained taut at the aperture of the horseshoe provided that the arms of the horseshoe are compressed slightly ($\approx 0.5\,mm$) until the adhesive sets. After the adhesive has set, the circuit is carefully removed with a scalpel. The beam lead diode and bias wires are then bonded onto the circuit using a single part gold loaded epoxy resin. A vee shaped insert made made from Plessy Materials SWAM is attached as shown in Figure (5.5) to suppress radiation pick–up by the printed bias lines and also to reduce reflections from the horseshoe frame. Finally the horseshoe frame is clamped to a TUFNOL

mounting bracket and the bias leads taken to an SMA jack.

The radiation pattern of the vee detector in the E and H–planes is shown in figures(5.6)a and (5.6)b respectively. The agreement between the theoretical radiation pattern calculated from equations(5.9) and (5.10) is seen to be quite good, except that the experimental E–plane radiation pattern shows a marked asymmmetry about boresight. The principal features of the theoretical E–plane radiation pattern are a main lobe on boresight with two sidelobes $\pm 7°$ from boresight, and two sidelobe clusters approximately $\pm 21°$ from boresight. The experimental E–plane radiation pattern shows very similar trends except:

(a) the main lobe and one of the first sidelobes have merged

(b) the sidelobe clusters are located slightly closer to the boresight direction

(c) the radiation pattern is not symmetric about boresight

Figure (5.6)c shows the cross polar E and H–plane radiation patterns. The H–plane cross polar signal is better than -25 dB with respect to the H–plane co–polar main beam. The E–plane cross polar response is only -1 dB below the co–polar E–plane signal level. The cross–polar E–plane radiation pattern resembles the grating lobe pattern obtained with two equally excited point sources spaced apart by a distance comparable to a free space wavelength and fed π radians out of phase. With this simple model maxima will occur whenever the path difference between the two sources to the observation point is an odd multiple of $\lambda_0/2$. Using the construction shown in Figure (5.7), the condition for a maximum is given by:

$$(n + \frac{1}{2})\lambda_0 = d\sin(\theta) \qquad 5.12$$

Where:

$$R \gg d$$

$$n = 0, \pm 1, \pm 2, ...$$

On substituting the angles from boresight of the first three maxima in the cross polar E–plane radiation pattern into equation(5.12), the separation of the sources, d, is found to be in the range 3.3 mm to 4.5 mm. This distance coincides

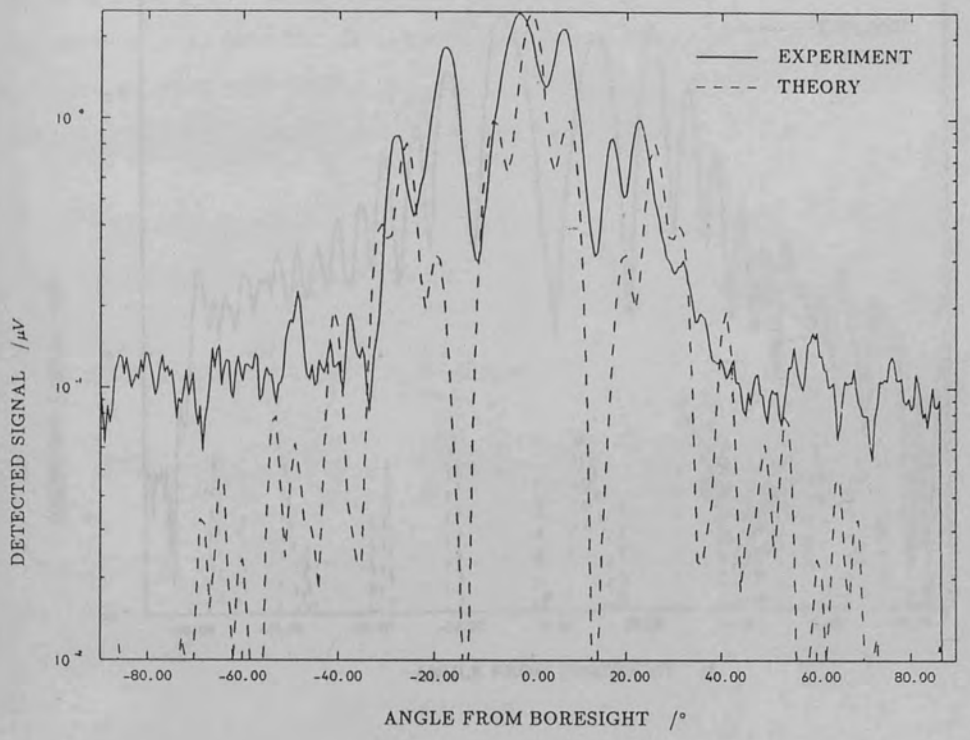

Figure (5.6)a 14.4 λ_{220} vee co–polar E–plane radiation pattern, F=221 *GHz*

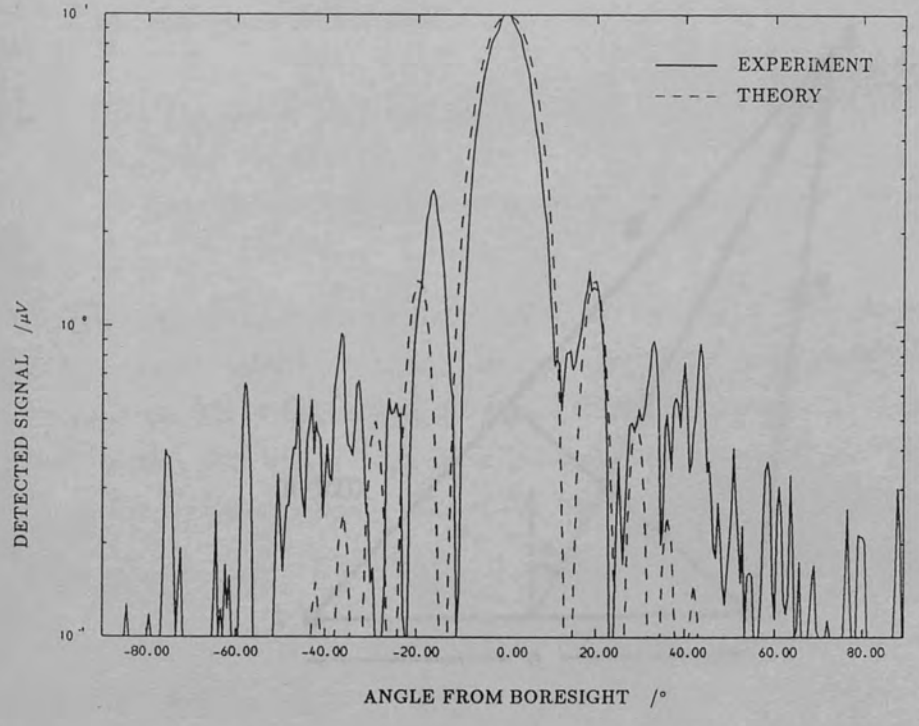

Figure (5.6)b 14.4 λ_{220} vee co–polar H–plane radiation pattern, F=221 *GHz*

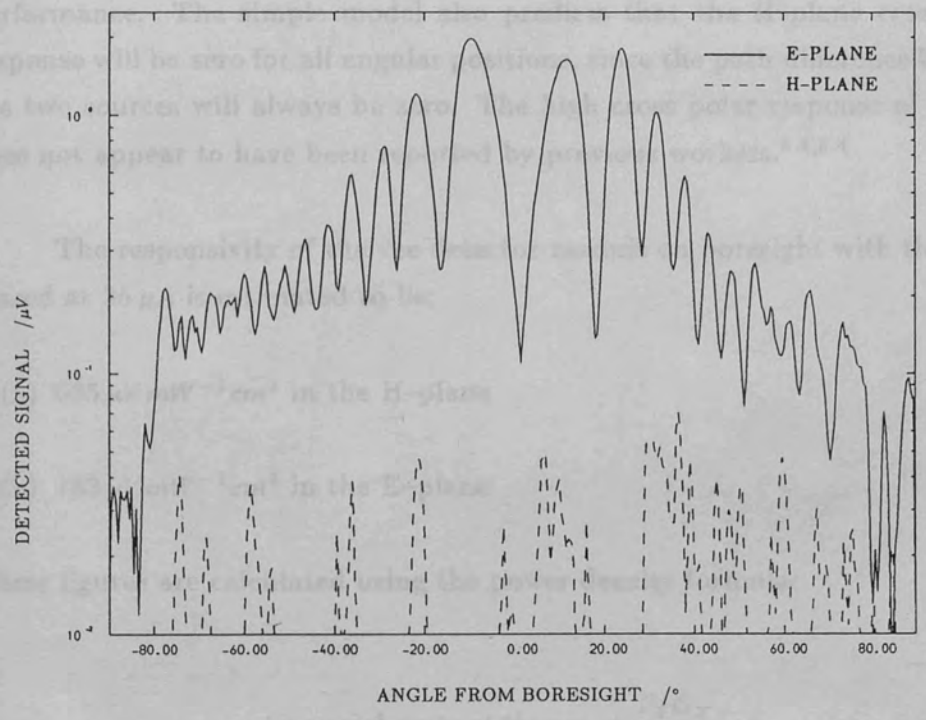

Figure (5.6)c $14.4\,\lambda_{220}$ vee cross–polar E and H–plane radiation pattern, F=221 *GHz*

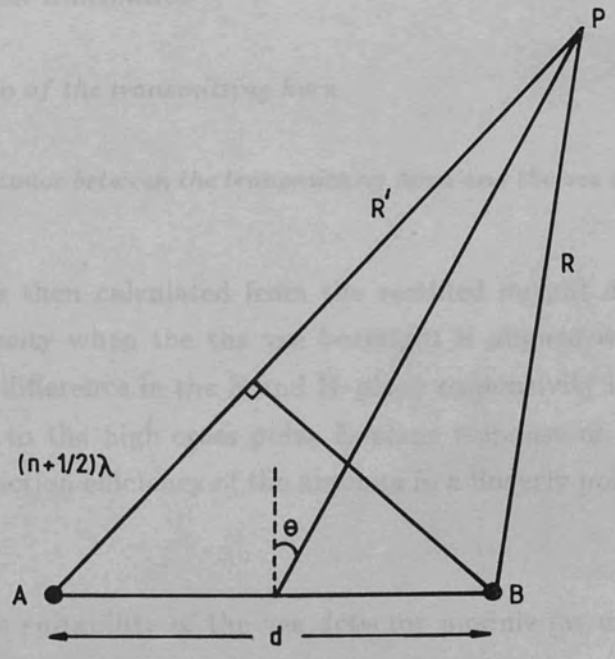

Figure (5.7) The far-field radiation from the cross–polar radiation sources at the vee aperture

with the aperture of the vee antenna, and suggests that the fringing fields at the open circuit end of the vee are responsible for the poor cross–polar E–plane performance. The simple model also predicts that the H–plane cross polar response will be zero for all angular positions, since the path difference between the two sources will always be zero. The high cross polar response of the vee does not appear to have been reported by previous workers.[5.2,5.4]

The responsivity of the vee detector module on boresight with the diode biased at $35\,\mu A$ is estimated to be:

(a) $685\,\mu V\,mW^{-1}cm^2$ in the H–plane

(b) $183\,\mu V\,mW^{-1}cm^2$ in the E–plane

These figures are calculated using the power density formula:

$$power\ density\ at\ the\ vee = \frac{P_T G_T}{4\pi D^2} \qquad 5.13$$

Where:

$P_T = the\ power\ transmitted$

$G_T = the\ gain\ of\ the\ transmitting\ horn$

$D = the\ distance\ between\ the\ transmitting\ horn\ and\ the\ vee\ antenna$

The responsivity is then calculated from the rectified output divided by the incident power density when the the vee boresight is aligned with the transmitting horn. The difference in the E and H–plane responsivity is marked, and is presumably due to the high cross polar E–plane response of the vee which reduces the transduction efficiency of the antenna in a linearly polarized electric field.

To assess the suitability of the vee detector module for use as a quasi–optic sub–harmonic mixer element, the radiation pattern and responsivity of the $14.4\lambda_{220}$ vee was obtained at frequencies of 95 GHz and 33 GHz. The radiation pattern of the $14.4\lambda_{220}$ vee in the principal planes at a frequency of 95 GHz is

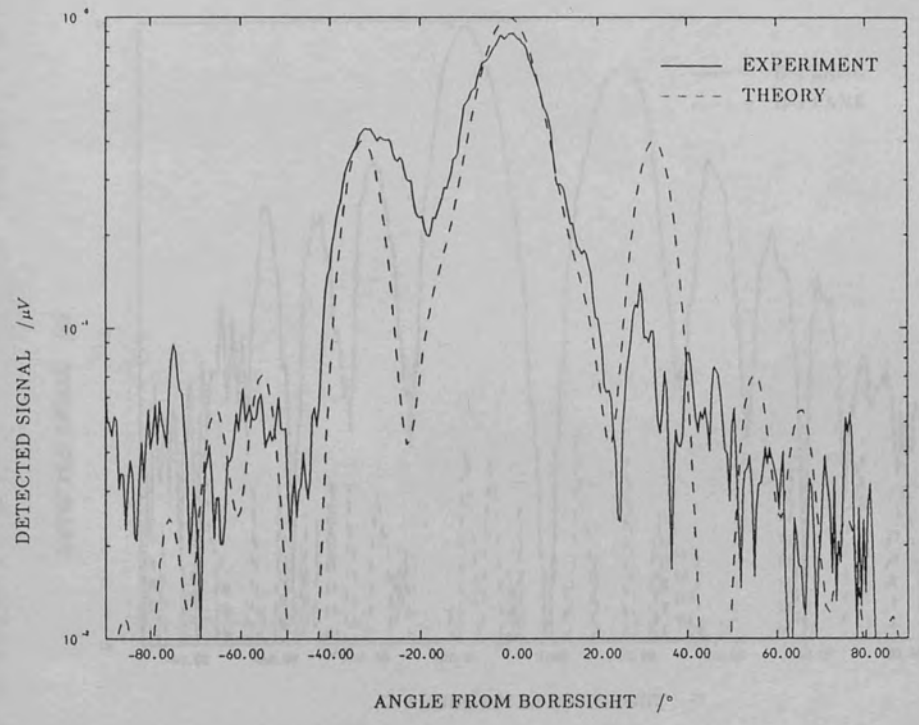

Figure (5.8)a 14.4 λ_{220} vee co–polar E–plane radiation pattern, F=95 *GHz*

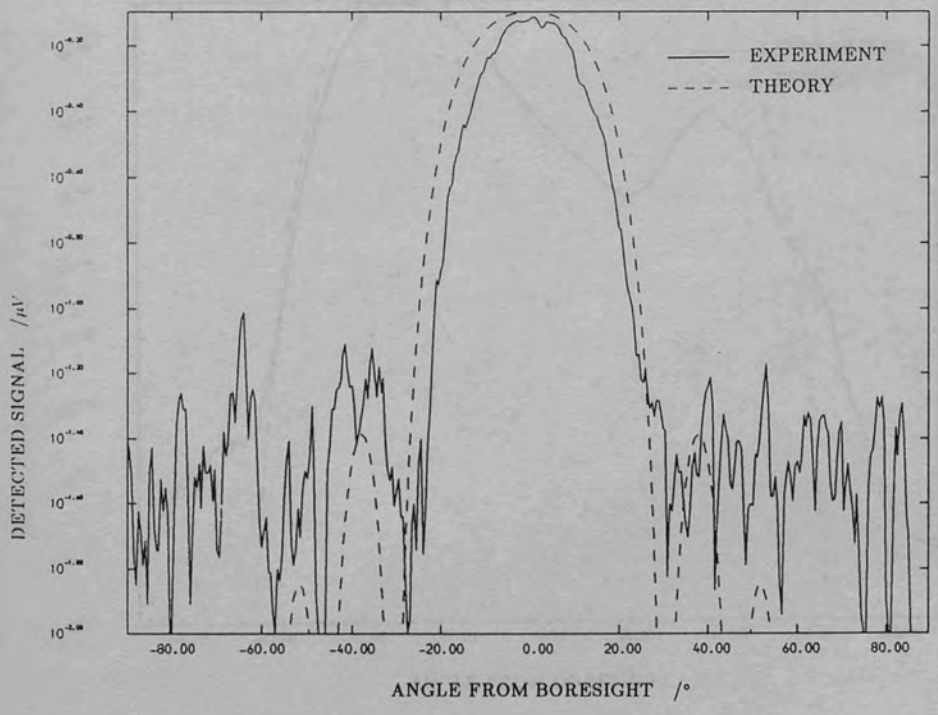

Figure (5.8)b 14.4 λ_{220} vee co–polar H–plane radiation pattern, F=95 *GHz*

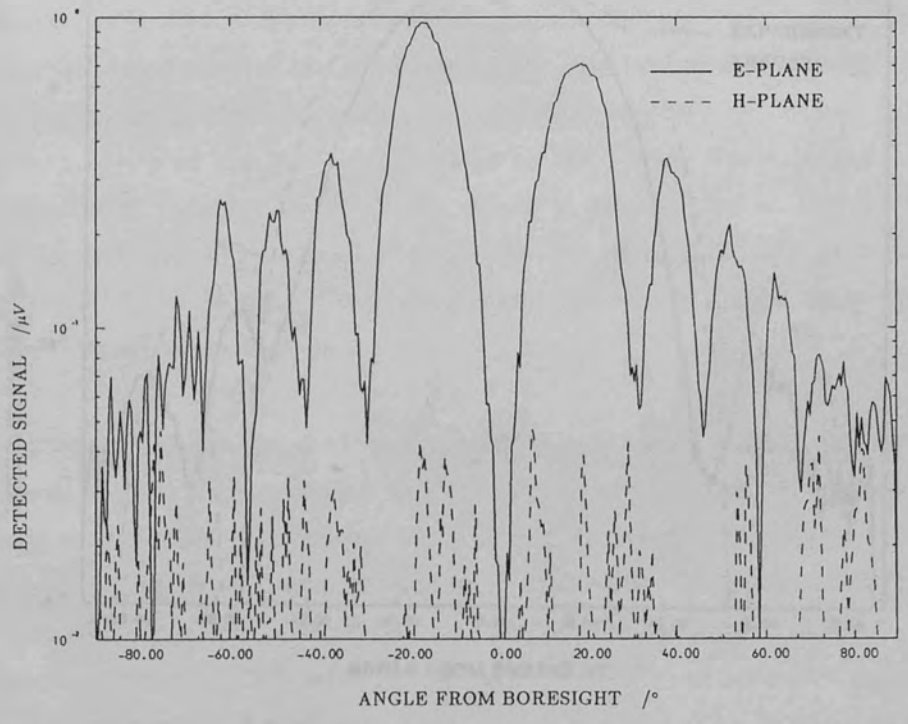

Figure (5.8)c $14.4\,\lambda_{220}$ vee cross–polar E and H–plane radiation pattern, F=95 *GHz*

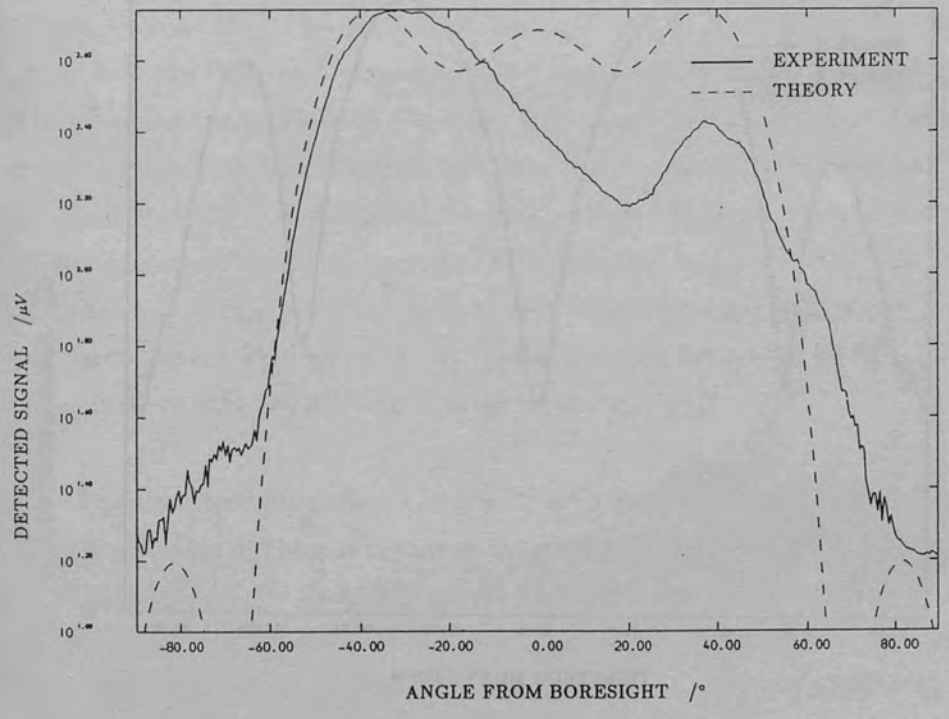

Figure (5.9)a $14.4\,\lambda_{220}$ vee co–polar E–plane radiation pattern, F=33 *GHz*

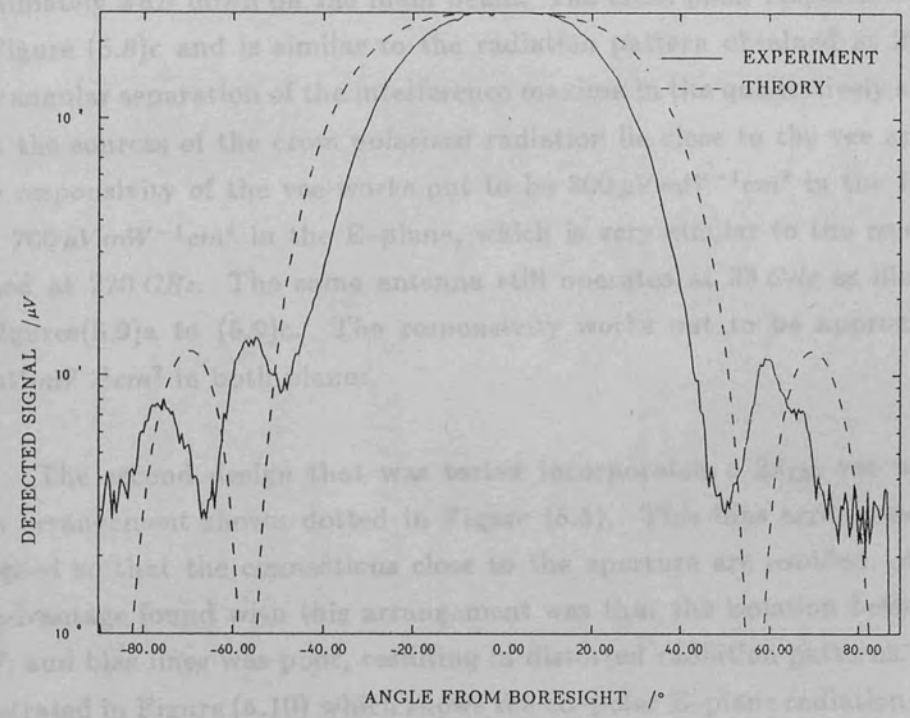

Figure (5.9)b $14.4\,\lambda_{220}$ vee co–polar H–plane radiation pattern, F=33 *GHz*

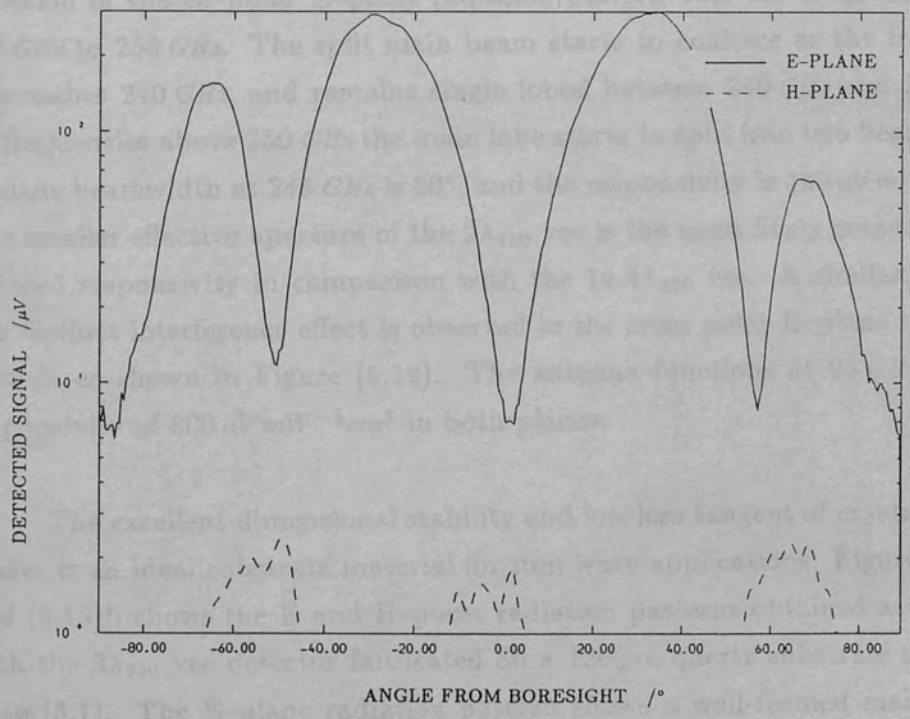

Figure (5.9)c $14.4\,\lambda_{220}$ vee cross–polar E and H–plane radiation pattern, F=33 *GHz*

illustrated in figures(5.8)a and (5.8)b. The antenna has a useful single lobed main beam, however the E–plane radiation pattern exhibits a large sidelobe approximately $3\,dB$ down on the main beam. The cross polar response is shown in Figure (5.8)c and is similar to the radiation pattern obtained at $220\,GHz$. The angular separation of the interference maxima in the qualitatively suggests that the sources of the cross polarized radiation lie close to the vee aperture. The responsivity of the vee works out to be $800\,\mu V\,mW^{-1}cm^2$ in the H–plane and $700\,\mu V\,mW^{-1}cm^2$ in the E–plane, which is very similar to the results obtained at $220\,GHz$. The same antenna still operates at $33\,GHz$ as illustrated in figures(5.9)a to (5.9)c. The responsivity works out to be approximately $85mV\,mW^{-1}cm^2$ in both planes.

The second design that was tested incorporated a $2\lambda_{220}$ vee with the bias arrangement shown dotted in Figure (5.5). This bias arrangement was adopted so that the connections close to the aperture are avoided. A major disadvantage found with this arrangement was that the isolation between the R.F. and bias lines was poor, resulting in distorted radiation patterns. This is illustrated in Figure (5.10) which shows the co–polar E–plane radiation pattern with the bias lines unloaded and loaded with SWAM. The E–plane radiation pattern exhibits a split main beam at the design frequency of $220\,GHz$, which indicates that the equivalent wire model is not accurate for short, unterminated vee antennas. The sequence of plots in figures(5.11)a to (5.11)f illustrates the variation of the co–polar E–plane radiation pattern over the frequency range $220\,GHz$ to $255\,GHz$. The split main beam starts to coalesce as the frequency approaches $240\,GHz$, and remains single lobed between $240\,GHz$ and $250\,GHz$. At frequencies above $250\,GHz$ the main lobe starts to split into two beams. The E-plane beamwidth at $245\,GHz$ is 50°, and the responsivity is $120\,\mu V\,mW^{-1}cm^2$. The smaller effective aperture of the $2\lambda_{220}$ vee is the most likely reason for the reduced responsivity in comparison with the $14.4\lambda_{220}$ vee. A similar, though less distinct interference effect is observed in the cross polar E–plane radiation pattern as shown in Figure (5.12). The antenna functions at $95\,GHz$ with a responsivity of $800\,\mu V\,mW^{-1}cm^2$ in both planes.

The excellent dimensional stability and low loss tangent of crystal quartz makes it an ideal substrate material for mm wave applications. Figure (5.13)a and (5.13)b shows the E and H–plane radiation patterns obtained at $220\,GHz$ with the $3\lambda_{220}$ vee detector fabricated on a $120\,\mu m$ quartz substrate shown in Plate (3.1). The E–plane radiation pattern shows a well formed main beam, but the H–plane radiation pattern shows asymmetry about boresight which is due to the relatively thick ($\approx \lambda_0/10$) substrate. The voltage responsivity of this

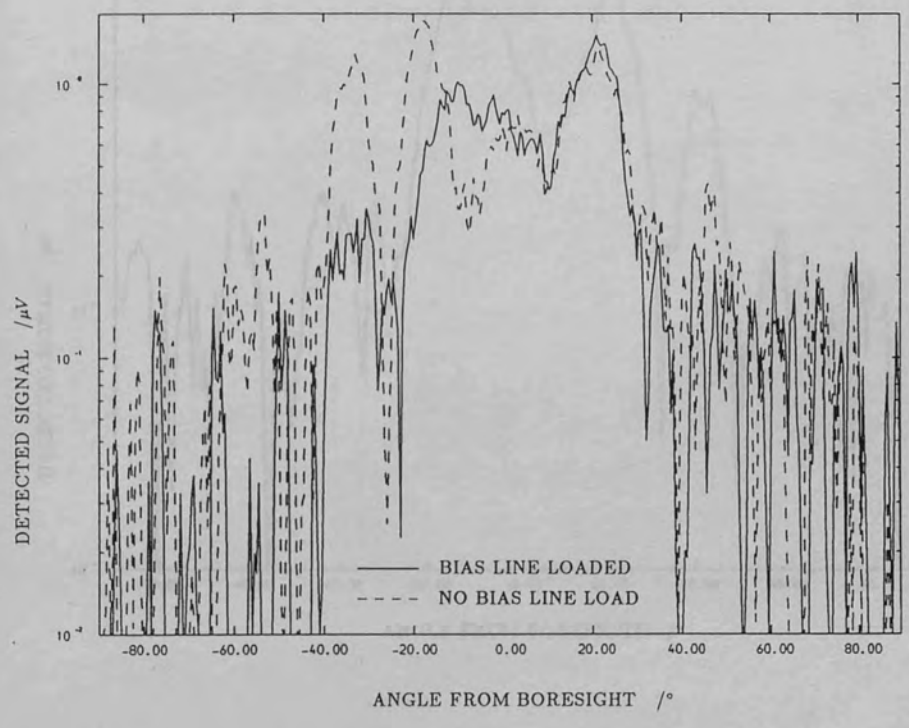

Figure (5.10) Distortion of the radiation pattern due to bias line pick–up

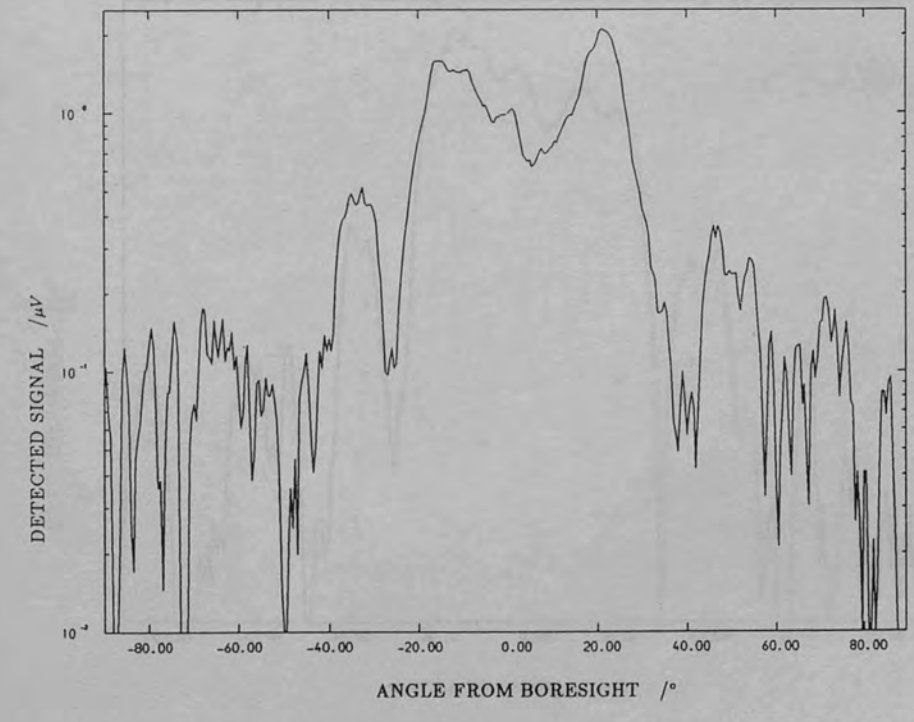

Figure (5.11)a $2\lambda_{220}$ vee co–polar E–plane radiation pattern, F=221 *GHz*

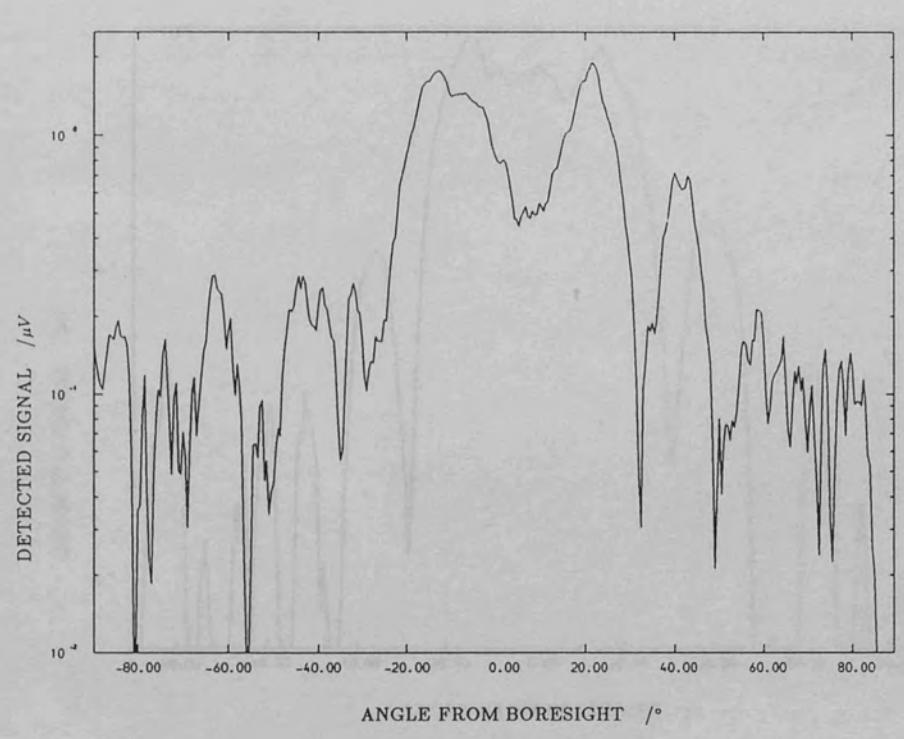

Figure (5.11)b $2\,\lambda_{220}$ vee co–polar E–plane radiation pattern, F=237 *GHz*

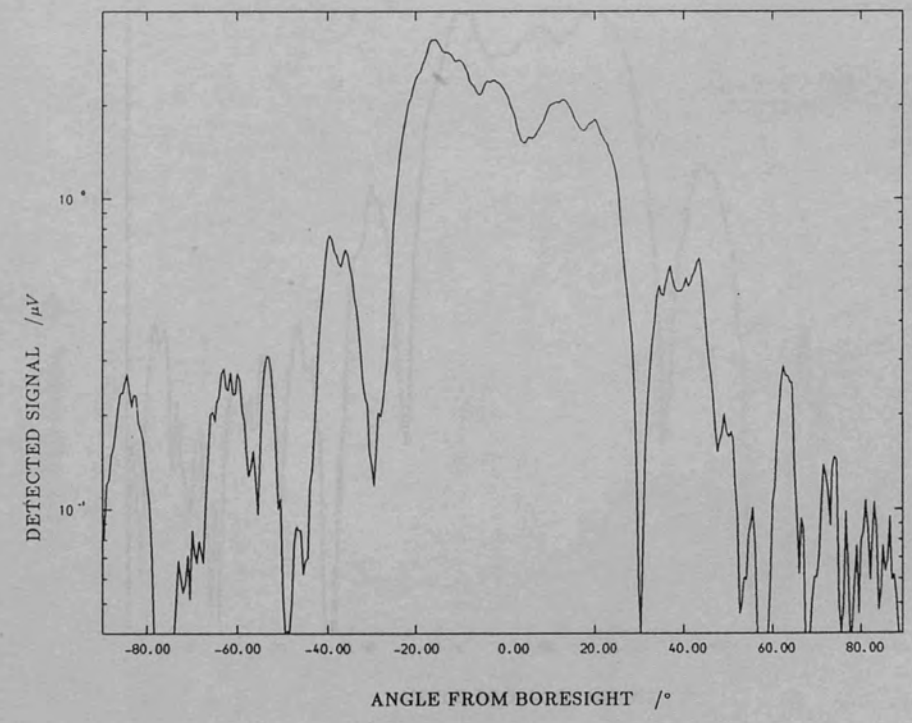

Figure (5.11)c $2\,\lambda_{220}$ vee co–polar E–plane radiation pattern, F=240 *GHz*

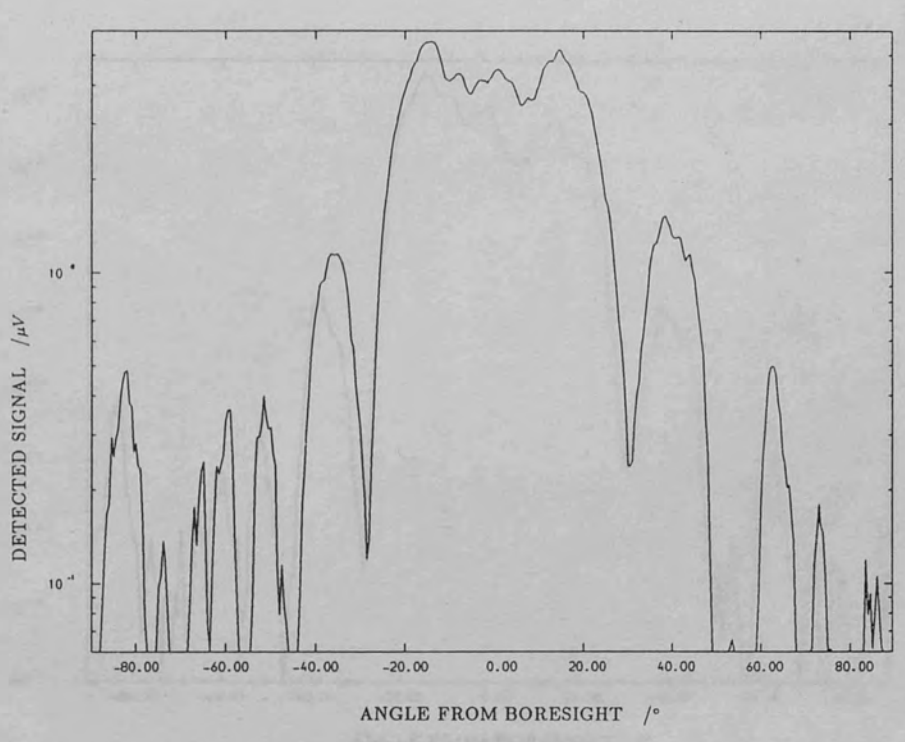

Figure (5.11)d $2\lambda_{220}$ vee co–polar E–plane radiation pattern, F=245 *GHz*

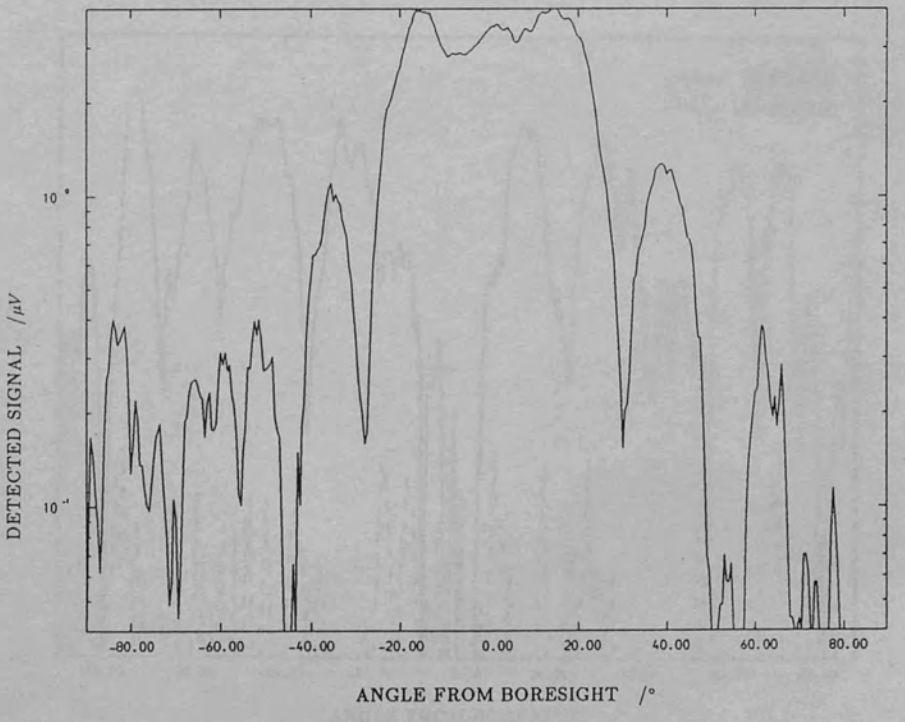

Figure (5.11)e $2\lambda_{220}$ vee co–polar E–plane radiation pattern, F=250 *GHz*

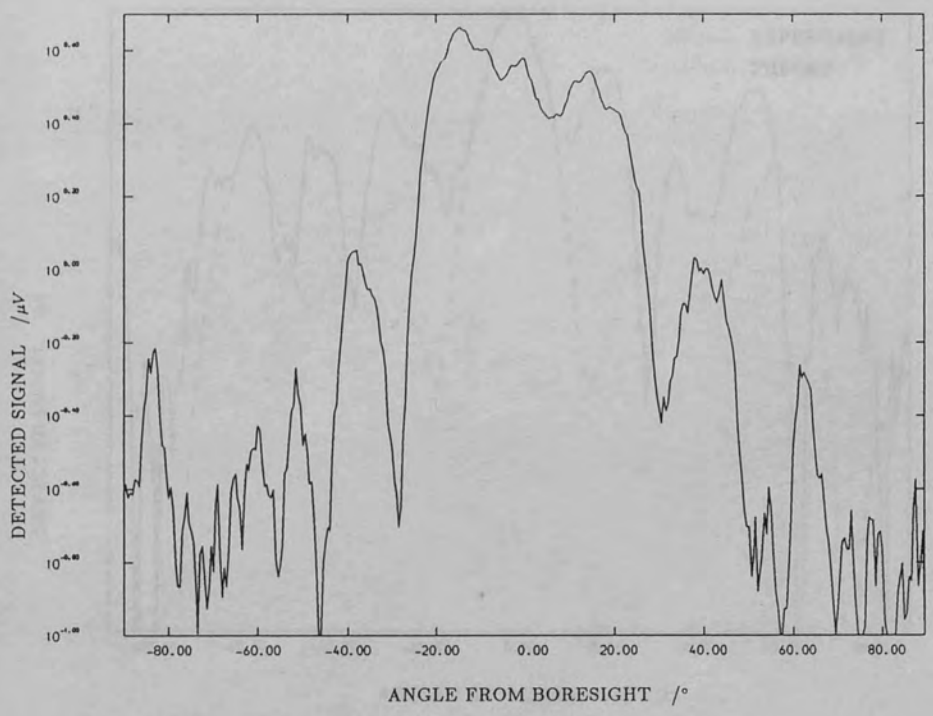

Figure (5.11)f $2\,\lambda_{220}$ vee co–polar E–plane radiation pattern, F=255 *GHz*

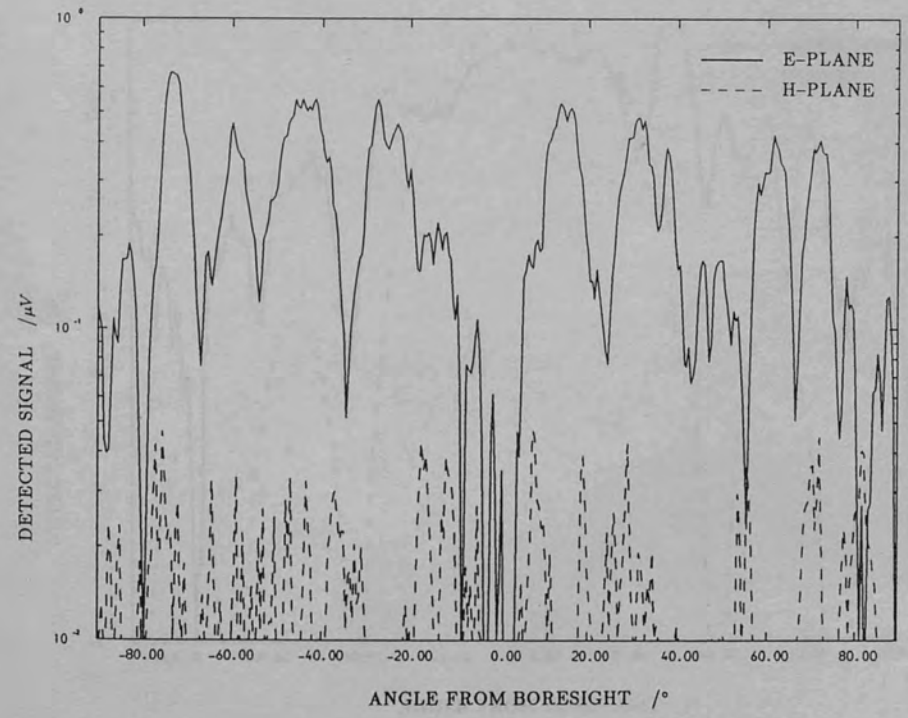

Figure (5.12) $2\,\lambda_{220}$ vee cross–polar E–plane radiation pattern, F=221 *GHz*

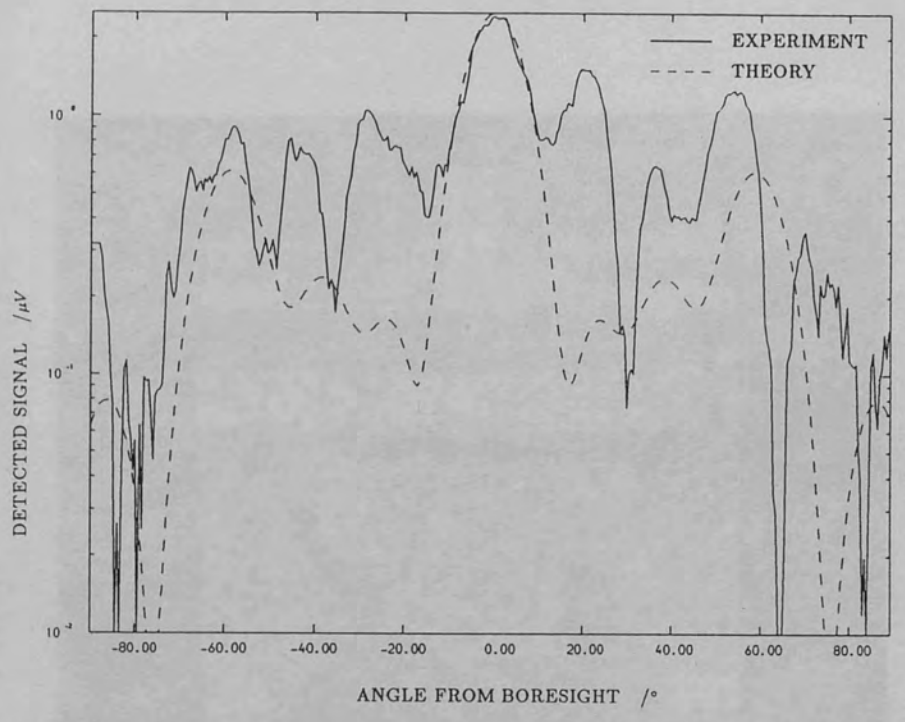

Figure (5.13)a $3\,\lambda_{220}$ vee co–polar E–plane radiation pattern, F=221 *GHz*

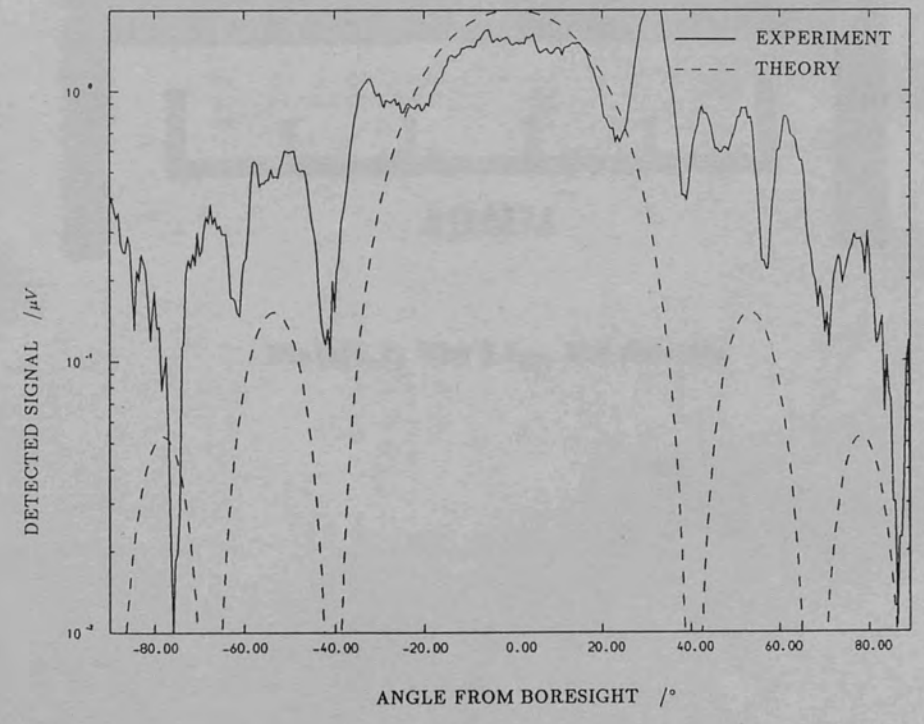

Figure (5.13)b $3\,\lambda_{220}$ vee co–polar H–plane radiation pattern, F=221 *GHz*

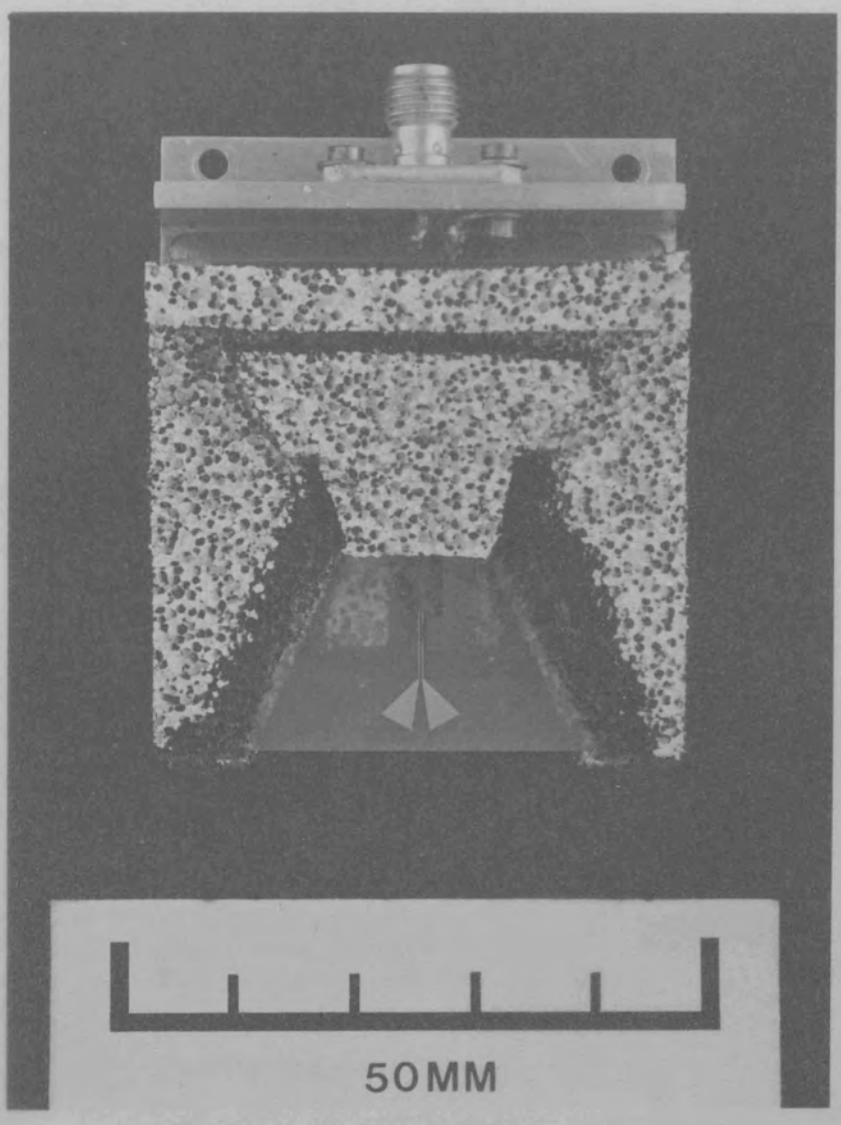

Plate(5.1) The $3\lambda_{220}$ Vee detector

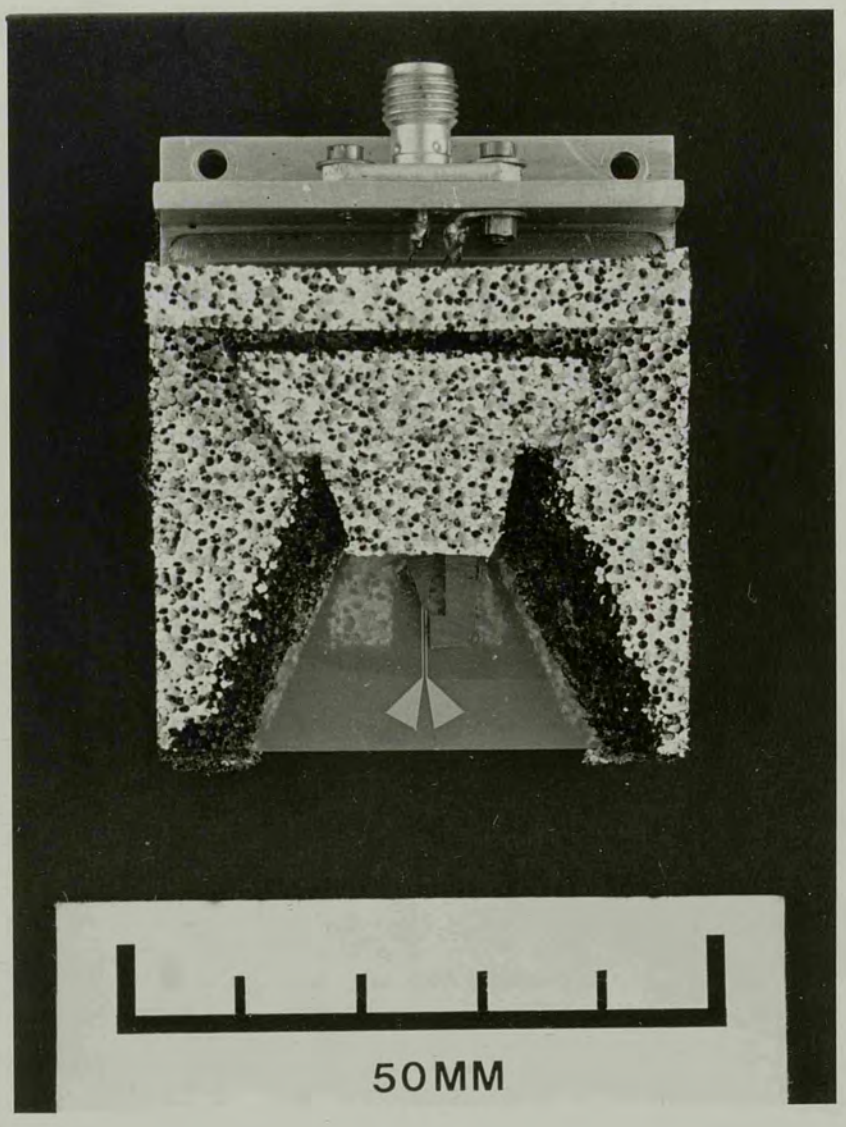
50MM

antenna works out to be $235\,\mu V mW^{-1}cm^2$, which is intermediate between the that of the two previous examples that were fabricated on thin MYLAR substrates.After allowing for the slightly higher directivity of the $3\lambda_{220}$ vee, the difference between the circuit fabricated on the low loss quartz substrate with a $5\,\mu m$ thick gold metallization and the $2\lambda_{220}$ vee fabricated on a MYLAR substrate with a $0.2\,\mu m$ thick metallization was marginal. This implies that the detector matching, and not the transmission line losses, is the major factor determining the vee detector performance.

The voltage responsivity of the vee designs were found to be poor compared to the figure of $2200\,\mu V mW^{-1}cm^2$ obtained by Kawasaki et al[5.7] using a whisker contacted Schottkey barrier diode in an oversize waveguide. A maximum limit to the detector voltage responsivity can be calculated from the effective aperture of the vee antenna and the basic diode parameters. The current sensitivity of a diode matched to its transmission line is given by:[5.7]

$$\beta = \frac{e}{2nkT}\,\frac{1}{\left(1+\frac{R_s}{R_j}\right)^2}\,\frac{1}{1+\frac{\omega^2 c_j^2 R_s R_j^2}{R_s+R_j}} \qquad \mu A\mu W^{-1} \quad 5.13$$

Where:

R_s = *the diode series resistance*

R_j = *the junction resistance*

c_j = *the junction capacitance*

ω = $2\pi \times$ *the frequency*

n = *the diode ideality factor*

e = *the electronic charge*

k = *the Boltzman constant*

T = *the absolute temperature*

The corresponding open circuit voltage sensitivity V is then given by:

$$V = \beta R_j \qquad \mu V\,\mu W^{-1} \qquad 5.14$$

Where:

$$R_j = \frac{dV}{dI}$$

$$= \frac{nkT}{I_s}$$

I_s = *the saturation current*

The characteristics of the DC 1346 diode quoted by the manufacturers are:

$$n = 1.15$$

$$R_s = 6\,Omega$$

$$c_j = 0.01\,pF$$

$$c_p = 0.02\,pF$$

$$L_p = 0.2\,nH$$

Inserting the above parameters into equations(5.13) and (5.14) gives a theoretical maximum voltage sensitivity of $2600\,\mu V\,\mu W^{-1}$ at $240\,GHz$. The effective aperture of a directional antenna is given by:

$$A_e = \frac{\lambda^2 G_r}{4\pi} \qquad 5.15$$

Where:

λ = *the wavelength*

G_r = *the antenna gain*

Assuming a directional gain of approximately $10\,dB$, which lies mid–way between the expected directivities of the $2\lambda_{220}$ and the $14.4\lambda_{220}$ vee antennas, the effective aperture works out to be $0.0124cm^2$. Therefore an incident radiation density of $1\,mW\,cm^{-2}$, will result in $12.4\mu W$ of power being coupled to the diode, assuming that the antenna and diode are perfectly matched, and that the transmission line loss is negligable. The voltage responsivity is then found to be $30{,}000\mu V\,mW^{-1}cm^2$. The $14.4\lambda_{220}$ approaches 2.5% of the maximum theoretical value of the maximum theoretical voltage responsivity, indicating that either:

(a) the diode parasitic capacitance and inductance have not been matched out

(b) the antenna input is mismatched

(c) the transmission line loss is excessively high

From the equivalent circuit of the beam lead diode shown in Figure (5.14), it is apparent that the package capacitance will divert current away from the rectifying junction if the reactance is not cancelled by a suitable matching network. Assuming that the shunt stub presents a near short circuit at the diode, then the equivalent circuit of the vee detector reduces to that shown in Figure (5.15). Under these conditions the fraction of the total current I_0 flowing through the rectifying junction is found to be $0.03I_0$. At a bias current of $35\mu A$, the dynamic resistance R_j is $714\,\Omega$, therefore the voltage generated across the rectifying junction is given by:

$$V = 0.03 I_0 R_j$$

$$V = 21.4 I_0 \qquad 5.16$$

The total load presented to the generator by the transmission line and the unmatched diode at $240\,GHz$ is given by:

$$Z_T = Z_0 + Z_{diode} \qquad 5.17$$

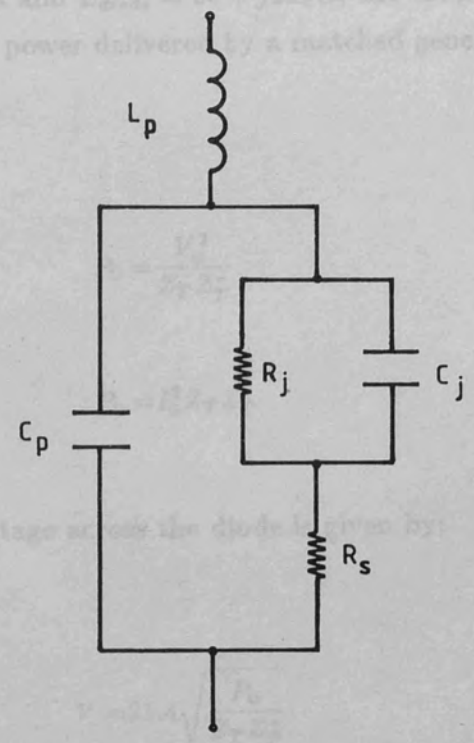

Figure (5.14) Beam lead diode equivalent circuit

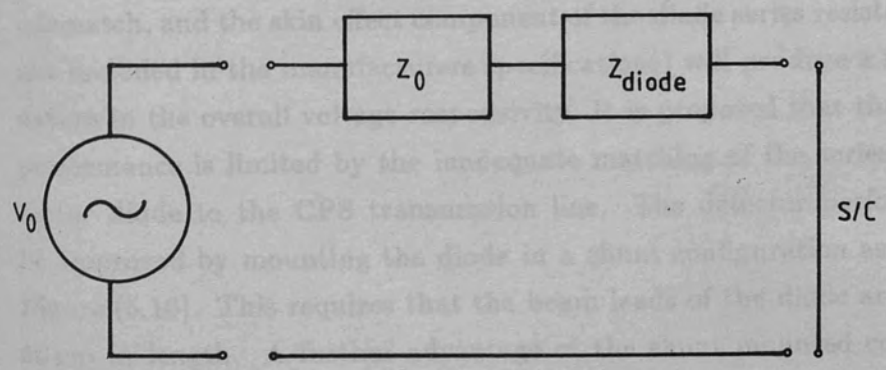

Figure (5.15) Vee detector equivalent circuit

Substituting for $Z_0 = 200\,\Omega$ and $Z_{diode} = 33 + j239\,\Omega$, the total load impedance becomes $233 + j239\,\Omega$. The power delivered by a matched generator to the load is then given by:

$$P_0 = \frac{V_0^2}{Z_T Z_T^*}$$

$$P_0 = I_0^2 Z_T Z_T^* \qquad 5.18$$

Therefore the rectified voltage across the diode is given by:

$$V = 21.4\sqrt{\frac{P_0}{Z_T Z_T^*}}$$

$$V = 1.2\sqrt{P_0} \qquad 5.19$$

For the hypothetical perfect vee with a gain of $10\,dB$, the power coupled from an incident field with a radiation density of $1 mW cm^{-2}$ is $12.4\mu W$, therefore the voltage responsivity of the vee is found to be approximately $4000\mu V\, mW^{-1} cm^2$. This represents 13% of the theoretical maximum responsivity calculated earliar, and is of a similar order of magnitude to the measured responsivities of the vee detectors tested. In reality the transmission line attenuation, the antenna mismatch, and the skin effect component of the diode series resistance (which is not included in the manufacturers specifications) will produce a further degradation in the overall voltage responsivity. It is proposed that the vee detector performance is limited by the inadequate matching of the series mounted detector diode to the CPS transmission line. The detector performance could be improved by mounting the diode in a shunt configuration as illustrated in Figure (5.16). This requires that the beam leads of the diode are cut down to $50\,\mu m$ in length. A further advantage of the shunt mounted configuration is that the balanced configuration of the CPS transmission line is undisturbed. The detector design shown in Figure (5.16) is yet to be tested.

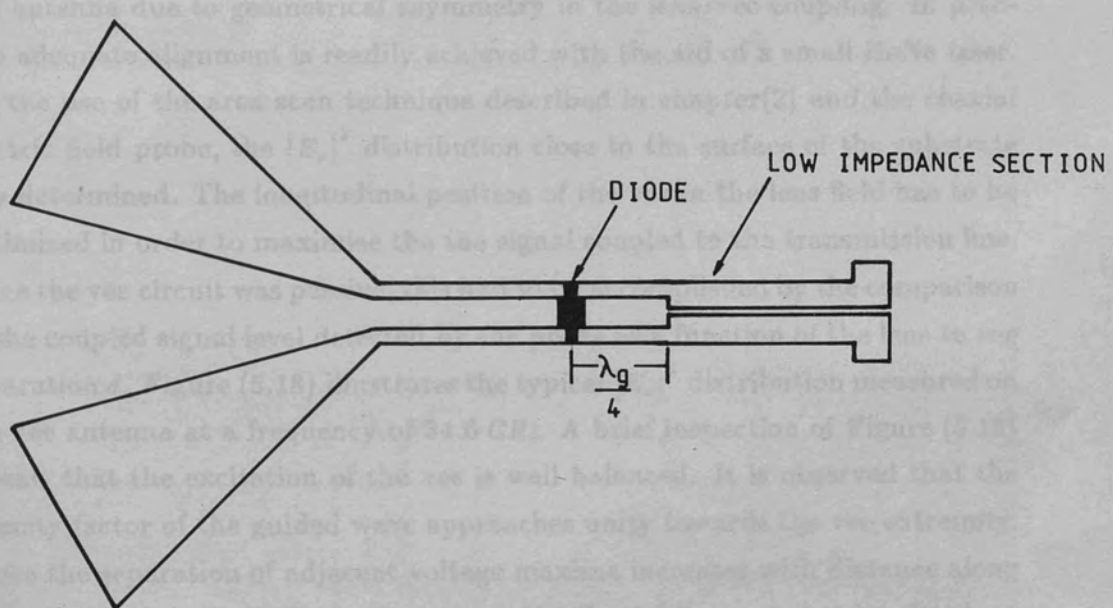

Figure (5.16) Proposed vee design employing a shunt mounted detector

5.4 Scanning Network Probe Investigation of a 2 Wavelength Vee Antenna

In order to assess the quality of the input match of the vee to the $200\,\Omega$ CPS transmission line, the $2\lambda_{220}$ vee was scaled up to $35\ GHz$ and the scanning network probe measurement technique employed. The CPS transmission line dimensions were also electromagnetically scaled to $35\ GHz$ from the original $220\ GHz$ design. A $25\ mm$ length of CPS transmission line, short circuited at the far end was attached to the vee input. The vee and transmission line were energized by a quasi–optic illumination system shown in Figure (5.17). The vee and CPS circuit were fabricated on a $70\ \mu m$ thick MYLAR substrate metallized with a $0.2\ \mu m$ silver coating. The axes of the vee, lens, and transmitting horn have to be carefully aligned in order to avoid an unbalanced excitation in the vee antenna due to geometrical asymmetry in the lens/vee coupling. In practice adequate alignment is readily achieved with the aid of a small HeNe laser. By the use of the area scan technique described in chapter(2) and the coaxial electric field probe, the $|E_z|^2$ distribution close to the surface of the substrate was determined. The longitudinal position of the vee in the lens field has to be optimized in order to maximize the the signal coupled to the transmission line. Since the vee circuit was passive, this had to be accomplished by the comparison of the coupled signal level detected by the probe as a function of the lens to vee separation d. Figure (5.18) illustrates the typical $|E_z|^2$ distribution measured on the vee antenna at a frequency of $34.6\ GHz$. A brief inspection of Figure (5.18) reveals that the excitation of the vee is well balanced. It is observed that the velocity factor of the guided wave approaches unity towards the vee extremity. (since the separation of adjacent voltage maxima increases with distance along the vee) The longitudinal standing wave distribution is generated by the short circuit in the CPS transmission line, as will be demonstrated later. It is also observed that there is a marked proximity effect, with the majority of the current flowing in a narrow strip close to the inner edges of the vee conductors. The graph shown in Figure (5.19) illustrates the variation in amplitude of the first two standing wave peaks as a function of lens to vee separation, where it is observed that the peak coupling occurs at $d = 60\ mm$. The ripple superimposed on the graph has a periodicity of approximately $2.5\lambda_0$, and is presumed to be due to the interference between the scattered wave from the vee and its reflection from the back surface of the lens, the coarse sampling interval that was employed ($\approx 1.25\lambda_0$) being responsible for the apparent periodicity of $2.5\lambda_0$. The input matching characteristics of the vee were estimated by comparing the standing wave pattern on the vee conductors with the CPS transmission line short circuited, and terminated with a matched load. The effect of the CPS load on the measured $|E_z|^2$ distribution can be seen in figures(5.20)a and(5.20)b

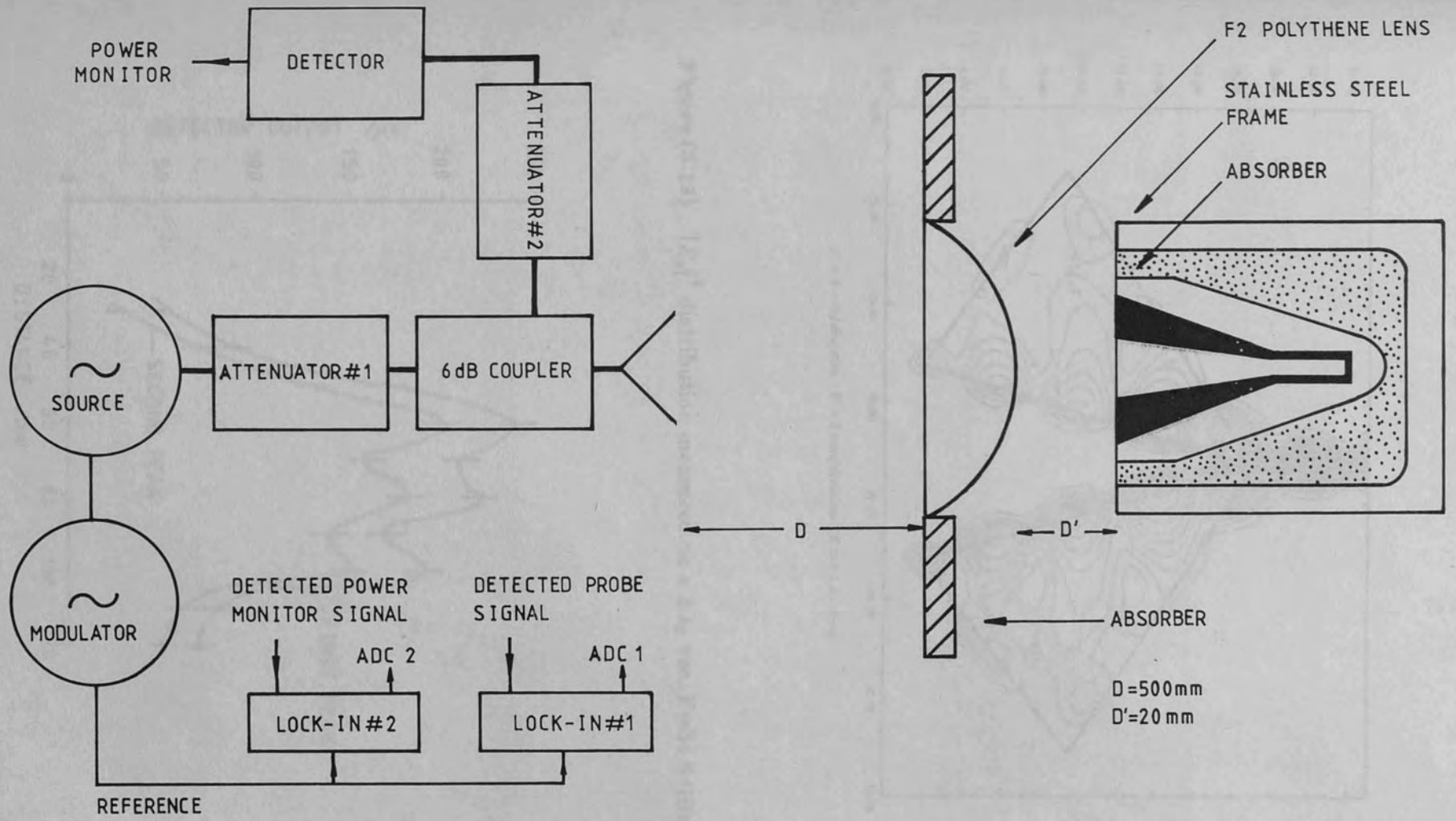

Figure(5.17) Experimental arrangement for exciting the vee antennas

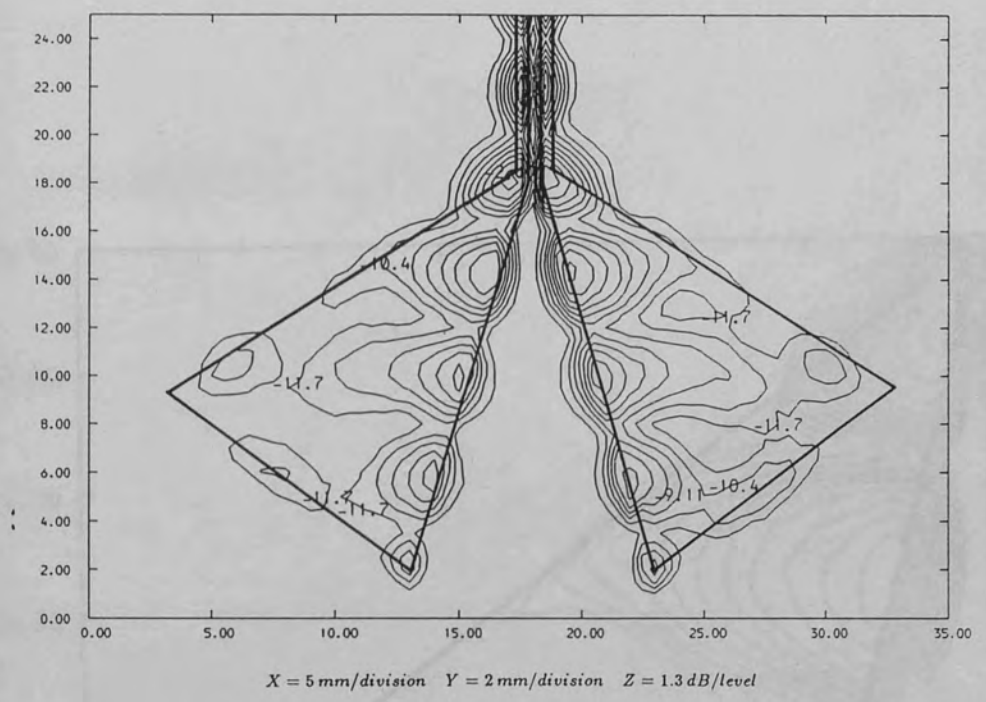

Figure (5.18) $|E_z|^2$ distribution measured on a $2\lambda_0$ vee, F=34.6 *GHz*

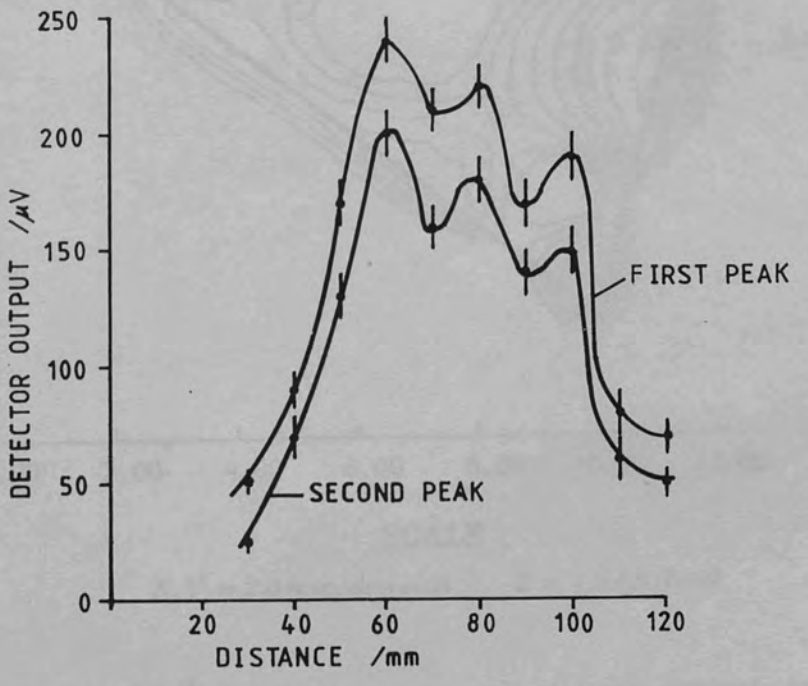

Figure (5.19) Peak signal level against vee–to–lens separation

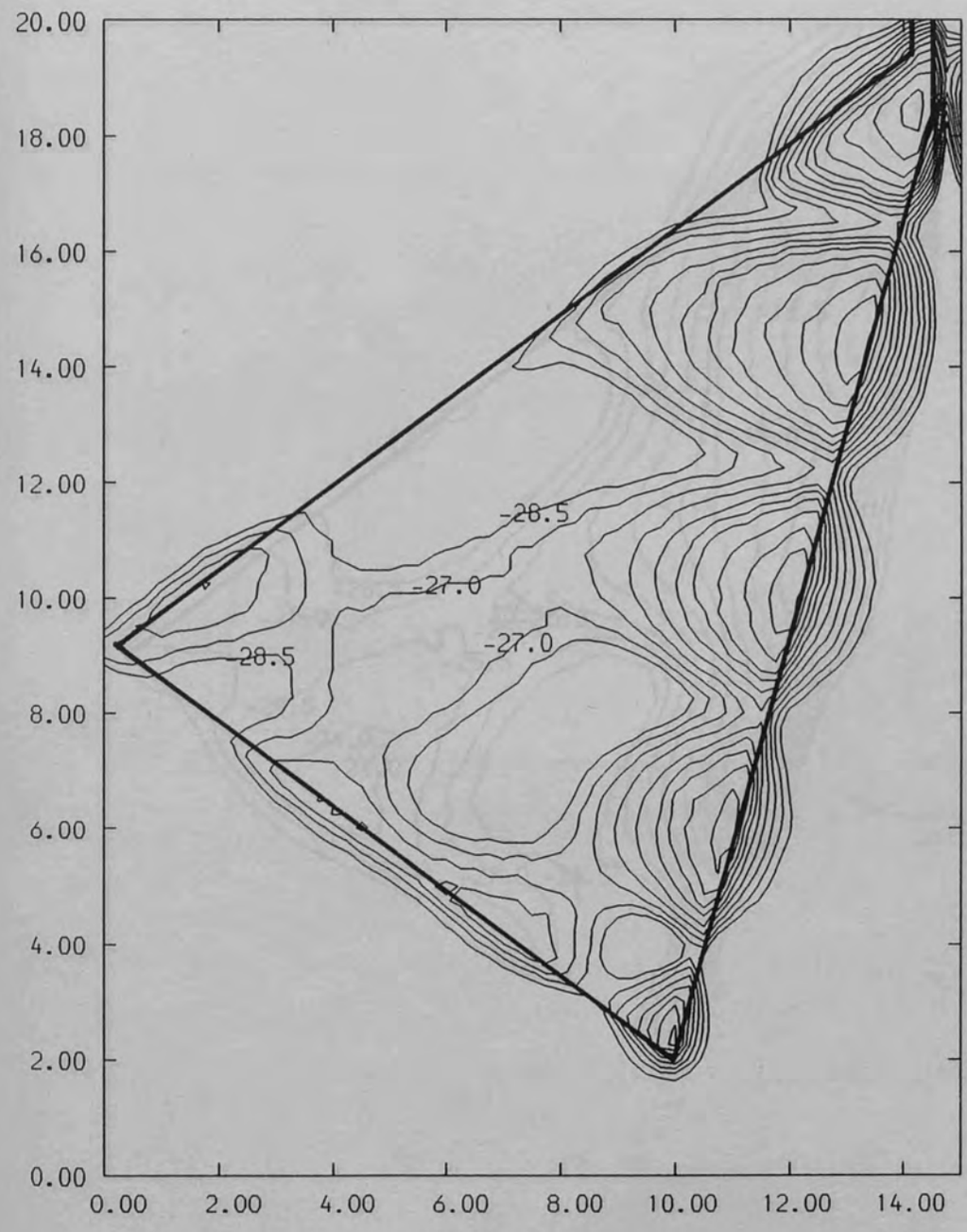

SCALE

$X, Y = 2.0\,mm/division \qquad Z = 1.5\,dB/level$

Figure (5.20)a $|E_z|^2$ distribution measured on a vee element, transmission line shorted, F=34.1 *GHz*

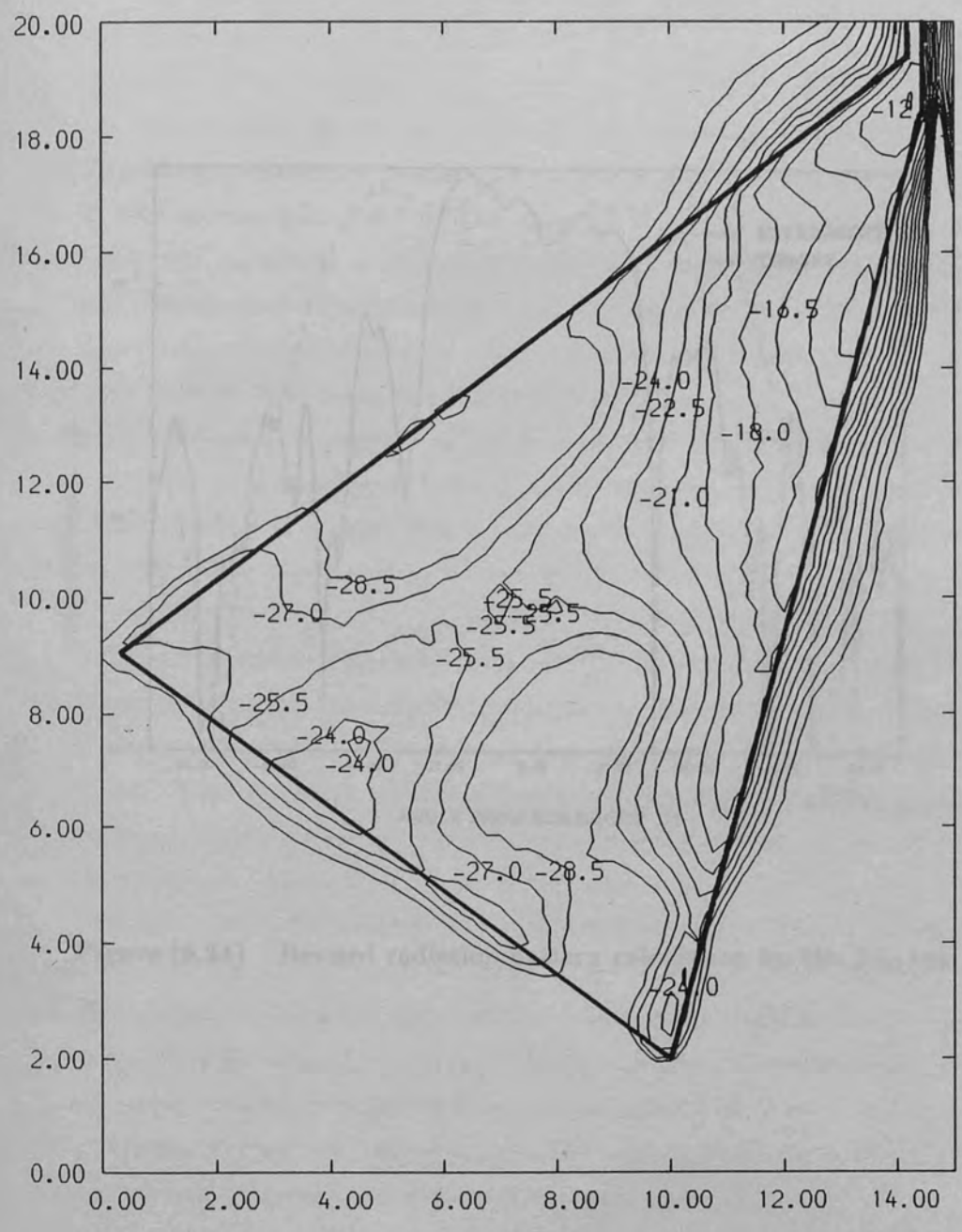

SCALE

$X, Y = 2.0\,mm/division \qquad Z = 1.5\,dB/level$

Figure (5.20)b $|E_z|^2$ distribution measured on a vee element, transmission line matched, F=34.1 *GHz*

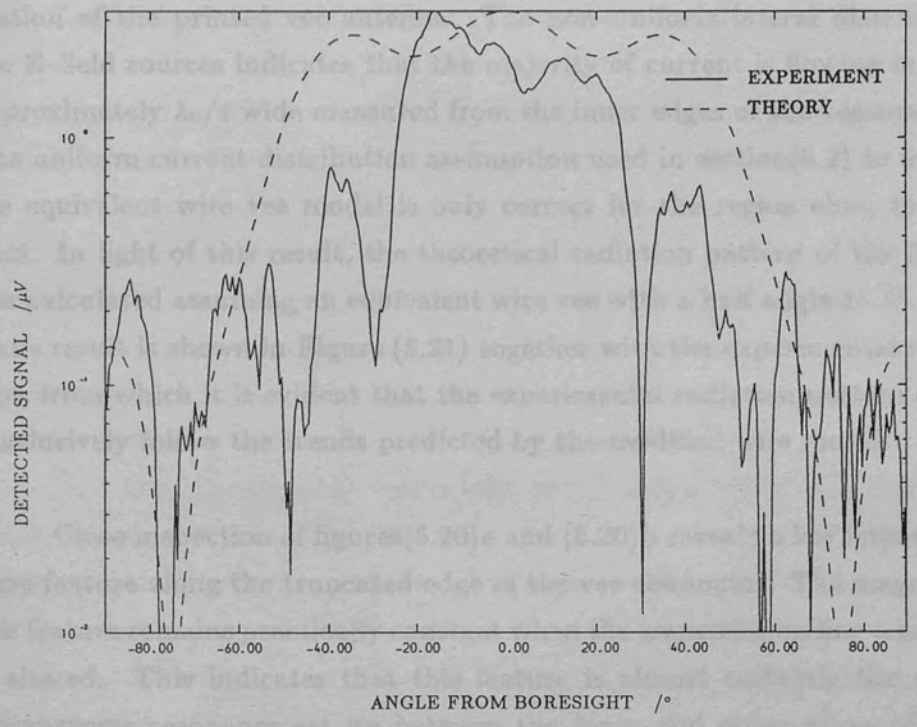

Figure (5.21) Revised radiation pattern calculation for the $2\lambda_0$ vee

which show the $|E_z|^2$ distribution close to the top surface of the vee conductors with the CPS transmission line short circuited and terminated with a surface absorber respectively. The longitudinal standing wave is reduced to a gentle linear decay of approximately $0.2\,dBmm^{-1}$ by removing the transmission line mismatch. The residual ripple close to the vee apex indicates that the antenna/CPS junction reflection coefficient is of the order of 0.1, which is very close to the reflection coefficient of the surface absorbing load measured by separate linear line scan measurements.

Figures(5.20)a, (5.20)b also provide useful physical insight into the operation of the printed vee antenna. The non–uniform lateral distribution of the E–field sources indicates that the majority of current is flowing in ribbons approximately $\lambda_0/4$ wide measured from the inner edges of the vee conductors. The uniform current distribution assumption used in section(5.2) to formulate the equivalent wire vee model is only correct for the region close to the vee apex. In light of this result, the theoretical radiation pattern of the $2\lambda_{220}$ vee was calculated assuming an equivalent wire vee with a half angle 15.5°. The E–plane result is shown in Figure (5.21) together with the experimental radiation plot, from which it is evident that the experimental radiation pattern does not conclusively follow the trends predicted by the modified wire model.

Close inspection of figures(5.20)a and (5.20)b reveals a low level standing wave feature along the truncated edge of the vee conductor. The magnitude of this feature remains practically constant when the transmission line termination is altered. This indicates that this feature is almost certainly the result of a transverse resonance set up between the inner and outer edges of the vee conductor. In the absence of phase information it is impossible to state the direction of current flow, but it is clear that the current distribition is very complicated and could not be represented by the equivalent wire model with any degree of accuracy. Reducing the conductor width might suppress the transverse resonance, thus allowing the wire vee model to be used with reasonable accuracy. In this respect better correlation between the equivalent wire vee model and the experimental results would be expected for high impedance or very long vee antennas which inherently use narrow vee conductors.

5.5 A Brief Investigation of Tapered Slot Excitation Modes Using the Scanning Network Probe

The tapered slot antenna has been subject to limited investigation in comparison with other printed antenna geometries. The early work has been

exclusively experimental and based on empirical design criteria.[5.8–5.11] Of this early work the results presented by Thungeren[5.11] are the most useful, containing extensive data concerning the radiation characteristics of the Vivaldi and the linearly tapered slot antenna. Sufficient data was collected over a 2:1 frequency range to isolate the effect of the antenna design parameters on the radiation characteristics. It was found that:

(a) the H–plane beamwidth is primarily determined by the length of the antenna

(b) the E–plane beamwidth is dependant on the aperture size of the terminal zone

(c) the beam efficiency, defined in terms of the $10\,dB$ beamwidth improves with increasing the flare angle of the linearly tapered slot, or increasing the rate of flare of the Vivaldi antenna

These workers also tried to model the tapered slot antenna as a travelling wave wire antenna coincident with the inner edges of the slot, under the assumption that the current is confined to the edge region. The agreement between this model and the experimental results was poor, except when the ground plane metallization was reduced to two strips $\lambda_0/8$ wide. Their results are in total agreement with the findings of the scanning network probe investigation of the vee antenna.

More recently attempts have been made to theoretically model the tapered slot antenna in order to optimize the impedance[5.12,5.13] and the radiation characteristics.[5.14] These theoretical models have all used numerical techniques. Analytic expressions for the radiation pattern of a linearly tapered slot over a ground plane have also been derived.[5.15]

Similar scanning network probe measurements to those carried out on the vee antenna have been repeated for the tapered slot geometry. Figures(5.22)a and (5.22)b show the measured $|E_z|^2$ distribution close to the top surface of a two wavelength long linearly tapered slot antenna when the parallel slot line feed is open circuited and terminated with a matched load respectively. The tapered slot dimensions were selected such that the throat angle and throat depth were made equal to the angle between the inner conductors and the axial length of the two wavelength vee design. The width of the parallel slot feed was made equal to the CPS transmission line strip separation. The illumination

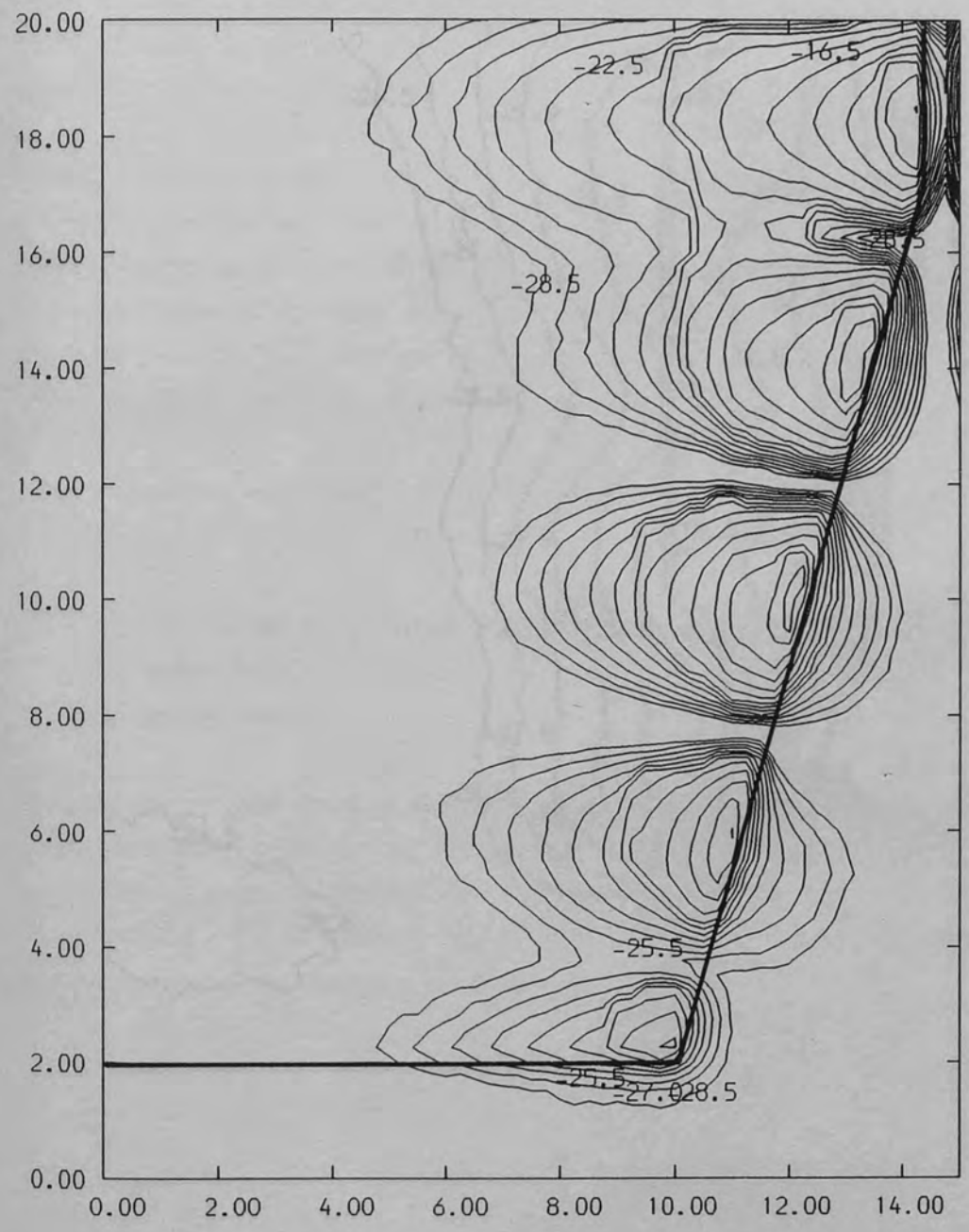

SCALE

$X, Y = 2.0\,mm/division \qquad Z = 1.5\,dB/level$

Figure (5.22)a $|E_z|^2$ distribution measured on a tapered slot, transmission line shorted, F=34.1 *GHz*

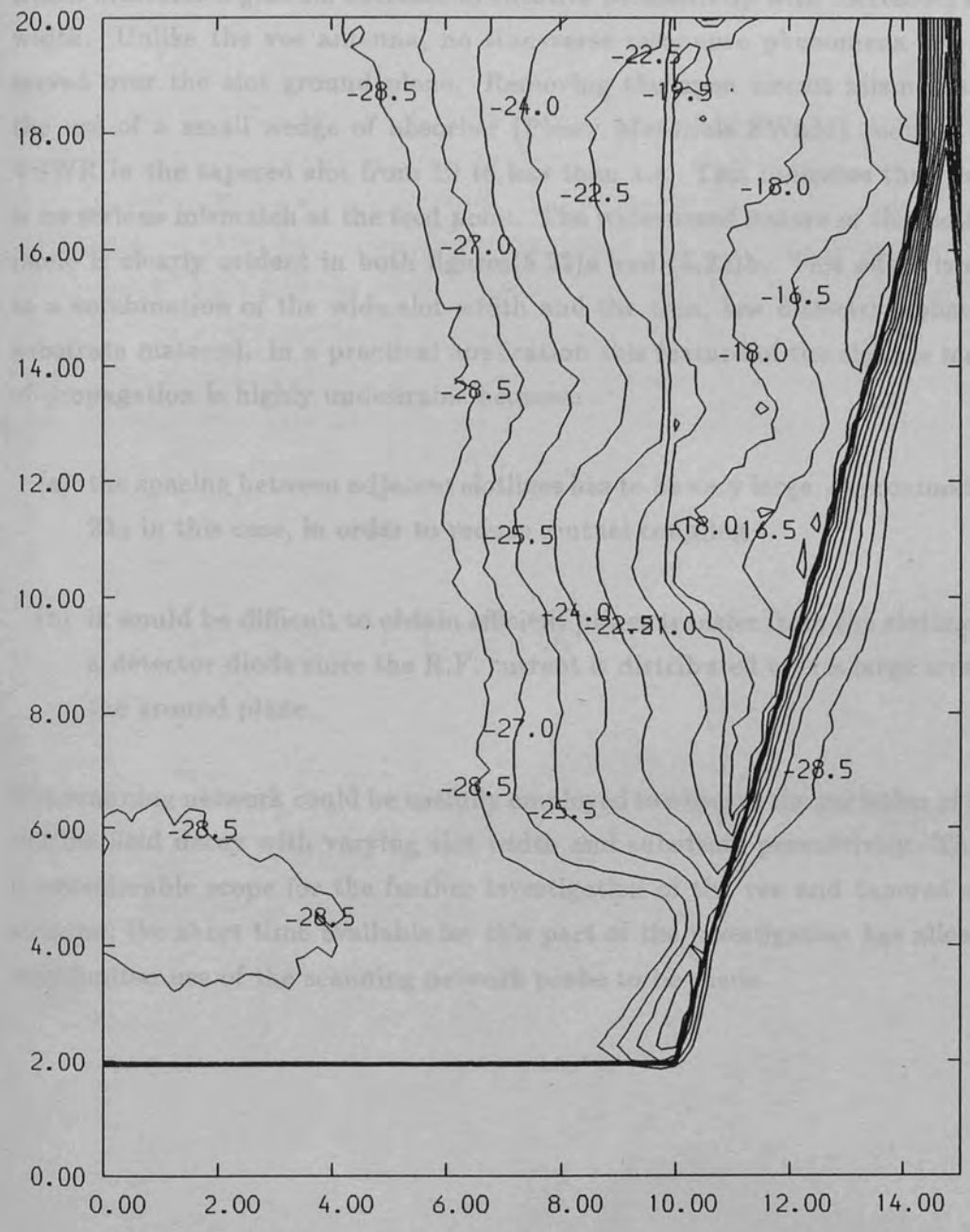

SCALE

$X, Y = 2.0\,mm/division \qquad Z = 1.5\,dB/level$

Figure (5.22)b $|E_z|^2$ distribution measured on a tapered slot, transmission line loaded, F=34.1 *GHz*

and probing conditions were identical to those employed for the vee measurements in figures(5.20)a,(5.20)b. The voltage standing wave generated by the reflection of the incident coupled wave from the slotline open circuit is clearly visible in Figure (5.22)a. In common with the vee antenna measurement, the tapered slot exhibits a pronounced proximity effect. Furthermore, the separation of the maxima increases with distance away from the tapered slot apex, which indicates a gradual decrease in effective permittivity with increasing slot width. Unlike the vee antenna, no transverse resonance phenomena are observed over the slot ground plane. Removing the open circuit mismatch by the use of a small wedge of absorber (Plessy Materials SWAM) reduces the VSWR in the tapered slot from 10 to less than 1.4. This indicates that there is no serious mismatch at the feed point. The widespread nature of the slotline mode is clearly evident in both figures(5.22)a and (5.22)b. This effect is due to a combination of the wide slot width and the thin, low dielectric constant substrate material. In a practical application this feature of the slotline mode of propagation is highly undesirable because:

(a) the spacing between adjacent slotlines has to be very large, approximately $2\lambda_0$ in this case, in order to reduce mutual coupling

(b) it would be difficult to obtain efficient power transfer from the slotline to a detector diode since the R.F. current is distributed over a large area of the ground plane.

The scanning network could be usefully employed to observe the variation of the slotline field decay with varying slot width and substrate permittivity. There is considerable scope for the further investigation of the vee and tapered slot antenna; the short time available for this part of the investigation has allowed only limited use of the scanning network probe to be made.

CHAPTER 6

Printed Transmission Line Measurements Using the Scanning Network Probe

6.1 Theory of Reflections on Transmission Lines

When a transmission line is terminated by a load with an impedance Z_L other than the characteristic impedance of the transmission line Z_0, the power transfer to the load is incomplete. Any power that is not absorbed by the load is reflected back towards the generator, and the interference between this reflected wave and the incident wave results in a standing wave being set up in the transmission line. The idealized case of a lossless transmission line terminated at one end by a load impedance Z_L, and by a matched generator at the other end is illustrated in Figure (6.1). At the load plane $z = 0$, therefore the voltage across the load, V_L, and the current through the load, I_L, are given by:

$$V_L = V^+ + V^- \tag{6.1}$$

$$I_L = I^+ + I^- \tag{6.2}$$

From the definition of load impedance:

$$I^+ = \frac{V^+}{Z_0} \tag{6.3}$$

$$I^- = \frac{V^-}{Z_0} \tag{6.4}$$

$$Z_L = \frac{V_L}{I_L} \tag{6.5}$$

Substituting equations(6.3)–(6.5) into equation(6.2) gives:

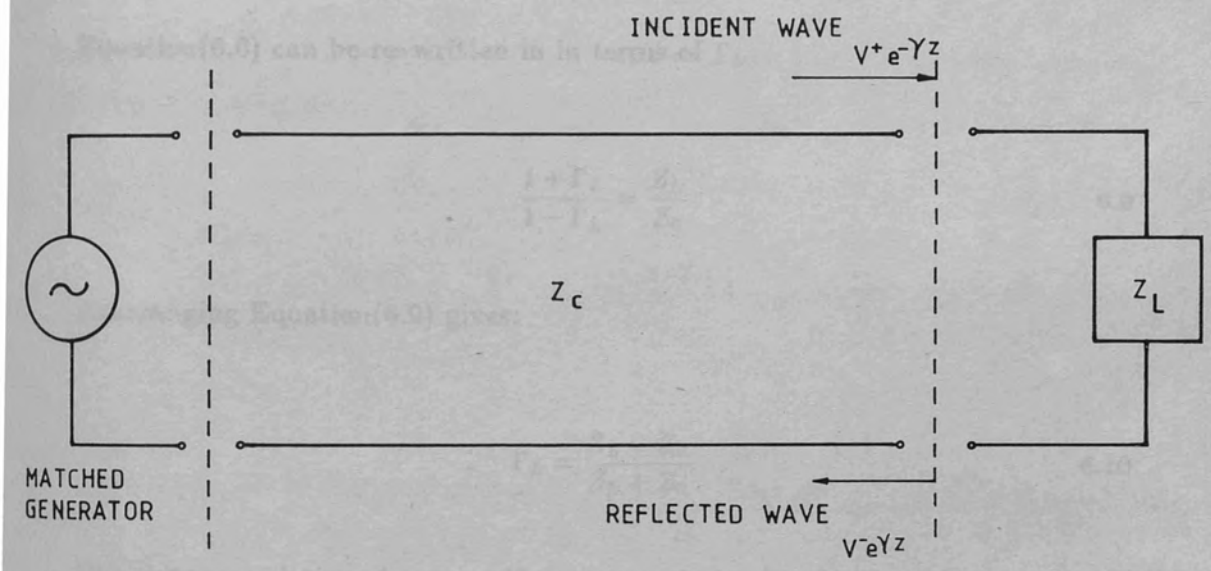

Figure (6.1) Reflection on a transmission line due to an arbitrary load Z_L

$$V^+ - V^- = \frac{Z_0}{Z_L} \tag{6.6}$$

Dividing equation(6.1) by equation(6.6) gives:

$$\frac{V^+ + V^-}{V^+ - V^-} = \frac{Z_L}{Z_0} \tag{6.7}$$

The voltage reflection coefficient at the load is defined by:

$$\Gamma_L = \frac{V^-}{V^+} \tag{6.8}$$

Equation(6.6) can be re–written in in terms of Γ_L:

$$\frac{1 + \Gamma_L}{1 - \Gamma_L} = \frac{Z_L}{Z_0} \tag{6.9}$$

Rearranging Equation(6.9) gives:

$$\Gamma_L = \frac{Z_L - Z_0}{Z_L + Z_0} \tag{6.10}$$

The voltage variation along a uniform transmission line can be written in terms of the voltage reflection coefficient at the load terminals, i.e.:

$$\frac{V}{V^+} = \exp(-\gamma z) + \Gamma_L \exp(\gamma z) \tag{6.11}$$

Where:

$$\gamma = \alpha + j\beta$$

$$= \textit{the propagation constant}$$

$$\alpha = \textit{loss in Nepers } m^{-1}$$

$$\beta = \frac{2\pi}{\lambda_g}$$

In general the voltage reflection coefficient will be complex, and it can be conveniantly expressed as:

$$\Gamma_L = \rho \exp(j\phi_L)$$

Where:

$$\rho = |\Gamma_L|$$

$$\phi_L = \arg(\Gamma_L)$$

$$= \textit{phase change on reflection}$$

Substituting $l = -z$ in equation(6.11), where l is the positive distance towards the generator, gives:

$$\frac{V}{V^+} = \exp(\gamma l)\left(1 + \rho \exp(\phi_L) \exp(-2\gamma l)\right)$$

$$= \exp(\alpha l) \exp(j\beta l)\left(1 + \rho \exp(-2\alpha l) \exp j(\phi_L - 2\beta l)\right) \qquad 6.12$$

The magnitude of the voltage standing wave is given by:

$$\left|\frac{V}{V^+}\right| = \exp(\alpha l)\left|1 + \rho \exp(-2\alpha l) \exp j(\phi_L - 2\beta l)\right|$$

$$= \exp(\alpha l)\left[(1 + \rho \exp(-2\alpha l))^2 - 4\rho \exp(-2\alpha l) \sin^2(\beta l - \frac{\phi_L}{2})\right]^{\frac{1}{2}} \qquad 6.13$$

In the case when the line loss tends to zero, then:

$$\left|\frac{V}{V^+}\right| = \left[(1 + \rho)^2 - 4\rho \sin^2(\beta l - \frac{\phi_L}{2})\right]^{\frac{1}{2}} \qquad 6.14$$

Figure (6.2) illustrates the form of the voltage standing wave in a lossless transmission line when $\Gamma_L = 1\angle 0°$, $0.1\angle 0°$, and $0.01\angle 0°$. In this case we find the

voltage standing wave oscillates between values $(1+\rho)$ and $1-\rho)$ when $\beta l = n\pi$ or $(n+1/2)\pi$ respectively. Figure (6.3) illustrates the the voltage standing wave when a load with $\Gamma_L = 1\angle 0°$ is connected to a lossy transmission line with a line loss of α = 1,0.1, and 0.01 Nepers/guide wavelength. The voltage standing wave now oscillates about the value $\exp(\alpha l)$, which is simply the envelope of the incident wave. The amplitude of the oscillation decreases with distance away from the load, and the rate of decay increases with increasing line attenuation.

The phase shift on reflection from a complex load corresponds to a phase lead when ϕ_L is positive and is given by:

$$\phi_L = 2\beta l_p \qquad 6.15$$

Where:

$$l_p = \textit{the position of first maximum relative to the load}$$

An ideal transmission line is characterized by zero attenuation, and the ratio V_{max}/V_{min} is constant along the length of the transmission line. This quantity is called the voltage standing wave ratio, and is given by the expression:

$$S = \frac{1+\rho}{1-\rho} \qquad 6.16$$

When there is significant transmission line attenuation, the standing wave ratio is given by:

$$S(l) = \frac{1+\rho\exp(-2\alpha l)}{1-\rho\exp(-2\alpha(l \pm \lambda_g/4))} \qquad 6.17$$

From equation(6.17) it is observed that:

(a) the VSWR tends to 1 at a large distance from the load

(b) the exact value depends on whether the ratio is taken with respect to preceeding or following minimum

The line loss can be neglected in most practical cases; a line attenuation of $.01\,dB/\lambda_g$ resulting in a 0.5% variation in the factor $\exp(-2\alpha l)$ between adjacent maxima and minima.

6.2 The Principles of VSWR Measurement on Printed Transmission Lines Using the Scanning Network Probe

The voltage reflection coefficient can be determined in terms of its magnitude and phase with equations(6.16) and (6.17) by simple measurements of relative voltage amplitude. The waveguide realization of this measurement technique is the familiar slotted line[6.1] shown in Figure (6.4). The technique employs a small electric field probe inserted through a narrow slot at the centre of the broad wall to measure the relative electric field intensity as a function of position along the waveguide. Provided that the probe coupling remains constant along the measurement path then:

$$detected\ probe\ output\ = K|E|^2 \tag{6.18}$$

The VSWR is then given by:

$$S = \sqrt{\frac{V_{max}}{V_{min}}} \tag{6.19}$$

Where:

$$V_{max} = detected\ output\ at\ a\ maximum$$

$$V_{min} = detected\ output\ at\ a\ minimum$$

The precision slide arrangement in Figure (6.4) ensures that the probe is tracked in a linear fashion, and that the probe penetration into the waveguide is kept constant.

The scanning network probe operates on printed transmission lines in an analagous manner; sampling the electric field close to the top surface of the

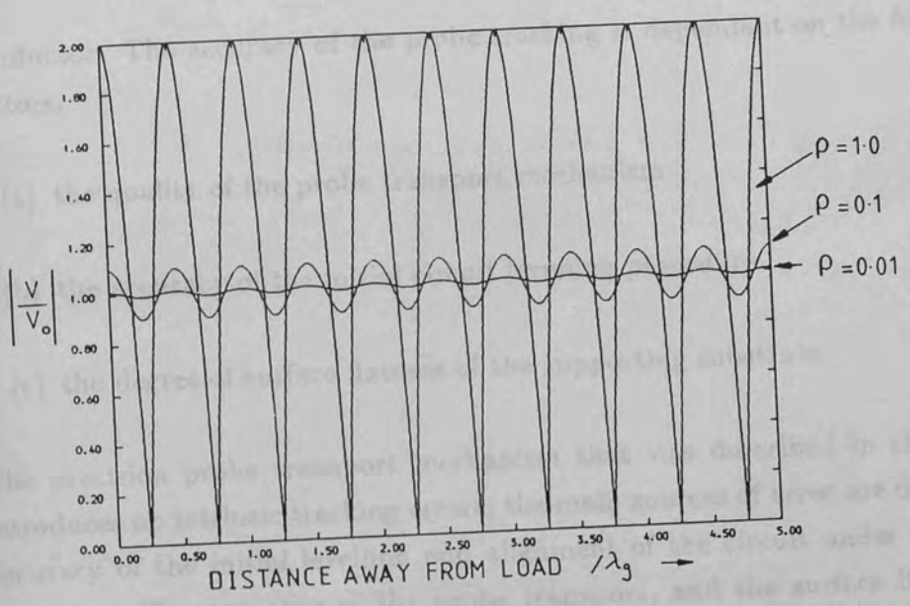

Figure (6.2) Voltage standing waves on a lossless transmission line

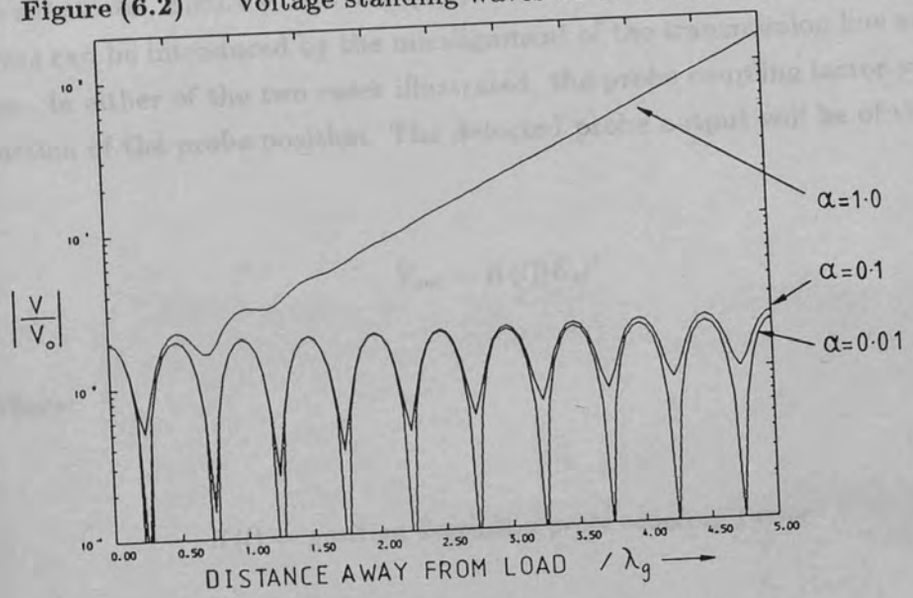

Figure (6.3) Voltage standing waves on a lossy transmission line

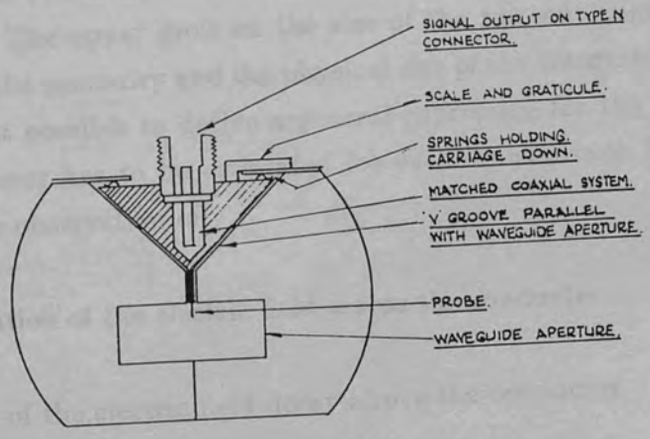

Figure (6.4) Practical realization of a waveguide slotted line

conductor. The accuracy of the probe tracking is dependant on the following factors:

(a) the quality of the probe transport mechanism

(b) the accuracy of the initial circuit levelling procedure

(c) the degree of surface flatness of the supporting substrate

The precision probe transport mechanism that was described in chapter(2) introduces no intrinsic tracking errors, the main sources of error are due to the accuracy of the initial levelling and alignment of the circuit under test with respect to the scan axes of the probe transport, and the surface flatness of the substrate. Figure (6.5)a and (6.5)b illustrate the way in which systematic errors can be introduced by the misalignment of the transmission line and scan axes. In either of the two cases illustrated, the probe coupling factor will be a function of the probe position. The detected probe output will be of the form:

$$V_{out} = K(l)|E_z|^2 \qquad 6.20$$

Where:

$$K(l) = \textit{position dependant probe coupling factor}$$

Provided that the variation of $K(l)$ between adjacent maxima and minima is negligably small, equation(6.19) can still be used to calculate the VSWR with minimal error. The upper limit on the size of the run–out angles α, and β is determined by the geometry and the physical size of the transmission line being tested. It is not possible to derive a general expression for the run–out error, therefore the error has to be estimated for each transmission line under test based upon the observation of:

(a) the variation of the electric field across the conductor

(b) the rate of the electric field decay above the conductor

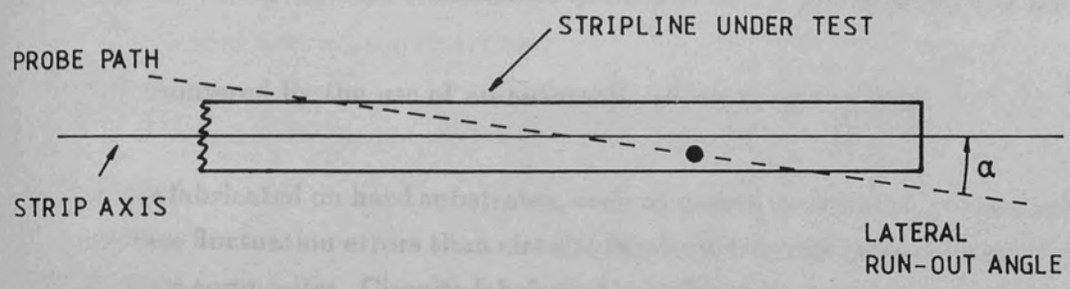

Figure (6.5)a An example of lateral run–out error

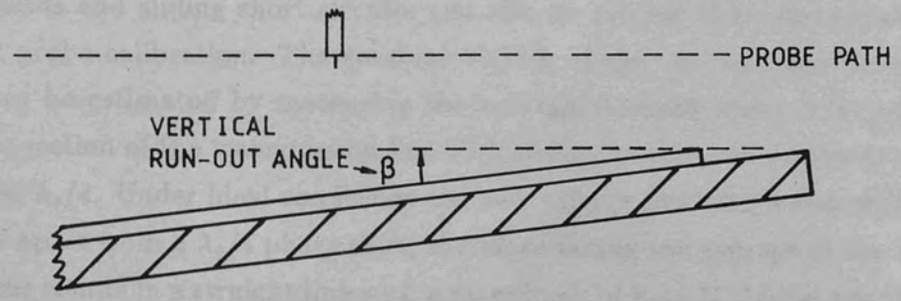

Figure (6.5)b An example of vertical run–out error

(c) the absolute accuracy that can be achieved in the initial levelling procedure

Surface imperfections, such as those caused by poor substrate bonding or mechanical damage, will cause random fluctuations in the probe to substrate separation. The probe output is a sensitive function of height, (due to the rapid decay of the electric field and the proximity effect) therefore significant measurement errors may be incurred. This source of error can be either:

(a) avoided by the use of substrate materials with a precision surface finish

(b) countered by the use of an automatic probe height control

Circuits fabricated on hard substrates, such as quartz or alumina, are less prone to surface fluctuation errors than circuits fabricated on soft substrates such ptfe glass fibre composites. Circuits fabricated on soft substrates have to be soldered to a flat brass backplane using a precision solder press. Surface flatness of the order of 0.0001" has been achieved over a $50\,mm \times 50\,mm$ substrate area. The test circuits used throughout this investigation were all fabricated to a high surface flatness, it was considered unnecessary to incorporate an automatic height control system into the scanning network probe measurement system at this stage.

In addition to the previously described sources of error due to the geometrical misalignment of the scan and transmission line axes, measurement errors caused by the perturbation of the circuit under test by the probe must also be considered. Techniques used for the calibration of network analysers involving sliding loads and sliding short circuits can also be employed for the scanning network probe calibration. The residual VSWR of the the scanning network probe can be estimated by measuring the voltage standing wave obtained in the same section of the transmission line with sliding load in two positions separated by $\lambda_g/4$. Under ideal conditions the two voltage standing waves will be identical apart from a $\lambda_g/4$ phase shift, therefore taking the average of the two waveforms results in a straight line with a magnitude of $V_{max}/2$. In the practical case, there will be a small residual VSWR due to reflections originating from the probe coupling to the circuit under test. The voltage standing wave due to the probe remains unaffected by the shift in the load position, therefore the residual voltage standing wave remaining after the averaging operation is an indication of the VSWR due to the probe.

Treating the probe as a normalized shunt admittance, the flow diagram representation of the probe and transmission line under test (assuming that the source is matched to the transmission line input) is shown in Figure (6.6)a. The reflection coefficient of the probe Γ_p is given by:

$$\Gamma_p = \frac{-\hat{Y}_p}{(2+\hat{Y}_p)} \tag{6.21}$$

Figures(6.6)b and (6.6)c show the first stages in flow graph reduction to obtain the forward and reflected waves due to the probe. On further reduction it can be shown that the voltage standing wave V is given by:

$$\begin{aligned} V =& V_{inc} + V_{ref} \\ =& \frac{(1+\Gamma_p)(1+\Gamma_L \exp(-2j\phi))}{1-\Gamma_p\Gamma_L \exp(-2j\phi)} \end{aligned} \tag{6.22}$$

When the probe is matched, then $\hat{Y}_p$ is pure real, and Γ_p is given by $-\rho$, where ρ is positive and real. Under these conditions the positions of the maxima and minima in the voltage standing wave $|V|$ remain unchanged from the ideal zero loading case when $Y_p \rightarrow 0$. The VSWR measured under these conditions will be lower than the true value by an amount $1/S'$, where:

$$S' = \frac{1+\rho|\Gamma_L|}{1-\rho|\Gamma_L|} \tag{6.23}$$

When the probe acts a pure imaginary shunt admittance then the maximum amplitude of the voltage standing wave remains unchanged, but the position of the maxima relative to the mid point between the voltage minima by an amount δ given by:[6.2]

$$\delta = \arcsin\left\{ \frac{2|\hat{Y}_p||\Gamma_L|}{\left\{4+|\hat{Y}_p|^2\left[1+|\Gamma_L|^2\right]^2\right\}^{\frac{1}{2}}} \right\} \tag{6.24}$$

When the probe appears capacitive, then the maxima shifts in a direction towards the load. The distortion of the voltage standing wave by a finite probe shunt admittance is illustrated in Figure (6.7).

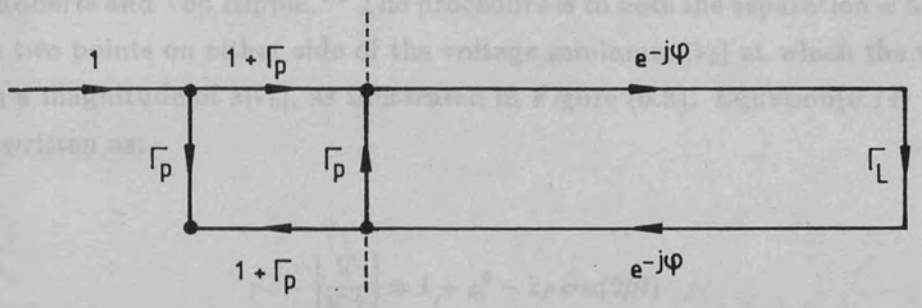

Figure (6.6)a Flow graph of complete circuit

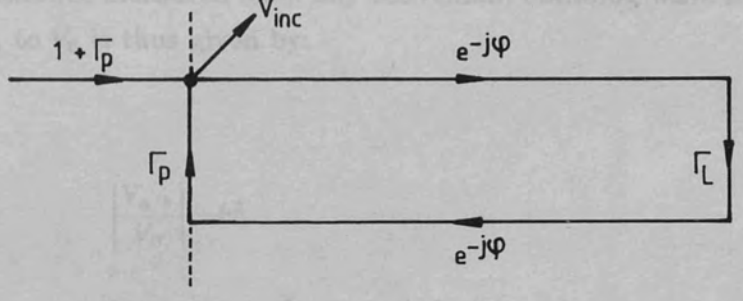

Figure (6.6)b Flow graph reduced to find incident voltage

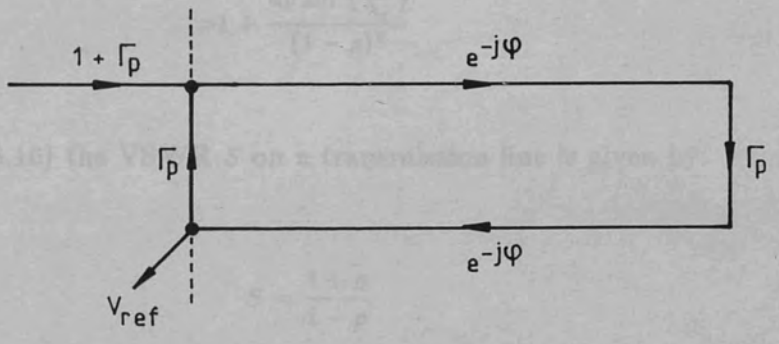

Figure (6.6)c Flow graph reduced to find reflected voltage

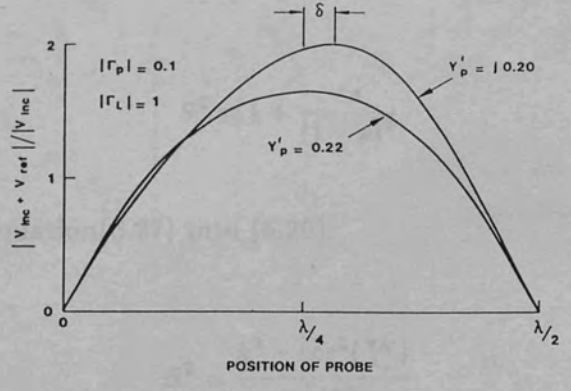

Figure (6.7) The distortion of a voltage maximum produced by capacitive probe loading

The errors caused by probe loading effects and detector non–linearities when measuring high VSWR ratios can be minimized by employing the method of Roberts and Von Hipple.[6.3] The procedure is to note the separation w between the two points on either side of the voltage minimum $|V_0|$ at which the voltage has a magnitude of $k|V_0|$, as illustrated in Figure (6.8). Equation(6.14) can be re–written as:

$$\left|\frac{V}{V^+}\right| = 1 + \rho^2 - 2\rho\cos(2\beta l) \qquad 6.25$$

Where l is the distance measured from any conveniant standing wave minima. The ratio of $V_{a/b}$ to V_0 is thus given by:

$$\left|\frac{V_{a/b}}{V_0}\right| = k^2$$

$$= \frac{1 + \rho^2 - 2\rho\cos(2\beta w/2)}{(1-\rho)^2}$$

$$= 1 + \frac{4\rho\sin^2(\frac{\pi w}{\lambda_g})}{(1-\rho)^2} \qquad 6.26$$

From equation(6.16) the VSWR S on a transmission line is given by:

$$S = \frac{1+\rho}{1-\rho}$$

From which:

$$S^2 = 1 + \frac{4\rho}{(1-\rho)^2} \qquad 6.27$$

On substituting equation(6.27) into (6.26):

$$S^2 = \frac{k^2 - \cos^2(\frac{\pi w}{\lambda_g})}{\sin^2(\frac{\pi w}{\lambda_g})} \qquad 6.28$$

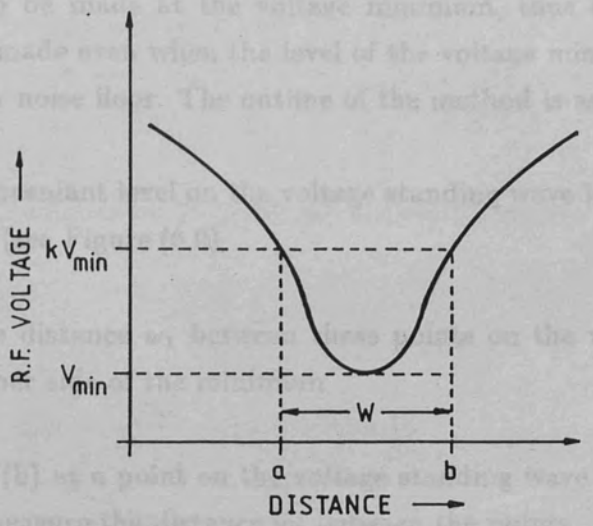

Figure (6.8) Voltage standing wave pattern near a voltage minimum

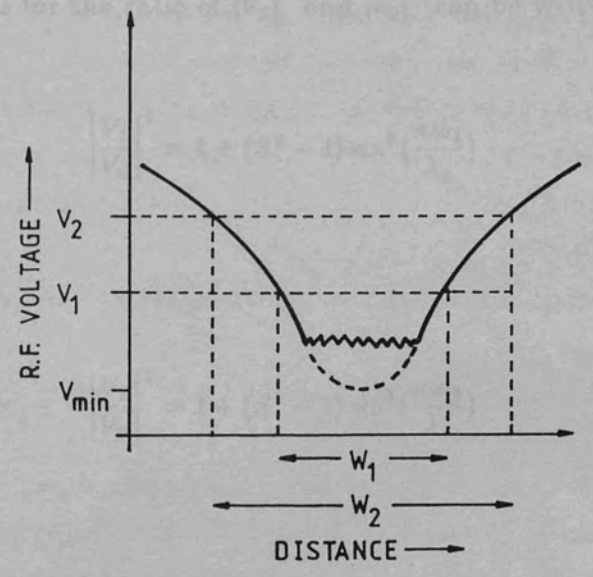

Figure (6.9) Voltage standing wave pattern near a voltage minimum when V_{min} is below the detector noise floor

This method requires the accurate determination of V_0 in order that k can be accurately established. Problems arise when the VSWR is very large, or the incident power is very low, because the level of $|V_0|$can approach and in some circumstances disappear below, the detector noise floor. When this occurs large errors are introduced into the measurement due to the uncertainty of the voltage minimum level. The method proposed by Owens[6.4] does not require a measurement to be made at the voltage minimum, thus enabling VSWR measurements to made even when the level of the voltage minimum has fallen below the detector noise floor. The outline of the method is as follows:

(a) choose a conveniant level on the voltage standing wave V_1 just above the noise floor. (see Figure (6.9)

(b) measure the distance w_1 between these points on the voltage standing wave on either side of the minimum

(c) repeat step (b) at a point on the voltage standing wave such that $|V_2| = c|V_1|$, and measure the distance w_2 between the points

Rearranging equation(6.28) gives:

$$k^2 = (S^2 - 1)\sin(\frac{\pi w}{\lambda_g}) + 1 \qquad 6.29$$

Similar expressions for the ratio of $|V_1|^2$ and $|V_2|^2$ can be written:

$$\left|\frac{V_1}{V_0}\right|^2 = 1 + (S^2 - 1)\sin^2(\frac{\pi w_1}{\lambda_g}) \qquad 6.30a$$

and:

$$\left|\frac{V_2}{V_0}\right|^2 = 1 + (S^2 - 1)\sin^2(\frac{\pi w_2}{\lambda_g}) \qquad 6.30b$$

Since:

$$\left|\frac{V_2}{V_1}\right| = c$$

Dividing equations(6.30)a and (6.30)b and rearranging gives:

$$S^2 = 1 + \frac{(c^2 - 1)}{\sin^2\left(\frac{\pi w_2}{\lambda_g}\right) - c^2 \sin^2\left(\frac{\pi w_1}{\lambda_g}\right)} \qquad 6.31$$

Therefore even when the true minimum is masked by detector noise, the VSWR can be calculated using equation(6.31). An extensive treatment of the errors incurred by the Roberts and Von Hipple method and Owens's method is given in reference(6.4).

6.3 VSWR Measurements on Printed Microstrip Using the Scanning Network Probe

6.3.1 Initial Investigation of Printed Microstrip

For the initial investigation of microstrip transmission lines, a test piece composed of a $40\,mm$ length of $50\,\Omega$ microstrip fabricated on $0.254\,mm$ RT–DUROID 5880 and terminated at both ends with waveguide to microstrip transitions was constructed. The two port test piece was employed so that the VSWR due to different waveguide loads could be measured in both the waveguide and microstrip line, as illustrated in Figure (6.10). When comparing the two measurements, unwanted reflection due to mismatch at the waveguide to microstrip transitions must be taken into account. The effect of the finite transition mismatch is illustrated by the following example. Let us consider measuring the VSWR due to a waveguide component with a reflection coefficient of Γ_L in the waveguide through an imperfect waveguide to microstrip transition with a reflection coefficient Γ_T. The imperfect transition will introduce measurement errors due to:

(a) the mismatch loss due to reflections at the transition plane

(b) the lumped series loss which dissipates power in the transition

The full signal flow graph representing this experimental situation is given in figure (6.11)a. For simplicity the generator is assumed to be matched, and the waveguide and microstrip line are assumed to be lossless. The mismatch loss is represented by a lossless two port error box, and the lumped series loss is included into the error box transmission coefficients as a constant multiplier α.

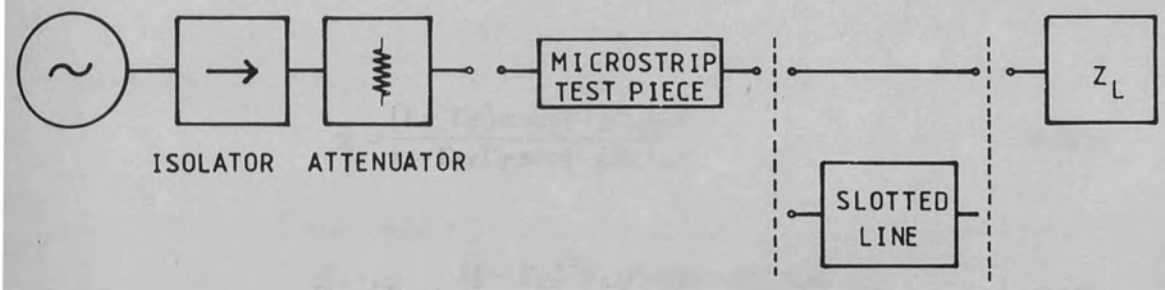

Figure (6.10) Experimental set up to compare VSWR measurements made using a slotted line and the scanning network probe

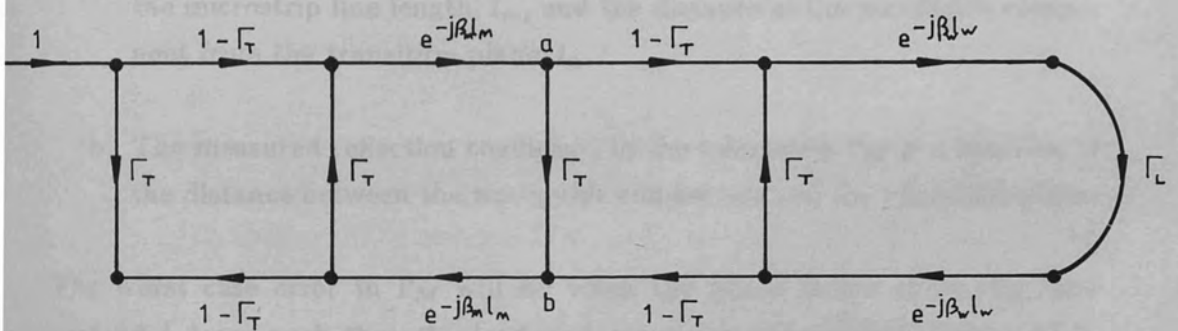

Figure (6.11)a Complete signal flow graph representation of Figure (6.10)

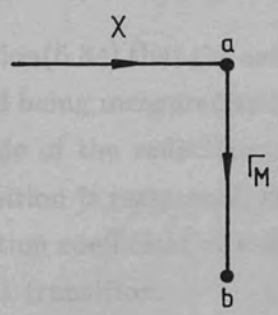

Figure (6.11)b Reduced signal flow graph to find the effective reflection coefficient of the load measured in the microstrip line

The effective reflection coefficient of the waveguide load measured in the microstrip is found by reducing the signal flow graph to a single branch connecting the nodes a and b. After extensive reduction, the flow graph reduces to that shown in Figure (6.11)b where:

$$\chi = \frac{(1-\Gamma_T)\alpha \exp(-j\beta_m l_m)}{1-\Gamma_M \Gamma_T \exp(-j\beta_m l_m)} \qquad 6.32a$$

$$\Gamma_M = \Gamma_T + \frac{(1-\Gamma_T)^2 \Gamma_L \alpha^2 \exp(-j2\beta_w l_w)}{1-\Gamma_T \Gamma_L \exp(-j2\beta_w l_w)} \qquad 6.32b$$

Where: $\Gamma_T = \rho_T \exp(j\phi_T)$ *and* $\Gamma_L = \rho_L \exp(j\phi_L)$

The signal flow graph analysis shows that:

(a) The power incident on the measurement port given by χ is a function of the microstrip line length, l_m, and the distance of the waveguide component from the transition plane, l_w.

(b) The measured reflection coefficient in the microstrip Γ_M is a function of the distance between the waveguide component and the transition plane.

The worst case error in Γ_M will be when the phase terms of Γ_T, Γ_L, and $\exp(j2\beta_w l_w)$ are such that the load and transition mismatches either add in phase or anti-phase. In terms of magnitudes the extreme values of Γ_M will be given by:

$$\left|\Gamma_M\right| = \rho_T + \frac{(1-\rho_T)^2 \rho_L \alpha^2}{1 \pm \rho_T \rho_L} \qquad 6.33$$

It is clear from equation(6.34) that the series loss in the transition acts a resistive pad between the load being measured and the measurement plane, and will thus reduce the magnitude of the reflection coefficient measured in the microstrip line. Since the transition is reciprocal, then the same problem will arise when measuring the reflection coefficient of a microstrip circuit in the waveguide feed through an imperfect transition.

The initial experiments carried out were intended to establish the probe response in the planes orthogonal to the transmission line in order to estimate

the run out errors that were discussed in section(6.2). Using the experimental set up shown in Figure (6.12) the probe response in the transverse and vertical planes at a voltage maximum were measured using the scanning network probe operating in a linear line scan mode. Typical examples of the probe's response in the transverse and vertical planes are shown in Figures(6.13)a and (6.13)b respectively. The procedure used to align the transmission line axis to the scan axis was as follows:

(a) level the substrate with respect to the scan plane to a first approximation using a two axis spirit level

(b) Check that the probe to substrate separation at the extremes of the scan are equal. If this was not the case then the table angle was altered using the micrometer drive on the circuit holder. (see chapter(2) for details) The accuracy to which the probe height can be set is determined by two factors:

   (a) the micrometer control

   (b) the minimum probe to substrate separation that can be reproducibly detected by the operator; in practice it was found that changes of the order of $6\,\mu m$ could be distinguished by observation of the sharp rise in the probe signal when contact is made with the circuit metallization.

(c) with the probe almost touching the surface of the substrate, the scan and transmission line axes are aligned by observing and correcting for any lateral run–out using the rotary table control. By scanning the probe along the edge of the microstrip, it was estimated that the maximum lateral run–out was of the order of one probe tip radius. ($\approx 50\,\mu m$)

The scan length was $40\,mm$, therefore the above positioning errors give rise to run–out angles of $\alpha = 0.07°$ and $0.009°$, where α and β are defined in Figure (6.5). At the measurement frequency of 34.1 GHz the lateral run–out angle α gives rise to a positional error of $2.0\,\mu m$ over one quarter of a guide wavelength. From Figure (6.13) it is apparent that a positional error of this order will have negligable effect on the VSWR measurement, provided that the scan is centred on the strip axis where the probe response is a slow function of

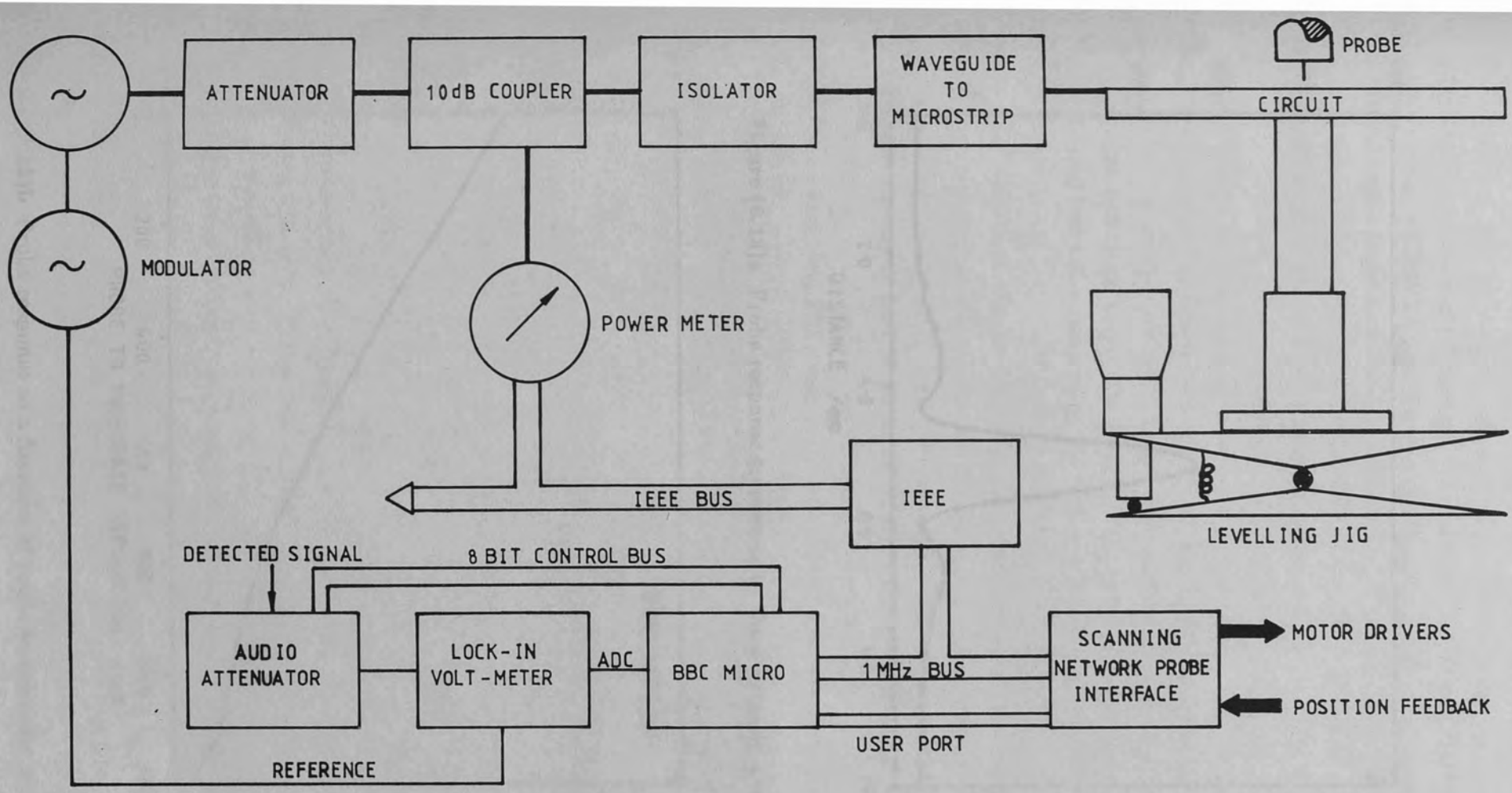

Figure (6.12) Experimental set up for the initial microstrip line investigation

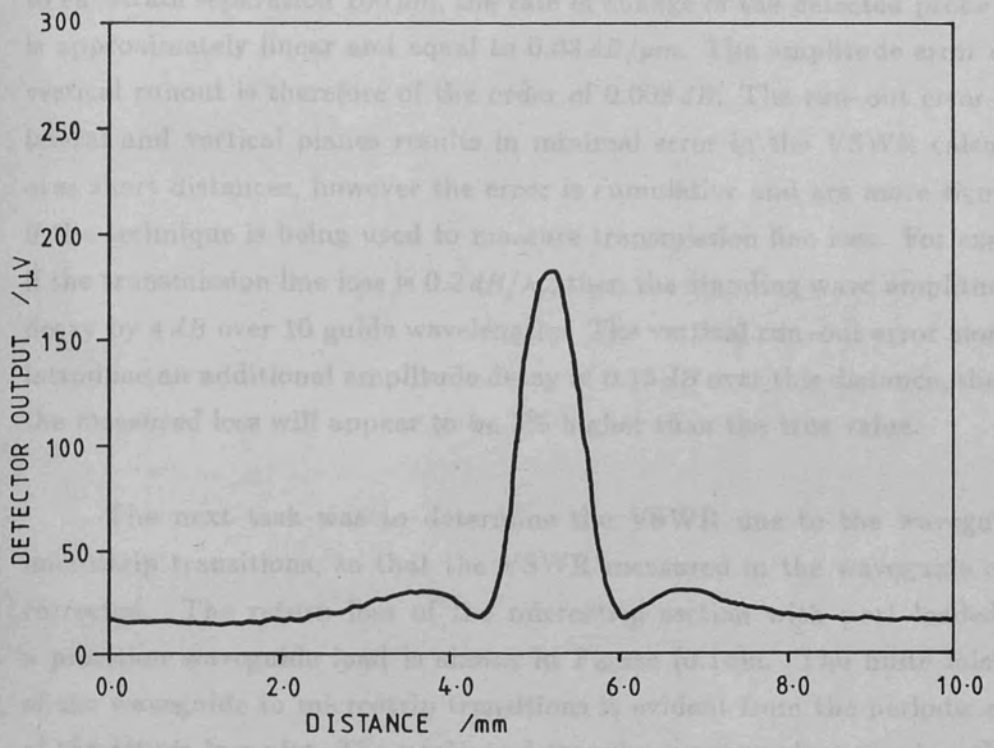

Figure (6.13)a Probe response transverse to the microstrip axis

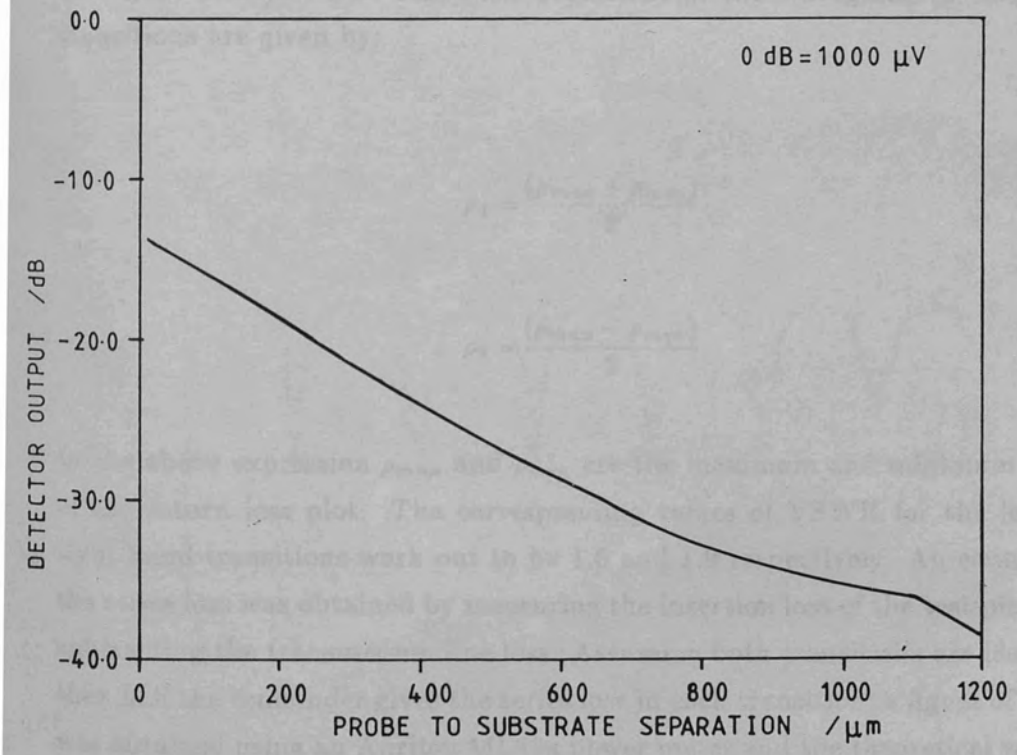

Figure (6.13)b Probe response as a function of probe to substrate separation

lateral position. The vertical run–out angle β gives rise to a change in the probe to substrate separation of $0.25\,\mu m$ over the same distance. At a nominal probe to substrate separation $100\,\mu m$, the rate of change of the detected probe signal is approximately linear and equal to $0.03\,dB/\mu m$. The amplitude error due to vertical runout is therefore of the order of $0.008\,dB$. The run–out error in the lateral and vertical planes results in minimal error in the VSWR calculation over short distances, however the error is cumulative and are more significant if the technique is being used to measure transmission line loss. For example, if the transmission line loss is $0.2\,dB/\lambda_g$, then the standing wave amplitude will decay by $4\,dB$ over 10 guide wavelengths. The vertical run–out error alone will introduce an additional amplitude decay of $0.15\,dB$ over this distance, therefore the measured loss will appear to be 3% higher than the true value.

The next task was to determine the VSWR due to the waveguide to microstrip transitions, so that the VSWR measured in the waveguide can be corrected. The return loss of the microstrip section with port loaded with a precision waveguide load is shown in Figure (6.14)a. The finite mismatch of the waveguide to microstrip transitions is evident from the periodic nature of the return loss plot, The peaks and troughs corresponding to when the two mismatches add in phase or anti–phase. Performing the same measurement with the microstrip test piece reversed gave a slightly different result which is shown in Figure (6.14)b. The reflection coefficient of the waveguide to microstrip transitions are given by:

$$\rho_1 = \frac{(\rho_{max} + \rho_{min})}{2} \qquad 6.34a$$

$$\rho_2 = \frac{(\rho_{max} - \rho_{min})}{2} \qquad 6.34b$$

In the above expression ρ_{max} and ρ_{min} are the maximum and minimum values of the return loss plot. The corresponding values of VSWR for the left and right hand transitions work out to be 1.6 and 1.9 respectively. An estimate of the series loss was obtained by measuring the insertion loss of the test piece and subtracting the transmission line loss. Assuming both transitions are identical, then half the remainder gives the series loss in each transition; a figure of $0.4\,dB$ was obtained using an Anritsu ML83a power meter and the theoretical value of transmission line loss calculated from reference(6.5). This gives a value of $\alpha = 0.91$ and then using equation(6.33) the maximum and minimum values of VSWR

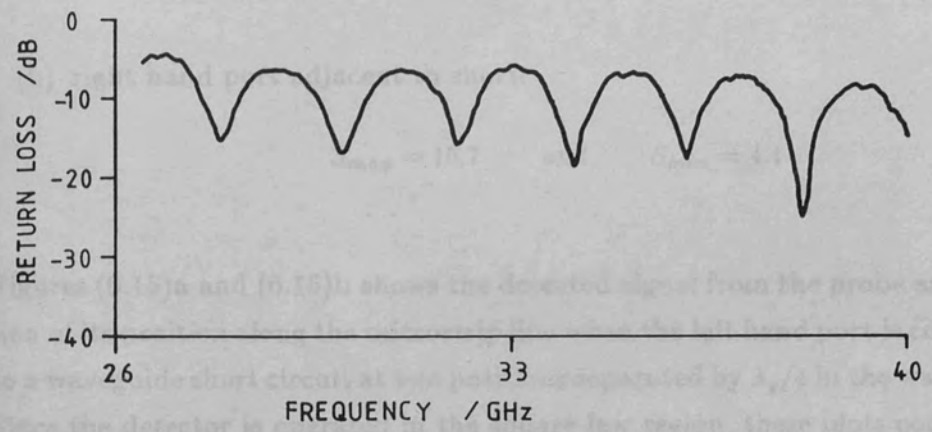

Figure (6.14)a Two port microstrip test piece return loss measured from port (1)

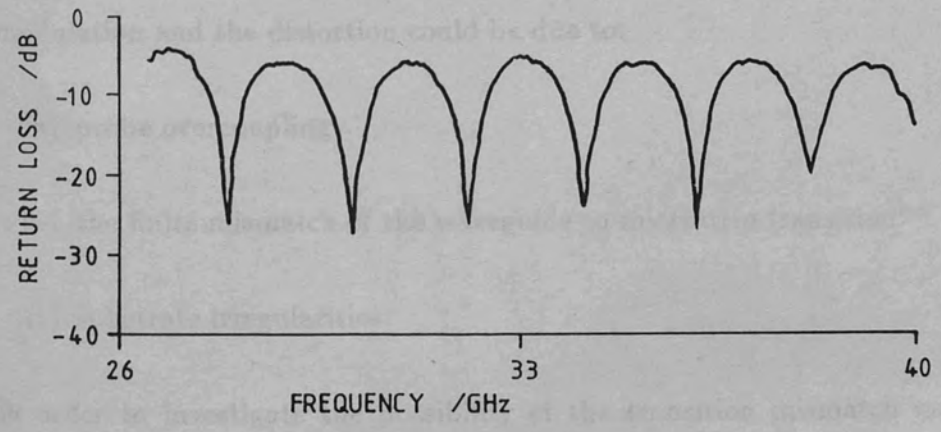

Figure (6.14)b Two port microstrip test piece return loss measured from port (2)

that would be measured in the microstrip when one of the ports is terminated by a short circuit are:

(a) left hand port adjacent to short:

$$S_{max} = 14.4 \qquad and \qquad S_{min} = 4.4$$

(b) right hand port adjacent to short:

$$S_{max} = 15.7 \qquad and \qquad S_{min} = 4.1$$

Figures (6.15)a and (6.15)b shows the detected signal from the probe as a function of its position along the microstrip line when the left hand port is connected to a waveguide short circuit at two positions separated by $\lambda_g/4$ in the waveguide. Since the detector is operated in the square law region, these plots correspond to the power standing wave on the microstrip. A visual inspection of the two plots reveals a noticable distortion of the standing wave maxima, combined with a low frequency amplitude modulation. The amplitude modulation gives rise to a large spread in the measured VSWR. The values of VSWR calculated from Figures (6.15)a and (6.15)b with the aid of equation(6.19) after allowing for the detector and amplifier offset are 7.7±4.4 and 5.4±1.0.

The guide wavelength of the microstrip was calculated from the separation of the adjacent maxima and adjacent minima and was found to be $5.98 \pm 0.10\, mm$ which is in excellent agreement with the theoretical guide wavelength of $5.94\, mm$ calculated using reference(6.5). The cause of the amplitude modulation and the distortion could be due to:

(a) probe overcoupling

(b) the finite mismatch of the waveguide to microstrip transition[6.4]

(c) substrate irregularities

In order to investigate the possibility of the transition mismatch modifying the measured standing wave, the short circuit was replaced by a matched load (VSWR=1.1 in the waveguide) and E–H tuner. Figure (6.16)a shows the measured standing wave on the microstrip when the E and H arms of the tuner are set to zero. In this example the power is incident from left to right.

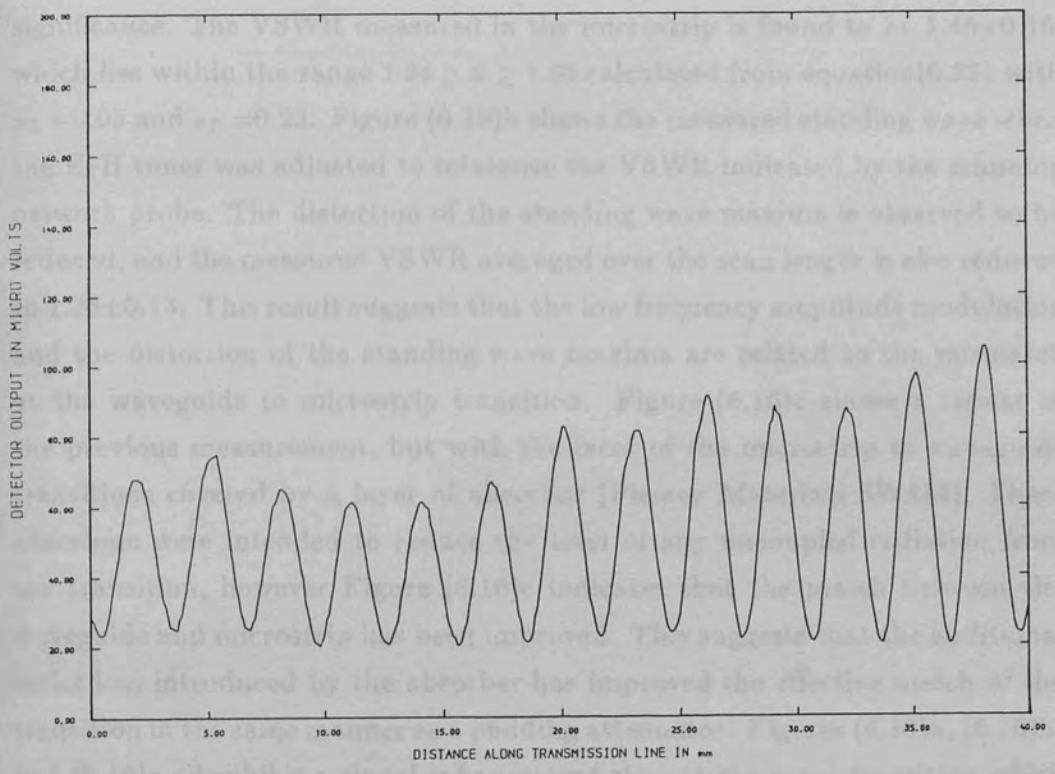

Figure (6.15)a Power standing wave plot measured with waveguide short circuit set to zero

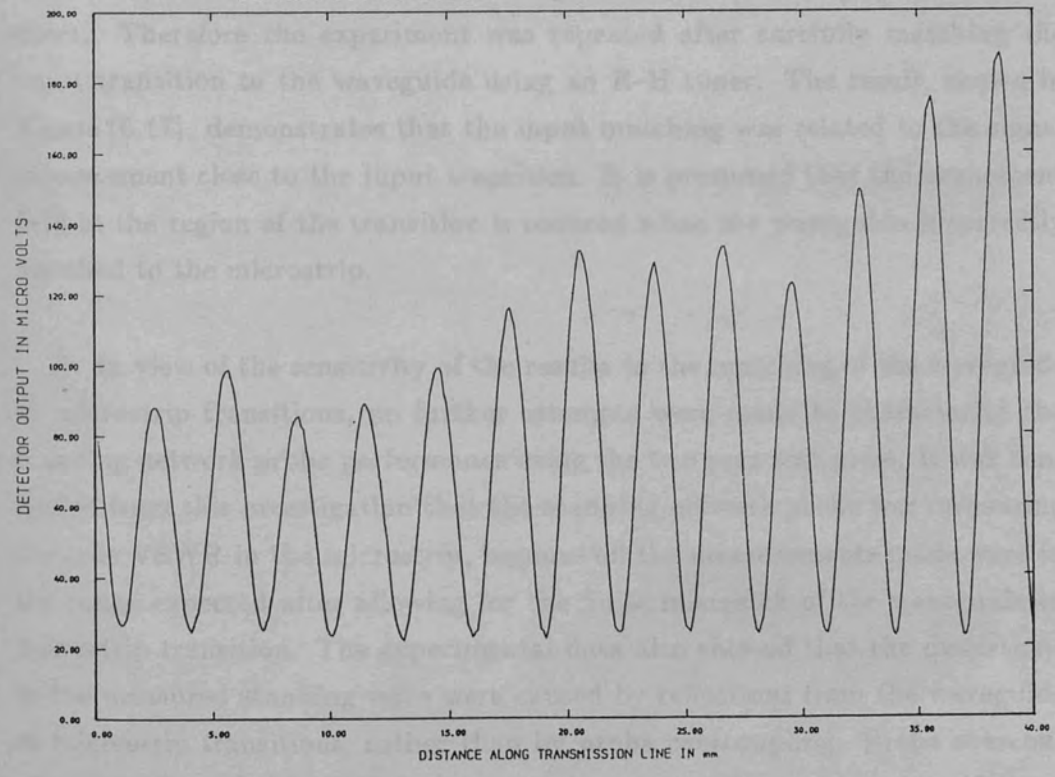

Figure (6.15)b Power standing wave plot measured with waveguide short circuit shifted by $\lambda_g/4$

The standing wave exhibits similar distortions to those found in the earlier short circuit experiments, however the amplitude modulation is now of greater significance. The VSWR measured in the microstrip is found to be 1.48±0.16, which lies within the range $1.34 \geq S \geq 1.60$ calculated from equation(6.33) with ρ_L =0.05 and ρ_T =0.23. Figure (6.16)b shows the measured standing wave when the E–H tuner was adjusted to minimize the VSWR indicated by the scanning network probe. The distortion of the standing wave maxima is observed to be reduced, and the measured VSWR averaged over the scan length is also reduced to 1.28±0.13. This result suggests that the low frequency amplitude modulation and the distortion of the standing wave maxima are related to the mismatch at the waveguide to microstrip transition. Figure (6.16)c shows a repeat of the previous measurement, but with the faces of the microstrip to waveguide transitions covered by a layer of absorber (Plessey Materials SWAM). These absorbers were intended to reduce the level of any uncoupled radiation from the transition, however Figure (6.16)c indicates that the match between the waveguide and microstrip has been improved. This suggests that the additional series loss introduced by the absorber has improved the effective match of the transition in the same manner as a padding attenuator. Figures (6.16)a, (6.16)b, and (6.16)c all exhibit a signal enhancement close to the input transition which could not be related to any surface imperfection. The mismatch at the input transition, which had hitherto been neglected, could be responsible for this effect. Therefore the experiment was repeated after carefully matching the input transition to the waveguide using an E–H tuner. The result, shown in Figure (6.17), demonstrates that the input matching was related to the signal enhancement close to the input transition. It is presumed that the evanescent field in the region of the transition is reduced when the waveguide is correctly matched to the microstrip.

In view of the sensitivity of the results to the matching of the waveguide to microstrip transitions, no further attempts were made to characterize the scanning network probe performance using the two port test piece. It was concluded from this investigation that the scanning network probe was measuring the true VSWR in the microstrip, because all the measurements made were in the range expected after allowing for the finite mismatch of the waveguide to microstrip transition. The experimental data also showed that the distortions in the measured standing wave were caused by reflections from the waveguide to microstrip transitions, rather than by probe overcoupling. Probe overcoupling would cause the maxima to be asymmetrically disposed between adjacent minima, and since there was no evidence for this it is assumed to be a negligable effect for the range of VSWR encountered during this investigation.

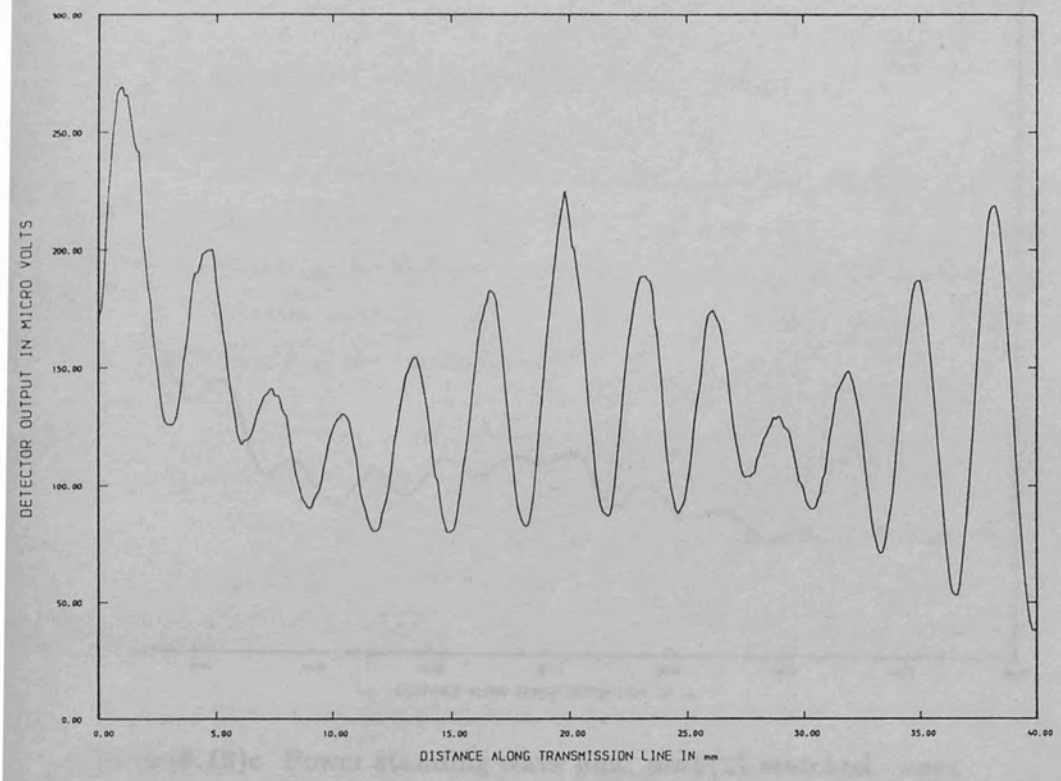

Figure (6.16)a Power standing wave plot, port (2) unmatched, input unmatched

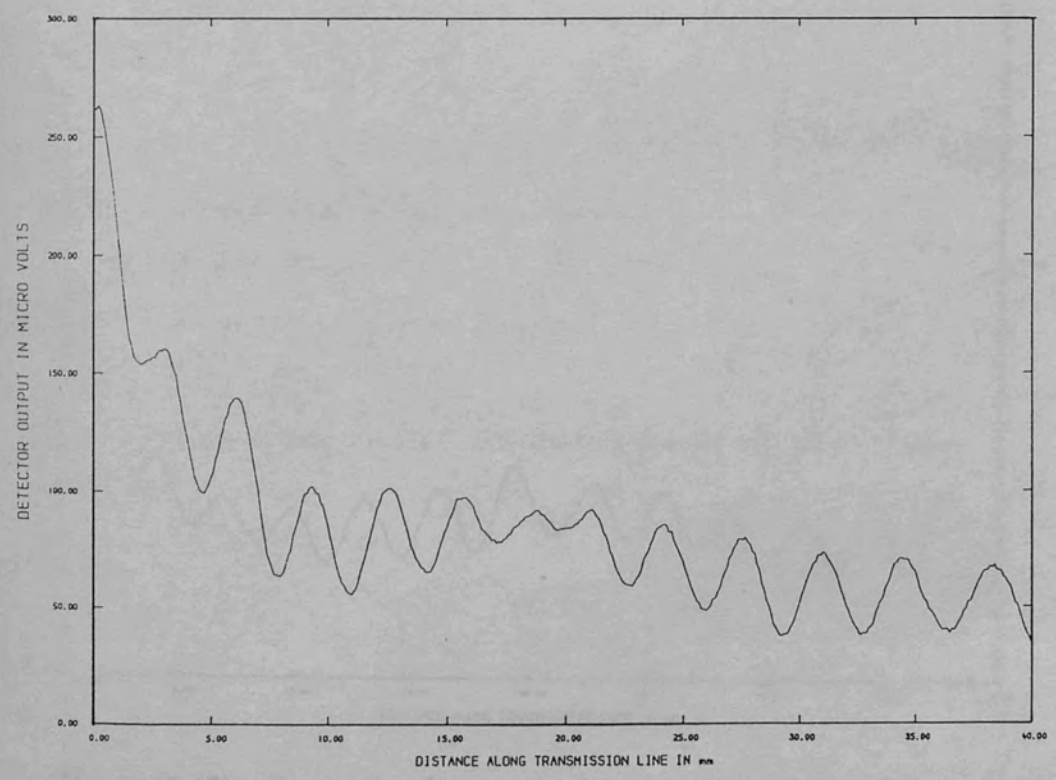

Figure (6.16)b Power standing wave plot, port (2) matched, input unmatched

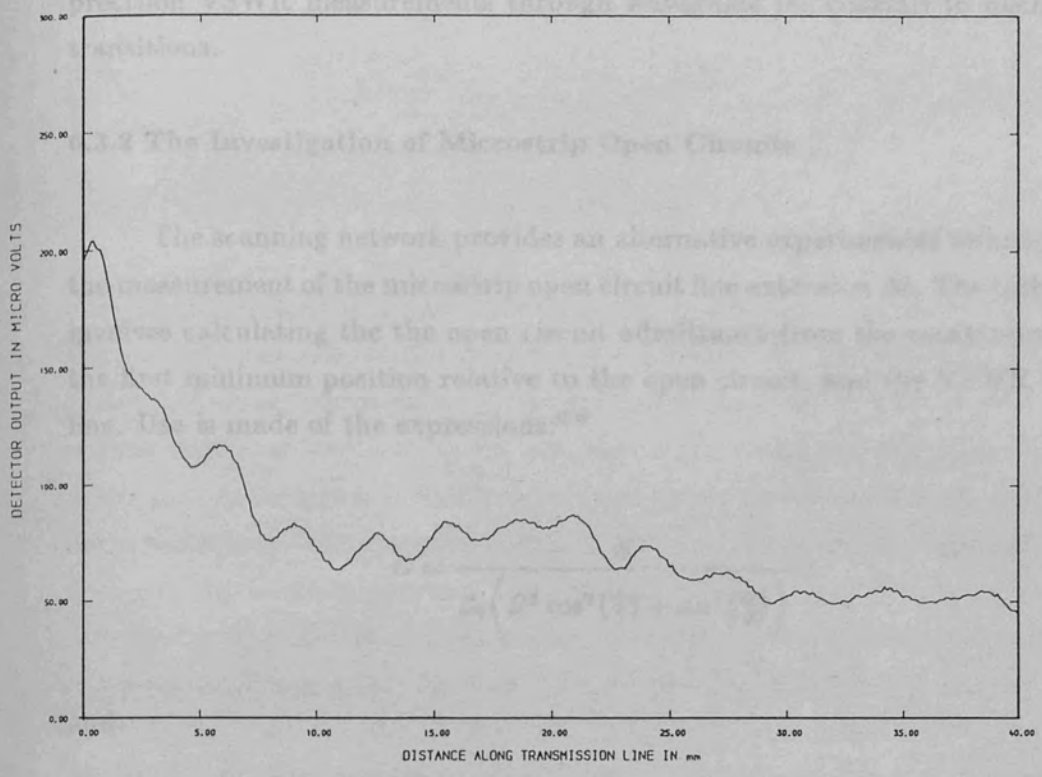

Figure (6.16)c Power standing wave plot, port (2) matched, input unmatched, SWAM covered transitions

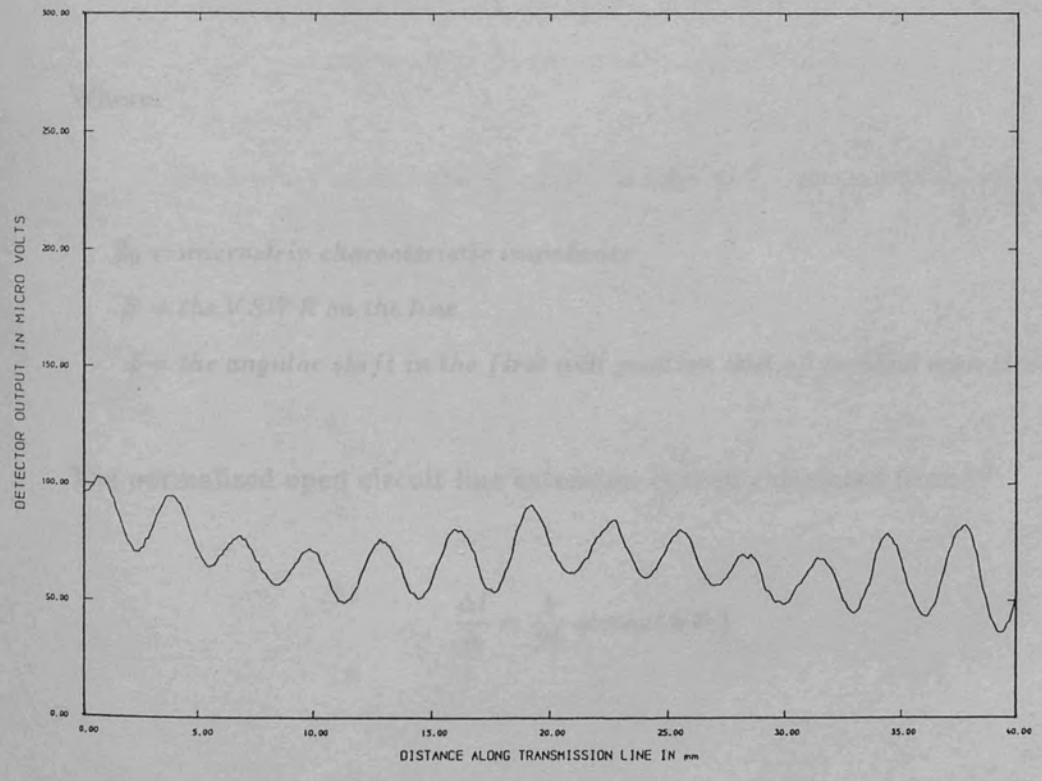

Figure (6.17) Power standing wave plot, port (2) matched, input matched, SWAM covered transitions

The theory and experimental results both highlight the problem of making precision VSWR measurements through waveguide (or coaxial) to microstrip transitions.

6.3.2 The Investigation of Microstrip Open Circuits

The scanning network provides an alternative experimental technique for the measurement of the microstrip open circuit line extension Δl. The technique involves calculating the the open circuit admittance from the measurement of the first minimum position relative to the open circuit, and the VSWR in the line. Use is made of the expressions:[6.6]

$$G = \frac{S}{Z_0\left(S^2\cos^2\left(\frac{\phi}{2}\right) + \sin^2\left(\frac{\phi}{2}\right)\right)} \qquad 6.35a$$

and:

$$B = \frac{(S^2-1)\sin\left(\frac{\phi}{2}\right)\cos\left(\frac{\phi}{2}\right)}{Z_0\left(S^2\cos^2\left(\frac{\phi}{2}\right) + \sin^2\left(\frac{\phi}{2}\right)\right)} \qquad 6.35b$$

Where:

Z_0 = *microstrip characteristic impedance*

S = *the VSWR on the line*

ϕ = *the angular shift in the first null position that of an ideal open circuit*

The normalized open circuit line extension is then calculated from:[6.7]

$$\frac{\Delta l}{h} = \frac{1}{\beta h}\arctan(BZ_0) \qquad 6.36$$

Where:

$$\beta = \frac{2\pi}{\lambda_g}$$

$B = measured\ susceptance\ in\ Siemens$

$h = the\ substrate\ thickness$

This method is similar to the experiments carried out by Ladbrooke[6.8] in which the electric field *beneath* the microstrip was sampled. The scanning network probe technique, which samples the vertical component of electric field *above* the microstrip, is less likely to perturb the circuit under test since the majority of the microwave signal is confined between the bottom surface of the strip and the groundplane. The scanning network probe technique can be employed to investigate any microstrip circuit, whereas the technique described by Ladbrooke is limited to specially fabricated microstrip circuits. Six microstrip open circuit test pieces utilizing 0.254 *mm* thick RT–DUROID 5880 substrates were designed with the aid of the frequency corrected design equations given in reference(6.5). The design data for the range of impedances selected are given in Table(6.1).

TABLE(6.1)

Microstrip Open Circuit Design Data

impedance at 35GHz /Ω	line width /*mm*	aspect ratio w/h
105	0.2	0.79
78	0.4	1.6
50	0.96	3.8
40	1.5	5.9
30	2.6	10.2
22	4.8	18.9

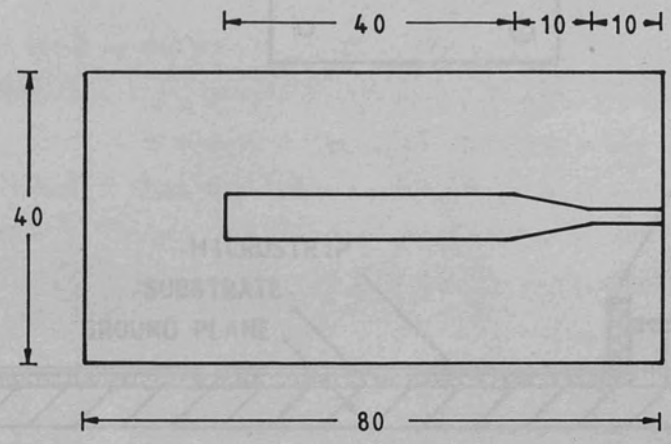

Figure (6.18)a General layout of the microstrip open circuit test pieces

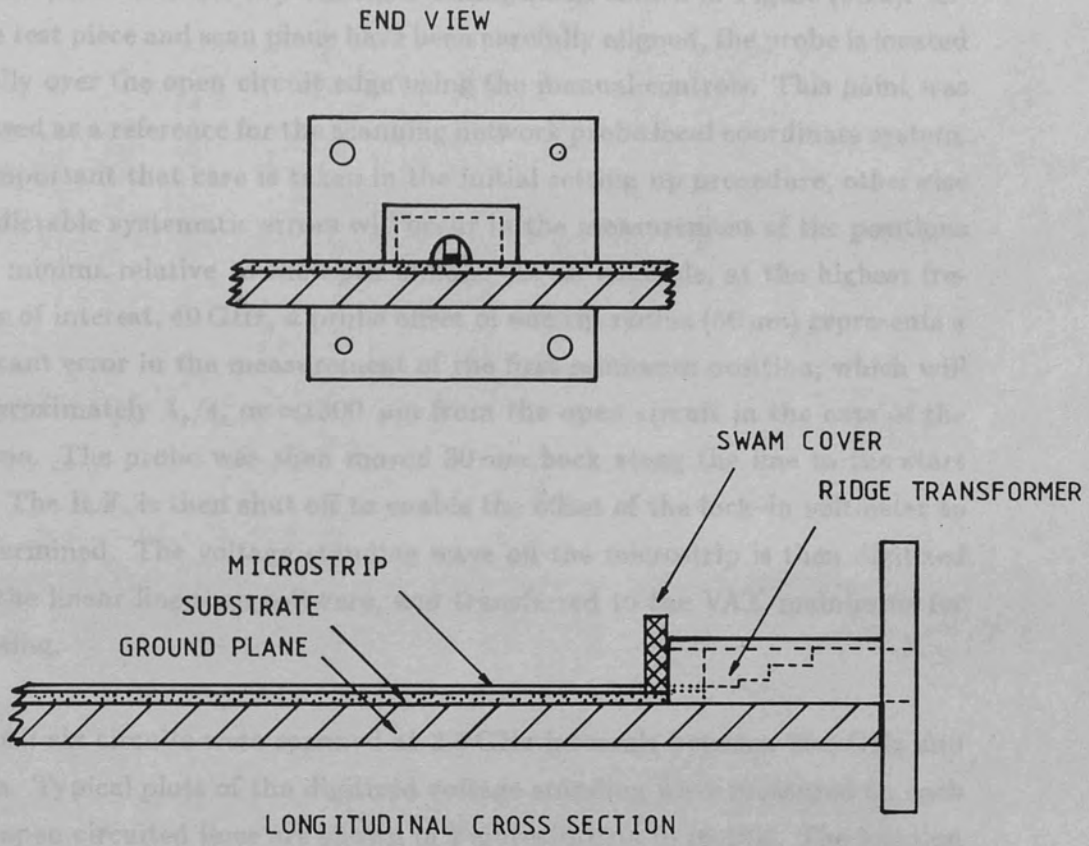

Figure (6.18)b Waveguide to microstrip transition detail

Since it was impracticable to construct a matched waveguide to microstrip transition for each individual line width, the lines were linearly tapered over $10\,mm$ to $50\,\Omega$ so that the existing $50\,\Omega$ waveguide to microstrip transitions could be employed. The general layout of the test circuits is illustrated in Figures (6.18)a and (18)b.

The initial measurements were made using the $0.6\,mm$ diameter nickel sheathed probe and the experimental arrangement shown in Figure (6.12). After the test piece and scan plane have been carefully aligned, the probe is located centrally over the open circuit edge using the manual controls. This point was then used as a reference for the scanning network probe local coordinate system. It is important that care is taken in the initial setting up procedure, otherwise unpredictable systematic errors will occur in the measurement of the positions of the minima relative to the open circuit. As an example, at the highest frequency of interest, 40 GHz, a probe offset of one tip radius ($50\,\mu m$) represents a significant error in the measurement of the first minimum position, which will be approximately $\lambda_g/4$, or $\approx 1300\ \mu m$ from the open circuit in the case of the $30\,\Omega$ line. The probe was then moved $30\,mm$ back along the line to the start point. The R.F. is then shut off to enable the offset of the lock–in voltmeter to be determined. The voltage standing wave on the microstrip is then digitized using the linear line scan software, and transferred to the VAX mainframe for processing.

All six circuits were scanned at 2.5 GHz intervals between 26.5 GHz and 39 GHz. Typical plots of the digitized voltage standing wave measured on each of the open circuited lines are shown in Figures(6.19)a to (6.19)f. The location of the physical open circuit is at $30\,mm$ in each case. The following qualitative observations can be made:

(a) the maxima and minima show a periodic modulation similar to that observed on the two port test piece

(b) the magnitude of the detected signal on the transmission line greatest on the $105\,\Omega$ transmission line, systematically decreasing with decreasing line impedance

(c) the magnitude of the fringe field region beyond the microstrip open circuit increases with decreasing line impedance.

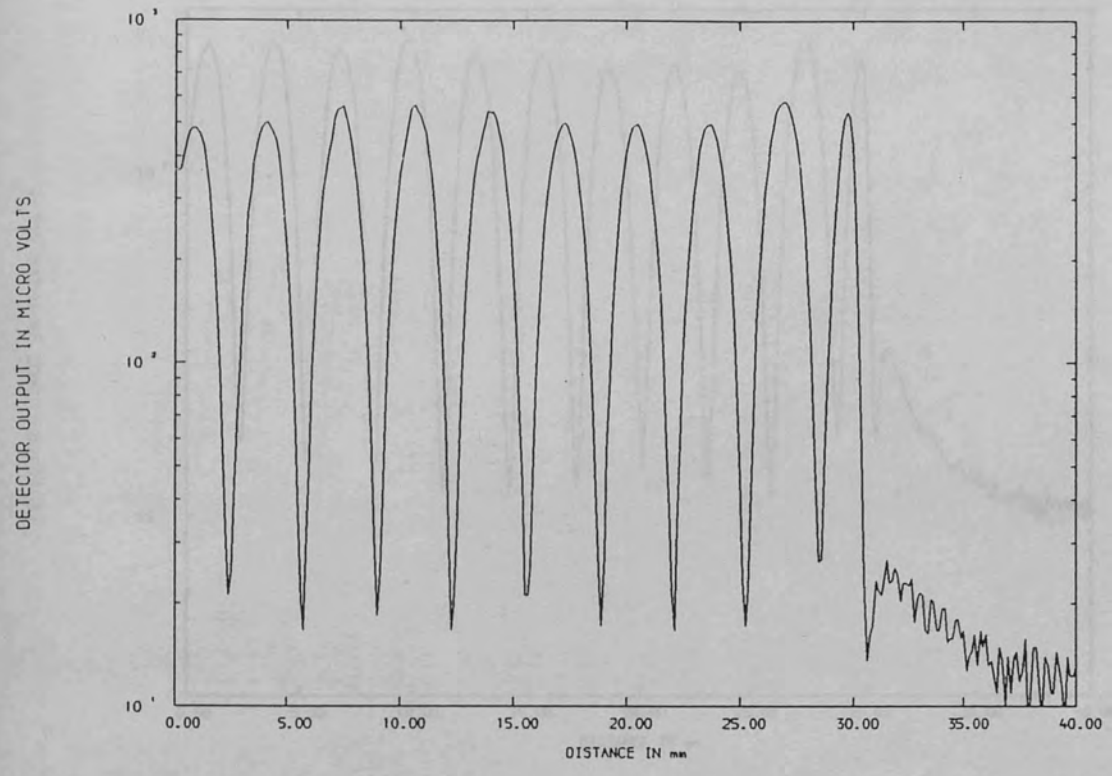

Figure (6.19)a Open circuit microstrip line scan, Z_0=105 Ω, F=36.5 *GHz*

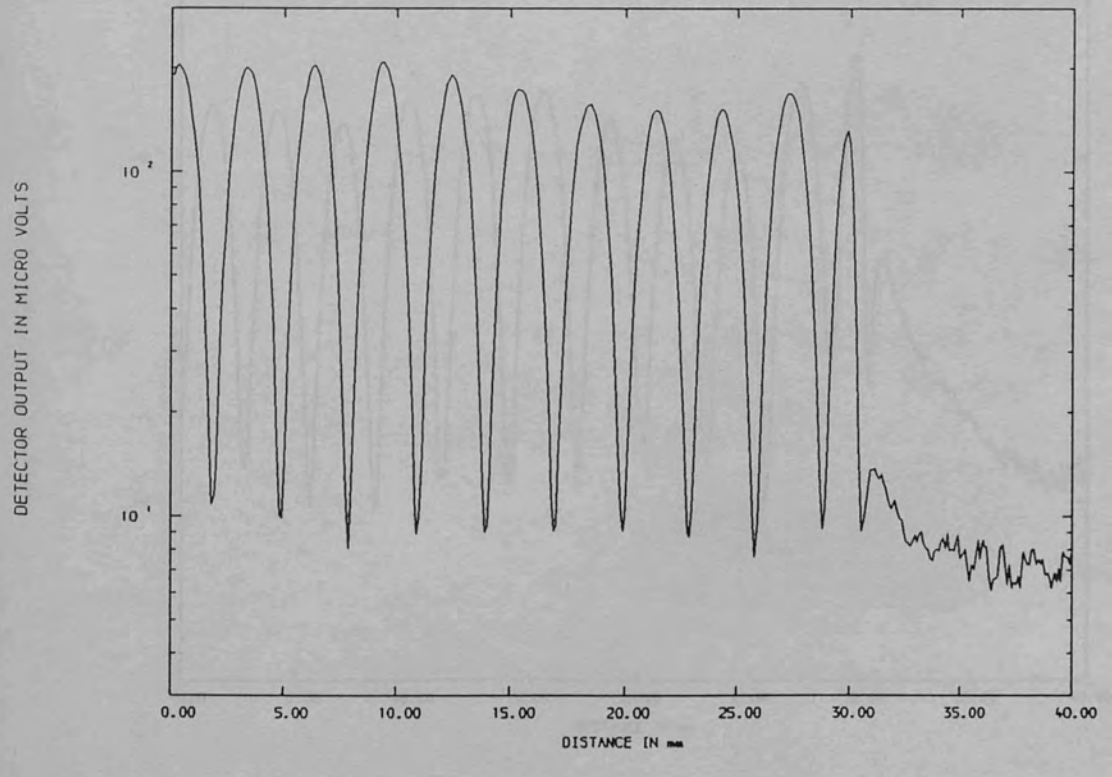

Figure (6.19)b Open circuit microstrip line scan, Z_0=78 Ω, F=36.5 *GHz*

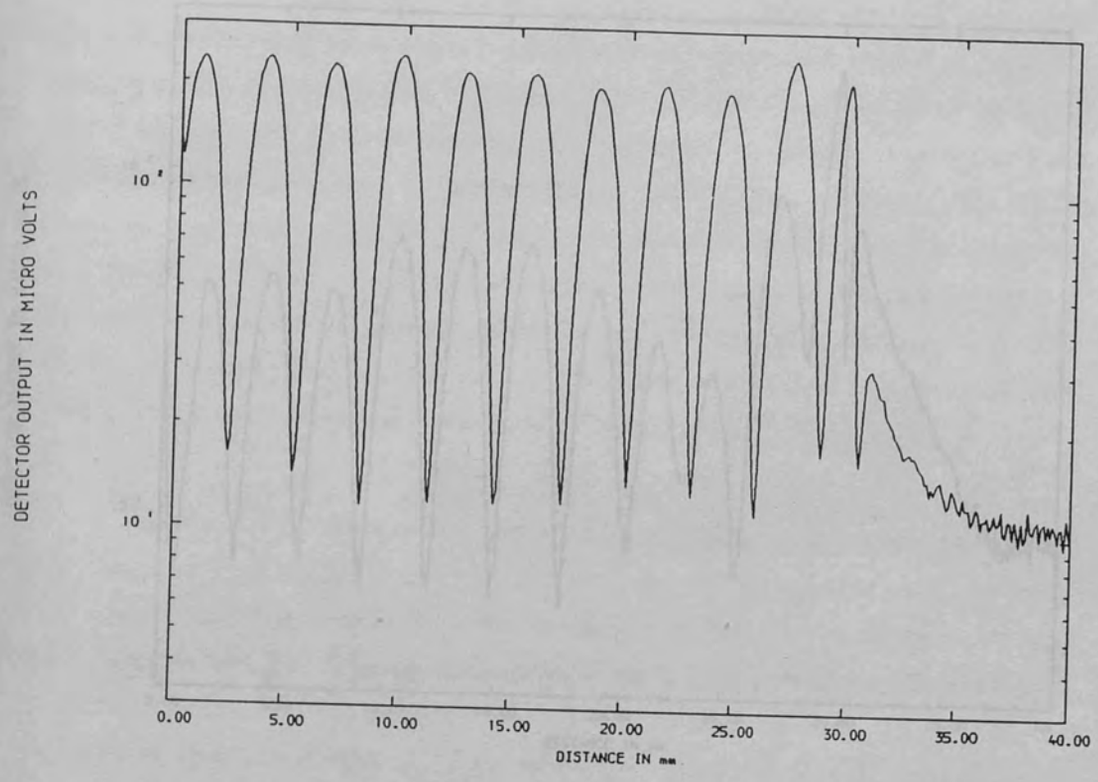

Figure (6.19)c Open circuit microstrip line scan, Z_0=50 Ω, F=36.5 *GHz*

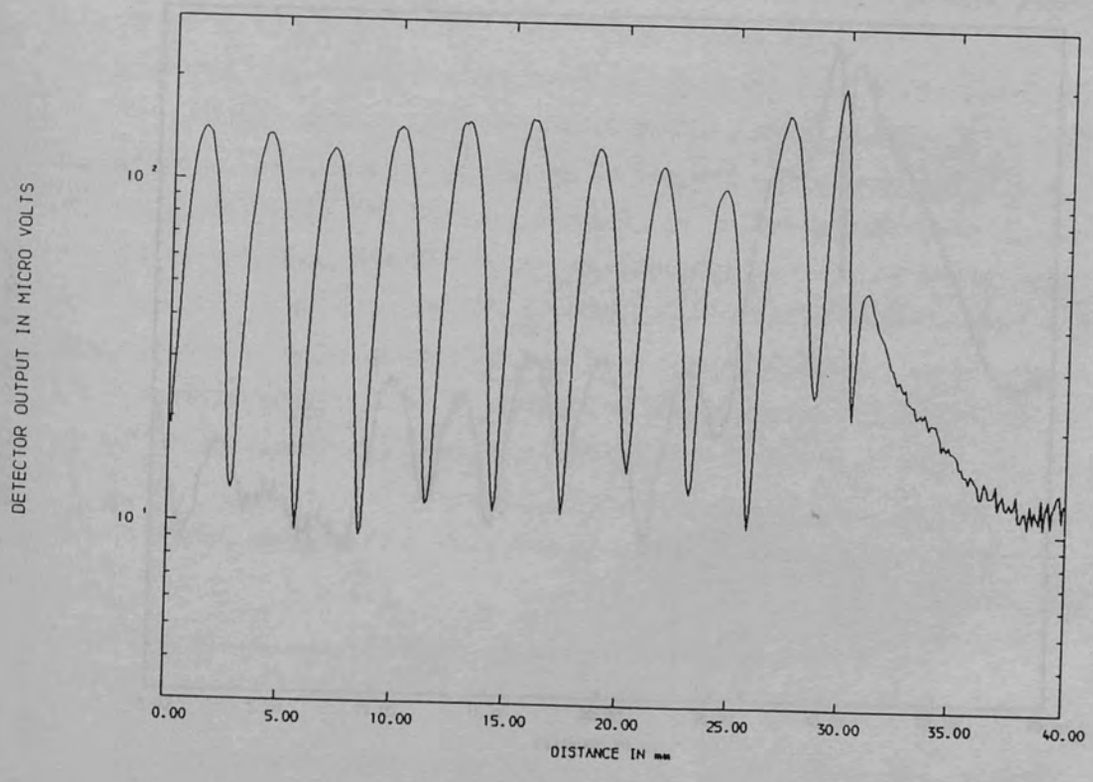

Figure (6.19)d Open circuit microstrip line scan, Z_0=40 Ω, F=36.5 *GHz*

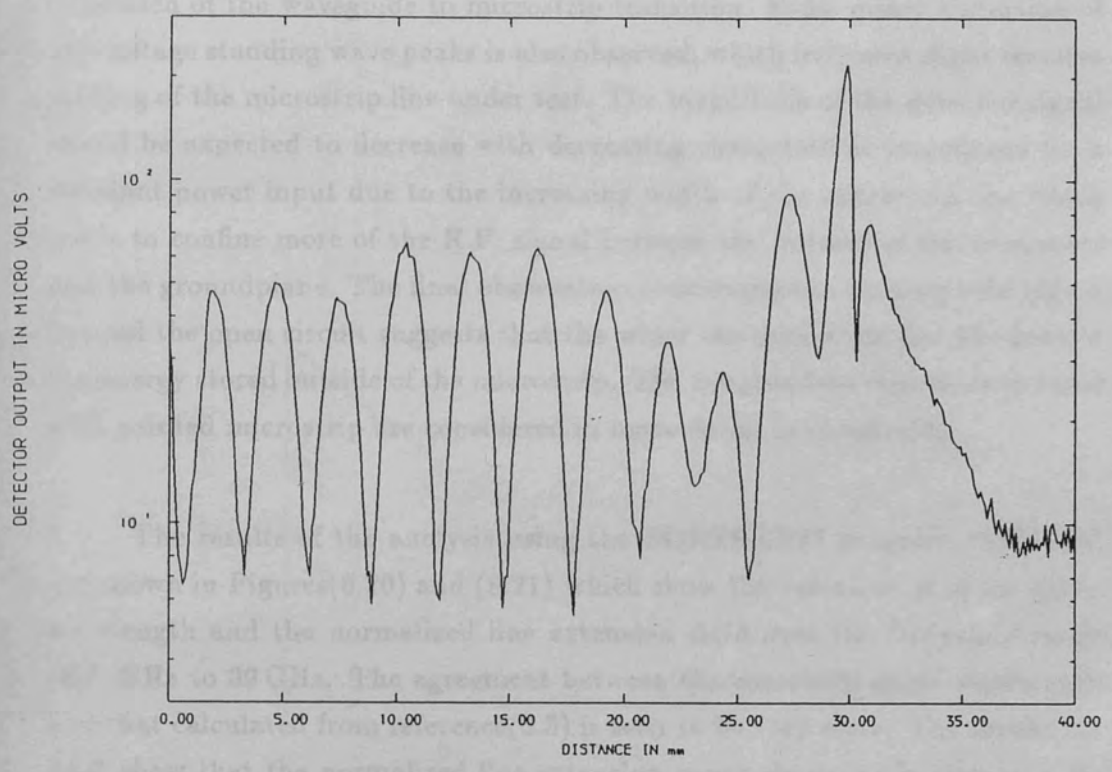

Figure (6.19)e Open circuit microstrip line scan, Z_0=30 Ω, F=36.5 *GHz*

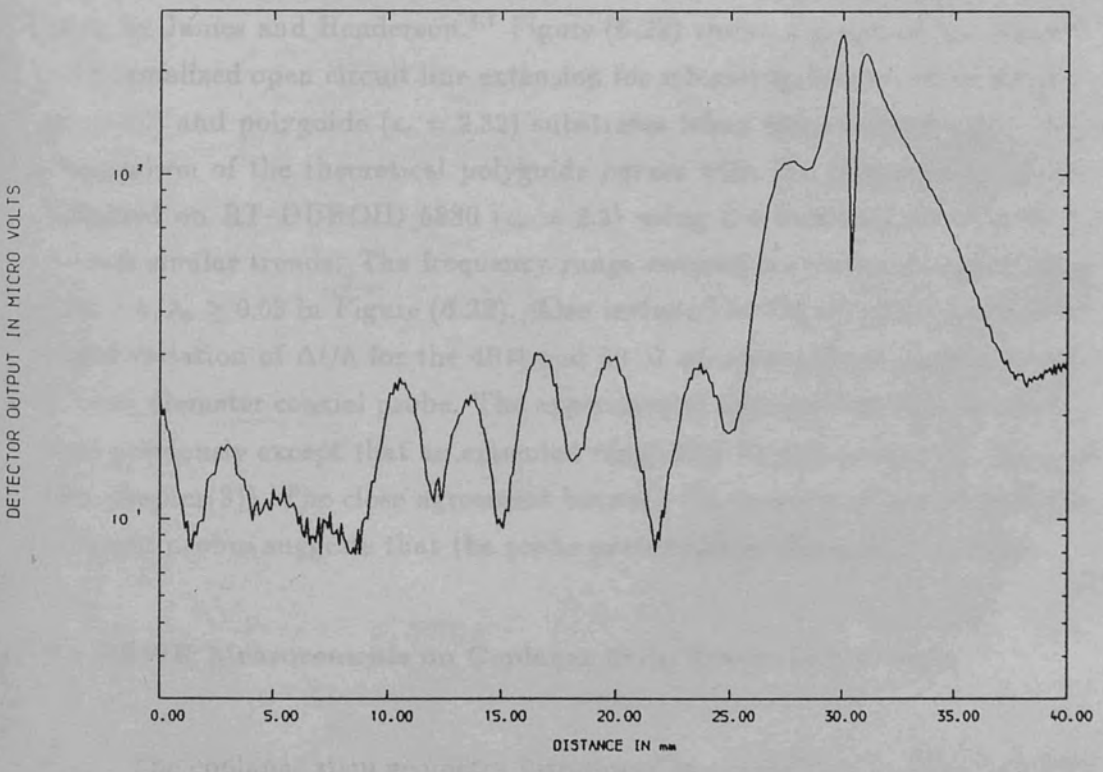

Figure (6.19)f Open circuit microstrip line scan, Z_0=22 Ω, F=36.5 *GHz*

The periodic modulation or "beat effect" is thought to be due to the finite mismatch of the waveguide to microstrip transition. Some minor distortion of the voltage standing wave peaks is also observed, which indicates slight reactive loading of the microstrip line under test. The magnitude of the detected signal would be expected to decrease with decreasing characteristic impedance for a constant power input due to the increasing width of the microstrip line which tends to confine more of the R.F. signal between the bottom of the conductor and the groundplane. The final observation concerning the fringing field region beyond the open circuit suggests that the wider the microstrip line the greater the energy stored outside of the microstrip. The fringing field regions associated with printed microstrip are considered in more detail in chapter(8).

The results of the analysis using the FORTRAN77 program "SWAVE" are shown in Figures(6.20) and (6.21) which show the variation of of the guide wavelength and the normalized line extension $\Delta l/h$ over the frequency range 26.5 GHz to 39 GHz. The agreement between the measured guide wavelength and that calculated from reference(6.5) is seen to be very close. The results for $\Delta l/h$ show that the normalized line extension varies slowly with frequency for the substrate material employed. The results were found to be higher than predicted by the quasi-static expression given in equation(4.4). The only attempt to characterize the high frequency behaviour of microstrip open circuits has been by James and Henderson.[6.7] Figure (6.22) shows a graph of the theoretical normalized open circuit line extension for microstrip fabricated on alumina ($\epsilon_r = 10$) and polyguide ($\epsilon_r = 2.32$) substrates taken from reference(6.7). The comparison of the theoretical polyguide curves with the experimental results obtained on RT–DUROID 5880 ($\epsilon_r = 2.2$) using the scanning network probe reveals similar trends. The frequency range covered is equivalent to the range $0.02 \geq h/\lambda_0 \geq 0.03$ in Figure (6.22). Also included in Figure (6.21) is the measured variation of $\Delta l/h$ for the 40 Ω and 50 Ω microstrip lines using a smaller 0.3 mm diameter coaxial probe. The experimental arrangement was identical to that previously except that an extended range lock–in voltmeter was employed (see chapter(3)). The close agreement between the two sets of data taken with different probes suggests that the probe perturbation effects are negligible.

6.4 VSWR Measurements on Coplanar Strip Transmission Lines

The coplanar strip geometry introduced in chapter(5) is useful for applications where a balanced transmission line system is required with impedance

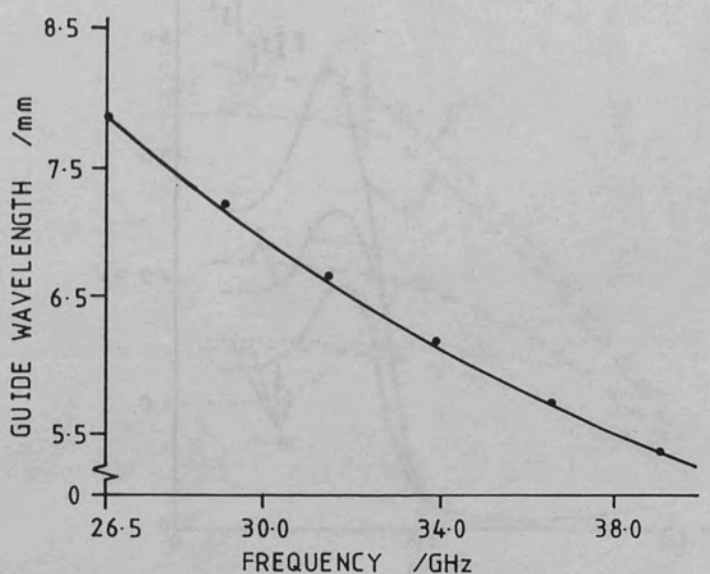

Figure (6.20) Measured variation of λ_g with frequency

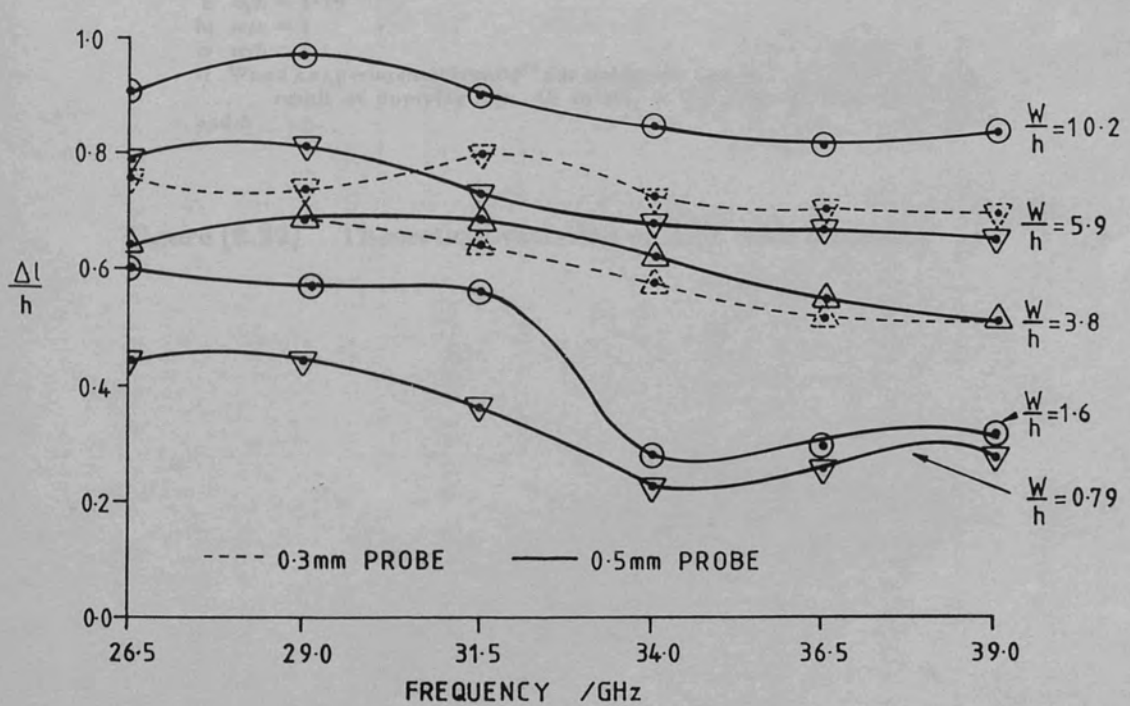

Figure (6.21) Measured variation of Δ_l/h with frequency

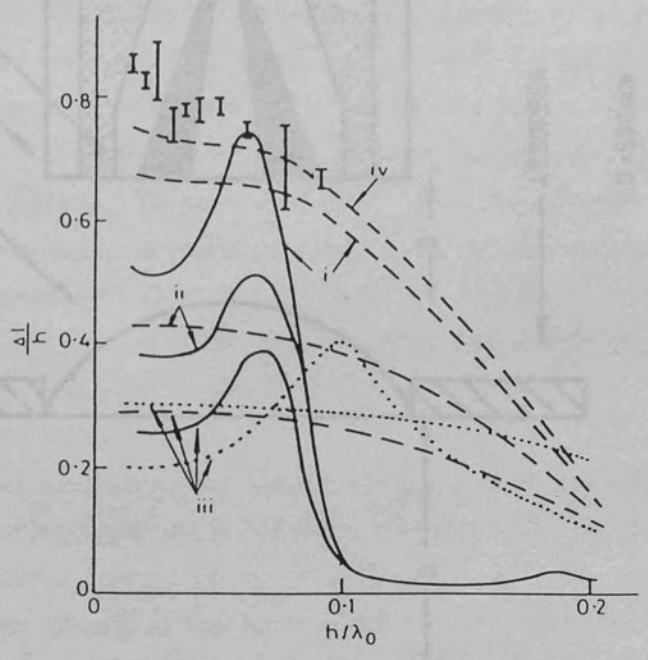

——— alumina $\epsilon_r = 10$
– – – – polyguide $\epsilon_r = 2{\cdot}32$
i $w/h = 5$
ii $w/h = 1{\cdot}79$
iii $w/h = 1$
iv $w/h = 6{\cdot}1$
II Wood's experimental results[18] for polyguide case iv
..... result of applying eqn. 40 to $(G_r + G_s)$ given in Figs. 6*a* and *b*

Figure (6.22) Theoretical variation of Δ_l/h with frequency

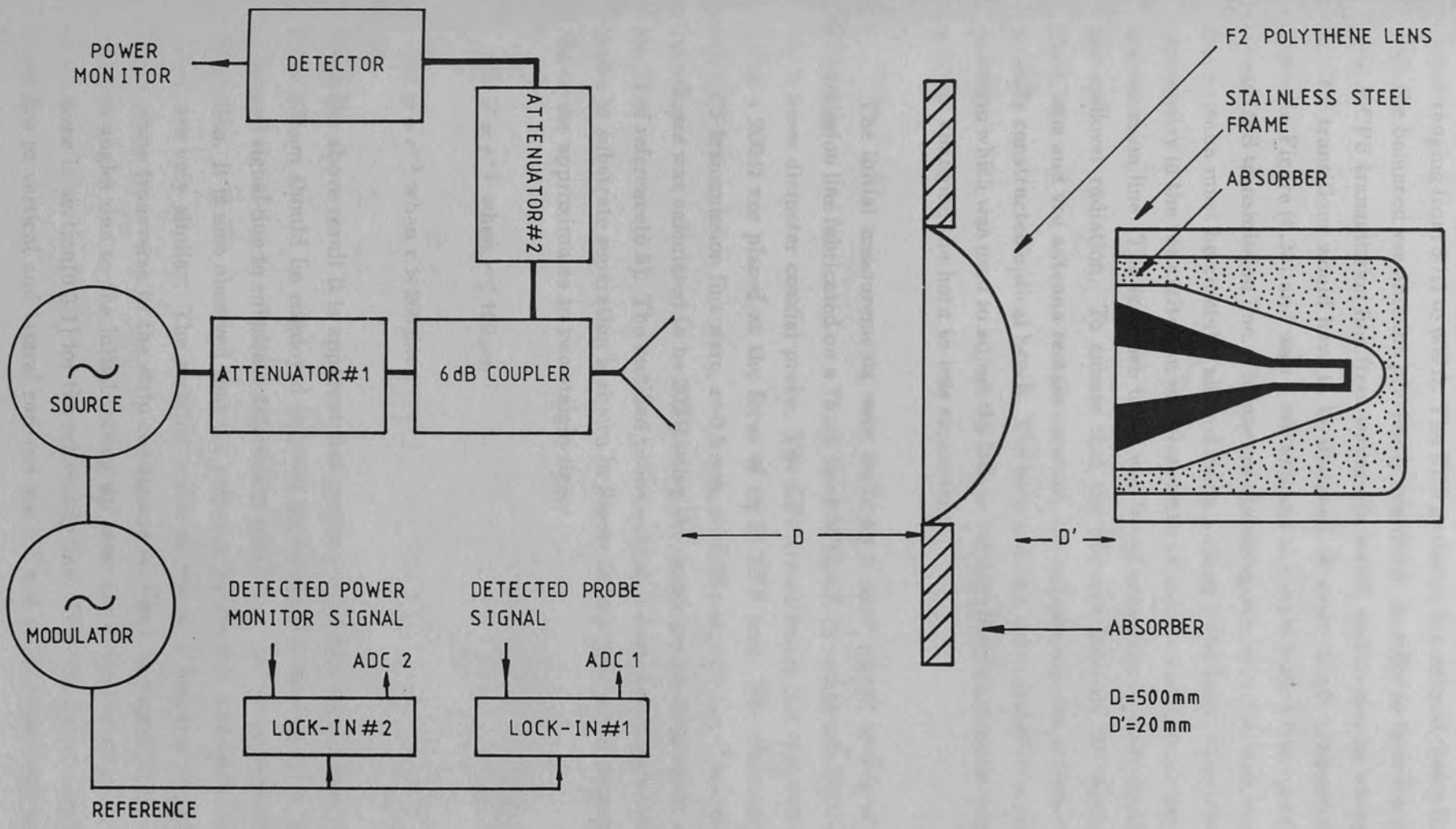

Figure(6.22) Method employed to energize C.P.S. transmission lines for the scanning network probe measurements.

values ranging from 50 Ω to 600 Ω. The CPS geometry is a natural choice for use with the balanced vee antenna previously described. In order to launch a signal onto a CPS transmission line from waveguide would require special waveguide to CPS transitions would have to be designed. A more simple arrangement is shown in Figure (6.23) and uses a vee antenna to couple from a free space field to the CPS transmission line. The axes of the waveguide horn, the lens, and the vee antenna must be carefully aligned using a small HeNe laser, otherwise the asymmetry in the vee excitation will give rise to an unbalanced wave on the CPS transmission line. The eccosorb baffle was found necessary in order to absorb the spillover radiation. To ensure that the distance between the waveguide horn, lens and vee antenna remain constant, the components are attached to a sturdily constructed optical bench. The horn and lens were carried on a moving platform which was used to adjust the lens to vee distance for optimum coupling without changing the horn to lens separation.

The initial measurements were made on a short circuit length of CPS transmission line fabricated on a 75 μm thick MYLAR ($\epsilon_r = 3.1$) substrate using the 0.5 mm diameter coaxial probe. The CPS transmission line was energized using a 200 Ω vee placed at the focus of an f2 TPX lens. The dimensions of the CPS transmission line were, s=0.5 mm, w=0.25 mm, and the characteristic impedance was calculated to be 202 Ω using the design equations given in chapter(7) of reference(6.5). The rectified probe output voltage as a function of the probe to substrate separation is shown in Figure (6.24). The power response of the probe approximates to two staight lines:

(a) $P \propto r^{-\frac{1}{2}}$ when $r \leq 100\,\mu m$

(b) $p \propto r^{-2}$ when $r > 200\,\mu m$

From the above result it is apparent that probe to substrate separations of less than 100 μm should be employed in order to reduce the random error in the measured signal due to substrate deformities which alter the probe to substrate separation. It is also observed that the response for the two monopole lengths tested are very similar. The rectified probe output as a function of position in the plane transverse to the strip conductors is shown in Figure (6.25). The run–out angles due to the initial setting up error are of similar magnitude to those given in section(6.3.1) for the microstrip line. The cumulative amplitude error due to vertical and lateral run–out are 5% and 4.5% respectively over a 40 mm scan.

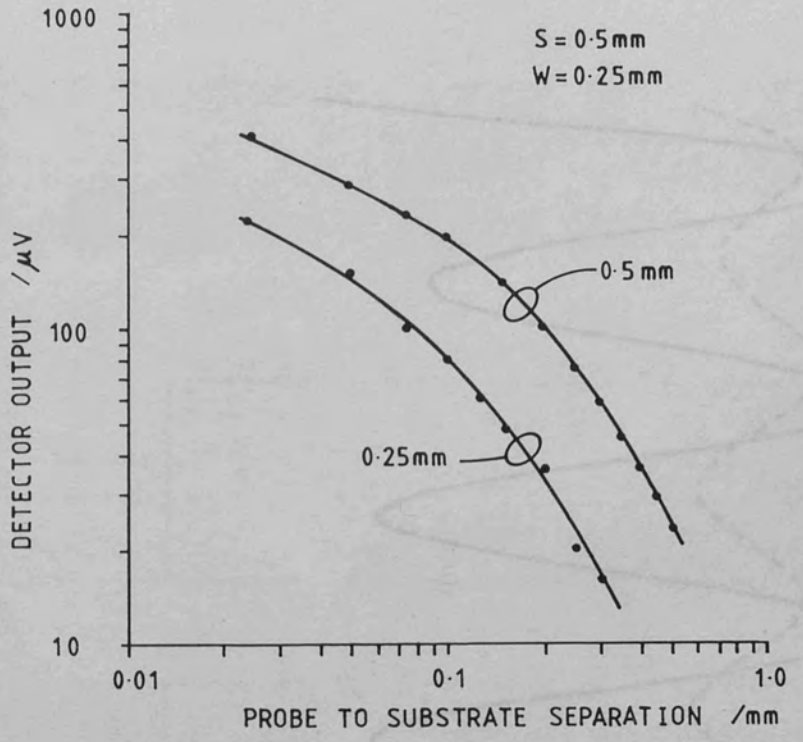

Figure (6.24) Variation of the detected signal with probe to substrate separation

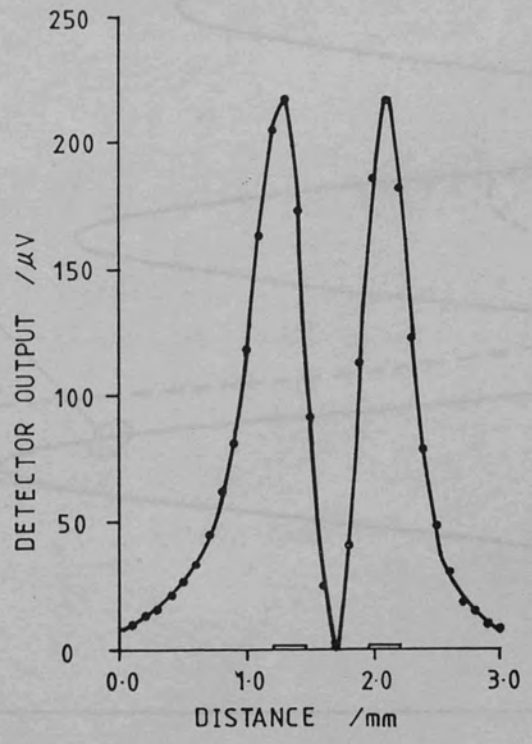

Figure (6.25) Variation of the detected signal transverse to the axis of the CPS transmission line

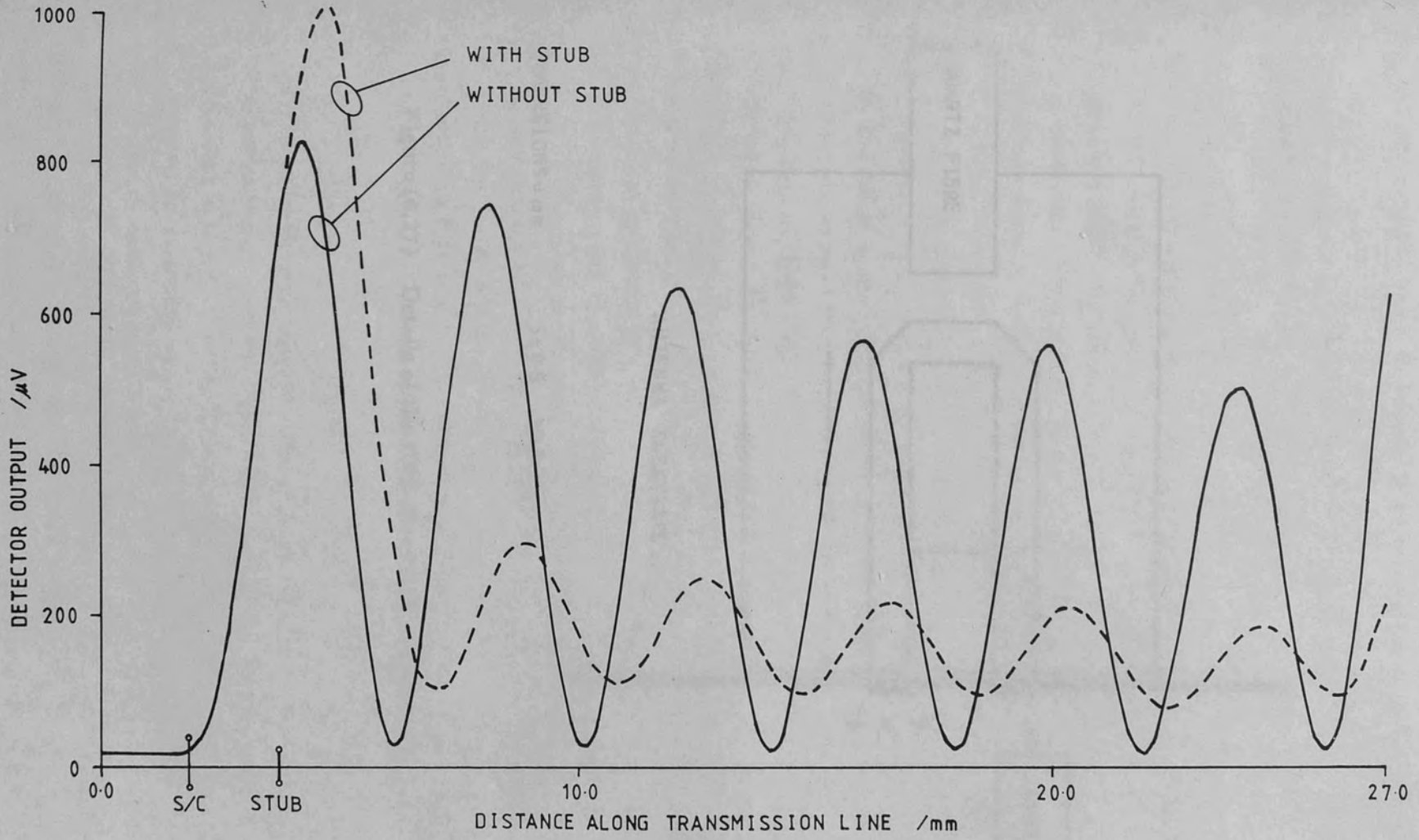

Figure(6.26) Power standing wave plots illustrating stub matching in a 200 Ω C.P.S. transmission line

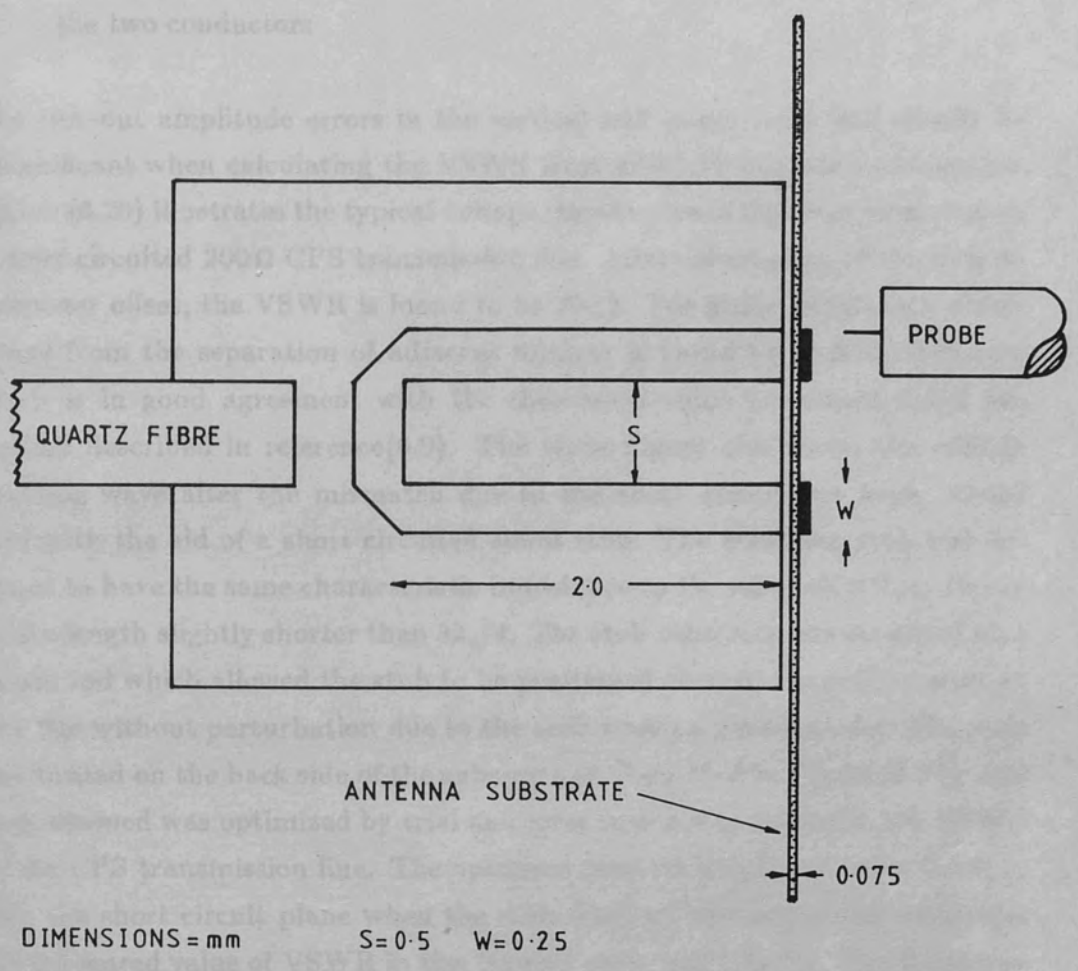

Figure (6.27) Details of the CPS shunt stub construction

These estimates assume:

(a) the probe output is $\propto r^{-\frac{1}{2}}$, where r is the probe to substrate separation

(b) the measurement is performed close the peak signal response on either of the two conductors

The run–out amplitude errors in the vertical and lateral axes will clearly be insignificant when calculating the VSWR from adjacent maxima and minima. Figure (6.26) illustrates the typical voltage standing wave that was measured on a short circuited $200\,\Omega$ CPS transmission line. After subtraction of the lock–in voltmeter offset, the VSWR is found to be 20 ± 2. The guide wavelength determined from the separation of adjacent minima is found to be $3.95\pm0.03\,mm$, which is in good agreement with the theoretical value calculated using the method described in reference(6.9). The same Figure also shows the voltage standing wave after the mismatch due to the short circuit has been "tuned out" with the aid of a short circuited shunt stub. The matching stub was designed to have the same characteristic impedance as the main CPS line, and to have a length slightly shorter than $3\lambda_g/4$. The stub substrate was mounted on a quartz rod which allowed the stub to be positioned close to the main transmission line without perturbation due to the stub transport mechanism. The stub was located on the back side of the substrate as illustrated in Figure (6.27), and its positioned was optimized by trial and error in order to minimize the VSWR on the CPS transmission line. The optimum position was found to be $0.256\,\lambda_g$ from the short circuit plane when the stub was just contacting the substrate. The measured value of VSWR in the "tuned" state was 1.7 ± 0.2. The finite line attenuation gave rise to the amplitude taper observed in both standing wave plots illustrated in Figure (6.26), however the effect was too small to enable the transmission line loss to be determined over such a short length of transmission line.

The standing wave plot shown in Figure (6.28) was measured on an identical CPS transmission line, but terminated with a matched load constructed from nichrome coated MYLAR. The load construction is illustrated in Figure (6.29), and is designed to attenuate the signal over approximately one guide wavelength. The match obtained using a nichrome layer $0.1\,\mu m$ thick was 1.8 ± 0.2.

Figure (6.30) shows a design for a simple integrated vee quasi–optic detector for use at Q–band. The R.F. was decoupled from from the bias lines by alternate low and high impedance quarter wavelength sections of transmission

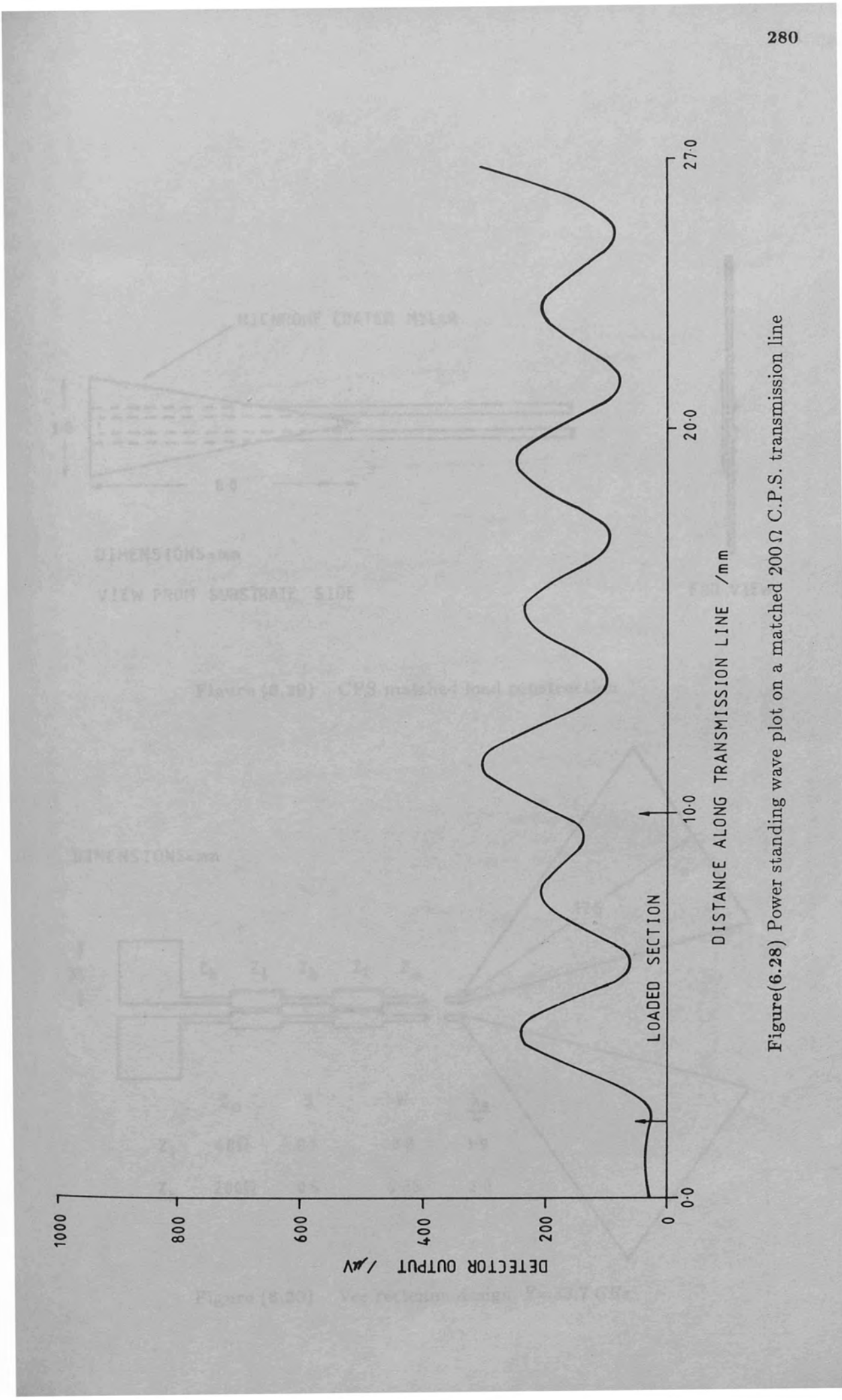

Figure(6.28) Power standing wave plot on a matched 200 Ω C.P.S. transmission line

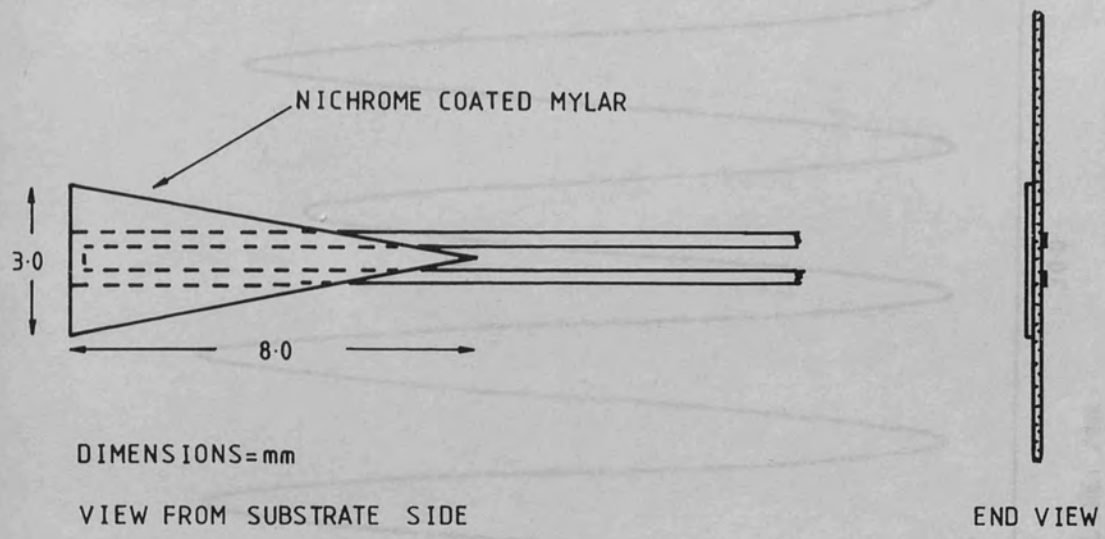

Figure (6.29) CPS matched load construction

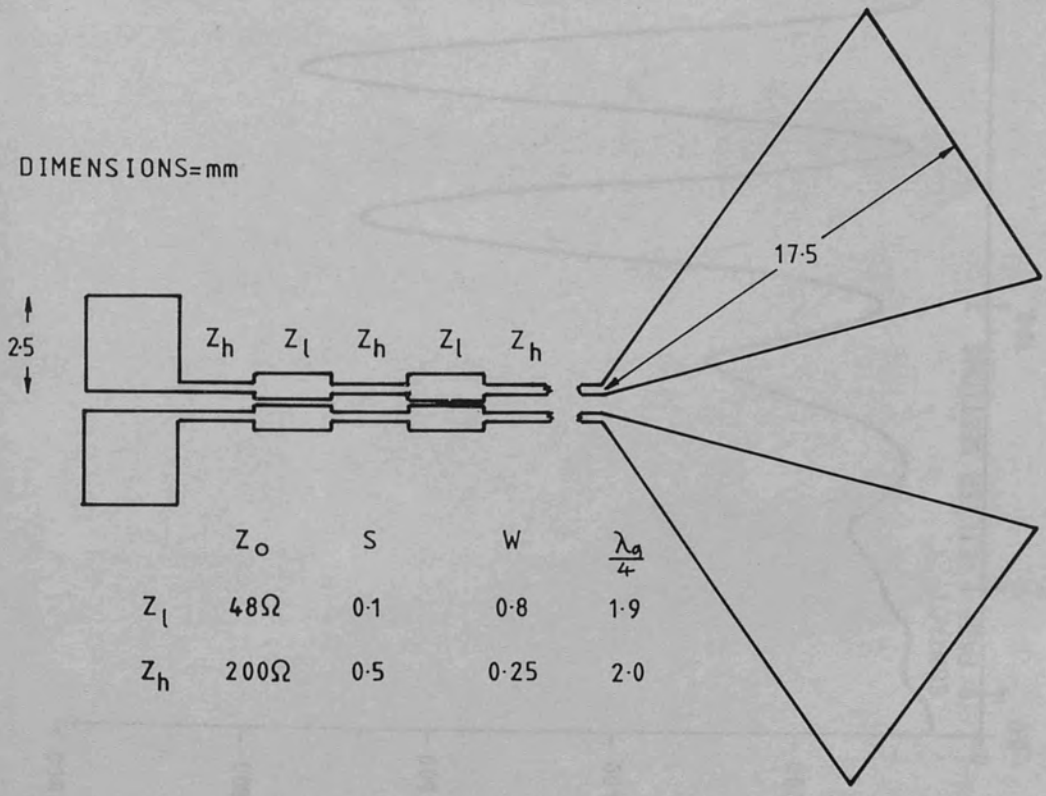

	Z_o	S	W	$\frac{\lambda_g}{4}$
Z_l	48Ω	0·1	0·8	1·9
Z_h	200Ω	0·5	0·25	2·0

Figure (6.30) Vee rectenna design, F=33.7 *GHz*

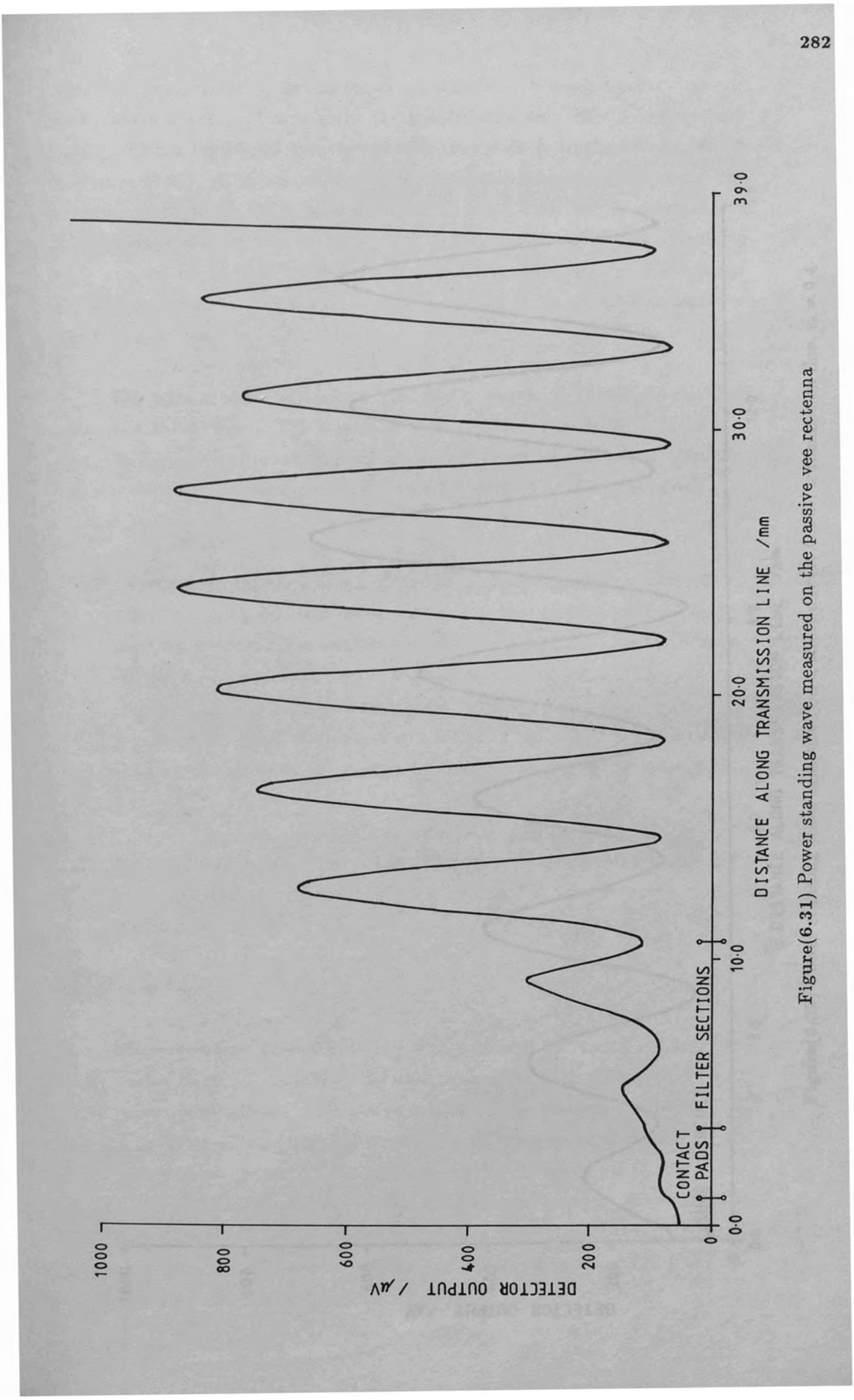

Figure(6.31) Power standing wave measured on the passive vee rectenna

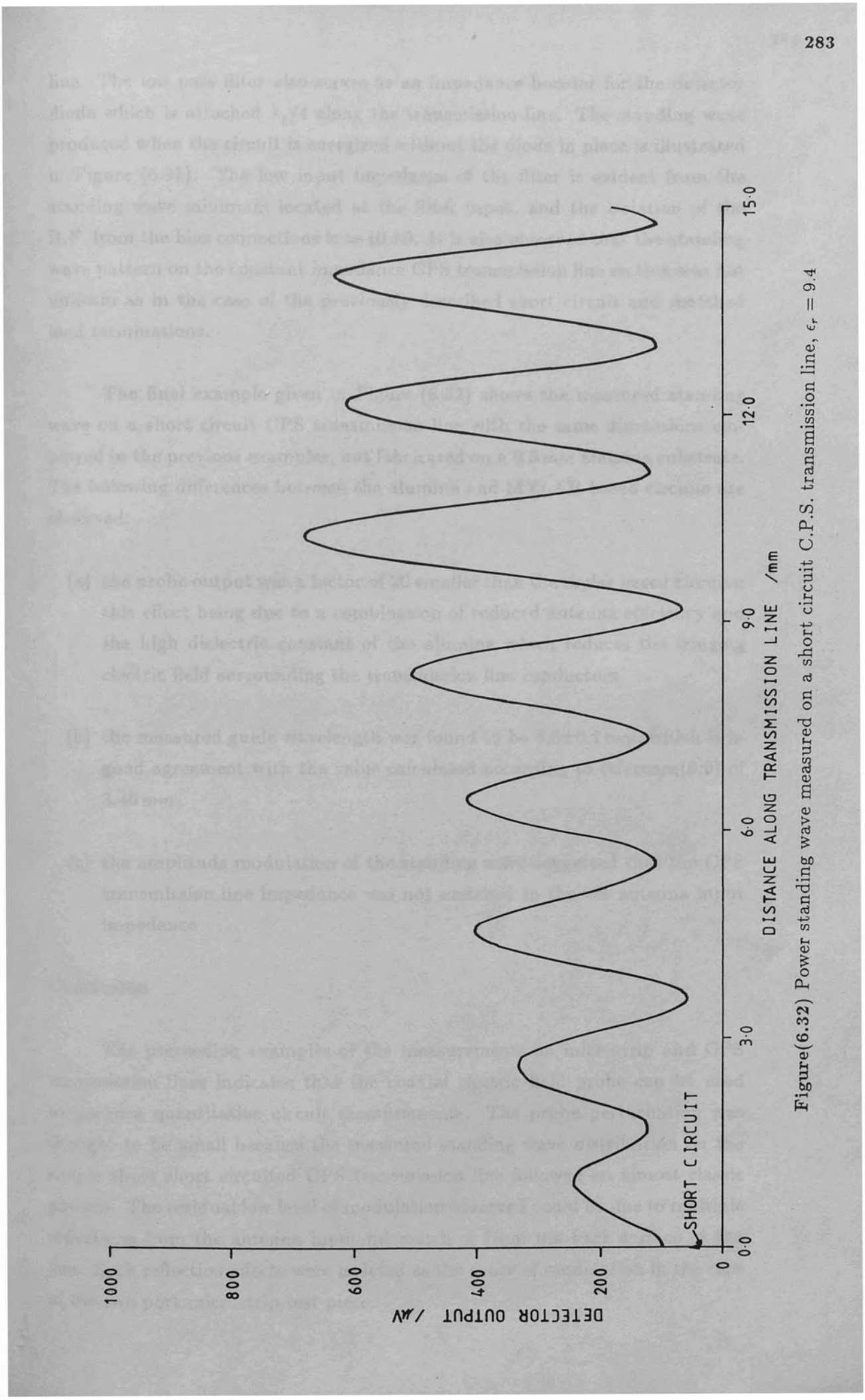

Figure(6.32) Power standing wave measured on a short circuit C.P.S. transmission line, $\epsilon_r = 9.4$

line. The low pass filter also serves as an impedance booster for the detector diode which is attached $\lambda_g/4$ along the transmission line. The standing wave produced when the circuit is energized without the diode in place is illustrated in Figure (6.31). The low input impedance of the filter is evident from the standing wave minimum located at the filter input, and the isolation of the R.F. from the bias connections is $\approx$-10 dB. It is also observed that the standing wave pattern on the constant impedance CPS transmission line section was not uniform as in the case of the previously described short circuit and matched load terminations.

The final example given in Figure (6.32) shows the measured standing wave on a short circuit CPS transmission line with the same dimensions employed in the previous examples, but fabricated on a 0.5 mm alumina substrate. The following differences between the alumina and MYLAR based circuits are observed:

(a) the probe output was a factor of 20 smaller than the mylar based circuits; this effect being due to a combination of reduced antenna efficiency and the high dielectric constant of the alumina which reduces the fringing electric field surrounding the transmission line conductors

(b) the measured guide wavelength was found to be 3.6$\pm$0.1 mm, which is in good agreement with the value calculated according to reference(6.9) of 3.45 mm

(c) the amplitude modulation of the standing wave suggested that the CPS transmission line impedance was not matched to the vee antenna input impedance

Conclusion

The preceeding examples of the measurements on microstrip and CPS transmission lines indicates that the coaxial electric field probe can be used to perform quantitative circuit measurements. The probe perturbation was thought to be small because the measured standing wave distribution on the simple short short circuited CPS transmission line followed an almost classic pattern. The residual low level of modulation observed could be due to multiple reflections from the antenna input mismatch or from the back surface of the lens. Such reflection effects were isolated as the cause of modulation in the case of the two port microstrip test piece.

The accuracy of the scanning network probe transmission line measurements could possibly be improved by the use of smaller diameter probes. The use of such small probes will require a more sensitive detection system, such as a superheterodyne receiver. The accuracy of the initial setting up procedure is the predominant factor determining the measurement accuracy and repeatability. The stringent circuit levelling requirements and the need for precision flat circuits would be eased if a servo control loop were added to maintain the probe at a constant height above the circuit.

CHAPTER 7

Microstrip Antenna Array Diagnostics

7.1 Introduction

Single microstrip radiators do not provide sufficient gain for most communications and radar applications, therefore the use of arrays becomes essential. The combination of several patch antennas on a single substrate is made difficult at millimetre wavelengths due to the additional complexity introduced into the array design by surface wave coupling between the array elements.[7.1] To date, no satisfactory means of measuring or calculating the effect of surface wave coupling between the patch elements except reference (7.2) which employs a rigorous Green's function technique. The mode analysis and transmission line measurement techniques that were described in chapters (4) and (6) can be combined to form a powerful diagnostic tool for microstrip arrays. The scanning network probe allows:

(a) the mode of excitation of the individual elements to be found

(b) the matching of an individual array element to its microstrip feed to be determined

(c) excessive surface wave launching to be detected

The practical application and potential usefulness of the scanning network probe technique as a diagnostic tool for microstrip array evaluation is demonstrated by the following examples.

7.2 A Linear 4–Element Rectangular Patch Array

7.2.1 Theoretical Design Considerations

The conditions for maximum broadside radiation from a multi–element linear array can be derived from general array theory. For the array of n uniformly spaced radiators along the Z–axis illustrated in Figure (7.1) the

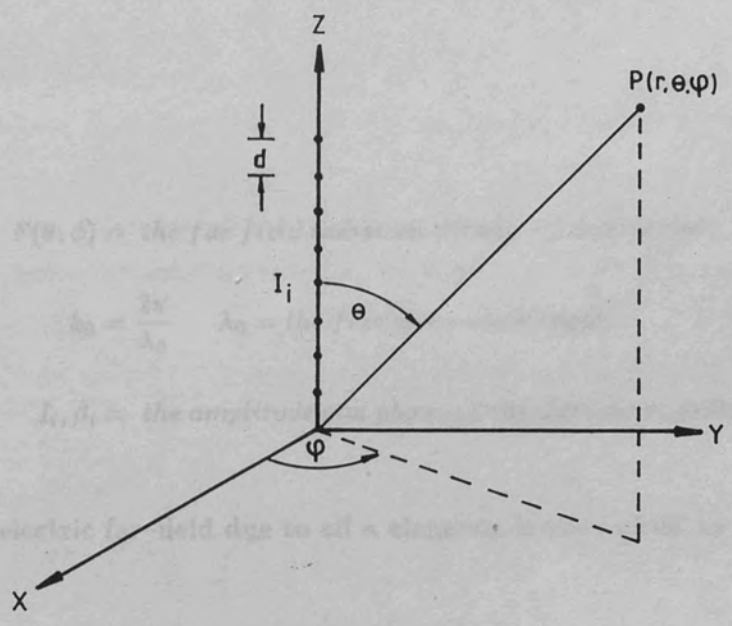

Figure (7.1) A linear point source array

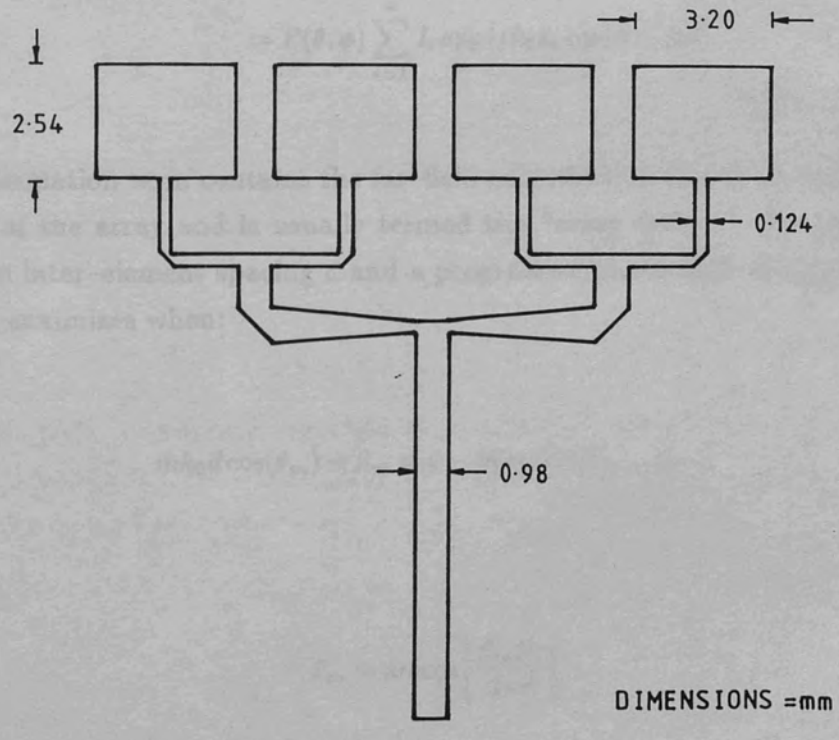

Figure (7.2) Linear 4–element patch array outline

far–field contribution due to the i^{th} element is given by:

$$E_i = F(\theta,\phi) I_i \exp\left[jk_0 z_i \cos(\theta) + \beta_i)\right] \qquad 7.1$$

Where:

$F(\theta,\phi) =$ *the far field radiation pattern of one element*

$k_0 = \dfrac{2\pi}{\lambda_0}$ $\quad \lambda_0 =$ *the free space wavelength*

$I_i, \beta_i =$ *the amplitude and phase of the element excitation*

The total electric far–field due to all n elements is then given by:[7.4]

$$E(\theta,\phi) = \sum_{i=1}^{n} E_i(\theta,\phi)$$

$$= F(\theta,\phi) \sum_{i=1}^{n} I_i \exp\left[jk_0 z_i \cos(\phi + \beta_i)\right] \qquad 7.2$$

The summation term contains the far–field contribution due to the geometrical layout of the array and is usually termed the "array factor." For the case of uniform inter–element spacing d and a progressive phase shift of β_m, the array factor maximizes when:

$$mk_0 d \cos(\theta_m) + \beta_m = 0 \quad m = 0, 1, 2, \ldots n-1 \qquad 7.3$$

or:

$$\theta_m = \arccos\left[\frac{\beta_m \lambda_0}{2\pi d}\right] \qquad 7.4$$

where:

$\theta_m =$ *the direction of the main beam*

$\beta_m = m\beta_0$

$\beta_0 =$ *the phase shift between successive elements*

Restricting our attention to the case when the elements are excited with equal amplitude, then the magnitude of the of the array factor $|T|$ is given by:

$$|T| = \frac{\sin\left(\frac{nu}{2}\right)}{\sin\left(\frac{u}{2}\right)} \tag{7.5}$$

where:

$$u = k_0 d\{\cos(\theta) - \cos(\theta_m)\}$$

The directivity function of the array in the far–field is thus given by:

$$|E_i(\theta, \phi)| = |F(\theta, \phi)|\,|T| \tag{7.6}$$

For a broadside radiator $\theta_m = \pi/2$, therefore from equation(7.4):

$$\arccos\left[\frac{\beta_m \lambda_0}{2\pi d}\right] = \frac{\pi}{2} \tag{7.7}$$

Equation(7.7) is only satisfied when $\beta_m = 0$, which requires that the phase shift between adjacent elements is zero. The nulls in the radiation pattern due to the array factor occur whenever:

$$\sin\left(\frac{nu}{2}\right) = 0$$

or:

$$\frac{nk_0d}{2}(\cos(\theta) - \cos(\theta_m)) = m\pi \quad m = \pm 1, \pm 2 \ldots \tag{7.8}$$

For a broadside radiator $\cos(\theta_m) = 0$, so:

$$\cos(\theta) = \frac{2m\pi}{nk_0d}$$

$$= \frac{m\lambda_0}{nd} \tag{7.9}$$

The first minima occur when $m = \pm 1$ giving angles of:

$$\theta_1 = \pm \arccos\left[\frac{\lambda_0}{nd}\right] \tag{7.10}$$

The location of the sidelobes is found by differentiating the array factor and equating the result to zero which gives:

$$n\tan(\frac{u}{2}) = \tan(\frac{nu}{2}) \tag{7.11}$$

Therefore, in order to make a broadside radiating array, it is necessary to excite the array elements with equal amplitude and phase. Is also apparent from equations(7.4), and (7.9) that the grating lobe structure will be eliminated provided that the element spacing is maintained below one free space wavelength.

The linear 4 element rectangular patch array shown in Figure (7.2) was designed using these simple criteria. The patch radiators were designed to be resonant $35\,GHz$ when fabricated on RT–DUROID 5880 using the expressions given in chapter (4). No attempt was made to allow for mutual coupling between the patch elements. An inter–element spacing of $\lambda_0/2$ between the patch centre lines was selected in order to eliminate any grating lobe structure. The array elements were excited by a "binary tree" corporate feed network employing non–isolating microstrip T–junctions. The advantages of the microstrip T–junction splitter are its simplicity of design and very wide bandwidth. The disadvantage

of this type of power splitter is the lack of isolation between the output arms which will result in complex inter–element interaction if the elements themselves are mismatched. If the corporate feed network utilized isolating power splitting components such as the Wilkinson coupler or hybrid coupler, then the reflected power from the mismatched patch feed points would simply be routed back to the matched input, and there would be no resulting modification of the desired power distribution on the array. However, the power distribution of a corporate feed network constructed from non–isolating power splitters will be subject to modification if the elements are mismatched, since some of the reflected power is routed to the other array elements. The impedance of the input and output arms of the microstrip T–junction are approximately related by:

$$\frac{1}{Z_{in}} = \frac{1}{Z_{out1}} + \frac{1}{Z_{out2}} \qquad 7.12$$

For a $3dB$ power split, $Z_{out1} = Z_{out2}$, therefore:

$$Z_{out} = 2Z_{in} \qquad 7.13$$

When the impedance of the input arms is $50\,\Omega$, the required impedance of the output arms is $100\,\Omega$. Rather than split the two $100\,\Omega$ outputs of the primary power splitter into four $200\,\Omega$ outputs, each of the $100\,\Omega$ outputs was linearly tapered to $50\,\Omega$ and then split into two $100\,\Omega$ outputs. This avoids the problem of etching the very narrow $200\,\Omega$ lines. The linearly tapered impedance transformer was selected due to its wide bandwidth compared to the quarter wave matching sections employed by Munson.[7.4] The path lengths from the corporate feed input to each of the radiating elements was identical, therefore all the array elements should be excited in the same phase. The interconnections between the power splitters were made using straight lengths of microstrip that were either parallel, or perpendicular to the main $50\,\Omega$ microstrip feed line. Any change in the direction of the microstrip lines was effected using the optimized mitred bends as suggested by Edwards.[7.5] This was alien to normal microstrip design practice which would aim to:

(a) connect the circuit elements by the shortest possible route, thus minimizing transmission line loss

(b) avoid sharp deviations of the microstrip line which result in increased radiation losses

The relatively widespread, orthogonal layout of the corporate feed was selected for the sole purpose of simplifying the data analysis software.

7.2.2 4 Element Linear Array Performance

The photographic mask for the array was produced by the CALMA CAD system available at MDS. The antenna was fabricated on 0.254 mm, rolled copper clad RT–DUROID 5880 using a copper "etch–back" technique. After etching, the substrate was cut to size and soft soldered to a 1 $\frac{1}{2}$" square 3/16" thick brass plate which provided the necessary mechanical support for the substrate and the waveguide to microstrip transition. The array in its final form is shown in plate (7.1) at the end of this chapter. The return loss measured in the frequency range 30–40 GHz using a waveguide scalar network analyser is shown in Figure (7.3). The array exhibited a return loss of 18 dB at a frequency of 33.8 GHz, and a return loss of 9.6 dB at 37.8 GHz. The radiation pattern of the array in the E and H–planes at each of these frequencies is shown in Figures (7.4)a,b and (7.5)a,b. The array performance is summarized in Table (7.1).

TABLE (7.1)

Linear Array Performance Summary

Plane	F	$\theta_{3\,dB}$	1^{st} Sidelobe	X– Polar	Directivity
	$/GHz$	$/^\circ$	$/dB$	$/dB$	$/dB_i$
E	33.8	68	-9	<-20	
H	33.8	24.7	-15.6	-17.8	16.1
E	37.8	57.6	-9.3	<-20	
H	37.8	25.3	-13.6	-20.1	18.5

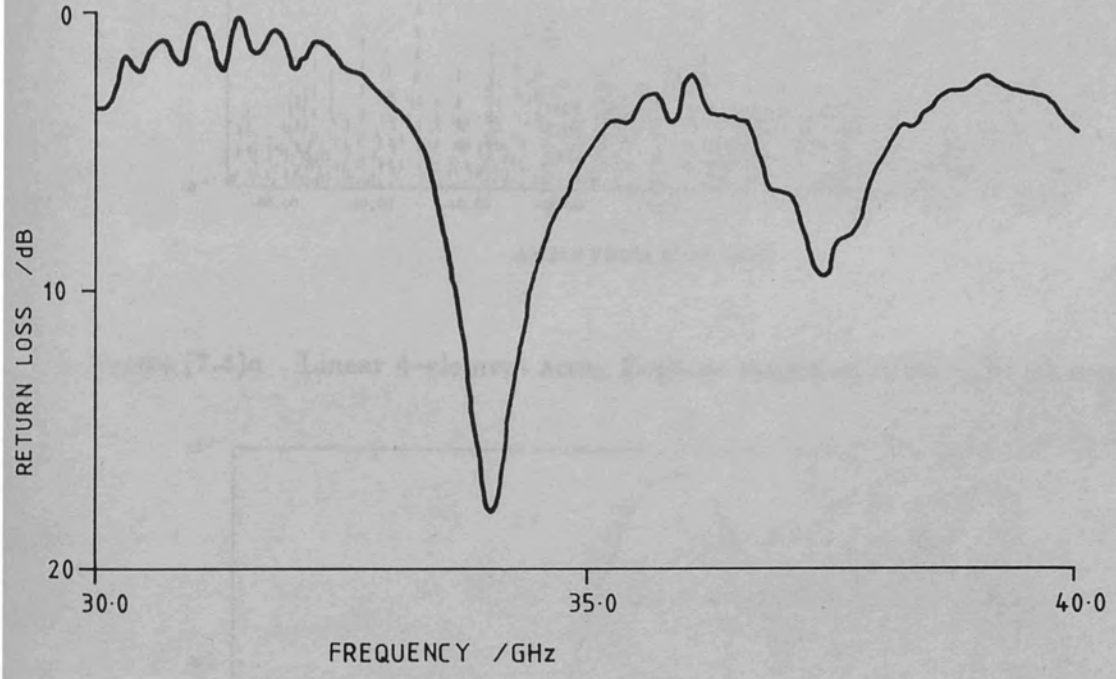

Figure (7.3) Linear 4–element array return loss

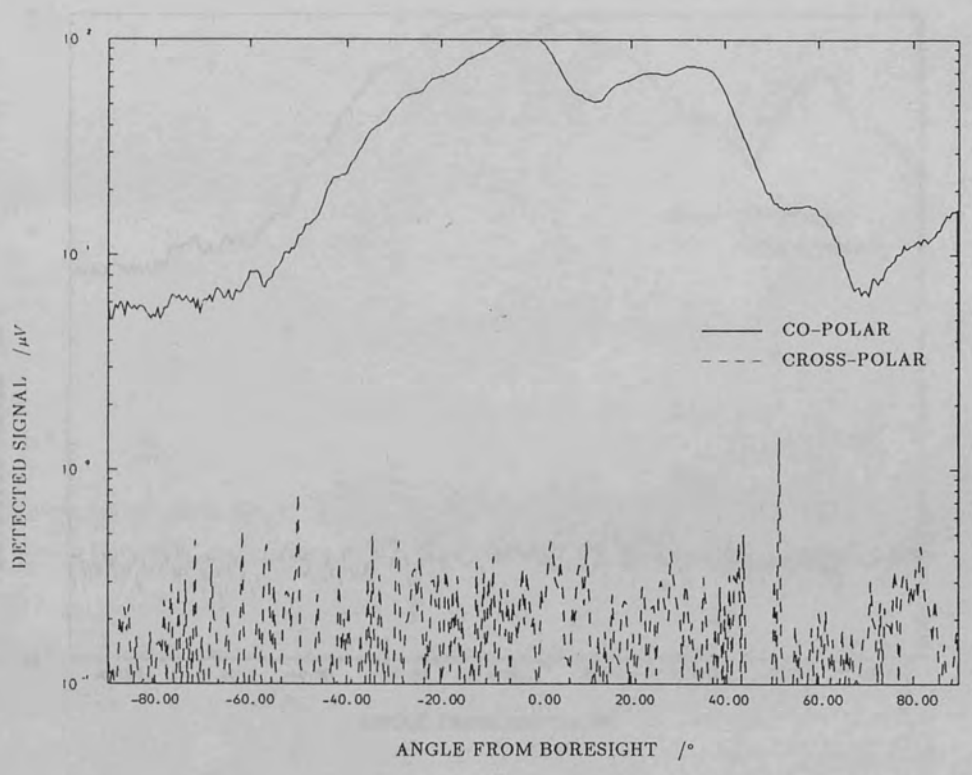

Figure (7.4)a Linear 4–element array E–plane radiation pattern, F=33.8 *GHz*

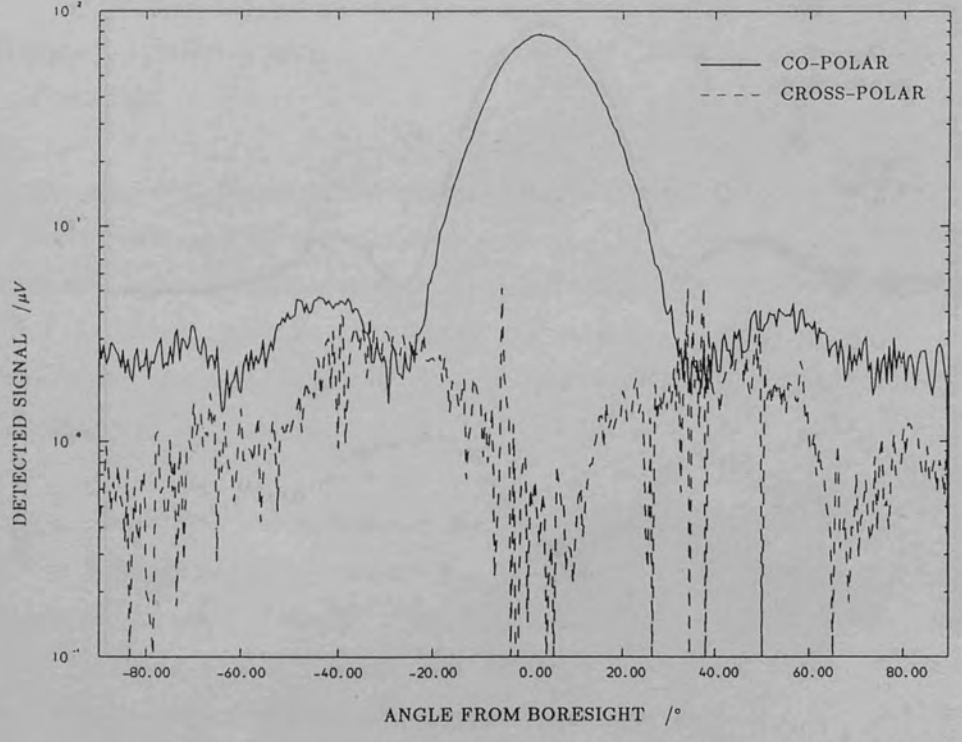

Figure (7.4)b Linear 4–element array H–plane radiation pattern, F=33.8 *GHz*

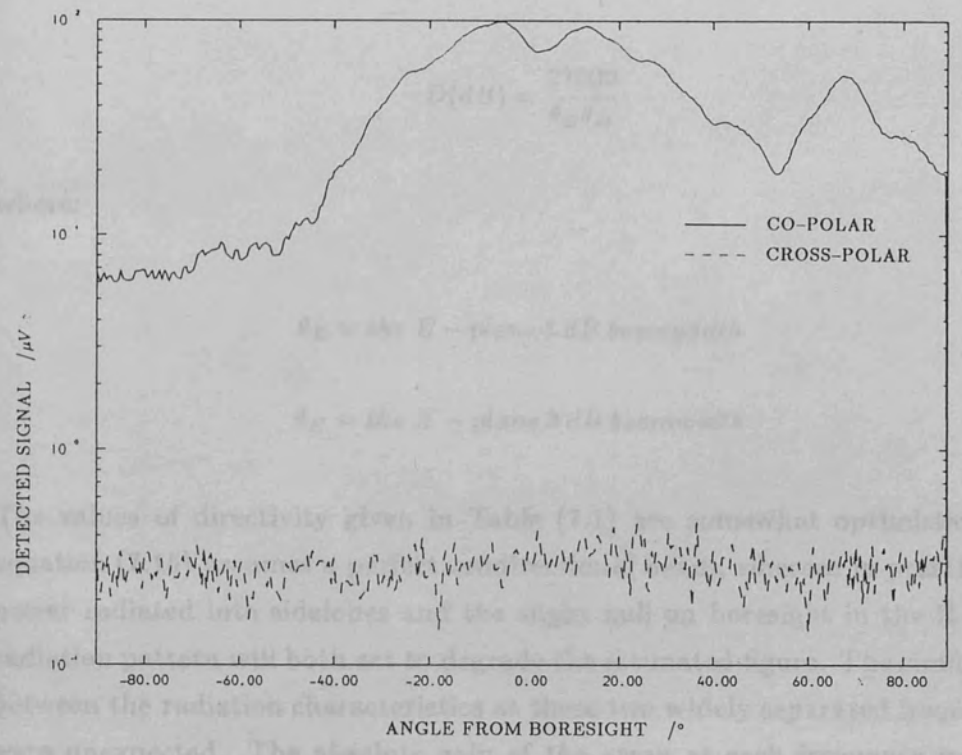

Figure (7.5)a Linear 4–element array E–plane radiation pattern, F=37.8 *GHz*

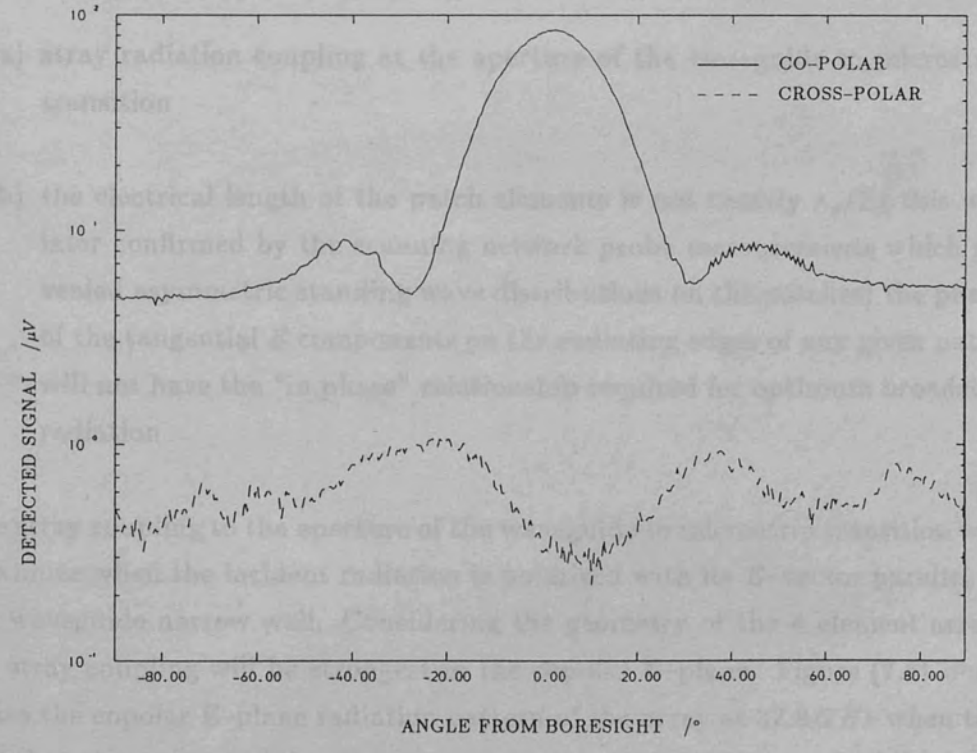

Figure (7.5)b Linear 4–element array H–plane radiation pattern, F=37.8 *GHz*

The directivity was calculated using the approximate relation:[7.6]

$$D(dB) = \frac{27000}{\theta_E \theta_H} \qquad 7.14$$

where:

$$\theta_E = the\ E - plane\ 3\,dB\ beamwidth$$

$$\theta_H = the\ H - plane\ 3\,dB\ beamwidth$$

The values of directivity given in Table (7.1) are somewhat optimistic since equation (7.15) assumes a perfect unidirectional beam, whereas in practice the power radiated into sidelobes and the slight null on boresight in the H–plane radiation pattern will both act to degrade the estimated figure. The similarities between the radiation characteristics at these two widely separated frequencies were unexpected. The absolute gain of the array at each frequency was not measured, however the relative level of the detected signal was approximately $10\,dB$ higher at the lower frequency. The slight splitting observed in the E-plane radiation pattern might be caused by:

(a) stray radiation coupling at the aperture of the waveguide to microstrip transition

(b) the electrical length of the patch elements is not exactly $\lambda_g/2$,(this was later confirmed by the scanning network probe measurements which revealed asymmetric standing wave distributions on the patches) the phase of the tangential E components on the radiating edges of any given patch will not have the "in phase" relationship required for optimum broadside radiation

The stray coupling to the aperture of the waveguide to microstrip transition will maximize when the incident radiation is polarized with its E–vector parallel to the waveguide narrow wall. Considering the geometry of the 4 element array, the stray coupling will be strongest in the copolar E–plane. Figure (7.6) illustrates the copolar E–plane radiation pattern of the array at $37.8\,GHz$ when the absorber that was shielding the waveguide aperture was removed. The boresight splitting is seen to increase, and the side lobe level at angles close to 90° has been raised. The high sidelobe level at approximately 70° from boresight

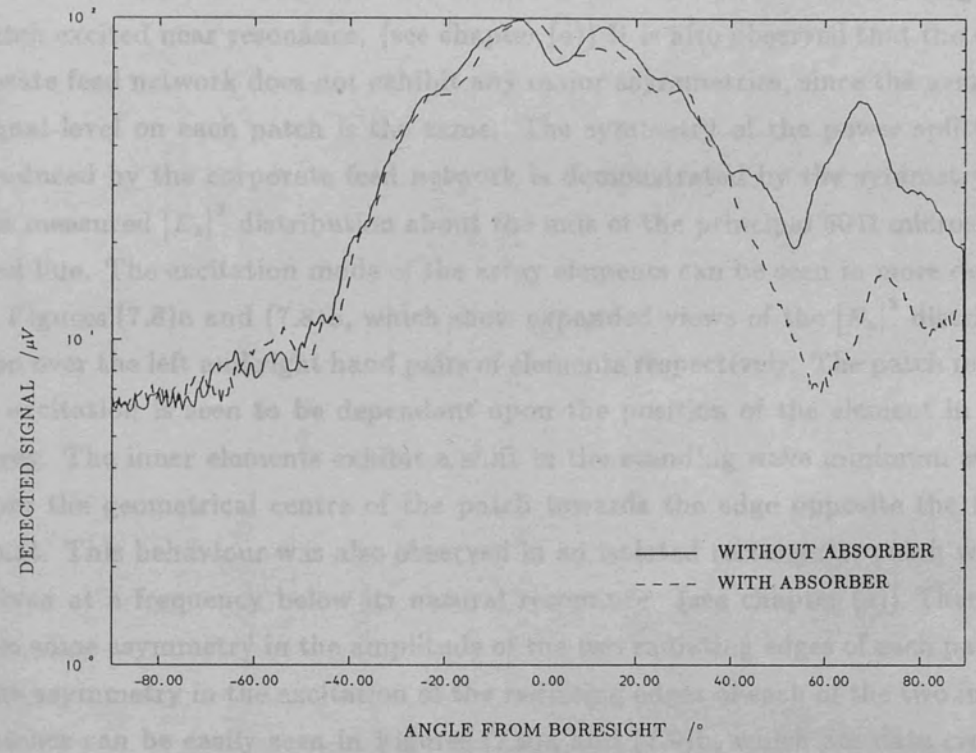

Figure (7.6) Radiation pattern distortion caused by direct coupling to the waveguide aperture

is correlated with the waveguide aperture pointing towards the transmitting horn, suggesting that the stray radiation coupling to the waveguide aperture of the transition is partly responsible for the degraded E–plane radiation pattern.

The scanning network probe technique described in the preceeding chapters was used to observe the mode of excitation of the array at $33.8\,GHz$ and $37.8\,GHz$. The $|E_z|^2$ distribution measured $50\,\mu m$ above the antenna metallization at $33.8\,GHz$ is shown in Figure (7.7). The patch array elements all exhibited a mode structure similar to that found with the isolated rectangular patch excited near resonance. (see chapter (4)) It is also observed that the corporate feed network does not exhibit any major asymmetries, since the average signal level on each patch is the same. The symmetry of the power splitting produced by the corporate feed network is demonstrated by the symmetry of the measured $|E_z|^2$ distribution about the axis of the principal $50\,\Omega$ microstrip feed line. The excitation mode of the array elements can be seen in more detail in Figures (7.8)a and (7.8)b, which show expanded views of the $|E_z|^2$ distribution over the left and right hand pairs of elements respectively. The patch mode of excitation is seen to be dependant upon the position of the element in the array. The inner elements exhibit a shift in the standing wave minimum away from the geometrical centre of the patch towards the edge opposite the feed point. This behaviour was also observed in an isolated rectangular patch when driven at a frequency below its natural resonance. (see chapter (4)) There is also some asymmetry in the amplitude of the two radiating edges of each patch. The asymmetry in the excitation of the radiating edges of each of the two inner patches can be easily seen in Figures (7.9)a and (7.9)b, which are data cross–sections taken along the axis of the $100\,\Omega$ feed line to each of the patches. The cross–sections show very similar trends and confirm the symmetry of the power split. The slight difference in the two cross–sections close to the patch feed point is attributed to the slight offset of the scan window, which has prevented the cross–sections being taken along the same region of the $100\,\Omega$ microstrip in each case. Returning to Figures (7.8)a and (7.8)b, it is observed that the standing wave minimum on the two inner patches is not parallel to the radiating edges, but progressively shifts towards the patch centre as one proceeds along the axis defined by the patch radiating edges and away from the axis of symmetry. This suggests that the line extension Δl is a function of position along the patch width. The implication made here is that the phase of the reflected wave from the open circuit patch edge is also a function of position along the patch width. The excitation mode of the outer two patches is slightly from the the inner pair,

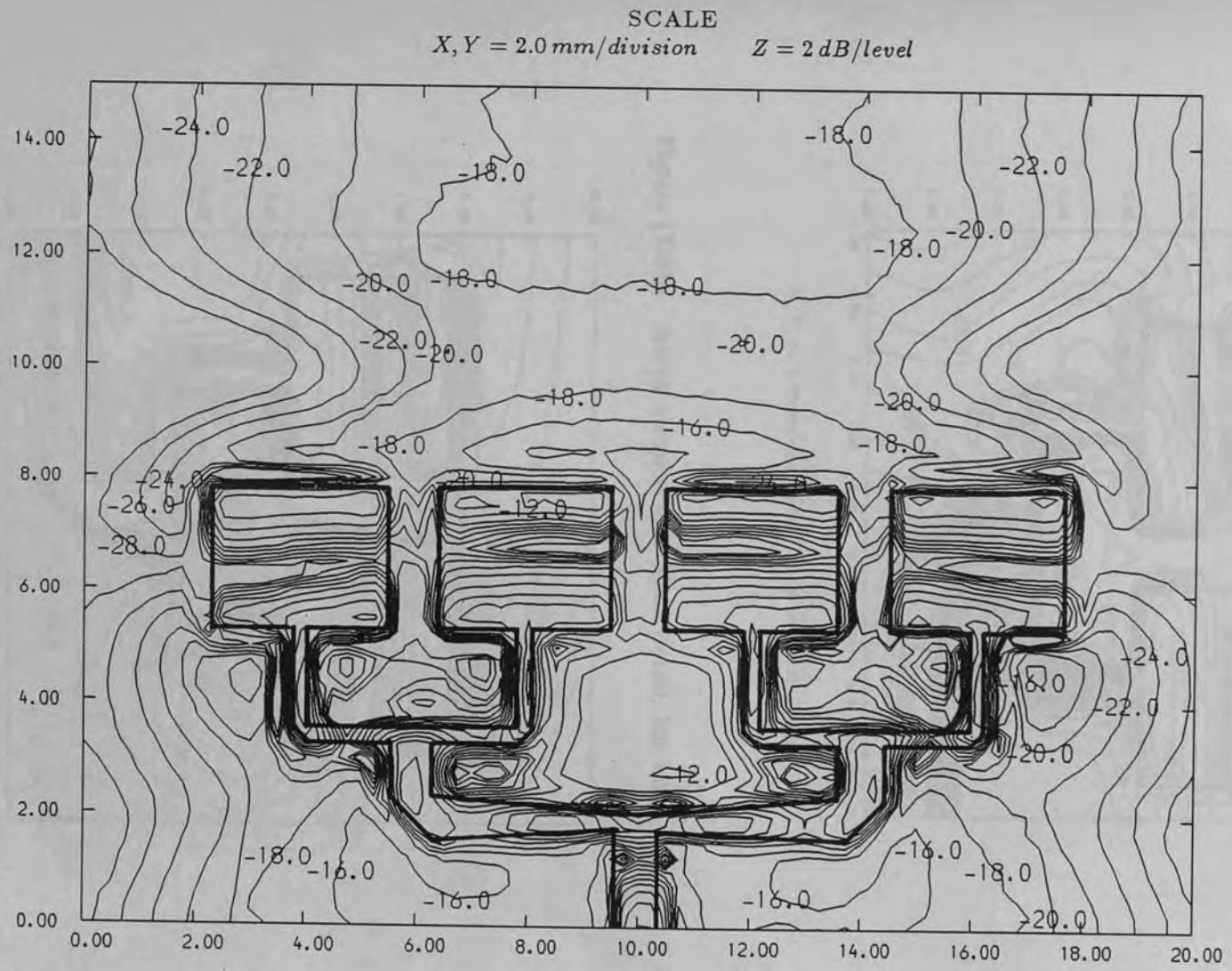

Figure(7.7) Linear 4 Element Array $|E_z|^2$ Distribution, F=33.8 *GHz*

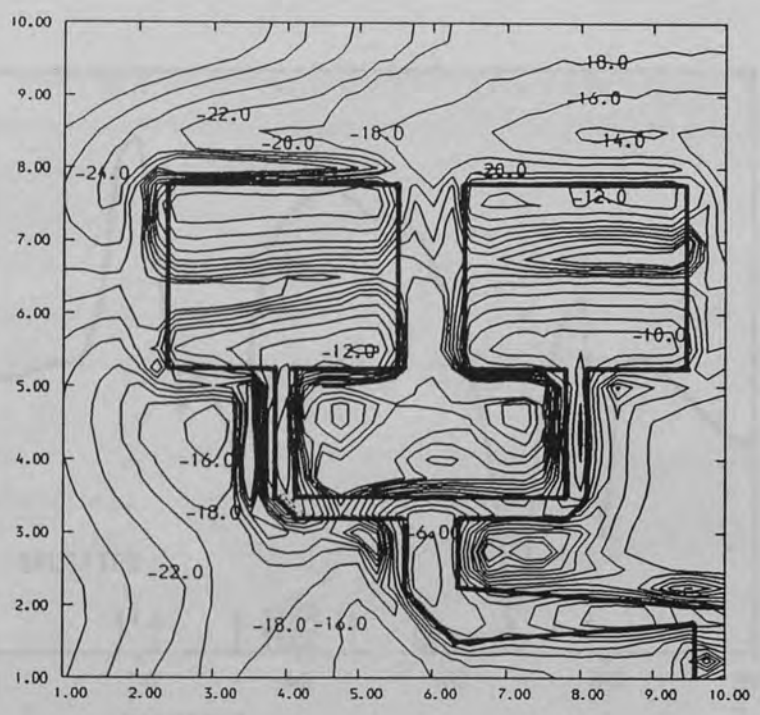

$X, Y = 1\,mm/division \qquad Z = 2\,dB/level$

Figure (7.8)a Array element excitation detail, left hand pair

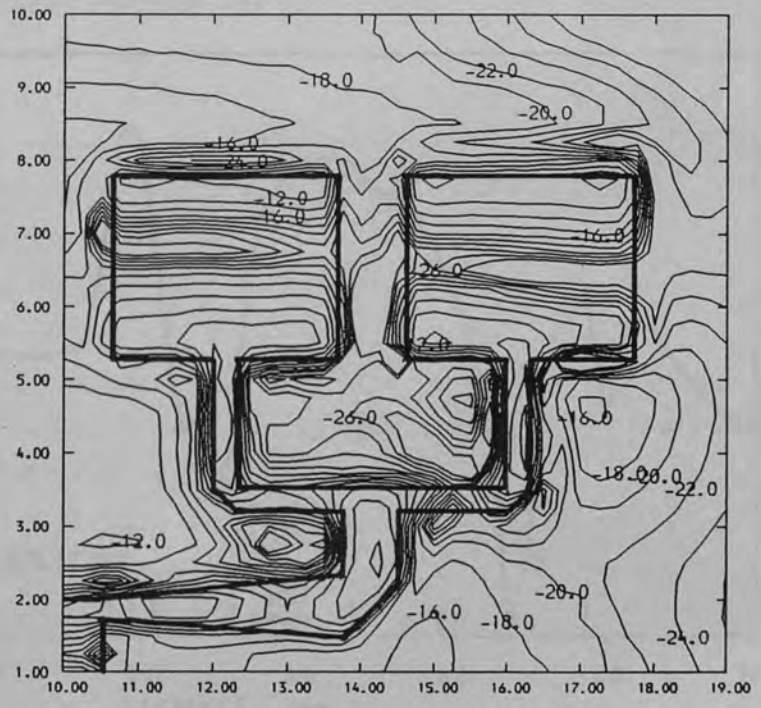

$X, Y = 1\,mm/division \qquad Z = 2\,dB/level$

Figure (7.8)b Array element excitation detail, right hand pair

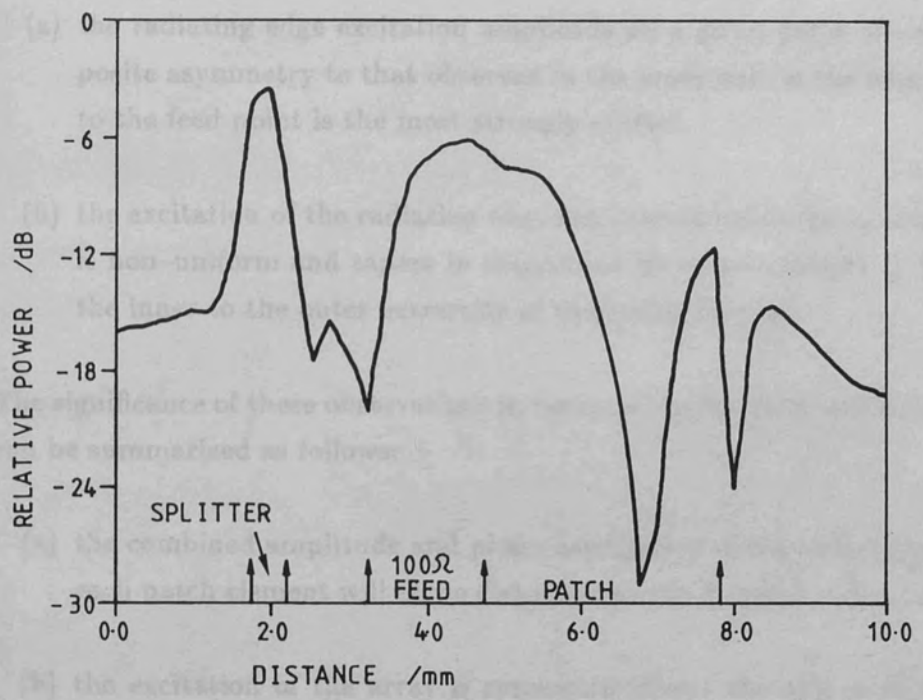

Figure (7.9)a Cross section along the axis of the microstrip feed, inner left hand element

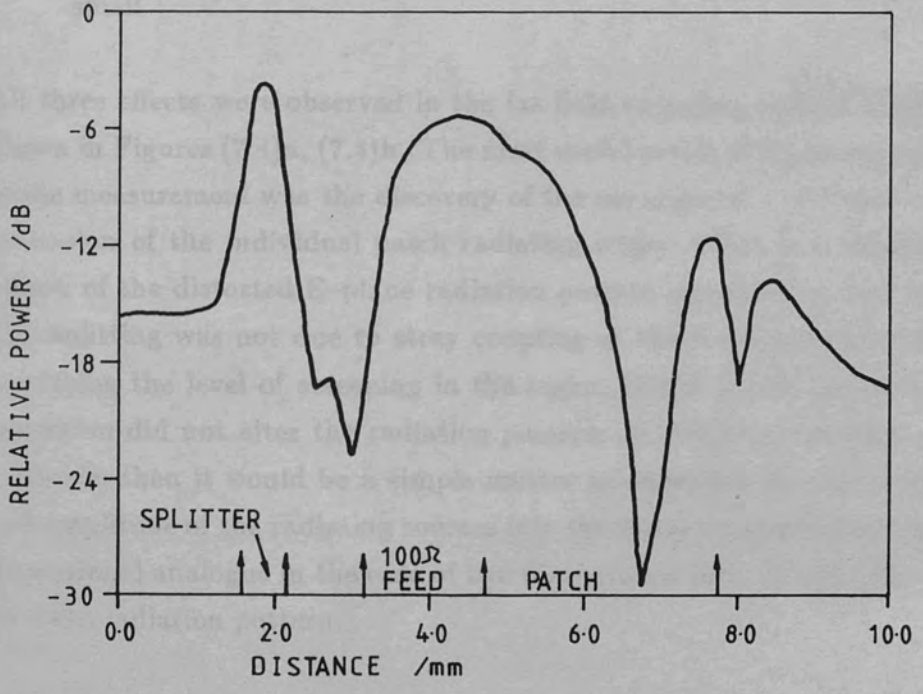

Figure (7.9)b Cross section along the axis of the microstrip feed, inner right hand element

viz.:

(a) the radiating edge excitation amplitude on a given patch shows the opposite asymmetry to that observed in the inner pair, ie the edge opposite to the feed point is the most strongly excited.

(b) the excitation of the radiating edge that incorporates the microstrip feed is non–uniform and tapers in magnitude by approximately -7.5 dB from the inner to the outer extremity of the radiating edge.

The significance of these observations in terms of the far–field radiation pattern can be summarized as follows:

(a) the combined amplitude and phase asymmetry of the radiating edges on each patch element will cause distortion of the E–plane radiation pattern

(b) the excitation of the array is symmetric about the axis of the primary 50 Ω microstrip feed, therefore the H–plane radiation pattern will be free from distortion

(c) there is no evidence of a strong cross polarized component in the patch excitation, therefore the cross–polar radiation in the far field should be small

All three effects were observed in the far field radiation pattern measurement shown in Figures (7.4)a, (7.4)b. The most useful result of the scanning network probe measurement was the discovery of the asymmetric phase and amplitude excitation of the individual patch radiating edges, which is a possible explanation of the distorted E–plane radiation pattern measured at this frequency. The splitting was not due to stray coupling at the waveguide aperture, since increasing the level of screening in the region of the waveguide to microstrip transition did not alter the radiation pattern. If phase information were also available, then it would be a simple matter to substitute the measured phase and amplitude of the radiating sources into the linear array equation (or its two dimensional analogue in the case of two dimensional arrays) and hence find the far–field radiation pattern.

The $|E_z|^2$ distribution at the higher operating frequency of 37.8 GHz is shown in Figure (7.10). Unlike the $|E_z|^2$ distribution measured at 33.8 GHz, the individual patch excitation modes are not clearly visible. Since the power

SCALE

$X, Y = 2.0\,mm/division \qquad Z = 2\,dB/level$

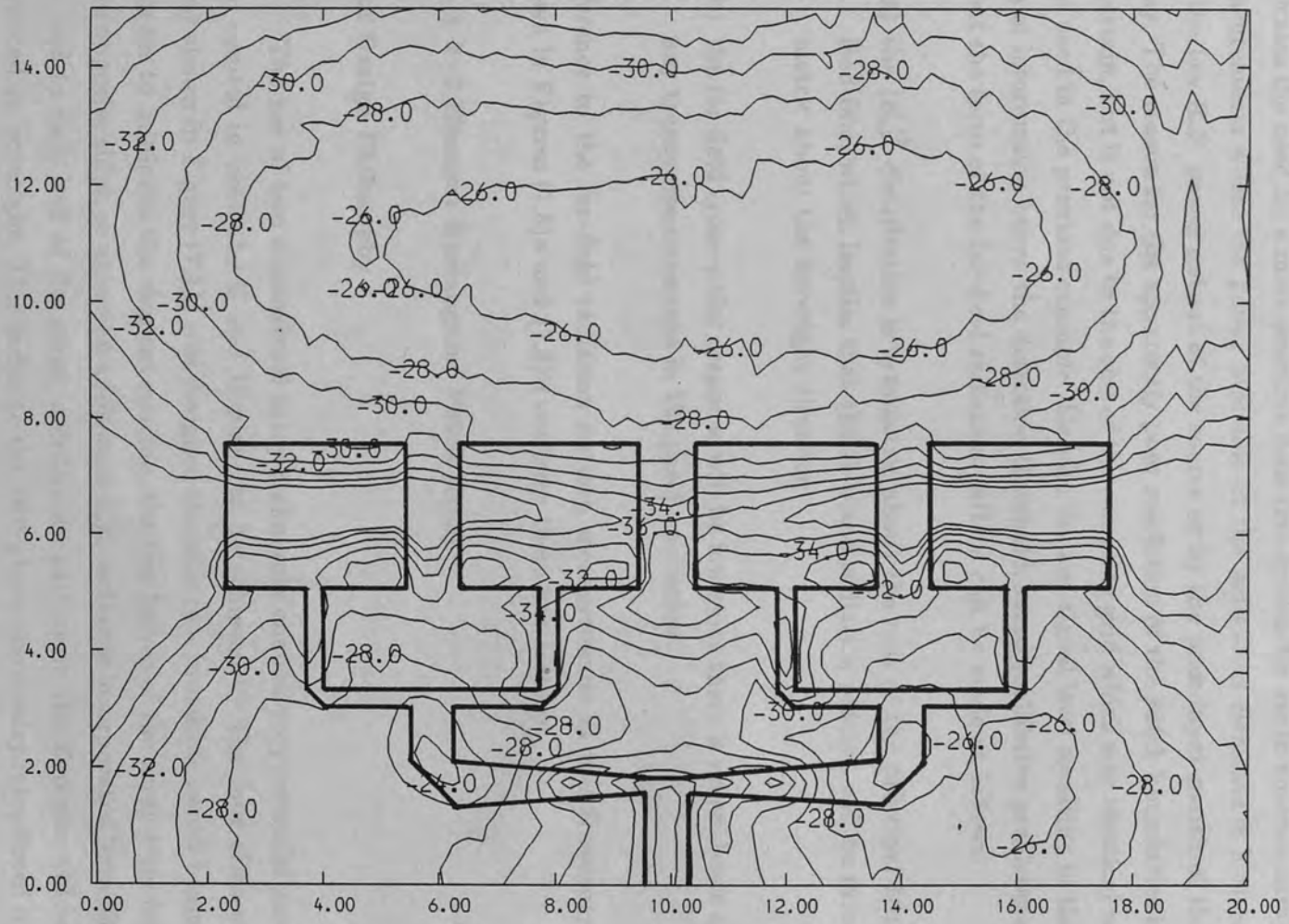

Figure(7.10) Linear 4 Element Array $|E_z|^2$ Distribution, F=37.8 *GHz*

launched into the array was reduced by approximately $10\,dB$ due to the poor input match of the array, the amplitude of the probe signal detected in the array is correspondingly low. The low power input has limited the dynamic range of the detection system, the maximum signal detected being only $15\,dB$ above the minimum detectable signal for square law operation. This highlights the problem of the limited sensitivity afforded by direct video detection, and indicates the need for a more sensitive detection system for use in antenna array measurements where the power available at the individual elements is limited by the low R.F. power output of the source or by the poor input match of the array. The reason for the apparently poor resolution of the patch boundaries is uncertain, but it not due to the size of the sampling grid which was identical to that used in the previous example. Despite the low signal level resulting in the loss of information below the detection threshold, some qualitative predictions about the form of the far–field radiation pattern can be made as follows:

(a) the $|E_z|^2$ distribution is symmetric about the axis of the principal $50\,\Omega$ feed line, which implies that the H–plane radiation pattern will be symmetric about the boresight direction

(b) the far field cross–polar response will be low since there is no evidence of any transverse resonance in the patch excitation.

Reference to the far–field radiation pattern measurements at this frequency, shown in Figures (7.5)a and (7.5)b confirms these two features.

7.3 A 2×2 Element Rectangular Patch Array

7.3.1 Design Philosophy

The use of two dimensional array techniques enables very versatile pattern control in both the E and H–plane to be achieved.[7.1] The four element array shown in Figure (7.11) was designed to produce a broadside pencil beam. In order to minimize the element spacing, the two halves of the array were fed from opposite sides, so unless an additional $\lambda_g/2$ section is incorporated between the feed to each half of the array, a difference pattern in the E–plane will be produced on boresight. This is due to the 180° phase asymmetry introduced by the feed geometry. The $\lambda_g/2$ phasing section was overlooked when the final artwork for the mask was produced, thus the array was expected to exhibit a split E–plane radiation pattern. The dimensions of the patch elements were identical to those employed in the four element linear array design, and correspond to

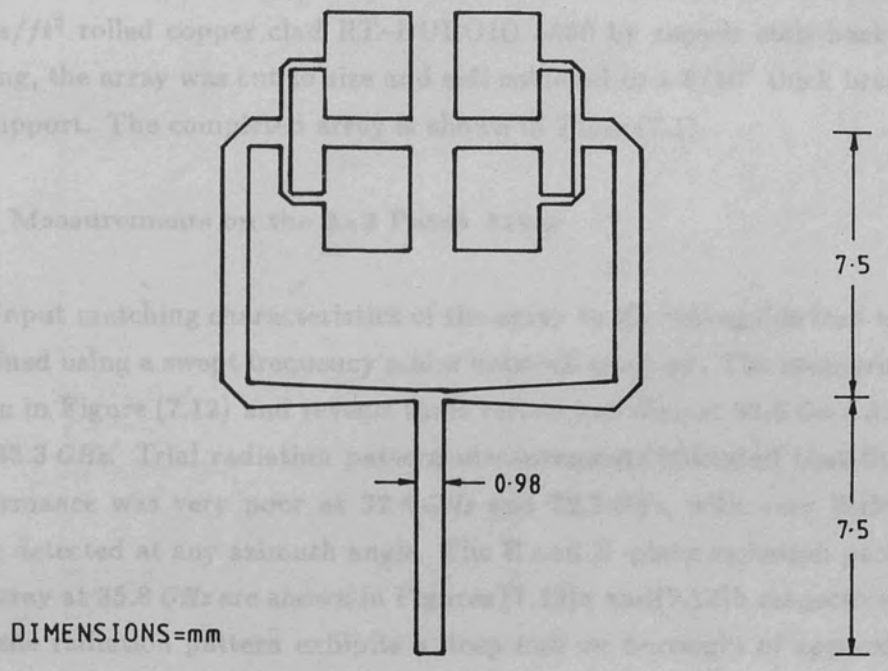

Figure (7.11) 2×2 patch array outline

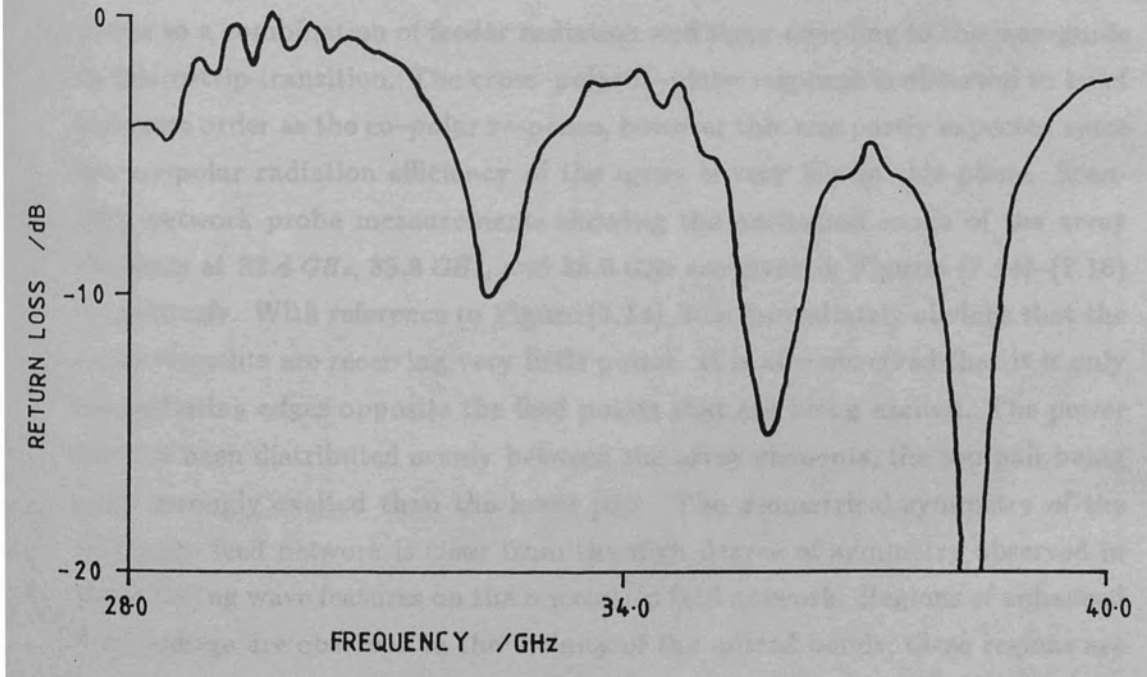

Figure (7.12) 2×2 patch array return loss

an isolated patch resonant frequency of $35\,GHz$. The corporate feed network was constructed using three microstrip T–junction power splitters of the same design described in section (7.2.1). The array was fabricated on $0.254\,mm$ thick, $1/2\,oz/ft^2$ rolled copper clad RT–DUROID 5880 by copper etch–back. After etching, the array was cut to size and soft soldered to a 3/16" thick brass plate for support. The completed array is shown in Plate (7.1).

7.3.2 Measurements on the 2×2 Patch Array

The input matching characteristics of the array to the waveguide feed were determined using a swept frequency scalar network analyser. The measurement is shown in Figure (7.12) and reveals three return loss dips at 32.4 *GHz*, 35.8 *GHz*, and 38.3 *GHz*. Trial radiation pattern measurements indicated that the array performance was very poor at 32.4 *GHz* and 38.3 *GHz*, with very little power being detected at any azimuth angle. The E and H–plane radiation patterns of the array at 35.8 *GHz* are shown in Figures (7.13)a and(7.13)b respectively. The E–plane radiation pattern exhibits a deep null on boresight of approximately -20 *dB* relative to the peak response which occurs at angles of ±30° from boresight. The cause of the split beam is the 180° phase difference introduced by the corporate feed geometry, as described in the previous section. The E–plane cross–polar response is approximately -13 *dB* down with respect to the co–polar beam. The slight asymmetry in the E–plane radiation pattern suggests that the element excitation was not equal about the array axis of symmetry. The co–polar H–plane response of the array is poor, and exhibits distortion which is due to a combination of feeder radiation and stray coupling to the waveguide to microstrip transition. The cross–polar H–plane response is observed to be of the same order as the co–polar response, however this was partly expected since the co–polar radiation efficiency of the array is very low in this plane. Scanning network probe measurements showing the excitation mode of the array elements at 32.4 *GHz*, 35.8 *GHz*, and 38.3 *GHz* are given in Figures (7.14)–(7.16) respectively. With reference to Figure (7.14), it is immediately obvious that the array elements are receiving very little power. It is also observed that it is only the radiating edges opposite the feed points that are being excited. The power has not been distributed evenly between the array elements, the top pair being more strongly excited than the lower pair. The geometrical symmetry of the corporate feed network is clear from the high degree of symmetry observed in the standing wave features on the microstrip feed network. Regions of enhanced field leakage are observed in the vicinity of the mitred bends; these regions are also symmetric about the H–plane axis of the array. The VSWR estimated by cross–sectioning the data along each of the $50\,\Omega$ microstrip feed lines located at

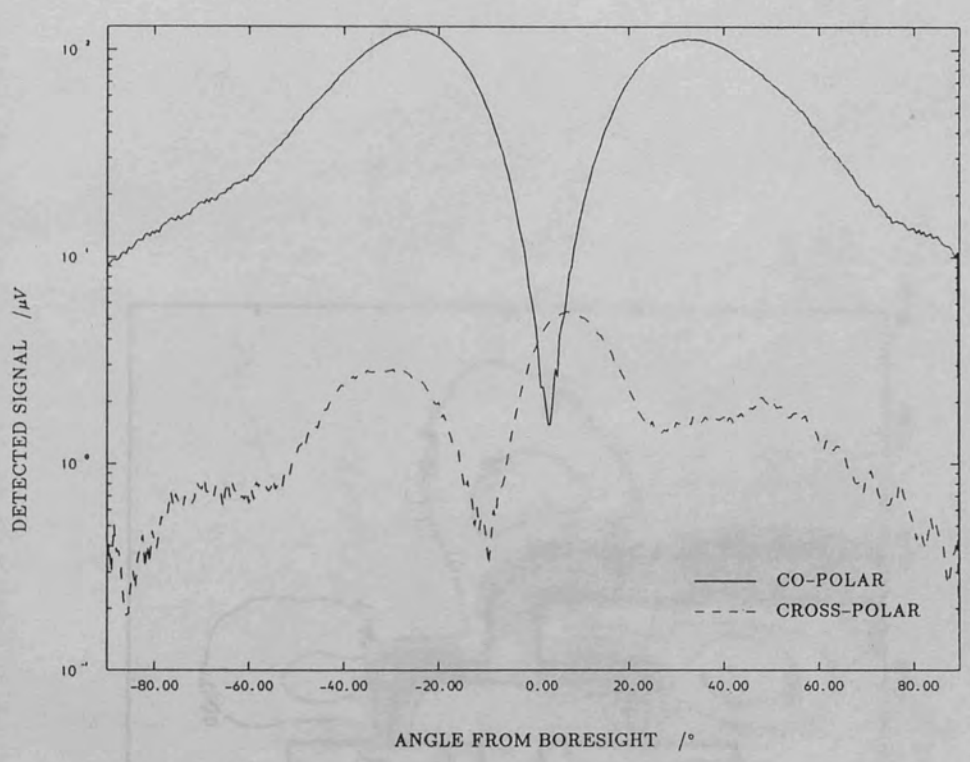

Figure (7.13)a 2×2 element array E–plane radiation pattern, F=35.8 *GHz*

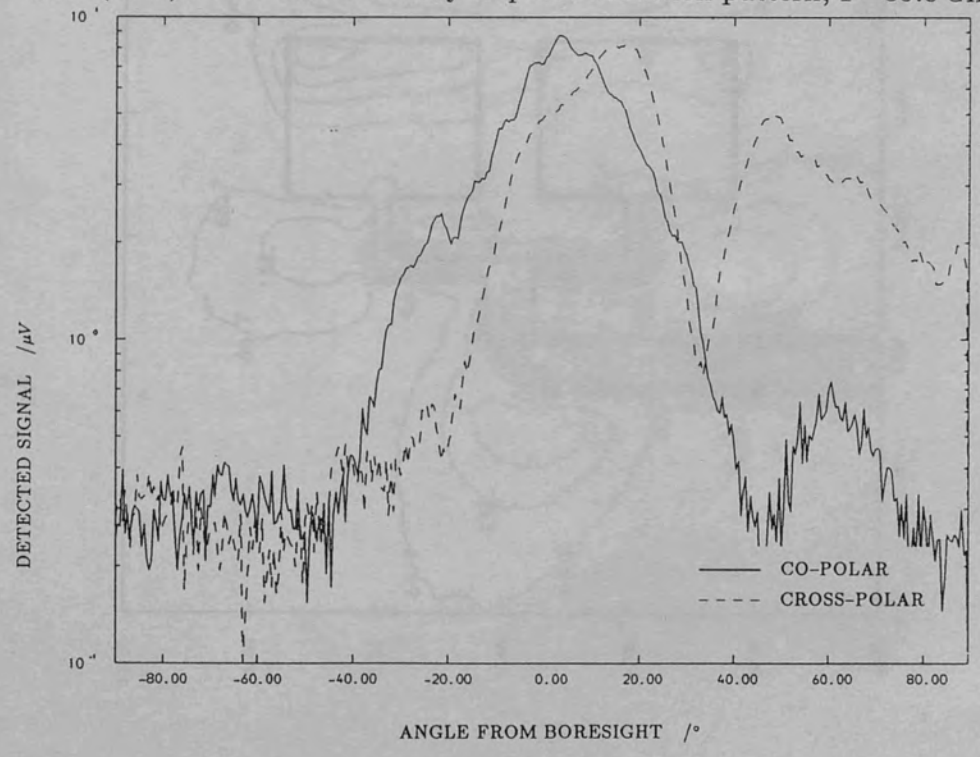

Figure (7.13)b 2×2 element array H–plane radiation pattern, F=35.8 *GHz*

SCALE

$X, Y = 2.0\,mm/division \qquad Z = 66.66\,\mu V/level$

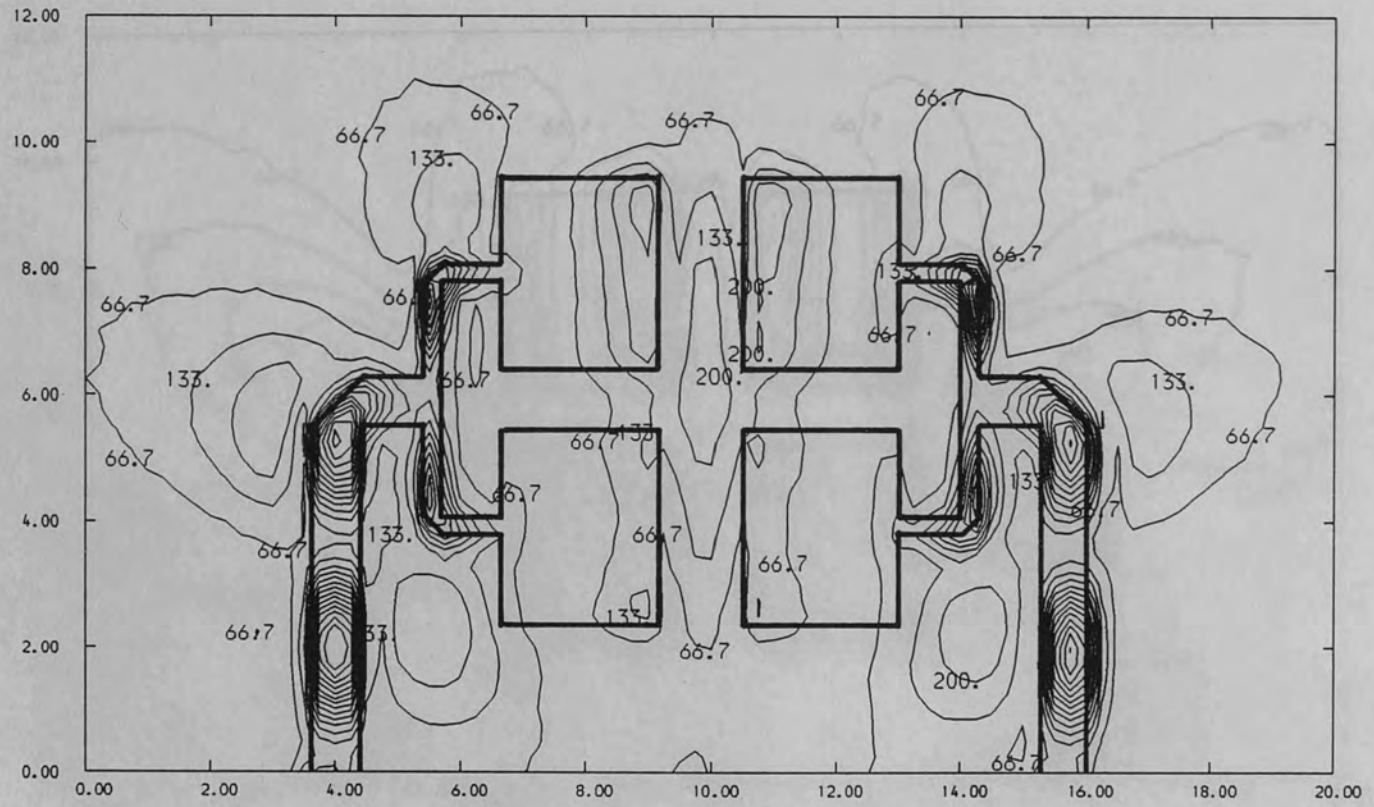

Figure(7.14) 2×2 Element Patch Array $|E_z|^2$ Distribution, F=32.4 *GHz*

SCALE

$X, Y = 2.0\,mm/division \qquad Z = 66.66\,\mu V/level$

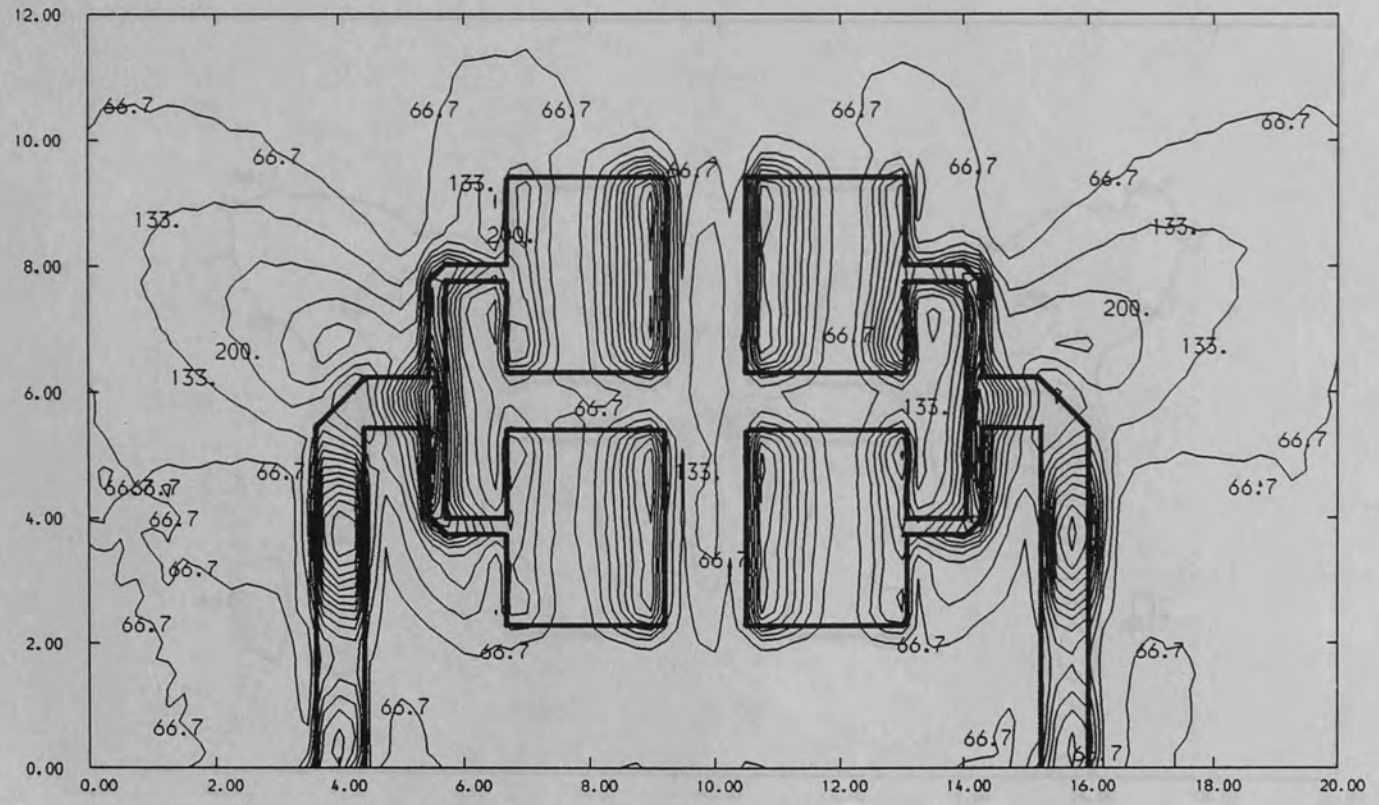

Figure(7.15) 2×2 Element Patch Array $|E_z|^2$ Distribution, F=35.6 *GHz*

SCALE

$X, Y = 2.0\,mm/division \qquad Z = 66.66\,\mu V/level$

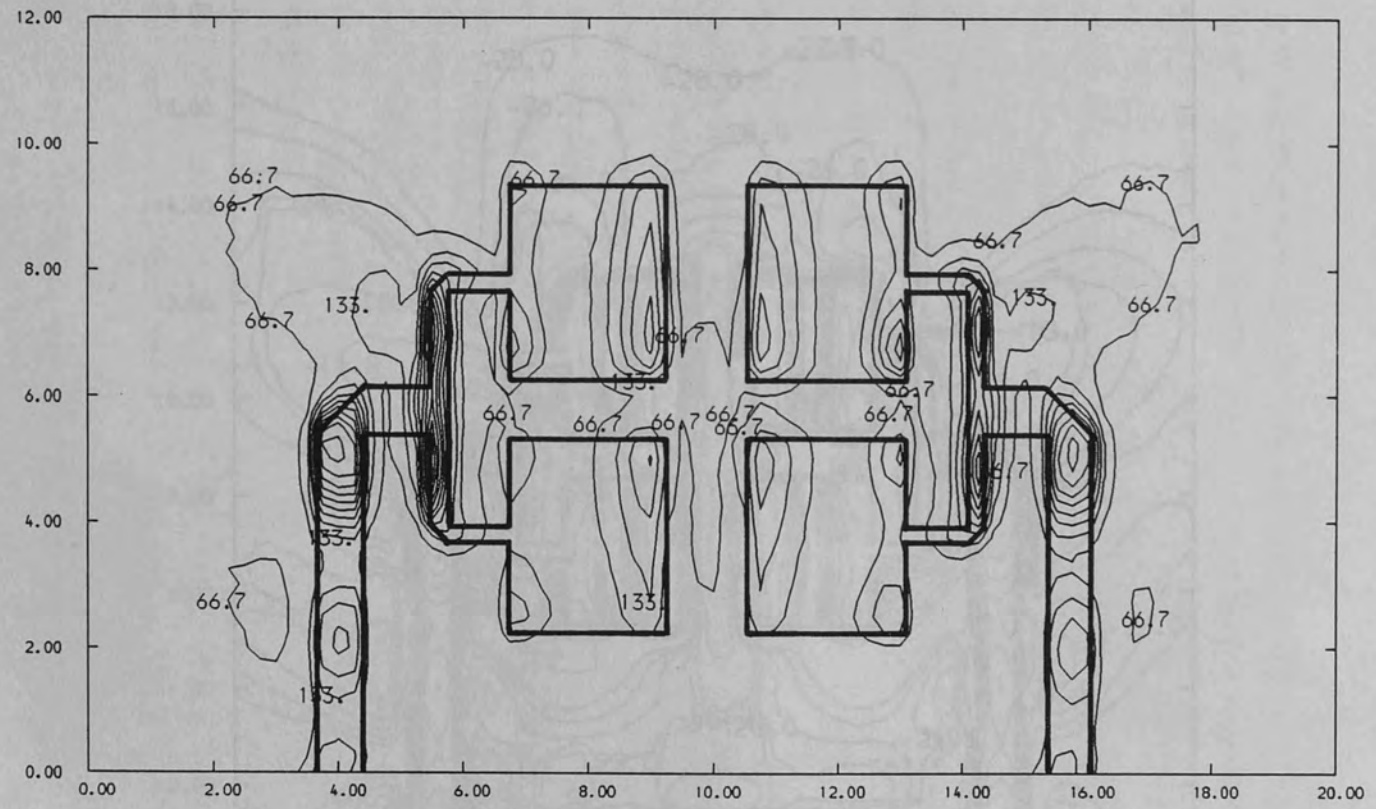

Figure(7.16) 2×2 Element Patch Array $|E_z|^2$ Distribution, F=38.3 *GHz*

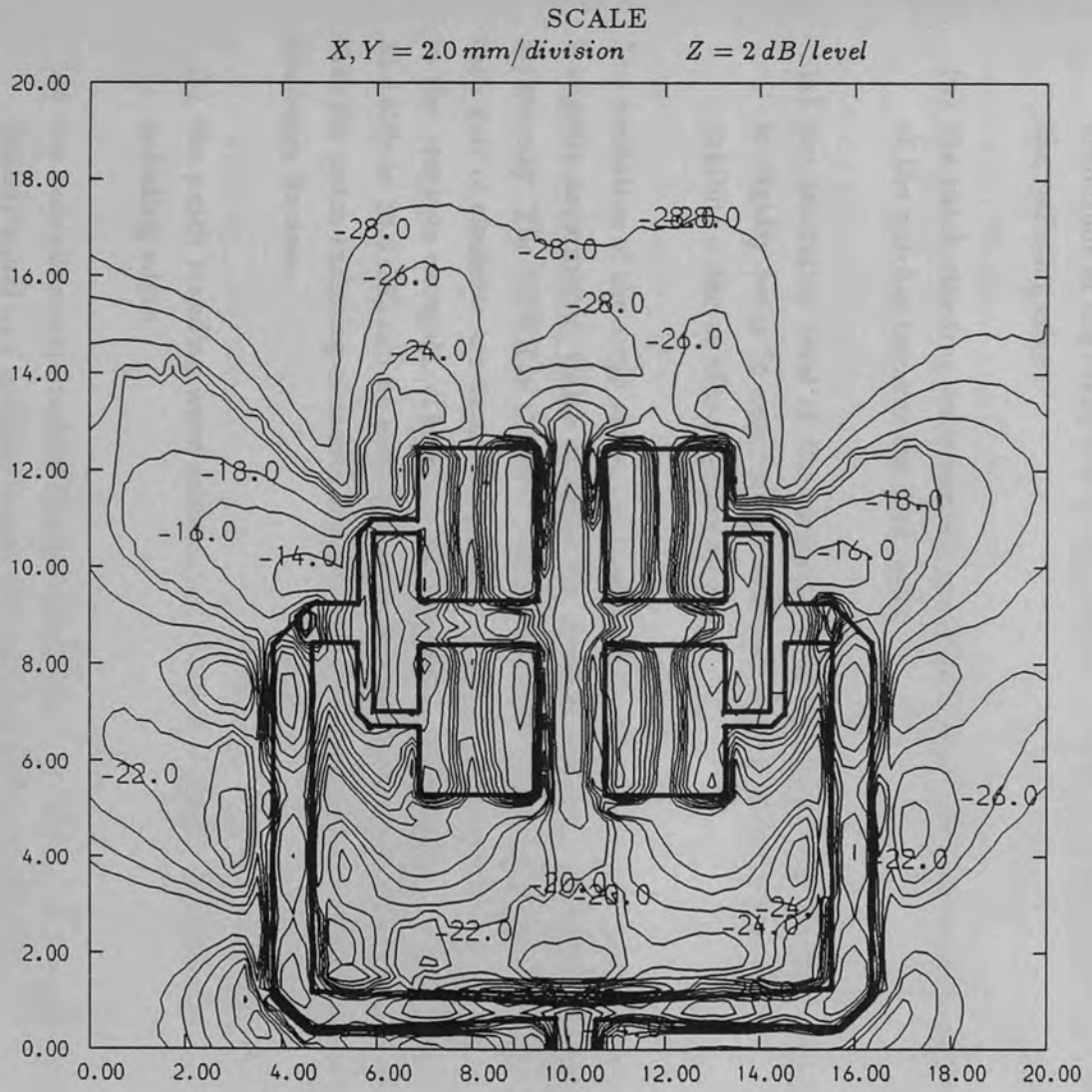

Figure(7.17) 2×2 Element Patch Array $|E_z|^2$ Distribution, F=36.8 *GHz*

$x = 4.00\,mm$, and $x = 15.75\,mm$ is found to be approximately 4.0 in both lines.

The equivalent measurement at 35.8 *GHz* is shown in Figure (7.15). At this frequency the patch radiators were strongly excited, therefore indicating that the array will radiate efficiently. The excitation mode exhibited by the patches is characteristic of that observed in an isolated patch excited below its resonant frequency, i.e.:

(a) the radiating edge opposite the feed point is strongly excited and the amplitude of the excitation is approximately uniform along the length of the radiating edge

(b) the patch standing wave minima are shifted from the geometrical centre of the patches towards the feed point

(c) the excitation level of the radiating edge incorporating the feed point is slightly lower in comparison with the opposing radiating edge, and exhibits a degree of non–uniformity

The excitation of the array about the H–plane axis of symmetry at $x = 10.00\,mm$ is slightly asymmetric, which explains the E–plane observed radiation pattern asymmetry. The VSWR in the $50\,\Omega$ feed lines is found to be 2.5, indicating that each pair of elements are better matched to the $50\,\Omega$ microstrip feed lines than in the previous example. The effect of increasing the frequency slightly from 35.8 *GHz* to 36.8 *GHz* can be seen in Figure (7.17). The measurement indicates that the patch radiating elements are being excited very close to their resonant frequency because:

(a) the patch standing wave minima are located centrally between the two radiating edges

(b) the excitation amplitude of the radiating edges on each patch are approximately equal and uniform across the patch non–resonant width

The VSWR in the $50\,\Omega$ feedlines is found to be 2.0.

The final scanning network probe measurement on this array was carried out at 38.3 *GHz* and is shown in Figure (7.16). The result shows that excitation of the patch radiating edges is relatively weak compared to previous example, and from cross-section data the VSWR in the $50\,\Omega$ feed lines is found to be 4.5.

The high VSWR indicates that over 40% of the power incident on each of the patch array element pairs was being reflected back towards the generator and is in direct conflict with the return loss of $26\,dB$ measured in the waveguide feed. It is assumed that the relative phases of the antenna and waveguide to microstrip transition mismatches were such that cancellation occurred in the waveguide feed.

The cross polar performance of this array was poor compared to the four element linear array. No evidence of high order transverse patch modes was observed in either of the two arrays examined, therefore the source of the cross–polar radiation must be related to the corporate feed network. The significant difference between the two examples is the form of the leakage field regions. In the first example the majority of the returning E–field lines possess tangential components that are co–polar with those generated by the patch radiating edges, therefore they do not act as sources of cross–polar radiation, but will contribute to the co–polar radiation pattern. In the second example of the 2×2 array it is observed from symmetry that the resolved tangential components of the electric field lines at the mitred bends will cancel in the co–polar plane, but will add in phase to produce a net cross–polar response. The total effect of these sources in the far–field is dependant on their relative phase and amplitude in addition to their geometric location and orientation. The lack of a phase sensitive measurement system prevented the full exploitation of the scanning network probe technique in this respect. The ability to measure phase and amplitude in this example would have allowed a quantitative prediction of the spurious components of the far–field radiation pattern to be made.

7.4 A Four Element Patch Array for Circularly Polarized Applications

7.4.1 Design Considerations

Circularly polarized radiation can be obtained from microstrip antennas in a variety of ways, for example:

(a) exciting orthogonal modes in a nearly square patch antenna, either by a dual feed[7.7] or corner feed technique

(b) exciting coupled modes in more "exotic" geometry antennas such as the pentagonal patch antenna[7.8]

(c) adjusting the phase and amplitude distribution of the radiation from microstrip bends in the "rampart" line antenna described by James, Hall, and Wood.[7.9]

(d) using an array of linearly polarized microstrip elements arranged in a suitable geometry

The proposed design for a circularly polarized microstrip array employing rectangular patch antennas is shown in Figure (7.18). The patches are arranged so that their E–vectors are mutually orthogonal, and are fed with a progressive phase shift of $\pi/2$ radians between each successive element. The secondary power splitters incorporate an extra $\lambda_g/4$ section in one output arm in order to obtain a relative phase shift of $\pi/2$ between the power splitter outputs. The primary power splitter includes a $\lambda_g/2$ phasing section in one output arm, therefore each of the secondary power splitters is excited with a relative phase difference of π. The corporate feed network shown in Figure (7.18) generates a progressive phase lag of $\pi/2$ between adjacent elements in a clockwise sense. The array design does not represent an optimum solution to obtain circular polarization, however the array geometry is of interest because:

(a) it allows the behaviour of the microstrip T-junction to be observed when its output arms are asymmetrically mismatched

(b) the orthogonal layout of the patch radiators should reduce the mutual coupling between the array elements

The patch array elements and the power splitter utilized were identical to those employed in the previous array designs. The array was etched onto $1/2oz/ft^2$ rolled copper clad $0.254\,mm$ thick RT–DUROID 5880 and then soft soldered to a 3/16" thick brass plate for mechanical support. Power was coupled to the array via a stepped ridged waveguide to microstrip transformer as before.

7.4.2 Array Measurements

Figure (7.19) shows the measured return loss in the waveguide feed over the frequency range 28 GHz to 40 GHz. Four principal resonances are observed at frequencies of 28.9 GHz, 31.8 GHz, 34.9 GHz, and 39.8 GHz. The $|E_z|^2$ area scan measurements made with the $0.5\,mm$ diameter nickel sheathed probe corresponding to these frequencies are given in Figures (7.20) to (7.23). The contour plots have been thresholded $10\,dB$ above the noise floor of the detector in order

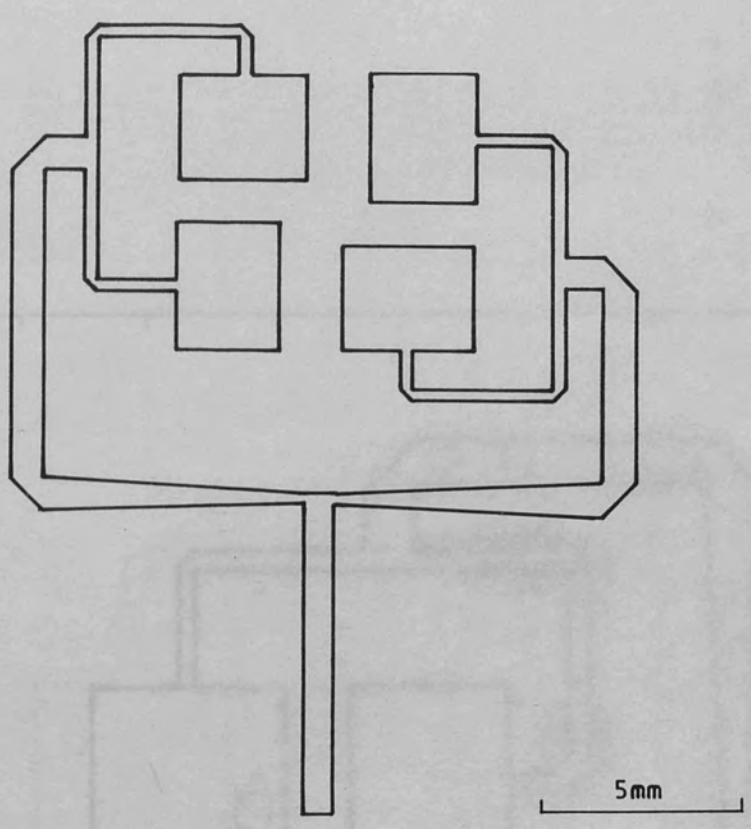

Figure (7.18) C.P. array outline

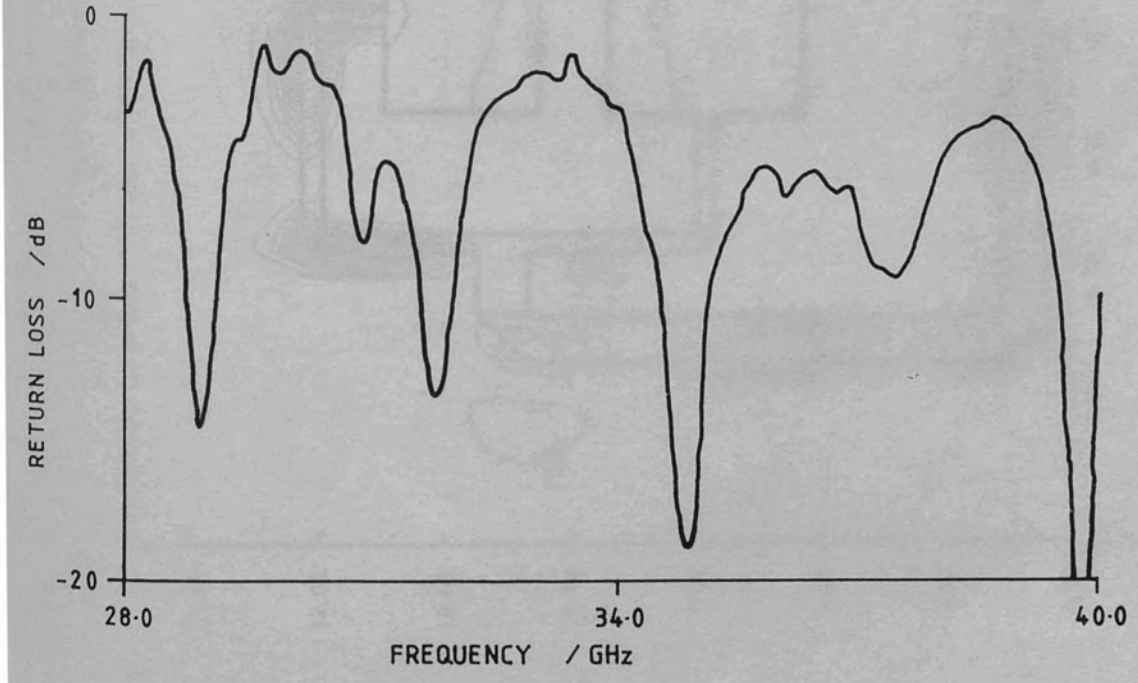

Figure (7.19) C.P. array return loss

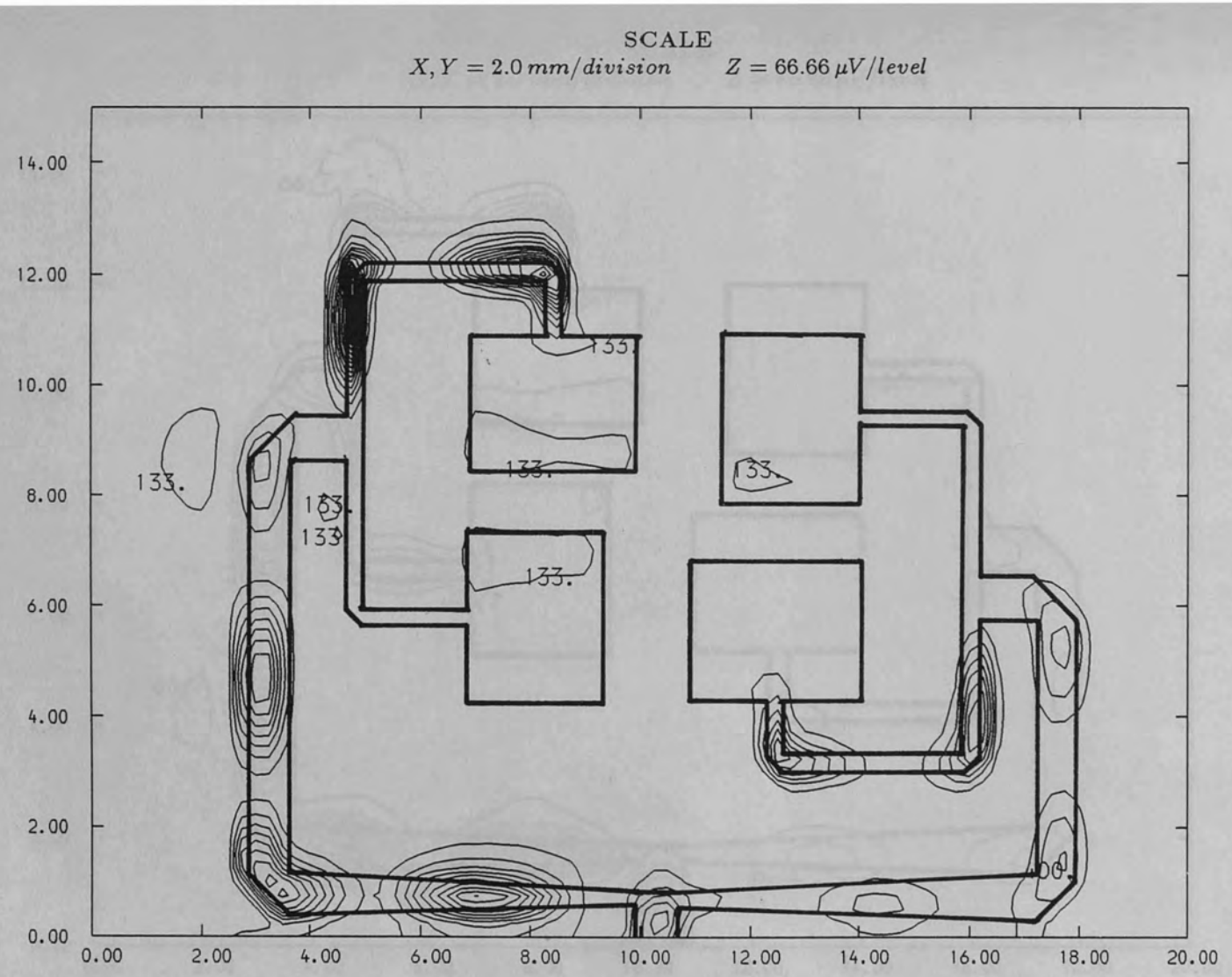

Figure(7.20) 4 Element C.P. Array $|E_z|^2$ Distribution, F=28.9 *GHz*

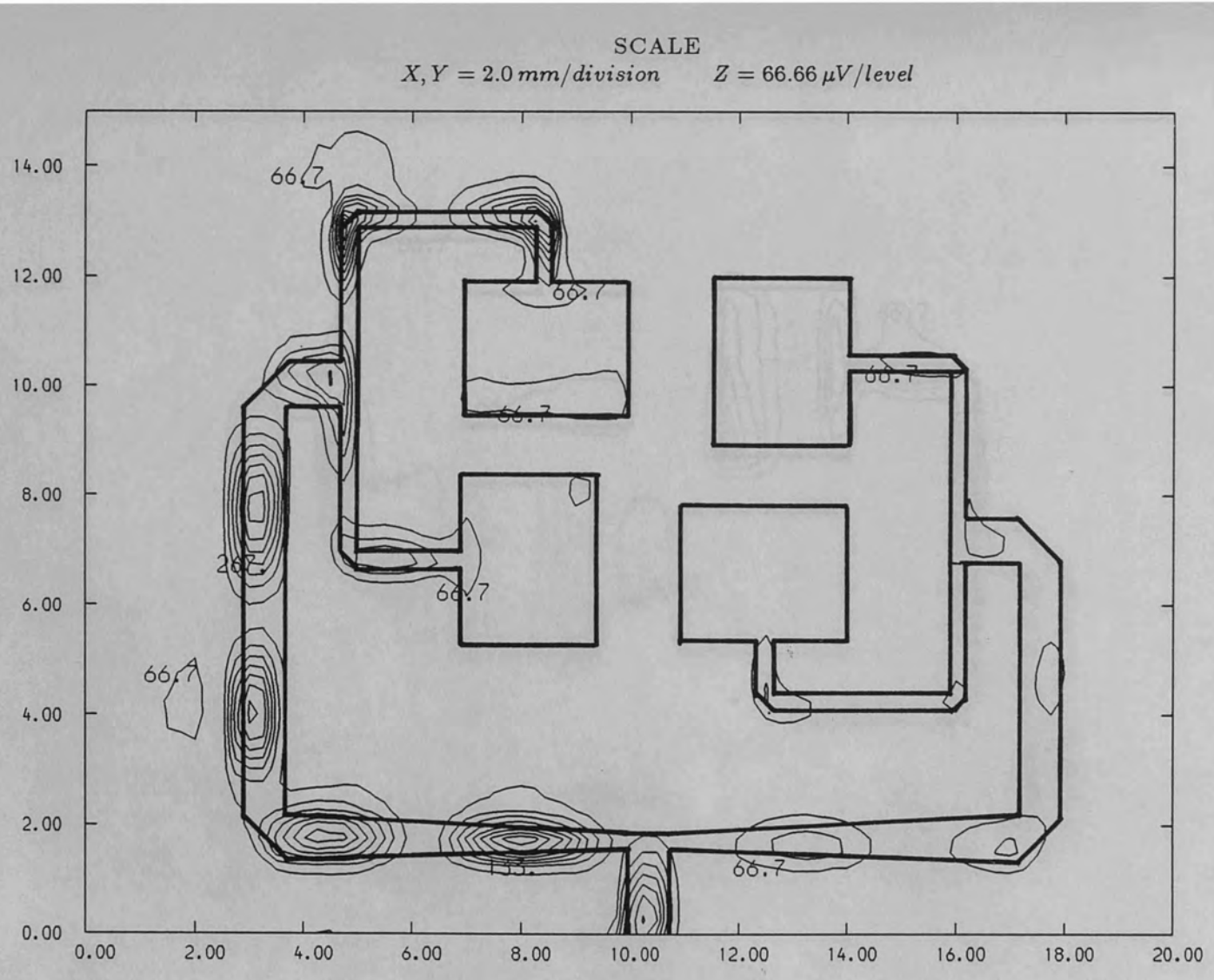

Figure(7.21) 4 Element C.P. Array $|E_z|^2$ Distribution, F=31.8 *GHz*

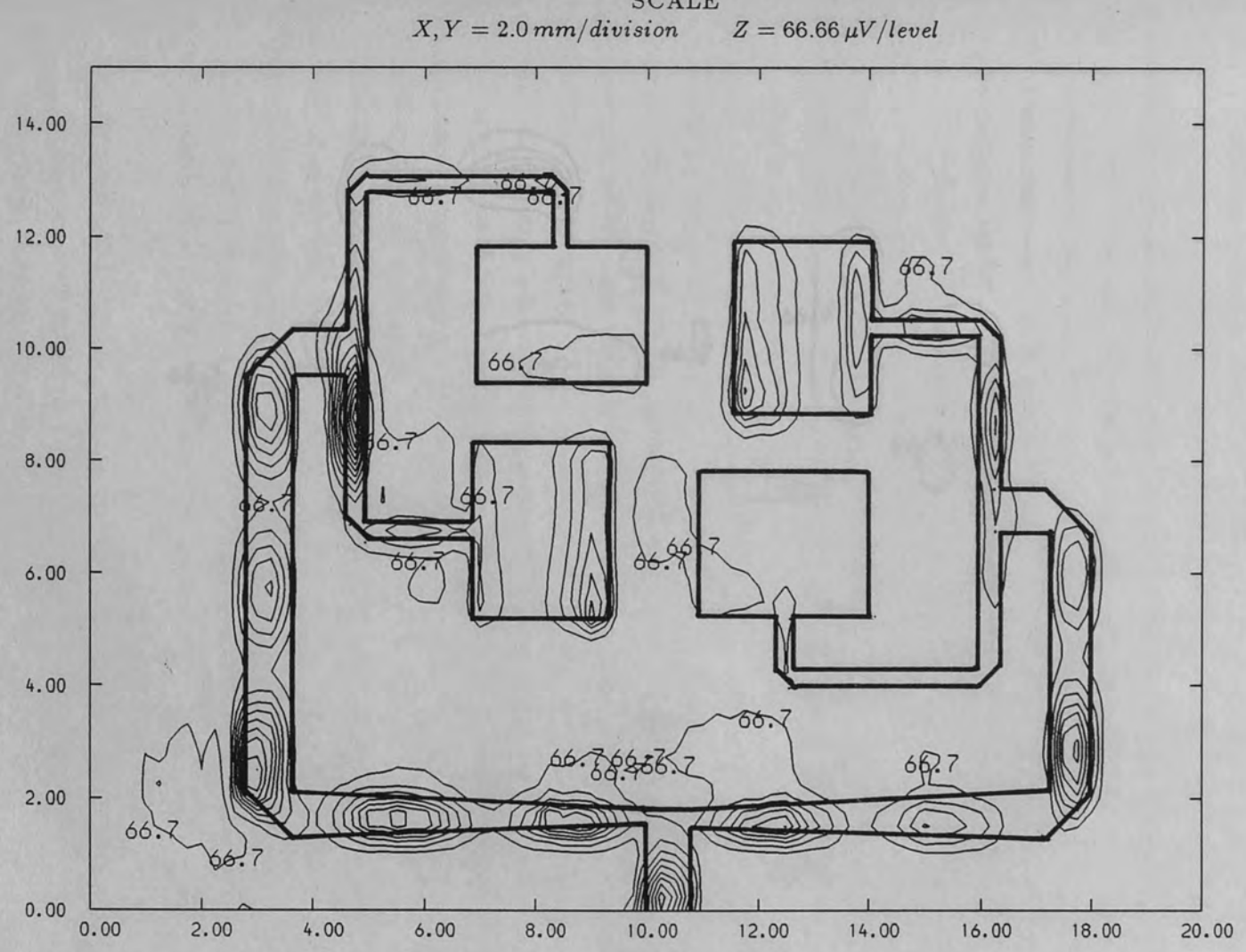

Figure(7.22) 4 Element C.P. Array $|E_z|^2$ Distribution, F=34.9 *GHz*

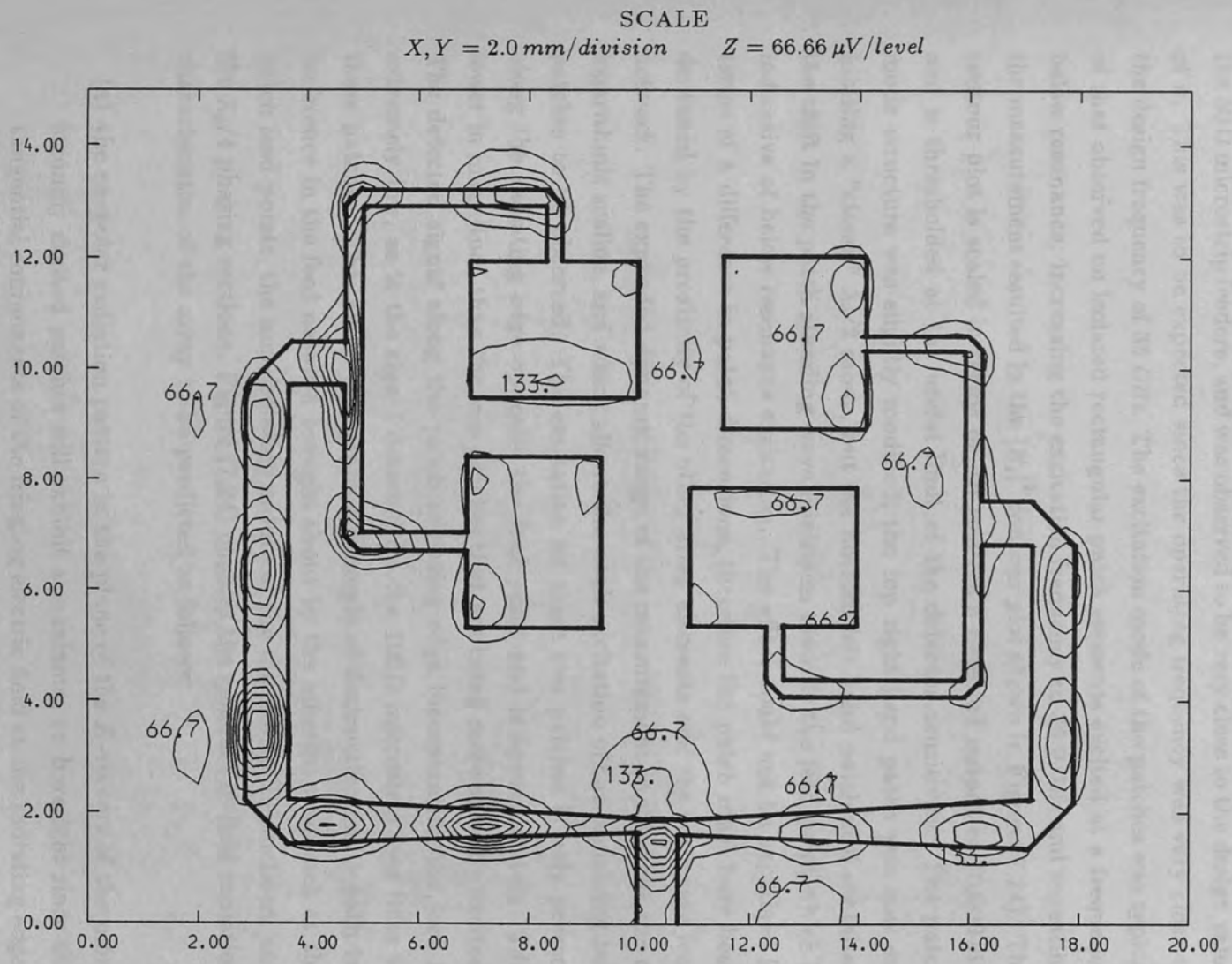

Figure(7.23) 4 Element C.P. Array $|E_z|^2$ Distribution, F=39.8 *GHz*

to enhance the visibility of the regions of high excitation. It was clear from these measurements that the only frequency at which any of the elements were strongly excited was 34.9 *GHz*. It was also observed that the power split between the elements was unequal at this frequency; the patches fed via the $\lambda_g/4$ phasing section apparently receiving no power. The phasing of the inputs to the secondary power splitters can be estimated from the standing wave distribution on the $50\,\Omega$ microstrip feeders, and was observed to be very close to the design value of π. This was to be expected since the operating frequency was very close to the design frequency of 35 *GHz*. The excitation mode of the patches was typical of that observed on isolated rectangular patch elements excited at a frequency below resonance. Increasing the excitation frequency to 35.9 *GHz* and repeating the measurement resulted in the $|E_z|^2$ contour plot shown in Figure (7.24). The contour plot is scaled in terms of *dB* relative a detected output of $10{,}000\,\mu V$, and is thresholded at the useful limit of the detector sensitivity. The patch mode structure was slightly modified; the top right hand patch was now exhibiting a "classic" $\lambda_g/2$ mode, but the bottom left hand patch still exhibited the shift in the patch standing wave minimum towards the feed point which is indicative of below resonance excitation. The effect could not be explained in terms of a difference in patch dimensions, therefore the patch must have been de–tuned by the proximity of the other array elements and the corporate feed network. The expanded dynamic range of the measurement enabled the use of logarithmic scaling, and which allows the weak excitation of the remaining two patches to be observed. The excitation on these two patches is only present along the radiating edge opposite the feed point and is approximately $12\,dB$ lower in magnitude than the two patches that are being more strongly excited. The detected signal along the patch radiating edge incorporating the feed is extremely low, as is the signal detected on the $100\,\Omega$ microstrip feed lines to these patches. This result is a graphic example of destructive multi–path interference in the feed network brought about by the inherent mismatch at the patch feed points, the non–isolating nature of the microstrip T–junctions, and the $\lambda_g/4$ phasing sections. Figure (7.24) enables the general far–field radiation characteristics of the array to be predicted as follows:

(a) the co–polar radiation pattern in the plane of the E–vectors of the more strongly excited patches will exhibit a maximum on boresight since the tangential components of the fringing electric field at the radiating edges of the two patches will be in phase

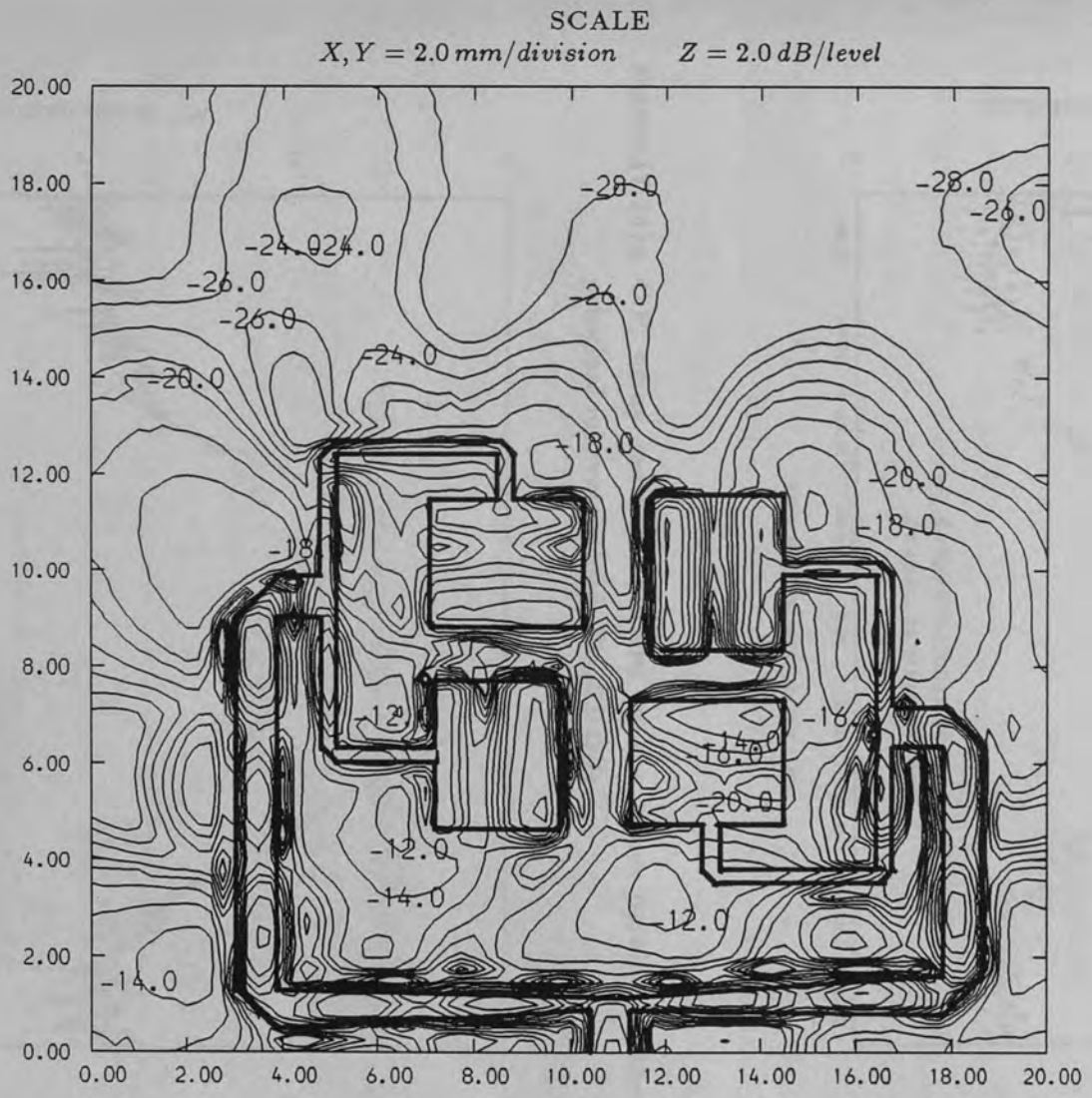

Figure(7.24) 4 Element C.P. Array $|E_z|^2$ Distribution, F=35.9 *GHz*

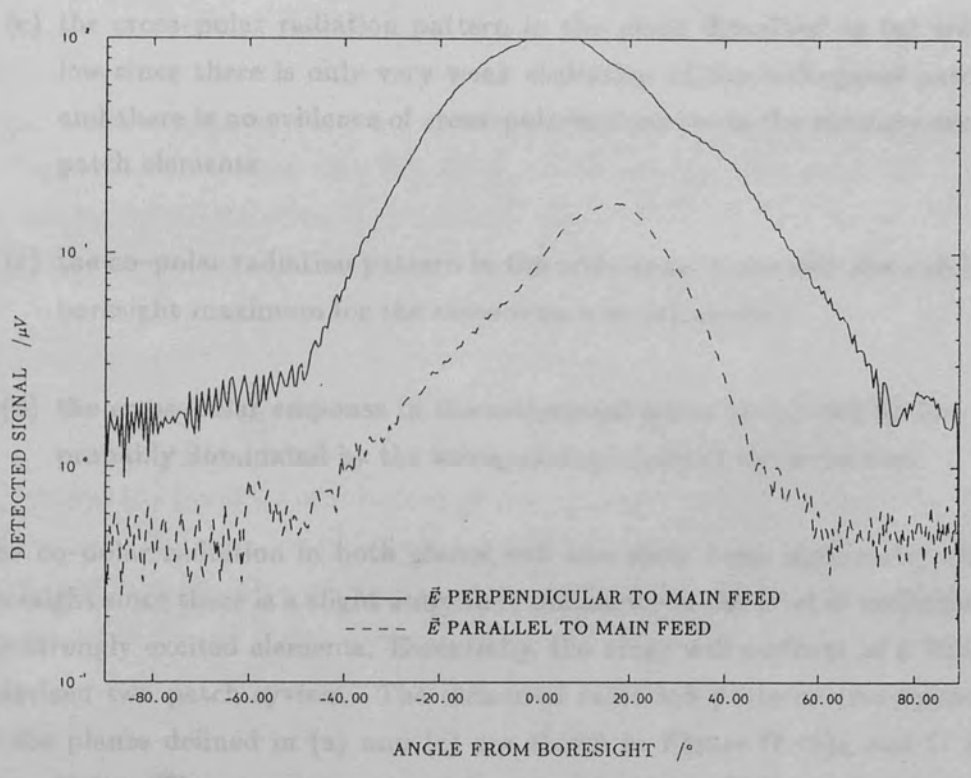

Figure (7.25)a C.P. array radiation pattern in the plane parallel to the principal microstrip feed, F=35.9 *GHz*

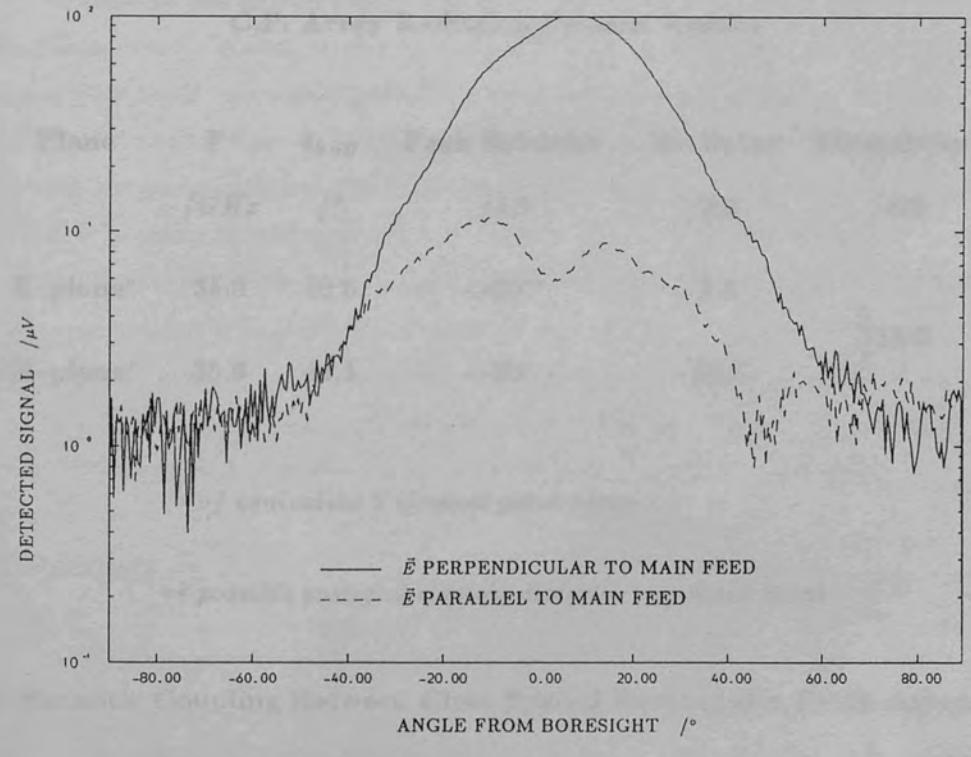

Figure (7.25)b C.P. array radiation pattern in the plane perpendicular to the principal microstrip feed, F=35.9 *GHz*

(c) the cross–polar radiation pattern in the plane described in (a) will be low since there is only very weak excitation of the orthogonal patches, and there is no evidence of cross–polarized modes in the strongly excited patch elements

(c) the co–polar radiation pattern in the orthogonal plane will also exhibit a boresight maximum for the same reason as (a) above

(d) the cross–polar response in the orthogonal plane to (a) will be low and probably dominated by the waveguide aperture of the transition

The co–polar radiation in both planes will also show some asymmetry about boresight since there is a slight amplitude imbalance in the level of excitation of the strongly excited elements. Essentially, the array will perform as a linearly polarized two patch system. The measured radiation patterns corresponding to the planes defined in (a) and (c) are shown in Figure (7.25)a and (7.25)b respectively. The measurements summarized in Table (7.2) confirm that the array is indeed operating as a pair of linearly polarized patch radiators.

TABLE (7.2)

C.P. Array Radiation Pattern Results

Plane	F /GHz	$\theta_{3\,dB}$ /°	Peak Sidelobe /dB	X– Polar /dB	Directivity /dB_i
E–plane*	35.9	40.6	<-20**	-7.5	15.0
H–plane*	35.9	44.1	<-20**	-10.7	

* *of equivalent 2 element patch array*

** *possible vestigial sidelobe distortion of main beam*

7.5 Parasitic Coupling Between Close Spaced Rectangular Patch Antennas

Several papers have been published concerning the mutual coupling between microstrip antennas.[7.2,7.10–12] Even in the simplest case where only

space wave coupling is considered,[7.11] the calculation requires the use of numerical techniques. In order to estimate the level of parasitic coupling between microstrip patch antennas the simple experimental arrangement shown in Figure (7.26) was set up. The single patch radiator which was fabricated for the mode investigation in chapter (4) was employed as the driven element of a two element parasitically coupled patch array. The parasitic element was cut from 20 μm thick copper foil to the same dimensions as the driven element. The parasitic patch could therefore be positioned anywhere on the surface of the substrate. The level of parasitic coupling was determined by measuring the amplitude of excitation at each of the patch edges using the 0.5 mm nickel sheathed probe. For the purposes of this experiment, the probe was operated under manual control. The variation of the measured excitation amplitude of the radiating edges with the patch to parasite separation for the E–plane coupled geometry illustrated in Figure (7.26) is shown in Figure (7.27). The measurements were all normalized to the amplitude of the driven patch radiating edge located at the feed point. It was observed that the excitation level falls off linearly with increasing separation. The amplitude of the signal measured on the edge of parasitic element closest to the driven element is seen to peak slightly at a parasite separation of 0.06 λ_0. The other parasite radiating edge peaks at a slightly closer separation of 0.05 λ_0. At separations greater than 0.07 λ_0, the measurement is limited by the noise floor of the detector. Figure (7.26) also shows the variation of the driven patch feed point amplitude with the patch–parasite separation, which is seen to decrease at the same rate as the radiating edges of the parasite until the patch–parasite separation reaches 0.06 λ_0 after which the amplitude remains constant. This indicates that the loading of the driven patch becomes insignificant when the element separation is greater than 0.06 λ_0. With the aid of a more sensitive detection system, (or a high power R.F. source) it would be possible to plot the amplitude of the parasitic element excitation at larger separations which would be more representative of typical array spacings. The parasitic coupling is observed to be strong up to separations of about one substrate thickness, which suggests that the coupling between the parasite and the driven element is via the fringing electric field at the patch edges.

7.6 Summary

In this chapter it has been demonstrated that the scanning network probe is capable of providing more physical insight into the operation of microstrip antenna arrays than is possible from simple return loss and radiation pattern

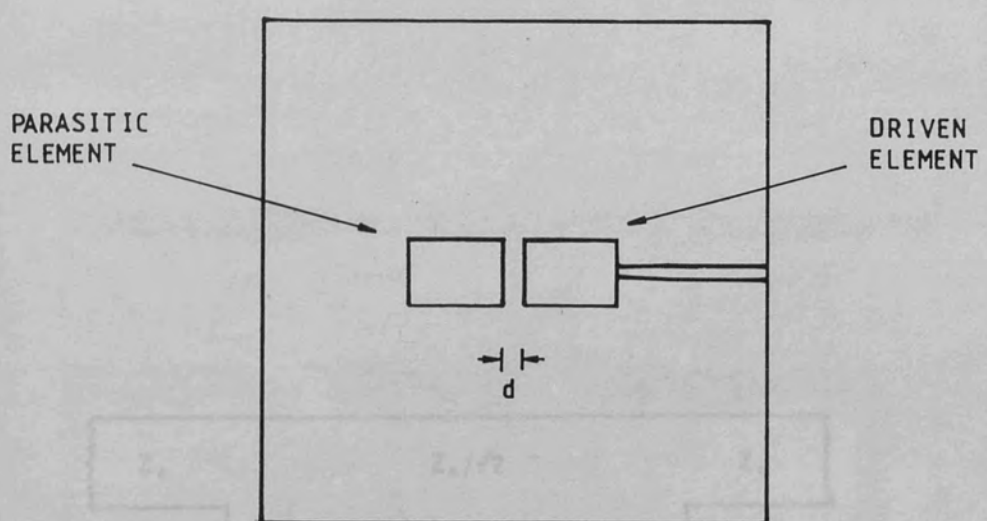

Figure (7.26) Parasitic patch layout

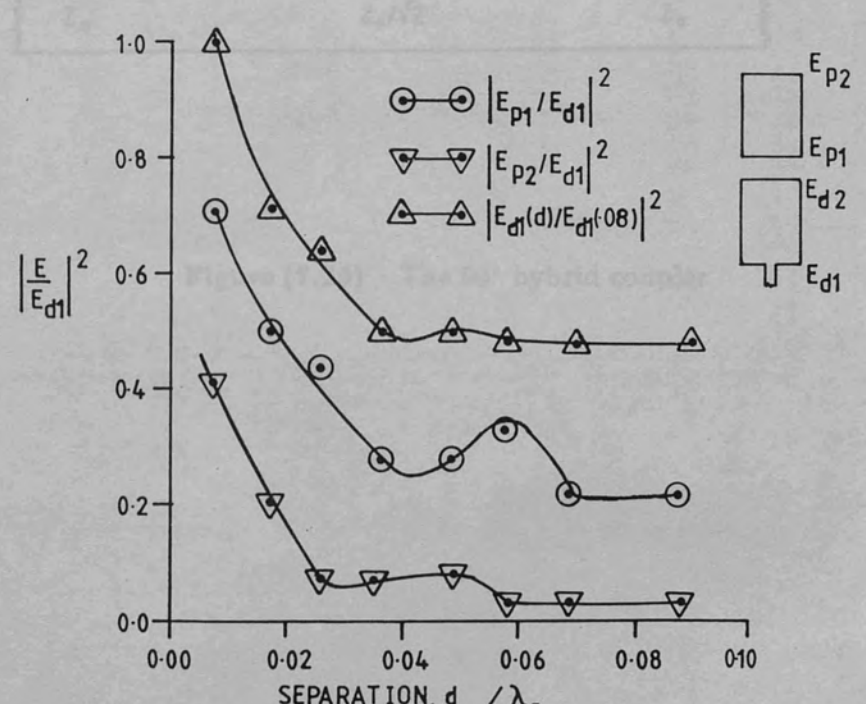

Figure (7.27) Variation of parasite excitation with patch–parasite separation

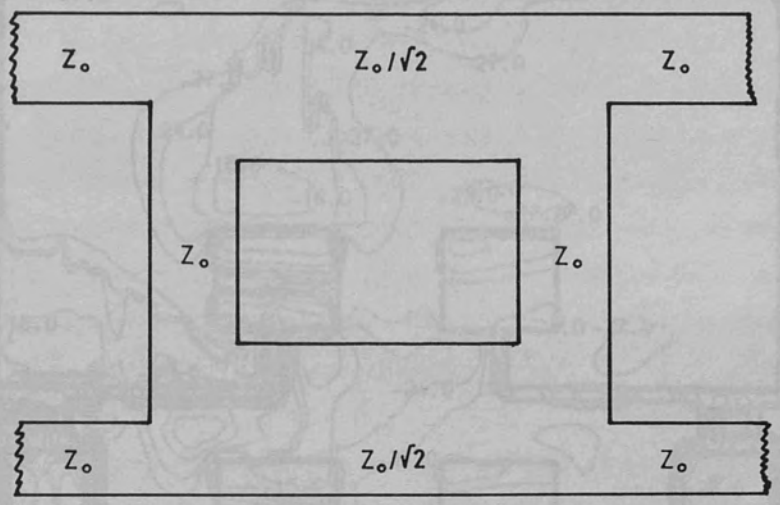

Figure (7.28) The 90° hybrid coupler

SCALE

$X, Y = 2.0, 5.0\, mm/division \qquad Z = 3\, dB/level$

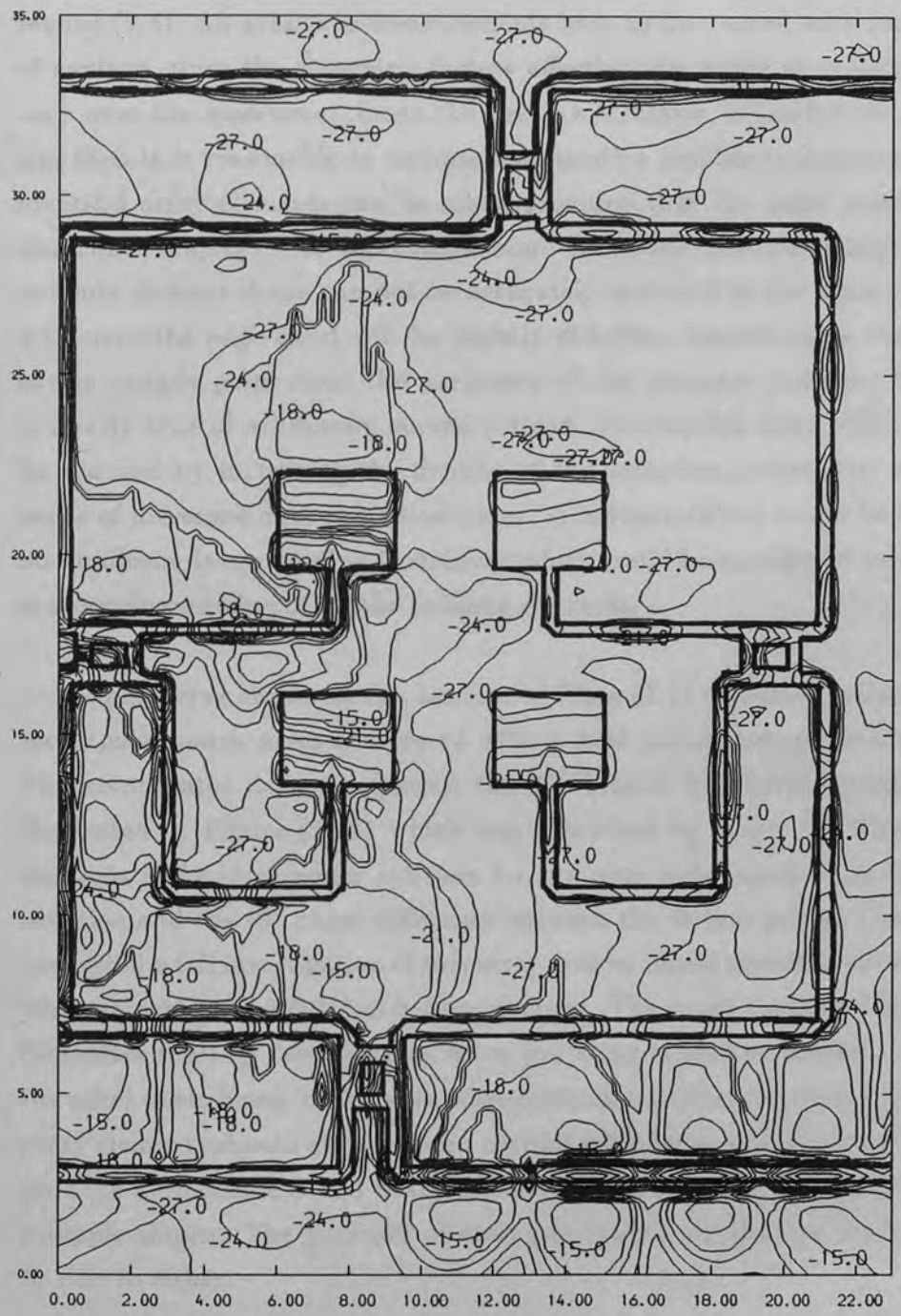

Figure (7.29) 4 Element Monopulse Array $|E_z|^2$ Distribution, F=34.9 *GHz*

measurements. The power distribution produced by the feed network can be quantitatively determined, and the effect of mismatched elements within the feed network assessed by the standing wave structure in the feed lines. Modifications to the desired amplitude distribution caused by mutual coupling of the array elements via space or surface wave coupling can also be determined. An additional source of coupling is the corporate feed network, which can result in the total destruction of the desired amplitude distribution, as demonstrated in section (7.4). All area scan measurements have to be treated with some degree of caution, since the geometric factors affecting the probe to circuit coupling vary over the scan area. Since the probe interaction is limited to the probe tip, then it is reasonable to assume that relative amplitude measurements on identical array elements can be made provided that the same point on each element is employed for the comparison. A further problem arises when the antenna element shape can not be accurately matched by the square sampling grid since the edge effect will be slightly different, depending on the distance of the sample point from the periphery of the antenna element. The same is clearly true of arbitrarily curved printed transmission lines. The error can be reduced by increasing the density of the sampling points, but at the expense of increased data aquisition times. A better solution would be to employ non-uniform data sampling techniques which could be configured to guarantee symmetric sampling of all the antenna elements.

The array shown at the bottom of Plate (7.1) comprises a four element rectangular patch array integrated with a dual plane monopulse comparator. The comparator design employed the 90° branch line hybrid power splitter illustrated in Figure (7.28) which was described by Rosen.[7.13] These circuit elements make ideal power splitters for the monopulse application due to the isolation and the 90° phase difference between the output ports. Time has not permitted a full investigation of this array, but an initial scanning network probe measurement at 34.9 GHz has been performed. The result shown in Figure (7.29) illustrates the $|E_z|^2$ distribution when the array is excited from its sum port, the other ports being loaded with waveguide matched terminations. Ideally, the array elements should all have been excited with equal amplitude and phase to produce a broadside pencil beam, however this was clearly not achieved in the example shown. The presence of strong excitation on the top feedlines could be due to either:

(a) a significant reflection at the patch feed points which, by the nature of the power splitter network, will be divided equally between the four output ports

(b) the power splitters are not functioning correctly

The phase of the reflected wave from each of the patch feed points arriving at each of the array ports will be dependent on the path taken, for example the first order reflections from each patch element will add in phase at the sum input and result in a high VSWR. In this example the VSWR in the 50 Ω sum feedline was found to be approximately 10. The reflected waves incident on the remaining three ports will tend to cancel because of the 180° phase relationship between the pairs of radiators set up by the feed network. Perfect cancellation will only be achieved if the power reaching each element is of equal amplitude, and if the feed network is phased correctly. The standing wave nature of the excitation in the feed lines connected to the matched loads indicates that there is a significant reflection from either the microstrip to waveguide transitions or from the remaining 90° bend which is not visible in Figure (7.29). The VSWR is found to be about 2 in the feed lines connecting to the loaded off ports. In this example the advantage of the isolation between the outputs of the hybrid power splitter is negated by the poor matching of the waveguide to microstrip transformers. Further work is necessary on this array to isolate the cause of poor power distribution. The use of sliding surface loads would allow various parts of the circuit to be loaded off, thus allowing small sections of the circuit to be energized and examined under matched conditions. Although incomplete, this example illustrates the potential of the scanning network probe as a diagnostic tool in microstrip array design.

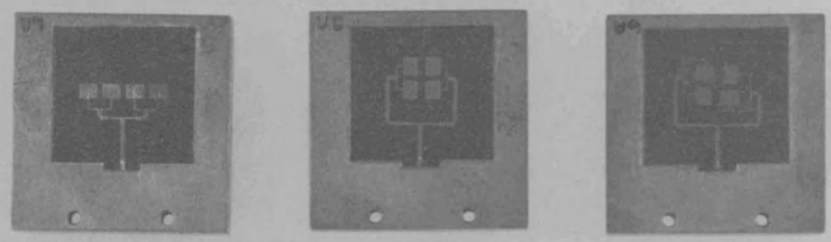

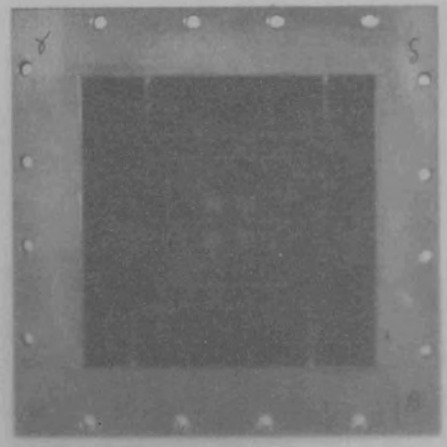

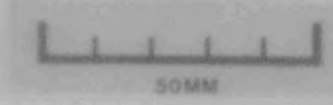

Plate(7.1) The corporately fed patch antenna arrays

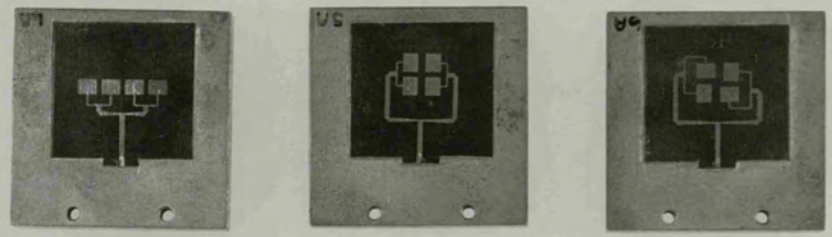

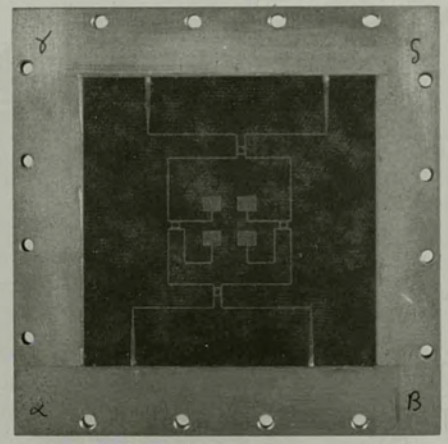
γ
δ
α
β

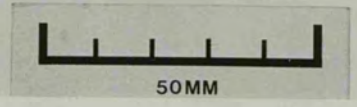
50MM

CHAPTER 8

Conclusions and Future Areas of Research

8.1 Conclusions

The aim of this research was to develop a measurement system that enabled the evaluation of microwave printed circuit antenna systems. The technique is specifically intended for printed circuit antenna or MICs that do not have accessible R.F. test ports and therefore can not be tested by conventional methods. A system has been developed which uses a mechanically scanned, non contacting coaxial probe to sample the electric field component perpendicular to the plane of the substrate. Two measurement strategies were considered in Chapter (2), these being:

(a) Linear line scan measurements in which the probe is scanned in one dimension parallel to the section of transmission line under test.

(b) Area scan measurements in which the probe is scanned in two dimensions, thus generating a map of the surface $|E_z|^2$ distribution.

The linear line scan measurement technique provides a means of measuring VSWR on printed transmission lines in a manner analogous to the slotted line, thus enabling the engineer to obtain a quantitative measurement of any mismatches within a printed circuit. The linear line scan technique would greatly reduce the time required to optimize a given circuit design, since the measurement provides the engineer with the mismatch location, and hence the area of the circuit that requires attention. Such information would not be available from conventional network analyser measurements. The measurement error introduced by undesirable coupling to the transverse magnetic field was treated in Chapter (3). Using a simple dual magnetic loop model, expressions were derived for the amplitude and phase errors introduced into the coaxial monopole probe output voltage. The use of the expressions developed is limited to microstrip-like transmission lines which propagate a near TEM mode, and requires that the probe to substrate separation is much smaller than the monopole length. The model predicted that the amplitude and phase error due to magnetic coupling would be negligible for the coaxial monopole probes that were employed for the investigation of microstrip lines fabricated on low permittivity substrates and operated in the frequency range 26.5 *GHz* to 40 *GHz*. The model also predicted a substantially reduced magnetic coupling error if the same probes were used to study microstrip circuits at the lower microwave frequencies, i.e. 1–10 *GHz*.

Chapter (6) demonstrated the practical application of the linear line scan measurement technique using microstrip and coplanar strip test circuits. Reasonable agreement was obtained between waveguide slotted line measurements

and the scanning network probe data for the two port microstrip test piece (see section 6.3.1) after taking proper account of the finite mismatch of the waveguide to microstrip transitions. The results obtained for the microstrip open circuit line extension, using the scanning network probe, were also in good agreement with the available theory. These results also suggested that the perturbing effects of the probe on the microstrip line were minimal. The voltage standing waves observed on open circuit microstrip lines with aspect ratios between 0.79 and 10.2 indicated only minimal reactive loading. Resistive loading of the microstrip was not evident for the range of VSWR's encountered. Since the probe loading is only significant near voltage maxima, and the majority of measurements are taken near voltage minima, the minor reactive loading noted in Chapter (6) was considered to be insignificant. The results are difficult to quantify further without a microstrip 'standard' with which the scanning network probe measurements can be rigorously compared.

A useful means of assessing the level of probe perturbation and other quantities such as line loss, substrate deformities, and generator mismatch is the sliding load calibration. The concept of the sliding load calibration is illustrated in Figure (8.1). The technique requires that the voltage standing wave due to an imperfect, resistive load is measured. The load is then advanced along the transmission line by $\lambda_g/4$, and the voltage standing wave on the same section of transmission line as the previous measurement then measured. On a perfect transmission line the result of averaging the two sets of data will be a straight line, since shifting the load by $\lambda_g/4$ simply displaces the voltage standing wave by $\lambda_g/4$. In practice, both the probe and generator mismatch will be the source of additional standing waves which are *independent* of the load position, and will give rise to a residual standing wave component in the averaged data. It is also noted that any error in the probe output due to substrate surface imperfections or local dielectric constant variations will also be independent of the load position and therefore give rise to a component in the averaged standing wave data. Such errors would normally be random, and thus easily distinguished from the generator and probe loading effects which would possess a $\lambda_g/2$ periodicity.

The equivalent circuit of the probe and terminated microstrip line is shown in Figure (8.2). The generator is assumed to be matched and the series impedance Z_T represents the mismatched waveguide to microstrip transition. In addition to the first order standing wave generated by the interference of the incident and reflected waves at the termination Z_L, there will be other components due to:

(a) a second order standing wave generated by the partial reflection of the reflected wave at the waveguide to microstrip transition

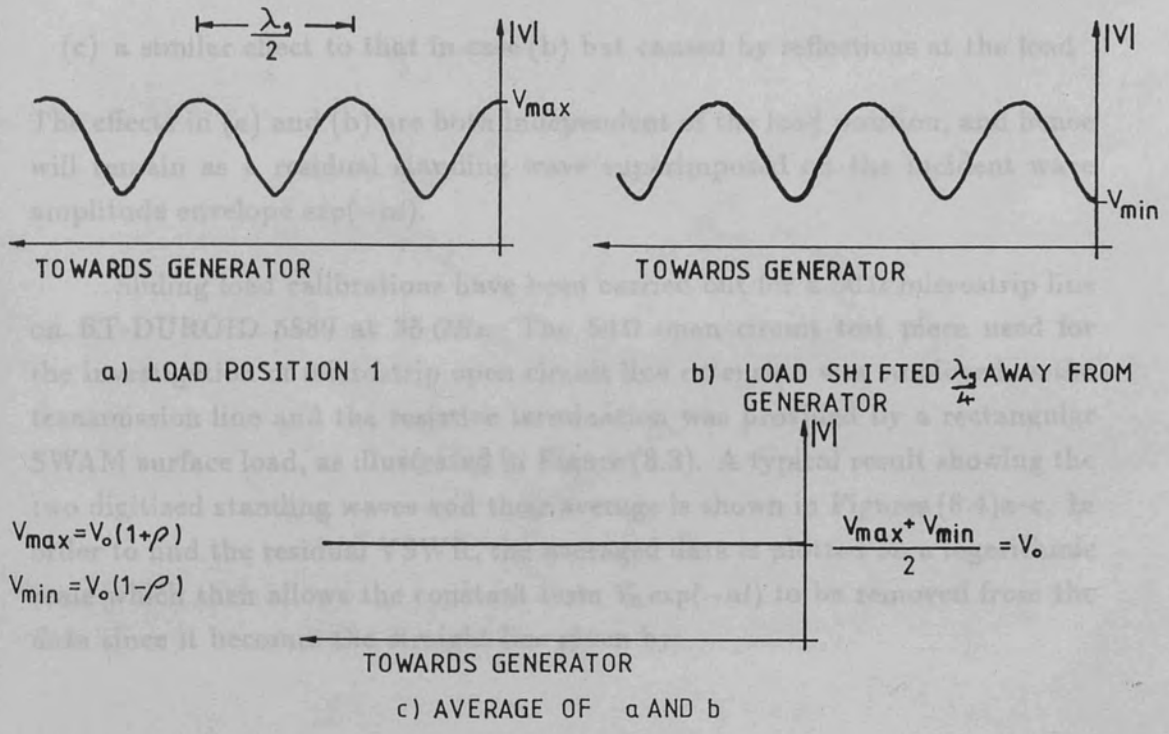

Figure (8.1) Idealized result of a sliding load calibration

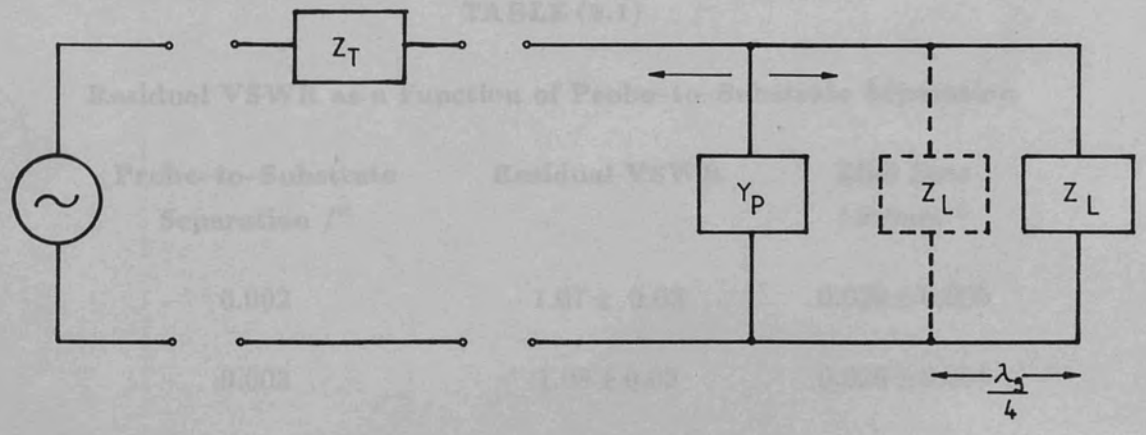

Figure (8.2) Equivalent circuit of the microstrip line and probe

(b) a second order standing wave generated by the partial reflection of the reflected wave from the *probe* at the waveguide to microstrip transition; this effect is analogous to the probe-slot resonance found in slotted lines[8.1]

(c) a similar effect to that in case (b) but caused by reflections at the load

The effects in (a) and (b) are both independent of the load position, and hence will remain as a residual standing wave superimposed on the incident wave amplitude envelope $\exp(-\alpha l)$.

Sliding load calibrations have been carried out for a $50\,\Omega$ microstrip line on RT-DUROID 5880 at $35\,GHz$. The $50\,\Omega$ open circuit test piece used for the investigation of microstrip open circuit line extension was employed as the transmission line and the resistive termination was provided by a rectangular SWAM surface load, as illustrated in Figure (8.3). A typical result showing the two digitized standing waves and their average is shown in Figures (8.4)a–c. In order to find the residual VSWR, the averaged data is plotted on a logarithmic scale which then allows the constant term $V_0 \exp(-\alpha l)$ to be removed from the data since it becomes the straight line given by:

$$y = -0.4343\alpha l + \log_{10}(V_0) \qquad 8.1$$

After removing the constant term, the residual VSWR is calculated from the peak to valley ratio of the remaining standing wave. The results in Table (8.1) illustrate the measured variation of the residual VSWR as a function of probe to substrate separation.

TABLE (8.1)

Residual VSWR as a Function of Probe–to–Substrate Separation

Probe–to–Substrate Separation /"	Residual VSWR	Line Loss / $dBmm^{-1}$
0.002	1.07 ± 0.03	0.029 ± 0.005
0.003	1.08 ± 0.02	0.026 ± 0.005
0.004	1.08 ± 0.02	0.040 ± 0.005
0.005	1.06 ± 0.03	0.032 ± 0.005
0.006	1.07 ± 0.03	0.029 ± 0.005

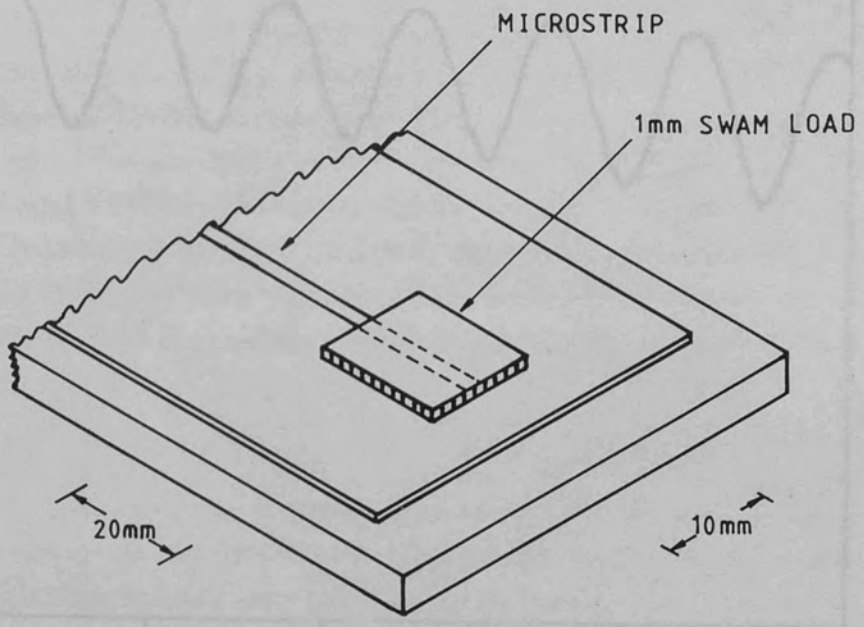

Figure (8.3) Microstrip sliding load construction

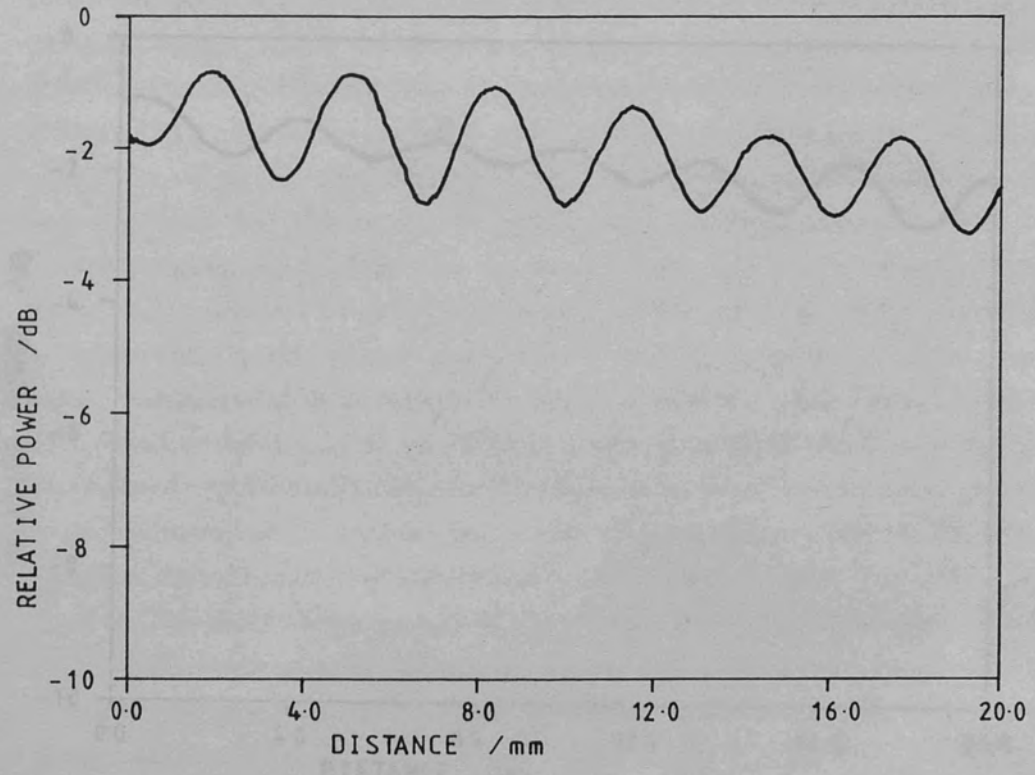

Figure (8.4)a Measured power standing wave, load position # 1

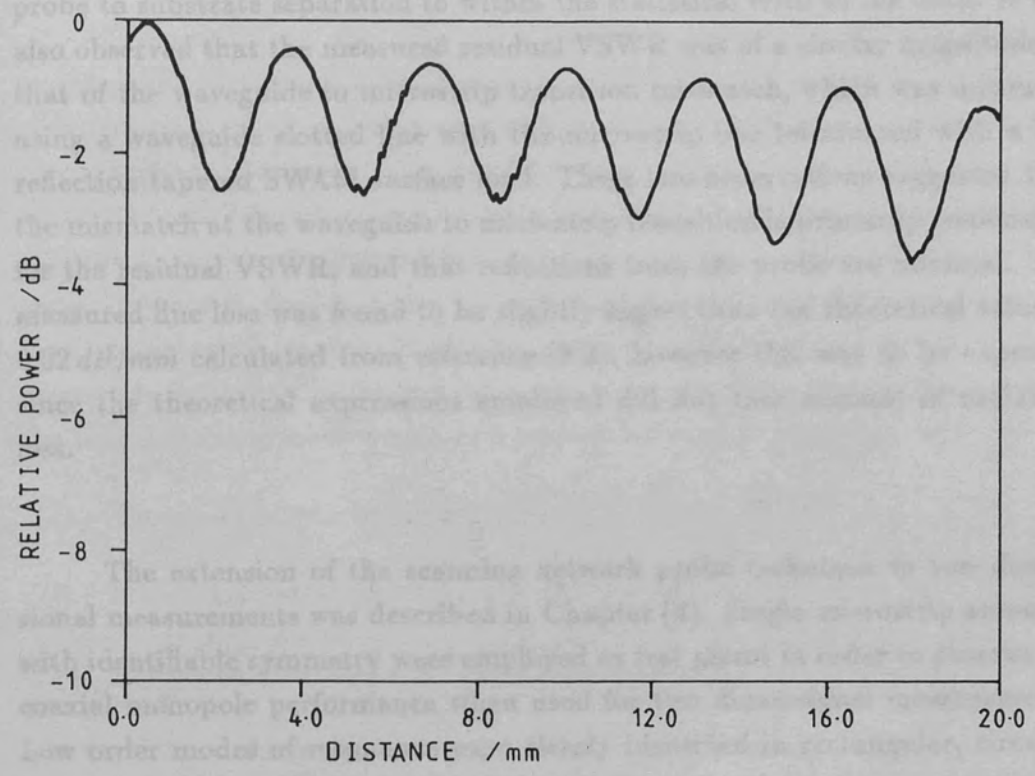

Figure (8.4)b Measured power standing wave, load position # 2

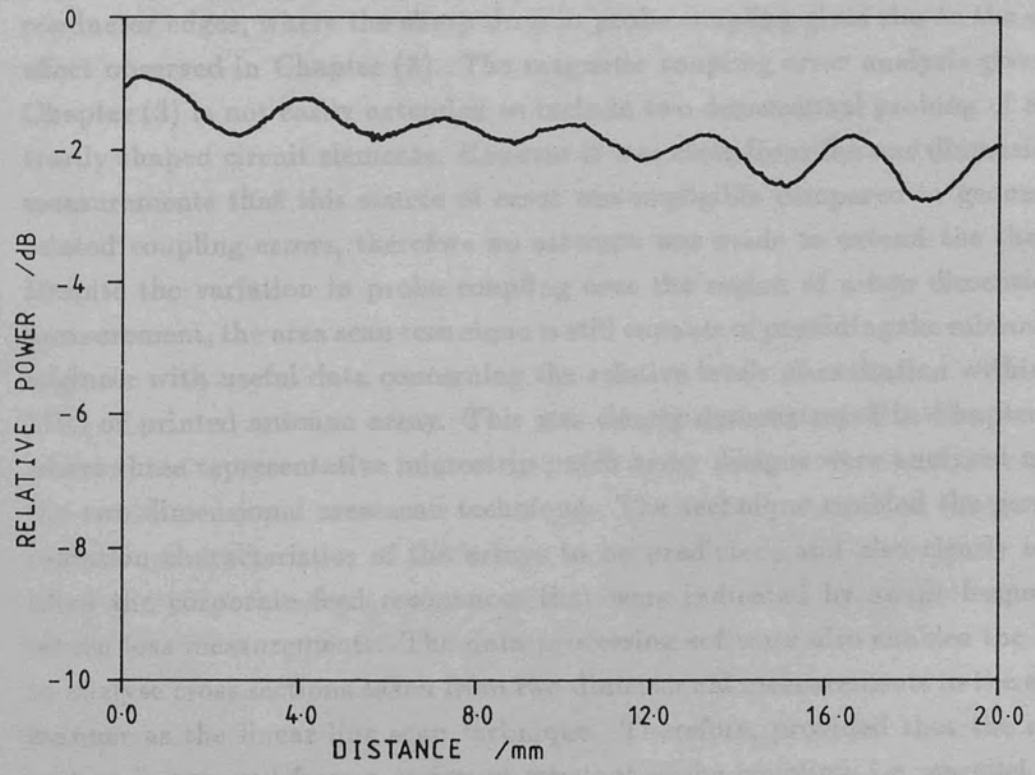

Figure (8.4)c Residual power standing wave

It was observed that the residual VSWR remained constant with increasing probe to substrate separation to within the statistical error in the data. It was also observed that the measured residual VSWR was of a similar magnitude to that of the waveguide to microstrip transition mismatch, which was measured using a waveguide slotted line with the microstrip line terminated with a low reflection tapered SWAM surface load. These two observations suggested that the mismatch at the waveguide to microstrip transition is primarily responsible for the residual VSWR, and that reflections from the probe are minimal. The measured line loss was found to be slightly higher than the theoretical value of $0.02\,dB/mm$ calculated from reference (8.2), however this was to be expected since the theoretical expressions employed did not take account of radiation loss.

The extension of the scanning network probe technique to two dimensional measurements was described in Chapter (4). Single microstrip antennas with identifiable symmetry were employed as test pieces in order to observe the coaxial monopole performance when used for two dimensional measurements. Low order modes of resonance were clearly identified in rectangular, circular, and triangular patch antennas. The two dimensional measurements are not readily quantifiable, since the geometric factors governing the probe coupling to the antenna or MIC under test do not remain constant as a function of probe position. The variable probe coupling is most evident on and close to conductor edges, where the sharp drop in probe coupling gives rise to the edge effect observed in Chapter (3). The magnetic coupling error analysis given in Chapter (3) is not easily extended to include two dimensional probing of arbitrarily shaped circuit elements. However it was clear from the one dimensional measurements that this source of error was negligible compared to geometric related coupling errors, therefore no attempt was made to extend the theory. Despite the variation in probe coupling over the region of a two dimensional measurement, the area scan technique is still capable of providing the microwave engineer with useful data concerning the relative levels of excitation within an MIC or printed antenna array. This was clearly demonstrated in Chapter (7) where three representative microstrip patch array designs were analysed using the two dimensional area scan technique. The technique enabled the general radiation characteristics of the arrays to be predicted, and also clearly identified the corporate feed resonances that were indicated by swept frequency return loss measurements. The data processing software also enables the user to analyse cross sections taken from two dimensional measurements in the same manner as the linear line scan technique. Therefore, provided that the cross section is removed from a region of constant probe coupling, i.e. parallel to a section of transmission line, such data can provide a quantitative measurement of VSWR within the MIC or printed antenna array.

8.2 Future Exploitation of The Scanning Network Probe System

The aim of the research was to develop a measurement technique that would enable the characterization of integrated circuit systems with no accessible test ports. This has been successfully achieved with the scanning network probe system. The technique has only been demonstrated in the frequency range 26.5–40 *GHz*, although the extension of the technique to the lower microwave bands should present few problems. The use of the technique above these frequencies would require the development of smaller probes and a more sensitive detection system. Even though the scanning network probe provides amplitude only data in its current form, there are still many applications for the technique in printed circuit and printed antenna research, for example:

(a) The study of microstrip line modes.

(b) The investigation of irregular printed antenna geometries.

(c) The mode analysis of self oscillating antennas.

Figures(8.5)a–e show the result of area scan measurements on the open circuit microstrip lines described in Chapter(6). The main point of interest in these measurements is the location of the leakage field peaks beyond the circuit metallization. The magnitude of the leakage field at the open circuit termination is observed to increase with increasing line width. The same is also true of the leakage field features along the edges of the microstrip, and in the case of the 22 Ω microstrip line some of these features are greater in magnitude than the primary source on the edge of the microstrip conductor. In all of the examples it is observed that the fringing field maxima on either side of the line in the vicinity of the open circuit are shifted towards the open circuit. In the case of the 50 Ω and 78 Ω lines the maxima on the microstrip metallization and the fringe field maxima re-align approximately 1 1/2 guide wavelengths from the open circuit. The lower impedance lines exhibit a similar effect except that instead of re-aligning with the maxima on the microstrip line, the fringe field maxima start to shift *away* from the open circuit. It was observed in Chapter(6) that the voltage standing waves measured on wide microstrip lines exhibited a pronounced beat envelope, which indicates the propagation of multiple modes with slightly differing guide wavelengths. The possibility exists of Fourier transforming the digitized standing wave data from such a measurement, thus allowing the spatial frequency components of the composite standing wave to be found. The guide wavelengths of the different modes could then be identified and compared to the theoretical work of Rozzi et al.[8.3] A more novel approach for open circuit microstrip lines would be to treat the open circuit microstrip as a dielectric loaded cavity and use a modal expansion technique[8.4] to deduce the allowed modes and hence find the resultant electric field underneath

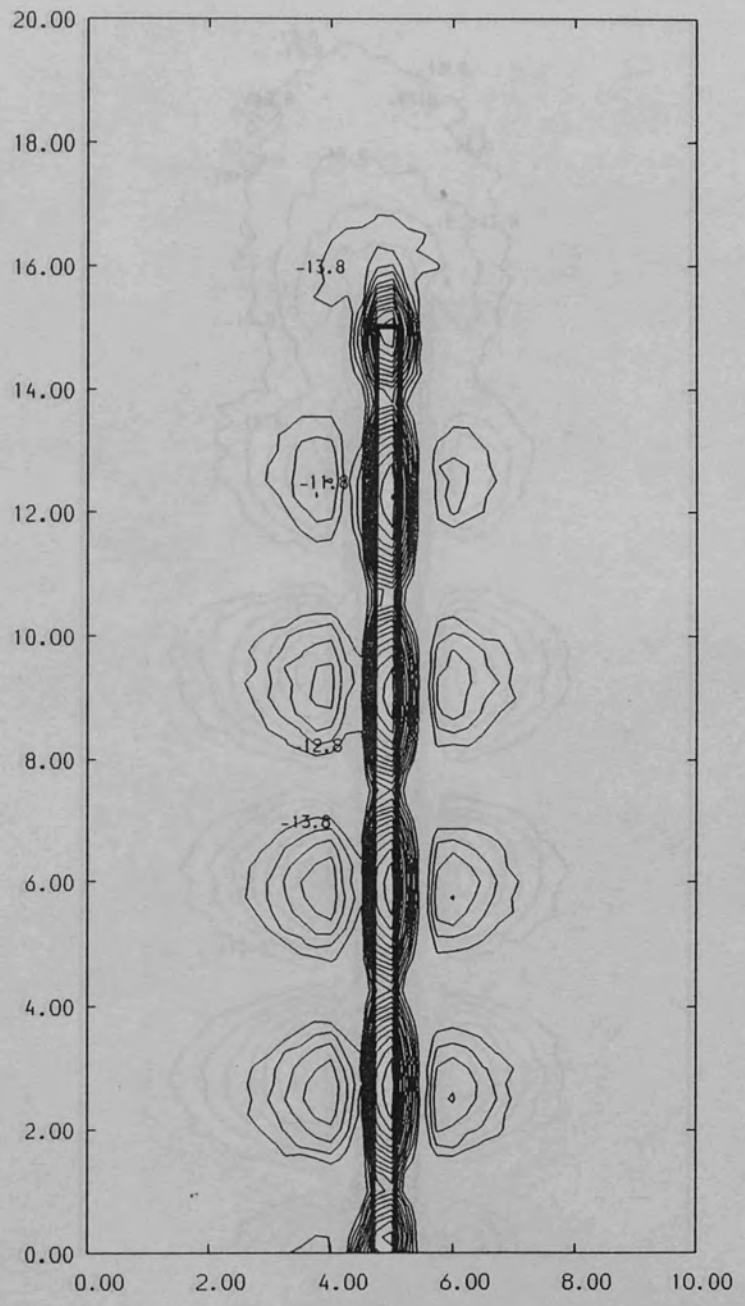

SCALE

$X, Y = 2.0\,mm/division \qquad Z = 1.0dB/level$

Figure (8.5)a Measured $|E_z|^2$ distributions on a 78 Ω microstrip line, F=34.5 *GHz*

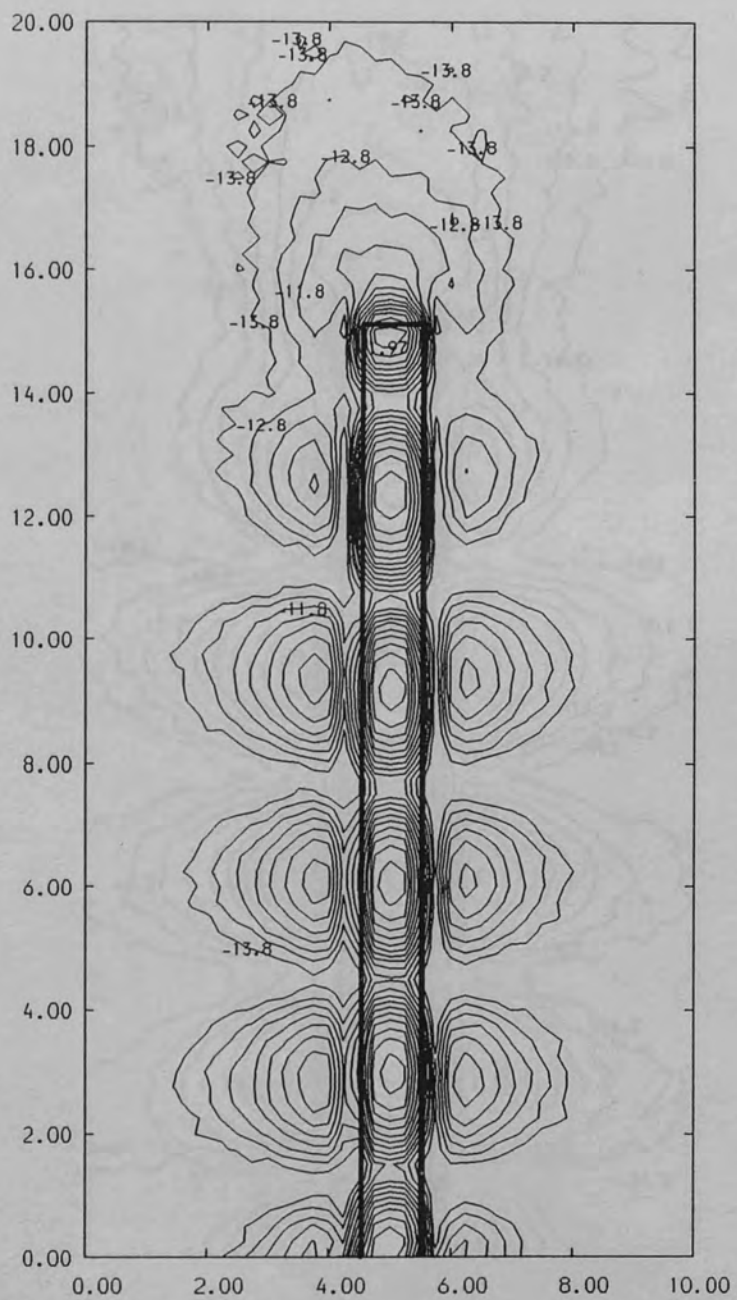

SCALE

$X, Y = 2.0\,mm/division \qquad Z = 1.0dB/level$

Figure (8.5)b Measured $|E_z|^2$ distributions on a 50 Ω microstrip line, F=34.5 *GHz*

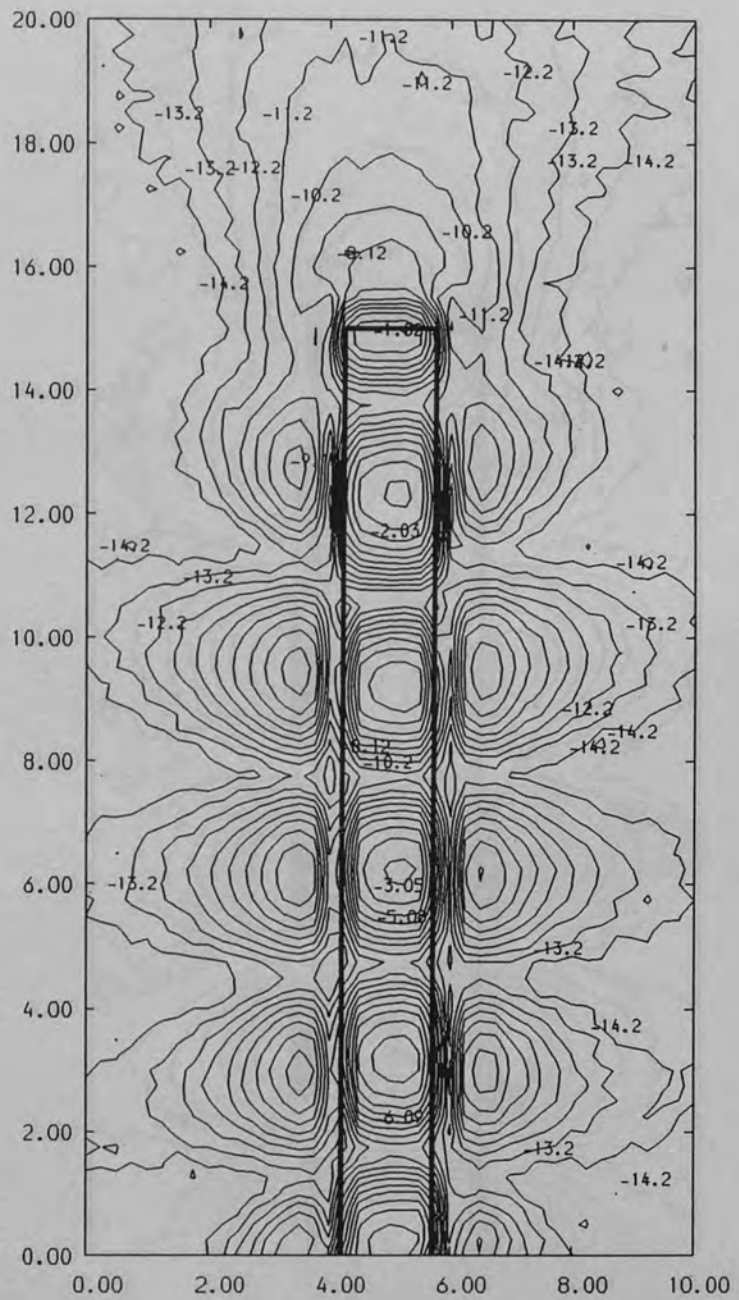

SCALE

$X, Y = 2.0\,mm/division \qquad Z = 1.0dB/level$

Figure (8.5)c Measured $|E_z|^2$ distributions on a 40 Ω microstrip line, F=34.5 *GHz*

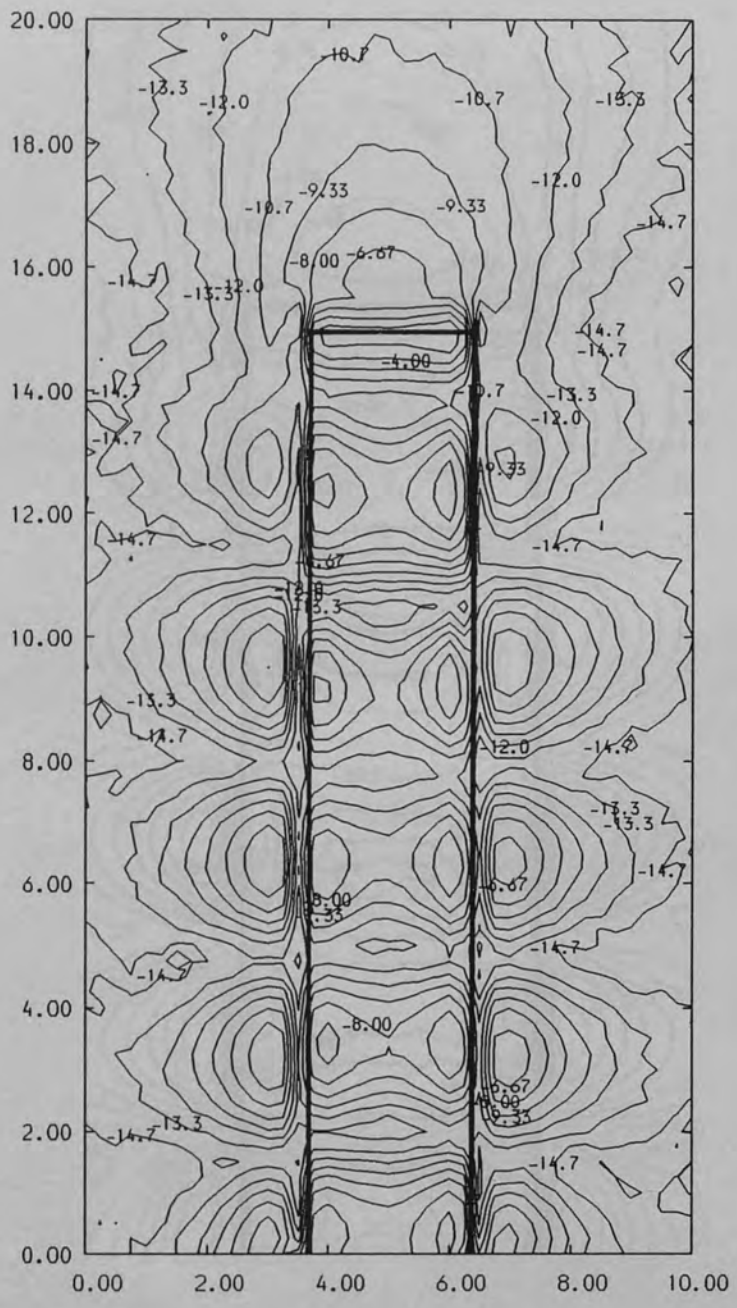

SCALE

$X, Y = 2.0\,mm/division \qquad Z = 1.33dB/level$

Figure (8.5)d Measured $|E_z|^2$ distributions on a 30 Ω microstrip line, F=34.5 *GHz*

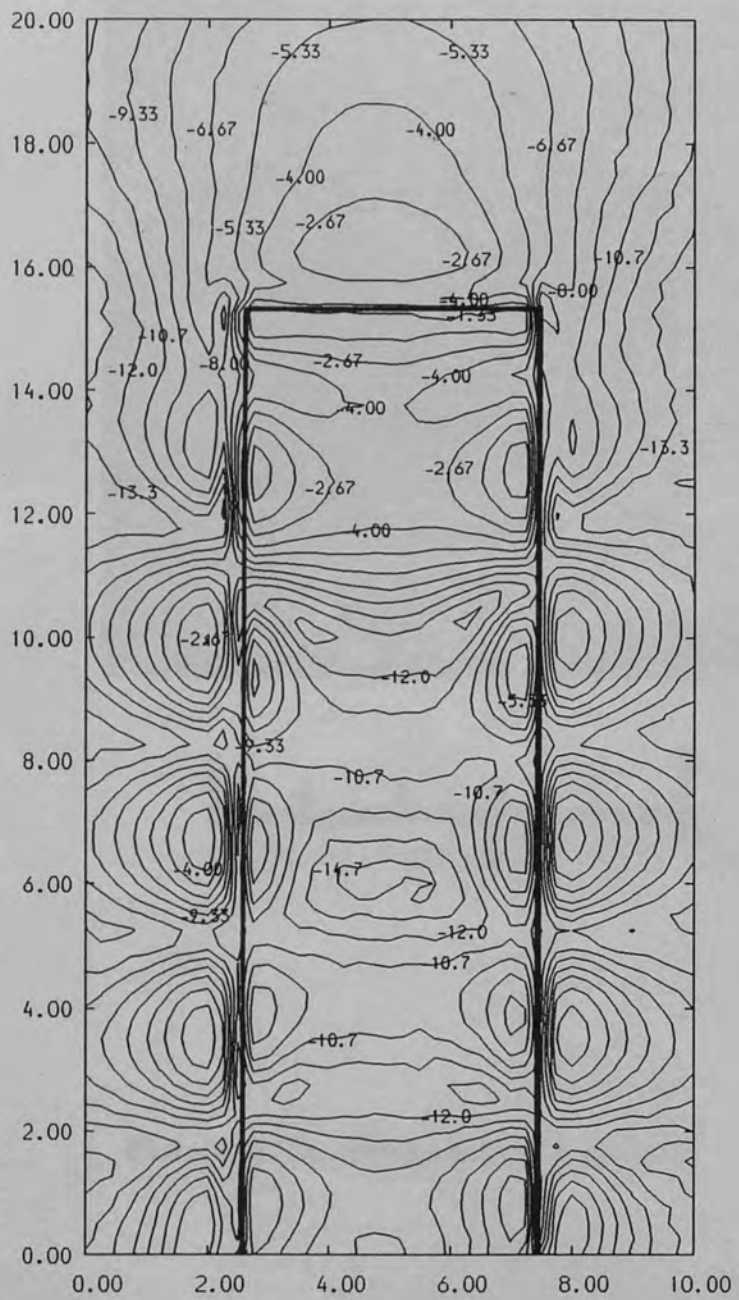

SCALE

$X, Y = 2.0\,mm/division \qquad Z = 1.33dB/level$

Figure (8.5)e Measured $|E_z|^2$ distributions on a 22 Ω microstrip line, F=34.5 *GHz*

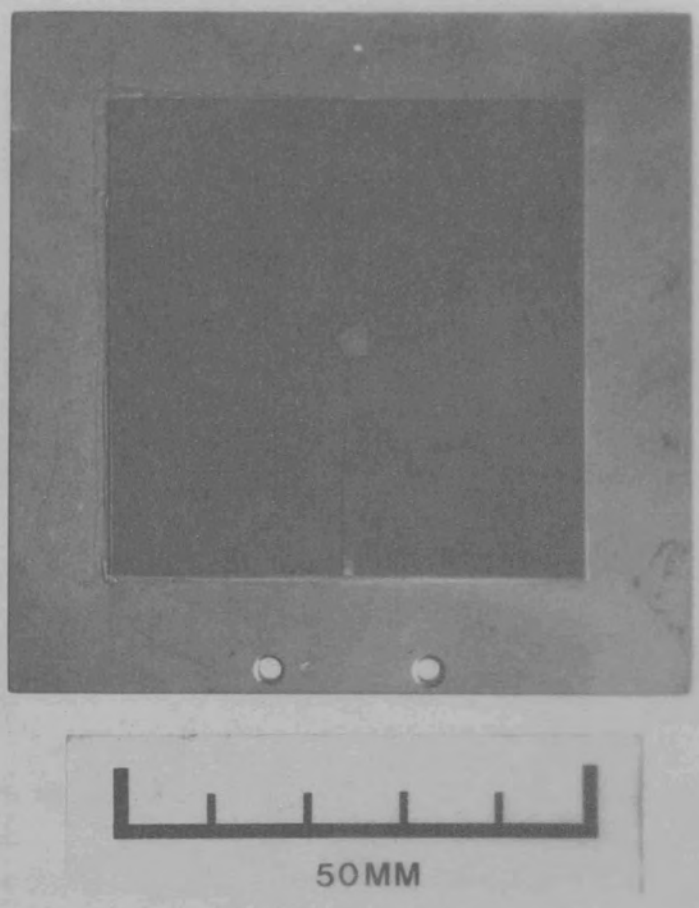

Plate(8.1) The pentagonal patch antenna

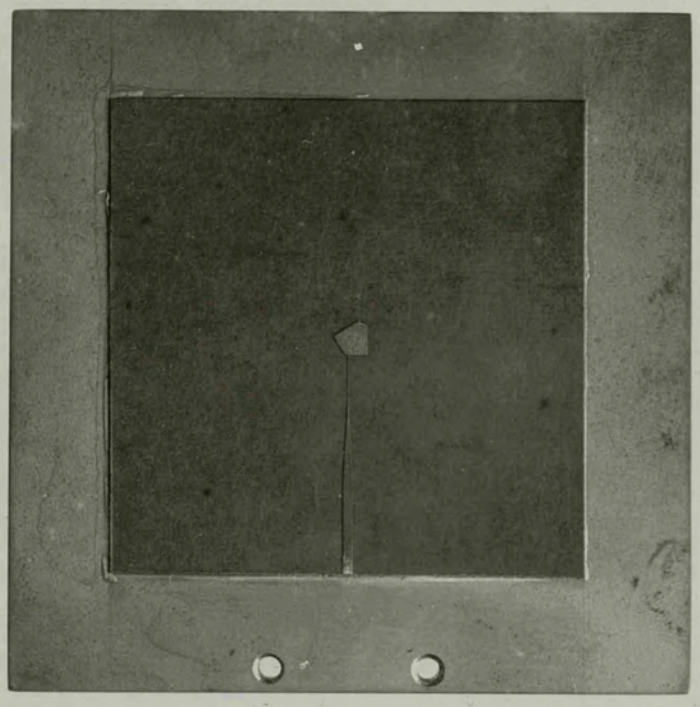

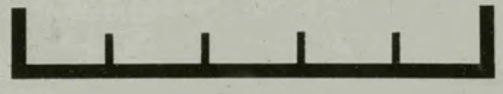

50MM

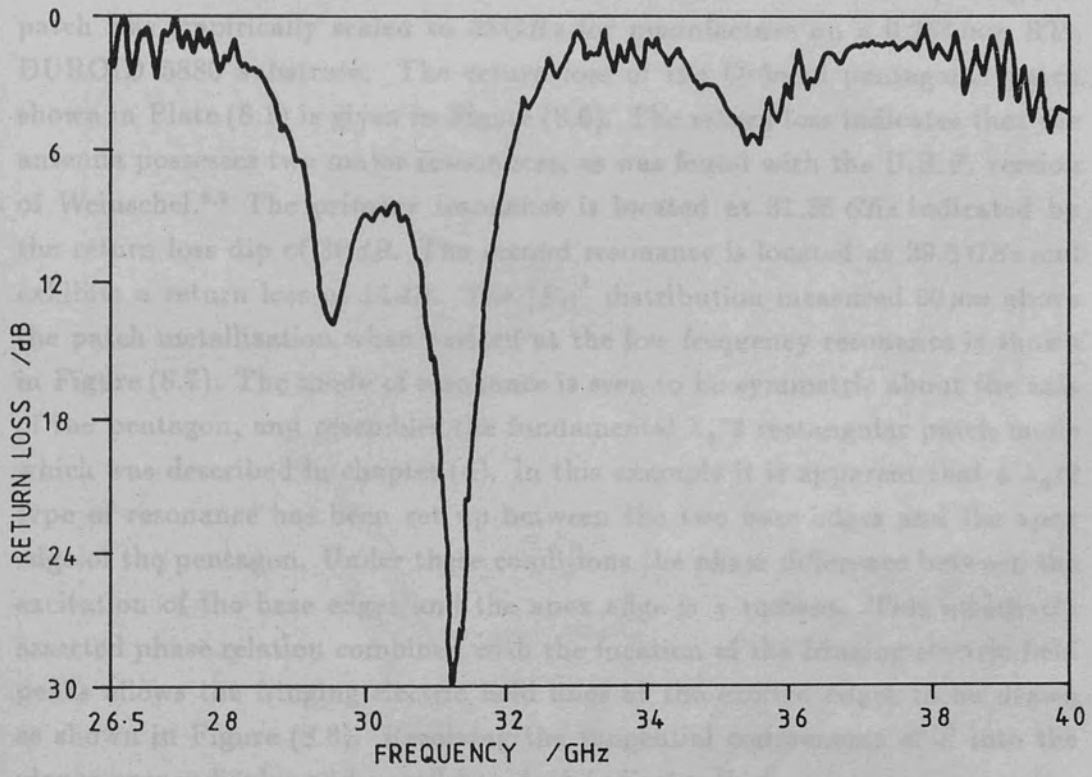

Figure (8.6) Pentagonal patch return loss

the microstrip. A comparison of the scanning network probe measurements with such theory would serve as a useful validation of the scanning network probe technique in general.

The area scan measurement technique offers a unique solution to the problem of identifying resonant modes in irregular microstrip patch antennas. Antenna designs with irregular geometry, such as the pentagonal patch[8.5,8.6] are usually empirically derived, and very little is known about the exact nature of the resonant modes. As an example, Weinschel's[8.5] U.H.F. pentagonal patch was empirically scaled to $35\,GHz$ for manufacture on a $0.254\,mm$ RT-DUROID 5880 substrate. The return loss of the Q-band pentagonal patch shown in Plate (8.1) is given in Figure (8.6). The return loss indicates that the antenna possesses two major resonances, as was found with the U.H.F. version of Weinschel.[8.5] The primary resonance is located at $31.35\,GHz$ indicated by the return loss dip of $30\,dB$. The second resonance is located at $29.5\,GHz$ and exhibits a return loss of $14\,dB$. The $|E_z|^2$ distribution measured $50\,\mu m$ above the patch metallization when excited at the low frequency resonance is shown in Figure (8.7). The mode of resonance is seen to be symmetric about the axis of the pentagon, and resembles the fundamental $\lambda_g/2$ rectangular patch mode which was described in chapter (4). In this example it is apparent that a $\lambda_g/2$ type of resonance has been set up between the two base edges and the apex edge of the pentagon. Under these conditions the phase difference between the excitation of the base edges and the apex edge is π radians. This intuitively asserted phase relation combined with the location of the fringing electric field peaks allows the fringing electric field lines at the excited edges to be drawn as shown in Figure (8.8). Resolving the tangential components of $\vec{E}$ into the planes perpendicular and parallel to A–A indicates that:

(a) at the base of the pentagon the resolved components of tangential $\vec{E}$ perpendicular to A–A will be π out of phase and hence make no contribution to the boresight radiation pattern

b) there will be no tangential $\vec{E}$ in the plane perpendicular to A–A at the apex edge

(c) at base edges and the apex edge, the components of tangential $\vec{E}$ resolved in the plane of A–A will be in phase and thus act as sources for broadside radiation

When excited in this mode, the pentagonal patch will therefore behave as a *linearly* polarized radiator with the E-plane defined by the axis A–A shown in Figure (8.8). The linear polarization was confirmed by the far-field radiation pattern measurements made at $29.5\,GHz$ which are shown in Figure (8.9)a and (8.9)b. The measured radiation patterns in the E and H-plane both show

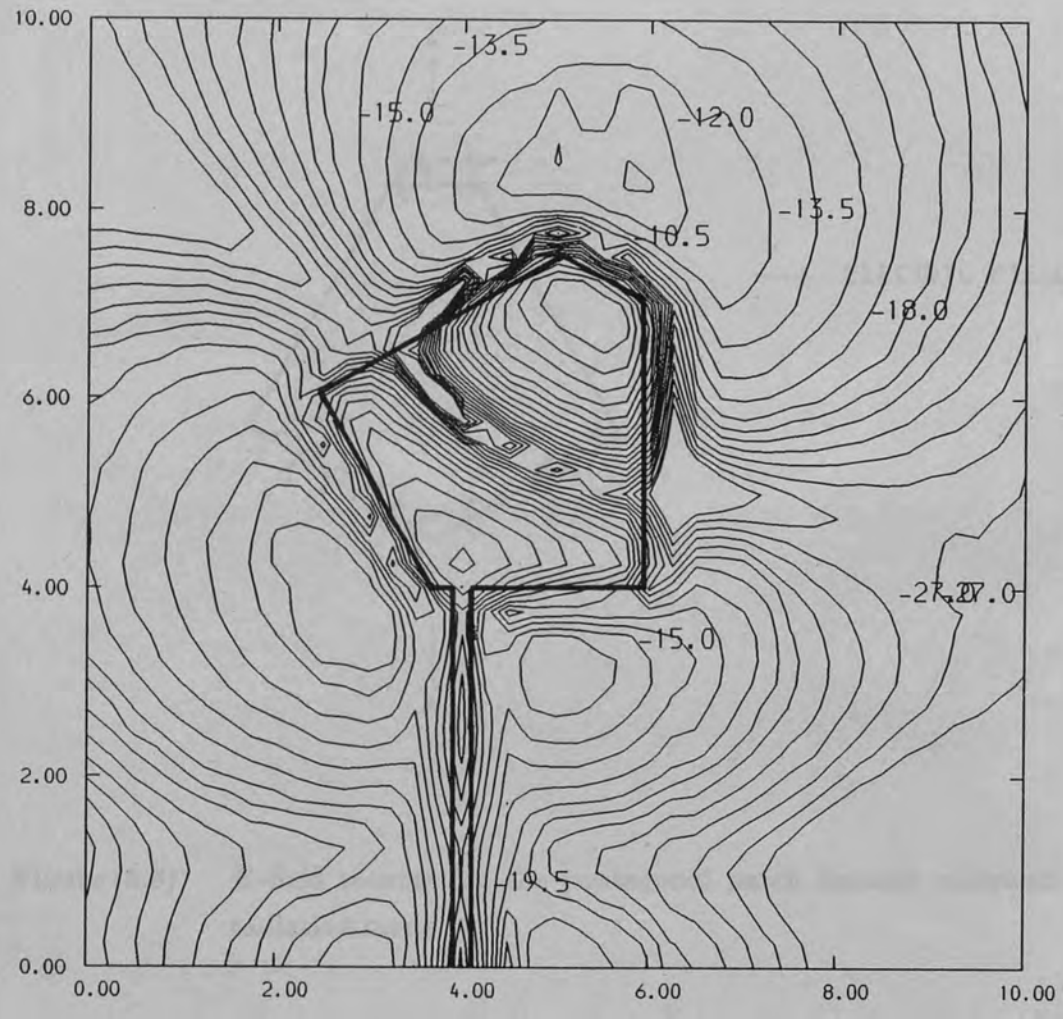

SCALE

$X, Y = 2\,mm/division \qquad Z = 1.5dB/level$

Figure (8.7) Measured $|E_z|^2$ distribution on the pentagonal patch, F=29.5 GHz

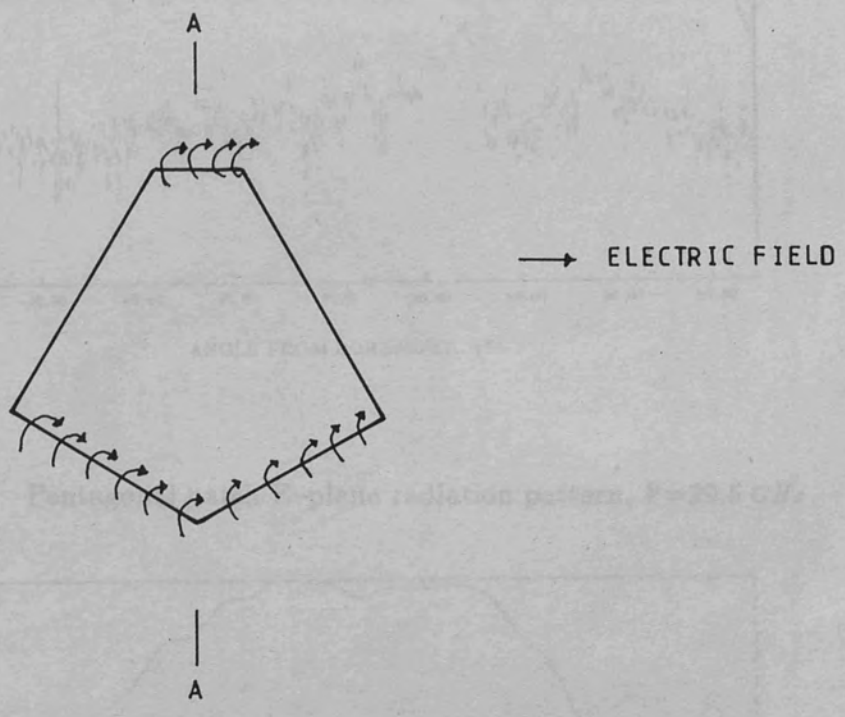

Figure (8.8) *E*–field sources for the pentagonal patch linearly polarized radiation mode

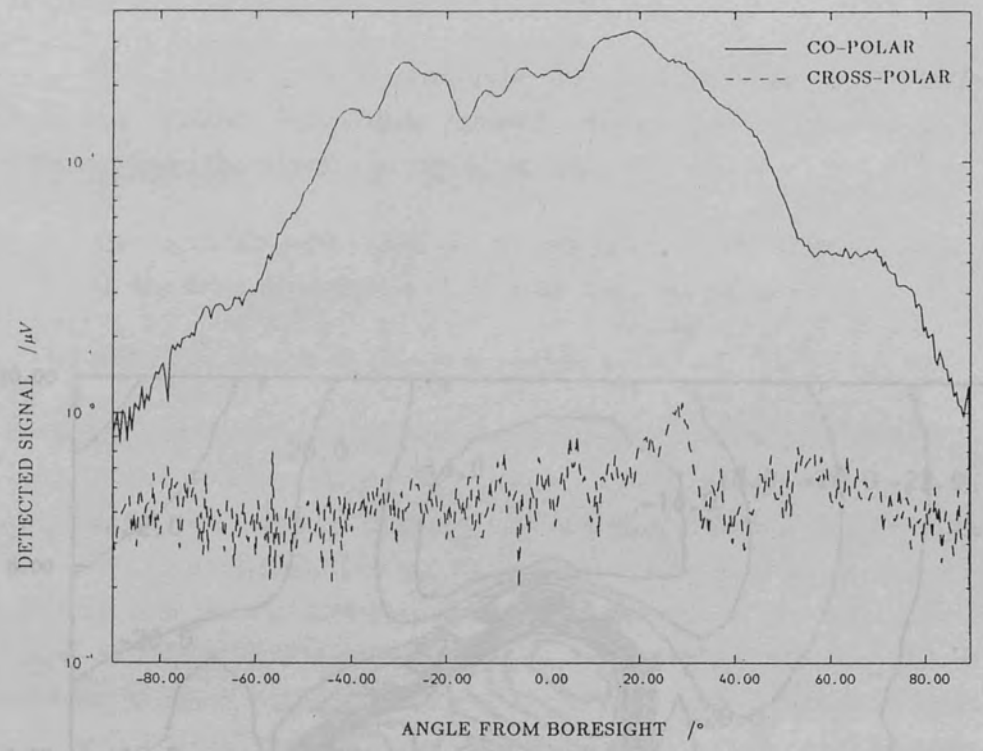

Figure (8.9)a Pentagonal patch E–plane radiation pattern, F=29.5 *GHz*

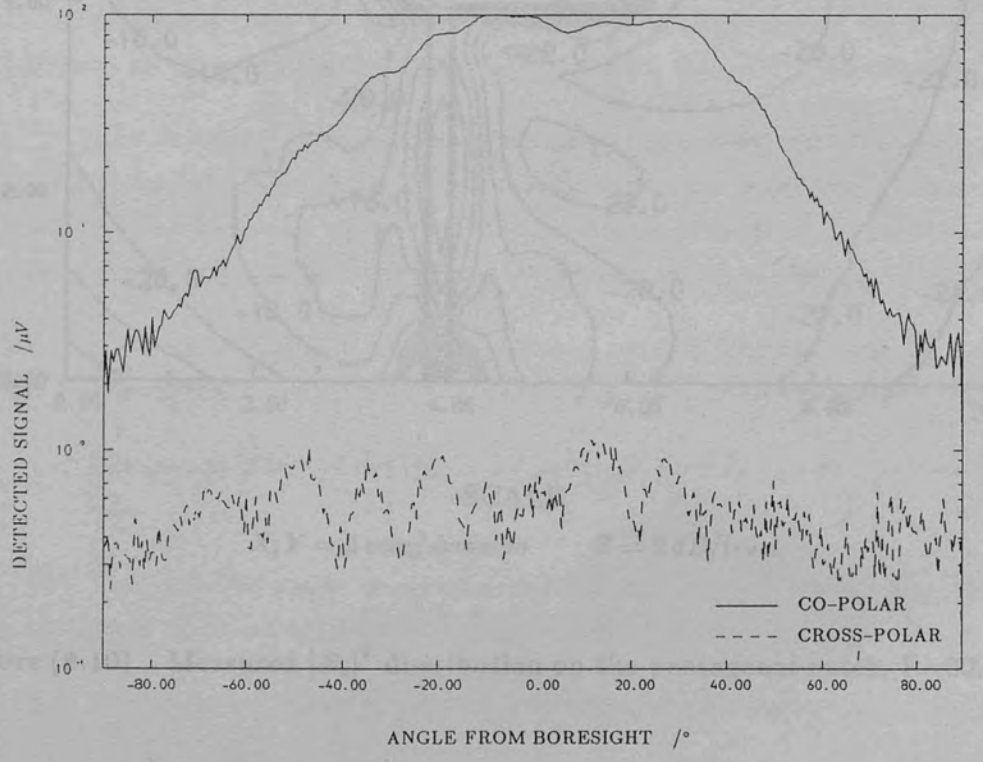

Figure (8.9)b Pentagonal patch H–plane radiation pattern, F=29.5 *GHz*

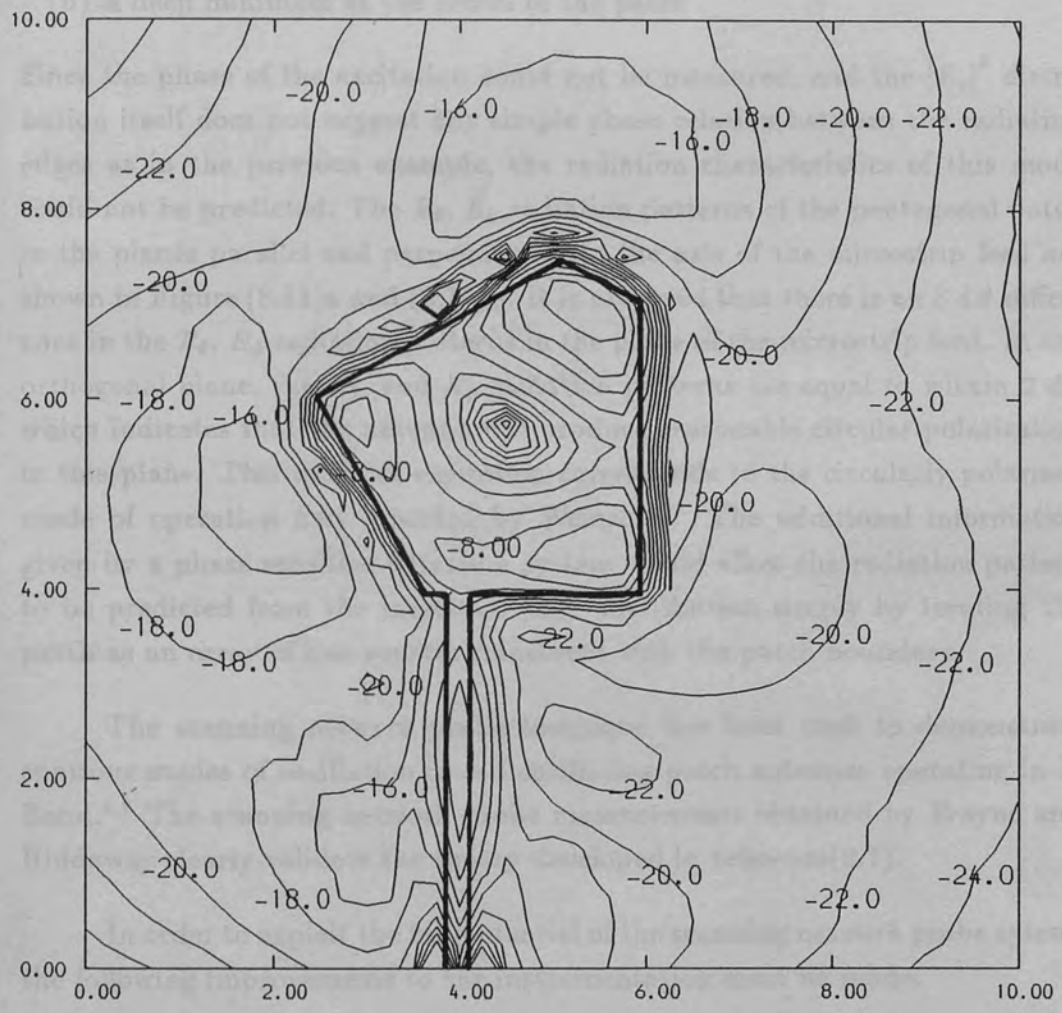

SCALE

$X, Y = 2\,mm/division \qquad Z = 2\,dB/level$

Figure (8.10) Measured $|E_z|^2$ distribution on the pentagonal patch, F=30.35 *GHz*

a single broadside beam with a low cross–polarized response of -20 dB in the H–plane and -15 dB in the E–plane.

The second mode of excitation, which was located at 31.35 GHz, is illustrated by $|E_z|^2$ distribution shown in Figure (8.10). This mode is totally different from the linearly polarized example and exhibits:

(a) strong excitation around the periphery of the patch, in a similar manner to the azimuthal modes of the disk and ring patches

(b) a deep minimum at the centre of the patch

Since the phase of the excitation could not be measured, and the $|E_z|^2$ distribution itself does not suggest any simple phase relation between the radiating edges as in the previous example, the radiation characteristics of this mode could not be predicted. The E_θ, E_ϕ radiation patterns of the pentagonal patch in the planes parallel and perpendicular to the axis of the microstrip feed are shown in Figure (8.11)a and (8.11)b. It is observed that there is an 8 dB difference in the E_θ, E_ϕ radiation patterns in the plane of the microstrip feed. In the orthogonal plane, the E_θ, and E_ϕ radiation patterns are equal to within 2 dB which indicates that the antenna will produce reasonable circular polarization in this plane. This mode of excitation corresponds to the circularly polarized mode of operation first reported by Weinschel. The additional information given by a phase sensitive detection system would allow the radiation pattern to be predicted from the measured $|E_z|^2$ distribution simply by treating the patch as an array of line sources coincident with the patch boundary.

The scanning network probe technique has been used to demonstrate spurious modes of oscillation in self oscillating patch antennas operating in J-Band.[8.7] The scanning network probe measurements obtained by Frayne and Riddaway clearly validate the theory developed in reference(8.7).

In order to exploit the full potential of the scanning network probe sytem, the following improvements to the instrumentation must be made:

(a) The probe size could be further reduced, thus improving spatial resolution.

(b) The R.F. detection technique must be modified to enable the measurement of phase and also to improve the minimum detectable signal level.

(c) The technique must be extended to allow swept frequency measurements.

A reduction in probe size will require the investigation of new probe construction methods, such as metallized, drawn quartz tube. The most economical way to measure phase and amplitude at millimetric wavelengths would be to employ

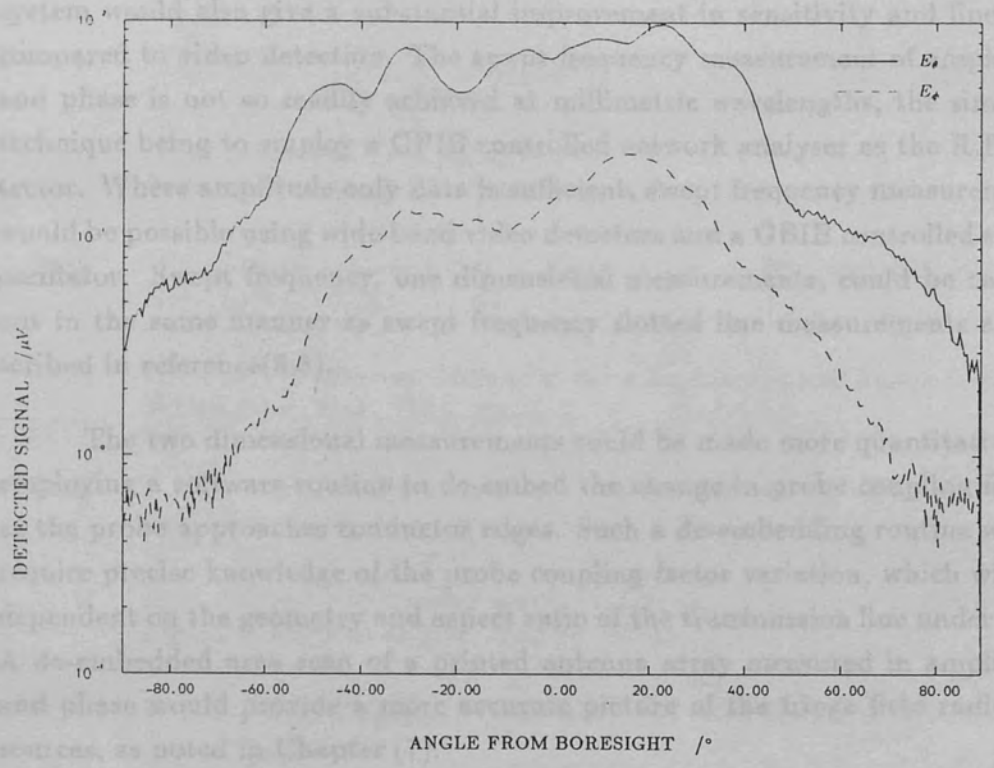

Figure (8.11)a Pentagonal patch radiation pattern in the plane parallel to the microstrip feed, F=30.35 *GHz*

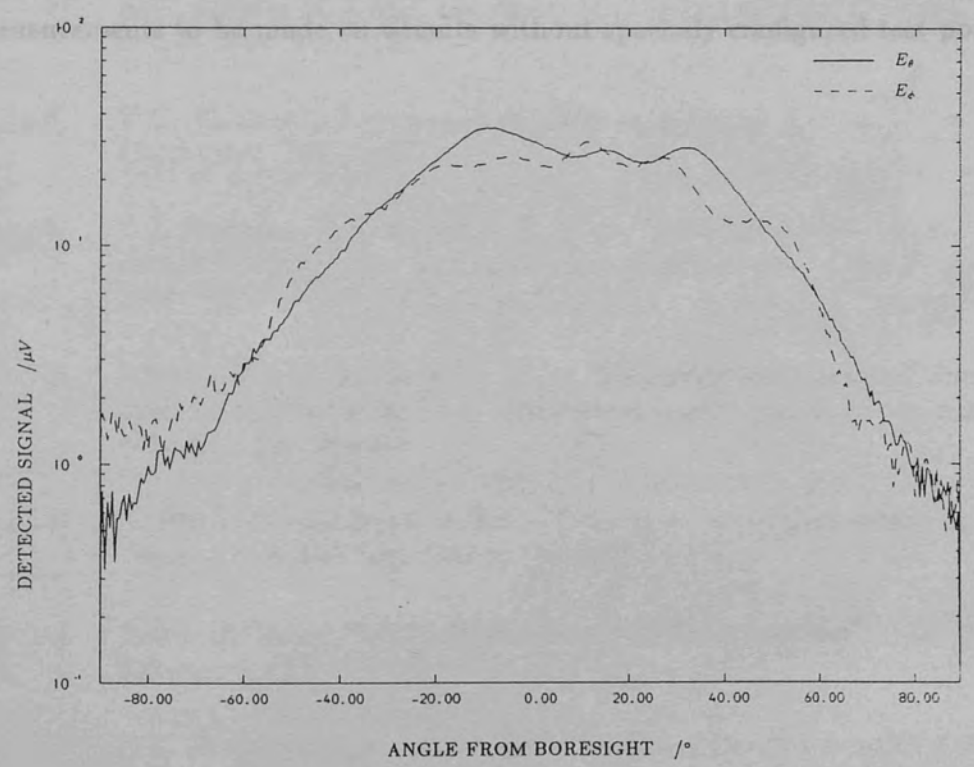

Figure (8.11)b Pentagonal patch radiation pattern in the plane perpendicular to the microstrip feed, F=30.35 *GHz*

a homodyne detector, as discussed in Chapter (3). The homodyne detection system would also give a substantial improvement in sensitivity and linearity compared to video detection. The swept frequency measurement of amplitude and phase is not so readily achieved at millimetric wavelengths, the simplest technique being to employ a GPIB controlled network analyser as the R.F. detector. Where amplitude only data is sufficient, swept frequency measurements would be possible using wide band video detectors and a GBIB controlled sweep oscillator. Swept frequency, one dimensional measurements, could be carried out in the same manner as swept frequency slotted line measurements as described in reference(8.8).

The two dimensional measurements could be made more quantitative by employing a software routine to de-embed the change in probe coupling factor as the probe approaches conductor edges. Such a de-embedding routine would require precise knowledge of the probe coupling factor variation, which will be dependent on the geometry and aspect ratio of the transmission line under test. A de-embedded area scan of a printed antenna array measured in amplitude and phase would provide a more accurate picture of the fringe field radiation sources, as noted in Chapter (7).

In conclusion, this research has demonstrated the basis of a new technique to aid the evaluation of printed circuit antennas which does not require direct connection between the circuit and measurement system, thus allowing measurements to be made on circuits without specially configured test ports.

REFERENCES

Chapter (1)

[1.1] C.R. Seashore, D.R. Singh, "mm–Wave Component Tradeoffs for Tactical Systems," *Microwave Journal June 1982 pp. 41–62*

[1.2] M.I. Skolnik, *Introduction to Radar Systems*, McGraw-Hill Book Co., New York, 1962 pp. 30–40

[1.3] I.J. Bahl, P. Bhartia, *Millimeter Wave Engineering and Applications*, John Wiley, New York, 1984, pp. 1–7

[1.4] B. Mantz, "Finally, a market in millimeter waves.," *Microwaves & RF Sep. 1984 pp. 90–94*

[1.5] R.T. Davies, "Millimeter waves: Controversy brews over transmission media.," *Microwaves Mar. 1976 pp. 32–42*

[1.6] J. Rheindel, "Printed WG circuits trim component costs," *Microwaves Oct. 1980 pp60–63*

[1.7] W.M. Sharpless, "Wafer type mm–wave rectifiers," *Bell S.T.J. vol 35 Nov 1956 pp1385–1402*

[1.8] K.C. Gupta, R. Garg, I.J. Bahl, *Microstrip Lines and Slotlines*, Artech House, New York, 1979

[1.9] T.C. Edwards, *Foundations for Microstrip Circuit Design.*, John Wiley, Chichester. Feb. 1983

[1.10] B.J. Andrews, T.S. Moore, A.T. Niazi, "Millimeter wave Microstrip antennas for dual polar and monopulse applications.," *I.C.A.P. conference 1984*

[1.11] J.R. James, A.Henderson., "High frequency behaviour of microstrip open circuit terminations," *Microwaves Optics and Acoustics, Sep. 1979 vol 3 No 4 pp. 205–219*

[1.12] B. Pozar, "Considerations for millimeter wave printed antennas," *IEEE Trans. AP-31 No5 Sep. 1983 pp740–747*

[1.13] Research–Brief, "Millimetric Microstrip Components," *GEC Research Laboratories*

[1.14] R.E. Forsythe, V.T. Brady, G.T. Wrixon, "Development of a 183 *GHz* subharmonic mixer," *IEEE Trans. MTT-5 May 1979 pp. 640-645*

[1.15] R.E. Forsythe, S.M. Halpern, "Subharmonic mixers for 183–225 *GHz*," *IEEE conf. on IR and mm waves, Miami, Florida, Dec. 1981*

[1.16] R.E. Forsythe, "A coherent solid state receiver for 225 *GHz*," *Microwave Journal 1982 pp64–71*

[1.17] M.V. Schneider, W.W. Snell, "Harmonically pumped stripline down converter," *IEEE Trans. MTT Mar. 1975 pp. 271–275*

[1.18] S.B. Cohn, "Slotline on a dielectric substrate," *IEEE Trans. MTT-17 No 10 1969 pp. 768–778*

[1.19] P.J. Gibson, "The Vivaldi Aerial," *Proc. 9th Eur. Microwave Conf. pp101–105 Sept. 1979*

[1.20] S.N. Prasad, S.Mahapatra, "A Novel MIC slotline antenna.," *Proc. 9th Eur. Microwave Conf. Sept. 1979 pp120–124*

[1.21] A.M.K. Saad, G. Bergmann, "Electrical performance of finlines of various configurations," *Microwaves, optics, and Accoustics Jan. 1977 No2 pp82–87*

[1.22] R.N. Bates, "Millimetre wave finline balanced mixers," *Proc. 9th European Mic. Conf. Sep. 1979 pp721–725*

[1.23] M.D. Coleman, P.J. Meir, "4mm and 5mm printed circuit balanced mixers," *Microwave Journal, Aug. 1979 pp66–68*

[1.24] E.G. Cristal, A.R. Podell, D. Parker, "Microguide, a new microwave integrated circuit transmission line," *IEEE G-MTT symposium digest 1972 p212*

[1.25] R. Knox, "Dielectric wave guide: a low cost option for I.C.s," *microwaves Mar. 1976 pp56–67*

[1.26] M. Dydyk, "Image guide: A promising medium for EHF circuits," *Microwaves April 1981 pp71–80*

[1.27] T.Itoh, "Open guiding structures for mm–wave integrated circuits," *Microwave Journal Sep 1982 pp133–125*

[1.28] R.Knox, P.P. Toulios, "Integrated circuits for the millimeter through optical frequency range," *Proc. Symp. on submillimeter waves, New York March 31- April 2nd 1970 pp497–516*

[1.29] H. Brian, "Microslab: a waveguide medium for the future," *Microwaves & RF. Sept 1986 pp83–88*

[1.30] R.H. Rainwater R.W. Mc Millan, "A hybrid technology for near mm waves," *Microwaves & RF Sept. 1986 pp83–88*

[1.31] G Beadin, M.Gheudin, G.Ruffie,L.Pagani, "230 GHz cosmic receiver: keeping noise down," *Microwaves & RF Sep. 1986 pp91–108*

[1.32] P. Goldsmith, "Infared and mm waves," *Vol. 6, chapter 5, Academic press ISBN 0-12-1477006-1*

[1.33] T.S. Chu, "Geometrical representation of gaussian beam propagation," *B.S.T. Jour. Feb 1966 pp287–299*

[1.34] D.B. Rutledge, D.P.Neikirk, D.P. Kasilingham, *Infrared and mm. waves*, Vol. 10, chapter 1, Academic press

[1.35] S. Mao, S. Jones, G.D. Vendelin, "Millimeter–wave integrated circuits," *IEEE Trans. Vol. MTT-16, No 7, Jul. 1968, pp455–461*

[1.36] P.H. Ladbrooke, "A novel standing wave indicator in microstrip," *The Radio and Electronic Engineer, Vol. 44, No. 5, May 1974, pp273–280*

[1.37] J.R. James, G.J. Wilson, "microstrip antennas and arrays. Part 1, Fundamental action and limitations," *IEE Proc. MOA, Sep. 1977, Vol. 1,No. 5, pp165–174*

[1.38] L. Lewin, "Radiation from discontinuities in striplines," *Proc. IEE, 1960, 107C, pp. 163–170*

[1.39] H. Sobol, "Radiation conductance of open circuit microstrip," *IEEE Trans. 1971, Vol. MTT-19, pp. 885–887*

[1.40] E.O. Hammerstad, "Equations for microstrip circuit design," *Proc. 5^{th} Eur. Microwave conf., 1975, pp. 268–272*

[1.41] G. Kompa, "Approximate calculation of radiation from open ended wide microstrip lines," *Electron. Lett., 1976,12, pp. 222–224*

[1.42] S.E. Schwarz, C.W. Turner, "Measurement techniques for planar high frequency circuits," *IEEE Trans. MTT-34, No 4, Apr. 1986, pp463–467*

Chapter (2)

[2.1] Instructions for the MODULYNX motion control microstep translator card MIF012 and MIF013, The Superior Electric Company, Bristol, Connecticut, USA.

[2.2] The ECONET level 3 user guide, Acorn publications, UK.

Chapter (3)

[3.1] G.S. Smith, "Analysis of Miniature Electric Field Probes with Resistive Transmission Lines," *IEEE Trans. MTT vol. MTT-29, No 11, Nov. 1981, pp1213–1214*

[3.2] S.Ramo, J.R. Whinnery, T. Van Duzer, *Fields and Waves in communication Electronics*, John Wiley, New York 1965, pp. 444

[3.3] R.J. King, *Microwave Homodyne Systems*, Peter Peregrinus 1978, pp178–284

[3.4] R.F. Diode Detectors, application note AN23, Wavetek Pacific Measurements Ltd. USA.

[3.5] I.J. Bahl, P. Bhartia, *Millimeter Wave Engineering and Applications*, John Wiley, New York, 1984, pp.432,445

[3.6] J.H. Richmond, "Measurement of time quadrature components of microwave signals," *IRE Trans. 1955, MTT-3 No2 pp13–15*

CHAPTER 4

[4.1] I.J. Bahl, P. Bhartia, *Microstrip Antennas*, Artech House, New York 1980

[4.2] J.R. James, P.S. Hall, C.Wood, *Microstrip Antenna Theory and Design*, Peter Peregrinus Ltd. 1981

[4.3] A.G.Derneryd, "A theoretical investigation of the rectangular microstrip antenna element," *IEEE Trans. AP-26, No4, pp532–535, July 1978*

[4.4] R.E. Munson, "Conformal Antennas and Microstrip Phased Arrays," *IEEE Trans. AP-27, 1979, pp137–445*

[4.5] Y.T. Lo, D. Soloman, W.F. Richards, "Theory and Experiment on Microstrip Antennas," *El.lett. vol. 15, 1979, pp42–44*

[4.6] W.F. Richards, Y.T. Lo, D.D. Hanson, "Improved theory for microstrip antennas," *El.lett. vol. 15, 1979, pp42–44*

[4.7] K.R. Carver, J.W. Mink, "Microstrip Antenna Technology ," *IEEE Trans. AP-29, No 1, Jan. 1981, pp2–23*

[4.8] Microwave Scalar Measurements, Hewlett Packard Seminar, course notes

[4.9] K.C. Gupta, R. Garg, I.J. Bahl, *Microstrip Lines and Slotlines*, Artech House, New York, 1979

[4.10] J.R. James, A.Henderson., "High frequency behaviour of microstrip open circuit terminations," *Microwaves Optics and Acoustics, Sep. 1979 vol 3, No 4, pp205–219*

[4.11] S.P. Schelkunoff, *Electromagnetic Waves*, Van Nostrand Rheinhold New York 1943 ch.10

[4.12] J. Helszajn, D.S. James, "Planar triangular resonators with Magnetic walls," *IEEE Trans. MTT-26, 1978, pp95-100*

[4.13] Y.S. Wu, F.J. Rosenbaum, "Mode chart for microstrip ring resonators," *IEEE Trans. MTT-21, Jul. 1973, pp487–489*

CHAPTER 5

[5.1] P.J. Gibson, "The Vivaldi Aerial," *Proc. 9th Eur Microwave Conf. pp101–105 Sept. 1979*

[5.2] D.B. Rutledge, S.E. Schwarz, A.T. Adams, "Infrared and submillimetre antennas," *Infrared physics vol 18, pp713–729*

[5.3] W. Hilberg, "From approximations to exact relations for characteristic impedances," *IEEE Trans. Vol. MTT-17, 1969, pp259–265*

[5.4] H.J. Cummins, *Submillimetre Scattering Antennas*, Ph.D. Thesis London 1982, pp.307

[5.5] H. Jasik, *Antenna Engineering Handbook*, McGraw Hill New York, first edition, pp.4-1–4-37

[5.6] S.Ramo, J.R. Whinnery, T. Van Duzer, *Fields and Waves in communication Electronics*, John Wiley, New York 1965, pp.683–686

[5.7] I.J. Bahl, P. Bhartia, *Millimeter Wave Engineering and Applications*, John Wiley, New York, 1984, pp.421–431

[5.8] S.N. Prasad, S.Mahapatra, "A Novel MIC slotline antenna.," *Proc. 9th Eur. Microwave Conf. Sept. 1979, pp120–124*

[5.9] E.L. Kolberg, T. Thungeren, K.S. Yngvesson, "Vivaldi antenna/finline circuit for SIS mixers," *6th Int. Conf. on IR and mm waves, Miami Beach 1981*

[5.10] E.L. Kolberg, T. Thungeren, K.S. Yngvesson, "Vivaldi antennas for single beam integrated receivers," *Proc. 12th European Microwave Conf. Helsinki, 1982, pp361–366*

[5.11] A. Beyer, D. Köther, "Theoretical considerations of finline antennas," *Proc. 5th ICAP conf. York, 1987, pp181–184*

[5.12] M. Helier, P. Lartigue, D. Lecointe, "Analysis of planar non-uniform slotline antennas," *Proc. 5th ICAP conf. York 1987, pp181–184*

[5.13] Y. Abdel-Aziz, H. El-Hennaway, S. Mahrous, K.S. Schunemann, "Design of Vivaldi antennas for microwave integrated circuit applications," *Proc. 14th European Microwave Conf. pp637–642*

[5.14] Cao Ju-liang, Li Wen-Xiang, "Radiation field of tapered slotline antennas," *IEEE AP-S Symp. APS-3-10 1984*

CHAPTER 6

[6.1] A.W. Cross, *Experimental Microwaves*, Saunders Microwave Ltd.

[6.2] P.I. Somlo, J.D. Hunter, *Microwave Impedance Measurement*, Peter Peregrinus U.K. 1985, pp.97

[6.3] S. Roberts, A. Von Hipple, "A new method for measuring the dielectric constant and loss in the range of centimetre waves," *J. Appl. Phys. No 17, 1946, pp610–616*

[6.4] R.P. Owens, "Technique for the measurement of standing wave ratios at low power levels," *Proc. IEE, Vol. 116, No. 6, Jun. 1979, pp933–940*

[6.5] K.C. Gupta, R. Garg, I.J. Bahl, *Microstrip Lines and Slotlines*, Artech House, New York, 1979

[6.6] J.R. James, P.S. Hall, C.Wood, *Microstrip Antenna Theory and Design*, Peter Peregrinus Ltd. 1981

[6.7] J.R. James, A.Henderson., "High frequency behaviour of microstrip open circuit terminations," *Microwaves Optics and Acoustics, Sep. 1979, vol 3, No 4, pp205–219*

[6.8] P.H. Ladbrooke, "A novel standing wave indicator in microstrip," *The Radio and Electronic Engineer, Vol. 44, No. 5, May 1974, pp273–280*

[6.9] E. Yamashita, S. Yawazaki, "Parallel strips embedded in or on a dielectric substrate," *IEEE Trans. MTT-16, 1968, pp972–973*

CHAPTER 7

[7.1] J.R. James, P.S. Hall, C.Wood, *Microstrip Antenna Theory and Design*, Peter Peregrinus Ltd. 1981, chapter 3

[7.2] D.M. Pozar, "Input impedance and mutual coupling of rectangular microstrip antennas," *IEEE Trans. Vol. AP-30, No. 6, Nov. 1982, pp.1191–1196*

[7.3] C.A. Balanis, *Antenna Theory and Design*, Harper Row, New York

[7.4] R.E. Munson, "Conformal microstrip antennas and phased arrays," *IEEE Trans. Vol. AP-22, 1974, pp74–78*

[7.5] T.C. Edwards, *Foundations for Microstrip Circuit Design.*, John Wiley, Chichester, Feb. 1983

[7.6] H. Jasik, *Antenna Engineering Handbook*, McGraw Hill New York, first edition

[7.7] A.G. Derneryd, "Microstrip array antenna," *Proc. 6th European Microwave Conf. Rome, 1976, pp339–343*

[7.8] H.D. Weinschel, "A cylindrical array of circularly polarized microstrip antennas," *IEEE AP-S Symp. Digest, 1975, pp170–180*

[7.9] C. Wood, P.S. Hall, J.R. James, "Design of wideband circularly polarized microstrip antennas and arrays," *ICAP 1978, London, pp312–316*

[7.10] R.P. Jeddlicka, M.T. Poe, K.R. Carver, "Measured mutual coupling between microstrip antennas," *IEEE Trans. Vol. AP-29, No 1, Jan. 1981*

[7.11] H. Van Lil, A.R. Van de Capelle, "Transmission line model for mutual coupling between microstrip antennas," *IEEE Trans. Vol. AP-32, No 8, Aug. 1984, pp.816–821*

[7.12] G. Dubost, A. Rabaa, "Mutual impedance between short circuited flat resonant dipoles," *IEEE Trans. Vol. AP-29, No 4, Jul. 1981, pp.668–671*

[7.13] A.R. Rosen, "Silicon as a monolithically integrated substrate—A new look," *RCA Rev., Vol. 42, Dec. 1981, pp633–660*

CHAPTER 8

[8.1] A.W. Cross, *Experimental Microwaves*, Saunders Microwave Ltd.

[8.2] K.C. Gupta, R. Garg, I.J. Bahl, *Microstrip Lines and Slotlines*, Artech House, New York, 1979

[8.3] C. Railton, T.E. Rozzi,J. Kot, "The efficient calculation of high order shielded microstrip modes for use in discontinuity problems," *Proc. 16th European Microwave Conf. Dublin, Sep. 1986, pp529–534*

[8.4] Y.T. Lo, D. Solomon, W.F. Richards, "Theory and Experiment on Microstrip Antennas," *IEEE Trans. Vol. AP-27,1979,pp.137,145*

[8.5] H.D. Weinschel, "A cylindrical array of circularly polarized microstrip antennas," *IEEE AP-S Symp. Digest, 1975, pp170–180*

[8.6] H.D. Weinschel, "A medium gain circularly polarized microstrip UHF antenna for marine DCP Communication to the GOES Satallite system," *IEEE AP-S Symp. Digest, 1976, pp391–394*

[8.7] P.G. Frayne, C.J. Riddaway, "Resonance in self-oscillating antennas," *Electronic Letters Nov.,1986 Vol. 22, No. 23, pp1269–1270*

[8.8] Weinschel Engineering, *R.F. and Microwave Equipment and Components Catalogue*, 1987, pp. 232–234

Acknowledgements

Grateful thanks are due to Dr P.G. Frayne for his help and encouragement during the course of this research, and for his persistence in obtaining the supporting grants. The mechanical design of the scanning network probe transport and the original concept of in–situ circuit measurements are also attributed to him.

I would like to thank the S.E.R.C. for providing support in the form of a CASE studentship, and for the provision of supporting grants: GR/C/62772 and GR/D/42221.

The project was also partially funded by Marconi Defence Systems Ltd. Stanmore, and thanks are extended for the provision of a 6 month extension of the CASE award. The provision of hard substrates for the 220 *GHz* work by MDS and the use of a return loss measurement facility is also acknowledged. Thanks are due to my various industrial supervisors, Dr G. Morris, Mr D.L. Fudge, Mrs M.S.A.S. Rizk, and Mr P.J. Topley for their helpful discussions and guidance during the course of this work.

The departmental mechanical workshop staff must also be thanked for the provision of high quality service throughout the research period.

The translation of the system specification into an operational electronic control and driver for the probe transport system was superbly accomplished by Mr L.P. Ellison of the electronic workshop. The patience and dedication of Mr Ellison and Mr D.R. Clements in the construction and final commissioning of the scanning network probe electronic hardware was instrumental in getting the system operational in the shortest possible time.

The help and assistance of Mr M. Thyer who carried out the numerous vacuum depositions required for the 220 *GHz* vee experiments, and matched load tests is also gratefully acknowledged.

I would like to acknowledge the assistance given by the thin film department at the GEC Research Centre, Wembley, who made available the facility to process the delicate hard substrates for the 220 *GHz* work.

Thanks are due to the departmental photographic technician Miss S. May who provided the photographic material in this thesis.

The patience, dedication and support of my wife Michelle will not be forgotten.

This thesis was typeset by the author using TEX.

J. Whitehurst April 1988

APPENDIX

Computer Listings

A.1 SCANNING NETWORK PROBE SOFTWARE

CONTENTS

(1) SNP-DRIVE

(2) AREA

(3) LINE

(4) PPLOT

(5) IPLOT

(6) SWAVE

(1) SNP-DRIVE

PRIMITIVE SCANNING NETWORK PROBE DRIVERS

```
25000 DEF PROCm1(ST%,DI%,SP%)
25010 PROChex(ST%)
25020 PROClatch1
25030 PROCmset1(SP%,DI%)
25040 PROCms1
25050 REPEAT
25060   PROCmstat
25070 UNTIL PP%=241
25080 ENDPROC
25090 DEF PROCm2(ST%,DI%,SP%)
25100 PROChex(ST%)
25110 PROClatch2
25120 PROCmset2(SP%,DI%)
25130 PROCms2
25140 REPEAT
25150   PROCmstat
25160 UNTIL PP%=242
25170 ENDPROC
25180 DEF PROCm3(ST%,DI%,SP%)
25190 PROChex(ST%)
25200 PROClatch3
25210 PROCmset3(SP%,DI%)
25220 PROCms3
25230 ENDPROC
25240 DEF PROCm4(ST%,DI%,SP%)
25250 PROChex(ST%)
25260 PROClatch4
25270 PROCmset4(SP%,DI%)
25280 PROCms4
25290 ENDPROC
25300 DEF PROCmstat
25310 PROCwio(&FD19,1)
25320 PROCwio(&FD18,1)
25330 PP%=FNrio(&FE60)
25340 ENDPROC
25350 DEF PROCmset1(SP%,DI%)
25360 PROCwio(&FD01,SP%)
25370 PROCwio(&FD05,DI%)
25380 ENDPROC
25390 DEF PROCmset2(SP%,DI%)
25400 PROCwio(&FD02,SP%)
25410 PROCwio(&FD06,DI%)
25420 ENDPROC
25430 DEF PROCmset3(SP%,DI%)
25440 PROCwio(&FD03,SP%)
25450 PROCwio(&FD07,DI%)
25460 ENDPROC
25470 DEF PROCmset4(SP%,DI%)
25480 PROCwio(&FD04,SP%)
25490 PROCwio(&FD08,DI%)
25500 ENDPROC
25510 DEF PROChex(ST%)
25520 ST%=ST%-1
25530 IF ST%>4068 THEN ST%=4068
25540 D%=ST% DIV 256
25550 E%=(ST%-D%*256) DIV 16
25560 F%=ST%-D%*256-E%*16
25570 ENDPROC
25580 DEF PROClatch1
```

```
25590 PROCwio(&FD1E,F%)
25600 PROCwio(&FD0E,E%)
25610 PROCwio(&FDCE,D%)
25620 PROCwio(&FD8E,1)
25630 ENDPROC
25640 DEF PROClatch2
25650 PROCwio(&FD3E,F%)
25660 PROCwio(&FD2E,E%)
25670 PROCwio(&FDDE,D%)
25680 PROCwio(&FD9E,1)
25690  ENDPROC
25700 DEF PROClatch3
25710 PROCwio(&FD5E,F%)
25720  PROCwio(&FD4E,E%)
25730 PROCwio(&FDEE,D%)
25740 PROCwio(&FDAE,1)
25750 ENDPROC
25760 DEF PROClatch4
25770 PROCwio(&FD7E,F%)
25780 PROCwio(&FD6E,E%)
25790 PROCwio(&FDFE,D%)
25800 PROCwio(&FDBE,1)
25810 ENDPROC
25820 DEF PROCms1
25830 PROCwio(&FD09,1)
25840 ENDPROC
25850 DEF PROCms2
25860 PROCwio(&FD0A,1)
25870 ENDPROC
25880 DEF PROCms3
25890 PROCwio(&FD0B,1)
25900 ENDPROC
25910 DEF PROCms4
25920 PROCwio(&FD0C,1)
25930 ENDPROC
25940 DEF PROCtheta
25950 PROCwio(&FD19,1)
25960 TH=FNrio(&FE60)*360/255
25970 ENDPROC
25980 DEF PROCyread
25990 LOCAL Y1,Y2,Y3,J
26000 PROCwio(&FE62,0)
26010 PROCwio(&FE6E,127)
26020 PROCwio(&FE6C,0)
26030 FORJ=0TO1000:NEXT
26040 PROCwio(&FD19,1)
26050 Y1=FNrio(&FE60)
26060 PROCwio(&FD19,1)
26070 PROCwio(&FD1A,1)
26080 Y1=FNrio(&FE6D)
26090 IF Y1=16 THEN Y1=0 ELSE Y1=255
26100 Y2=FNrio(&FE60)
26110 PROCwio(&FD19,1)
26120 PROCwio(&FD1C,1)
26130 Y3=FNrio(&FE60)
26140 Y=Y3+(Y1+Y2)/512
26150 ENDPROC
26160 DEF PROCxread
26170 LOCAL X1,X2,X3,J
26180 PROCwio(&FE62,0)
26190 PROCwio(&FE6E,127)
```

```
26200 PROCwio(&FE6C,0)
26210 FORJ=0TO1000:NEXT
26220 PROCwio(&FD19,1)
26230 X1=FNrio(&FE60)
26240 PROCwio(&FD19,1)
26250 PROCwio(&FD1B,1)
26260 X1=FNrio(&FE6D)
26270 IF X1=16 THEN X1=0 ELSE X1=255
26280 X2=FNrio(&FE60)
26290 PROCwio(&FD19,1)
26300 PROCwio(&FD1D,1)
26310 X3=FNrio(&FE60)
26320 X=X3+(X1+X2)/512
26330 ENDPROC
26340 DEF PROCinhibit
26350 PROCwio(&FD01,0)
26360 PROCwio(&FD02,0)
26370 PROCwio(&FD03,0)
26380 PROCwio(&FD04,0)
26390 PROCwio(&FD09,1):PROCwio(&FD0A,1):PROCwio(&FD0B,1):PROCwi
o(&FD0C,1)
26400 ENDPROC
26410 DEF FNrio(addr):!X%=addr:A%=5:CALLOSWORD
26420 =X%?4
26430 DEF PROCwio(addr,data):!X%=addr:X%?4=data
26440 A%=6:CALL OSWORD:ENDPROC
```

(2) AREA

EXAMPLE OF AN AREA SCAN ROUTINE

```
  232 FLAG=-1
 1010 MODE7
 1020 K=1000
 1030 @%=&20307
 1040 DIM X% 20:Y%=X% DIV 256 :OSWORD=&FFF1
 1050 PROCinhibit
 1060  R%=0:RR%=0
 1070 PROCintro
 1080 PROCdetchar
 1090 REPEAT:TAT=-1:PROCsetup:UNTIL TAT
 1100 PROCschar
 1110 PROCorigin
 1120 IF R%=0 THEN DIM N$(5),N0$(6,2)
 1130 CLS
 1140 PRINT TAB(1,5)"INPUT FILE HEADER TITLE"
 1150 PRINT TAB(1,7)"UP TO TWO LINES"
 1160 N=1:REPEAT
 1170 INPUT N$(N):N=N+1:UNTILN=3:CLS
 1180 REM ? ON ERROR PROCerror
 1190 PRINT TAB(1,0)"ENTER OUTPUT FILENAME SPECIFICATION"
 1200 INPUT TAB(6,1)":"ANS$
 1210 X=OPENOUT(ANS$):PTR#X=(GY+1)*(GX+1)*GM%*GM%*5:BPUT#X,2:CL
OSE#X
 1220 FIL=OPENOUT(ANS$):CLOSE#FIL:OSCLI("*ACCESS "+ANS$+" "+"LW
R/")
 1230 REM TEST SEE IF FILE WILL FIT AND THEN RESIZE FILE TO ZER
O
 1240  REM
 1250 ON ERROR GOTO1480
 1260 FIL=OPENUP(ANS$):FORN=1TO2:PRINT#FIL,N$(N):NEXT:PROCpush(
NFD,5):PROCpush(T%,5):PROCpush(GX,5):PROCpush(GY,5):PROCpush(GM
%,5)
 1270 MODE0
 1280 PROCarea
 1290 MODE7
 1300 PRINT TAB(0,5)"DO YOU WISH TO RE-SCAN WITH THE SAME "
 1310 PRINT TAB(0,7)"PARAMETERS?"
 1320 PRINT TAB(5,10) "PRESS <Y> OR <N>"
 1330 SE$=GET$
 1340 IF SE$="Y" THEN GOTO1120
 1350 CLS
 1360 PRINT TAB(2,5) "DO YOU WISH TO <E>XIT OR <C>ONTINUE?"
 1370 PRINT TAB(5,10)"PRESS <E> OR <C>"
 1380 SE$=GET$
 1390 IF SE$="E" THEN CHAIN "MENU"
 1400 CLS
 1410 PRINT TAB(2,5)"DO YOU WISH TO CHANGE THE DETECTOR"
 1420 PRINT TAB(2,7)"CHARACTERISTICS??"
 1430 PRINT TAB(2,10)"PRESS <Y> OR <N>"
 1440 SE$=GET$
 1450 IF SE$="Y"  GOTO 1080
 1460 GOTO1100
 1470 CLS
 1480 REM ERROR HANDLING ROUTINE
 1490 IF ERR=220 THEN PRINT TAB(2,5)" YOU HAVE ENTERED SOMETHIN
G THAT I":PRINT TAB(2,7)" DO NOT UNDERSTAND,PLEASE TRY AGAIN":G
OTO1530
 1500 IF ERR=222 THEN PRINT TAB(2,5)" THERE ARE TOO MANY FILES
OPEN ON THE DATA DISK":GOTO1530
```

```
 1510 IF ERR=223 THEN PRINT TAB(2,5)" THE END OF FILE WAS REACH
ED DURING":PRINT TAB(2,7)" THE READ,PLEASE CHECK":GOTO1530
 1520 GOTO1570
 1530 CLOSE#FIL
 1540 PRINT TAB(5,12)"PRESS ANY KEY TO CONTINUE"
 1550 SE$=GET$
 1560 GOTO1290
 1570 REPORT:PRINT ERL:STOP
 1580 END
 1590  REM "EXPERIMENT DRIVER PROCEDURES"
 1600 DEF PROCintro
 1610 CLS
 1620 PRINT TAB(10,5) CHR$(141);"AREA SCAN ROUTINE"
 1630 PRINT TAB(10,6) CHR$(141);"AREA SCAN ROUTINE"
 1640 PRINT TAB(13,9) CHR$(141);"ECONET V2.1"
 1650 PRINT TAB(13,10) CHR$(141);"ECONET V2.1"
 1660  REM
 1670  REM
 1680 PRINT TAB(12,19)"PRESS ANY KEY"
 1690 TMP$=GET$:CLS
 1700 PRINT TAB(5,8) CHR$(141);"PLEASE TELL ME ;"
 1710 PRINT TAB(5,9) CHR$(141);"PLEASE TELL ME ;"
 1720 PRINT TAB(2,10) CHR$(141);"YOUR USER NAME :"
 1730 PRINT TAB(2,11) CHR$(141);"YOUR USER NAME :"
 1740  logon$=""
 1750  REPEAT
 1760    logon$=logon$+GET$
 1770    IF ASC(RIGHT$(logon$,1))=127 THEN logon$=LEFT$(logon$,
LEN(logon$)-1)
 1780    IF ASC(RIGHT$(logon$,1))=13 THEN 1810
 1790    PRINT TAB(20,10);logon$+"    "
 1800    PRINT TAB(20,11);logon$+"    "
 1810  UNTIL RIGHT$(logon$,1)=CHR$(13)
 1820 PRINT TAB(2,12) CHR$(141);"YOUR PASSWORD :"
 1830 PRINT TAB(2,13) CHR$(141);"YOUR PASSWORD :"
 1840 TMP$=" "
 1850 REPEAT
 1860   TMP$=TMP$+GET$
 1870   IF ASC(RIGHT$(TMP$,1))=127 THEN TMP$=LEFT$(TMP$,LEN(TMP
$)-1)
 1880 UNTIL RIGHT$(TMP$,1)=CHR$(13)
 1890  logon$="*I AM "+LEFT$(logon$,LEN(logon$)-1)+TMP$
 1900  CLS:OSCLI("*NET"):OSCLI(logon$)
 1910 ENDPROC
 1920 DEF PROCdetchar
 1930 CLS
 1940 INPUT TAB(1,5)"INPUT DETECTOR TC IN mSECS"T%
 1950 INPUT TAB(1,8)"INPUT DETECTOR NFSD IN uV"NFD
 1960  PRINT TAB(2,20) CHR$(141);"PRESS ANY KEY TO CONTINUE"
 1970  PRINT TAB(2,21) CHR$(141);"PRESS ANY KEY TO CONTINUE"
 1980 SE$=GET$
 1990 ENDPROC
 2000 DEF PROCschar
 2010 CLS
 2020 INPUT TAB(1,5)"INPUT MAXIMUM X EXCURSION IN mm:" GX
 2030 INPUT TAB(1,8)"INPUT MAXIMUM Y EXCURSION IN mm:" GY
 2040 INPUT TAB(1,11)"INPUT MESH IN SAMPLES PER mm   :" GM%
 2050 INPUT TAB(1,15)"LENGTH OF VDU WINDOW IN mm     :" VW
 2060 IF VW=0 THEN VW=GY
 2070 PRINT TAB(1,18)"SELECT SPEED BY KEY,1=FAST,10=SLOW"
 2080 PRINT TAB(9,21)"PRESS KEY NOW"
```

```
2090 SP$=GET$
2100 IF SP$="1" THEN SP%=2
2110 IF SP$="2" THEN SP%=3
2120 IF SP$="3" THEN SP%=4
2130 IF SP$="4" THEN SP%=5
2140 IF SP$="5" THEN SP%=6
2150 IF SP$="6" THEN SP%=7
2160 IF SP$="7" THEN SP%=8
2170 IF SP$="8" THEN SP%=9
2180 IF SP$="9" THEN SP%=10
2190 IF SP$="0" THEN SP%=11
2200 STX=2000 DIV GM%
2210 ENDPROC
2220 DEF PROCorigin
2230 CLS
2240 PRINT TAB(1,5)"SWITCH TO MANUAL AND SET THE ORIGIN"
2250 PRINT TAB(1,8)"ZERO THE COORDINATES!"
2260  PRINT TAB(1,11)"THEN SWITCH BACK TO COMPUTER CONTROL"
2270 PRINT TAB(1,15)"PRESS ANY KEY TO CONTINUE"
2280 SE$=GET$
2290 PROCxread
2300 PROCyread
2310 X0=X:Y0=Y
2320 ENDPROC
2330 DEF PROCdump
2340 LOCAL Z
2350 Z=0:REPEAT:PROCpush(RES(Z),5):Z=Z+1:UNTILZ=GY*GM%+1
2360 ENDPROC
2370 DEF PROCtime
2380 FINI=TIME+7*T%
2390 REPEAT
2400 UNTIL TIME>=FINI
2410 ENDPROC
2420 DEF FNadc
2430 P=ADVAL(1)
2440 =P*1.8/65520*FSD
2450 DEF PROCarea
2460 STX%=2000 DIV GM%
2470 SX=GX*GM%
2480 XP=0
2490 REPEAT
2500   PROCscreen
2510   PROClin
2520   PROCdump
2530   IFXP=SX GOTO2560
2540   PROCinhibit
2550   PROCm2(STX%,0,SP%)
2560   XP=XP+1
2570 UNTIL XP=SX+1
2580  CLOSE#0
2590 PRINT"PRESS <Y> TO HOME PROBE"
2600 S$=GET$:IF S$="Y" THEN GOTO 2610 ELSE GOTO2620
2610 PROChome
2620 ENDPROC
2630 DEF PROClin
2640 LOCAL Z
2650 IF R%=1 GOTO2680
2660 SP=GY*GM%
2670 DIM RES(SP)
2680 CO=0:XX=0
2690 ST%=2000 DIV GM%
```

```
 2700 FOR Z=0 TO GY*GM%
 2710   PROCtime
 2720   V=FNvout(K)
 2730   PROCxread:X=X-X0
 2740   PROCyread:Y=Y-Y0
 2750   RES(Z)=V
 2760   PROCplot
 2770   PROCinhibit
 2780   IF Z=GM%*GY THEN GOTO 2810
 2790   PROCm1(ST%,0,SP%)
 2800    IF CO>VW*GM% THEN CO=0:XX=500/GM%:PROCscreen:MOVE180,V
/U%*600+100
 2810   CO=CO+1
 2820 NEXT Z
 2830  R%=1:RR%=1:FLAG=NOT(FLAG)
 2840 FOR Z=1 TO GY*GM%
 2850   PROCm1(ST%,32,SP%)
 2860 NEXTZ
 2870 ENDPROC
 2880 DEF PROCscreen
 2890 VDU24,0;224;1279;1023;
 2900 VDU28,0,31,79,25
 2910 VDU29,0;224;
 2920 MOVE 0,0
 2930 CLG:CLS
 2940 PROCxaxis
 2950 PROCyaxis
 2960 PROCxlabel
 2970 PROCylabel
 2980  MOVE 180,100
 2990 ENDPROC
 3000 DEF PROCxaxis
 3010 MOVE 180,100
 3020 FORN%=1TO20
 3030   PLOT1,50,0:PLOT1,0,-10:PLOT0,0,10
 3040 NEXT
 3050 MOVE180,100
 3060 ENDPROC
 3070 DEF PROCyaxis
 3080 MOVE 180,100
 3090 FORN%=1TO10
 3100   PLOT1,0,60:PLOT1,-10,0:PLOT0,10,0
 3110 NEXT
 3120 ENDPROC
 3130 DEF PROCxlabel
 3140 VDU5
 3150 MOVE 180,70:PRINT"0.0"
 3160 MOVE 580,70:PRINTVW/2
 3170 MOVE 1100,70:PRINTVW
 3180 MOVE400,28:PRINT"DISTANCE IN mm"
 3190 VDU4
 3200 ENDPROC
 3210 DEF PROCylabel
 3220 VDU5
 3230 MOVE0,120:PRINT"-50dB"
 3240 MOVE0,420:PRINT"-25dB"
 3250 MOVE0,720:PRINT"0dB"
 3260 VDU4
 3270 ENDPROC
 3280 DEF PROCplot
 3290 V1=(50-10*LOG(10000/V))*600/50
```

```
 3300 IF V1<0 THEN V1=0
 3310 V1=INT(V1+100)
 3320 DRAW ABS(XX+180),V1
 3330 XX=XX+1000/VW/GM%
 3340 XX=INT(XX)
 3350 PRINT TAB(0,2)"X=";"        "
 3360 PRINT TAB(0,2)"X=";X
 3370 PRINT TAB(15,2)"Y=";"        "
 3380 PRINT TAB(15,2)"Y=";Y
 3390 PRINT TAB(30,2)"V=";"        "
 3400 PRINT TAB(30,2)"V=";V
 3410 ENDPROC
 3420 DEF PROChome
 3430 LOCAL DX,DY,ST%,DI%
 3440 REPEAT
 3450   FOR J=0TO4000:NEXT
 3460   PROCxread
 3470   DX=X-X0
 3480    IF SGN(DX)=1 THEN DI%=32 ELSE DI%=0
 3490   IF ABS(DX)<=0.001 THEN GOTO 3540
 3500   ST%=INT(DX*2000+.5)
 3510   PROCinhibit
 3520   PROCm2(ST%,DI%,7)
 3530 UNTIL ABS(DX)<=0.001
 3540 REPEAT
 3550   FOR J=0TO4000:NEXT
 3560   PROCyread
 3570   DY=Y-Y0
 3580   IF SGN(DY)=1 THEN DI%=32 ELSE DI%=0
 3590   IF ABS(DY)<=0.001 THEN ENDPROC
 3600   ST%=INT(DY*2000+.5)
 3610   PROCinhibit
 3620   PROCm1(ST%,DI%,7)
 3630 UNTIL ABS(DY)<=0.001
 3640 ENDPROC
 5100 REM file_error
 5110 DEF PROCerror
 5120 IF ERR=191 THEN PROCnotloggedon
 5130 IF ERR=214 THEN GOTO ERL+30
 5140 IF ERR=17 THEN REPORT:STOP
 5150 PRINT" ":PRINT"PRESS ANY KEY TO CONTINUE":SE$=GET$
 5160 ON ERROR OFF:CLS:GOTO1220
 5170 ENDPROC
 5180 DEF FNvout(FSCALE)
 5190 LOCAL IT
 5200 IT=1:PROCatten(FSCALE)
 5210 PROCtime:IT=IT+1
 5220 IFK=10 THEN OSET=K1
 5230 IFK=100 THEN OSET=K2
 5240 IFK=1000 THEN OSET=K3
 5250 IFK=10000 THEN OSET=K4
 5260 V=ADVAL(1)*FSD*1.8/65520-OSET
 5270 IF V<=0 THEN V=0.1
 5280  IF FSCALE=10 THEN GOTO5310
 5290  IF IT>=5 AND V<FSD*.2 THEN GOTO 5320:REM PANIC JUMP OUT!
!!!!
 5300  IF V<FSD*.1:FSCALE=FSCALE/10:PROCatten(FSCALE):PROCtime:
PROCtime:GOTO5210
 5310 IF V>=FSD*1.1 :FSCALE=FSCALE*10:PROCatten(FSCALE):PROCtim
e:PROCtime:GOTO5210
 5320 =V
```

```
5330 DEF PROCatten(FU)
5340 IF FU=10:V%=255:FSD=10
5350 IF FU=100:V%=242:FSD=94.43
5360 IF FU=1000:V%=229:FSD=892.286
5370 IF FU=10000:V%=215:FSD=10000
5380 K=FU
5390 PROCwio(&FE6C,12)
5400 PROCwio(&FE6F,V%)
5410 PROCwio(&FE6C,14):PROCwio(&FE6C,12)
5420 ENDPROC
5430 DEF PROCsetup
5440 TAT=-1
5450 CLS:PRINT TAB(1,4)"SWITCH OFF RF,THEN PRESS ANY KEY"
5460 SE$=GET$
5470 PROCatten(10)
5480 PROCtime
5490 K1=FNadc
5500 PROCatten(100)
5510 PROCtime
5520 K2=FNadc
5530 PROCatten(1000)
5540 PROCtime
5550 K3=FNadc
5560 PROCatten(10000)
5570 PROCtime
5580 K4=FNadc
5590 IF K1>1 THEN CLS:PRINT TAB(1,4)"RF STILL ON OR PSD OFFSET
TOO GREAT":TAT=0:ENDPROC
5600 PRINT TAB(1,4)"SWITCH ON RF,THEN
"
5610 PRINT TAB(1,8)"PRESS ANY KEY"
5620 SE$=GET$
5630 ENDPROC
```

(3) LINE

EXAMPLE OF A LINEAR SCAN ROUTINE

```
  10 MODE7
  20 AC%=1:K=1000:FLAG=-1
  30 @%=&20307
  40 DIM X% 20:Y%=X% DIV 256 :OSWORD=&FFF1
  50 PROCinhibit
  60  R%=0:RR%=0
  70 PROCintro
  80 PROCdetchar
  90 REPEAT:TAT=-1:PROCsetup:UNTIL TAT
 100 PROCschar
 110 PROCorigin
 120 PROClfeature
 130  IF ST$="O" GOTO160
 140  IF ST$="L" GOTO200
 150  IF ST$="S" GOTO200
 160 MODE 0
 170 PROCscreen
 180 PROCoptscan
 190 GOTO230
 200 MODE0
 210 PROCscreen
 220 PROClin
 230 PROCdatastore
 240 MODE7
 250 CLS
 260 PRINT TAB(0,5)"DO YOU WISH TO RE-SCAN WITH THE SAME "
 270 PRINT TAB(0,7)"PARAMETERS?"
 280 PRINT TAB(5,10) "PRESS <Y> OR <N>"
 290 SE$=GET$
 300 IF SE$="N" THEN GOTO 330
 310 PROChome
 320 GOTO 120
 330 CLS
 340 PRINT TAB(2,5) "DO YOU WISH TO <E>XIT OR <C>ONTINUE?"
 350 PRINT TAB(5,10)"PRESS <E> OR <C>"
 360 SE$=GET$
 370 IF SE$="E" THEN CHAIN MENU
 380 CLS
 390 PRINT TAB(2,5)"DO YOU WISH TO CHANGE THE DETECTOR"
 400 PRINT TAB(2,7)"CHARACTERISTICS??"
 410 PRINT TAB(2,10)"PRESS <Y> OR <N>"
 420 SE$=GET$
 430 IF SE$="Y"  GOTO 70
 440 GOTO100
 450 CLS
 460 REM ERROR HANDLING ROUTINE
 470 IF ERR=198 THEN PRINT TAB(2,5)"THE DATA DISK IS FULL,PLEA
SE USE "
 480 PRINT TAB(2,7)"ANOTHER DISK"
 490 IF ERR=199 THEN PRINT TAB(2,5)"THERE IS A FAULT ON THE DA
TA DISK,"
 500 PRINT TAB(2,7)"PLEASE RE-FORMAT OR DISCARD."
 510  IF ERR=220 THEN PRINT TAB(2,5)"YOU HAVE ENTERED SOMTHING
 THAT I"
 520 PRINT TAB(2,7)"DO NOT UNDERSTAND,PLEASE TRY AGAIN"
 530 IF ERR=222 THEN PRINT TAB(2,5)"THERE ARE TOO MANY FILES O
PEN ON THE "
 540 PRINT TAB(2,7)"DATA DISK,PLEASE CHECK"
 550 IF ERR=223 THEN PRINT TAB(2,5)"THE END OF FILE WAS REACHE
```

```
D DURING"
  560 PRINT TAB(2,7)"THE READ,PLEASE CHECK"
  570 PRINT TAB(5,12)"PRESS ANY KEY TO CONTINUE"
  580 SE$=GET$
  590 GOTO240
  600 END
  610  REM "EXPERIMENT DRIVER PROCEDURES"
  620 DEF PROCintro
  630 CLS
  640 PRINT TAB(2,3) CHR$(141);"LINEAR LINE SCAN ROUTINE"
  650 PRINT TAB(2,4) CHR$(141);"LINEAR LINE SCAN ROUTINE"
  660 PRINT TAB(4,9)"SELECT SCAN OPTIONNOW"
  670  PRINT TAB(2,11)"<L>INEAR LINE SCAN ROUTINE"
  680 PRINT TAB(2,13)"<O>PTIMISED LINE SCAN ROUTINE"
  690 PRINT TAB(2,15)"<S>UBSTRATE PROFILE SCAN"
  700 ST$=GET$
  710 PRINT TAB(2,19)"OPTION  ",ST$;"   SELECTED"
  720 FORJ=0TO5000:NEXT
  730 ENDPROC
  740 DEF PROCdetchar
  750 CLS
  760 INPUT TAB(1,5)"INPUT DETECTOR TIME CONSTANT IN mSECS";T%
  770 INPUT TAB(1,10)"INPUT PSD FSD";TFSD
  780   INPUT TAB(1,15)"LENGTH OF VDU WINDOW IN mm";VW
  790  PRINT TAB(2,20) CHR$(141);"PRESS ANY KEY TO CONTINUE"
  800  PRINT TAB(2,21) CHR$(141);"PRESS ANY KEY TO CONTINUE"
  810 SE$=GET$
  820 ENDPROC
  830 DEF PROCschar
  840 CLS
  850 INPUT TAB(1,5)"INPUT SCAN LENGTH IN mm";L
  860 INPUT TAB(1,8)"INPUT NUMBER OF SAMPLES PER mm";S%
  870 PRINT TAB(1,11)"SCAN IN <X> OR <Y>"
  880 SE$=GET$
  890 IF SE$="X" THEN M%=2 ELSE M%=1
  900 PRINT TAB(1,14)"<F>ORWARD OR <R>EVERSE SCAN?"
  910 SE$=GET$
  920 IFSE$="F" THEN G%=0 ELSE G%=32
  930 ENDPROC
  940 DEF PROCorigin
  950 CLS
  960 PRINT TAB(1,5)"SWITCH TO MANUAL AND SET THE ORIGIN"
  970 PRINT TAB(1,8)"DO NOT ZERO THE COORDINATES!"
  980  PRINT TAB(1,11)"THEN SWITCH BACK TO COMPUTER CONTROL"
  990 PRINT TAB(1,15)"PRESS ANY KEY TO CONTINUE"
 1000 SE$=GET$
 1010 PROCxread
 1020 PROCyread
 1030 X0=X:Y0=Y
 1040 ENDPROC
 1050 DEF PROClfeature
 1060 IF R%=0 THEN DIM N$(5),N0$(6,2)
 1070 CLS
 1080 PRINT TAB(1,5)"INPUT THE NAMES OF ANY FEATURES YOU "
 1090  PRINT TAB(1,7)"WISH TO LABEL (UP TO 5,":PRINT TAB(1,9)"T
YPE A SPACE TO FINISH)"
 1100 N=1
 1110 REPEAT
 1120   INPUT N$(N)
 1130   N=N+1
 1140 UNTIL LENN$(N-1)=0 OR N=6
```

```
 1150 PRINT TAB(1,15)"NOW INPUT THE X AND Y COORDINATES IN"
 1160 PRINT TAB(1,17)"THE SAME ORDER"
 1170 N=1
 1180 REPEAT
 1190   INPUT N0$(N,1),N0$(N,2)
 1200   N=N+1
 1210 UNTIL LENN0$(N-1,1)=0 OR N=6
 1220 ENDPROC
 1230 DEF PROCpause
 1240 FINI=TIME+7*T%
 1250 REPEAT
 1260 UNTIL TIME>=FINI
 1270 ENDPROC
 1280 DEF FNadc
 1290 P=ADVAL(1)
 1300 =P*1.8/65520*FSD:REM IN uVOLTS
 1310 DEF PROClin
 1320 LOCAL Z
 1330 IF R%=1 GOTO1360
 1340 SP=L*S%
 1350 DIM RES(SP,3)
 1360 Z=0:CO=0:XX=0
 1370 SP%=8:ST%=2000 DIV S%:DI%=G%
 1380 REPEAT
 1390   PROCpause
 1400   VV=FNvout(K)
 1410   PROCxread:X=X-X0
 1420   PROCyread:Y=Y-Y0
 1430   RES(Z,1)=X:RES(Z,2)=Y:RES(Z,3)=VV
 1440   PROCplot
 1450   PROCinhibit
 1460   IFM%=1 THEN PROCm1(ST%,DI%,SP%) ELSE PROCm2(ST%,DI%,SP%
)
 1470   Z=Z+1:CO=CO+1
 1480    IF CO>VW*S% THEN CO=0:XX=500/S%:PROCscreen:MOVE180,V/U
%*600+100
 1490 UNTIL Z=L*S%+1
 1500  R%=1:RR%=1
 1510 ENDPROC
 1520 DEF PROCoptscan
 1530 LOCAL ST%,SP%,DI%
 1540 IF R%=1 GOTO1560
 1550 DIM RES(L*S%,3),A(11,3)
 1560 IF RR%=0THEN GOTO 1580
 1570 DIM A(11,3)
 1580 Z=0:CO=0:XX=0
 1590 REPEAT
 1600   PROCoset
 1610   PROCtran
 1620   PROCmax
 1630   RES(Z,1)=X:RES(Z,2)=Y:RES(Z,3)=V
 1640   PROCplot
 1650   SP%=8:DI%=G%:ST%=2000 DIV S%
 1660   PROCinhibit
 1670   IFM%=1 THEN PROCm1(ST%,DI%,SP%) ELSE PROCm2(ST%,DI%,SP%
)
 1680   Z=Z+1:CO=CO+1
 1690    IF CO>VW*S% THEN CO=0:XX=0:PROCscreen:MOVE180,V/U%*600
+100
 1700 UNTIL Z=L*S%+1
 1710 R%=1
```

```
1720 ENDPROC
1730 DEF PROCoset
1740 PROCinhibit
1750 IFM%=1 THEN PROCm2(50,0,10) ELSE PROCm1(50,0,10)
1760 ENDPROC
1770 DEF PROCtran
1780 K=1
1790 REPEAT
1800   PROCpause
1810   VV=FNvout(K)
1820   PROCxread:X=X-X0
1830   PROCyread:Y=Y-Y0
1840   A(K,1)=X:A(K,2)=Y:A(K,3)=V
1850   PROCinhibit
1860   IFM%=2 THEN PROCm1(10,32,10) ELSE PROCm2(10,32,10)
1870   K=K+1
1880 UNTIL K=11
1890 IFM%=1 THEN PROCm2(50,0,8) ELSE PROCm1(50,0,8)
1900 ENDPROC
1910 DEF PROCmax
1920 VM=0
1930 FOR K=1 TO 10
1940   H=A(K,3)
1950   IFH>=VM THEN PROCmax1
1960 NEXT
1970 ENDPROC
1980 DEF PROCmax1
1990 X=A(K,1):Y=A(K,2):V=A(K,3)
2000 ENDPROC
2010 DEF PROCscreen
2020 VDU24,0;224;1279;1023;
2030 VDU28,0,31,79,25
2040 VDU29,0;224;
2050 MOVE 0,0
2060 CLG:CLS
2070 PROCxaxis
2080 PROCyaxis
2090 PROCxlabel
2100 PROCylabel
2110  MOVE 180,100
2120 ENDPROC
2130 DEF PROCxaxis
2140 MOVE 180,100
2150 FORN%=1TO20
2160   PLOT1,50,0:PLOT1,0,-10:PLOT0,0,10
2170 NEXT
2180 MOVE180,100
2190 ENDPROC
2200 DEF PROCyaxis
2210 MOVE 180,100
2220 FORN%=1TO10
2230   PLOT1,0,60:PLOT1,-10,0:PLOT0,10,0
2240 NEXT
2250 ENDPROC
2260 DEF PROCxlabel
2270 VDU5
2280 MOVE 180,70:PRINT"0.0"
2290 MOVE 580,70:PRINTVW/2
2300 MOVE 1100,70:PRINTVW
2310 MOVE400,28:PRINT"DISTANCE IN mm"
2320 VDU4
```

```
2330 ENDPROC
2340 DEF PROCylabel
2350 VDU5
2360 MOVE0,120:PRINT"-50dB"
2370 MOVE0,420:PRINT"-25dB"
2380 MOVE0,720:PRINT"  0dB"
2390 VDU4
2400 ENDPROC
2410 DEF PROCplot
2420 V1=(50-10*LOG(10000/VV))*600/50
2430 IF V1<0 THEN V1=0
2440 V1=INT(V1+100)
2450 DRAW ABS(XX+180),V1
2460 XX=XX+1000/VW/S%
2470 XX=INT(XX)
2480 PRINT TAB(0,2)"X=";"       "
2490 PRINT TAB(0,2)"X=";X
2500 PRINT TAB(15,2)"Y=";"       "
2510 PRINT TAB(15,2)"Y=";Y
2520 PRINT TAB(30,2)"V=";"       "
2530 PRINT TAB(30,2)"V=";V
2540 ENDPROC
2550 DEF PROCdatastore
2560 CLS
2570 PRINT TAB(6,2)"DO YOU WISH TO STORE RAW DATA? <Y> OR <N>"
2580 ANS$=GET$
2590 IF ANS$="N" THEN ENDPROC
2600 CLS
2610 INPUT TAB(6,2)"ENTER FILENAME",ANS$
2620 Z=0
2630 X=OPENOUTANS$
2640 N=1
2650 REPEAT
2660   PRINT#X,N$(N),N0$(N,1),N0$(N,2)
2670   N=N+1
2680 UNTILN=6
2690 REPEAT
2700   PRINT#X,RES(Z,1),RES(Z,2),RES(Z,3)
2710   Z=Z+1
2720 UNTIL Z=L*S%+1
2730 CLOSE#X
2740 CLS
2750 PRINT TAB(6,2)"FILE SAVED AND CALLED   ";ANS$
2760 FORJ=0TO4000:NEXT
2770 ENDPROC
2780 DEF PROChome
2790 LOCAL DX,DY,ST%,DI%
2800 REPEAT
2810   PROCxread
2820   DX=X-X0
2830    IF SGN(DX)=1 THEN DI%=32 ELSE DI%=0
2840   ST%=INT(DX*2000)
2850   IF ABS(DX)<=0.005 GOTO2890
2860   PROCinhibit
2870   PROCm2(ST%,DI%,7)
2880 UNTIL ABS(DX)<=0.005
2890 REPEAT
2900   PROCyread
2910   DY=Y-Y0
2920   IF SGN(DY)=1 THEN DI%=32 ELSE DI%=0
2930   IF ABS(DY)<=0.005 THEN ENDPROC
```

```
 2940   ST%=INT(DY*2000)
 2950   PROCinhibit
 2960   PROCm1(ST%,DI%,7)
 2970 UNTIL ABS(DY)<=0.005
 2980 ENDPROC
 2990 DEF FNvout(FSCALE)
 3000 LOCAL IT
 3010 IT=1:PROCatten(FSCALE)
 3020 PROCpause:IT=IT+1
 3030 IFK=10 THEN OSET=K1
 3040 IFK=100 THEN OSET=K2
 3050 IFK=1000 THEN OSET=K3
 3060 IFK=10000 THEN OSET=K4
 3070 V=ADVAL(1)*FSD*1.8/65520-OSET
 3080 IF V<=0 THEN V=0.1
 3090  IF FSCALE=10 THEN GOTO3120
 3100  IF IT>=5 AND V<FSD*.2 THEN GOTO 3130:REM PANIC JUMP OUT!
!!!!
 3110  IF V<FSD*.1:FSCALE=FSCALE/10:PROCatten(FSCALE):PROCpause
:PROCpause:GOTO3020
 3120 IF V>=FSD*1.1 :FSCALE=FSCALE*10:PROCatten(FSCALE):PROCpau
se:PROCpause:GOTO3020
 3130 =V
 3140 DEF PROCatten(FU)
 3150 IF FU=10:V%=255:FSD=TFSD
 3160 IF FU=100:V%=242:FSD=9.443*TFSD
 3170 IF FU=1000:V%=229:FSD=89.2286*TFSD
 3180 IF FU=10000:V%=215:FSD=1000*TFSD
 3190 K=FU
 3200 PROCwio(&FE6C,12)
 3210 PROCwio(&FE6F,V%)
 3220 PROCwio(&FE6C,14):PROCwio(&FE6C,12)
 3230 ENDPROC
 3240 DEF PROCsetup
 3250 TAT=-1
 3260 CLS:PRINT TAB(1,4)"SWITCH OFF RF,THEN PRESS ANY KEY"
 3270 SE$=GET$
 3280 PROCatten(10)
 3290 PROCpause
 3300 K1=FNadc
 3310 PROCatten(100)
 3320 PROCpause
 3330 K2=FNadc
 3340 PROCatten(1000)
 3350 PROCpause
 3360 K3=FNadc
 3370 PROCatten(10000)
 3380 PROCpause
 3390 K4=FNadc
 3400 IF K1>FSD*0.1 THEN CLS:PRINT TAB(1,4)"RF STILL ON OR PSD
OFFSET TOO GREAT":TAT=0:ENDPROC
 3410 PRINT TAB(1,4)" SWITCH ON RF,THEN                        "
 3420 PRINT TAB(1,8)"PRESS ANY KEY"
 3430 SE$=GET$
 3440 ENDPROC
```

(4) PPLOT

EXAMPLE OF A POLAR PLOT ROUTINE

```
  5 DIM X% 20:Y%=X% DIV 256 :OSWORD=&FFF1
 10 REM RADIATION PLOT SOFTWARE V 1.0
 20  PROCinhibit
 25 @%=&20205
 30  DIM PO(360)
 40 MODE 1
 50 PROCsetscreen
 60 PROCinput
 70 PROCposn
 80 PROCpplot
 90 PROCdatastore
100 PROCreset
110 END
120 DEF PROCsetscreen
130 REM SPLIT SCREEN
140 VDU 24,0;224;1279;1023;
150 VDU 28,0,31,39,25
160 COLOUR 1:COLOUR 130
170 GCOL 0,3:GCOL 0,129
180 VDU 29,0;224;
190 MOVE 0,0
200 CLG:CLS
210 PROCxaxis
220 PROCyaxis
230 PROCylabel
240 PROCxlabel
250 ENDPROC
260  DEF PROCxaxis
270 MOVE 180,100
280 FORN%=1TO18
290   PLOT 1,50,0:PLOT 1,0,-10:PLOT 0,0,10
300 NEXT
310 ENDPROC
320 DEF PROCyaxis
330 MOVE 180,100
340 FORN%=1TO10
350   PLOT 1,0,60:PLOT 1,-10,0:PLOT0,10,0
360 NEXT
370 ENDPROC
380 DEF PROCxlabel
390 VDU 5
400 MOVE 180,70:PRINT"-90"
410 MOVE 630,70:PRINT"0"
420 MOVE 1080,70:PRINT"90"
430 MOVE 200,28:PRINT"ANGLE FROM BORESIGHT IN DEG."
440 VDU 4
450 ENDPROC
460 DEF PROCylabel
470 VDU 5
480 MOVE 0,120:PRINT"0.0V"
490 MOVE 0,420:PRINT"0.5V"
500 MOVE 0,720:PRINT"1.0V"
510 VDU 4
520 ENDPROC
530 DEF PROCinput
540 PRINT TAB(3,2)"SPEED  <F>AST OR <S>LOW":SP$=GET$
550 CLS
560 PRINT TAB(3,2)"DIRECTION  <F>WD. OR <R>EV.":DI$=GET$
570 CLS
```

```
 580 IF SP$="F" THEN SP%=8 ELSE SP%=10
 590 IF DI$="F" THEN DI%=0 ELSE DI%=32
 600 PRINT TAB(3,2)"POSITION ANTENNA ON BORESIGHT"
 610 PRINT TAB(9,4)"THEN PRESS ANY KEY"
 620 X$=GET$
 630 CLS:PRINT TAB(3,2)"POSITIONING IN PROGRESS"
 640 ENDPROC
 650 DEF PROCposn
 660  LOCAL SP%,ST%
 670 ST%=3000:SP%=8
 680 J%=0
 690  PROCinhibit
 700  IF DI%=0 THEN DD%=32 ELSE DD%=0
 720 REPEAT
 730   PROChex(ST%)
 740   PROClatch4
 745   PROCmset4(SP%,DD%)
 750   PROCms4
 760   PROCmstat
 770   IF P%=248 THEN GOTO 780 ELSE GOTO 760
 780   J%=J%+1
 790 UNTIL J%=6
 800 FORH%=0TO50000:NEXT
 810 ENDPROC
 820 DEF PROChex(ST%)
 830 ST%=ST%-1
 840 IF ST%>4068 THEN ST%=4068
 850 D%=ST% DIV 256
 860 E%=(ST%-D%*256) DIV 16
 870 F%=ST%-D%*256-E%*16
 880 ENDPROC
 890 DEF PROClatch4
 900 PROCwio(&FD7E,F%)
 910 PROCwio(&FD6E,E%)
 920 PROCwio(&FDFE,D%)
 930 PROCwio(&FDBE,1)
 940 ENDPROC
 950 DEF PROCmset4(SP%,DI%)
 960 PROCwio(&FD04,SP%)
 970 PROCwio(&FD08,DI%)
 980 ENDPROC
 990 DEF PROCmstat
1000 PROCwio(&FD19,1)
1010 PROCwio(&FD18,1)
1020 P%=FNrio(&FE60)
1030 ENDPROC
1040 DEF PROCms4
1050 PROCwio(&FD0C,1)
1060 ENDPROC
1070 DEF PROCinhibit
1080 PROCwio(&FD01,0):PROCwio(&FD02,0):PROCwio(&FD03,0):PROCwi
o(&FD04,0)
1090 PROCwio(&FD09,1):PROCwio(&FD0A,1):PROCwio(&FD0B,1):PROCwi
o(&FD0C,1)
1100 ENDPROC
1110 DEF PROCpplot
1120 X=0:J%=1
1130  MOVE 180,100
1140 CLS:PRINT TAB(3,2)"SCAN INITIATED"
1150 REPEAT
1160   ST%=100
```

```
 1170   PROCmset4(SP%,DI%)
 1180   PROChex(ST%)
 1190   PROClatch4
 1200    FORH%=0TO10000:NEXT
 1210   PO(J%)=ADVAL(1)
 1220   PROCplot
 1230   PROCms4
 1240   PROCmstat
 1250   IF P%=248 THEN GOTO 1260 ELSE GOTO1240
 1260   J%=J%+1
 1270 UNTIL J%=360
 1280 ENDPROC
 1290 DEF PROCplot
 1300 LOCAL Y,XX
 1320 V=PO(J%)
 1325 V=V/65520*1.8*600
 1330  IF V<0 THEN V=0
 1340 Y=INT(V+100)
 1350  PRINT TAB(6,4) PO(J%)/65520*1.8
 1360 XX=INT(X+180)
 1370 DRAW XX,Y
 1380 X=X+.5*5
 1390 ENDPROC
 1400 DEF PROCdatastore
 1410 CLS
 1420 PRINT TAB(3,2)"DO YOU WISH TO STORE RAW DATA Y/N":ANS$=GE
T$
 1430 IF ANS$="N" THEN ENDPROC
 1440 CLS
 1450 INPUT TAB(3,2)"ENTER FILENAME",ANS$
 1460 IF ANS$="" THEN GOTO 1440
 1470 J%=1
 1480 X=OPENOUTANS$
 1490 REPEAT
 1500   PRINT#X,PO(J%)
 1510   J%=J%+1
 1520 UNTIL J%=360
 1530 CLOSE#X
 1540 CLS
 1550 PRINT TAB(0,3)"FILE SAVED AND CALLED  ";ANS$
 1555 FORJ=0TO4000:NEXT
 1560 ENDPROC
 1570 DEF PROCreset
 1580 CLS
 1590 PRINT TAB(0,3)"PRESS Y TO RUN PROGRAM AGAIN"
 1600 Y$=GET$
 1610 IF Y$="Y" THEN RUN ELSE
 1620 ENDPROC
 1630 DEF FNrio(addr):!X%=addr:A%=5:CALL OSWORD
 1640 =X%?4
 1650 DEF PROCwio(addr,data):!X%=addr:X%?4=data
 1660 A%=6:CALL OSWORD:ENDPROC
```

(5) IPLOT

EXAMPLE OF PROGRAMMING WITH THE IEEE INTERFACE

```
  5 DIM X% 20:Y%=X% DIV 256 :OSWORD=&FFF1
 10 REM RADIATION PLOT SOFTWARE V 1.0
 20  PROCinhibit
 25 @%=&20205
 30  DIM PO(360)
 40 MODE 1
 50 PROCsetscreen
 60 PROCinput
 65 PROCpm
 70 PROCposn
 80 PROCpplot
 90 PROCdatastore
100 PROCreset
110 END
120 DEF PROCsetscreen
130 REM SPLIT SCREEN
140 VDU 24,0;224;1279;1023;
150 VDU 28,0,31,39,25
160 COLOUR 1:COLOUR 130
170 GCOL 0,3:GCOL 0,129
180 VDU 29,0;224;
190 MOVE 0,0
200 CLG:CLS
210 PROCxaxis
220 PROCyaxis
230 PROCylabel
240 PROCxlabel
250 ENDPROC
260  DEF PROCxaxis
270 MOVE 180,100
280 FORN%=1TO18
290   PLOT 1,50,0:PLOT 1,0,-10:PLOT 0,0,10
300 NEXT
310 ENDPROC
320 DEF PROCyaxis
330 MOVE 180,100
340 FORN%=1TO10
350   PLOT 1,0,60:PLOT 1,-10,0:PLOT0,10,0
360 NEXT
370 ENDPROC
380 DEF PROCxlabel
390 VDU 5
400 MOVE 180,70:PRINT"-90"
410 MOVE 630,70:PRINT"0"
420 MOVE 1080,70:PRINT"90"
430 MOVE 200,28:PRINT"ANGLE FROM BORESIGHT IN DEG."
440 VDU 4
450 ENDPROC
460 DEF PROCylabel
470 VDU 5
480 MOVE 0,120:PRINT"-60dBm"
490 MOVE 0,420:PRINT"-40dBm"
500 MOVE 0,720:PRINT"-20dBm"
510 VDU 4
520 ENDPROC
530 DEF PROCinput
540 PRINT TAB(3,2)"SPEED  <F>AST OR <S>LOW":SP$=GET$
550 CLS
560 PRINT TAB(3,2)"DIRECTION  <F>WD. OR <R>EV.":DI$=GET$
```

```
 570 CLS
 580 IF SP$="F" THEN SP%=8 ELSE SP%=10
 590 IF DI$="F" THEN DI%=0 ELSE DI%=32
 600 PRINT TAB(3,2)"POSITION ANTENNA ON BORESIGHT"
 610 PRINT TAB(9,4)"THEN PRESS ANY KEY"
 620 X$=GET$
 630 CLS:PRINT TAB(3,2)"POSITIONING IN PROGRESS"
 640 ENDPROC
 650 DEF PROCposn
 660  LOCAL SP%,ST%
 670 ST%=3000:SP%=8
 680 J%=0
 690  PROCinhibit
 700  IF DI%=0 THEN DD%=32 ELSE DD%=0
 720 REPEAT
 730   PROChex(ST%)
 740   PROClatch4
 745   PROCmset4(SP%,DD%)
 750   PROCms4
 760   PROCmstat
 770   IF P%=248 THEN GOTO 780 ELSE GOTO 760
 780   J%=J%+1
 790 UNTIL J%=6
 800 FORH%=0TO50000:NEXT
 810 ENDPROC
 820 DEF PROChex(ST%)
 830 ST%=ST%-1
 840 IF ST%>4068 THEN ST%=4068
 850 D%=ST% DIV 256
 860 E%=(ST%-D%*256) DIV 16
 870 F%=ST%-D%*256-E%*16
 880 ENDPROC
 890 DEF PROClatch4
 900 PROCwio(&FD7E,F%)
 910 PROCwio(&FD6E,E%)
 920 PROCwio(&FDFE,D%)
 930 PROCwio(&FDBE,1)
 940 ENDPROC
 950 DEF PROCmset4(SP%,DI%)
 960 PROCwio(&FD04,SP%)
 970 PROCwio(&FD08,DI%)
 980 ENDPROC
 990 DEF PROCmstat
1000 PROCwio(&FD19,1)
1010 PROCwio(&FD18,1)
1020 P%=FNrio(&FE60)
1030 ENDPROC
1040 DEF PROCms4
1050 PROCwio(&FD0C,1)
1060 ENDPROC
1070 DEF PROCinhibit
1080 PROCwio(&FD01,0):PROCwio(&FD02,0):PROCwio(&FD03,0):PROCwi
o(&FD04,0)
1090 PROCwio(&FD09,1):PROCwio(&FD0A,1):PROCwio(&FD0B,1):PROCwi
o(&FD0C,1)
1100 ENDPROC
1110 DEF PROCpplot
1120 X=0:J%=1
1130  MOVE 180,100
1140 CLS:PRINT TAB(3,2)"SCAN INITIATED"
1150 REPEAT
```

```
 1160   ST%=100
 1170   PROCmset4(SP%,DI%)
 1180   PROChex(ST%)
 1190   PROClatch4
 1200    FORH%=0TO10000:NEXT
 1210   PO(J%)=FNpower_value(pm%)
 1220   PROCplot
 1230   PROCms4
 1240   PROCmstat
 1250   IF P%=248 THEN GOTO 1260 ELSE GOTO1240
 1260   J%=J%+1
 1270 UNTIL J%=360
 1280 ENDPROC
 1290 DEF PROCplot
 1300 LOCAL Y,XX
 1320 V=PO(J%)
 1325 V=(40-(-20-V))*600
 1330  IF V<0 THEN V=0
 1340 Y=INT(V+100)
 1350  PRINT TAB(6,4) PO(J%)/65520*1.8
 1360 XX=INT(X+180)
 1370 DRAW XX,Y
 1380 X=X+.5*5
 1390 ENDPROC
 1400 DEF PROCdatastore
 1410 CLS
 1415 *DISK
 1420 PRINT TAB(3,2)"DO YOU WISH TO STORE RAW DATA Y/N":ANS$=GE
T$
 1430 IF ANS$="N" THEN ENDPROC
 1440 CLS
 1450 INPUT TAB(3,2)"ENTER FILENAME",ANS$
 1460 IF ANS$="" THEN GOTO 1440
 1470 J%=1
 1480 X=OPENOUTANS$
 1490 REPEAT
 1500   PRINT#X,PO(J%)
 1510   J%=J%+1
 1520 UNTIL J%=360
 1530 CLOSE#X
 1540 CLS
 1550 PRINT TAB(0,3)"FILE SAVED AND CALLED  ";ANS$
 1555 FORJ=0TO4000:NEXT
 1560 ENDPROC
 1570 DEF PROCreset
 1580 CLS
 1590 PRINT TAB(0,3)"PRESS Y TO RUN PROGRAM AGAIN"
 1600 Y$=GET$
 1610 IF Y$="Y" THEN RUN ELSE
 1620 ENDPROC
 1630 DEF FNrio(addr):!X%=addr:A%=5:CALL OSWORD
 1640 =X%?4
 1650 DEF PROCwio(addr,data):!X%=addr:X%?4=data
 1660 A%=6:CALL OSWORD:ENDPROC
 2000 DEF PROCpm
 2010 *IEEE
 2020 PROCinitialize
 2030 pm%=OPENIN(1,1)
 2040 PROCoutput(pm%,"G")
 2050 PROCoutput(pm%,"L")
 2060 ENDPROC
```

```
5000 REM IEEE DRIVER PROCEDURES
5010  DEF PROCinitialize
5020 CLOSE#0
5030 cmd%=OPENIN("COMMAND")
5040 data%=OPENIN("DATA")
5050 PRINT#cmd%,"BBC DEVICE NO",0
5060 PRINT#cmd%,"CLEAR"
5070 PRINT#cmd%,"REMOTE ENABLE"
5080 PRINT#cmd%,"UNTALK"
5090 PRINT#cmd%,"UNLISTEN"
5100 ENDPROC
5110 REM INPUT FUNCTION
5120 DEF FNinput(device%)
5130 LOCAL message$
5140 PRINT#cmd%,"TALK",device%
5150 INPUT#data%,message$
5160 PRINT#cmd%,"UNTALK"
5170 =message$
5180 REM OUTPUT PROCEDURE
5190  DEF PROCoutput(device%,message$)
5200 PRINT#cmd%,"LISTEN",device%,"EXECUTE"
5210 PRINT#data%,message$
5220 PRINT#cmd%,"UNLISTEN"
5230 ENDPROC
5240  DEF FNpower_value(dev%)
5250 LOCAL T$
5260 R$=FNinput(dev%)
5270  T$=MID$(R$,4,9)
5280 =VAL(T$)
```

(6) SWAVE

VSWR ANALYSER FOR SNP DATA

```
C     PROGRAM TO ANALYSE MICROWAVE FIELD PLOTTER VSWR DATA
C
C
C                BY J. WHITEHURST BSc.
C
C
C          note  that the maximum/minimum seeker is
C                optimised for high vswrs
C
      integer imax,imin
      real noise(5),glen1(50),glen2(50),vswr(50)
      logical flag
      common nmin,nmax,imax,imin,data(1000,3),vm(50,3),vn(50,3)
,vim,flag
      print*,' input position of load and analysis extent in mm
 '
      read*,scp,ssp
      print*,' '
      print*,'input number of data points and scan length in mm
  '
      read*,points,slen
      print*,' '
      print*,'input line impedance, loss (dB/mm), substrate hei
ght (mm)'
      read*,z0,alpha,shei
c convert alpha to nepers
      alpha=4.343*alpha
      print*,'is data:'
      print*,' '
      print*,'         1> absolute power'
      print*,' '
      print*,'         2> relative power'
      read*,psel
      points2=int(points*ssp/slen)
      do 1 k=1,points
      read(7,*) data(k,1),data(k,2),data(k,3)
   1  continue
c     array set up now find noise average
      if(psel.eq.2) then
      print*,'enter  1> to insert detector plateau'
      print*,' '
      print*,'       2> for auto plateau set (o/c scans only)'
      read*, dse
      if (dse.eq.1) then
      print*,'enter plateau height in uV'
      read*,avnoise
      else
      do 2 k=1,5
      noise(k)=50.
    2 continue
      do 3 k=1,points
      if(data(k,3).le.noise(1)) then
      noise(1)=data(k,3)
       else if(data(k,3).le.noise(2)) then
        noise(2)=data(k,3)
         else if(data(k,3).le.noise(3)) then
          noise(3)=data(k,3)
           else if(data(k,3).le.noise(4)) then
            noise(4)=data(k,3)
```

```
            else if(data(k,3).le.noise(5)) then
             noise(5)=data(k,3)
          end if
        3 continue
          avnoise=average(noise,5)
          errnoise=sdev(noise,5,avnoise)
c now subtracting noise pedestal from array....
          endif
          do 4 k=1,points
           data(k,3)=data(k,3)-avnoise
            if (data(k,3).le.0) then
             data(k,3)=0.1
            end if
        4 continue
          else
          endif
c         now to find max and min
          vim=data(1,3)
          nmax=0
          nmin=0
          imax=0
          imin=0
          if(data(1,3).gt.data(2,3)) then
          flag=.true.
           else
            flag=.false.
          end if
          do 5 k=1,points
          if( .not. flag) then
           call vmax(k,ssp)
            else if (flag) then
            call vmin(k,ssp)
           end if
        5 continue
c         max and min data now in vm and vn resp...
c
c         now to find effective permittivity..
          do 6 k=2,imax-2
          glen1(k-1)=2*(vm(k+1,2)-vm(k,2))
          glen2(k-1)=2*(vn(k+1,2)-vn(k,2))
        6 continue
c         now average and find standard deviation
          wl1=average(glen1,(imax-3))
          wl2=average(glen2,(imin-3))
          sd1=sdev(glen1,(imax-3),wl1)
          sd2=sdev(glen2,(imin-3),wl2)
c now find vswr...  loss corrected.
          do 7 k=2,imax-2
          swr=sqrt(vm(k,3)/vn(k,3))
          posmax=scp-vm(k,2)
          p1=alpha*posmax
          p2=wl2*alpha/4
          if (flag) then
          s1=cvswr(swr,p1,p2)
            else
            p2=-p2
            s1=cvswr(swr,p1,p2)
          endif
          vswr(k-1)=s1
        7 continue
          vsw=average(vswr,imax-3)
```

```
      svsw=sdev(vswr,imax-3,vsw)
c find position of first min
      dsum=wl2
      do 8 k=2,nmin
      delta=scp-vn(k,2)
      if(delta.lt.dsum.and.delta.ge.0.) then
      dsum=delta
      else
      endif
    8 continue
c     now find radiation resistance and susceptance
      dphi2=(wl2/4-dsum)*2*3.1415/wl2
      b2=z0*(vsw**2*(cos(dphi2/2))**2+(sin(dphi2/2))**2)
      gr=vsw/b2
      b=(vsw**2-1)*sin(dphi2/2)*cos(dphi2/2)/b2
      dphi1=(wl1/4-dsum)*2*3.1415/wl1
      b2=z0*(vsw**2*(cos(dphi1/2))**2+(sin(dphi1/2))**2)
      gr1=vsw/b2
      b1=(vsw**2-1)*sin(dphi1/2)*cos(dphi1/2)/b2
c find delta l/h
      dl1=(wl1/4-dsum)/shei
      dl2=(wl2/4-dsum)/shei
c find delta l/h according james and henderson
      dd1=ddash(wl1,b,z0)/shei
      dd2=ddash(wl2,b1,z0)/shei
c     data output
      print*,'guide wavelength in mm= ',wl1,'+/- ',sd1
      print*,' '
      print*,'guide wavelength in mm= ',wl2,'+/- ',sd2
      print*,' '
      print*,'first minimum= ',dsum,' mm',' dl1=',dl1,'  dl2=',
dl2
      print*,' Henderson delta l/h = ',dd1,' and ',dd2
      print*,'load vswr= ',vsw,' +/- ',svsw
      print*,' '
      print*,'load conductance= ',gr1,' s'
      print*,' '
      print*,'end susceptance      = ',b1,' s'
      print*,' '
      print*,'load conductance= ',gr,' s '
      print*,' '
      print*,'end susceptance      = ',b,' s '
      end
      subroutine vmax(k,ssp)
      logical flag
      common nmin,nmax,imax,imin,data(1000,3),vm(50,3),vn(50,3)
,vim,flag
      if(data(k,3).ge.vim) then
      vim=data(k,3)
      kappa=k
        else if(data(k,3).lt.(vim-10).and.data(k,2).le.ssp) the
n
        nmax=nmax+1
        imax=nmax
        vm(nmax,1)=data(kappa,1)
        vm(nmax,2)=data(kappa,2)
        vm(nmax,3)=data(kappa,3)
        flag= .not.flag
           else if(data(k,3).lt.(vim-10).and.data(k,2).gt.ssp)
then
           nmax=nmax+1
```

```
            vm(nmax,1)=data(kappa,1)
            vm(nmax,2)=data(kappa,2)
            vm(nmax,3)=data(kappa,3)
            flag= .not. flag
        end if
        end
        subroutine vmin(k,ssp)
        logical flag
        common nmin,nmax,imax,imin,data(1000,3),vm(50,3),vn(50,3)
,vim,flag
        if(data(k,3).le.vim) then
        vim=data(k,3)
        kappa=k
         else if(data(k,3).gt.(vim+50).and.data(k,2).le.ssp) then
         nmin=nmin+1
         imin=nmin
         vn(nmin,1)=data(kappa,1)
         vn(nmin,2)=data(kappa,2)
         vn(nmin,3)=data(kappa,3)
         flag=.not. flag
           else if(data(k,3).gt.(vim+10).and.data(k,2).gt.ssp) th
en
           nmin=nmin+1
           vn(nmin,1)=data(kappa,1)
           vn(nmin,2)=data(kappa,2)
           vn(nmin,3)=data(kappa,2)
           flag= .not. flag
        end if
        end
        function average(darray,n)
        dimension darray(1000)
        sum=0.
        do 1  k=1,n
        sum=sum+darray(k)
      1 continue
        average=sum/float(n)
        end
        function sdev(darray,n,a)
        dimension darray(1000)
        sum=0.
        do 1 k=1,n
        sum=sum+(darray(k)-a)**2
      1 continue
        sum=sum/float(n)
        sdev=sqrt(sum)
        end
        real function ddash(w,s,z)
        a=w/2/3.142
        b=atan(s*z)
        ddash=a*b
        end
c loss correction function for vswr
c taken from Somlo and Hunter
        real function cvswr(swrp,r1,r2)
c uses nag routine s11aaf to find ATANH(x)
        real S11AAF
        ifail=1
        x=1/swrp+r2
        b=S11AAF(x,ifail)
        cvswr=1/tanh(b-r1)
        end
```

A.2 ANTENNA DESIGN SOFTWARE

CONTENTS

(1) PATCH

(2) TRIMODE

(3) DMODE

(4) WIRE

(5) V-IMP

(1) PATCH

FINDS VSWR AND FIRST MINIMUM LOCATION ON AN EDGE FED PATCH

```
      real ll,lh,impede,induct,plen
      dimension gout(201,4)
      parameter(pi=3.1415)
      print*,'input linewidths of patch and feed'
      read*,wil,wih
      print*,' '
      print*,' input patch length in mm'
      read*, plen
      if(wih.gt.wil) then
      wlow=wih
      whi=wil
      else
      wlow=wil
      whi=wih
      endif
      print*,' '
      print*,'input substrate height and relative permittivity'
      read*,h,er
      print*,' '
      print*,'start and stop frequencies in GHz'
      read*, f1,f2
      print*,' '
c set up loop
      fint=(f2-f1)/200
      n=1
c find resonant frequency....
      rf=fret(wlow/h,er,plen,h)
      print*,rf
      do 1 f=f1,f2,fint
      wlen=300/f
c first find characteristic impedances
      ratl=wlow/h
      eel=eef(ratl,er,h)
      zlow=impede(wlow,eel,h,f)
      elo=efperm(er,eel,f,zlow,h)
      ll=induct(zlow,eel)
      rat=whi/h
      ee=eef(rat,er,h)
      zhi=impede(whi,ee,h,f)
      ehi=efperm(er,ee,f,zhi,h)
c find inductances
      lh=induct(zhi,ee)
c now find capacitive line extension
      res1=deltal(ratl,eel)
      res1=res1*h
c find b
      b=2*pi*res1*sqrt(elo)/zlow/wlen
c find g
      g=1/(60*wlen/wlow)
c characteristic admittance
      y0=1/zlow
c useful brackets
      be=2*pi*sqrt(elo)/wlen
      t=tan(be*plen)
      fu1=y0-b*t
      fu2=b+y0*t
c find g' and b'
      fu3=fu1**2
      fu4=g*t
```

```
      de1=fu3+fu4**2
      bdash=b+y0*(fu1*fu2-g**2*t)/de1
      gdash=g+y0*(g*fu1+g*t*fu2)/de1
      bh=2*pi*sqrt(ehi)/wlen
      de2=gdash**2+bdash**2
      r1=gdash/de2
      b1=-bdash/de2
      xl=2*pi*ll*f
      top1=2*b1*zhi+xl*de2
      bot1=r1**2-zhi**2+b1**2
      hpangle=atan(top1/bot1)
      if((f.lt.(rf-.5)).and.(hpangle.lt.0)) then
       hpangle=hpangle+pi
      else if((f.gt.(rf+.5)).and.(hpangle.gt.0)) then
       hpangle=hpangle-pi
      endif
      de3=(zhi+r1)**2+b1**2
      rho=(sqrt(bot1**2+top1**2))/de3
      rloss=20*alog10(rho)
      vswr=(1+rho)/(1-rho)
      smax=hpangle/2/bh
      gout(n,1)=f
      gout(n,2)=vswr
      gout(n,3)=rloss
      gout(n,4)=smax
      n=n+1
1     continue
c data output
      do 2 n=1,201
      write(100,*) gout(n,1)
      write(100,*) gout(n,2)
      write(101,*) gout(n,1)
      write(101,*) gout(n,3)
      write(102,*) gout(n,1)
      write(102,*) gout(n,4)
2     continue
      end
      real function eef(a,b,c)
      co=(b-1)/4.6*(.017/c)/sqrt(a)
      if(a.le.1) then
      fwh=(1+12/a)**-.5+0.04*(1-a)**2
      else
      fwh=(1+12/a)**-.5
      endif
      eef=(b+1)/2+(b-1)/2*fwh-co
      end
      real function deltal(a,b)
      top=(b+0.3)*(a+.264)
      bot=(b-.258)*(a+0.8)
      deltal=0.412*top/bot
      end
      real function efperm(permr,perme,fr,zo,hi)
      fp=zo*15.66/25.4/hi
      g=sqrt((zo-5)/60)+0.004*zo
      efperm=permr-(permr-perme)/(1+(g*(fr/fp)**2))
      end
      real function impede(wid,c,hei,ff)
      rt=wid/hei
      a=1/3.142/2
      if(rt.le.a) then
      rt1=rt+1.25/3.142*.017/hei*(1+alog(4*3.142*wid/.017))
```

```
      else
      rt1=rt+1.25/3.142*0.017/hei*(1+alog(2*hei/.017))
      endif
      if (rt.le.1.) then
      b=120./2./sqrt(c)*alog(8./rt1+0.25*rt1)
      else
      b=120.*3.142/sqrt(c)*(rt1+1.393+0.667*(alog(rt1+1.444)))*
*-1
      endif
      rt2=rt1/2
      if(rt2.le.1) then
      zb=120./sqrt(c)*alog(8./rt2+0.25*rt2)
      else
      zb=240.*3.142/sqrt(c)*(rt2+1.393+0.667*(alog(rt2+1.444)))
**-1
      endif
      g=sqrt((b-5)/60)+0.004*b
      fp=b*15.66/hei/25.4
      zf=zb-(zb-b)/(1+g*(ff/fp)**2)
      impede=zf
      end
      real function induct(z,eeff)
      induct=z*sqrt(eeff)/3.0e8
      end
      real function dl(widl,widh,l1,l2,hi)
      real l1,l2,ls
      a=widl/widh-1
      ls=hi*(40.5*a-75.*alog10(widl/widh)+0.2*a**2)
      ls=ls*1e-9
      dl=ls/(l1+l2)
      end
      real function di(g,z,ed)
      di=g*3.0e10/sqrt(ed)/z
      end
      real function fret(a,b,c,hi)
      real impede
      dl=hi*deltal(a,b)
      ef=eef(a,b,hi)
      bot=sqrt(ef)*2*(c+2*dl)
      fret=300/bot
      end
```

(2) TRIMODE

CREATES DATA FOR THEORETICAL $|E_z|^2$ DISTRIBUTION IN A TRIANGULAR PATCH

```
c program to calculate theoretical mode plots for
c
c equalateral triangular resonators.
c
c by J. Whitehurst BSc.
c
c for use with general plotting package
c
c
      real m,n,l
      dimension ez(101,101)
      common x0,x1
      a=5
      x0=5-5/sqrt(3.)
      x1=5+5/(2*sqrt(3.))
      print*,'input required mode number m,n,l'
      read*,m,n,l
      print*,'input number of samples/mm'
      read*,isample
      write(99,*) 1000,1,10,10,isample
      istop=10*isample
      x=0
      do 1 ix=1,istop+1
      y=0
      if((x.ge.x0).and.(x.le.x1)) then
      do 2 iy=1,istop+1
      ez(ix,iy)=ef(x,y,a,m,n,l)
      y=y+1/float(isample)
2     continue
      x=x+1/float(isample)
      else
      do 4 i=1,istop+1
      ez(ix,i)=0.
4     continue
      x=x+1/float(isample)
      endif
1     continue
      do 3 i=1,istop+1
      write(99,*) (ez(i,j),j=1,istop+1)
3     continue
      write(99,*) 'triangular  mode plot, m= ',m,'n= ',n,'l= ',
1
      end
ccccccccccccccccccccccccccccccccccccccccccccccccccccccccccccccccc
ccccccccccc
c
c
      real function ef(xd,yd,b,d,e,f)
      common x0,x1
      tang=0
      yfactor1=5+1/sqrt(3.)*(xd-x0)
      yfactor2=5-1/sqrt(3.)*(xd-x0)
      if (xd.eq.x0) then
      x=xd-5
      y=0
      else if((yd.ge.yfactor2).and.(yd.le.yfactor1)) then
      x=xd-5
      y=yd-5
      else
```

```
      tang=1.
      endif
      if(tang.eq.1.) then
      f1=0.
      f2=0.
      f3=0.
      else
      f1=funt(d,e,f,b,x,y)
      f2=funt(e,f,d,b,x,y)
      f3=funt(f,d,e,b,x,y)
      endif
      ef=(f1+f2+f3)**2*1000/9
      end
ccccccccccccccccccccccccccccccccccccccccccccccccccccccccccccccccccc
ccccccc
c
c
      real function funt(a,b,c,bb,xx,yy)
      pi=3.1415
      f1=cos((2*pi*xx/sqrt(3.)/bb+2*pi/3)*c)
      f2=cos(2*pi*(a-b)*yy/3/bb)
      funt=f1*f2
      end
```

(3) DMODE

CREATES DATA FOR THEORETICAL $|E_z|^2$ DISTRIBUTION IN A CIRCULAR PATCH

```
c program to compute theoretical Ez distributions by
c the simple cavity model
c uses nag routines s17aef to find j0(x)
c and s17aff to find j1(x)
c
c
c another J. Whitehurst software production.......
c
c
      common ez(101,101),a
      print*,'select mode required by number'
      print*,' '
      print*,'  1> TM 11'
      print*,' '
      print*,'  2> TM 21'
      print*,' '
      print*,'  3> TM 02'
      print*,' '
      print*,'  4> TM 31'
      print*,' '
      read*,mode
      print*,'input grid sample, max 10'
      print*,' '
      read*,grid
c select bessel function zero and calculate dummy waveno.
      if(mode.eq.1) then
        x0=1.84118
      else if(mode.eq.2) then
        x0=3.05424
      else if(mode.eq.3) then
        x0=3.83171
      else if(mode.eq.4) then
        x0=4.20119
      endif
      wnum=x0/2.5
c
c now generate plot data
c
      call tmnm(wnum,grid,mode)
c
c now output data to for099.dat
c
      write(99,*)1000,15,10,10,grid
      imax=int(10*grid+1)
      d=a**2/1000
      do 1 i=1,imax
      do 2 j=1,imax
      write(99,*) (ez(i,j))**2/d
2     continue
1     continue
      write(99,*)'disk mode plot number ',mode
      end
c
c
c subroutine to find ez value and assign array ele's
c
c
      subroutine tmnm(w,g,m)
      real s17aef,s17aff
```

```
      integer ifail
      common ez(101,101),a
      a=0.
      imax=int(10*g+1)
      do 1 i=1,imax
      do 2 j=1,imax
      x=float(i-1)/g
      y=float(j-1)/g
      if(x.lt.2.5) then
        ez(i,j)=0.
      else if((x.le.7.5).and.(x.ge.2.5)) then
          rmod=sqrt((x-5)**2+(y-5)**2)
          if(abs(rmod).le.2.5) then
          if((x-5).eq.0.) then
          xx=1.e-8
          else
          xx=x-5
          endif
          rthi=(y-5)/xx
          thi=atan(rthi)
          rmod=rmod*w
c
c now select mode mutiplier....
c
          if(m.eq.1) then
            ifail=0
            ez(i,j)=s17aff(rmod,ifail)*cos(thi)
          if(ifail.ne.0) then
            print*,'failed in s17aff'
          endif
          else if(m.eq.2) then
            thi=2*thi
            ez(i,j)=bessj(2,rmod)*cos(thi)
          else if(m.eq.3) then
            ifail=0
            ez(i,j)=s17aef(rmod,ifail)
          else if(m.eq.4) then
            thi=3*thi
            ez(i,j)=bessj(3,rmod)*cos(thi)
          endif
        else
          ez(i,j)=0.
        endif
      endif
      if(abs(ez(i,j)).gt.a) then
      a=ez(i,j)
      endif
2     continue
1     continue
      end
c
c now bessel function generator for other than j0,j1..
c
      real function bessj(n,x)
      real s17aef,s17aff
      integer ifail
      parameter(iacc=40,bigno=1.e10,bigni=1.e-10)
      if(abs(x).eq.0.) x=1.e-8
      tox=2./x
      if(x.gt.float(n)) then
        ifail=0
```

```
        bjm=s17aef(x,ifail)
        ifail=0
        bj=s17aff(x,ifail)
        do 1 j=1,n-1
          bjp=j*tox*bj-bjm
          bjm=bj
          bj=bjp
1     continue
      bessj=bj
      else
        m=2*((n+int(sqrt(float(iacc*n))))/2)
        bessj=0.
        jsum=0
        sum=0.
        bjp=0.
        bj=1.
        do 2 j=m,1,-1
c backward do loop..... bug *>>>>>>
          bjm=j*tox*bj-bjp
          bjp=bj
          bj=bjm
          if(abs(bj).gt.bigno) then
            bj=bj*bigni
            bjp=bjp*bigni
            bessj=bessj*bigni
            sum=sum*bigni
          endif
          if(jsum.ne.0) sum=sum+bj
          jsum=1-jsum
          if(j.eq.n) bessj=bjp
2     continue
      sum=2.*sum-bj
      bessj=bessj/sum
      endif
      end
```

(4) WIRE

RADIATION PATTERNS OF WIRE VEES AND RHOMBICS

```
C WIRE ANTENNA RADIATION PLOT PROGRAM
C
C BY J. WHITEHURST BSc
C
C FOR USE WITH VAX 11/780 + ULCC DIMFILM PLOTTING PACKAGE
C
      REAL L
      COMMON ALPHA,L,R(361),PI,SEL,EPS
      PI=3.1415
    1 PRINT*,'WIRE RADIATION PLOT PROGRAM'
      PRINT*,' '
      PRINT*,'SELECT OPTION BY NUMBER FROM MENU'
      PRINT*,' '
      PRINT*,'1) VEE ANTENNA  H-PLANE'
      PRINT*,' '
      PRINT*,'2) VEE ANTENNA  E-PLANE'
      PRINT*,' '
      PRINT*,'3) RHOMBIC ANTENNA H-PLANE'
      PRINT*,' '
      PRINT*,'4) RHOMBIC ANTENNA E-PLANE'
      PRINT*,' '
      PRINT*,'5) VELOCITY CORRECTED VEE H-PLANE'
      PRINT*,' '
      PRINT*,'6) VELOCITY CORRECTED VEE E-PLANE'
      PRINT*,' '
      PRINT*,'7) VELOCITY CORRECTED RHOMBIC H-PLANE'
      PRINT*,' '
      PRINT*,'8) VELOCITY CORRECTED RHOMBIC E-PLANE'
      READ*, SEL
      PRINT*,' '
      PRINT*,'INPUT LENGTH OF ELEMENTS IN WAVELENGTHS'
      READ*,L
      PRINT*,' '
      PRINT*,'INPUT ELEMENT ANGULAR SEPERATION IN DEGREES'
      READ*, ALPHA
      alpha=alpha/180*pi
      IF (SEL. GT .4) THEN
         PRINT*,' '
         PRINT*,'INPUT VELOCITY FACTOR OF ANTENNA'
         READ*, EPS
      EPS=1/EPS
      ELSE
         CONTINUE
      END IF
      IF (SEL. EQ .1) THEN
         CALL HVEE
              B=(SIN(ALPHA))**2
      ELSE IF (SEL. EQ .2) THEN
         CALL EVEE
              B=0.125
      ELSE IF (SEL. EQ .3) THEN
         CALL HROM
              B=8*(SIN(ALPHA))**2
      ELSE IF (SEL. EQ .4) THEN
         CALL EROM
              B=8*(SIN(ALPHA))**2
      ELSE IF (SEL. EQ .5) THEN
         CALL VCHVEE
              B=(SIN(ALPHA))**2
```

```
      ELSE IF (SEL. EQ .6) THEN
         CALL VCEVEE
              B=0.125
      ELSE IF (SEL. EQ .7) THEN
         CALL VCHROM
              B=8*(SIN(ALPHA))**2
      ELSE IF (SEL. EQ .8) THEN
         CALL VCEROM
              B=8
      ELSE
         GOTO 1
      END IF
C ARRAY R(J) PRODUCED, NOW FIND MAX. AND NORMALISE
      R1=0.
      DO 2 J=1,91
      IF (R(J) .GT. R1) THEN
      R1=R(J)
      END IF
    2 CONTINUE
      C=R1*B
      PRINT*,'KMAX = ',C,' *IZ/(4*PI)'
      DO 3 J=1,181
      A=R(J)

      R(J)=A/R1
      WRITE(8,*) J-91,R(J)
    3 CONTINUE
      CALL CARTES
      PRINT*,' '
      PRINT*,'ALPHA= ',ALPHA,'L= ',L,' EPS= ',EPS,'KMAX= ',C
      END
C  SUBROUTINES TO GENERATE PLOT DATA
      SUBROUTINE HROM
      REAL L
      COMMON ALPHA,L,R(361),PI,SEL,EPS
      J=1
      DO 1 PHI=0,PI,PI/180
      A=1-SIN(PHI)*COS(ALPHA)
      RADVEC=(SIN(PI*L*A))**4/A**2
      R(J)=RADVEC
      J=J+1
    1 CONTINUE
      RETURN
      END
      SUBROUTINE EROM
      REAL L
      COMMON ALPHA,L,R(361),PI,SEL,EPS
      J=1
      DO 1 PHI=-PI/2,PI/2,PI/180
      A=1-COS(PHI+ALPHA)
      B=1-COS(PHI-ALPHA)
      IF (A .EQ. 0.) THEN
          A=0.00000001
      END IF
      IF (B .EQ. 0.)THEN
          B=0.00000001
      END IF
      RADVEC=(SIN(PI*L*A))**2*(SIN(PI*L*B))**2/A/B
      R(J)=RADVEC
      J=J+1
    1 CONTINUE
```

```
      RETURN
      END
      SUBROUTINE HVEE
      REAL L
      COMMON ALPHA,L,R(361),PI,SEL,EPS
      J=1
      DO 1 PHI=0,pi,PI/180
      A=(1-SIN(PHI)*COS(ALPHA))
      RADVEC=(1-COS(2*PI*L*A))/A**2
      R(J)=RADVEC
      J=J+1
    1 CONTINUE
      RETURN
      END
      SUBROUTINE EVEE
      REAL L
      COMMON ALPHA,L,R(361),PI,SEL,EPS
      J=1
      DO 1 PHI=pi/2,-pi/2,-PI/180
      A=SIN(PHI+ALPHA)
      B=SIN(PHI-ALPHA)
      C=1-COS(PHI+ALPHA)
      D=1-COS(PHI-ALPHA)
      F1=(1-COS(2*PI*L*C))/C*A
      F2=(1-COS(2*PI*L*D))/D*B
      F3=SIN(2*PI*L*C)*A/C
      F4=SIN(2*PI*L*D)*B/D
      RADVEC=(F1-F2)**2+(F3-F4)**2
      R(J)=RADVEC
      J=J+1
    1 CONTINUE
      RETURN
      END
      SUBROUTINE VCHVEE
      REAL L
      COMMON ALPHA,L,R(361),PI,SEL,EPS
      J=1
      DO 1 PHI=0,PI,PI/180
      U=EPS-SIN(PHI)*COS(ALPHA)
      RADVEC=((1-COS(2*PI*L*U)))/U**2
      R(J)=RADVEC
      J=J+1
    1 CONTINUE
      RETURN
      END
      SUBROUTINE VCEVEE
      REAL L
      COMMON ALPHA,L,R(361),PI,SEL,EPS
      J=1
      DO 1 PHI=-PI/2,PI/2,PI/180
      A=SIN(PHI-ALPHA)
      B=SIN(PHI+ALPHA)
      C=EPS-COS(PHI-ALPHA)
      D=EPS-COS(PHI+ALPHA)
      F1=SIN(2*PI*L*C)/C*A
      F2=SIN(2*PI*L*D)/D*B
      F3=(1-COS(2*PI*L*C))/C*A
      F4=(1-COS(2*PI*L*D))/D*B
      RADVEC=(F1-F2)**2+(F3-F4)**2
      R(J)=RADVEC
      J=J+1
```

```
    1 CONTINUE
      RETURN
      END
      SUBROUTINE VCHROM
      REAL L
      COMMON ALPHA,L,R(361),PI,SEL,EPS
      J=1
      DO 1 PHI=0,PI,PI/180
      A=EPS-SIN(PHI)*COS(ALPHA)
      RADVEC=(SIN(EPS*L*PI*A))**4/A**2
      R(J)=RADVEC
      J=J+1
    1 CONTINUE
      RETURN
      END
      SUBROUTINE VCEROM
      REAL L
      COMMON ALPHA,L,R(361),PI,SEL,EPS
      J=1
      DO 1 PHI=-PI/2,PI/2,PI/180
      A=EPS-COS(PHI+ALPHA)
      B=EPS-COS(PHI-ALPHA)
      C=(COS(PHI+ALPHA)-COS(PHI-ALPHA))**2*(EPS-1)/4/A/B
      D=(SIN(ALPHA))**2-C
      RADVEC=(SIN(L*A*PI))**2*(SIN(L*B*PI))**2*D/A/B
      R(J)=RADVEC
      J=J+1
    1 CONTINUE
      RETURN
      END
C     PLOTTING ROUTINE
      SUBROUTINE CARTES
C CARTESIAN RADIATION PLOT ROUTINE
      REAL X(361),Y(361)
      COMMON ALPHA,L,R(361),PI,SEL,EPS
      Q=-90
      DO 1 J=1,181
      A=R(J)
C SET UP ARRAYS FOR PLOTTING
      X(J)=Q
      Y(J)=A
      Q=Q+1
    1 CONTINUE
C NOW THE DIMFILM ROUTINES
      CALL CAM35MM
      CALL NEWFRAM
      CALL AUTOXY
      CALL GRAPHIC(X,Y,181)
      CALL GRFRAME
      CALL LYTICK
      CALL LXTICK
      CALL LYVAL
      CALL LXVAL
      CALL LXLABEL(31HANGLE FROM BORESIGHT IN DEGREES,31)
      CALL LYLABEL(14HRELATIVE POWER,14)
      IF (SEL .EQ. 1) THEN
         CALL UTITLE(26HVEE H-PLANE RADIATION PLOT,26)
      ELSE IF (SEL .EQ. 2) THEN
         CALL UTITLE(26HVEE E=PLANE RADIATION PLOT,26)
      ELSE IF (SEL .EQ. 3) THEN
         CALL UTITLE(30HRHOMBIC H-PLANE RADIATION PLOT,30)
```

```
      ELSE IF (SEL .EQ. 4) THEN
         CALL UTITLE(30HRHOMBIC E-PLANE RADIATION PLOT,30)
      ELSE IF (SEL. EQ .5) THEN
      CALL UTITLE(45HVELOCITY CORRECTED VEE H-PLANE RADIATION P
LOT,45)
      ELSE IF (SEL. EQ .6) THEN
      CALL UTITLE(45HVELOCITY CORRECTED VEE E-PLANE RADIATION P
LOT,45)
      ELSE IF (SEL.EQ.7) THEN
      CALL UTITLE
     1(49HVELOCITY CORRECTED RHOMBIC H-PLANE RADIATION PLOT,49)
      ELSE IF (SEL.EQ.8) THEN
      CALL UTITLE
     1(49HVELOCITY CORRECTED RHOMBIC E-PLANE RADIATION PLOT,49)
      END IF
      CALL ENDFILM
      END
```

(5) V-IMP

VEE INPUT IMPEDANCE CALCULATOR

```
  5  *FX6,11
 10 CLS
 20 LET FLAG=0
 30 REM PROGRAM TO CALCULATE THE INPUT IMPEDANCE OF A PRINTED
V ANTENNA
 40 ITEM$="ANT"
 50 F=0.1*PI/180
 60 PROCLEN
 70 PROCSTART
 80 CLS
 90 PRINT TAB(5)"************************"
100 PRINT
110 PRINT TAB(5)" I'M THINKING ABOUT IT"
120 PRINT
130 PRINT TAB(5)"************************"
140 REPEAT
150   PROCIMPEDANCE
160   PROCDES
170 UNTIL ABS(T0)<T
180 T0=50
190 F=A/100
200 PROCline
210 DEF PROCLEN
220 INPUT" FREQUENCY F IN GHz ",FF
230 INPUT"LENGTH OF V ELEMENT IN wavelengths",L
240 DEF FNL(N)=360/PI*ASN(0.431/SQR(N))
250 LET THETA=FNL(L)
260 IF L<=5THEN LET TH1=THETA-25:LET TH2=THETA+25
270 IF L>5 THEN LET TH1=THETA-5:LET TH2=THETA+5
280 LET TH1=RAD(TH1)
290 LET TH2=RAD(TH2)
300 ENDPROC
310 DEF PROCSTART
320 INPUT"TARGET IMPEDANCE IN OHMS",Z0
330 INPUT"DIELECTRIC CONSTANT OF SUBSTRATE",DK1
340 INPUT "TOLERANCE IN Z0",T
350 INPUT"LINE WIDTH IN mm",W
360 ENDPROC
370 DEF PROCIMPEDANCE
380 LET K=TAN(TH1/2)/TAN(TH2/2)
390 IF K<=0.707 THEN PROC1
400 IF K>0.707 THEN PROC2
410 ENDPROC
420 DEF PROC1
430 LET KDASH=SQR(1-K^2)
440 LET DEN=LN(2*(1+SQR(KDASH))/(1-SQR(KDASH)))
450 LET RATIO=PI/DEN
460 PROCIMP
470 ENDPROC
480 DEF PROC2
490 LET RATIO=LN(2*(1+SQR(K))/(1-SQR(K)))/PI
500 PROCIMP
510 ENDPROC
520 DEF PROCIMP
530 IF ITEM$="ANT" DK=1 ELSE DK=DK1
540 LET Z1=377*SQR(2/(DK+1))*RATIO
550 ENDPROC
560 DEF PROCINCR1
570 LET TH1=TH1+F
```

```
 580 LET TH2=TH2-F
 590 ENDPROC
 600 DEF PROCINCR2
 610 LET TH1=TH1-F
 620 LET TH2=TH2+F
 630 ENDPROC
 640 DEF PROCDES
 650 LET T0=Z0-Z1
 660 IF (T0*-1)>T THEN PROCINCR2:GOTO370
 670 IF T0>T THEN PROCINCR1:GOTO370
 680 LET TH1=DEG(TH1):LET TH2=DEG(TH2)
 690 CLS
 700 PRINT:PRINT:PRINT
 710 INPUT"HARD COPY Y/N";A$:IF A$="Y" THEN VDU2
 720 IF A$="y" THEN VDU2
 730 PRINT:PRINT:PRINT
 740 PRINT "TARGET IMPEDANCE REACHED"
 750 PRINT
 755 PRINT"LENGTH = ",L," WAVELENGTHS"
 760 PRINT
 770 PRINT"THETA1=";TH1;" DEGREES"
 780 PRINT
 790 PRINT
 800 PRINT"THETA2=";TH2;" DEGREES"
 810 PRINT
 820 PRINT
 830 PRINT"THETA3=";THETA;" DEGREES"
 840 PRINT
 850 PRINT
 860 PRINT"V IMPEDANCE=";Z1;" OHMS"
 870 VDU3
 880 PRINT""
 890 DEF PROCline
 900 INPUT"LINE IMPEDANCE REQUIRED IN OHMS",Z0
 910 ITEM$="LINE"
 920 A=2*W
 930 F=A/100
 940 CLS:PRINT TAB(5)"************************"
 950 PRINT
 960 PRINT TAB(5)"  I'M THINKING ABOUT IT"
 970 PRINT
 980 PRINT TAB(5)"************************"
 990 REPEAT
1000   PROCratio
1010   PROCdes
1020   PROCdes1
1030 UNTIL ABS(T0)<T
1040 PROClin
1050 PROCRESTART
1060 ENDPROC
1070 DEF PROCratio
1080 K=A/(A+2*W)
1090 ENDPROC
1100 DEF PROCdes
1110 IF K<=0.707 THEN PROC1
1120 IF K>0.707 THEN PROC2
1130 ENDPROC
1140 DEF PROCincr1
1150 A=A-F
1160 ENDPROC
1170 DEF PROCincr2
```

```
 1180 A=A+F
 1190 ENDPROC
 1200 DEF PROCdes1
 1210 T0=Z0-Z1
 1220 IF (T0*-1)>T PROCincr1:GOTO 1000
 1230 IF T0>T PROCincr2:GOTO 1000
 1240 ENDPROC
 1250 DEF PROClin
 1260 CLS:INPUT"HARD COPY Y/N ";A$:IF A$="Y" VDU2
 1270 PRINT"TARGET IMPEDANCE REACHED"
 1280 PRINT""
 1290 PRINT"LINE IMPEDANCE = ",Z1," OHMS"
 1300 PRINT
 1310 PRINT"STRIP SEPRATION = ",A," mm"
 1320 PRINT
 1330 PRINT"STRIP WIDTH = ",W," mm"
 1340 VDU3
 1350 ENDPROC
 1360 DEF PROCRESTART
 1370 PRINT""
 1380 PRINT
 1390 INPUT"DO YOU REQUIRE COORDINTATES ";Q$
 1400 IF Q$="Y" PROCcoor ELSE 10
 1410 ENDPROC
 1420 DEF PROCcoor
 1430  *FX 6,1
 1440 PRINT:PRINT:PRINT
 1450 INPUT"DO YOU REQUIRE HARD COPY OF COORDINATES ";A$:F1=0
 1460 IF A$="Y" THEN LET F1=1:VDU2
 1470 LET A1=TH1:LET A2=TH2:LET A3=THETA
 1480 A1=RAD(A1):A2=RAD(A2):A3=RAD(A3)
 1490 S=A
 1500 REM SUBROUTINE TO CALCULATE COORDINATES OF VEE IN UNITS O
F 1 MICRON (10E-6M)
 1510 L2=L*300/FF/COS(A2-A3)
 1520 X1=S*TAN(A1):Y1=S/2
 1530 X2=S*TAN(A1):Y2=S/2+W
 1540 X4=L2*COS(A1):Y4=L2*SIN(A1)
 1550 X3=L2*COS(A2):Y3=L2*SIN(A2)
 1560 PRINT:PRINT:PRINT" FREQUENCY = ";FF;"GHz":PRINT:PRINT
 1570 PRINT"X1= ";X1;"  Y1= ";Y1
 1580 PRINT"X2= ";X2;"  Y2= ";Y2
 1590 PRINT"X3= ";X3;"  Y3= ";Y3
 1600 PRINT"X4= ";X4;"  Y4= ";Y4
 1610 PRINT"X5= ";X1;"  Y5= ";-Y1
 1620 PRINT"X6= ";X2;"  Y6= ";-Y2
 1630 PRINT"X7= ";X3;"  Y7= ";-Y3
 1640 PRINT"X8= ";X4;"  Y8= ";-Y4
 1645 PRINT:PRINT
 1650 IF F1=1 :VDU3
 1660 IF F1=1 :VDU3
 1670 GOTO 10
 1680 ENDPROC
```

CONFERENCE PAPERS

[1] P.G. Frayne, J. Whitehurst, "A Surface Scanning Probe for Microstrip Diagnostics," *IEE Colloquium on 'The Technology of Measuring Microwave and Millimetric Components,' Digest No: 1986/121, Nov. 1986, pp3/1–3/7*

[2] P.G. Frayne, J. Whitehurst, "Mode Analysis in Radiating and Non-Radiating Planar Open Structures Using a Scanning Microwave Probe," *5^{th} ICAP Conference, York, 1987, pp501–505*

A SURFACE SCANNING PROBE FOR MICROSTRIP DIAGNOSTICS

P G Frayne and J Whitehurst

Introduction

A noncontacting scanning microwave probe technique has been developed which measures the surface charge density distribution over any planar network. The method is applicable to a wide range of transmission line geometries and a single capacitatively coupled sensor will measure the scalar source density distribution over microstrip, slotline, co-planar stripline and co-planar waveguide networks or any combination of these on a single substrate. Partially shielded networks may also be characterized provided that there is some means of access through an end wall of the structure. Furthermore, the method may be applied to active as well as passive systems and to non-radiating transmission lines as well as antennas. In the context of antenna measurements, it should be made clear at the outset that the present technique should not be confused with the more familiar procedure for determining a far-field radiation pattern by Fourier transformation of the near radiation field measured in the aperture plane of the antenna. However, if it is so desired, this type of measurement can be made with an appropriate choice of sensor geometry.

The aim of the present scanning network probe technique (S.N.P.) is to provide a method for the rapid characterization of monolithic or hybrid microwave integrated circuits as well as radiating structures. We believe that the method has sufficient generality to justify both the precision microcomputer controlled transport mechanism necessary for its implementation and the dedicated computational facilities required for rapid data reduction.

The modular approach to microwave system design has the advantage of permitting each component to be fully characterized by well established Network Analyser techniques. However, there are now many situations where a high degree of component integration has become essential. This is particularly true where requirements for small size and low mass have dictated the use of operating frequencies around 100 GHz. The present trend towards more complete circuit integration, if only as a means of reducing unit costs, will continue and the SNP system may well satisfy the growing need for an integrated circuit test and optimisation capability.

Instrumentation

The essential components of the system are as follows:-

(1) A microcomputer controlled precision transport mechanism.

The authors are with the Physics Department, Royal Holloway & Bedford New College, Egham, Surrey.

(2) A sensor with geometry appropriate to the type of measurement required e.g. E_n for scalar source density distributions

E_t for near radiation field measurements

H_t for magnetic measurements.

The subscripts n, t indicate the components normal and tangential to the plane of the substrate.

(3) Separate information channels for microwave phase and amplitude data. Each channel will normally employ lock-in amplifiers.

(4) Data storage system (Winchester or floppy disc) and a data processing computer with graphics software and plotting facilities.

The transport mechanism employs precision leadscrews which are driven from sine/cosine pole interpolating microstep motors with a 2000 step per revolution capability. The coordinates of the sensor are determined by 9-bit absolute shaft encoders and ROM based software which gives the position in millimetres over a measurement field 250 × 350 mm. The minimum step interval is 0.5 μm and the worst case random error is 2 μm on either axis.

Different types of sensors have been investigated which can measure either the R.F. electric fields or R.F. magnetic fields close to the surface of the substrate. The sensor is scanned in a raster pattern at constant height h over the substrate using incremental steps of the order of $\frac{\lambda_o}{40}$. The mesh size of the scan can be varied by the operator to suit the requirement for low or high spatial resolution. For a given probe geometry the coupling factor and limiting spatial resolution are sensitive and complex functions of the height. Normally $h \sim \frac{\lambda_o}{150}$ which dictates the use of precision bonded substrates for microstrip and warp free materials for the coplanar strip and slot line geometries. In order to maintain constant probe coupling, it is important that the circuit is accurately levelled over the entire area under investigation. This slight inconvenience is a small price to pay for the large amount of information that subsequently becomes available.

The most versatile sensor, shown in fig 1, is based upon a miniature rigid co-axial structure with an extended inner conductor approximately 0.1 mm diameter. Clearly, with this arrangement the probe excitation will be determined by the vertical component of the local potential gradient. In the case of antenna measurements, it is important to make the probe shaft as long as possible consistent with mechanical rigidity. Typically we employ probes of length $20\ \lambda_o$ and an overall diameter of 0.5 millimetre is satisfactory for use at Q band. In order to minimise any capacitative loading of the test circuit by the outer sheath, the surface impedance of the screen is made much larger than that of the inner conductor. This arrangement ensures that the test circuit is totally unaffected by added hand capacity at the probe support, but necessarily results in a high loss coefficient $\alpha = 150\ m^{-1}$. At Q-band more than 80% of the received signal will be dissipated in the surface resistance.

The subject of the limiting spatial resolution is a complex matter which is strongly dependent upon the power law that determines the probe coupling. It has been experimentally observed that the resolution is also a function of the geometry of the probe tip and is greatest when the inner conductor extends

approximately one probe radius beyond the sheath. We do not imply that the dimensions given in fig 1 are necessarily state of the art, nevertheless they are adequate for most applications up to Q-band. Higher resolution may be achieved by substantially reducing the diameter of the sheath and also by using edge detection techniques which may be implemented at either the hardware or software level. The angular response of the probe may then be de-convolved but only at the expense of larger data files and longer processing times.

It should be noted that a small Q-band patch antenna array covering approximately 25 square centimetres of ground plane with simultaneous measurement of phase and amplitude, using a constant 0.25 millimetre sampling grid, would generate 80,000 raw data points per unit of frequency. Measurement at four separate frequencies using two dimensional hardware implemented edge detection would generate over a million data points.

Implementation

The examples given in the last section of this summary clearly demonstrate that the S.N.P. is a versatile instrument, the most striking feature of which is the tutorial nature of the contour plotting routines. The highly pictorial output is unparalleled as a means of gaining physical insight into the mode structure supported by a complex circuit. With the added facility of three dimensional surface plotting, some of the low level features become more significant and unexpected symmetry is more easily recognised.

To obtain the salient features of a plot, the two-dimensional mapping is thresholded at a relatively high level thus suppressing unwanted detail. Conversely, for high resolution the threshold is set just above the noise level and a small contour increment is selected. The ability to "zoom in" on a small area of a high resolution plot is also a very useful feature. More importantly, the data is quantitative. The contours can be sectioned in any specified direction and the voltage standing wave ratio automatically computed provided that maxima and minima can be identified. A wide dynamic range of measurement is of paramount importance for the determination of a large V.S.W.R. and this may be achieved with the help of a programmable post detection attenuator.

Circuit analytical techniques may be employed to locate sources of mis-match in a complex network. These techniques are analogous to the use of matched load and short circuit terminations in Network Analyser practice. For example, it is usually possible to non-destructively "load off" any part of the test circuit with a surface mounted absorber. Systematic elimination of each point of discontinuity in the structure will enable the problematic areas to be identified.

Discussion

Figure (2). Open circuited 50 ohm microstrip line on 5880 substrate material.

The line was energised from W.G. 22 at 34 GHz using a stepped ridge transformer and the waveguide aperture was loaded with an absorbing material to attenuate any uncoupled radiation. The guide wavelength was found to be 6.0 ± 0.19 mm and the V.S.W.R. averaged over a 16 mm length of line was 8.5 ± 1. The boundary of the upper conductor is shown by the broken line. Since the probe signal is only proportional to surface charge density under conditions of constant capacitative coupling, the shape of the contours will be distorted close to an edge. The width of this particular line is only twice the probe diameter, consequently the peak current density does not appear on the edges

as theoretically expected. If the probe diameter is much smaller than the guide wavelength an accurate value for the V.S.W.R. can be found by sectioning the contours along the axis of the top conductor. In the case of lower impedance lines, the axial depression of the current density due to the lateral skin effect is proportionately greater and the edges are also more remote. In such cases the current density is seen to maximise close to the edges. This figure also shows some additional structure over the ground plane which is not thought to be a probe related effect.

Figure (3) Q-band $\frac{\lambda_G}{2}$ rectangular patch antenna.

Below resonance (fig 3a), only one edge is strongly excited and the first V.S.W.R. maximum in the line is shifted towards the generator. At resonance (fig 3b), the return loss measured in the waveguide is 12 db. Again, one edge is more strongly excited than the other because of the loading effect of the microstrip line. Above resonance (fig 3b), the maximum at the feedpoint withdraws from the edge, whilst at the opposite end of the patch the maximum remains close to the edge. At this frequency the lateral break up into two separate peaks is due to the onset of a transverse resonance. The antenna presents almost a short circuit to the feed line as evidenced by the deep minimum at the end of the line and also an 0 db return loss in the waveguide. In all three scans the low level features on the ground plane are significantly different.

Figure (4) 4-element Q-band microstrip array.

At the selected frequency we have a relatively deep return loss minimum in the waveguide feed of 13 db. As in the case of an isolated patch, the aperture furthermost from the feed is more strongly excited and there is some imbalance of excitation between the four patches. The V.S.W.R. in the various feed lines can be measured and there is some evidence for R-F leakage at the mitred bends. There is scope for experimental circuit analysis with surface mounted loads in this example.

Figure (5a) One half of a $2\lambda_o$ short Vee antenna.

This is a logarithmic contour plot for a linearly tapered coplanar strip travelling wave antenna using a 70 μm mylar substrate. The V.S.W.R. in the short circuited c.p.s. transmission line running out of the top right-hand edge of the figure is 8 and in the tapered section close to the feed point is 5. This indicates the presence of some mismatch at the feed point. The antenna is fed in reception from a microwave lens and the increase of the antenna coupling towards the focus (antenna apex) is clearly evident. The velocity factor in the tapered line increases towards the apex owing to a steady increase of the substrate effective permittivity. The current density is observed to peak on the inner edge of the Vee because this represents the current path of minimum reactance. There are also significant non-uniformities at the extremity of the Vee.

Figure (5b) As in (5a), but with a matched feed.

This is also a logarithmic contour plot, but with respect to a different reference level. A surface load is placed over the c.p.s. short circuit which reduces the V.S.W.R. in the line close to the apex to less than 1·1.

Figure (6a) One half of a short $2\lambda_o$ tapered slot with inner edge identical to the Vee.

In this example the parallel sided slot line is open circuited giving a VSWR of 15. The distribution close to the feed is obviously quite different from that in the c.p.s. line. No low level features are seen distant from the tapered edge and the velocity factor now varies more slowly along the edge.

Figure (6b) As in (6a)

In this example the feed point is matched with a surface mounted load. The V.S.W.R. in the tapered slot is less than 1·1 . A new low level feature is now apparent remote from the tapered edge.

Note, there is an anomaly in the contour plotting in this particular example.

Acknowledgements

We wish to thank the S.E.R.C. for the receipt of a research grant, the Marconi Company for supporting a CASE Studentship (J.W.), Mr J Williams for his superb craftmanship and Mr L Ellison for designing the electronic control system.

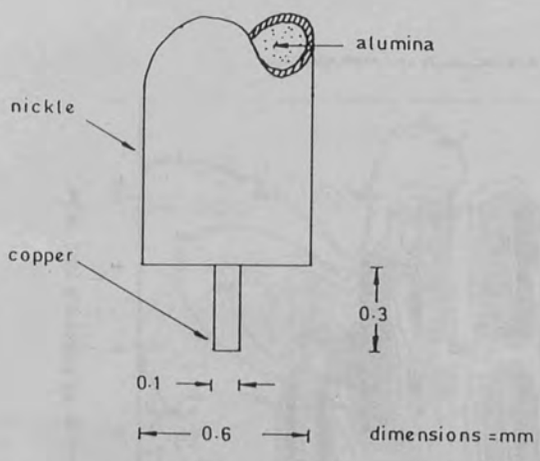

Fig (1) Q-band co-axial probe.

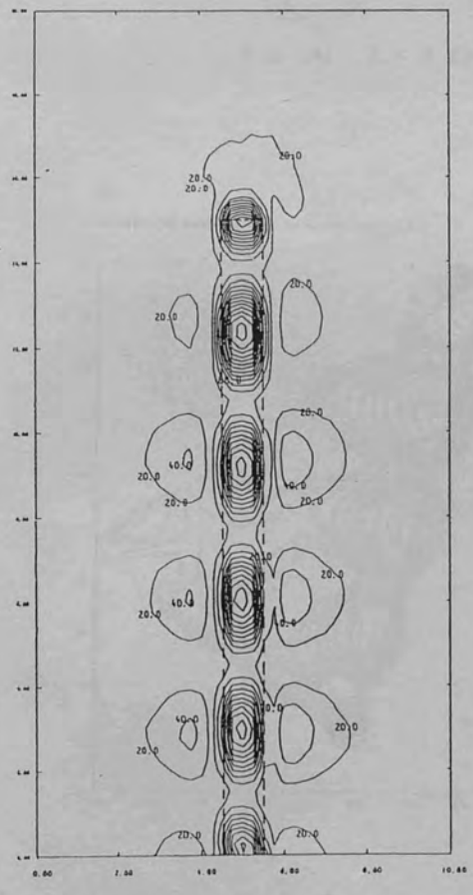

Fig (2) Open circuit 50Ω microstrip.

F = 34.0 GHz.

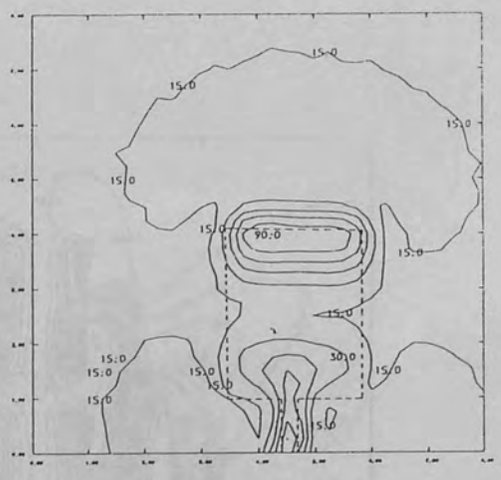

(a) below resonance

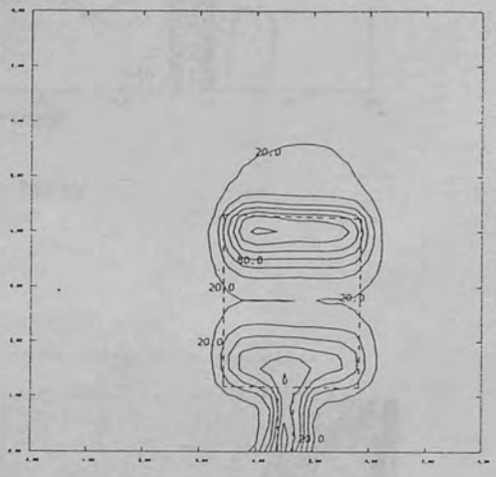

(b) at resonance

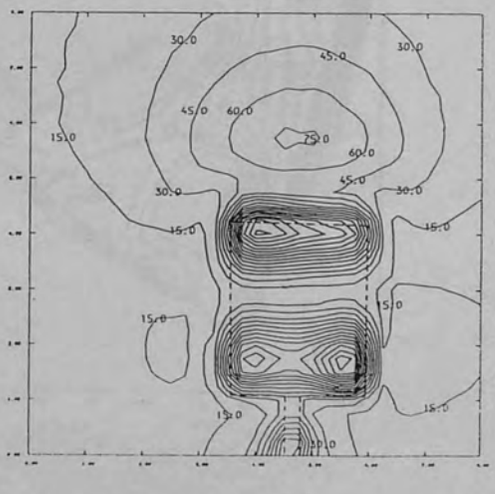

(c) above resonance

Fig (3) half wavelength Patch Resonances

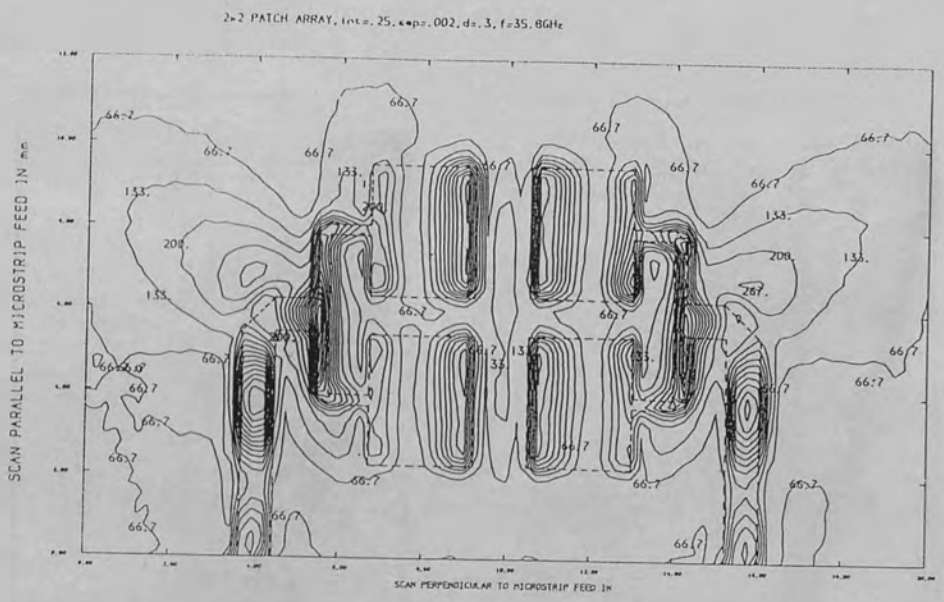

Fig (4) 2 × 2 Element Patch Array

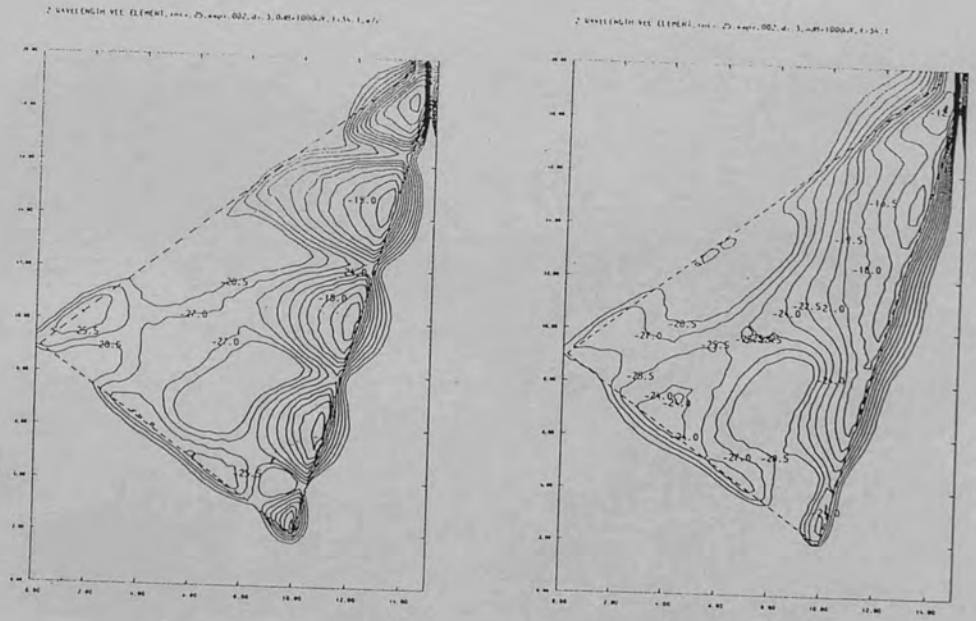

(a) (b)

Fig. (5) Reception modes of a short Vee antenna.

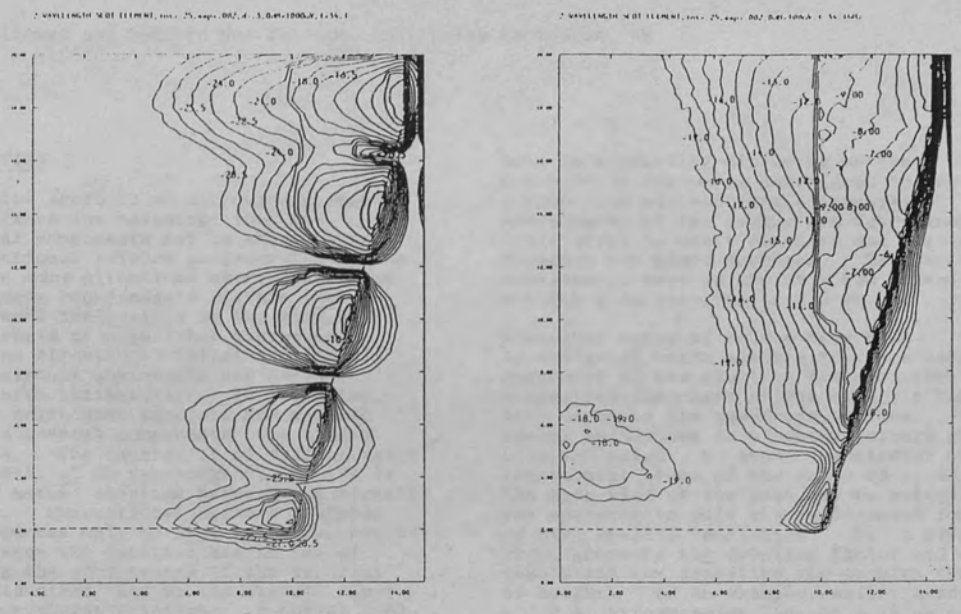

(a) (b)

Fig. (6) Reception modes of a short slot antenna.

MODE ANALYSIS IN RADIATING AND NON RADIATING PLANAR OPEN STRUCTURES USING A SCANNING MICROWAVE PROBE

P. G. Frayne and J. Whitehurst

Royal Holloway and Bedford New College, University of London, UK

INTRODUCTION

The modular approach to microwave systems design offers the advantage that the individual components may be characterized by conventional network analyser techniques. There are many situations where small size and low mass requirements dictate the use of component integration in the form of either hybrid or monolithic microwave integrated circuits. Whilst individual printed circuit components can be manufactured satisfactorily in isolation, problems arise when attempts are made to integrate several components on a single substrate. The excitation of surface waves, particularly at mm wavelengths, results in unwanted mutual coupling between the circuit elements. Conventional network analyser techniques can only be applied to the device ports, hence the designer has no way of assessing the performance of the internal components other than by the circuit input and output characteristics. A useful tool for the microwave integrated circuit engineer is an instrument that enables the characterization of the internal components. For example, sources of enhanced surface wave excitation and high VSWR can be located within the mic. Once the circuit design is modified, the effect of the corrective measures can be quantified. This paper describes a non-contacting scanning microwave probe technique which essentially measures the surface charge density over any planar network. The application of the scanning network probe (S.N.P.) technique to the study of printed antenna systems, and non-radiative transmission lines is demonstrated with a range of basic circuits employing the microstrip, slotline and coplanar strip line (C.P.S.) geometries.

INSTRUMENTATION

The essential components of the scanning network probe system are:

a) a microcomputer controlled precision transport mechanism.

b) a sensor with geometry appropriate to the type of measurement required, i.e. for charge density, current density or near radiation field.

c) a microwave detection system; simple video detection combined with a lock-in amplifier is employed for amplitude only measurements whilst a homodyne bridge is used for simultaneous amplitude and phase measurement.

d) a data processing computer with a high resolution graphics capability and facilities for mass data storage.

The transport mechanism employs precision leadscrews which are driven from sine/cosine pole interpolating microstep motors. The motor drive system is configured to provide a 2000 step per revolution capability. The coordinates of the sensor are determined by 9-bit absolute shaft encoders and custom designed ROM based decoders. The maximum measurement area is 250 mm × 350 mm and the minimum step interval is 0.5 μm.

Different types of sensor have been investigated which sense either the normal component of the electric field or the tangential component of the magnetic field very close to the substrate surface. The sensor is scanned in a raster pattern at a constant height h above the circuit using incremental steps of the order of $\lambda_o/40$. The mesh size of the scan can be varied by the operator to suit the requirement for low or high spatial resolution. For a given probe geometry the coupling factor and spatial resolution are sensitive and complex functions of height. As an example, whilst scanning a C.P.S. transmission line on a 70 μm mylar substrate, a local fluctuation in height of ± 1% produces an amplitude change of ± 5% when $h \simeq \lambda_o/150$. When $h \simeq \lambda_o/300$, the same height fluctuation produces an amplitude variation of ± 10%. The implication derived here is that when small values of h are employed, the substrate height fluctuations must be kept to a minimum. In practice this is achieved by the use of precision bonded soft substrates or precision ground hard substrates.

The most versatile sensor, shown in figure (1), is based upon a miniature rigid coaxial structure with an extended inner conductor. Clearly with this configuration the probe excitation will be determined by the vertical component of the local potential gradient. In the case of antenna measurements it is also necessary to make the probe shaft as long as possible consistent with mechanical rigidity. A typical 0.5 mm diameter probe has an overall length of approximately 20 λ_o for use at Q-band frequencies. The capacitative loading of the circuit under test by the outer sheath of the probe is minimized by using a material of high surface impedance (e.g. nickel) for the outer screen. This arrangement ensures that the test circuit is totally unaffected by added hand capacity at the probe support, but this necessarily results in a high loss coefficient $\alpha = 150$ Nepers m^{-1}. The spatial resolution of the probe is governed by the power law that determines the probe coupling and the effective length of the exposed tip. It has been observed that the physical length of the probe tip should be approximately one probe radius long for optimum edge resolution. In order to achieve higher spatial resolution the overall size of the probe must be substantially reduced, and deconvolution techniques applied. Deconvolution of the probe response can be obtained at the hardware level by the use of

multiple sensors, or at the software level by implementing a deconvolution algorithm on the single sensor scan data.

APPLICATIONS

Transmission Line Measurements

The ability to perform impedance measurements on *any* printed transmission line is the most useful application of the scanning network probe. The accuracy of the VSWR measurements using the S.N.P. technique is dependent on the following factors:

a) the coupling coefficient between the transmission line and the probe must remain constant over the length of the measurement.

b) the effective capture area of the probe should be as small as possible.

c) the detection system should possess a wide dynamic range and be sensitive enough to detect the deep voltage minima produced by high VSWR loads. The probe coupling coefficient is solely determined by geometrical factors, i.e. the probe separation and orientation, and the transmission line geometry. Clearly, all these geometric features can be kept constant for a sensor scan parallel to the transmission line axis of symmetry. For VSWR measurements it is of no consequence which region of the conductor is scanned, however one would usually scan the region of the highest average charge density in order to maximise the signal to noise ratio. In addition to the change in coupling coefficient introduced by varying the sensor height h, increasing h beyond $\lambda_0/100$ results in a degradiation of the spatial resolution. The reduced spatial resolution manifests itself by:

a) a broadening of the voltage maxima

b) a broadening and reduction in the depth of the voltage minima.

Experiments have indicated that the VSWR measurements on microstrip using low K substrates converge rapidly when $h < \lambda_0/100$.

The detection system employed sets an ultimate limit on the range of VSWR that can be accurately measured. For amplitude only measurements the test circuit is energised with an A.M. modulated signal. The detected probe output is then fed to a lock-in voltmeter via a programmable attenuator. The lock-in voltmeter is an extremely narrow band detection system which filters out the d.c. and even harmonic components of the modulation frequency that are present in the video detected output. The minimum detectable signal depends on the integration time constant of the lock-in voltmeter, and typically we employ a time constant of 300 mS to achieve a minimum detectable video signal of 0.1 μV. Better sensitivity can be achieved, but only at the expense of longer integration times. The programmable attenuation is calibrated in 10 dB steps from 0 dB to -70 dB. The maximum VSWR that can be measured is determined by the attenuator range and the minimum detectable signal. For a short circuit 50Ω microstrip carrying 4.0 mW of power, the highest VSWR observed using the 0.5 mm coaxial probe is of the order of 170. As an example of the transmission line measurements that can be made using the S.N.P., figure (2) shows the variation of the normalized open circuit line extension $\Delta\ell/h$ and guide wavelength with frequency, as measured on a microstrip line with an aspect ratio w/h of 10.3 and fabricated on a 0.254 mm RT-Duroid 5880 substrate. The experimental values for the guide wavelength are in good agreement with Bhal and Bhartia's results (1), and the experimental points for $\Delta\ell/h$ are of the same order as those predicted by James and Henderson (2) for wide microstrip lines on low dielectric constant substrates.

Study of Planar Resonators

Previously reported methods of microstrip resonator mode analysis have utilized liquid crystal overlays (Derneryd (3)) and thermal imaging of a thin resistive layer deposited over the circuit under test (M. Malkomes, A. Quitmann (4)). Both techniques will perturb the circuit under test by the presence of the diagnostic layer, and require high input powers (1 watt) to obtain good results. More importantly the techniques are purely qualitative and provide amplitude only data. The scanning network probe permits examination of the resonances without the need for a perturbing diagnostic layer. The higher sensitivity and enhanced resolution of the S.N.P. system enables low level resonance features to be observed. The significant advantage of the SNP is that the power measurements are quantitative, and enable the relative excitation levels in a complex resonant system to be compared. When the SNP is applied to two dimensional charge density distribution measurements, the following factors must be considered:

a) the probe orientation must be kept perpendicular to the plane of the substrate, otherwise a systematic asymmetry in the probe response will result.

b) the diameter of the probe must be kept as small as possible so that the probe edge effect is minimised.

c) the sampling mesh must be small enough to yield a representative measurement of the edge charge density distribution. If the sampling mesh is too coarse, the contouring and surface plot software routines are unable to map the edge regions accurately due to the large scale point to point interpolation that is required. The mesh size is determined by the operator to suit the requirement for high or low spatial resolution but the smallest sampling interval that can be usefully employed will depend on the limiting spatial resolution of the sensor. The application of the SNP technique to mode analysis in microstrip resonators is demonstrated by the following examples.

Figure 3(a) shows a contour map representation of the surface charge distribution on a microstrip ring resonator excited in a TM_{51} mode. The mode structure of this azimuthal mode is clearly demonstrated, and compares favourably with the theoretical E-field source distribution shown in Figure (3)b (1). The features located beyond the ring metallization are due to the excitation of surface waves. By symmetry all E-field sources should be of equal amplitude, however reference to figure (3)a shows that some asymmetry was present in this example. It is interesting to note that each surface wave feature is centred on a source charge density peak. It may also be seen that the charge

density peaks corresponding the highest amplitude surface wave features are lower in intensity than the others. The generation of unwanted surface waves will reduce both the microstrip resonator Q and the radiation efficiency.

The S.N.P. has been used to study the mode structure in resonant microstrip disks. Figure (4)a shows an example of a TM_{21} disk mode excited by a high impedance microstrip feed. Comparison of the contour map of charge density with the theoretical E-field source distribution shown in figure (4)b shows qualitative agreement with the theory. (1) Close inspection reveals that the charge density peaks are of equal magnitude to within the measurement uncertainty, as would be expected from the azimuthal symmetry. The surface wave features are of approximately equal intensity and exhibit different propagation patterns compared with those observed in the previous example. The difference between the surface wave patterns is attributed to the different geometry and phase of the sources in the two cases. The probe edge effect is visible in both examples and manifests itself in two ways:

a) the edge maxima are located slightly inside the conductor boundary.

b) Owing to the finite size of the probe sheath, the probe does not measure a sharp change of amplitude on traversing a conductor boundary. This is particularly noticeable with the high impedance microstrip feedlines.

Despite the edge effect, the resonant modes of microstrip and other planar structures can be identified easily using the SNP technique.

Planar Antenna Array Analysis

In addition to the mode analysis of isolated resonators, the effect of combining several resonators on a single substrate has been investigated. Figure (5) shows the charge density distribution over a four element patch array with its elements phased to provide circular polarization. One immediately observes that only two of the four elements are strongly excited. The frequency of the measurement was 34.9 GHz in this particular example and is close to the patch design centre frequency of 35 GHz. The primary power splitter at the bottom of figure (5) has split the power evenly between the output arms, but the secondary power splitters have not functioned correctly. The design employs a quarter wavelength transmission line section to obtain the required $\pi/2$ phase shift between adjacent elements. Although this method would work satisfactorily if the load was perfectly matched, any other impedance will be transformed by the quarterwave section, and if the branch arms of the simple T-splitter are not terminated with the same impedance then the power split will not be equal. The reason for the low excitation of the two patches incorporating the additional quarterwave sections is now clear; the high input impedance of the patch at resonance is transformed to a near short circuit at the T-splitter, with the result that the majority of the power flows into the opposing branch arm. We also note that the mode of excitation of the two patches that *are* receiving power as shown in figure (5) is not symmetric. An isolated patch of the same dimensions as those used in this array demonstrated a nearly balanced edge excitation at this frequency. This indicates that the mutual interaction of the array elements has modified the resonance condition of the individual patches. The antenna design could be improved by the use of 3db branch line couplers to perform the secondary power splitter function. This would:

a) enable the $\pi/2$ phase shift to be obtained without the use of an additional quarterwave section.

b) prevent coupling between adjacent elements due to the isolation properties of the branch line coupler.

c) reduce the input VSWR due to the fact that half the reflected power from any element would be dissipated in the loaded port of the coupler.

The SNP unambiguously shows the pitfalls of this particular design. Conventional return loss and radiation pattern measurements are incapable of providing the physical insight necessary to deduce the cause of failure.

Application to slot and coplanar strip circuits

The SNP also has been employed in the investigation of linearly tapered coplanar stripline and slotline antennas. The charge density distribution shown in figure (5) was measured on a single element of a tapered coplanar strip vee antenna which was fabricated on a 70 μm Mylar substrate. The vee was placed in the converging field of a microwave lens and optimised for maximum coupling and balanced excitation. The standing wave is produced by the interference of the incident coupled wave and its reflection from a short circuit termination in the C.P.S. feed. When the short circuit termination is replaced by a matched load the standing wave is almost entirely removed, indicating that the antenna-transmission line junction is not a major source of mismatch (Frayne, Whitehurst (5)). The progressive decrease in the separation of the maxima and minima indicates a steady increase in the vee effective permittivity towards the vee apex. The amplitude of the coupled signal also increases towards the vee apex due to the increase in antenna coupling near the lens focus. Significant non-uniformities in the charge density distribution are visible at the vee extremities. Transverse strip resonances such as revealed by the SNP will give rise to radiation pattern distortion.

Figure (7) shows the charge density distribution over one half of a tapered slotline antenna fabricated on a similar 70 μm thick mylar substrate and illuminated under identical conditions to those of the vee in figure (6). The tapered slot flare angle is equal to the inner flare angle of the vee antenna shown in figure (5). A similar standing wave distribution is observed but the charge density now decays more slowly away from the conductor edge than in the previous example. In this instance the standing wave is primarily due to an open circuit in the parallel slotline feed. The widepsread nature of the slotline mode is particularly noticeable at the antenna feed-point where the charge density distribution has spread approximately a free space wavelength inside the edge of the slot.

The effective permittivity of the tapered slot section progressively increases towards the feed point. indicating that the field lines are becoming more tightly bound as the slot width narrows. It is clear that the SNP is a very useful tool for the characterization of wide slots for which there is no accurate theoretical model.

CONCLUSION

A new diagnostic technique for the study of planar mics has been presented. Several examples have been given to demonstrate the potential of the scanning network probe in the analysis of radiating and non-radiating structures. There are obvious future applications of the instrument to the characterization of monolithic microwave integrated circuits.

Acknowledgements

The authors wish to thank the S.E.R.C. for the receipt of a research grant and Marconi Defence Systems Ltd for supporting a CASE Studentship (JW).

References

1. Bahl, I.J., Bhartia, P., 1980 "Microstrip Antennas", Artech House, New York.

2. James, J.R., Henderson, A., 1979, Microwaves Optics and Acoustics Vol. 3, No. 5, pp 205-218.

3. Derneryd, A.G., 1978, IEE TRANS. ANT. PROP., AP-26, No. 4, pp 532, 535.

4. Malkomes, M., Quitmann, A., 1981, Electronic Letters, 17, pp 198, 199.

5. Frayne, P. G., Whitehurst, J., 1986, "The Technology of Measuring Microwave and Millimetric Components", IEE Colloquium, digest No. 1986/121.

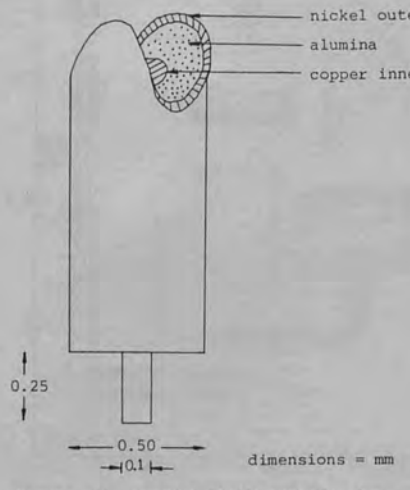

Figure (1) Coaxial Probe construction

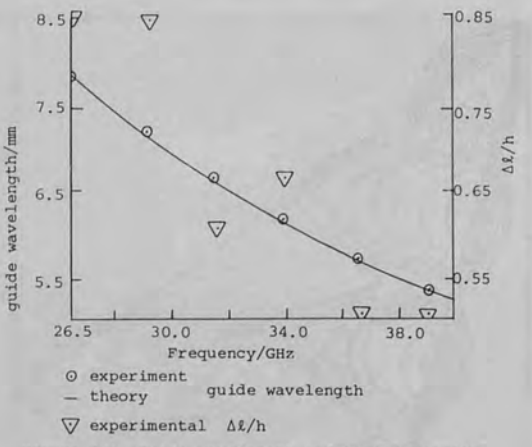

Figure (2) Guide wavelength and line extension variation with frequency

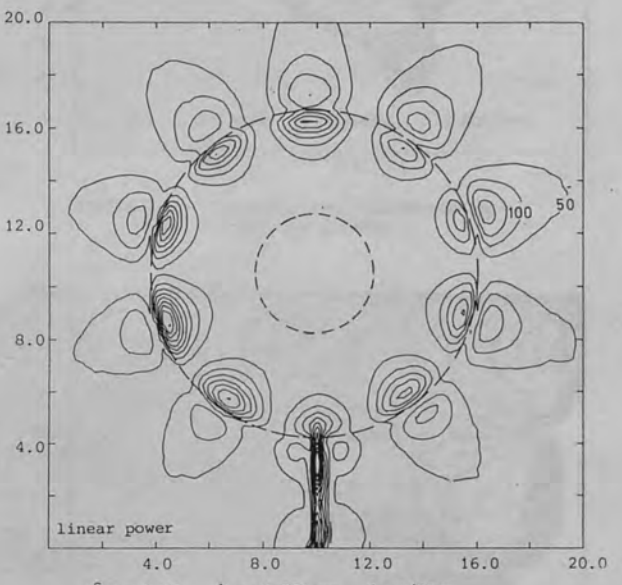

$\varepsilon_r = 2.32$ h = 0.254 mm 2 mm/div

Figure (3)a TM_{51} Source Charge Distribution on a Microstrip Annulus

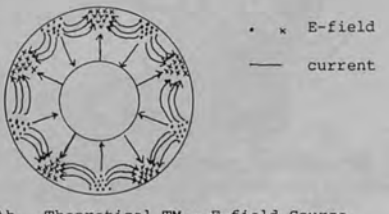

Figure (3)b Theoretical TM_{51} E-field Source Distribution

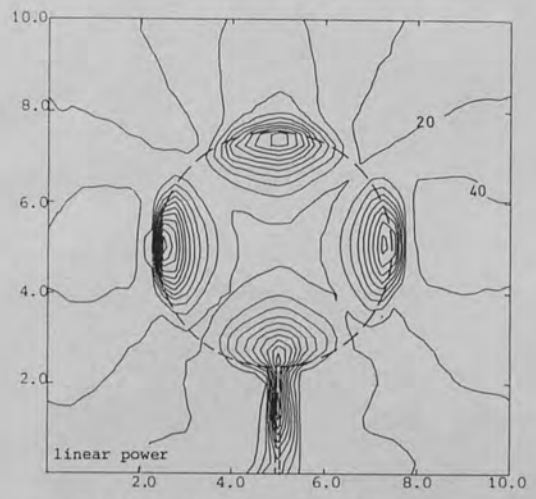

ε_r = 2.32 h = 0.254 mm 2 mm/div

Figure (4)a TM_{21} Source Charge Distribution on a Microstrip Disk

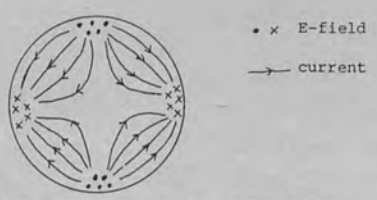

Figure (4)b Theoretical TM_{21} E-Field Source Distribution

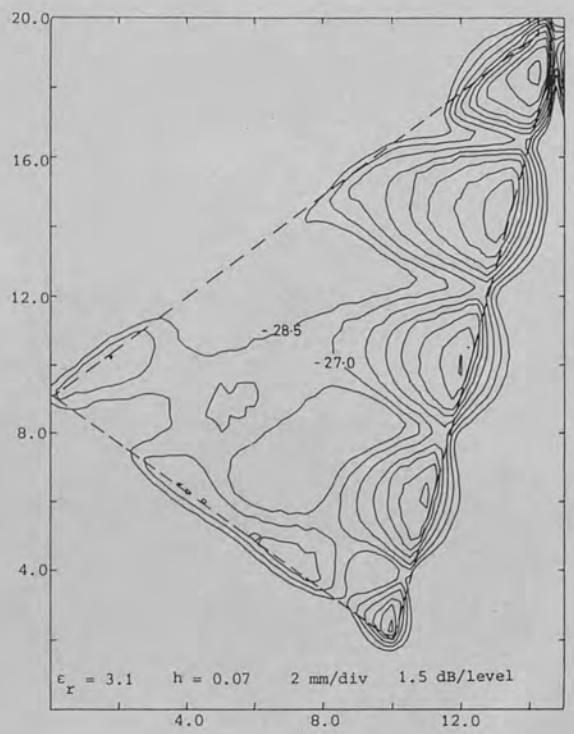

Figure (6). Source Charge Distribution on a Single Vee Element

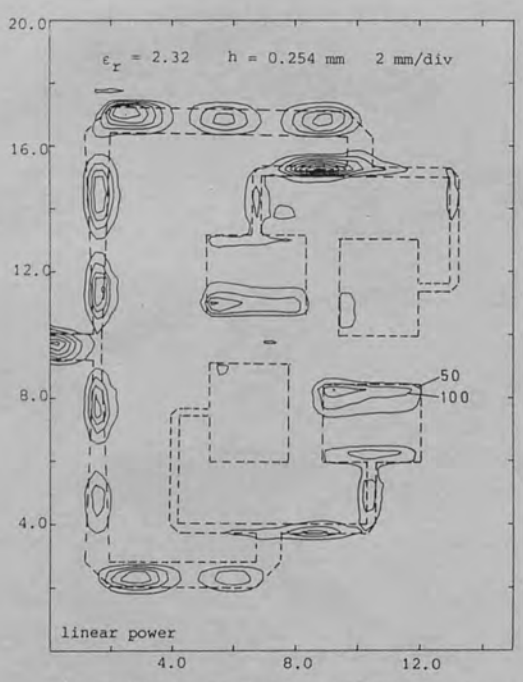

Figure (5) Source Charge Distribution on a Four Element Patch Array

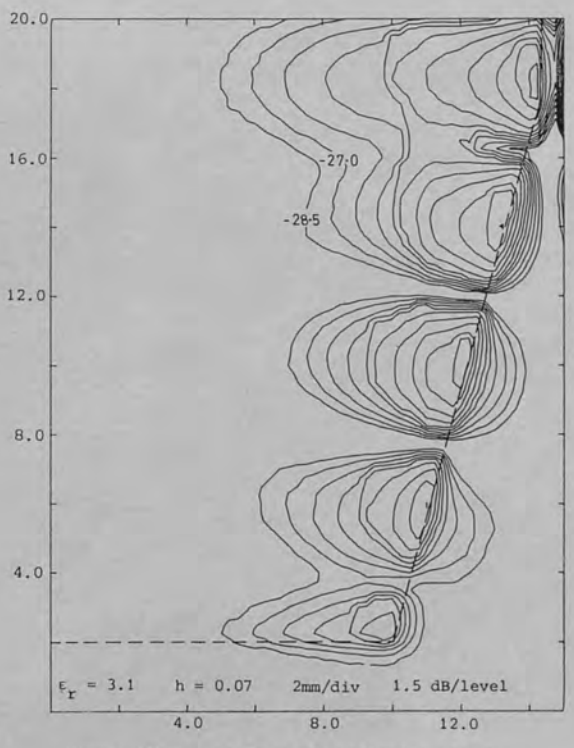

Figure (7) Source Charge Distribution on one Half of a Tapered Slot Antenna